

Dissertation zur Erlangung des Doktorgrades
der Fakultät für Chemie und Pharmazie
der Ludwig-Maximilians-Universität München

Real structure - property relationships of metastable ternary antimony tellurides and related compounds

Matthias Nikolaus Schneider

aus

München

2011

Erklärung

Diese Dissertation wurde im Sinne von § 13 Abs. 3 bzw. 4 der Promotionsordnung vom 29. Januar 1998 (in der Fassung der sechsten Änderungssatzung vom 16. August 2010) von Herrn PD Dr. Oliver Oeckler betreut.

Ehrenwörtliche Versicherung

Diese Dissertation wurde selbständig, ohne unerlaubte Hilfe erarbeitet.

München, den 30.11.2011

.....
(Matthias Schneider)

Dissertation eingereicht am 01.12.2011

1. Gutacher PD Dr. Oliver Oeckler

2. Gutachter Prof. Dr. Wolfgang Schnick

Mündliche Prüfung am 20.12.2011

Copyrights

Parts of this work have been published in peer-reviewed journals and are subject to the following copyrights. They have been reproduced with permission of the corresponding publisher and have only been adapted with respect to the format of this thesis.

Atom distribution in SnSb₂Te₄ by resonant X-ray diffraction (Chapter 2.2, Page 14)

O. Oeckler, M. N. Schneider, F. Fahrnbauer, G. Vaughan

Solid State Sci. **2011**, 13 (5), 1157-1161.

DOI: 10.1016/j.solidstatesciences.2010.12.043, <http://dx.doi.org/10.1016/j.solidstatesciences.2010.12.043>

Copyright © 2011 Elsevier Masson SAS. All rights reserved.

Unusual solid solutions in the system Ge-Sb-Te : The crystal structure of 33R-Ge_{4-x}Sb_{2-y}Te₇ (x, y ≈ 0.1) is isostructural to that of Ge₃Sb₂Te₆ (Chapter 2.3, Page 26)

M. N. Schneider, O. Oeckler

Z. Anorg. Allg. Chem. **2008**, 634 (14), 2557 – 2561.

DOI: 10.1002/zaac.200800334, <http://onlinelibrary.wiley.com/doi/10.1002/zaac.200800334/abstract>

Copyright © 2008 WILEY-VCH Verlag GmbH & Co. KGaA, Weinheim

Ambiguities in the structure determination of antimony tellurides arising from almost homometric structure models and stacking disorder (Chapter 2.4, Page 39)

M. N. Schneider, M. Seibald, P. Lagally, O. Oeckler

J. Appl. Crystallogr. **2010**, 43 (5-1), 1012-1020.

DOI: 10.1107/S0021889810032644, <http://journals.iucr.org/j/issues/2010/05/01/issconts.html>

Copyright © 2010 International Union of Crystallography, Reproduced with permission of the International Union of Crystallography

GeSb₄Te₄ – a new 9P-type phase in the system Ge-Sb-Te (Chapter 3.2, Page 63)

M. N. Schneider, O. Oeckler

Z. Anorg. Allg. Chem. **2010**, 636 (1), 137 – 143.

DOI: 10.1002/zaac.200900453, <http://onlinelibrary.wiley.com/doi/10.1002/zaac.200900453/abstract>

Copyright © 2010 WILEY-VCH Verlag GmbH & Co. KGaA, Weinheim

A new series of long-range ordered metastable phases in the system M-Sb-Te (M = Ge, Ag) (Chapter 3.3, Page 81)

M. N. Schneider, M. Seibald, O. Oeckler

Dalton Trans. **2009**, (11) 2004 – 2011.

DOI: 10.1039/B814000F, <http://pubs.rsc.org/en/Content/ArticleLanding/2009/DT/b814000f>

Copyright © 2009 Royal Society of Chemistry, Reproduced by permission of The Royal Society of Chemistry (RSC)

The layered tellurides $39R-M_{0.067}Sb_{0.667}Te_{0.266}$ (M = Ge, Sn): element distribution and thermoelectric properties (Chapter 3.4, Page 99)

M. N. Schneider, F. Fahrnbauer, T. Rosenthal, M. Döblinger, C. Stiewe, O. Oeckler

Chem. Eur. J. **2012**, *18* (4), 1209-1218.

DOI: 10.1002/chem.201102331, <http://onlinelibrary.wiley.com/doi/10.1002/chem.201102331/abstract>

Copyright © 2012 WILEY-VCH Verlag GmbH & Co. KGaA, Weinheim

From phase-change materials to thermoelectrics? (Chapter 4.1, Page 124)

M. N. Schneider, T. Rosenthal, C. Stiewe, O. Oeckler

Z. Kristallogr. **2010**, *225* (11), 463-470.

DOI: 10.1524/zkri.2010.1320, <http://www.oldenbourg-link.com/doi/abs/10.1524/zkri.2010.1320>

Copyright © 2010 Oldenbourg Wissenschaftsverlag, München

Nanostructures in metastable $GeBi_2Te_4$ obtained by high-pressure synthesis and rapid quenching and their influence on physical properties (Chapter 4.2, Page 142)

T. Schröder, M. N. Schneider, T. Rosenthal, A. Eisele, C. Gold, E.-W. Scheidt, W. Scherer, R. Berthold, O. Oeckler

Phys. Rev. B **2011**, *84* (18), 184104.

DOI:10.1103/PhysRevB.84.184104, <http://link.aps.org/doi/10.1103/PhysRevB.84.184104>

Copyright © 2011 American Physical Society

The influence of stress and strain on the kinetic stability and phase transitions of cubic and pseudocubic Ge-Sb-Te materials (Chapter 5.2, Page 173)

M. N. Schneider, P. Urban, A. Leineweber, M. Döblinger, O. Oeckler

Phys. Rev. B **2010**, *81* (18), 184102.

DOI:10.1103/PhysRevB.81.184102, <http://link.aps.org/doi/10.1103/PhysRevB.81.184102>

Copyright © 2010 by the American Physical Society

Real structure and thermoelectric properties of GeTe-rich Germanium Antimony Tellurides (Chapter 5.3, Page 194)

T. Rosenthal, M. N. Schneider, C. Stiewe, M. Döblinger, O. Oeckler

Chem. Mater. **2011**, *23* (19), 4349-4356.

DOI: 10.1021/cm201717z, <http://pubs.acs.org/doi/abs/10.1021/cm201717z>

Copyright © 2011 American Chemical Society, Reprinted (adapted) with permission of the American Chemical Society

From metastable to stable modifications – *in situ* Laue diffraction investigation of diffusion processes during the phase transitions of GeTe-rich $(GeTe)_n(Sb_2Te_3)$ ($6 < n < 15$) crystals (Chapter 5.5, Page 240)

M. N. Schneider, X. Biquard, C. Stiewe, T. Schröder, P. Urban, O. Oeckler

Chem. Commun. **2012**, *48* (16), 2192-2194.

DOI: 10.1039/C1CC15808B, <http://pubs.rsc.org/en/content/articlelanding/2012/cc/c1cc15808b#divAbstract>

Copyright © 2011 Royal Society of Chemistry, Reproduced by permission of The Royal Society of Chemistry (RSC)

Meiner Familie

*If a tree falls in a forest and no one is around to hear it,
does it make a sound?*

Acknowledgement

First and foremost I would like to thank PD Dr. O. Oeckler not only for offering me an intriguing and fruitful research project but also for his open mind with respect to my ideas of scientific research. He did not only act as mentor during my doctorate but also as friend for which I like to express my deepest gratitude.

I also would like to thank Prof. Dr. W. Schnick for being my second referee and for his generous support of my work and our group.

I am thankful to PD. Dr. H.-C. Böttcher, Prof. Dr. D. Johrendt, Prof. Dr. Karaghiosoff and Prof. Dr. W. Schmahl for being available as examiners in my doctoral examination and some inspiring discussions on various occasions.

I also want to thank our great staff members: W. Wunschheim for technical support on more than one occasion, C. Minke for his patience during lots of EDX measurements always showing the same elements (fortunately) and finally T. Miller who did so often pave the way into reciprocal space by measuring more than just one crystal...

I also want to thank the following alumni of different groups at the chair of solid state chemistry, S. Pagano, M. Zeuner, A. Zurawski, C. Höller, M. Tegel, M. Rotter and D. Bichler which did enlighten my "early years" not only from the scientific point of view.

It was also a great pleasure to work with many excellent research students and I am indebted to P. Lagally, A. Eisele, M. Ehrensperger, J. Holz, R. Hailer and L. Sposato. Special thanks; however, go to P. Urban and F. Fahrnbauer. Not only did they both do great jobs at the synchrotron facility but they became integral members of our group and close friends.

The doctorate would not have been the same without our basecamp in lab D2.100, occupied by a gang of great people, including M. Seibald and F. Hintze. It was very pleasant to share this second home with them and I really would like to thank them for the nice time I had there.

Besides the aforementioned group members and lab-mates I also want to thank all the nice and friendly co-workers at the "chair of inorganic solid state" chemistry. Special thanks go to F. Pucher who shares my passion for cooking which did yield some excellent "food coproductions". I will always remember the skiing trip with S. Sedlmaier whom I highly respect as scientist and friend.

To my first fellow PhD students in our group I want to express my deepest gratitude. T. Rosenthal was ever a great support starting from the first days in the course of our studies and we managed to overcome ups and downs in many ways, I just say "let's meet for one coffee...". Equal thanks I like to express to T. Schröder whom I reckon to be the probably best metal-rockstar in reciprocal space... With these guys I can only think "we were like brothers" which by the way is true anyway with respect to our doctoral advisor.

Above all I like to thank my family for their help and love in any situation of life. My parents have supported me in good and in bad times and I can not thank them enough for the possibilities only they made available. Of course, this is also true for my brother Andreas whom I highly respect as humanist and journalist. With him I had the best times of my life and hopefully will ever have. Finally I want to thank my greatest finding during the doctorate, Saskia.

Table of contents

1	Introduction	1
1.1	Tellurides - an interesting class of materials.....	1
1.2	Structural chemistry of pnictogen tellurides.....	2
1.3	Pnictogen tellurides as phase-change materials and thermoelectrics - Synthesis and required properties.....	5
1.4	Structure elucidation of disordered materials.....	7
2	Challenges in the structure elucidation of layered tellurides.....	10
2.1	Overview	10
2.2	Atom distribution in SnSb ₂ Te ₄ by resonant X-ray diffraction.....	14
2.2.1	Introduction	15
2.2.2	Experimental section	17
2.2.2.1	Sample preparation and characterization	17
2.2.2.2	Single-crystal X-ray diffraction data collection and processing	18
2.2.3	Results and discussion.....	20
2.2.3.1	Diffraction data analysis	20
2.2.3.1	Structure description.....	21
2.2.4	Conclusion	22
2.2.5	References.....	23
2.3	Unusual solid solutions in the system Ge-Sb-Te: The crystal structure of 33R-Ge _{4-x} Sb _{2-y} Te ₇ (x, y ≈ 0.1) is isostructural to that of Ge ₃ Sb ₂ Te ₆	26
2.3.1	Introduction	27
2.3.2	Results and discussion.....	30
2.3.2.1	Characterization of Ge ₄ Sb ₂ Te ₇ samples.....	30
2.3.2.2	Single crystal structure determination	31
2.3.3	Conclusion	35
2.3.4	Experimental section	36
2.3.4.1	Synthesis.....	36
2.3.4.2	Chemical analysis	36
2.3.4.3	X-ray characterization	36
2.3.5	References.....	37
2.4	Ambiguities due to almost homometric structure models and stacking disorder concerning the structure determination of antimony tellurides	39
2.4.1	Introduction	40
2.4.2	Experimental	43
2.4.2.1	Sample preparation and characterization	43
2.4.2.2	Single-crystal structure determination	43
2.4.2.3	Simulation of diffraction patterns of disordered polytypes.....	45
2.4.3	Ambiguities of structure solution and ‘almost homometric’ structure models.....	46
2.4.4	Influence of positional disorder on the reliability of structure solution	50
2.4.5	Ambiguities arising from stacking disorder	52
2.4.6	Conclusion	54
2.4.7	References.....	55
3	Long-periodic ordered layered structures (MTe)_nM'₂Te₃(M₂)_k as model systems for “multilayer superlattices”	59
3.1	Overview	59
3.2	GeSb ₄ Te ₄ – a new 9P-type phase in the system Ge-Sb-Te	63
3.2.1	Introduction.....	64
3.2.2	Results and discussion.....	67
3.2.2.1	Sample characterization.....	67
3.2.2.2	Crystal structure determination.....	68

3.2.2.3	Comparison of 9 <i>P</i> polytypes in the system Ge/Sb/Te	71
3.2.2.4	Stability of GeSb ₄ Te ₄	73
3.2.2.5	Electrical conductivity	74
3.2.3	Conclusions	75
3.2.4	Experimental section	76
3.2.4.1	Synthesis	76
3.2.4.2	EDX analyses	76
3.2.4.3	X-ray diffraction	77
3.2.4.4	Thermal analysis	77
3.2.4.5	Electrical conductivity measurement	78
3.2.5	References	78
3.3	A new series of long-range ordered metastable phases in the system M-Sb-Te (M = Ge, Ag).....	81
3.3.1	Introduction	82
3.3.2	Experimental	84
3.3.2.1	Synthesis and chemical analysis	84
3.3.2.2	Thermal analysis	84
3.3.2.3	Conductivity measurements	85
3.3.2.4	X-ray characterization	85
3.3.3	Results and discussion	87
3.3.3.1	Powder patterns and structural homologies	87
3.3.3.2	Single-crystal structure refinement	89
3.3.3.3	Structure description	91
3.3.3.5	Metastability of phases (MTe) _{<i>n</i>} (Sb ₂ Te ₃) _{<i>m</i>} (Sb ₂) _{<i>k</i>}	93
3.3.3.6	Electrical properties	94
3.3.4	Conclusion	95
3.3.5	References	96
3.4	The layered tellurides 39<i>R</i>-M_{0.067}Sb_{0.667}Te_{0.266} (M = Ge, Sn): element distribution and thermoelectric properties	99
3.4.1	Introduction	100
3.4.2	Results and discussion	102
3.4.2.1	Synthesis, homogeneity and stability	102
3.4.2.2	Electron microscopy and diffraction	104
3.4.2.3	X-ray diffraction data analysis	105
3.4.2.4	Structure description and element distribution	107
3.4.2.5	Thermoelectric properties	110
3.4.3	Conclusion	111
3.4.4	Experimental section	113
3.4.4.1	Synthesis and elemental analysis	113
3.4.4.2	Thermal analysis	113
3.4.4.3	X-ray powder diffraction	113
3.4.4.4	Single-crystal X-ray crystallography	114
3.4.4.5	Electron microscopy	114
3.4.4.6	Thermoelectric properties	115
3.4.5	References	115
4	From phase-change materials to thermoelectrics	119
4.1	Overview	119
4.2	From phase-change materials to thermoelectrics?	124
4.2.1	Introduction	125
4.2.1.1	Thermoelectrics	125
4.2.1.1	Phase-change materials	126
4.2.2	Structure of metastable GST bulk materials with different GeTe content and their thermoelectric properties	128
4.2.2.1	Structural aspects	128
4.2.2.2	Thermoelectric properties	134
4.2.3	Conclusion	135
4.2.4	Experimental	136
4.2.4.1	Synthesis	136
4.2.4.2	Scanning electron microscopy and chemical analysis	136
4.2.4.3	X-ray diffraction	137

4.2.4.4	Transmission electron microscopy	137
4.2.4.5	Thermal analysis.....	138
4.2.4.6	Thermoelectric properties.....	138
4.2.5	References.....	138
4.3	Nanostructures in metastable GeBi₂Te₄ obtained by high-pressure synthesis and rapid quenching and their influence on physical properties.....	142
4.3.1	Introduction.....	143
4.3.2	Experimental details.....	145
4.3.2.1	Synthesis.....	145
4.3.2.2	Energy dispersive x-ray analysis	146
4.3.2.3	X-ray diffraction.....	146
4.3.2.4	Transmission electron microscopy	147
4.3.2.5	Electrical and thermal transport measurements	147
4.3.3	Results and discussion.....	148
4.3.3.1	Structure of quenched HP-GeBi ₂ Te ₄	148
4.3.3.2	Nucleation mechanism and nanostructuring.....	151
4.3.3.3	Influence of the nanostructure on the electrical resistivity	154
4.3.3.4	Influence of grain boundaries on <i>ZT</i>	159
4.3.4	Conclusion	162
4.3.5	References.....	163
5	Characterization of the real structure of metastable germanium antimony tellurides and its influence on their properties.....	165
5.1	Overview.....	165
5.2	Influence of stress and strain on the kinetic stability and phase transitions of cubic and pseudocubic Ge-Sb-Te materials	173
5.2.1	Introduction.....	175
5.2.2	Experimental details.....	177
5.2.2.1	Synthesis.....	177
5.2.2.2	Scanning electron microscopy and chemical analysis	177
5.2.2.3	X-ray diffraction.....	177
5.2.2.4	Transmission electron microscopy	179
5.2.3	Results and discussion.....	179
5.2.3.1	Electroneutrality and phase separation	179
5.2.3.2	Average crystal structure of the quenched samples	180
5.2.3.3	<i>In situ</i> temperature-dependent powder diffraction study	183
5.2.3.4	Transmission electron microscopy	184
5.2.3.5	Influence of the powder-particle size on the establishment of the rhombohedral distortion ...	186
5.2.4	Conclusions.....	190
5.2.5	References.....	191
5.3	Real structure and thermoelectric properties of GeTe-rich germanium antimony tellurides	194
5.3.1	Introduction.....	195
5.3.1.1	Tellurides as thermoelectrics	195
5.3.1.2	Sb ₂ Te ₃ (GeTe) _n as phase-change materials.....	195
5.3.1.3	Structure and properties of Sb ₂ Te ₃ (GeTe) _n	196
5.3.2	Experimental section.....	197
5.3.3	Results and discussion.....	199
5.3.3.1	Stability of the phases Sb ₂ Te ₃ (GeTe) _n (3 ≤ n ≤ 17)	199
5.3.3.2	Influence of thermal treatment on the nanostructure	200
5.3.3.3	Influence of the composition on the nanostructure of quenched Sb ₂ Te ₃ (GeTe) _n samples.....	203
5.3.3.4	Structural relaxation around the defect layers in Sb ₂ Te ₃ (GeTe) ₁₂	204
5.3.3.5	Influence of the microstructure on the thermoelectric characteristics of Sb ₂ Te ₃ (GeTe) _n (n = 3-19).....	205
5.3.4	Conclusion	208
5.3.5	References.....	210
5.4	Diffuse X-ray scattering and the real structure of GeTe-rich metastable germanium antimony tellurides (GeTe)_nSb₂Te₃ (2 > n > 12)	212
5.4.1	Introduction.....	214
5.4.2	Experimental	215

5.4.2.1	Sample preparation and characterization.....	215
5.4.2.2	Single-crystal data collection and processing.....	216
5.4.2.3	Treatment of diffuse scattering data and calculation of diffraction patterns from disordered structures.....	218
5.4.3	Determination of the average structure of metastable $(\text{GeTe})_n\text{Sb}_2\text{Te}_3$ ($n = 5$ and 6).....	219
5.4.4	Diffuse Scattering.....	220
5.4.4.1	Diffraction patterns of disordered phases $(\text{GeTe})_n\text{Sb}_2\text{Te}_3$	220
5.4.4.2	Modelling of diffuse scattering in metastable $(\text{GeTe})_n\text{Sb}_2\text{Te}_3$ phases.....	221
5.4.4.3	Influence of different structural features on the diffuse scattering.....	224
5.4.5	Examples for matching simulated and experimental data.....	230
5.4.5.1	Cubic vs. hexagonal stacking around planar faults in $(\text{GeTe})_2\text{Sb}_2\text{Te}_3$ and $(\text{GeTe})_{12}\text{Sb}_2\text{Te}_3$...	230
5.4.5.2	Fitting simulated to experimental synchrotron data of $(\text{GeTe})_5\text{Sb}_2\text{Te}_3$ and $(\text{GeTe})_6\text{Sb}_2\text{Te}_3$...	232
5.4.6	Conclusion.....	236
5.4.7	References.....	237
5.5	From metastable to stable modifications – <i>in situ</i> Laue diffraction investigation of diffusion processes related to the phase transitions of GeTe-rich $(\text{GeTe})_n(\text{Sb}_2\text{Te}_3)$ ($n = 6 < n < 15$) crystals.....	240
5.5.1	Introduction.....	241
5.5.2	Results and discussion.....	243
5.5.3	Conclusion.....	247
5.5.4	References.....	247
5.5.5	Supporting information.....	248
5.5.5.1	Experimental.....	248
5.5.5.2	Additional Figures.....	251
6	Conclusion and prospects.....	254
7	Summary.....	257
7.1	Resonant X-ray diffraction to distinguish Sn, Sb and Te in $21R\text{-SnSb}_2\text{Te}_4$	257
7.2	Limitations of structure predictions based on the composition of germanium antimony tellurides.....	257
7.3	Homometry and stacking disorder in antimony tellurides.....	258
7.4	A new metastable long-periodic layered germanium antimony telluride $9P\text{-GeSb}_4\text{Te}_4$	258
7.5	Long-range ordered metastable phases as models for "superlattices".....	259
7.6	Concentration gradients of the elements in new metastable layered tellurides $39R\text{-M}_{0.067}\text{Sb}_{0.667}\text{Te}_{0.266}$ ($M = \text{Ge}, \text{Sn}$).....	259
7.7	Similarities between phase-change materials and thermoelectrics.....	260
7.8	High-pressure synthesis of metastable germanium bismuth tellurides.....	260
7.9	Influence of stress and strain on the stability of metastable germanium antimony tellurides.....	261
7.10	Real structure and properties of quenched germanium antimony tellurides.....	262
7.11	Analysis of diffuse scattering from metastable germanium antimony tellurides.....	262
7.12	In situ Laue diffraction investigation of diffusion processes involved in the phase transitions of germanium antimony tellurides.....	263
8	Appendix.....	264
8.1	Publications within this thesis.....	264
8.2	Contributions to conferences.....	265

1 Introduction

1.1 Tellurides - an interesting class of materials

Tellurium minerals mainly comprise tellurides of noble metals, bismuth or lead, often in multinary variants. Although tellurium itself is named after the latin word *tellus* meaning *earth*, such minerals are extremely rare, as tellurium is one of the least abundant elements in the lithosphere. Nevertheless, this chalcogenide has gained increasing importance in modern society as many tellurides are small band gap semiconductors interesting for diverse technical applications. For example, it is well known that CdTe is used in thin-film solar cells to harvest energy of the sun ^[1,2] and most commercial thermoelectric heat-to-electrical-energy converters are based on compounds such as PbTe or Bi₂Te₃.^[3,4] It is less known that alloys containing elements such as Ag, In, Ge, Sb in combination with Te, such as Ge₂Sb₂Te₅ or Ag₅In₅Sb₆₀Te₃₀,^[5,6] dominate the field of phase-change materials which are essential for new rewriteable data storage technologies. Tellurides therefore play an important role in our energy management, but also allow one to address the ever increasing need to efficiently handle huge amounts of information. With respect to the application as thermoelectric as well as phase-change materials, multinary pnictogen tellurides are the most promising materials. Their structural diversity is huge and ranges from amorphous phases to crystalline modifications with simple average structures as well as long-periodic layered structures (cf. Chapter 1.2). The properties of these materials are strongly related to their atomic structures (cf. Chapter 1.3), including disorder on various length scales ranging from nano- to microstructures in stable and metastable materials. Nowadays, the study of structure-property relationships need not be restricted to the average structure of materials (cf. Chapter 1.4) but can also include effects of the real structure on a material's properties. However, due to the complexity of such investigations, the scientific significance, i. e. the question "What can one learn from such studies?" needs to be evaluated in advance. Pnictogen tellurides are a class of materials for which a better understanding of the material properties can be anticipated based on real structure-property relationships by both *ex situ* and *in situ* investigations.

1.2 Structural chemistry of pnictogen tellurides

Many multinary pnictogen tellurides exhibit at least one highly disordered modification crystallizing in a simple structure type. Typical structures with only one Wyckoff site for the average structure of disordered compounds can be derived from the simple cubic α -Po structure

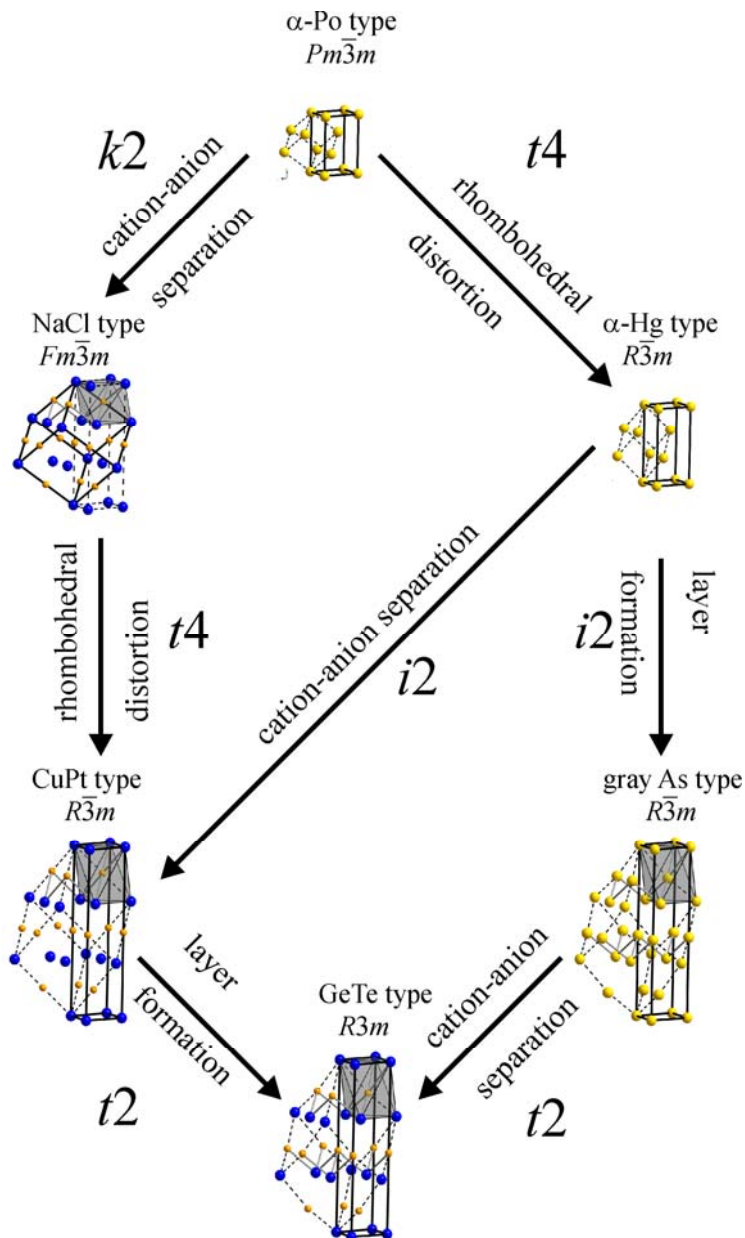


Figure 1. Structural relation between simple structure types that can be derived from the cubic α -Po structure type; the unit cells in trigonal and cubic settings are depicted as continuous or fragmented lines. For binary variants one coordination sphere of the cations is shown as grey polyhedra; gray bonds indicate which atoms are affected by layer formation; atoms are depicted yellow; for binary variants cations are depicted orange and anions blue.

type by rhombohedral distortion leading to the α -Hg type. Doubling the unit cell can be accompanied by atom displacements to form layers in the gray arsenic (A7) type. Simple AB structures in this class of compounds are characterized by cation-anion separation. The simplest one is the NaCl type which can be rhombohedrally distorted (so-called CuPt type). The additional formation of layers involves the loss of centrosymmetry and leads to the GeTe type. Figure 1 depicts the group-subgroup relationships that interrelate the simple structure types. In these simple average structures, several atom types and possibly additional vacancies

share only few Wyckoff positions.^[7,8] At first glance, it is somewhat surprising that positively and negatively polarized atoms as well as additional vacancies share the same crystallographic sites, and a plethora of short-range ordering effects can be expected. In fact, many of these modifications are metastable, although some have been reported to be stable. For example, In_3SbTe_2 exhibits rocksalt-type structure that is stable at room temperature, whereas for phases $(\text{GeTe})_n\text{Sb}_2\text{Te}_3$ ($n \geq 3$) the rocksalt-type modifications are stable only at elevated temperatures.^[9,10] For $\text{Ag}_{3.4}\text{In}_{3.7}\text{Sb}_{76.4}\text{Te}_{16.5}$ and $\text{Ge}_{7.1}\text{Sb}_{76}\text{Te}_{16.9}$ a metastable gray As type was found, whereas their high temperature polymorphs exhibit an α -Hg type.^[7,8] Metastable $\text{Au}_{25}\text{Ge}_4\text{Sn}_{11}\text{Te}_{60}$ exhibits a metastable α -Po structure which was also reported for metastable GeBi_2Te_4 .^[7,8] As discussed in Chapter 4.3, samples of GeBi_2Te_4 obtained by high-pressure high-temperature synthesis crystallize in a CuPt-type structure, and as demonstrated in Chapter 5.2 quenched crystals $\text{Ge}_{0.7}\text{Sb}_{0.2}\text{Te}$ can be described with a GeTe-type average structure.

Interestingly, some structural features of the simple average structures are also found in long-periodically ordered layered structures of binary or multinary pnictogen tellurides (e.g. on the pseudobinary lines $\text{Sb-Sb}_2\text{Te}_3$, $\text{Bi-Bi}_2\text{Te}_3$, $\text{GeTe-Sb}_2\text{Te}_3$, $\text{PbTe-Bi}_2\text{Te}_3$,...) which in many cases represent the polymorphs stable at room temperature.^[11-14] A schematic overview of such layered structures is given in Figure 2.

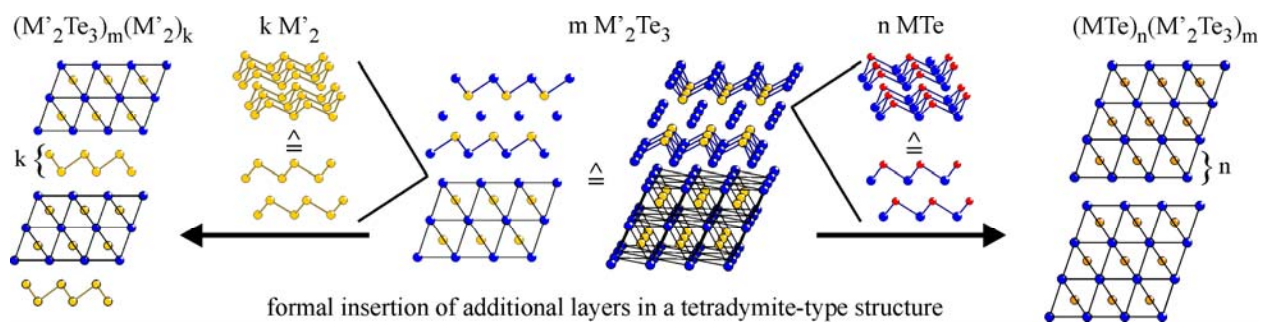


Figure 2. Long-periodic layered structures $(\text{MTe})_n(\text{M}'_2\text{Te}_3)_m$ (right) and $(\text{M}'_2\text{Te}_3)_m(\text{M}'_2)_k$ (left); cations are depicted yellow, red and orange, anions blue; the structures can be formally derived from a tetradymite structure $\text{M}'_2\text{Te}_3$ (centre) by insertion of M' layers in the van der Waals gap or by extension of the alternating sequence of cations and anions in the rocksalt-type slabs with additional layers MTe .

In phases $(\text{MTe})_n(\text{M}'_2\text{Te}_3)_m$ ($\text{M} = \text{Ge}, \text{Sn}, \text{Pb}$; $\text{M}' = \text{As}, \text{Sb}, \text{Te}$), 2D infinite slabs of a distorted rocksalt-type structure are present whose thickness, i. e. the number of alternating cation and anion layers, depends on n and m .^[15] The frequency of van der Waals gaps between the Te-atom layers terminating these slabs determines the periodicities and thus the structure type of the layered structures. Although the hypothetical number of such ternary layered structures is very

large, the number of discrete compounds recorded in crystallographic databases like PCD (Pearson's Crystal Data) and ICSD (Inorganic Crystal Structure Database) is rather small as the number of stable compounds depends on the element combination.^[16,17] The series $(\text{GeTe})_n(\text{Sb}_2\text{Te}_3)_m$ is the most comprehensive one whereas in other systems, the pseudobinary sections $\text{MTe-M}'_2\text{Te}_3$ are dominated by the compounds $\text{MM}'_2\text{Te}_4$, and no comparable phases in the systems Sn-As-Te or Pb-As-Te have been reported yet. In general, an increasing number of discrete compounds is found with increasing atomic number of the group V element. In binary phases $(\text{M}'_2\text{Te}_3)$ ($\text{M}' = \text{Sb, Bi}$), the rocksalt-type slabs contain 5 alternating cation and anion layers, and hence resemble those of tetradymite ($\text{Bi}_2\text{Te}_2\text{S}$, sulfur atoms formally being replaced by additional Te atoms) which is homeotypic with Sb_2Te_3 and Bi_2Te_3 .^[18,19] In contrast to the ternary compounds $(\text{MTe})_n(\text{M}'_2\text{Te}_3)_m$, the binary phases $(\text{M}'_2\text{Te}_3)_m(\text{M}'_2)_k$ contain k corrugated gray-arsenic type layers between consecutive rocksalt-type slabs. These gray-arsenic type layers are similar to the layers in the structures of the elements Sb and Bi.^[15] Similar to the ternary phases, van der Waals gaps interconnect the different slabs. For both series of compounds, these gaps between the different slabs significantly influence the neighboring atom layers, e.g. the interatomic distance set as well as the element distribution. The interatomic distances between atoms across the gap, i.e. Te-Te atom distances in ternary phases or Te-M' ($\text{M}' = \text{Sb, Bi}$) atom distances in binary ones, are slightly smaller than the sum of van der Waals radii, which indicates a certain degree of covalence. Cation positions in the vicinity of the van der Waals gap are displaced towards the gap, leading to a 3+3 coordination in the $[\text{MTe}_6]$ octahedra of the distorted rocksalt-type blocks that decreases with increasing distance from the gap. In a similar way, the inter- and intra-layer atomic distances of gray-arsenic type layers which neighbour $\text{M}'_2\text{Te}_3$ blocks are influenced, although the resulting atom displacements are less pronounced. In all ternary layered structures, the cation positions are occupied by M and M' - usually in a disordered fashion - the anion positions are occupied by Te. In general, the group V elements prefer to occupy the cation positions next to the van der Waals like gap which probably results from the interaction with Te-atoms terminating the slabs which are coordinated by cations from one side only.

1.3 Pnictogen tellurides as phase-change materials and thermoelectrics - Synthesis and required properties

Compounds which are potential candidates for an application as thermoelectric generators or Peltier elements need to simultaneously fulfill various demands that are, at least in part, also crucial for phase-change materials in data-storage technology.^[3-5,20-26] As thermoelectrics rely on a temperature gradient in order to interconvert heat and electrical energy, it is evident that these materials need to exhibit sufficient electrical conductivity σ whereas heat flow due to the temperature gradient across the material needs to be hindered by a low thermal conductivity κ . In addition, a high Seebeck coefficient S , which specifies the magnitude of the voltage induced by the thermal gradient across the material, is required. The efficiency η of a thermoelectric material is given by a combination of its figure of merit ZT defined according to $ZT = \sigma S^2 / \kappa$ and the Carnot efficiency $\Delta T / T_{\text{hot}}$ according to

$$\eta = \frac{\Delta T}{T_{\text{hot}}} \frac{\sqrt{1 + ZT_{\text{avg}}} - 1}{\sqrt{1 + ZT_{\text{avg}}} + \frac{T_{\text{cold}}}{T_{\text{hot}}}}$$

where T_{hot} and T_{cold} are the temperatures of the hot and cold ends in a thermoelectric module, respectively, ΔT is the corresponding difference and T_{avg} is the average temperature. This definition implies that a high efficiency requires a large figure of merit ZT and a large temperature gradient across the thermoelectric material.

In the past decades, fundamental research has focused on the search for compounds with high figures of merit and simultaneously increasing interest has been attributed to the optimization of known thermoelectrics. Both approaches are challenging: On the one hand, “design rules“ that guide the development of new materials are sparse; on the other hand there are few “adjusting screws” regarding the properties. Whereas the electrical conductivity and the Seebeck coefficient as well as the electronic part of the thermal conductivity depend on the charge carrier concentration and thus cannot be varied independently, the phononic part of the thermal conductivity strongly depends on the structure of the material which often can be optimized with respect to the thermal conductivity without significantly influencing the electronic structure. For example, the introduction of phonon scattering centers, e.g. point defects or grain boundaries, as well as large lattice periodicities, i.e. large unit cell parameters, provides short mean path lengths for heat carrying phonons and therefore significantly influences the thermal conductivity. Compounds that feature "rattling" atoms in structural cages also may exhibit reduced thermal conductivities; such materials are known as phonon glass electron crystals. Hence, various

synthetic approaches have been used to prepare new nano- or microstructures of known thermoelectrics, the most important ones being layer-by-layer deposition of “superlattice” structures as thin films, cold and hot pressing of ball-milled bulk material or the preparation of nanocomposites to name only a few.^[27-31]

Comparable to thermoelectrics, phase-change materials for rewriteable data storage need to unite several requirements. These compounds exhibit a reversible transition between an amorphous and a crystalline polymorph which can be induced by providing a precisely controlled amount of heat through local application of laser irradiation or electrical currents.^[5,6,26,32,33] The phase transition is accompanied by a large change in the optical reflectivity or electrical resistivity, which ensures that two distinguishable logical states - represented by amorphous and crystalline areas in the storage media - can be defined and used for the read process. Write-erase cycling involves a complex interplay of thermodynamics and kinetics. Whereas high cooling rates of about 10^{10} K/s ensure that molten spots can be quenched to yield amorphous recording marks, crystallization proceeds within several nanoseconds if the small amorphous areas are heated to elevated temperatures.^[25] At these temperatures, the atom mobility is high enough for structural rearrangements that only require small diffusion pathways. These are sufficient as the crystalline phases exhibit simple average structures whose local structures may be comparable to the amorphous modifications. However, in order to ensure data retention and cyclability, the crystallization kinetics of phase-change materials must meet the demand that the transition between amorphous and crystalline modifications does not take place at ambient conditions and that no irreversible structural changes, e.g. chemical reactions with the environment or decomposition into different compounds occur during the read-write-erase cycles or the storage of the media for many years. Since phase-change recording is the state-of-art technique for rewritable optical data storage discs (e.g. CD-RW, RW-DVD, or BD-RE), the synthesis has focused on thin-film layers for which sputter deposition (physical vapor deposition) is the preferred fabrication technique. However, with the upcoming application as non-volatile solid-state random access memory (PCRAM), alternative methods for the deposition of phase-change materials have been investigated, which include for example chemical vapor deposition, electrodeposition or solution-phase deposition.^[5,23,34,35] All these techniques have the advantage that amorphous as well as crystalline phases can be obtained (depending on the deposition conditions) and stable as well as metastable phases can be accessed. However, all thin-film samples share the disadvantage that the range of applicable characterization techniques is limited, e. g. the measurement of properties often requires bulk samples and the powerful tool of single-crystal diffraction (cf. Chapter 1.4) can not be applied.

1.4 Structure elucidation of disordered materials

A century ago, the discovery of X-ray diffraction on crystalline materials opened a new world of structure determination techniques for solid-state scientists which has been explored and developed ever since. Nowadays, single-crystal X-ray structure determination from Bragg reflection intensities - resulting from diffraction on a three-dimensionally long-range ordered arrangement of unit cells - has become a standard technique for all but the most complex questions. Remaining challenges concern the description and structure elucidation of aperiodic crystals without 3D translational symmetry, e.g. quasicrystals, incommensurately modulated crystals or incommensurate composite compounds that require the application of superspace symmetry.^[36] Chemical disorder or local distortions, e.g. short-range order even leads to statistical deviations from 3D translational symmetry and gives rise to diffuse scattering, i.e. intensity distributed between the Bragg reflections.^[37] In general, diffuse scattering is several orders of magnitude less intense than Bragg reflections; however, due to the advent of efficient X-ray optics and optimized detection systems, it has become feasible to collect this continuously distributed intensity. Its interpretation often requires a detailed understanding of the structural chemistry of the compounds investigated and although the analysis of diffuse scattering is still far from routine it can yield structural information that reaches far beyond the average structure. Experimental challenges of modern crystallography include the differentiation of elements with similar atomic number and the characterization of microcrystalline or heterogeneous samples but also concern for example the characterization of materials under extreme conditions or time resolved structural investigations. Many complex questions can be addressed by X-ray diffraction if it is supplemented by additional knowledge, e.g. obtained by a range of theoretical methods or other experimental techniques such as electron microscopy, neutron diffraction or spectroscopic methods. X-ray diffraction, however, is an essential pillar for structure determination.

References for Chapter 1

- [1] P. Würfel, T. Trupke, *Phys. J.* **2003**, 2, 45.
- [2] R. W. Miles, G. Zoppi, I. Forbes, *Mater. Today* **2007**, 10, 20.
- [3] J. R. Sootsman, D. Y. Chung, M. G. Kanatzidis, *Angew. Chem. Int. Ed.* **2009**, 48, 8616.
- [4] G. J. Snyder, E. S. Toberer, *Nat. Mater.* **2008**, 7, 105.
- [5] S. Raoux, *Annu. Rev. Mater. Res.* **2009**, 39, 9.1.
- [6] M. Wuttig, N. Yamada, *Nat. Mater.* **2007**, 6, 824.
- [7] T. Matsunaga, N. Yamada, *Jpn. J. Appl. Phys.* **2004**, 43, 4704.
- [8] T. Matsunaga, N. Yamada, *Jpn. J. Appl. Phys.* **2002**, 41, 1674.
- [9] K. Deneke, A. Rabenau, *Z. Anorg. Allg. Chem.* **1964**, 333, 201.
- [10] T. Matsunaga, H. Morita, R. Kojima, N. Yamada, K. Kifune, Y. Kubota, Y. Tabata, J.-J. Kim, M. Kobata, E. Ikenaga, K. Kobayashi, *J. Appl. Phys.* **2008**, 103, 093511.
- [11] K. Kifune, Y. Kubota, T. Matsunaga, N. Yamada, *Acta Crystallogr.* **2005**, B61, 492.
- [12] J. W. G. Bos, H. W. Zandbergen, M.-H. Lee, N. P. Ong, R. J. Cava, *Phys. Rev. B* **2007**, 75, 195203.
- [13] L. E. Shelimova, O. G. Karpinsky, P. P. Konstantinov, M. A. Kretova, E. S. Avilov, V. S. Zemskov, *Inorg. Mater.* **2001**, 37, 342.
- [14] L. E. Shelimova, O. G. Karpinsky, T. E. Svechnikova, E. S. Avilov, M. A. Kretova, V. S. Zemskov, *Inorg. Mater.* **2004**, 40, 1264.
- [15] L. E. Shelimova, O. G. Karpinsky, M. A. Kretova, V. I. Kosyakov, V. A. Shestakov, V. S. Zemskov, F. A. Kuznetsov, *Inorg. Mater.* **2000**, 36, 768.
- [16] F. H. Allen, G. Bergerhoff, R. Sievers, *Crystallographic Databases*, **1987**, International Union of Crystallography, Bonn/Cambridge/Chester.
- [17] P. Villars, K. Cenzual, *Pearson's Crystal Data: Crystal Structure Database for Inorganic compounds (on CD-ROM), Version 1.0*, Release **2007/8**, ASM International, Materials Park Ohio, USA.
- [18] D. Harker, *Z. Kristallogr.* **1934**, 89, 175.
- [19] P. Bayliss, *Am. Mineral.* **1991**, 76, 257.
- [20] A. V. Shevelkov, *Russ. Chem. Rev* **2008**, 77, 1.
- [21] J. Sommerlatte, K. Nielsch, H. Böttner, *Phys. J.* **2007**, 6, 35.
- [22] F. J. DiSalvo, *Science* **1999**, 285, 703.
- [23] S. Raoux, W. Wojciech, D. Ielmini, *Chem. Rev.* **2009**, 110, 240.

-
- [24] D. Lencer, M. Salinga, B. Grabowski, T. Hickel, J. Neugebauer, M. Wuttig, *Nat. Mater.* **2008**, *7*, 972.
- [25] D. Lencer, M. Salinga, M. Wuttig, *Adv. Mater.* **2011**, *23*, 2030.
- [26] W. Bensch, M. Wuttig, *Chem. Unserer Zeit* **2010**, *44*, 92.
- [27] M. S. Dresselhaus, G. Chen, M. Y. Tang, R. Yang, H. Lee, D. Wang, Z. Ren, J.-P. Fleurial, P. Gogna, *Adv. Mater.* **2007**, *19*, 1.
- [28] M. G. Kanatzidis, *Chem. Mater.* **2010**, *22*, 648.
- [29] H. Böttner, G. Chen, R. Venkatasubramanian, *MRS Bull.* **2006**, *31*, 211.
- [30] D. L. Medlin, G. J. Snyder, *Curr. Opin. Colloid Interface Sci.* **2009**, *14*, 226.
- [31] Y. C. Lan, A. J. Minnich, G. Chen, Z. F. Ren, *Adv. Funct. Mater.* **2010**, *20*, 357.
- [32] A. V. Kolobov, *Nat. Mater.* **2008**, *7*, 351.
- [33] A. V. Kolobov, P. Fons, J. Tominaga, *Thin Solid Films* **2007**, *515*, 7534.
- [34] A. L. Lacaita, D. J. Wouters, *Phys. Stat. Sol. A* **2008**, *205*, 2281.
- [35] S. Raoux, R. M. Shelby, J. Jordan-Sweet, B. Munoz, M. Salinga, Y.-C. Chen, Y.-H. Shih, E.-K. Lai, M.-H. Lee, *Microelectron. Eng.* **2008**, *85*, 2330.
- [36] S. van Smaalen, *Incommensurate Crystallography*, **2007**, Oxford University Press, Oxford.
- [37] T. R. Welberry, *Diffuse X-Ray Scattering and Models of Disorder*, **2010**, Oxford University Press, Oxford.

2 Challenges in the structure elucidation of layered tellurides

2.1 Overview

At ambient conditions, thermodynamically stable phases of compounds on the pseudobinary sections $M\text{Te} - \text{Sb}_2\text{Te}_3$ ($M = \text{Ge}, \text{Sn}, \text{Pb}$) and $\text{Sb} - \text{Sb}_2\text{Te}_3$ (including substituted variants thereof) exhibit long-periodically ordered layered structures as discussed in Chapter 1.2. They can be prepared by slow cooling stoichiometric melts, by quenching stoichiometric melts and subsequent annealing or by chemical transport reactions in the stability range of the corresponding phases. These stability ranges can be extracted from the phase diagrams, which also indicate if quenching is necessary to hinder peritectic decomposition upon slow cooling.^[1-6] Simple rules based on homology principles have been derived that allow one the prediction of the layer types, stacking sequences and space groups from the composition.^[7] These rules can be used as guidelines for structure solution as well as for the evaluation of structure refinements; however, as will be shown in the following sections they also show some exemptions and can not be used for all questions arising during structural characterization of compounds constituting the series $(M\text{Te})_n(M'_2\text{Te}_3)_m$ and $(M'_2\text{Te}_3)_m(M''_2)_k$.

For example, in all ternary layered structures, positional disorder on cation positions is observed. One important task of the structure analysis, hence, is the determination of the element distribution. However, this becomes challenging when elements with small scattering contrast for laboratory X-rays or neutrons are present. In this work, resonant scattering techniques with synchrotron radiation were used to distinguish elements with similar atomic number that share the same crystallographic sites, e.g., in $21R\text{-SnSb}_2\text{Te}_4$ (cf. Chapter 2.2). For the simultaneous refinement ($R\bar{3}m$, $a = 4.298(1)$, $c = 41.50(1)$ Å, $R1 = 0.028$) of mixed site occupancies and anisotropic displacement parameters, multiple high-resolution data sets collected at the Sn-, Sb- and Te-edges (29.20 keV, 30.49 keV, 31.81 keV) and at wavelengths far away from the edges were used. The manual variation of correction terms $\Delta f'$ and $\Delta f''$ interpolated from various databases and compared to calculated values did show that the refined element distribution is very robust and does not change more than a few standard deviations when $\Delta f'$ is changed by ± 0.5 . Therefore $\Delta f'$ for those values that are strongly affected by resonant scattering were refined, whereas all others were kept as an average from different calculations. The analysis indicates the absence of significant amounts of Sb-Te or Sn-Te anti-site defects. Mixed site

occupancies on cation positions are comparable to those of $21R\text{-GeSb}_2\text{Te}_4$ and $21R\text{-PbSb}_2\text{Te}_4$ and show that antimony prefers cation positions close to the van der Waals gaps between rocksalt-type slabs. Resonant scattering proved to be an elegant method to enhance the scattering contrast in pnictogen tellurides that contain elements with similar atomic number. It allows one to unequivocally determine the elemental ratios on crystallographic sites also in more complex cases as discussed in Chapter 3.4.

The ratio between different cations sharing crystallographic sites in the long-periodic layered structures is slightly variable and therefore allows for certain compositional homogeneity ranges of individual structure types. However, due to such homogeneity ranges, minute deviations from ideal compositions or small defect concentrations may lead to samples with unexpected structures that are not in accordance with the simple rules for structure prediction. For example, for $\text{Ge}_4\text{Sb}_2\text{Te}_7$ a $39R$ -type layered structure with rocksalt-type slabs comprising 13 alternating cation and anion layers is expected.^[7] In contrast to this prediction, single-crystal diffraction revealed a $33R$ layer stacking ($R\bar{3}m$, $a = 4.1891(5)$ Å, $c = 62.169(15)$, $R = 0.047$) of rocksalt-type slabs which comprise 11 cation and anion layers each (cf. Chapter 2.3). This $33R$ -type structure is known for $\text{Ge}_3\text{Sb}_2\text{Te}_6$ with similar metrics ($R\bar{3}m$, $a = 4.2128(2)$, $c = 62.309(3)$ Å),^[8] which exhibits a closely related interatomic distance set, but different site occupancies. On the one hand, this indicates that different compositions and variable degrees of Ge/Sb disorder can exist for the same structure type. Structure predictions based on the composition therefore need to be further corroborated, e.g. by comparison of experimentally determined and predicted metrics. On the other hand, this finding implies that interatomic distance sets derived from single-crystal or powder diffraction data are characteristic for the corresponding structure type and can be used to identify structural building units found in layered pnictogen tellurides.

The interatomic distance set of a structure and the scattering density on its Wyckoff sites can be unambiguously derived from the corresponding diffraction pattern. However, two non-congruent interatomic distance sets between atoms weighted with the product of their form factors might yield the same Patterson function, resulting in identical diffracted intensities. This problem, known as homometry, has already been realized by Patterson himself,^[9,10] but occurs very seldom during practical structure determination. Crystals of binary and Pb doped phases $(\text{Sb}_2)_k(\text{Sb}_2\text{Te}_3)_m$ ($m = 1$, and $k = 8$ or 6 , respectively), however, exemplify that ambiguities in the interpretation of both single-crystal and powder diffraction data of pnictogen tellurides can arise from pseudo-homometry (cf. Chapter 2.4). Initial structure solutions and crystal chemical considerations yielded different non-congruent structure models for $39R\text{-Sb}_{10}\text{Te}_3$ ($R\bar{3}m$, $a = 4.2874(6)$, $c = 64.300(16)$ Å, $R1 = 0.0298$) and $33R\text{-(Sb}_{0.978(3)}\text{Pb}_{0.022(3)})_8\text{Te}_3$ ($R\bar{3}m$,

$a = 4.2890(10)$, $c = 75.51(2)$ Å, $R1 = 0.0615$). Correct and wrong models exhibit reasonable interatomic distances. Therefore, the almost homometric structure models can only be distinguished by chemical analysis, because structure analysis in such cases is ambiguous. The correct and wrong models can be equally well refined on experimental single-crystal diffraction data; the refinement of the wrong structure models on calculated data of the correct models yields residuals $R < 0.01$. The ambiguities of the correct interpretation of diffraction data are further enhanced if variations in the stacking sequence of building units are assumed in a more or less disordered fashion. Different polytypes might yield rather similar diffraction patterns, and simulations of powder patterns show that certain reflections characteristic for the periodicity of long-periodically ordered structures weaken with increasing block disorder. The average structure then corresponds to a simple α -Hg type which might be erroneously be interpreted in terms of a 3D randomly disordered arrangement of all atom types, although the structure contains distinct building units arranged in a disordered fashion.

The structure elucidation of layered compounds $(MTe)_n(M'_2Te_3)_m$ and $(M'_2Te_3)_m(M'_2)_k$ is not only interesting from a crystallographic point of view but also leads to a deeper understanding of the structural chemistry of pnictogen tellurides. Such knowledge is obviously essential if structure-property relationships are to be investigated but can also be helpful during the search for new compounds and the characterization of disordered phases. The results presented in the following chapters therefore fundamentally rely on the knowledge of typical element distributions and interatomic distance sets of characteristic structural building units. Not only the structural characterizations of novel long-periodic layered phases which combine structural elements of the both series $(MTe)_n(M'_2Te_3)_m$ and $(M'_2Te_3)_m(M'_2)_k$, respectively, (cf. Chapter 3) but also the analysis of diffuse scattering from metastable samples $(GeTe)_n(Sb_2Te_3)$ ($n \geq 3$) were based on the information about homogeneity ranges of pnictogen tellurides or the influence of one dimensional disorder on the diffraction patterns of long-periodic layered structures.

References for Chapter 2.1

- [1] A. Stegherr, *Philips Res. Repts. Suppl.* **1969**, 6, 1.
- [2] B. Legendre, C. Hancheng, S. Bordas, M. T. Clavaguera-Mora, *Thermochim. Acta* **1984**, 78, 141.
- [3] S. Bordas, M. T. Clavaguera-Mora, B. Legendre, C. Hancheng, *Thermochim. Acta* **1986**, 107, 239.
- [4] V. I. Kosyakov, V. A. Shestakov, L. E. Shelimova, F. A. Kuznetsov, V. S. Zemskov, *Inorg. Mater.* **2000**, 36, 1004.
- [5] L. E. Shelimova, O. G. Karpinsky, T. E. Svechnikova, E. S. Avilov, M. A. Kretova, V. S. Zemskov, *Inorg. Mater.* **2004**, 40, 1264.
- [6] Y. I. Buyanov, L. V. Goncharuk, V. R. Sidorko, *Powder Metall. Met. Ceram.* **1999**, 38, 270.
- [7] L. E. Shelimova, O. G. Karpinsky, M. A. Kretova, V. I. Kosyakov, V. A. Shestakov, V. S. Zemskov, F. A. Kuznetsov, *Inorg. Mater.* **2000**, 36, 768.
- [8] T. Matsunaga, R. Kojima, N. Yamada, K. Kifune, Y. Kubota, M. Takata, *Appl. Phys. Lett.* **2007**, 90, 161919.
- [9] A. L. Patterson, *Nature* **1939**, 3631, 939.
- [10] A. L. Patterson, *Phys. Rev.* **1944**, 65, 195.

2.2 Atom distribution in SnSb₂Te₄ by resonant X-ray diffraction

Oliver Oeckler, Matthias N. Schneider, Felix Fahrnbauer, and Gavin Vaughan

Solid State Sciences **2011**, *13*, 1157-1161.

Abstract

The atom distribution in SnSb₂Te₄ ($R\bar{3}m$, $a = 4.298(1) \text{ \AA}$, $c = 41.57(1) \text{ \AA}$) has been elucidated by resonant single-crystal diffraction using synchrotron radiation with wavelengths near the K absorption edges of the elements present and additional non-resonant data. Refinement of site occupancies for all atoms on all sites was done with a joint refinement using five datasets. It shows that there is almost no anti-site disorder and no significant amount of vacancies. The cations are neither fully ordered nor randomly distributed. The 21R-type structure consists of rocksalt-type blocks separated by van der Waals gaps. Each block consists of four anion and three cation layers. Sn atoms are distributed over all cation sites but cluster in the middle of the blocks.

Keywords: tin antimony telluride, element distribution, resonant scattering

Copyright: © 2011 Elsevier Masson SAS

2.2.1 Introduction

In recent years, multinary chalcogenides have attracted attention as materials for various applications such as phase-change materials for data storage or promising thermoelectrics with high figures of merit.^[1-6] Most of these compounds exhibit disordered crystal structures, so the relevant properties strongly depend on real-structure effects such as partial vacancy ordering and the associated local distortions. Very often, the compounds contain chemical elements with similar electron counts, so the element distribution over the crystallographic positions cannot be assigned *ab initio* by conventional X-ray diffraction. This problem is the same in electron diffraction and imaging; moreover, many heavy elements like In, Sn, Sb and Te also exhibit rather similar neutron scattering lengths. Therefore, even if conclusions about the element distribution can be drawn from interatomic distances, mixed site occupancies cannot be refined and effects like anti-site disorder cannot be analyzed.

A solution to this problem is the use of resonant (also called “anomalous”) scattering when radiation close to absorption edges of the elements is used. The large change of the dispersion correction for atomic form factors, especially $\Delta f'$, close to absorption edges allows to enhance the scattering contrast and hence to study the distribution of atoms with similar electron count on the crystallographic sites. “Traditional” δ -syntheses^[7-9] show the distribution of the anomalous scatterers in the structure, in the same way that a difference Fourier synthesis shows residual electron density. This method is based on a Fourier synthesis from $F - F'$ and phases calculated from the structure model (structure factors F measured far from absorption edges, i.e. not significantly affected by resonant scattering; F' on the low-energy side of the absorption edge of the lighter element in order not to not significantly change $\Delta f'$ and to keep absorption effects similar for both datasets). Concerning δ -syntheses, the relative scaling of both datasets is problematic and the dispersion correction factors need to be calculated. However, the drastic change of $\Delta f'$ close to absorption edges, which furthermore depends on the chemical environment of the atoms, makes its refinement very desirable. On first glance, refining $\Delta f'$ seems to bias the refinement of the element distribution as a resonant scatterer appears as a “lighter” atom, however, this correlation is not very pronounced as $\Delta f'$ does not depend on the resolution $\sin\theta/\lambda$. In cases where three elements with similar electron count need to be distinguished, the δ -synthesis method is not applicable. Instead, the structure model should be simultaneously refined on datasets measured at the corresponding absorption edges.

In this paper, we address the distribution of Sn, Sb and Te in $21R$ - SnSb_2Te_4 . This structure type is observed for many compounds AB_2E_4 ($A = \text{Ge, Sn, Pb}$; $B = \text{As, Sb, Bi}$; $E = \text{Se, Te}$),

representing the middle of the pseudobinary phase diagrams $(AE)_n(B_2E_3)_m$ with $n = m = 1$.^[10-18] The structure contains rocksalt-type blocks composed of seven alternating cation and anion layers, respectively, that interact through van der Waals gaps between hexagonal anion layers terminating the blocks. The unit cell contains three of these blocks as shown in Fig. 1.

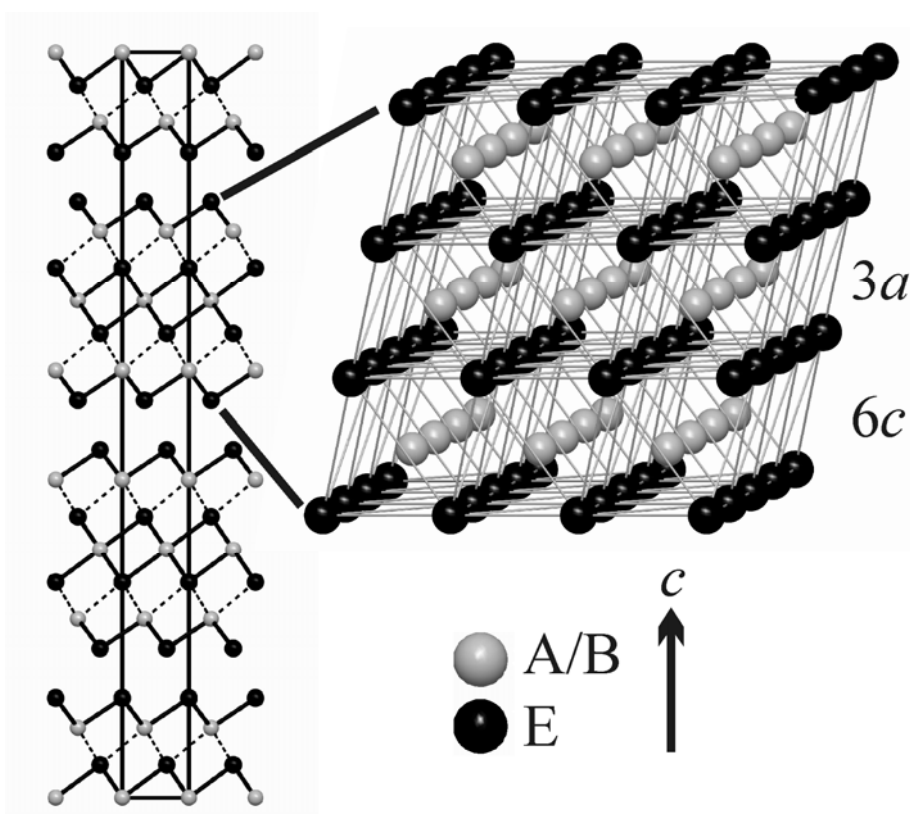


Figure 1. Projection of the unit cell of 21R-type compounds AB_2X_4 along $[100]$ (left), fragmented lines show longer distances within the rocksalt-type seven-layer block (right).

In compounds like $GeSb_2Te_4$,^[10,11] the Te atoms terminating the blocks at the van der Waals gaps are chemically different from the Te atoms within the blocks. This leads to a 3 + 3 coordination of the cations with shorter and longer bond lengths in the $[(Ge/Sb)Te_6]$ octahedra and also influences the atom distribution on the two different cation sites (see below). It has been shown in several investigations that $SnSb_2Te_4$ exhibits a similar 21R-type layered structure.^[13-17] However, as the three elements cannot be distinguished by conventional diffraction or imaging techniques, the element distribution in the structure, especially the metal distribution on cation positions, has been controversially discussed. By means of electron diffraction and high-resolution transmission electron microscopy, a stacking sequence of the atom layers in the rocksalt-type blocks $[Sn-Te-Te-Sb-Sb-Te-Te]$ has been favored, but the sequence $[Te-Sb-Te-Sn-Te-Sb-Te]$ has also been discussed.^[13] X-ray diffraction experiments confirmed the 21R-type structure but assumed the stacking sequence $[Te-(Sn/Sb)-Te-(Sn/Sb)-Te-(Sn/Sb)-Te]$ with a

random distribution of Sn and Sb on the cation positions,^[17] although the experimental data of course cannot exclude an ordered distribution [Te-Sb-Te-Sn-Te-Sb-Te] with Sb on $6c$ and Sn on $3a$. This ordered distribution has been corroborated by the results of ^{119}Sn Mößbauer investigations^[16]. These indicate that the local environment of Sn is not significantly distorted. Thus, it has been concluded that the $6c$ cation site next to the van derWaals gap with a $3 + 3$ coordination is occupied with Sb and the more symmetrically surrounded $3a$ site in the center of the blocks is occupied by Sn. This ordered distribution would match the overall composition SnSb_2Te_4 . In addition to the questions of cation distribution, some comparable tellurides like Sb_2Te_3 or ternary compounds Ge-Sb-Te and Pb-Sb-Te^[13,19,20] show certain amounts of anti-site defects. The purpose of our investigation on $21R\text{-SnSb}_2\text{Te}_4$ is to clarify these open questions on the atom distribution and to establish a straightforward way for the interpretation of resonant X-ray diffraction data as the method of choice for the system Sn-Sb-Te and comparable materials.

2.2.2 Experimental section

2.2.2.1 Sample preparation and characterization

Bulk samples were prepared by melting stoichiometric amounts of the pure elements Sn (99.999%, Smart Elements), Sb (99.999%, Smart Elements) and Te (99.999%, Alfa Aesar) at 950 °C in sealed silica glass ampoules under argon atmosphere and subsequent annealing at 450-500 °C for two to five days. Representative parts of the samples were crushed to powders and fixed on Mylar foils with silicon grease to collect powder diffraction patterns on a Huber G670 powder diffractometer equipped with an imaging plate detector ($\text{Cu-K}_{\alpha 1}$ radiation, Ge monochromator, $\lambda = 1.54051 \text{ \AA}$) in Guinier geometry. The powder data were evaluated using the program WINX^{POW}^[21] and indicate homogeneity of the samples. The metrics $a = 4.298(2) \text{ \AA}$ and $c = 41.57(2) \text{ \AA}$ was determined by a Pawley fit using the program TOPAS.^[22]

Single crystals suitable for data collection have been grown within three days from powdered SnSb_2Te_4 by chemical transport in evacuated silica glass ampoules using 10 weight percent SbI_3 as transport agent; a temperature gradient from 600 °C to 400 °C was employed. Hexagonal plate-like single crystals were obtained and residual SbI_3 was washed off with acetone. The crystals were fixed on glass fibers with silicone grease. Quality assessment was performed by Laue photographs on a Buerger precession camera. Diffuse streaks indicative of stacking disorder were not observed. The composition of the single crystals was confirmed by energy dispersive X-ray spectroscopy on planar crystal faces using a JSM-6500F scanning electron

microscope (Jeol, USA) with EDX detector (model 7418, Oxford Instruments, Great Britain). The results were averaged from 4 point analyses (in atom%): Sn 14.9(2), Sb 28.6(2), Te 56.5(5), calculated for SnSb_2Te_4 : Sn 14.3, Sb 28.6, Te 57.1. According to the phase diagram,^[23] SnSb_2Te_4 exhibits a certain range of homogeneity. As shown by the chemical analysis and the lattice parameters of the single crystals, which match well with those of the powder sample, the composition of our single crystals does not deviate significantly from the idealized one.

2.2.2.2 Single-crystal X-ray diffraction data collection and processing

Laboratory single-crystal datasets were collected on an STOE IPDS-I diffractometer with imaging plate detector using Mo- K_α radiation (graphite monochromator, $\lambda = 0.71073 \text{ \AA}$). Synchrotron data of the same single crystal were collected at beamline ID11 at the ESRF (Grenoble) on a heavy duty Huber diffractometer with vertical rotation axis equipped with a Frelon2K CCD detector.^[24] The X-ray optics at the undulator beamline give a good stability of the beam in the required energy range from 29 to 32 keV (0.42-0.39 \AA) at the K -edges of Sn (29.200 keV, 0.424607 \AA), Sb (30.491 keV, 0.406629 \AA) and Te (31.814 keV, 0.389700 \AA) and the small band pass required for resonant single-crystal scattering experiments. High-resolution resonant scattering data were obtained at the Sn, Sb and Te edges and at a wavelength far away of the edges. A detector offset was used to obtain high-angle data. After conversion of the frames, the data were indexed using SMART and integrated using SAINT.^[25,26]

Semiempirical absorption corrections based on equivalent reflections were applied to the laboratory data.^[27] Due to different detector settings and some technical problems, the synchrotron data consisted of several partial datasets. These were scaled, combined and corrected for absorption for each wavelength using SADABS.^[28] For these corrections, the Laue symmetry $\bar{3}m$ was assumed. The process of multi-scan absorption corrections (incl. scaling) describes the absorption surface using spherical harmonics (maximum order 8).^[29] The internal R value decreases to about half of the value for uncorrected data. The scaling process includes the anisotropy of absorption, the absolute value is introduced by a subsequent spherical absorption correction. Different other types of absorption corrections, including numerical ones based on the crystal shape, have been thoroughly tested for the laboratory data, they do not yield significantly different results for interatomic distances and anisotropic displacement parameters. This corroborates that there is no problem with the absorption correction process. The programs JANA2006^[30] and SHELX97^[31] were used for full-matrix least-squares refinement of both the dispersion correction factors as well as the 21 R -type structure model taken from the literature.^[16,17] The procedure is discussed in the following section. Further information may be

obtained from the Fachinformationszentrum Karlsruhe, D-76344 Eggenstein-Leopoldshafen (Germany), by quoting the deposition number CSD-421909, the names of the authors, and the citation of the paper. As there is no cif standard for multiple-wavelength joint refinements, the data that vary for different wavelengths (e.g. the absorption coefficient), have been given for $\lambda = 0.3897 \text{ \AA}$ in the deposited data, whereas the atomic parameters result from the joint refinement. Details on the individual data collections and refinement results are summarized in Tables 1 and 2.

Table 1. Crystallographic data on the structure refinement of $21R\text{-SnSb}_2\text{Te}_4$ at 293 K.

Formula	SnSb ₂ Te ₄				
Formula mass (in g mol ⁻¹)	872.59				
Crystal system / Space group	trigonal, $R\bar{3}m$				
Cell parameters (in Å)	$a = 4.298(1), c = 41.57(1)$				
Cell volume (in Å ³)	665.0(3)				
Formula units (per unit cell)	3				
$F(000)$	1080				
Crystal shape and size	platelet, 0.25 x 0.20 x 0.02 mm ³				
X-ray density (in g cm ⁻³)	6.493				
Parameters / restraints	29 / 4				
Resolution	0.75 Å, $\sin\theta/\lambda = 0.666$				
RI [all data in all datasets] ^(a)	0.0283				
$wR2$ [all data in all datasets] ^(b)	0.0710				
Wavelength (in Å)	0.389700	0.406629	0.424607	0.432758	0.71073
Absorption coefficient (in mm ⁻¹)	23.8	13.6	8.4	5.6	21.8
Measured / independent reflections	3330/254	3160/257	2789/253	2671/255	1390/241
R_{int}	0.065	0.055	0.051	0.072	0.089
R_{σ}	0.034	0.041	0.035	0.038	0.043
RI [$I > 2\sigma(I)$] ^(a)	0.0229	0.0228	0.0190	0.0324	0.0372
RI [all data] ^(a)	0.0230	0.0228	0.0191	0.0349	0.0398
$wR2$ [$I > 2\sigma(I)$] ^(b)	0.0552	0.0608	0.0555	0.0830	0.0938
$wR2$ [all data] ^(b)	0.0552	0.0608	0.0557	0.0842	0.0945
GooF [all data]	0.868	0.985	0.905	1.293	1.411
Residual electron density (min. / max.) (in eÅ ⁻³)	-0.90/1.23	-1.31/1.04	-0.99/1.09	-1.81/1.24	-3.43/3.68

^{a)} $RI = \sum |F_o - F_c| / \sum |F_o|$

^{b)} $wR2 = [\sum [w(F_o^2 - F_c^2)^2] / \sum [w(F_o^2)^2]]^{1/2}$; $w = 1 / [\sigma^2(F_o^2) + (0.0331P)^2 + 5.0P]$ with $P = [\text{Max}(0, F_o^2) + 2F_c^2] / 3$

Table 2. Wyckoff positions, atomic coordinates, equivalent isotropic temperature factors and anisotropic displacement parameters (in Å²) for 21R-SnSb₂Te₄; the positions are named after the atom types with the highest occupancy factors, all refined site occupancies are given in Fig. 2.

atom	Wyck.	x	y	z	U_{eq}	$U_{11} = U_{22} = 2 U_{12}$	U_{33}	$U_{13} = U_{23}$
Sn/Sb1	3a	0	0	0	0.0249(2)	0.0239(3)	0.0268(3)	0
Sn/Sb2	6c	0	0	0.427255(11)	0.02603(17)	0.0245(2)	0.0291(2)	0
Te3	6c	0	0	0.133695(10)	0.02152(16)	0.02235(17)	0.0198(2)	0
Te4	6c	0	0	0.289024(7)	0.01910(16)	0.01982(18)	0.0177(3)	0

2.2.3 Results and discussion

2.2.3.1 Diffraction data analysis

In order to obtain strong resonant scattering effects, the data were collected very close to the absorption edges. Tentative refinements using just one dataset clearly show that the distribution of the element near the corresponding absorption edge strongly influences R values and that the refinement of the corresponding site occupancy is highly significant. The aim of the final refinement was to refine the site occupancy of each element on all crystallographic positions, regardless of its value (e.g. if it is significantly larger than zero or not), in order to prove the element distribution ab initio and to employ as few presumptions as possible. In order to suppress the correlation with the overall scale factor, it proved sufficient to fix the overall composition (element ratios) according to the formula SnSb₂Te₄ (but not the total number of atoms in the unit cell). Vacancies were allowed on the cation positions. It is possible to also allow anion vacancies, however, such refinements yield slightly negative site occupancies for some atoms on some sites (but all of them are zero within their standard deviation). For the sake of positive site occupancies, which are required in refinement input files, the anion sites were constrained according to full occupancy, which is chemically reasonable as cation vacancies are much more likely than anion vacancies in comparable compounds. The dispersion correction factors $\Delta f'$ and $\Delta f''$ were calculated with the program CROSSEC implemented in the CCP4 program suite^[32] and compared to values interpolated from various databases.^[33,34] Manually varying the values for $\Delta f'$ in joint refinements shows that the refined element distribution is very robust and does not change more than a few standard deviations when $\Delta f'$ is changed by about ± 0.5 . Therefore, the overall result does not depend significantly on the exact values used. The best option was the refinement of $\Delta f'$ for those values that are strongly affected by resonant scattering (Sn at the Sn-K edge etc.) using JANA2006^[30] and to keep all others as an average

from different calculations. The refinement did not change the calculated values in an unreasonable way (max. 1.5 electrons). It is remarkable that increased absorption and fluorescence do not pose a serious problem even when data were collected at the Te-K edge which also means significant resonant scattering for Sn and Sb. The absorption coefficient for this unfavorable situation is still in the same range as for a normal laboratory measurement with Mo-K α radiation.

The final refinement (SHELX) converged at $R1 = 0.028$ for all five datasets. All site occupancies could be refined independently (Table 2). The precision of site occupancies is about 1%. The correlation between site occupancies is about 60-65%. In the same final refinement, all atoms have been refined anisotropically; the correlation between site occupancies and displacement parameters does not exceed 65%. Although the amount of Sn and Sb on the anion positions as well as the concentration of cation vacancies turns out not to be significant, the corresponding parameters have not been fixed to zero in order to demonstrate the stability of the refinement and to evaluate the standard deviations.

2.2.3.1 Structure description

In accordance with literature,^[14-17] the structure of $21R\text{-SnSb}_2\text{Te}_4$ exhibits three rocksalt-type blocks with 7 alternating cation and anion layers each as shown in Fig. 1. The distance between Te anion layers (distance Te-Te: 3.6973(7) Å) at the van der Waals gap points to a partially covalent character as it is significantly shorter than the sum of van der Waals radii (4.0 Å). The Te atoms in these Te layers show a unifacial cation coordination which leads to a stronger interaction with the cations in the $[\text{Sn/SbTe}_6]$ octahedra next to the gap. The cations form shorter bonds toward the gap and longer bonds toward the block center, leading to the 3 + 3 coordination with bond lengths of 2.9818(6) Å and 3.2266(7) Å. The $[\text{Sn/SbTe}_6]$ octahedra in the center of the blocks are more regular with bond lengths of 3.0905(5) Å. These bond lengths are in accordance with the results reported in the literature.

The refinement shows that cations and anions are almost perfectly separated in the structure (cf. Fig. 2). There is no anti-site disorder except for a small amount of Te on one cation position. Although it is statistically significant, this should not be over-interpreted (small systematic errors might occur in any refinement and are not represented by standard deviations based on counting statistics only). Sn and Sb are disordered on the cation positions, however. The disorder is not random. Sn concentrates on the $3a$ position in the center of the blocks while Sb is enriched on the $6c$ position near the van der Waals gaps. Probably, the higher formal charge of Sb^{III} compared to Sn^{II} is better suited to saturate the coordination of Te positions unifacially

surrounded by cations. This result is in accordance with the mixed site occupancies reported for the isotypic phases GeSb_2Te_4 and PbSb_2Te_4 , which also show a preferred occupation of the $6c$ position with Sb and a preferred occupation of the $3a$ position with Ge or Pb, respectively.^[10-13] The interatomic distances in these compounds vary in the same way with respect to their position in the blocks (cf. Fig. 2). This means that the Ge, Sn and Sb compounds are strictly isotypic also with respect to the cation distribution.

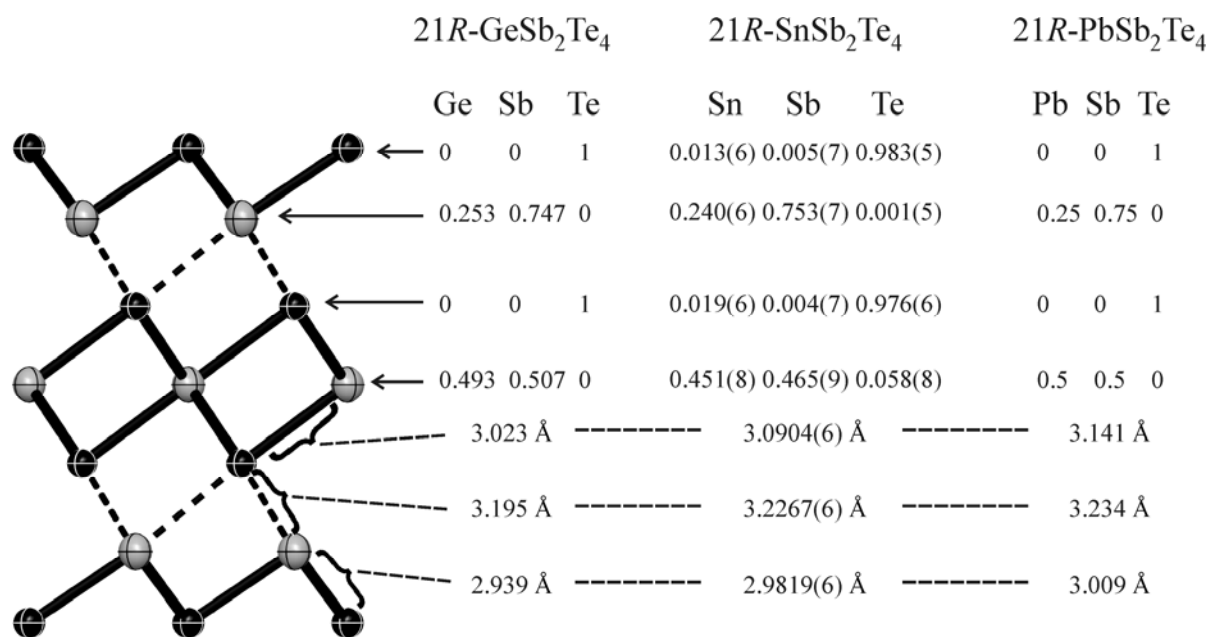


Figure 2. Atom distribution (occupancy factors for the elements in each compound, top right, arrows indicate the corresponding atom position) and selected interatomic distances (bottom right, the corresponding “bonds” are indicated) in the refined model of SnSb_2Te_4 (left, displacement ellipsoids are drawn at 90 % probability level). For comparison, the corresponding values are given for GeSb_2Te_4 ^[10] and PbSb_2Te_4 .^[12,13]

2.2.4 Conclusion

High-resolution synchrotron data at the absorption edges of all elements involved allowed the simultaneous refinement of site occupancies and anisotropic displacements in 21R- SnSb_2Te_4 . Although the application of resonant scattering is rather time-consuming, it is clearly the method of choice to increase the scattering contrast of Sn, Sb and Te, and can be applied to many compounds with similar element combinations when the element assignment is ambiguous.

The joint refinement using five datasets indicates no significant anti-site disorder or cation vacancies in SnSb_2Te_4 . The cation distribution is very similar to that in the isotypic compounds GeSb_2Te_4 and PbSb_2Te_4 . It is neither completely random nor fully ordered. A preferred

occupation with Sb is observed for the 6c position in the vicinity of the van der Waals gap whereas the 3a position is preferably occupied by Sn. This result seems to contradict the results obtained by ^{119}Sn Mößbauer spectroscopy.^[16] Although it cannot be excluded that the Bridgman grown crystal used in the Mößbauer study exhibits another element distribution than the crystal obtained from the gas phase, it seems unlikely that this is the case as both methods usually yield the thermodynamically stable materials. However, Mößbauer spectroscopy probes the local environment on the Sn atoms. The distortion around the 6c site derived from diffraction data is a space-averaged situation. If Sn atoms occupy this position, the local environment can be more regular, whereas it is a bit more distorted when Sb is present. Such variations might cause the slightly prolate displacement ellipsoids observed.

As the crystals have been slowly grown by chemical transport, they probably exhibit the thermodynamically stable element distribution, which in this case as well - as in the isotopic Ge and Pb compounds - is partially disordered. Such cation disorder has in fact been reported for many similar ternary tellurides such as $\text{Ge}_2\text{Sb}_2\text{Te}_5$, $\text{Ge}_{4-x}\text{Sb}_{2-y}\text{Te}_7$ ($x, y \approx 0.1$), GeSb_4Te_4 or $\text{Ge}_{2-x}\text{Sb}_{2+x}\text{Te}_5\text{Sb}_8$ ($x = 0.43$).^[35-38] It would be interesting to investigate the influence of different synthesis conditions and temperature treatment on the cation distribution. The high tendency toward cation disorder probably plays an important role concerning the thermoelectric characteristics of such materials. Although the thermoelectric figure of merit ZT of SnSb_2Te_4 is only 0.009 at 300 K,^[39] it might be worthwhile to investigate the corresponding structure property relationship.

2.2.5 References

- [1] D. Lencer, M. Salinga, B. Grabowski, T. Hickel, J. Neugebauer, M. Wuttig, *Nat. Mater.* **2008**, 7, 972.
- [2] S. Raoux, *Annu. Rev. Mater. Res.* **2009**, 39, 9.1.
- [3] M. Frumar, B. Frumarova, T. Wagner, M. Hrdlicka, *J. Mater. Sci. Mater. Electron* **2007**, 18, 169.
- [4] J.R. Sootsman, D.Y. Chung, M.G. Kanatzidis, *Angew. Chem. Int. Ed.* **2009**, 48, 8616.
- [5] G.J. Snyder, E.S. Toberer, *Nat. Mater.* **2008**, 7, 105.
- [6] A.V. Shevelkov, *Russ. Chem. Rev.* **2008**, 77, 1.
- [7] R. Wulf, *Acta Crystallogr. Sect A*, **1990**, 46, 681.
- [8] R. Wulf, *Mineral. Petrol.* **1995**, 52, 187.
- [9] J.-L. Hodeau, V. Favre-Nicolin, S. Bos, H. Renevier, E. Lorenzo, J.-F. Berar,

- Chem.Rev.* **2001**, *101*, 1843.
- [10] T. Matsunaga, N. Yamada, *Phys. Rev. B.* **2004**, *69*, 104111.
- [11] O.G. Karpinsky, L.E. Shelimova, M.A. Kretova, J.-P. Fleurial, *J. Alloys Compd.* **1998**, *268*, 112.
- [12] L.E. Shelimova, O.G. Karpinskii, T.E. Svechnikova, E.S. Avilov, M.A. Kretova, V.S. Zemskov, *Inorg. Mater.* **2004**, *40*, 1264.
- [13] L.E. Shelimova, O.G. Karpinskii, T.E. Svechnikova, I.Y. Nikhezina, E.S. Avilov, M.A. Kretova, V.S. Zemskov, *Inorg. Mater.* **2008**, *44*, 371.
- [14] H.W. Shu, S. Jaulmes, J. Flahaut, *J. Solid State Chem.* **1988**, *74*, 277.
- [15] A.G. Talybov, *Soviet Phys. Crystallogr.* **1961**, *6*, 40.
- [16] G. Concas, T.M. de Pascale, L. Garbato, F. Ledda, F. Meloni, A. Rucci, M. Serra, *J. Phys. Chem. Solids* **1992**, *53*, 791.
- [17] T.B. Zhukova, A.I. Zaslavskii, *Soviet Phys. Crystallogr.* **1972**, *16*, 796.
- [18] L.E. Shelimova, O.G. Karpinskii, P.P. Konstantinov, E.S. Avilov, M.A. Kretova, V.S. Zemskov, *Inorg. Mater.* **2004**, *40*, 451.
- [19] T. Thonhauser, G.S. Jeon, G.D. Mahan, J.O. Sofo, *Phys. Rev. B.* **2003**, *68*, 205207.
- [20] L.E. Shelimova, O.G. Karpinsky, P.P. Konstantinov, M.A. Kretova, E.S. Avilov, V.S. Zemskov, *Inorg. Mater.* **2001**, *37*, 342.
- [21] *WINXPOW, Version 2.12*, Stoe & Cie. GmbH, Darmstadt, **2005**.
- [22] A. Coelho, *TOPAS - Academic, V. 4.1*, Coelho Software, Brisbane, **2007**.
- [23] A. Stegherr, *Philips Res. Repts. Suppl.* **1969**, *6*, 1.
- [24] J.C. Labiche, O. Mathon, S. Pascarelli, M.A. Newton, G.G. Ferre, C. Curfs, G.B.M. Vaughan, A. Homs, D.F. Carreiras, *Rev. Sci. Instrum.* **2007**, *78*, 11.
- [25] J.L. Chambers, K.L. Smith, M.R. Pressprich, Z. Jin, *SMART, V.5.625*. Bruker AXS, Madison, USA, **1997-2001**.
- [26] *SAINT, V6.01*, Bruker AXS, Madison, USA, **1999**.
- [27] *XPREP, Version 6.12*, Siemens Analytical X-ray Instruments Inc, Madison, Wisconsin, USA, **1996**.
- [28] *SADABS, V2.03*, Bruker AXS, Madison, USA, **1999**.
- [29] Z. Otwinowski, W. Minor, in: C.W. Carter Jr., R.M. Sweet (Eds.), *Methods in Enzymology, Macromolecular Crystallography Part A*, Vol. 276, Academic Press, New York, **1997**, pp. 307-326.
- [30] V. Petricek, M. Dusek, L. Palatinus, *JANA2006 - The Crystallographic Computing System*, Institute of Physics, Praha, Czech Republic, **2006**.

-
- [31] G.M. Sheldrick, *Acta Crystallogr. Sect. A* **2008**, *64*, 112.
- [32] Collaborative Computational Project No. 4 The CCP4 suite: programs for protein crystallography, *Acta Crystallogr. Sect. D* **1994**, *50*, 760.
- [33] B.L. Henke, E.M. Gullikson, J.C. Davis, *At. Data Nucl. Data Tables* **1993**, *54*, 181.
- [34] C.T. Chantler, K. Olsen, R.A. Dragoset, J. Chang, A.R. Kishore, S.A. Kotochigova, D.S. Zucker, *X-Ray Form Factor, Attenuation and Scattering Tables, Version 2.1*, National Institute of Standards and Technology, Gaithersburg, MD, **2005**.
- [35] T. Matsunaga, N. Yamada, Y. Kubota, *Acta Crystallogr. Sect. B* **2004**, *60*, 685.
- [36] M.N. Schneider, O. Oeckler, *Z. Anorg. Allg. Chem.* **2008**, *634*, 2557.
- [37] M.N. Schneider, O. Oeckler, *Z. Anorg. Allg. Chem.* **2010**, *636*, 137.
- [38] M.N. Schneider, M. Seibald, O. Oeckler, *Dalton Trans.* **2009**, 2004.
- [39] J. Oestreich, *Ph.D. Thesis*, University of Konstanz, Germany, **2001**.

2.3 Unusual solid solutions in the system Ge-Sb-Te: The crystal structure of 33R-Ge_{4-x}Sb_{2-y}Te₇ (x, y ≈ 0.1) is isostructural to that of Ge₃Sb₂Te₆

Matthias N. Schneider and Oliver Oeckler

Zeitschrift für Anorganische und Allgemeine Chemie, **2009**, 634, 2557-2561.

Dedicated to Dr. Hansjürgen Mattausch on the occasion of his 65th birthday

Abstract

Whereas for a series of layered compounds with the general formula (GeTe)_n(Sb₂Te₃)_m the stoichiometry allows to predict the structure type and the average thickness of the hexagonal atom layers, these rules are not generally applicable for GeTe-rich compounds like Ge₄Sb₂Te₇. A 39R layer stacking is expected, however, single crystal diffraction studies reveal a 33R layered structure ($R\bar{3}m$, $a = 4.1891(5) \text{ \AA}$, $c = 62.169(15) \text{ \AA}$, $R = 0.047$) closely related to that of Ge₃Sb₂Te₆. This is also corroborated by the average layer thickness that can be determined from the strong reflections of powder patterns and exhibits a direct relation to the structure type. Mixed occupancy of cation positions with Ge and Sb and possibly defects allow this unusual range of homogeneity. Bulk material of the kinetically stable compound can be synthesized by quenching stoichiometric melts of the pure elements and subsequent annealing.

Keywords: germanium antimony tellurides; phase-change materials; thermoelectrics; phase homology; crystal structure determination

Copyright: © 2008 WILEY-VCH Verlag GmbH & Co. KGaA

2.3.1 Introduction

The phase-change behaviour of germanium antimony tellurides, which is of great importance for modern data storage technologies,^[1-3] as well as their thermoelectric characteristics^[4-6] have put this class of compounds into a focus of materials research and development. Both applications strongly depend on the compounds' structures which depend on synthesis conditions and composition. The knowledge of the exact atomic structures as a basis for the understanding of structure-property relationships and also for meaningful theoretical calculations is an important step to boost the efficiency of this class of materials. The goal is, of course, the prediction of new phases for future appliances.

Whereas in phase-change materials, amorphous and pseudo-cubic metastable phases are important, most well-characterized thermodynamically stable ternary compounds in the system Ge-Sb-Te have been found on the pseudobinary section GeTe - Sb₂Te₃.^[7-9] They constitute a homologous series (GeTe)_n(Sb₂Te₃)_m that includes, for example, the known compounds GeSb₄Te₇, GeSb₂Te₄, Ge₂Sb₂Te₅ and Ge₃Sb₂Te₆.^[10] Their structures follow the same principles as those of the stable compounds in analogous systems, e.g. with Sn or Pb substituting Ge and Bi or As replacing Sb.^[11-14] The trigonal structures can be formally described as “cubic” ABC stacking sequences of hexagonal layers. Each layer consists either of cationic (Ge, Sb) or anionic (Te) atoms. Of course, the *c/a* ratio strongly deviates from that of a cubic lattice in trigonal setting. Therefore, cations are octahedrally coordinated and might be viewed as centering octahedral voids in a *fcc* Te lattice. However, this rocksalt type structure is present only in slab-like Te-[(Ge/Sb)-Te-(Ge/Sb)]_n-Te building blocks that are stacked along [001]. These are not separated by layers of “empty” octahedral voids but shifted against each other to enable Te-Te bonding. Therefore, the complete Te partial structure does not correspond to a close sphere packing.

According to the literature,^[10, 11, 15, 16] the structures of the thermodynamically stable compounds (GeTe)_n(Sb₂Te₃)_m can be derived by rather simple rules, which can be used to interpret powder patterns as well as to predict reasonable models for structure refinement. Sb₂Te₃ itself crystallizes in the tetradymite (Bi₂Te₂S) structure type with three slabs per translation period, each containing an alternating sequence of three Te and two Sb layers (space group $R\bar{3}m$, $a = 4.264(1)$ Å, $c = 30.46(1)$ Å), which yields three Te-Te contacts per unit cell as shown in Figure 1.^[17]

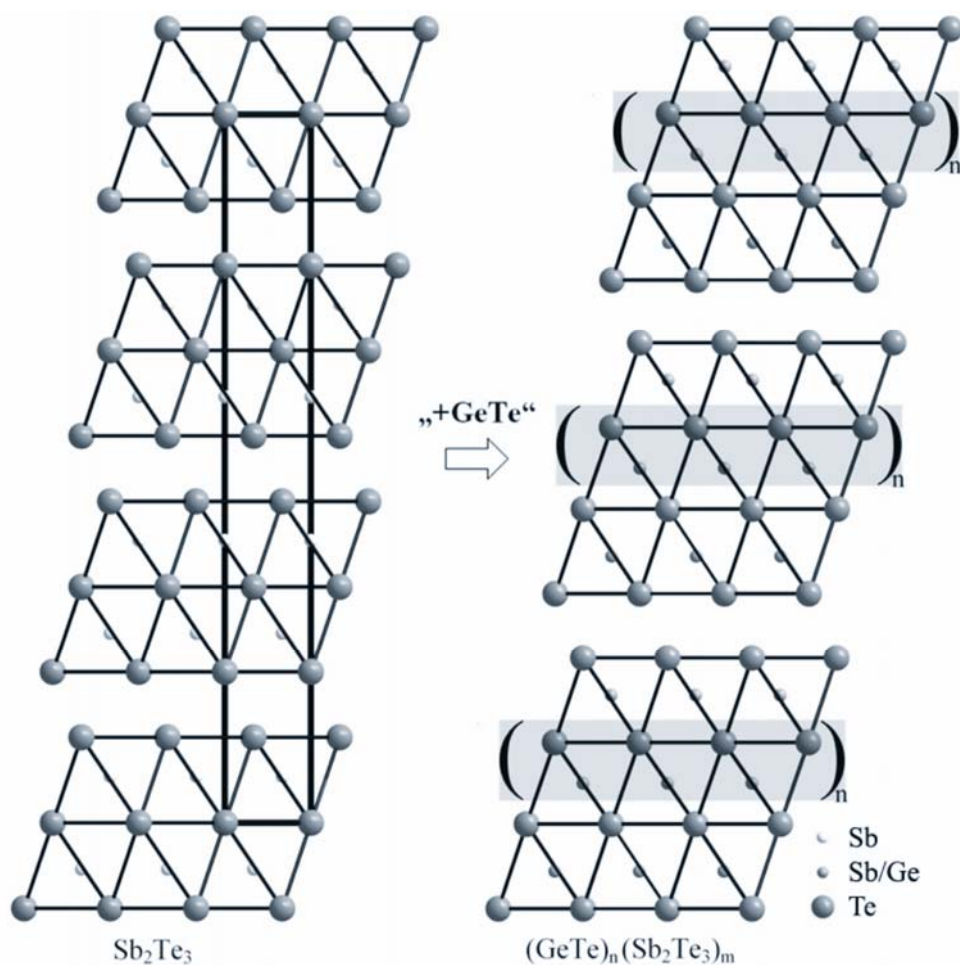


Figure 1. Formal insertion of GeTe-units into Sb_2Te_3 slabs leads to compounds $(\text{GeTe})_n(\text{Sb}_2\text{Te}_3)_m$.

Depending on the exact composition, differently sized building blocks can be obtained by formal insertion of n GeTe units in m Sb_2Te_3 slabs (cf. Fig. 1). Cation positions in these rocksalt-type slabs have been reported to be statistically occupied by Ge and Sb.^[10, 18, 19] The number N of anionic or cationic layers per translational period is a multiple of the number of atom layers within one building block. One formula unit GeTe contributes 2 layers to each block, whereas 5 layers must be taken into account per Sb_2Te_3 unit. As the pseudo-cubic ABC stacking sequence superimposes a periodicity that is a multiple of 3, one translational period comprises three slabs if $2n + 5m$ is not a multiple of 3. Then the space group is $R\bar{3}m$ (with $Z = 3$), whereas it is $P\bar{3}m1$ (with $Z = 1$) in case $2n + 5m$ is a multiple of 3.

Whereas the a lattice parameter is almost constant for all compounds, the c parameters of the trigonal structures strongly depend on the number of layers N/Z per building block and thus the bonding situation. The average thickness c/N of a single atom layer lies between the formal thickness of a single layer in the end members GeTe ($c/N = 1.78 \text{ \AA}$)^[20] and Sb_2Te_3 ($c/N = 2.03 \text{ \AA}$)^[21] of the pseudobinary section. The averaged “basic” lattice parameters c/N do not

follow a simple Vegard's law depending on the formal ratio of the end members in a specific compound as the Te-Te bonding between the building blocks is partly of Van der Waals character and therefore the distances Te-Te are much longer than the distances between cationic and anionic layers within the blocks. As N can be derived from the chemical formula, the lattice parameters $(\text{GeTe})_n(\text{Sb}_2\text{Te}_3)_m$ can be predicted if the relationship between the average layer thickness and the cation/anion ratio, which directly relates to the number of Te-Te contacts per unit cell, is known.^[10]

$$c/N = f(x) \text{ with } x = \frac{(n+2m)}{(n+3m)} = \frac{\text{number of Ge and Sb atoms}}{\text{number of Te atoms}}$$

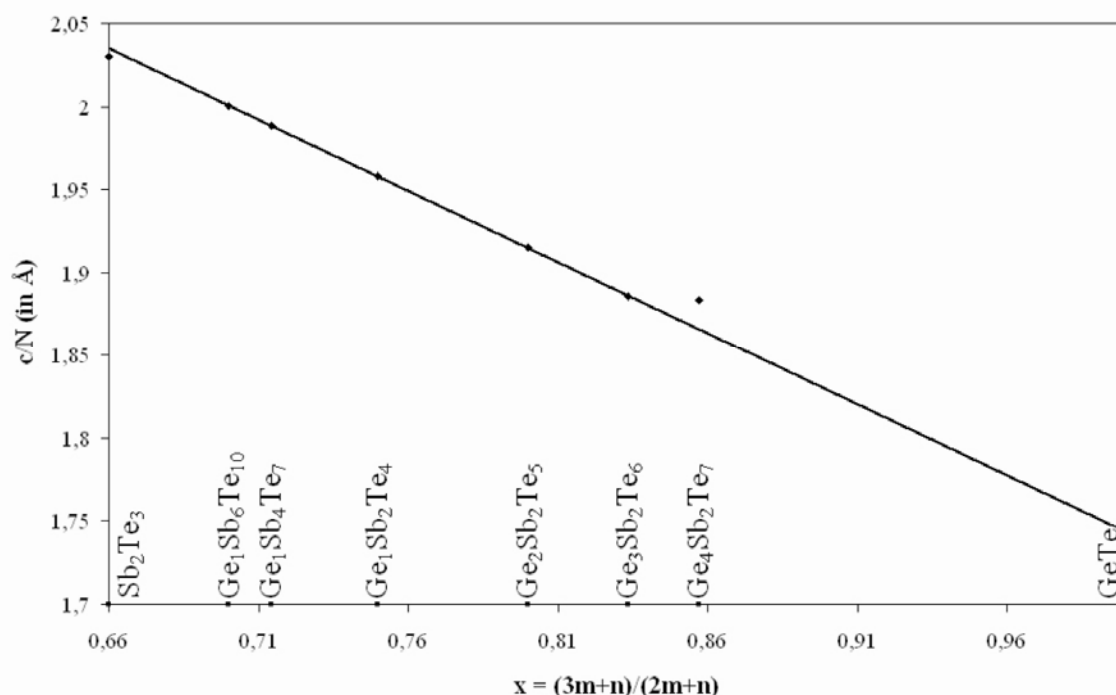


Figure 2. Relation between average layer thickness c/N and composition; the phases $(\text{GeTe})_n(\text{Sb}_2\text{Te}_3)_m$ with $n = 1, 2, 3$ and $m = 1$ as well as $n = 1$ and $m = 2, 3$ were taken into account to calculate the line of best fit.

c/N can easily be determined if only the strong reflections of powder patterns are considered. Owing to the ABC stacking sequence of individual layers, they correspond to a rhombohedral basic structure that can be viewed as an extremely distorted fcc lattice compressed along the stacking direction. Significant alternation between cation and anion layers suggests a rhombohedral unit cell that, in hexagonal setting, contains six atom layers per translation period along c . The strong reflections belonging to this basis maybe viewed as family reflections of different kinds of polytypic superstructures, although in contrast to OD structures the stacking cannot be viewed as more or less ordered sequence of almost equivalent layers. From samples with x between 0.71 and 0.86, *Karpinsky* and *Shelimova*^[10] derived $c/N(x) = 2.604 - 0.8614x$, which is in good agreement with our own result $c/N(x) = 2.6009 - 0.8575x$ (cf. Fig. 2).

On the GeTe rich side of pseudobinary line GeTe - Sb₂Te₃, additional members of the series can be found, but to our knowledge no single phase samples have been obtained so far. Those phases are expected to follow the simple linear equation described above; this has already been used to predict their structural parameters.^[10] In contrast to these results we observed a deviation from the relationship for a phase with the nominal composition Ge₄Sb₂Te₇ ($x = 0.86$). Single crystal diffraction studies reveal that the sample of “Ge₄Sb₂Te₇” crystallizes in a 33R type known from Ge₃Sb₂Te₆ which has a lower GeTe content.

2.3.2 Results and discussion

2.3.2.1 Characterization of Ge₄Sb₂Te₇ samples

Applying the rules for structure prediction described above, Ge₄Sb₂Te₇ is expected to form a 39R layer structure (space group $R\bar{3}m$). Extrapolating c/N to $x = 0.86$, the cell parameters are predicted to be $a = 4.18 \text{ \AA}$ and $c = 73.46 \text{ \AA}$ (from our own results, see above). This structure type has been reported for Ge₄As₂Te₇ from studies using transmission electron microscopy, but a local variation of layers per building block was observed^[13, 14] and analogous stacking disorder can be found for the compounds of the system Ge-Sb-Te.^[19] However, $c/N = 1.884 \text{ \AA}$ determined from the strong reflections of the powder pattern of our sample with the nominal composition Ge₄Sb₂Te₇ does not correspond to the value expected for this composition based on the linear relationship mentioned above ($c/N = 1.866 \text{ \AA}$, cf. Fig. 2), but to a 33R layer structure (space group $R\bar{3}m$) with cell parameters of $a = 4.189(1) \text{ \AA}$ and $c = 62.17(2) \text{ \AA}$. This corresponds to the phase Ge₃Sb₂Te₆,^[19, 21] whereas EDX spectroscopy clearly confirmed the composition of Ge₄Sb₂Te₇. Furthermore, the powder pattern corresponds to that calculated from single-crystal data (see below), no reflections from impurity phases can be detected. Also the weak reflections match better with simulations of the 33R type than with those of the 39R type (calculated from data on the phase Ge₄As₂Te₇^[22]) as shown in Figure 3.

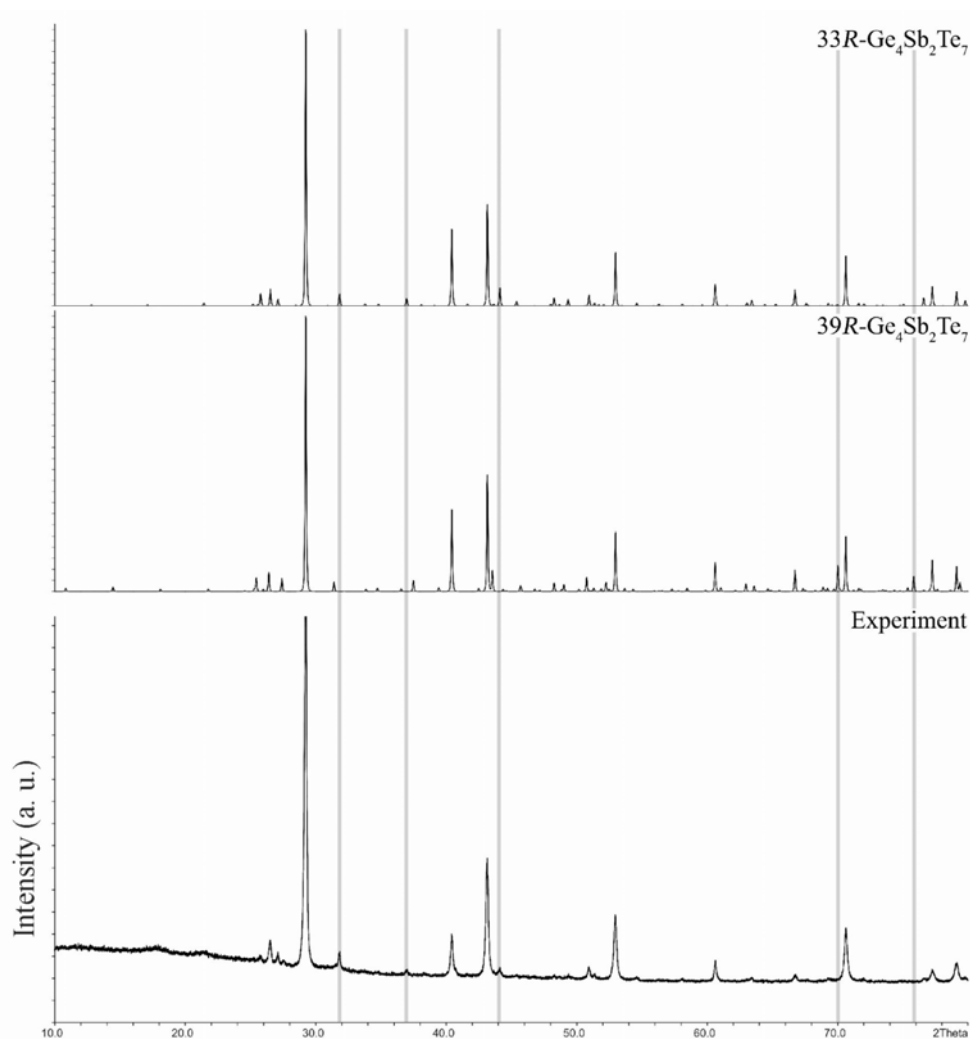


Figure 3. Comparison of the experimental powder pattern with calculated patterns based on the 33R and 39R types, respectively; lattice parameters were calculated from the experimental c/N (from strong reflections) for both types.

2.3.2.2 Single crystal structure determination

Single-crystal diffraction is the best method to analyze the discrepancy between well-known structural relationships, composition, and the powder diffraction pattern. The cell parameters determined from several crystals ($a = 4.203\text{--}4.209 \text{ \AA}$, $c = 62.3\text{--}62.5 \text{ \AA}$) confirmed the presence of the 33R type as suggested by the powder pattern. The metrics corresponds to the model of $\text{Ge}_3\text{Sb}_2\text{Te}_6$ in the space group $\overline{R}3m$, which has been determined by the Rietveld method from powder diffraction data.^[21] This structure type was used as a starting model for structure refinement. Refined lattice parameters from our powder data were used instead of the rather imprecise values determined from the crystals. The refinement including anisotropic displacement factors converged at $R1 = 0.048$. Crystal data and details of the refinement are summarized in Table 1. Atomic parameters are listed in Table 2, and anisotropic displacement factors are given in Table 3.

Table 1. Crystallographic data and structure refinement of 33R-Ge_{4-x}Sb_{2-y}Te₇ ($x \approx y \approx 0.1$) at 293 K.

Formula	Ge _{3.43(4)} Sb _{1.71(4)} Te ₆ ($\hat{=} \text{Ge}_{3.93(4)}\text{Sb}_{1.90(4)}\text{Te}_7$)
Formula mass (in g mol ⁻¹)	1208.68
Crystal system / Space group	trigonal / $R\bar{3}m$
Cell parameters (in Å)	$a = 4.189(1)$ $c = 62.17(2)$
Cell volume (in Å ³)	944.8(4)
X-ray density (in g cm ⁻³)	6.373(3)
Absorption coefficient (in mm ⁻¹)	24.97
Formula units (per unit cell)	3
$F(000)$	1509
Diffractometer	IPDS I
Radiation	MoK α ($\lambda = 0.71073$ Å)
2θ range (in °)	9.8 > 2θ > 55.0
$R_{\text{int}} / R_{\sigma}$	0.062 / 0.048
Absorption correction /	semiempirical
Transmission (max. / min.)	0.287 / 0.067
Measured reflections	1289
Independent data / parameters	340 / 21
Refinement	full-matrix least-squares on F^2
R indices [$I > 2\sigma(I)$] ^(a,b)	$R1 = 0.048$, $wR2 = 0.121$
R indices [all data] ^(a,b)	$R1 = 0.051$, $wR2 = 0.124$
GooF [all data]	1.026
$\Delta\rho_{\text{min}} / \Delta\rho_{\text{max}}$ (in eÅ ⁻³)	+2.1 / -3.0 (0.6 Å from Te2)

$$^a) R1 = \frac{\sum |F_o - F_c|}{\sum |F_o|}$$

$$^b) wR2 = \frac{[\sum [w(F_o^2 - F_c^2)^2]]^{1/2}}{\sum [w(F_o^2)]^{1/2}}; w = 1 / [\sigma^2(F_o^2) + (aP)^2 + bP] \text{ with } P = [\text{Max}(0, F_o^2) + 2F_c^2] / 3$$

Table 2. Wyckoff positions, atomic coordinates, site occupancy and equivalent isotropic displacement factors (in Å²) for 33R- Ge_{4-x}Sb_{2-y}Te₇ ($x \approx y \approx 0.1$).

atom	Wyckoff position	x	y	z	f.o.f.	U _{eq.}
Ge1/Sb1	3a	0	0	0	0.73(2)/ 0.27(2)	0.0340(9)
Ge2/Sb2	6c	0	0	0.27452(3)	0.77(2)/ 0.23(2)	0.0325(7)
Ge3/Sb3	6c	0	0	0.45227(3)	0.55(1)/ 0.45(1)	0.0300(6)
Te1	6c	0	0	0.085000(16)	1	0.0238(4)
Te2	6c	0	0	0.189440(18)	1	0.0276(4)
Te3	6c	0	0	0.361680(13)	1	0.0228(5)

Table 3. Anisotropic displacement parameters (in Å²) for 33R-Ge_{4-x}Sb_{2-y}Te₇ ($x \approx y \approx 0.1$).

atom	U_{11}	U_{22}	U_{33}	U_{12}	U_{13}	U_{23}
Ge1/Sb1	0.0301(9)	0.0301(9)	0.0417(15)	0.0151(5)	0	0
Ge2/Sb2	0.0300(8)	0.0300(8)	0.0374(12)	0.0150(4)	0	0
Ge3/Sb3	0.0277(6)	0.0277(6)	0.0346(9)	0.0138(3)	0	0
Te1	0.0230(5)	0.0230(5)	0.0252(7)	0.0115(2)	0	0
Te2	0.0270(5)	0.0270(5)	0.0288(8)	0.0135(2)	0	0
Te3	0.0218(5)	0.0218(5)	0.0250(8)	0.0109(2)	0	0

The structure can be described as an ordered stacking sequence of hexagonal atom layers with three building blocks of 11 layers each in the unit cell. Fully occupied Te layers alternate with cationic layers that exhibit mixed Ge/Sb occupancy. The building blocks are stacked along [001] and interconnected via Te-Te contacts. Each atom position within a building block is coordinated by an octahedron of six neighbouring atoms. All interatomic distances within the (001) planes correspond to the lattice parameter $a = 4.189(1)$ Å. The distance between Te atoms of adjacent blocks is $3.724(1)$ Å, which is significantly smaller than the sum of the Van der Waals radii (about 4.00 Å) and indicates a partially covalent character. Within the 11-layer slabs, an almost regular (Ge/Sb)Te₆ octahedron with a (Ge/Sb)-Te bond length of $2.992(1)$ Å can be observed only in the centre around Ge1/Sb1. The distortion of the (Ge/Sb)Te₆ octahedrons increases from the inversion centre in the middle of each block element towards the gap between adjacent blocks as depicted in Figure 4. The longer bonds are located towards the block centre ($3.072(1)$ Å at Ge2/Sb2, $3.209(2)$ Å at Ge3/Sb3) and shorter bonds face the block boundary ($2.915(1)$ Å at Ge2/Sb2, $2.873(1)$ Å at Ge3/Sb3). This asymmetry is due to the growing influence of the “unsaturated” coordination sphere of Te atoms in the layers terminating each 11-layer slab. They obviously compensate their formal charge by forming stronger bonds to the cations, resulting in a 3 + 3 coordination which leads to polar (Ge,Sb)-Te double layers as they are known from α -GeTe.^[17] Due to the inversion centre of each layer no polarity remains on a macroscopic scale.

In addition, the unifacial coordination of the terminal Te atom layers by cations also influences the ratio of Ge and Sb on the cation sites. The higher formal charge of Sb^{III} compared to Ge^{II} makes it more suitable to occupy cation positions neighbouring terminal Te layers. Cation positions close to the gap between adjacent blocks therefore exhibit a lower Ge/Sb ratio (cf. Fig. 4).

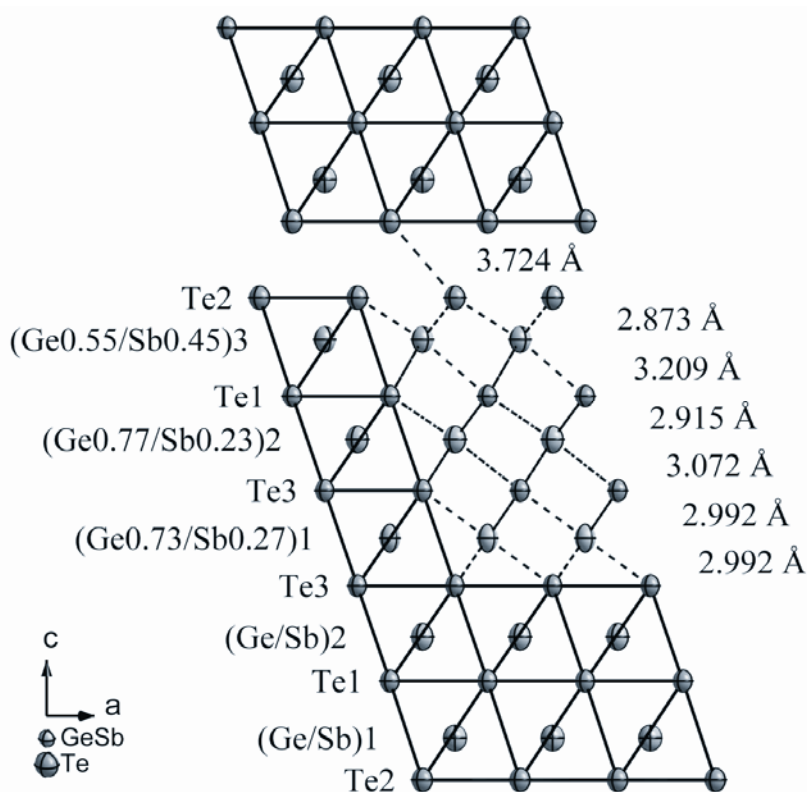


Figure 4. Projection of the crystal structure of $33R\text{-Ge}_{4-x}\text{Sb}_{2-y}\text{Te}_7$ ($x \approx y \approx 0.1$) along $[010]$: displacement ellipsoids are drawn at 90 % probability level and interatomic distances and site occupations are indicated.

As discussed above, the cation / anion ratio has been reported to have a strong impact on the crystal structures. In ideal $33R\text{-Ge}_3\text{Sb}_2\text{Te}_6$ [22] and $39R\text{-Ge}_4\text{Sb}_2\text{Te}_7$ this ratio is 0.83 and 0.86, respectively. For the $33R$ structure of “ $\text{Ge}_4\text{Sb}_2\text{Te}_7$ ” reported here, this ratio is 0.83 by definition if we assume full occupancy of all positions. The exact composition $\text{Ge}_4\text{Sb}_2\text{Te}_7$ can only occur if either defects are present in the Te anion partial structure or if anti-site disorder is assumed (since the electron count of Sb and Te is very similar, this can not be completely excluded by X-ray diffraction methods). However, a very slight deviation from the ideal composition is more likely. The structure refinement (assuming fully occupied Ge/Sb cation and Te anion positions) yields the composition $\text{Ge}_{3.43(4)}\text{Sb}_{1.71(4)}\text{Te}_6 = \text{Ge}_{3.93(4)}\text{Sb}_{1.90(4)}\text{Te}_7$ which is very close to the bulk material’s composition, both according to the mixture of starting materials as well as confirmed by EDX. As neither the structure models considered here nor experimental and refined compositions differ significantly when the standard deviations are taken into account, it is not mandatory to assume an unusually large amount of voids or non-stoichiometry. Minute amounts of Ge and Sb that might have separated from the material are certainly below the detection limit of EDX or powder diffraction.

2.3.3 Conclusion

We have shown that for $m/n > 0.33$, i. e. for high Ge contents, the structures of pseudobinary phases $(\text{GeTe})_n(\text{Sb}_2\text{Te}_3)_m$ cannot be predicted well on the basis of a homologous series taking into account only the stoichiometry. However, detailed analysis of powder patterns and common structural principles allow the reliable prediction of the block thickness, i. e. the number of atom layers in one slab. Contrary to simple rules, “ $\text{Ge}_4\text{Sb}_2\text{Te}_7$ ” does not form a $39R$ structure with 13-layer slabs. Owing to small amounts of defects or slight deviations from the ideal composition, the compound occurs in the $33R$ structure type known from $\text{Ge}_3\text{Sb}_2\text{Te}_6$. This means that the homogeneity range of this type is much larger than that of other pseudobinary $(\text{GeTe})_n(\text{Sb}_2\text{Te}_3)_m$ phases. The compound synthesized might be metastable from a thermodynamical point of view, and the $39R$ type might be found under other conditions, but the $33R$ type is at least kinetically stable when annealed at $550\text{ }^\circ\text{C}$ for several days. Therefore, different compositions and variable degrees of Ge/Sb disorder can exist in the same phase. This homogeneity range, including metastable structures, could be a major step towards a selective adjustment of the material’s properties. Furthermore, the disordered stable phases are very interesting model systems for metastable phases. In fact, the structure of one rocksalt-type block more or less corresponds to the structure of metastable pseudocubic phases of Ge-Sb-Te phase-change materials. Therefore, some conclusions drawn from this structure may be of general importance:

- 1.) Octahedral voids within the slightly distorted Te *fcc* sublattice are preferably occupied by Sb cations if they are closer to Te layers that are coordinated by cations from only one side. In addition, cations are generally displaced towards a Van der Waals gap between two adjacent Te layers.
- 2.) There is a strong tendency to avoid cation vacancies within the building blocks. Cation vacancies only formally concentrate in ordered layers between adjacent blocks, in fact Te-Te bonding leads to a shift of the blocks so that Te atoms form no continuous *fcc* sublattice.
- 3.) Slight non-stoichiometry due to a variable Ge/Sb ratio on cation sites allows to avoid extreme long-range order, i.e. the occurrence of very thick building blocks.

2.3.4 Experimental section

2.3.4.1 Synthesis

Bulk samples of the compounds were prepared by melting stoichiometric amounts of the pure elements Ge (99.999 %, Sigma Aldrich), Sb (99.999 %, Smart Elements) and Te (99.999 %, Alfa Aesar) in sealed silica glass ampoules under argon atmosphere at 950 °C. After quenching to room temperature in water, the samples were annealed at 550 °C for 100 h under Ar.

2.3.4.2 Chemical analysis

The composition of the metallic bulk material was confirmed by EDX spectroscopy using a JSM-6500F (Jeol, USA) scanning electron microscope with EDX detector (model 7418, Oxford Instruments, Great Britain). Averaging three analyses on different points of the crushed sample yields Ge:Sb:Te = 4.1(2): 2.02(3):7.

2.3.4.3 X-ray characterization

X-ray powder patterns were recorded on a Huber G670 powder diffractometer equipped with an imaging plate system using Cu-K $_{\alpha 1}$ radiation (Ge monochromator, $\lambda = 1.54051 \text{ \AA}$) in Guinier geometry. Specimens were prepared by crushing representative parts of the samples and fixing the powder on Mylar foils using silicone grease. Lattice parameters were determined by least-square refinement using the program WINX^{POW} [23] (see also results and discussion).

For single crystal analysis, irregularly shaped crystals were isolated from the crushed ingots, mounted on glass fibres and checked for quality by Laue photographs on a Buerger precession camera. Intensity data of the best crystal were collected on a STOE IPDS-I diffractometer with imaging plate detector using Mo-K $_{\alpha}$ radiation (graphite monochromator, $\lambda = 0.71093 \text{ \AA}$). The crystal used was almost single, however, three very small, randomly oriented fragments could be detected. Reflections of the main crystal that overlapped with reflections of fragments were discarded. Due to the high symmetry, this did not reduce the completeness of the dataset. Semiempirical absorption corrections based on equivalent reflections were applied before structure refinements with SHELX [24] were executed. Details about data collection and refinement are given in Table 1. Further details of the crystal structure investigation are available from the Fachinformationszentrum Karlsruhe, D-76344 Eggenstein-Leopoldshafen (Germany), on quoting the depository number CSD-419645 as well as the names of the authors and citation of the paper (Fax: _49-7247-808-666; E-mail:crysdata@fiz-karlsruhe.de).

2.3.5 References

- [1] M. Wuttig, N. Yamada, *Nat. Mater.* **2007**, *6*, 824.
- [2] T. Matsunaga, N. Yamada, *Jpn. J. Appl. Phys.* **2004**, *43*, 4704.
- [3] W. Welnic, M. Wuttig, *Mater. Today* **2008**, *11*, 20.
- [4] K. F. Hsu, S. Loo, F. Guo, W. Chen, J. S. Dyck, C. Uher, T. Hogan, E. K. Polychroniadis, M. G. Kanatzidis, *Science* **2004**, *303*, 818.
- [5] H. Böttner, G. Chen, R. Venkatasubramanian, *MRS Bulletin* **2006**, *31*, 211.
- [6] P. P. Konstantinov, L. E. Shelimova, E. S. Avilov, M. A. Kretova, V. S. Zemskov, *Inorg. Mater.* **2001**, *37*, 662.
- [7] L. E. Shelimova, O. G. Karpinsky, P. P. Konstantinov, M. A. Kretova, E. S. Avilov, V. S. Zemskov, *Inorg. Mater.* **2001**, *37*, 342.
- [8] a) B. Legendre, C. Hancheng, S. Bordas, M.-T. Clavaguera-Mora, *Thermochim. Acta* **1984**, *78*, 141; b) S. Bordas, M.-T. Clavaguera-Mora, B. Legendre, C. Hancheng, *Thermochim. Acta* **1986**, *107*, 239.
- [9] V. I. Kosyakov, V. A. Shestakov, L. E. Shelimova, V. S. Zemskov, F. A. Kuznetsov, *Inorg. Mater.* **2000**, *36*, 1004.
- [10] O. G. Karpinsky, L. E. Shelimova, M. A. Kretova, J.-P. Fleurial, *J. Alloys Compd.* **1998**, *268*, 112.
- [11] T. B. Zhukova, A. I. Zaslavskii, *Sov. Phys. Cryst.* **1971**, *16*, 796.
- [12] L. E. Shelimova, O. G. Karpinsky, P. P. Konstantinov, M. A. Kretova, E. S. Avilov, V. S. Zemskov, *Inorg. Mater.* **2004**, *40*, 451.
- [13] S. Kuypers, G. v. Tendeloo, J. v. Landuyt, S. Amelinckx, *J. Solid State Chem.* **1988**, *76*, 102.
- [14] S. Kuypers, G. v. Tendeloo, J. v. Landuyt, S. Amelinckx, H. W. Shu, S. Jaulmes, J. Flahaut, P. Laruelle, *J. Solid State Chem.* **1988**, *73*, 192.
- [15] F. Hulliger, *Structural Chemistry of Layer-Type Phases*, Springer-Verlag, **1977**.
- [16] O. G. Karpinsky, L. E. Shelimova, M. A. Kretova, V. S. Zemskov, *Inorg. Mater.* **2000**, *36*, 1108.
- [17] T. L. Anderson, H. B. Krause, *Acta Crystallogr. Sect. B* **1974**, *30*, 1307.
- [18] T. Matsunaga, N. Yamada, *Phys. Rev. B: Condens. Matter Mater. Phys.* **2004**, *69*, 104111.
- [19] B. J. Kooi, J. T. M. de Hosson, *J. Appl. Phys.* **2002**, *92*, 3584.
- [20] T. K. Chattopadhyay, J. X. Boucherle, H. G. von Schnering, *J. Phys. C* **1987**, *20*, 1431.

- [21] T. Matsunaga, R. Kojima, N. Yamada, K. Kifune, Y. Kubota, Y. Tabata, M. Takata, *Appl. Phys. Lett.* **2007**, *90*, 161919.
- [22] H. W. Shu, S. Jaulmes, J. Flahaut, *J. Solid State Chem.* **1988**, *74*, 277.
- [23] *WINXPOW, Version 2.12*, Stoe & Cie. GmbH, Darmstadt, **2005**.
- [24] G. M. Sheldrick, *Acta Crystallogr. Sect A* **2008**, *64*, 112.

2.4 Ambiguities due to almost homometric structure models and stacking disorder concerning the structure determination of antimony tellurides

Matthias N. Schneider, Markus Seibald, Patrick Lagally and Oliver Oeckler

Journal of Applied Crystallography **2010**, *43*, 1012-1020.

Synopsis

Ambiguities in the interpretation of diffraction data from layered chalcogenides arise from almost homometric non-congruent structure models, especially if mixed site occupancies are present. Further pitfalls can result from stacking disorder of distinct tetradymite and A7-type building units.

Abstract

Ambiguities in the interpretation of both single-crystal and powder diffraction data can lead to wrong conclusions concerning structure analysis of layered chalcogenides with interesting physical properties and potential applications. This is exemplified for binary and Pb doped phases of the homologous series $(\text{Sb}_2)_k(\text{Sb}_2\text{Te}_3)_m$. Almost homometric structure models for $39R\text{-Sb}_{10}\text{Te}_3$ ($R\bar{3}m$, $a = 4.2874(6)$ Å, $c = 64.300(16)$ Å, $R1 = 0.0298$) have been derived from initial structure solutions and crystal chemical considerations. The variation of the electron density on certain positions may further reduce the differences between the calculated diffraction patterns of non-congruent structure models as exemplified with the new compound $33R\text{-(Sb}_{0.978(3)}\text{Pb}_{0.022(3)})_8\text{Te}_3$ ($R\bar{3}m$, $a = 4.2890(10)$ Å, $c = 75.51(2)$ Å, $R1 = 0.0615$). Both compounds are long-range ordered, and in either case both ‘almost homometric’ models can be refined equally well on experimental data sets. The models can only be distinguished by chemical analysis, as reasonable atom assignments lead to different compositions for both models. Interestingly, all structure solution attempts led to the wrong models in both cases. In addition, it is shown that stacking disorder of characteristic layers may lead to powder diffraction patterns which can be misinterpreted in terms of 3D randomly disordered almost isotropic structures with a simple $\alpha\text{-Hg}$ type basic structure.

Copyright: © 2010 International Union of Crystallography

2.4.1 Introduction

Systematic crystal chemistry can be a powerful tool to categorize related structures in a class of compounds, especially if building blocks or characteristic structural features can be combined in a versatile way and physical properties follow a defined trend when the structures are systematically varied. An understanding of the corresponding structure–property relationships may allow one to predict and accordingly synthesize new materials with optimized properties.

Some layered chalcogenides have been reported to be promising superconductors such as $\text{Ba}_{1-x}\text{K}_x\text{BiO}_3$, meta-magnets like $\text{Sr}_2\text{MnO}_2\text{Cu}_{2m-\delta}\text{S}_3$, or thermoelectrics, for example $A_m[M_{1+l}\text{Se}_{2+l}]_{2m}[M_{2l+n}\text{Se}_{2+3l+n}]$ ($A = \text{K, Rb, Cs, Sr, Ba}$, $M = \text{Sn, Pb, Eu, Sb, Bi}$) or CsBi_4Te_6 .^[1-4] These and many similar phases can be described in terms of homologous series, where common structural motifs are repeated in different long-range ordered structures, which are in many ways similar to polysomatic series of minerals.^[5]

The layered structures of binary as well as multinary antimony or bismuth tellurides are prime examples of such homologous series. Some pnictogen-rich tellurides like $(\text{Sb}_2)_k(\text{Sb}_2\text{Te}_3)_m$ ^[6,7] or $(\text{Bi}_2)_k(\text{Bi}_2\text{Te}_3)_m$ ^[8,9] form series of numerous compounds between the end members Sb or Bi ($m = 0$) and Sb_2Te_3 or Bi_2Te_3 ($k = 0$), respectively. Slabs of k A7-type (grey As) layers^[10-12] alternate with m tetradymite-type ($\text{Bi}_2\text{Te}_2\text{S}$) building blocks, Sb_2Te_3 or Bi_2Te_3 , composed of five alternating anion and cation layers.^[13,14] This is shown in Fig. 1, which additionally depicts how such tetradymite-type blocks can formally be expanded by n additional layers $M\text{Te}$ ($M = \text{Ge, Sn, Pb}$), leading to phases $(M\text{Te})_n(\text{Bi}_2\text{Te}_3)_m$ and $(M\text{Te})_n(\text{Sb}_2\text{Te}_3)_m$ ($M = \text{Ge, Sn, Pb}$). These accordingly contain slabs of $2n + 5m$ alternately stacked cation and anion layers.^[15-19] In addition, metastable phases that combine both types of homologous series have been described recently.^[20,21] Such long-range ordered structures are described by the stacking sequences of the corresponding layer types; however, pronounced local relaxation and preferred occupancy of mixed cation sites occur in the vicinity of the van der Waals gaps between adjacent slabs, probably due to a different chemical environment. Different stacking sequences are often very similar in energy and can give rise to disorder or polytypism, which was reported, for example, for Sb_4Te_3 .^[6,22]

The strong reflections (corresponding to an average structure) of such polytypes are observed at almost equal positions in X-ray diffraction patterns, and only weak superstructure reflections allow one to distinguish them. If the composition of homologous compounds differs, of course chemical analysis can help to differentiate them. This is especially important when they crystallize in the same Ramsdell type. For example, $9P\text{-Ge}_2\text{Sb}_2\text{Te}_5$ ($n = 2$, $k = 0$; $P\bar{3}m1$,

$a = 4.225$, $c = 17.239$ Å) exhibits the sequence $[-(\text{Ge}_2\text{Sb}_2\text{Te}_5)-]_\infty$ with building units $\text{Ge}_2\text{Sb}_2\text{Te}_5$ of nine alternating cation and anion layers,^[23] whereas $9P\text{-GeSb}_4\text{Te}_4$ ($n = 1$, $k = 1$; $P\bar{3}m1$, $a = 4.247$, $c = 17.483$ Å) shows the sequence $[-(\text{GeSb}_2\text{Te}_4)-(\text{Sb}_2)-]_\infty$ ^[20] and $9P\text{-Sb}_6\text{Te}_3$ ($n = 0$, $k = 2$; $P\bar{3}m1$, $a = 4.272$, $c = 17.633$ Å) is a third type with the sequence $[-(\text{Sb}_2\text{Te}_3)-(\text{Sb}_2)-(\text{Sb}_2)-]_\infty$.^[24] The powder diffraction patterns of these three phases exhibit only very small differences because of the similar lattice parameters and the similar average structure. The average structure of all members of the homologous series mentioned above can be defined as a primitive rhombohedral structure ($\alpha\text{-Hg}$ type). The individual structures can be viewed as superstructures of this basic type, and a (three + one)-dimensional superspace formalism may be used to describe all phases with one unifying model. This has been shown e.g. for the similar homologous series $(\text{Bi}_2)_k(\text{Bi}_2\text{Se}_3)_m$ or $(\text{Bi}_2)_k(\text{Bi}_2\text{Te}_3)_m$.^[25-26]

Of course, single-crystal diffraction is more suitable for distinguishing between various polytypic or otherwise closely related structures. However, two of the non-congruent $9P$ -type structures described above ($9P\text{-GeSb}_4\text{Te}_4$, $9P\text{-Ge}_2\text{Sb}_2\text{Te}_5$) can be refined with comparable R values on the same single-crystal data. The false minimum observed, although significantly higher in R value than the true one, does not result from low data quality, nor is it due to the similar electron count of Sb and Te. It rather seems to be related to the problem of homometry. Two non-congruent structures yield the same diffraction pattern if they exhibit the same interatomic vector sets weighted with the corresponding scattering densities. The general assumption that a structure and its diffraction pattern are biuniquely related does not hold for such so-called homometric structures. X-ray crystal structure analysis relies on the singularity of the weighted interatomic vector set; however, it has already been shown by Patterson^[27,28] that this may indeed result from non-congruent atom arrangements. Although the existence of a large number of such homometric pairs was estimated during several theoretical discussions of the problem^[29-37] such ambiguities concerning X-ray structure analysis are, fortunately, extremely rare. Only very few experimental examples have been found since Dachs^[38] first reported a case of homometry for the mineral bixbyite. For example, homometric pairs have been described for CdI_2 , NiAs and FeTa_2O_6 .^[39-41]

Here we address two pairs of layered structures that are very close to homometry in order to point out that the resulting ambiguities in structure analysis are a rather general problem in chalcogenide chemistry. This may or may not involve the problem of distinguishing e.g. Sb and Te, and occupational disorder may render structures ‘more homometric’, *i.e.* yield wrong minima in structure refinements that cannot be distinguished from the correct one. Stacking disorder, which is not significant in the long periodically ordered structures of the new compounds

reported here, may further increase this problem in other cases. According to order–disorder theory,^[42,43] faults in layered materials primarily affect weak non-family reflections, indicative of the polytype, whereas the influence on strong family reflections which represent the average structure is marginal.

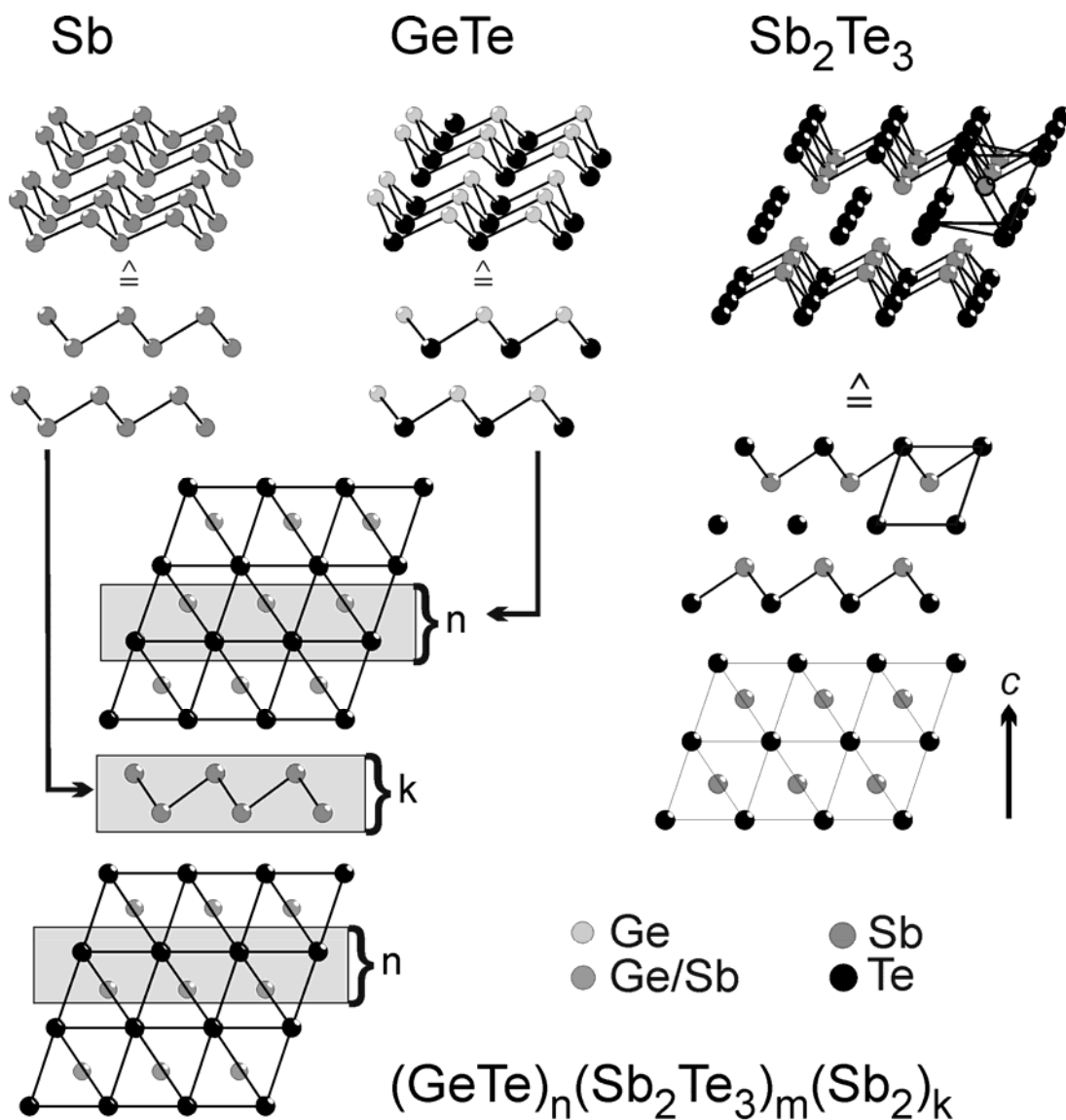


Figure 1. Schematic overview over structural features of layered compounds in the system Ge/Sb/Te.

2.4.2 Experimental

2.4.2.1 Sample preparation and characterization

Mixtures of the pure powdered elements Pb (99.995%, Sigma Aldrich), Sb (99.999%, Smart Elements) and Te (99.999%, Alfa Aesar) with the initial stoichiometric ratios Pb:Sb:Te = 1:10:4 and Sb:Te = 10:3 were heated in sealed silica glass ampoules under an argon atmosphere at 1223 K for 3–5 h to obtain homogeneous melts. Afterwards, the samples were either slowly cooled to the annealing temperature of 673 K (binary phase) or quenched to room temperature in air and reheated to the annealing temperature of 673 K (possible for both phases) which for both phases was maintained for 4–6 d to obtain homogeneous samples.

Representative parts of the metallic grey ingots were ground to powders and fixed on Mylar foils with silicone grease to collect X-ray powder diffraction patterns on a Huber G670 powder diffractometer equipped with an imaging-plate system using Cu $K\alpha_1$ radiation (Ge monochromator, $\lambda = 1.54051 \text{ \AA}$) in Guinier geometry. The powder data were evaluated using the program WinX^{POW}.^[44] The X-ray powder pattern of the binary $\text{Sb}_{10}\text{Te}_3$ specimens indicated homogeneity, whereas for the Pb-doped phase small amounts of PbTe were identified in the powder pattern of the original sample. Elemental analyses averaged from various point analyses on planar faces of the single crystal used for data collection were done by energy-dispersive X-ray spectroscopy (EDX) using a JSM-6500F (Jeol, USA) scanning electron microscope with an EDX detector (model 7418, Oxford Instruments, UK). They yielded the composition (in at.%) Sb 72.8, Pb 1.1, Te 26.1 [calculated for $(\text{Sb}_{0.978}\text{Pb}_{0.022})_8\text{Te}_3$: Sb 71.1, Pb 1.6, Te 27.3]. Homogeneous bulk samples of $(\text{Sb}_{0.978}\text{Pb}_{0.022})_8\text{Te}_3$ can be prepared by melting stoichiometric amounts of the pure elements using analogous temperature treatment.

2.4.2.2 Single-crystal structure determination

Irregularly shaped plate-like single crystals for data collection and elemental analysis were mechanically isolated from the ingots and fixed on glass fibres for quality assessment by Laue diffraction on a Buerger precession camera. Intensity data were collected on a Stoe IPDS-I diffractometer with an imaging-plate detector using Mo $K\alpha$ radiation (graphite monochromator, $\lambda = 0.71073 \text{ \AA}$). The rhombohedral metrics determined for single crystals of $(\text{Sb}_{0.978}\text{Pb}_{0.022})_8\text{Te}_3$ [$R\bar{3}m$, $a = 4.2874 (6)$, $c = 64.300 (16) \text{ \AA}$] and $\text{Sb}_{10}\text{Te}_3$ [$R\bar{3}m$, $a = 4.2874 (6)$, $c = 64.300 (16) \text{ \AA}$] revealed the presence of a $33R$ -type structure for $(\text{Sb}_{0.978}\text{Pb}_{0.022})_8\text{Te}_3$ and a $39R$ -type structure for $\text{Sb}_{10}\text{Te}_3$. Neither of the single crystals showed significant diffuse streaks along c^* , which indicates the absence of pronounced stacking disorder. After absorption correction, initial

structure solution by direct methods,^[45] Patterson interpretation or charge flipping^[46-48] confirmed that the Pb-doped and binary phases contain 33 and 39 hexagonal atom layers per unit cell, respectively. However, apart from this, all initial solutions were false minima. Details on false minima and the development of the final structure models are given in the following sections. Final full-matrix least-squares refinements including anisotropic displacements and, in the case of $(\text{Sb}_{0.978}\text{Pb}_{0.022})_8\text{Te}_3$, site occupancies (standard deviation on Sb/Pb occupancy: 0.003) were executed with SHELXL.^[45] For both phases, crystal data and details of the refinements are summarized in Table 1. Atomic coordinates and anisotropic displacement parameters are given in Tables 2 and 3, respectively. Further information may be obtained from the Fachinformationszentrum Karlsruhe, D-76344 Eggenstein-Leopoldshafen (Germany), by quoting the deposition numbers CSD-421727 for $\text{Sb}_{10}\text{Te}_3$ and CSD-421728 for $(\text{Sb}_{0.978}\text{Pb}_{0.022})_8\text{Te}_3$, the names of the authors, and the citation of the paper.

Table 1. Crystallographic data on the structure refinement of 33R- $(\text{Sb}_{0.978}\text{Pb}_{0.022})_8\text{Te}_3$ and 39R- $\text{Sb}_{10}\text{Te}_3$ at 293 K.

Formula	$(\text{Sb}_{0.978(3)}\text{Pb}_{0.022(3)})_8\text{Te}_3 =$ $\text{Pb}_{0.18(3)}\text{Sb}_{7.82(3)}\text{Te}_3$	$\text{Sb}_{10}\text{Te}_3$
Formula mass (in g mol^{-1})	1371.89	1600.30
Crystal system / Space group	trigonal / $R\bar{3}m$	trigonal / $R\bar{3}m$
Cell parameters (in Å)	$a = 4.2874(6)$ $c = 64.300(16)$	$a = 4.2890(10)$ $c = 75.51(2)$
Cell volume (in Å ³)	1023.6(3)	1202.9(5)
X-ray density (in g cm^{-3})	6.677	6.627
Absorption coefficient (in mm^{-1})	23.644	21.866
Formula units (per unit cell)	3	3
$F(000)$	1707.5	1998
Diffractometer	IPDS I	IPDS I
Radiation (in Å)	MoK_α ($\lambda = 0.71073$)	MoK_α ($\lambda = 0.71073$)
2θ range (in °)	$5.7 < 2\theta < 60.0$	$4.9 < 2\theta < 52.0$
$R_{\text{int}} / R_\sigma$	0.0811 / 0.0412	0.0965 / 0.0472
Absorption correction	numerical [49,50]	semiempirical [51]
Measured reflections	3739	2811
Independent data / parameters	462 / 19	375 / 22
Refinement	full-matrix least-squares on F^2	full-matrix least-squares on F^2
R indices [$I > 2\sigma(I)$] ^(a,b)	$R1 = 0.0298$ $wR2 = 0.0666$	$R1 = 0.0615$ $wR1 = 0.1128$
R indices [all data] ^(a,b)	$R1 = 0.0893$ $wR2 = 0.0833$	$R1 = 0.1015$ $wR2 = 0.1228$
Residual electron density (max. / min, in $\text{e}\text{Å}^{-3}$)	1.172 / -2.041	3.189 / -3.554

^{a)} $R1 = \sum |F_o - F_c| / \sum |F_o|$

^{b)} $wR2 = [\sum [w(F_o^2 - F_c^2)^2] / \sum [w(F_o^2)^2]]^{1/2}$; $w = 1 / [\sigma^2(F_o^2) + (aP)^2 + bP]$ with $P = [\text{Max}(0, F_o^2) + 2F_c^2] / 3$

Table 2. Wyckoff positions, atomic coordinates, site occupancy, equivalent isotropic temperature factors and anisotropic displacement parameters (in Å²) for 39R-Sb₁₀Te₃ ($U_{13} = U_{23} = 0$).

atom	Wyck.	x	y	z	s.o.f.	U_{eq}	$U_{11} = U_{22} = 2U_{12}$	U_{33}
Te1	3a	0	0	0	1	0.0375(12)	0.0235(15)	0.066(3)
Sb1	6c	2/3	1/3	0.02808(5)	1	0.0383(9)	0.0284(10)	0.058(2)
Te2	6c	1/3	2/3	0.05018(3)	1	0.0256(9)	0.0240(11)	0.0288(19)
Sb2	6c	0	0	0.07986(4)	1	0.0284(8)	0.0242(11)	0.0368(18)
Sb3	6c	2/3	1/3	0.10044(3)	1	0.0206(8)	0.0218(9)	0.0181(16)
Sb4	6c	1/3	2/3	0.13116(4)	1	0.0298(9)	0.0216(12)	0.046(2)
Sb5	6c	0	0	0.15135(3)	1	0.0258(9)	0.0225(11)	0.032(2)

Table 3. Wyckoff positions, atomic coordinates, site occupancy, equivalent isotropic temperature factors and anisotropic displacement parameters (in Å²) for 33R-(Sb_{0.978}Pb_{0.022})₈Te₃ ($U_{13} = U_{23} = 0$).

atom	Wyck.	x	y	z	s.o.f.	U_{eq}	$U_{11} = U_{22} = 2U_{12}$	U_{33}
Te1	3a	0	0	0	1	0.0186(8)	0.0181(12)	0.0196(11)
Sb1/Pb1	6c	1/3	2/3	0.03102(5)	Sb 0.911(14) Pb 0.089(14)	0.0315(7)	0.0239(8)	0.0466(11)
Te2	6c	2/3	1/3	0.05790(3)	1	0.0186(6)	0.0165(9)	0.0227(8)
Sb2	6c	0	0	0.09485(4)	1	0.0202(5)	0.0165(8)	0.0276(9)
Sb3	6c	1/3	2/3	0.11874(4)	1	0.0185(6)	0.0152(9)	0.0252(8)
Sb4	6c	2/3	1/3	0.15475(4)	1	0.0160(4)	0.0126(7)	0.0229(8)

2.4.2.3 Simulation of diffraction patterns of disordered polytypes

For the simulation of diffraction patterns of disordered stacking variants, a general recursion method for calculating intensity distribution from crystals with coherent planar faults was used as implemented in the program DIFFaX.^[52] This method has frequently been used successfully to simulate powder diffraction patterns of disordered compounds.^[53-62] It exploits the recurring patterns in an ordered or disordered arrangement of defined layers (the layer sequence is given by stacking vectors and transition probabilities) to compute the average interference wavefunction scattered by each layer with a given layer structure factor. Powder diffraction patterns were simulated for randomized arrangements of structural motifs of phases (Sb₂)_k(Sb₂Te₃)_m. Details on the models used for the simulation can be found in later sections. A pseudo-Voigt profile function was used to simulate the powder diffraction pattern profiles with the wavelength of Cu $K\alpha_1$ radiation ($\lambda = 1.54051$ Å). Pattern fitting based on the Rietveld method was done using TOPAS.^[63]

2.4.3 Ambiguities of structure solution and ‘almost homometric’ structure models

All structure solution attempts for the binary antimony telluride $\text{Sb}_{10}\text{Te}_3$ indicate a 39R-type layered structure, but the number of layers per unit cell does not uniquely define the building blocks present. Furthermore, the similar atomic form factors of Sb and Te do not allow a straightforward differentiation of these elements by X-ray diffraction. However, the comparison of interatomic distances with those in well known compounds of the same elements usually allows the assignment of atom types and thus the derivation of a suitable structure model as we have outlined earlier.^[21] All structure solution methods yield atom positions which, by means of such comparisons, can be consistently interpreted as a sequence of five A7-type Sb_2 layers and one hypothetical SbTe_2 slab, *i.e.* $[-(\text{SbTe}_2)-(\text{Sb}_2)-(\text{Sb}_2)-(\text{Sb}_2)-(\text{Sb}_2)-]_{\infty}$. The hypothetical composition of such a compound is $\text{Sb}_{11}\text{Te}_2$. However, a hypothetical structure model of 39R- $\text{Sb}_{10}\text{Te}_3$ composed of four A7-type Sb_2 layers and one Sb_2Te_3 slab, *i.e.* $[-(\text{Sb}_2\text{Te}_3)-(\text{Sb}_2)-(\text{Sb}_2)-(\text{Sb}_2)-]_{\infty}$ was described by Kifune et al.,^[7] although this structure has not been observed experimentally so far. The two structure models (cf. Fig. 2) are incongruent and exhibit different sequences of interatomic distances, even if Sb and Te are not distinguished. Both structure models can be refined equally well on the same experimental data and the refined models remain incongruent.

Both refinements yield $R1$ and $wR2$ values around 0.06 and 0.11, respectively, for the observed reflections. The exact R values depend on the weighting schemes used, and if these are optimized individually for both models, the differences are insignificant. Both models exhibit reasonable interatomic distances; however, the first model (39R- $\text{Sb}_{11}\text{Te}_2$) derived from the structure solution contains SbTe_2 slabs, which have not yet been reported for any antimony telluride. Most important, its formula is inconsistent with the composition $\text{Sb}_{10}\text{Te}_3$ which has been approximately confirmed by EDX and is further proved by the preparation of homogeneous samples from stoichiometric mixtures of the elements. On the contrary, samples with the composition $\text{Sb}_{11}\text{Te}_2$ yield neither homogeneous samples nor single crystals similar to the one discussed here.

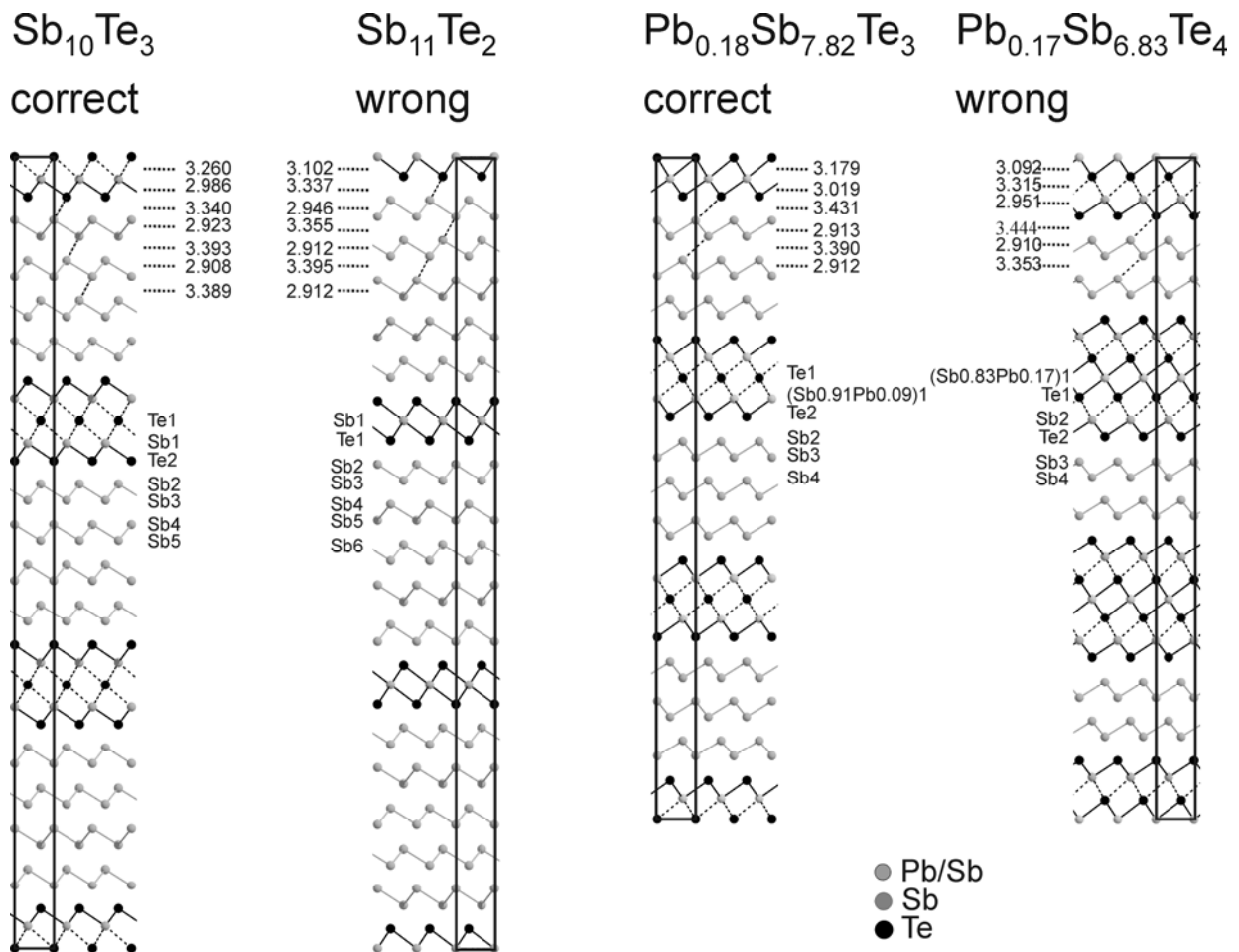


Figure 2. Projection of the correct and wrong ‘almost homometric’ structure models for $\text{Sb}_{10}\text{Te}_3$ and $(\text{Sb}_{0.978}\text{Pb}_{0.022})_8\text{Te}_3$ along [010], interatomic distances are given in Å (esd’s < 0.003 Å).

Therefore, the second model (39R- $\text{Sb}_{10}\text{Te}_3$) is the correct one as it is the only model that is consistent with the composition. The Sb atoms in the tetradymite-type Sb_2Te_3 layer exhibit a 3 + 3 coordination with Sb-Te bond lengths of 2.986 and 3.260 Å. These are comparable to values reported for other members of the homologous series $(\text{Sb}_2)_k(\text{Sb}_2\text{Te}_3)_m$. The four A7-type Sb_2 layers show a small distortion compared to those in elemental antimony, where the intra-layer distance is 2.908 Å and the inter-layer distance is 3.355 Å.^[11] In 39R- $\text{Sb}_{10}\text{Te}_3$, the distances depend on the position of the layers; however, the intra-layer distances (2.923, 2.908 Å) as well as the inter-layer distances (3.393, 3.389 Å) are still quite similar to those in elemental antimony and other antimony-rich antimony tellurides. The Sb-Te distance between the A7-type and the tetradymite-type blocks is 3.340 Å and indicates a van der Waals gap comparable to that in other homologous compounds of the series $(\text{Sb}_2)_k(\text{Sb}_2\text{Te}_3)_m$, where the corresponding distance lies between 3.3 and 3.5 Å.^[6,7] These distances are significantly shorter than the sum of the van der Waals radii^[64] for Sb (2.00 Å) and Te (2.06 Å), which indicates partial covalency.

Although the correct structure model can, in this case, be derived by chemical intuition and homology principles and is uniquely confirmed by chemical analysis, the two models yield almost identical diffraction patterns, which is shown by simulated powder patterns and in Fig. 3 (top). For these calculated patterns, isotropic displacement parameters were used in order to avoid levelling of small differences by anisotropic displacements with no physical meaning. The residual R_p calculated according to $|y(\text{correct model}) - y(\text{wrong model})| / y(\text{correct model}) = 0.0095$ represents the small degree of mismatch. If the wrong structure model is refined on a single-crystal data set calculated from the correct model in order to exclude the effect of experimental artefacts, the R value obtained is 0.0058.

Hence, for these examples, the unique relation between diffraction pattern and structure model does not hold within the typical error limits of data collection. In this context, the different non-congruent models for the $33R$ -type phase can be regarded as practically homometric and thus cannot be distinguished by X-ray diffraction alone. As can be seen from Fig. 2, the interatomic distance sets of the correct and wrong structure models are incongruent even when atom types are not distinguished; therefore, the ambiguity results neither from wrong atom-type assignments nor from anisotropic displacement parameters with no physical meaning, as described above. However, this effect is especially distinct as the interatomic vector sets, i.e. the Patterson functions of the wrong and correct structure models, are very similar and they consequently yield almost identical diffraction patterns. For $33R\text{-Sb}_{10}\text{Te}_3$, the coordinates x and y are zero for all positions ($3a$ and $6c$), so that the z coordinates define the interatomic distance sets of the structure models. The similar electron count of Sb and Te reduces the homometry effect to a onedimensional problem which can be described in terms of a cyclotomic set.^[27-29,65] However, the two structure models are almost, but not exactly, homometric.

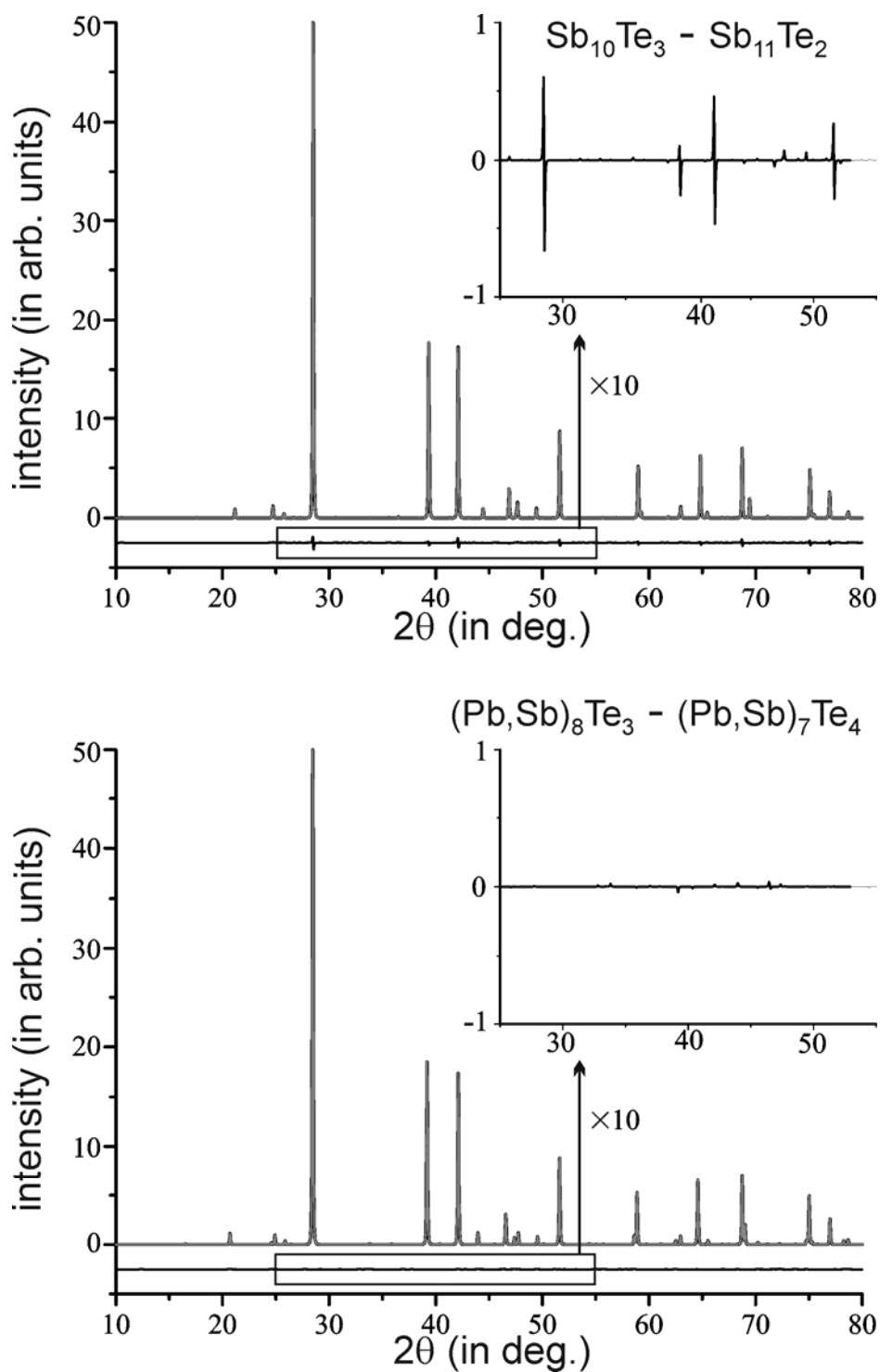


Figure 3. Powder diffraction patterns calculated from the correct and wrong models (cf. Figure 2) of $\text{Sb}_{10}\text{Te}_3$ (top) and $(\text{Sb}_{0.978}\text{Pb}_{0.022})_8\text{Te}_3$ (bottom) using the same isotropic displacement parameters for all atoms and a difference plot; the insert shows a magnified area to reveal the small difference between the respective models.

2.4.4 Influence of positional disorder on the reliability of structure solution

The ambiguities encountered during the structure determination of $(\text{Sb}_{0.978}\text{Pb}_{0.022})_8\text{Te}_3$, which exhibits a $33R$ -type structure, are similar to those observed during the analysis of $39R\text{-Sb}_{10}\text{Te}_3$. The initial (wrong) structure solution and atom assignment based on interatomic distances yielded a model containing rocksalt-type slabs composed of seven atom layers comparable to those in $21R\text{-PbSb}_2\text{Te}_4$.^[17,66] These alternate with pairs of two consecutive $A7$ -type Sb_2 layers, *i.e.* $[-(\text{PbSb}_2\text{Te}_4)-(\text{Sb}_2)-(\text{Sb}_2)-]_\infty$, as shown in Fig. 2. Again, another (correct) non-congruent structure model was constructed according to homology principles; it contains tetradymite-like $(\text{Pb,Sb})_2\text{Te}_3$ slabs that alternate with blocks of three $A7$ -type Sb_2 layers, *i.e.* $[-(\text{Pb,Sb})_2\text{Te}_3)-(\text{Sb}_2)-(\text{Sb}_2)-(\text{Sb}_2)-]_\infty$. This corresponds to a Pb-doped variant of Sb_8Te_3 .^[6,7,15]

In this case, both structure models are chemically very reasonable and contain only well known structural motifs. The seven-layer rocksalt-type blocks in the wrong model are very similar to those in both $21R\text{-GeSb}_2\text{Te}_4$ and $21R\text{-SnSb}_2\text{Te}_4$.^[67,68] These compounds are composed exclusively of such blocks, which consist of seven alternating cation and anion layers and are interconnected by Te–Te van der Waals interactions. It is well known that the different chemical surroundings of Te near these van der Waals gaps induce positional displacements of the nearest Sb atoms and furthermore influence the elemental distribution within the slabs^[69] in the same way as described below for the compound investigated in this study. The structure elements in the correct model have already been described above. In the structure analyses, Sb/Pb mixed site occupancies were refined for the cation positions and anisotropic displacement parameters were used for all atoms. No unusual displacements were observed. The wrong structure model based on the initial solution converged at $R1 = 0.0299$ and yielded the chemical composition $\text{Sb}_{6.83}\text{Pb}_{0.17}\text{Te}_4 = \text{Sb}_{1.71}\text{Pb}_{0.04}\text{Te}$, whereas the correct model derived from homology principles converged at $R1 = 0.0298$ and yielded the composition $\text{Sb}_{7.82}\text{Pb}_{0.18}\text{Te}_3 = \text{Sb}_{2.61}\text{Pb}_{0.06}\text{Te}$. The composition derived from the correct model is consistent with the element ratio derived by EDX, whereas the antimony content of the wrong model is significantly lower and thus strongly deviates from the analysis. This result is corroborated by the fact that homogeneous samples whose powder patterns correspond to the one calculated from the model obtained from single-crystal data can only be prepared with the correct stoichiometry. This means that, similar to the case of $\text{Sb}_{10}\text{Te}_3$, the correct structure model can only be assigned if the chemical composition is known. Despite the similar form factors of Sb and Te, the models themselves allow no other element distribution without accepting unreasonable interatomic distances.

Similar to $\text{Sb}_{10}\text{Te}_3$, the cation tetradymite-type layers in $(\text{Sb}_{0.978}\text{Pb}_{0.022})_8\text{Te}_3$ exhibit a 3 + 3 coordination with M—Te bond lengths (M = Sb, Pb) of 3.019 and 3.179 Å. The M—Te bonds facing the van der Waals gaps are shorter (cf. Fig. 2) as these Te atoms do not have strong bonds on one side. Compared to the isotypic binary phase $33R\text{-Sb}_8\text{Te}_3$ [2.956, 3.240 Å; described as $\text{Sb}_{72}\text{Te}_{28}$ by Kifune et al.^[7]], the mixed cation site occupancy with Pb and Sb reduces the distortion and leads to weaker bonding towards the van der Waals gap since $\text{Pb}^{+\text{II}}$ increases the degree of ionicity. The A7-type antimony layers show only a slight variation of the intra-layer distances depending on the position within the stacking sequence (cf. Fig. 2); they are very similar to the A7-type layers found in elemental antimony. The Sb—Te distance between the tetradymite-type and A7-type blocks (3.431 Å) indicates a van der Waals-like gap similar to those in the phases $(\text{Sb}_2)_k(\text{Sb}_2\text{Te}_3)_m$ (3.3–3.5 Å).^[6,7]

The correct structure model can be derived from the single-crystal data taking into account the chemical composition; however, the two non-congruent structure models cannot be distinguished on the basis of their experimental diffraction patterns. In this case, the residual Rp calculated from simulated powder patterns according to $|y(\text{correct model}) - y(\text{wrong model})| / y(\text{correct model})$ is just 0.0005 (cf. Fig. 3, bottom). This means that these two models are even closer to a homometric pair than those for $39R\text{-Sb}_{10}\text{Te}_3$. In this case, the similarity is not only due to the interatomic distance set itself as not all atoms exhibit similar form factors. If the Pb doping is neglected and the positions are solely occupied by Sb and Te, respectively, the difference between the diffraction patterns increases. A single-crystal data set calculated from the correct model of the Pb-doped phase yields $R1 = 0.013$ for the wrong model, whereas the same procedure yields only $R1 = 0.018$ for analogous models of $33R\text{-Sb}_8\text{Te}_3$ and $33R\text{-Sb}_7\text{Te}_4$ with the same positions. The small discrepancy between ‘almost homometric’ structures may thus be decreased (or, in other cases, increased) by doping and consequently varying the scattering density of specific positions. As homometry in a strict sense is not present, the differences between two models may be levelled by chemical disorder. Furthermore, it must be considered that anisotropic displacement parameters, although physically very reasonable, may level the R values by modelling experimental errors: the two models have almost the same R value of 0.030 when refined on experimental data, whereas it is 0 for the correct and 0.013 for the wrong model when refined on calculated data free of experimental error.

2.4.5 Ambiguities arising from stacking disorder

Additional ambiguities in structure analyses of layered chalcogenides may arise from stacking disorder. Of course, such disorder leads to diffuse streaks; however these may be rather weak and, especially in powder diffraction patterns, it may be almost impossible to distinguish intrinsic diffuse scattering from extrinsic background. If diffuse scattering is neglected, structure refinements based on Bragg data yield averaged structure models. Even if the average structure is correctly determined, it may be rather misleading from a chemical point of view and its interpretation may differ significantly from the actual situation.

We shall demonstrate such a situation for the compound $\text{Sb}_{14}\text{Te}_3$. Although the structure has not been refined in detail, Kifune et al.^[7] have taken into account the structural principles of the homologous series $(\text{Sb}_2)_k(\text{Sb}_2\text{Te}_3)_m$ and proposed a very reasonable structure model with a 51R-type structure of tetradymite-type Sb_2Te_3 blocks alternating with six A7-type Sb_2 layers in a long-range ordered fashion. We have calculated powder patterns for different types of disordered stacking variants and will demonstrate the influence of disorder on Rietveld pattern fitting. The disorder model employs two basic building units, *i.e.* the tetradymite-like Sb_2Te_3 slab and corrugated honeycomb nets of Sb atoms, *i.e.* the typical layers found in A7-type structures. Typical interatomic distances within the layers as well as typical translation vectors between layers were taken from the structure refinement of 9P- Sb_6Te_3 ^[24] which itself crystallizes with a stacking sequence of $[-(\text{Sb}_2\text{Te}_3)-(\text{Sb}_2)-(\text{Sb}_2)-]_\infty$ ($P\bar{3}m1$, $a = 4.272$, $c = 17.633$ Å). The influence of the stacking sequence on the structure of the individual layers and on average lattice parameters is very small and was neglected. The degree of disorder in the arrangements of the basic building units depends on the stacking probabilities. We assumed a completely random stacking of layers that yields the desired composition, except for the rule that tetradymite-type slabs do not follow each other in accordance with known structures of comparable phases. This means that the A7-type blocks randomly vary in thickness. Powder diffraction patterns of such disordered phases are shown in Fig. 4 (bottom) for compositions $(\text{Sb}_2)_k(\text{Sb}_2\text{Te}_3)$ with $k = 2-7$. For low Sb contents, diffuse intensities show pronounced maxima, which become smoother and smoother with increasing Sb content. The Bragg reflections corresponding to the primitive rhombohedral (α -Hg type) average structure (*cf.* §1) are almost unaffected by the Sb content. They may also be viewed as family reflections of order-disorder structures. The weak superstructure reflections indicative of distinct long periodically ordered polytypes develop into diffuse scattering in disordered phases.

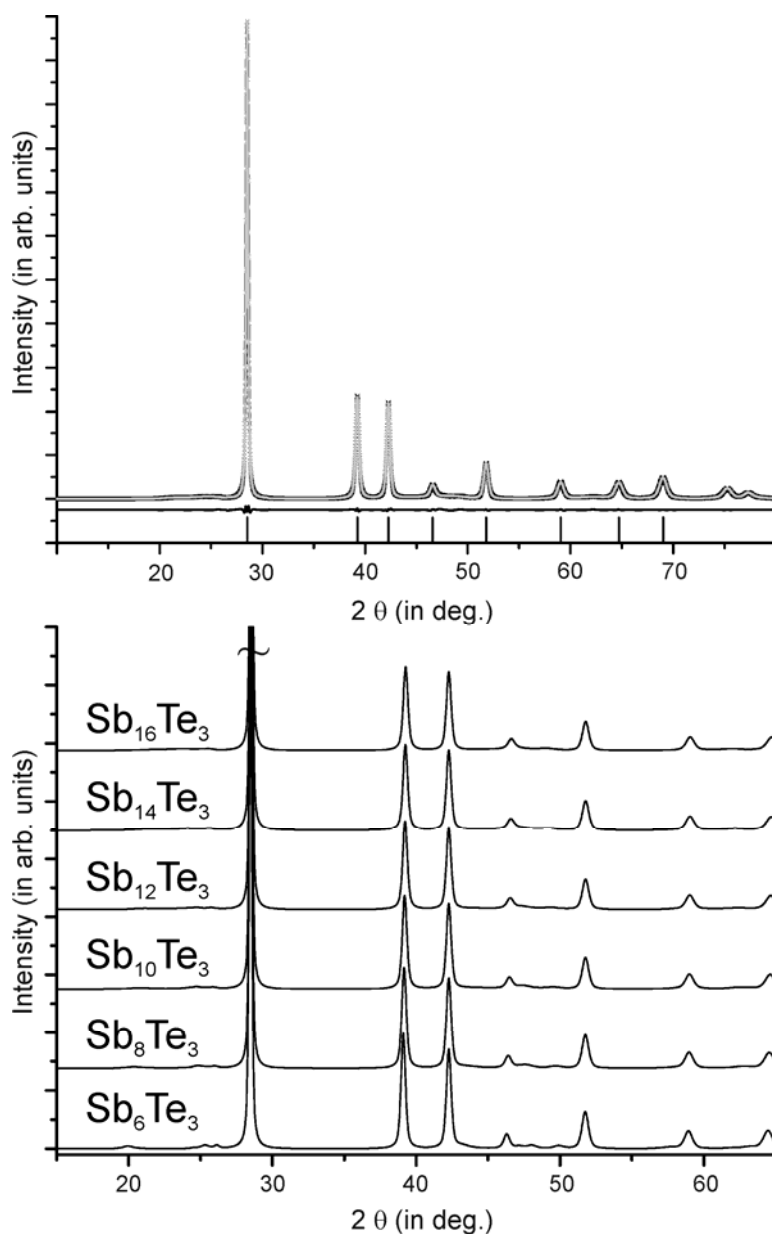


Figure 4. Powder patterns simulated for completely disordered phases $(\text{Sb}_2)_k(\text{Sb}_2\text{Te}_3)$ ($k = 2 - 7$) and a Rietveld plot obtained by fitting the calculated pattern for $k = 6$ with a randomly disordered α -Hg type model (cf. text).

If such diffraction patterns are encountered experimentally, the diffuse scattering will often be overlooked, especially if the Sb content is high. In such cases, the α -Hg-type average structure will be found. Fig. 4 (top) shows a seemingly very convincing Rietveld fit of the calculated diffraction pattern of completely disordered $\text{Sb}_{14}\text{Te}_3$ based on the average α -Hg-type model [$R\bar{3}m$, $a = 4.272(3)$, $c = 5.843(5)$ Å] with just the Wyckoff position $3a$ occupied with Sb and Te in the ratio 14:3. This refinement converges at $R_p = 0.0205$ ($R_{wp} = 0.0382$, goodness of fit = 1.389) if a small degree of preferred orientation and anisotropic peak broadening is taken into account, as would be done in any experimental pattern fitting. Except for the preferred orientation, which is of course not present in synthetic data, such an average structure is basically

correct. However, if the diffuse scattering is not recognized and one has no prior knowledge of the structural chemistry of such phases, one may tend to interpret this average structure as a random distribution of Sb and Te in the rhombohedral lattice. Such a structure appears like an almost isotropic metal lattice, whereas the real situation is a pronounced layered structure where, for example, Sb bonds either to three other Sb atoms of the A7-type layers or to six Te atoms of the tetradymite-type layer. This means that the atom arrangement is far from random as there are only two distinct environments for Sb. Although there is almost no mistake in the process of structure determination, there is a huge difference between a random atom distribution and the real structure from a chemical point of view. The structure contains very pronounced short-range order and is far from isotropic.

2.4.6 Conclusion

The ambiguities in the structure analysis of layered antimony tellurides described in this paper involve non-congruent structure models that correspond to almost homometric pairs, independent of the problem of differentiating Sb and Te. The correct and wrong models are characterized by comparable low R values and exhibit well behaved displacement parameters. It needs to be emphasized that even high-quality experimental diffraction data do not contain enough information to uniquely identify the correct model. Interestingly, most of the few practical examples of homometry, such as CdI_2 or FeTa_2O_6 ,^[39,41] are related to the stacking sequence in layer-like structures and/or to superstructure formation. Hence, such effects need to be considered in structure analyses, especially if the compounds form homologous series. The problems described here, and probably many others, too, can be resolved by using complementary data such as chemical analysis. In some cases it may also be possible to reduce the problem by enhancing the diffraction contrast by anomalous scattering which has the same effect as doping with lighter elements. High-resolution electron microscopy may also be a valuable complementary technique.

The synthetic powder diffraction data of a one-dimensional disordered stacking sequence of tetradymite- and A7-type layers may demonstrate that although the average structure is correctly refined, in this case using an α -Hg average structure with only one crystallographic position, one usually tends to incorrectly interpret it in terms of random disorder. This results from the fact that diffuse scattering can often not be distinguished from the background in experimental data. Especially in powder patterns, diffuse streaks in reciprocal space almost seem to vanish. This is almost trivial; however, it is especially relevant concerning disordered tellurides. For example,

simple disordered average structures have been reported for metastable phases of phase-change materials such as $\text{Ag}_{3.4}\text{In}_{3.7}\text{Sb}_{76.4}\text{Te}_{16.5}$ and $\text{Ge}_{7.1}\text{Sb}_{76.0}\text{Te}_{16.9}$, which are used for data storage media.^[71,72] High-temperature phases of these materials crystallize in the α -Hg average structure discussed above. Such compounds often exhibit long periodically ordered layered structures at equilibrium conditions, parts of which may be realistic models for the local structure in disordered modifications. This means that their structures are essentially layered on an intermediate length scale, i.e. much less isotropic than the (correct!) average structure model.

As multinary antimony and bismuth tellurides are also promising candidates for high-performance thermoelectric,^[73,74] the ambiguities described in this paper cannot of course be neglected if structure–property relationships are to be established. Crystallographers and materials scientists alike should be aware of such pitfalls in structure analysis, especially as these might not be detectable in a straightforward way.

2.4.7 References

- [1] Z. A. Gál, O. J. Rutt, C. F. Smura, T. P. Overton, N. Barrier, S. J. Clarke, J. Hadermann, *J. Am. Chem. Soc.* **2006**, *128*, 8530.
- [2] A. Mrotzek, G. M. Kanatzidis, *Acc. Chem. Res.* **2003**, *36*, 111.
- [3] D.-Y. Chung, T. Hogan, P. Brazis, M. Rocci-Lane, C. Kannewurf, M. Bastea, C. Uher, G. M. Kanatzidis, *Science* **2000** *287*, 1024.
- [4] L. A. Klinkova, M. Uchida, Y. Matsui, V. I. Nikolaichik, N. V. Barkovskii, *Phys. Rev. B* **2003**, *67*, 140501.
- [5] D. R. Veblen, *Am. Mineral.* **1991**, *76*, 801.
- [6] P. F. P. Poudeu, M. G. Kanatzidis, *Chem. Commun.* **2005**, *21*, 2672.
- [7] K. Kifune, Y. Kubota, T. Matsunaga, N. Yamada, *Acta Crystallogr. Sect. B* **2005**, *61*, 492.
- [8] K. Yamana, K. Kihara, T. Matsumoto, *Acta Crystallogr. Sect. B* **1997**, *35*, 147.
- [9] J. W. G. Bos, H. W. Zandbergen, M.-H. Lee, N. P. Ong, R. J. Cava, *Phys. Rev. B* **2007**, *75*, 195203.
- [10] D. Schiferl, C. S. Barrett, *J. Appl. Crystallogr.* **1969**, *2*, 30.
- [11] C. S. Barrett, P. Cucka, K. Haefner, *Acta Crystallogr.* **1963**, *16*, 451.
- [12] P. Cucka, C. S. Barrett, *Acta Crystallogr.* **1962**, *15*, 865.
- [13] T. L. Anderson, H. B. Krause, *Acta Crystallogr. Sect. B* **1974**, *30*, 1307.
- [14] P. Bayliss, *Am. Mineral.* **1991**, *76*, 257.

- [15] L. E. Shelimova, O. G. Karpinskii, M. A. Kretova, V. I. Kosyakov, V. A. Shestakov, V. S. Zemskov, F. A. Kuznetsov, *Inorg. Mater.* **2000**, *36*, 768.
- [16] L. E. Shelimova, O. G. Karpinskii, P. P. Konstantinov, E. S. Avilov, M. A. Kretova, V. S. Zemskov, *Inorg. Mater.* **2004**, *40*, 451.
- [17] L. E. Shelimova, O. G. Karpinskii, T. E. Svechnikova, E. S. Avilov, M. A. Kretova, V. S. Zemskov, *Inorg. Mater.* **2004**, *40*, 1264.
- [18] T. B. Zhukova, A. I. Zaslavskii, *Sov. Phys. Crystallogr.* **1972**, *16*, 796.
- [19] A. Stegherr, *Philips Res. Rep. Suppl.* **1969** Issue 6.
- [20] M. N. Schneider, O. Oeckler, *Z. Anorg. Allg. Chem.* **2010**, *636*, 137.
- [21] M. N. Schneider, M. Seibald, O. Oeckler, *Dalton Trans.* **2009**, 2004.
- [22] R. M. Imamov, S. A. Semiletov, *Sov. Phys. Crystallogr.* **1971**, *15*, 845.
- [23] T. Matsunaga, N. Yamada, Y. Kubota, *Acta Crystallogr.* **2004**, *B60*, 685.
- [24] V. Agafonov, N. Rodier, R. Céolin, R. Bellissent, C. Bergman, J. P. Gaspard, *Acta Crystallogr. Sect. C* **1991**, *47*, 1141.
- [25] H. Lind, S. Lidin, *Solid State Sci.* **2003**, *5*, 47.
- [26] C. L. Ciobanu, A. Pring, N. J. Cook, P. Self, D. Jefferson, G. I. Dima, V. Melnikov *Am. Mineral.* **2009**, *94*, 517.
- [27] A. L. Patterson, *Nature* **1939**, *3631*, 939.
- [28] A. L. Patterson, *Phys. Rev.* **1944**, *65*, 195.
- [29] J. M. Buerger, *Can. Mineral.* **1978**, *16*, 301.
- [30] J. N. Franklin, *Acta Crystallogr. Sect A* **1974**, *30*, 698.
- [31] U. Grimm, M. Baake, *Z. Kristallogr.* **2008**, *223*, 777.
- [32] M. Baake, U. Grimm, *Z. Kristallogr.* **2007**, *222*, 54.
- [33] J. Rosenblatt, *Commun. Math. Phys.* **1984**, *95*, 317.
- [34] J. Rosenblatt, P. D. Seymour, *SIAM J. Alg. Disc. Methods* **1982**, *3*, 343.
- [35] R. Hosemann, S. N. Bagchi, *Acta Crystallogr.* **1954**, *7*, 237.
- [36] P. C. Jain, G. C. Trigunayat, *Acta Crystallogr. Sect. A* **1977**, *33*, 257.
- [37] E. Zobetz, *Cryst. Res. Technol.* **1994**, *29*, 379.
- [38] H. Dachs, *Z. Kristallogr.* **1956**, *107*, 370.
- [39] K. Fichtner, *Acta Crystallogr. Sect A* **1986**, *42*, 98.
- [40] J. G. Thompson, A. D. Rae, R. L. Withers, T. R. Welberry, A. C. Willis, *J. Phys. C Solid State Phys.* **1988**, *21*, 4007.
- [41] S. Hansen, A. Landa-Cánovas, K. Ståhl, J. Nilsson, *Acta Crystallogr. Sect A* **1995**, *51*, 514.

- [42] K. Dornberger-Schiff, *Acta Crystallogr.* **1956**, *9*, 593.
- [43] S. Đurovič, J. Hybler, *Z. Kristallogr.* **2006**, *221*, 63.
- [44] Stoe & Cie, *WinXPOW*. Stoe & Cie, Darmstadt, Germany, **2005**.
- [45] G. M. Sheldrick, *Acta Crystallogr. Sect A* **2008**, *64*, 112.
- [46] G. Oszlányi, A. Sütő, *Acta Crystallogr. Sect A* **2004**, *60*, 134.
- [47] G. Oszlányi, A. Sütő, *Acta Crystallogr. Sect A* **2005**, *61*, 147.
- [48] V. Petricek, M. Dusek, L. Palatinus, *JANA2006* Institute of Physics, Prague, Czech Republic, **2006**.
- [49] Stoe & Cie, *X-SHAPE 1.05* Stoe & Cie, Darmstadt, Germany. Based on the program HABITUS by W. Herrendorf, University of Giessen, Germany, **1999**.
- [50] Stoe & Cie *XRED-32 1.03*. Stoe & Cie, Darmstadt, Germany, **2002**.
- [51] Bruker *XPREP*. Version 6.12. Bruker AXS Inc., Madison, Wisconsin, USA, **1996**.
- [52] Treacy, M. M. J., Newsam, J. M. & Deem, M. W. (1991). *Proc. R. Soc. London Ser. A*, **1991**, *433*, 499.
- [53] T. N. Ramesh, P. V. Kamath, C. Shivakumara, *Acta Crystallogr. Sect B* **2006**, *62*, 530.
- [54] A. V. Radha, C. Shivakumara, P. V. Kamath, *Clays Clay Miner.* **2005**, *53*, 520.
- [55] H. Dittrich, M. Wohlfahrt-Mehrens, *Int. J. Inorg. Mater.* **2001**, *3*, 1137.
- [56] J. Kim, T. Hughbanks, *J. Solid State Chem.* **2000**, *149*, 242.
- [57] L. Croguennec, C. Pouillier, A. N. Mansour, C. Delmas, *J. Mater. Chem.* **2001**, *11*, 131.
- [58] P. Norby, R. E. Johnsen, *J. Phys. Chem. C* **2009**, *113*, 19061.
- [59] M. Casas-Cabanas, J. Rodríguez-Carvajal, J. Canales-Vázquez, Y. Laligant, P. Lacorre, M. R. Palacín, *J. Power Sources* **2007**, *174*, 414.
- [60] J. Breu, W. Seidl, A. Stoll, *Z. Anorg. Allg. Chem.* **2003**, *629*, 503.
- [61] A. Leineweber, M. Leoni, *Z. Kristallogr. Suppl.* **2009**, *30*, 423.
- [62] A. F. Gualtieri, S. Ferrari, M. Leoni, G. Grathoff, R. Hugo, M. Shatnawi, G. Paglia, S. Billinge, *J. Appl. Crystallogr.* **2008**, *41*, 402.
- [63] A. Coelho, *TOPAS-Academic* Coelho Software, Brisbane, Australia, **2007**.
- [64] A. Bondi, *J. Phys. Chem.* **1964**, *68*, 441.
- [65] F. A. Grünbaum, C. C. Moore, *Acta Crystallogr. Sect A* **1995**, *51*, 310.
- [66] L. E. Shelimova, O. G. Karpinskii, T. E. Svechnikova, I. Y. Nikhezina, E. S. Avilov, M. A. Kretova, V. S. Zemskov, *Inorg. Mater.* **2008**, *44*, 371.
- [67] T. Matsunaga, N. Yamada, *Phys. Rev. B* **2004**, *69*, 104111.

- [68] G. Concas, T. M. de Pascale, L. Garbato, F. Ledda, F. Meloni, A. Rucci, M. Serra, *J. Phys. Chem. Solids* **1992**, *53*, 791.
- [69] M. N. Schneider, O. Oeckler, *Z. Anorg. Allg. Chem.* **2008**, *634*, 2557.
- [70] T. Matsunaga, N. Yamada, *Jpn. J. Appl. Phys.* **2002**, *41*, 1674.
- [71] T. Matsunaga, N. Yamada, *Jpn. J. Appl. Phys.* **2004**, *43*, 4704.
- [72] G. J. Snyder, E. S. Toberer, *Nat. Mater.* **2008**, *7*, 105.
- [73] J. R. Sootsman, D. Y. Chung, M. G. Kanatzidis, *Angew. Chem. Int. Ed.* **2009**, *48*, 8616.

3 Long-periodic ordered layered structures $(\text{MTe})_n\text{M}'_2\text{Te}_3(\text{M}_2)_k$ as model systems for “multilayer superlattices”

3.1 Overview

In recent years, more and more attention has been paid to the optimization of thermoelectrics as well as phase-change materials based on multinary chalcogenides. Interestingly, for both fields of application one promising approach is the use of superlattices that consist of thin lamellae of different materials deposited layer-per-layer in periodical arrangement.^[1-9] Such multilayer arrangements promise various advantages compared to bulk materials. While phonon scattering at the interfaces between the thin layers can be exploited to reduce the phononic part of the thermal conductivity, the modified band structure as a consequence of the superlattice structure allows one to maintain or even enhance the electron transport.^[1] In addition, the different lamellae can consist of materials with very different properties, e.g. metallic and insulating layers might be combined in superlattices and the design of such multilayer structures allows for an optimization of their properties. Concerning thermoelectrics, the main focus has been the reduction of the thermal conductivity. Superlattices based on $\text{Bi}_2\text{Te}_3\text{-Sb}_2\text{Te}_3$ (grown by chemical vapour deposition) or PbTe-PbSe (grown by molecular beam epitaxy) first exemplified that very low thermal conductivities can be obtained by a superlattice approach.^[4,10] For data storage media, in particular non-volatile memory based on phase-change materials, a reduced thermal conductivity also contributes to the heat transfer management of devices.^[11] The basic concept to optimize the write and erase properties by a superlattice approach, however, is to co-deposit a phase-change material of high kinetic stability but low crystallization speed with one of high crystallization speed which is less inert. At the interfaces, structural rearrangements are facilitated which allows for high switching speeds and low operating voltages as has been demonstrated for example for superlattice-like structures composed of GeTe lamellae and Sb_7Te_3 layers.^[9]

In this context, the structural elucidation of layered multinary chalcogenides $(\text{GeTe})_n\text{Sb}_2\text{Te}_3$ or $(\text{Sb}_2\text{Te}_3)_m(\text{Sb}_2)_k$ is of great interest as some of these compounds exhibit very large translation periods. In $(\text{GeTe})_6\text{Sb}_2\text{Te}_3$ ($R\bar{3}m$, $a = 4.1759(2)$, $c = 93.396(4)$ Å) these are due to very thick distorted rocksalt-type blocks,^[12] in $(\text{Sb}_2)(\text{Sb}_2\text{Te}_3)_3$ ($R\bar{3}m$, $a = 4.274(1)$, $c = 102.69(9)$ Å) they are due to the arrangement of Sb_2Te_3 units and Sb blocks;^[13] both are comparable to those of

superlattice structures obtained by layer-per-layer deposition, e.g. Bi₂Te₃ (10 Å)/Sb₂Te₃ (50 Å) multilayers.^[1,4] As shown in the following sections (Chapter 3.2 - 3.3), additional metastable long-periodic phases with combinations of building blocks found in the series of stable compounds (GeTe)_n(Sb₂Te₃)_m and (Sb₂Te₃)_m(Sb₂)_k can be obtained by “partial spinodal decomposition” and subsequent annealing. Such compounds with the general formulae (MTe)_nSb₂Te₃(Sb₂)_k (M = Ge or Ag/Sb), have not been previously reported. The first examples synthesized were *9P*-GeSb₄Te₄ = (GeTe)Sb₂Te₃(Sb₂) (*P* $\bar{3}m1$, $a = 4.2466(2)$ Å, $c = 17.483$ Å, $R1 = 0.0355$) (cf. Chapter 3.2), *51R*-Ge_{2-x}Sb_{10+x}Te₅ \approx (GeTe)₂Sb₂Te₃(Sb₂)₄ ($x = 0.43$; *R* $\bar{3}m$, $a = 4.258(1)$ Å, $c = 97.23(2)$ Å, $R = 4.38\%$) and *15P*-Ag_xSb_{11-x}Te₄ \approx (Ag_{0.5}Sb_{0.5}Te)Sb₂Te₃(Sb₂)₄ ($x = 0.24$; *P* $\bar{3}m1$, $a = 4.282(1)$ Å, $c = 28.638(5)$ Å, $R = 5.38\%$) (cf. Chapter 3.3). Ge atoms may be replaced by a mixture of Ag and Sb, as exemplified by *15P*-Ag_xSb_{11-x}Te₄. According to the phase diagrams, these phases are metastable; however, temperature-dependent powder diffraction on *9P*-GeSb₄Te₄ as well as thermoanalytical measurements for all three compounds neither reveal any structural changes nor indicate decomposition before the phases melt at 540 °C (*9P*-GeSb₄Te₄), 529 °C (*51R*-Ge_{2-x}Sb_{10+x}Te₅) or 525 °C (*15P*-Ag_xSb_{11-x}Te₄), respectively. All three compounds show a metallic temperature dependency of their electrical conductivities. Their absolute values of the conductivity at room temperature are rather low compared to typical metals (*9P*-GeSb₄Te₄: 33 Scm⁻¹, *51R*-Ge_{2-x}Sb_{10+x}Te₅: 2500 Scm⁻¹, and *15P*-Ag_xSb_{11-x}Te₄: 588 Scm⁻¹). Although the absolute values for the electrical conductivity should not be over-interpreted, the comparison of the three compounds indicates that with increasing lattice parameters of the layered structure, the conductivity increases. The structure of the compounds can be described as an ordered stacking sequence of corrugated honeycomb nets of antimony with distorted rocksalt-type slabs comprising alternating cation and anion layers. *9P*-GeSb₄Te₄ contains one antimony layer sandwiched between distorted rocksalt-type blocks as found in *21R*-GeSb₂Te₄.^[14,15] Interestingly, although the structure is clearly non-congruent with other *9P*-type tellurides like Ge₂Sb₂Te₅ = (GeTe)₂Sb₂Te₃^[16] and Sb₂Te = Sb₂Te₃(Sb₂)₂^[17], diffraction patterns are very similar, indicating the occurrence of pseudo-homometry which is further corroborated as models corresponding to the known layered phases represent false minima during structure solution and refinement (cf. Chapter 2.4). A combined approach based on structural predictions from metrics determined by powder diffraction and comparison of typical interatomic distance sets of similar phases those derived from initial structure solution on single-crystal data was used to determine the structure of *51R*-Ge_{2-x}Sb_{10+x}Te₅ ($x = 0.43$) and *15P*-Ag_xSb_{11-x}Te₄ ($x = 0.24$). Structure refinements reveal that both compounds exhibit layered structures with large lattice parameters that can be described as alternating stacking sequence of

four antimony layers (gray-arsenic type) with distorted rocksalt-type slabs similar to those in $9P\text{-Ge}_2\text{Sb}_2\text{Te}_5$ and $21R\text{-GeSb}_2\text{Te}_4$, respectively. Whereas no diffuse streaking indicative of stacking disorder was observed in reciprocal lattice sections, all three phases exhibit positional disorder with respect to cation site occupancies in the distorted rocksalt-type slabs. Whereas in the tetrelide pnictogen tellurides all cation positions are shared by Ge and Sb atoms in variable ratios, antimony prefers Wyckoff positions neighboring the adjacent antimony slab and Ag concentrates exclusively on these positions. According to the structure refinements based on laboratory data, the blocks between the distorted rocksalt-type slabs are composed exclusively of antimony which is further corroborated by the good agreement of refined and experimentally determined compositions.

In contrast to $\text{Ag}_x\text{Sb}_{11-x}\text{Te}_4$ ($x = 0.24$) = $(\text{Ag}_{0.5}\text{Sb}_{0.5}\text{Te})\text{Sb}_2\text{Te}_3(\text{Sb}_2)_4$ which exhibits a $15P$ -type structure as expected from the composition, $39R\text{-Ge}_{0.067}\text{Sb}_{0.667}\text{Te}_{0.266}$ = $(\text{GeTe})\text{Sb}_2\text{Te}_3(\text{Sb}_2)_4$ ($R\bar{3}m$, $a = 4.2649(1)$, $c = 75.061(2)$ Å) and $39R\text{-Sn}_{0.067}\text{Sb}_{0.667}\text{Te}_{0.266}$ = $(\text{GeTe})\text{Sb}_2\text{Te}_3(\text{Sb}_2)_4$ ($R\bar{3}m$, $a = 4.2959(1)$, $c = 75.392(2)$ Å) - which exhibit similar element ratios - do not form $15P$ -type structures (cf Chapter 3.4). Similar to $\text{Ge}_4\text{Sb}_2\text{Te}_7$ = $(\text{GeTe})_4\text{Sb}_2\text{Te}_3$ for which a $39R$ -type structure is predicted from the composition but which crystallizes in a $33R$ -type expected for the composition $\text{Ge}_3\text{Sb}_2\text{Te}_6$ = $(\text{GeTe})_3\text{Sb}_2\text{Te}_3$ (cf. Chapter 2.3), $39R\text{-Ge}_{0.067}\text{Sb}_{0.667}\text{Te}_{0.266}$ and $39R\text{-Sn}_{0.067}\text{Sb}_{0.667}\text{Te}_{0.266}$ crystallize in the $39R$ -type characteristic for $\text{Sb}_{10}\text{Te}_3$ = $\text{Sb}_2\text{Te}_3(\text{Sb}_2)_4$ (cf. Chapter 2.4). The compounds therefore basically might be described as GeTe or SnTe substituted variants of this binary pnictogen telluride which itself exhibits a periodic arrangement of four gray-arsenic type antimony layers with one Sb_2Te_3 slab. However, the structure of $39R\text{-Ge}_{0.067}\text{Sb}_{0.667}\text{Te}_{0.266}$ and $39R\text{-Sn}_{0.067}\text{Sb}_{0.667}\text{Te}_{0.266}$ is more complex as its homogeneity range results from interdependent concentration modulation of the site occupancies of all Wyckoff positions as revealed by STEM-HAADF Z-contrast imaging on $39R\text{-Ge}_{0.067}\text{Sb}_{0.667}\text{Te}_{0.266}$. In order to enhance the scattering contrast for the single-crystal structure determination, data of both phases were collected using synchrotron radiation at the K edges of elements with similar atomic number. Joint refinements on these single-crystal diffraction data confirm the concentration gradients for both phases and reveal that not only cation positions within the Sb_2Te_3 slabs are occupied by a mixture of Ge and Sb or Sn and Sb atoms, respectively, but that the antimony slabs adjacent to the Sb_2Te_3 blocks are partially substituted by GeTe and SnTe, respectively. This element distribution might be regarded as intermediate state of spinodal composition, but can also be viewed as model for the interdiffusion of different layers in superlattices prepared by layer-per-layer deposition. Interestingly, the thermal conductivity of both phases lies in between that of elemental antimony

and the compounds $(MTe)_n(Sb_2Te_3)_m$ ($M = Ge, Sn$). Although the maximal thermoelectric figure of merit of $39R-Ge_{0.067}Sb_{0.667}Te_{0.266}$ and $39R-Sn_{0.067}Sb_{0.667}Te_{0.266}$ does not exceed 0.06 at 400 °C, these compounds as well as the phases $9P-GeSb_4Te_4$, $51R-Ge_{2-x}Sb_{10+x}Te_5$ ($x = 0.43$) or $15P-Ag_xSb_{11-x}Te_4$ ($x = 0.23$) are intriguing model systems for metal (gray-arsenic type lamellae) – semiconductor $((MTe)_n(Sb_2Te_3)_m)$ $M = Ge, Sn, Ag/Sb$ heterostructures.

References for Chapter 3.1

- [1] H. Böttner, G. Chen, R. Venkatasubramanian, *MRS Bull.* **2006**, *31*, 211.
- [2] M. S. Dresselhaus, G. Chen, M. Y. Tang, R. Yang, H. Lee, D. Wang, Z. Ren, J.-P. Fleurial, P. Gogna, *Adv. Mater.* **2007**, *19*, 1.
- [3] D. L. Medlin, G. J. Snyder, *Curr. Opin. Colloid Interface Sci.* **2009**, *14*, 226.
- [4] R. Venkatasubramanian, E. Siivola, T. Colpitts, B. O'Quinn, *Nature* **2001**, *413*, 597.
- [5] T. C. Chong, L. P. Shi, R. Zhao, P. K. Tan, J. M. Li, H. K. Lee, X. S. Miao, A. Y. Du, C. H. Tung, *Appl. Phys. Lett.* **2006**, *88*, 3.
- [6] T. C. Chong, L. P. Shi, X. S. Miao, P. K. Tan, R. Zhao, Z. P. Cai, *Jpn. J. Appl. Phys.* **2000**, *39*, 737.
- [7] M. Hase, Y. Miyamoto, J. Tominaga, *Phys. Rev. B* **2009**, *79*, 174112.
- [8] J. Tominaga, P. Fons, A. Kolobov, T. Shima, C. C. Chong, R. Zhao, H. K. Lee, L. Shi, D. D. Johnson, *Jpn. J. Appl. Phys.* **2008**, *47*, 5763.
- [9] H. Yang, T. C. Chong, R. Zhao, H. K. Lee, J. Li, K. G. Lim, L. Shi, *Appl. Phys. Lett.* **2009**, *94*, 203110.
- [10] T. C. Harman, P. J. Taylor, M. P. Walsh, B. E. LaForge, *Science* **2002**, *297*, 2229.
- [11] H. Tong, X. S. Miao, X. M. Cheng, H. Wang, L. J. Zhang, J. J. Sun, F. Tong, J. H. Wang, *Appl. Phys. Lett.* **2011**, *98*, 101904.
- [12] T. Matsunaga, H. Morita, R. Kojima, N. Yamada, K. Kifune, Y. Kubota, Y. Tabata, J.-J. Kim, M. Kobata, E. Ikenaga, K. Kobayashi, *J. Appl. Phys.* **2008**, *103*, 093511.
- [13] P. F. P. Poudeu, M. G. Kanatzidis, *Chem. Commun.* **2005**, *21*, 2672.
- [14] O. G. Karpinsky, L. E. Shelimova, M. A. Kretova, J.-P. Fleurial, *J. Alloys Compd.* **1998**, *268*, 112.
- [15] T. Matsunaga, N. Yamada, *Phys. Rev. B* **2004**, *69*, 104111.
- [16] T. Matsunaga, N. Yamada, Y. Kubota, *Acta Crystallogr. Sect. B* **2004**, *60*, 685.
- [17] V. Agafonov, N. Rodier, R. Céolin, R. Bellissent, C. Bergman, J. P. Gaspard, *Acta Crystallogr. Sect. C* **1991**, *47*, 1141.

3.2 GeSb₄Te₄ – a new 9P-type phase in the system Ge-Sb-Te

Matthias N. Schneider and Oliver Oeckler

Zeitschrift für Anorganische und Allgemeine Chemie **2010**, 636, 137-143.

Dedicated to Professor Arndt Simon on the occasion of his 70th birthday

Abstract

9P-GeSb₄Te₄ is a new germanium antimony telluride that can be obtained from the elements as a homogeneous phase by quenching a stoichiometric melt and subsequently annealing the sample at 500 °C. The crystal structure consists of alternating antimony layers similar to those in elemental Sb and rocksalt-type blocks similar to those in GeSb₂Te₄. Although not thermodynamically stable according to the phase diagram, GeSb₄Te₄ is remarkably stable up to 540 °C, where it starts to melt incongruently according to DSC and DTA measurements. The crystal structure has been refined from single-crystal X-ray data ($P\bar{3}m1$, $a = 4.2466(2)$ Å, $c = 17.483$ Å, $R1 = 0.0355$). Its diffraction patterns are very similar to those of other 9P-type tellurides like Ge₂Sb₂Te₅ and Sb₂Te, which tend to occur as very pronounced false minima in structure refinements. The electrical conductivity is low (33 Scm⁻¹) but exhibits metallic temperature dependence.

Keywords: germanium antimony tellurides; crystal structure determination; metastable alloys

Copyright: © 2008 WILEY-VCH Verlag GmbH & Co. KGaA

3.2.1 Introduction

Metastable Ge/Sb/Te phases (GST materials) dominate the field of phase-change materials for non-volatile memory devices.^[1-5] Attempts were made to extend their performance using superlattices in thin films obtained by sputtering (e.g. consecutive GeTe layers and Sb₇Te₃ or Sb₂Te₃ layers, with overall composition GeSb₇Te₄ and Ge₂Sb₂Te₅, respectively).^[6-8] The atomic structures of multilayer films produced by magnetron sputtering strongly resemble the long-range ordered layered compounds that can be obtained by conventional solid-state synthesis.^[9-12] The latter can exhibit very long translation periods and, to a certain extent, the degree of stacking disorder present is tunable. Because of the disorder, the thermal conductivity is rather low (and might be tunable as well), and it coexists with rather high electrical conductivity. This is important for phase-change materials but also essential for thermoelectrics. The thermoelectric properties of some stable GST materials have been measured, however, the figures of merit reported are moderate so far.^[11,13] However, higher Figure of merits can be expected for superlattice structures, as the thermal conductivity is influenced by their more or less pronounced long-range order.^[14-17] Hence, the investigation of metastable GST phases might yield insight into the structural chemistry of both phase-change materials as well as thermoelectrics.

According to the ternary phase diagram Ge/Sb/Te, which has been determined very thoroughly,^[11,18-20] all stable ternary phases are members of a homologous series (GeTe)_n(Sb₂Te₃)_m.^[12] The end member GeTe (space group $R\bar{3}m$, $a = 4.1639 \text{ \AA}$, $c = 10.6922 \text{ \AA}$)^[21] is the only stable compound formed by germanium and tellurium. Its structure (cf. Figure 1) is a noncentrosymmetric binary variant of the A7 (gray arsenic) structure type. Antimony crystallizes in the A7 type and exhibits very similar metrics (space group $R\bar{3}m$, $a = 4.3084 \text{ \AA}$, $c = 11.274 \text{ \AA}$).^[22]

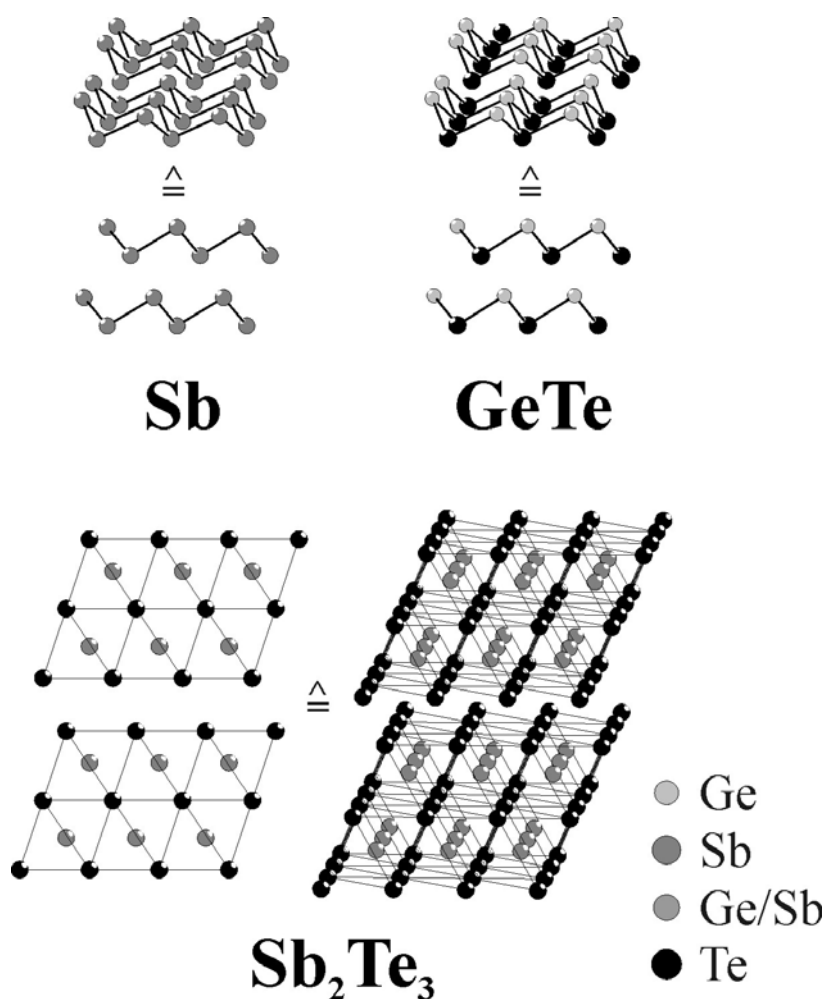


Figure 1. Crystal structures of Sb, GeTe and Sb₂Te₃.

The other end member Sb₂Te₃ (space group $R\bar{3}m$, $a = 4.264 \text{ \AA}$, $c = 30.458 \text{ \AA}$)^[23, 24] crystallizes in a binary variant of the tetradymite (Bi₂Te₂S)^[25, 26] structure type which exhibits three rocksalt-type slabs per unit cell. Each contains an ABC stacking sequence of hexagonal tellurium layers with antimony atoms in the octahedral voids (AcBaC). If cations and anions are not differentiated, the overall stacking corresponds to the cubic close packing. The slabs are separated by van der Waals gaps and stacked in a way so that the overall stacking remains a cubic layer sequence, whereas the tellurium substructure corresponds to a *hbc* sequence. The bonding between the individual slabs is van der Waals type with significant covalent Te–Te interactions, as indicated by the Te–Te distance of 3.736 Å which is shorter than the sum of the van der Waals radii (about 4.12 Å).

In the compounds (GeTe)_n(Sb₂Te₃)_m^[11, 27, 28] the rocksalt-type slabs of Sb₂Te₃ are formally expanded by insertion of GeTe. Their structures are long-periodically ordered trigonal stacking sequences of hexagonal atom layers. The more GeTe is incorporated, the more the spacing between the van der Waals gaps increases. Antimony and germanium cations are usually

disordered in these phases, the Ge/Sb ration depending on the relative distance to the van der Waals gap.^[9, 27, 29, 30] Since the a lattice parameter of elemental antimony is very similar to that of Sb_2Te_3 and the chemical bonding is similar too, A7-type antimony layers can be sandwiched by rocksalt-type slabs. This was observed in antimony-rich antimony tellurides which form a homologous series $(\text{Sb}_2\text{Te}_3)_m(\text{Sb}_2)_k$.^[10, 11, 24]

We have recently shown that A7-type antimony layers can also be sandwiched between expanded rocksalt-type layers known from the $(\text{GeTe})_n(\text{Sb}_2\text{Te}_3)_m$ series. $\text{Ge}_{2-x}\text{Sb}_{2+x}\text{Te}_5\cdot\text{Sb}_8$ ($x = 0.43$; space group $R\bar{3}m$, $a = 4.258 \text{ \AA}$, $c = 97.23 \text{ \AA}$)^[9] was characterized as the first member of a general series $(\text{GeTe})_n(\text{Sb}_2\text{Te}_3)_m(\text{Sb}_2)_k$ with $m, n, k \neq 0$. According to the ternary phase diagram, such phases are only stable at high temperatures if their composition is close to the lines $\text{Sb}_2\text{Te}_3\text{-Sb}$ or $\text{Sb}_2\text{Te}_3\text{-GeTe}$. In these cases they lie within the homogeneity range of the phases of the two homologous series. Longtime annealing at lower temperatures leads to germanium precipitation.^[11, 18-20] The homogeneity range of the stable phases is rather small. However, annealing times of more than half a year have sometimes been necessary to obtain the thermodynamic equilibrium. Furthermore, similar phases can be obtained by formally replacing germanium by a combination of silver and additional antimony, e.g. $\text{Ag}_x\text{Sb}_{3-x}\text{Te}_4\cdot\text{Sb}_8$ ($x = 0.24$, space group $P\bar{3}m1$, $a = 4.282 \text{ \AA}$, $c = 28.638 \text{ \AA}$).^[9]

Similar to Sb_2Te_3 (see above), all these long-periodically ordered layered structures exhibit a cubic stacking sequence of hexagonal atom layers when atom types are not distinguished. Therefore, the Ramsdell symbol is easy to predict. If the number of layers per slab ($2n + 5m + 2k$) is a multiple of three, the structure can be described with a primitive unit cell (space group $P\bar{3}m1$, $Z = 1$), if it is not, the structure is rhombohedral (space group $R\bar{3}m$, $Z = 3$) as three slabs are required per unit cell translation along the stacking direction. The total number of layers in the unit cell is $N = Z(2n + 5m + 2k)$ ($Z =$ formula units per unit cell) yields the Ramsdell symbol NP or NR for primitive and rhombohedral sequences, respectively.^[12, 30] If the total number of layers is the same, different polytypes may correspond to the same Ramsdell type. Of course, this also occurs for different compositions, for example $21R\text{-GeSb}_2\text{Te}_4$ ^[27, 31] and $21R\text{-Sb}_4\text{Te}_3$,^[10, 24] or $33R\text{-Ge}_3\text{Sb}_2\text{Te}_6$ ^[27, 32] and $33R\text{-Sb}_{10}\text{Te}_3$.^[10, 24] Here we report on a new $9P$ -type phase with $n = m = k = 1$, corresponding to the composition GeSb_4Te_4 , which is the simplest possibility to combine structure elements from both homologous series.

3.2.2 Results and discussion

3.2.2.1 Sample characterization

GeSb_4Te_4 can be obtained by quenching a stoichiometric melt and subsequently annealing it at 500 °C. Single-phase samples can be obtained as evident from powder diffraction patterns (cf. Figure 2). The average structure indicated by the strong reflections corresponds to a rhombohedral unit cell with $a = 4.2466(2)$ Å and $c = 5.828(2)$ Å, however, the positions of superstructure reflections indicate a $9P$ polytype structure. Based on the structure model from single-crystal data (see below), the powder pattern can be fitted well using the Rietveld method. As many reflections are weak, the refined atomic coordinates are rather imprecise but consistent with those from the single-crystal analysis, however, occupancy and displacement factors are meaningless.

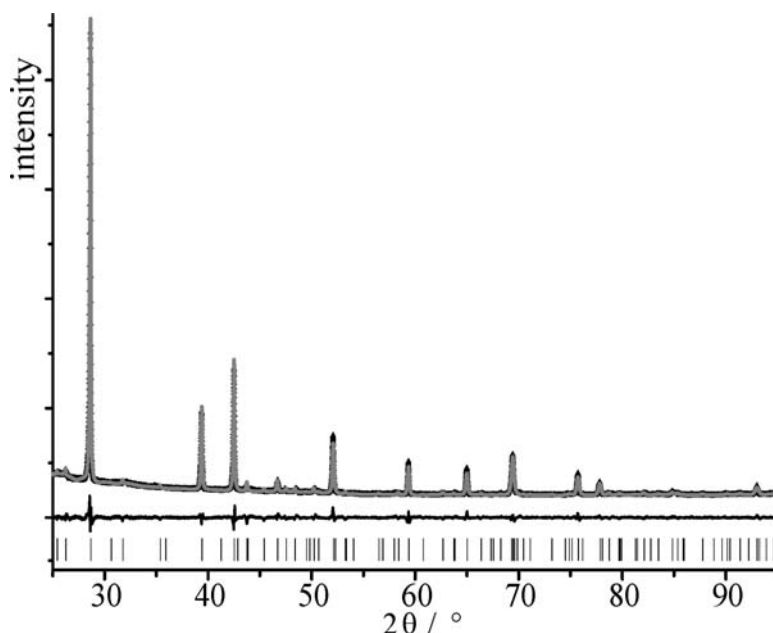


Figure 2. Result of a Rietveld fit (gray) of an experimental powder diffraction pattern of GeSb_4Te_4 (black).

As GeSb_4Te_4 melts incongruently (see below), the single-phase samples do not contain single crystals suitable for structure analysis. However, for the nominal composition GeSb_6Te_4 the liquidus lies below the stability range of the metastable phase GeSb_4Te_4 and lamina shaped crystals of the latter compound can be found in inhomogeneous GeSb_6Te_4 samples. Two such crystals were used for structure determination; the results were identical within 3σ limits concerning the structural parameters. EDX analyses were obtained from both crystals after the X-ray data collection. As the crystals exhibit large uncontaminated faces, EDX analyses are fairly reliable. They yield the compositions $\text{Ge}_{1.1(1)}\text{Sb}_{3.8(2)}\text{Te}_4$ and $\text{Ge}_{1.0(1)}\text{Sb}_{4.1(2)}\text{Te}_4$, respectively.

Thus GeSb_4Te_4 is a very good approximation to the actual composition and corroborated by the homogeneity of the product obtained with this nominal composition. For comparison: EDX analyses of the ingot with nominal composition GeSb_4Te_4 used for the conductivity measurement yielded $\text{Ge}_{1.1(1)}\text{Sb}_{4.2(2)}\text{Te}_4$.

3.2.2.2 Crystal structure determination

Both the stoichiometry GeSb_4Te_4 and the primitive lattice parameters [hP , $a = 4.2466(2)$ Å, $c = 17.483(3)$ Å] indicate a $9P$ polytype, thus, the expected space group is $\overline{P}3m1$. The initial structure solution from single-crystal data by direct methods consequently yielded a structure with nine hexagonal atom layers per unit cell. Of course, the similar atomic form factors of antimony and tellurium do not allow a straightforward differentiation of these elements by X-ray diffraction. As we outlined earlier,^[9] the building blocks in stable GST phases exhibit characteristic interatomic distance sets that allow a fairly reliable atom assignment. Hence, by comparison of the distance sets obtained from the initial structure solution with those of the compounds Sb_2Te_3 , Sb_2Te , SbTe , Sb_8Te_3 , GeSb_2Te_4 , $\text{Ge}_2\text{Sb}_2\text{Te}_5$ and $\text{Ge}_3\text{Sb}_2\text{Te}_6$, a structure model was derived. It corresponded to the structure of $\text{Ge}_2\text{Sb}_2\text{Te}_5$. Refining the Ge/Sb ratio on the cation positions (which usually exhibit mixed occupancy) yielded a total composition $\text{Ge}_{1.27}\text{Sb}_{2.73}\text{Te}_5$ (= " $\text{Ge}_{1.02}\text{Sb}_{2.18}\text{Te}_4$ ") and $R1 = 0.0364$. However, this structure model is not consistent with the chemical analysis and exhibits rather high residual electron density near the tellurium atom positions. The displacement parameters seem quite reasonable but are a bit more inconsistent than in comparable structure analyses. Therefore, a structure model was derived that is consistent with the stoichiometry present. For GeSb_4Te_4 , one can expect a sequence of GeSb_2Te_4 rocksalt-type blocks, which are known from $21R$ - GeSb_2Te_4 ,^[27, 31] and one A7-type antimony layer. The atomic coordinates of such a structure model were calculated to yield the typical interatomic distances. The refinement of this model converges at $R1 = 0.0355$, and the refined interatomic distances do not differ significantly from the values expected in comparison with similar phases (see above). This means that the initial structure solution was a false minimum with an R value only slightly higher than the optimal one. As discussed below, the two structure models are incongruent even when no differentiation between different atom types is considered. Thus, the wrong structure model does not just involve wrong atom type assignments owing to the similar form factors of antimony and tellurium. Its good R value is probably due to anisotropic displacement parameters with no physical meaning.

The refinement of site occupancy factors for tellurium atoms and antimony atoms in the A7-type layer did not show significant deviations from full occupancy. The Sb/Ge ratio on the cation

positions is consistent with the formula GeSb_4Te_4 considering $2\sigma - 4\sigma$ intervals. In the final refinement it was constrained to yield the ideal composition indicated by the analyses and the homogeneous samples with the same nominal composition. This constraint did not increase the R values significantly. Crystal data and refinement details are given in Table 1, atom positions, site occupancies and displacement parameters are given in Table 2.

Table 1. Crystallographic data and structure refinement of $9P\text{-GeSb}_4\text{Te}_4$ at 293 K.

Formula	GeSb_4Te_4
Formula mass (in g mol^{-1})	1069.99
Crystal system / Space group	trigonal, $P\bar{3}m1$
Cell parameters (in \AA)	$a = 4.2466(2)$, $c = 17.483(3)$
Cell volume (in \AA^3)	273.04(5)
X-ray density (in g cm^{-3})	6.507(1)
Absorption coefficient (in mm^{-1})	22.890
Formula units (per unit cell)	1
$F(000)$	444
Diffractometer	Stoe IPDS I
Radiation	Mo- K_α ($\lambda = 0.71073 \text{ \AA}$)
2θ range (in $^\circ$)	$7 < 2\theta < 58$
Absorption correction	numerical
Transmission (max. / min.)	0.285 / 0.145
Measured reflections	1321
Independent data / parameters	337 / 17 (1 restraint)
Refinement	full-matrix least-squares on F^2
R indices ^(a,b)	$R1 [I > 2\sigma(I)] = 0.0355$, $wR2[\text{all data}] = 0.0777$
Goof [all data]	0.801
$\Delta\rho_{\text{min}} / \Delta\rho_{\text{max}}$ (in $\text{e}\text{\AA}^{-3}$)	-1.53 / 2.09

$$^a) R1 = \frac{\sum |F_o - F_c|}{\sum |F_o|}$$

$$^b) wR2 = \frac{[\sum [w(F_o^2 - F_c^2)^2]]^{1/2}}{[\sum [w(F_o^2)^2]]^{1/2}}; w = 1 / [\sigma^2(F_o^2) + (aP)^2 + bP] \text{ with } P = [\text{Max}(0, F_o^2) + 2F_c^2] / 3$$

Table 2. Wyckoff positions, atomic coordinates, site occupancy, equivalent isotropic temperature factors and anisotropic displacement parameters (in \AA^2) for $9P\text{-GeSb}_4\text{Te}_4$.

atom	Wyck.	x	y	z	s.o.f.	U_{eq}	$U_{11}=U_{22}=2U_{12}$	U_{33}	$U_{13}=U_{23}$
Ge1/Sb1	1a	0	0	0	0.50(3)/ 0.50(3)	0.0358(14)	0.033(2)	0.041(2)	0
Te1	2d	2/3	1/3	0.10280(16)	1	0.0278(5)	0.0244(6)	0.0346(10)	0
Ge2/Sb2	2d	1/3	2/3	0.21925(13)	0.250(15)/ 0.750(15)	0.0431(10)	0.0345(14)	0.060(2)	0
Te2	2c	0	0	0.31261(11)	1	0.0306(6)	0.0301(8)	0.0317(10)	0
Sb3	2d	2/3	1/3	0.45519(19)	1	0.0483(8)	0.0249(10)	0.0950(18)	0

The structure of GeSb_4Te_4 can be described as an ordered stacking sequence of hexagonal atom layers. They build up alternating A7-type antimony layers (formally a sequence of two hexagonal atom layers) and rocksalt-type GeSb_2Te_4 blocks. Within their alternating cation and anion layers, the cations are located in distorted tellurium octahedra, with three shorter and three longer distances (Ge,Sb)–Te. The occupancy and the displacement of the cation positions depend on the distance to the neighboring A7-type antimony layer. The (Ge,Sb) Te_6 octahedra near the van der Waals gaps show a preferred occupancy by antimony and their deviation from an ideal octahedron is more pronounced. This corresponds to the situation in 21R- GeSb_2Te_4 itself^[27, 31] as illustrated in Figure 3.

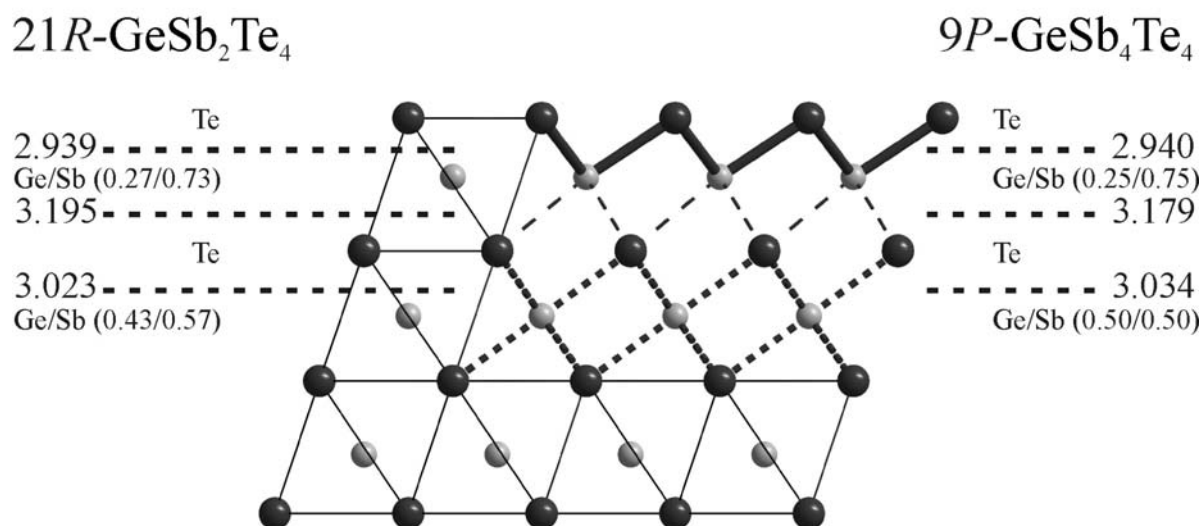


Figure 3. Comparison of interatomic distances (in Å) and site occupancies of the GeSb_2Te_4 blocks in 9P- GeSb_4Te_4 and 21R- GeSb_2Te_4 .

The distances Sb–Te between the layers [3.497(3) Å] terminating the rocksalt-type block and the adjacent A7-type layer are significantly shorter than the sum of the van der Waals radii (Sb: 2.00 Å, Te: 2.06 Å),^[33] which indicates partial covalent bonding. Within the A7-type antimony layer the distance Sb–Sb [2.910(3) Å] is close to that in elemental antimony (2.908 Å). A small fraction of these layers might be substituted by GeTe layers which could expand the adjacent rocksalt-type blocks. However, as no significant diffuse streaks have been observed, stacking disorder is not very pronounced. The structure refinement vaguely indicates a slightly reduced scattering density at the antimony positions. However, as it was not statistically significant, this possibility has not been investigated in detail so far.

3.2.2.3 Comparison of 9P polytypes in the system Ge/Sb/Te

According to the structural principles of phases $(\text{GeTe})_n(\text{Sb}_2\text{Te}_3)_m(\text{Sb}_2)_k$, 9P-type structures are possible for three combinations of n and k (m must be 1). Two of them are well known stable phases (cf. Figure 4). The structure of 9P- $\text{Ge}_2\text{Sb}_2\text{Te}_5$ ($n = 2, k = 0$; $P\bar{3}m1$, $a = 4.225 \text{ \AA}$, $c = 17.239 \text{ \AA}$)^[34] contains 9 alternating layers of cation and anions per unit cell. Cation positions exhibit a mixed occupancy by germanium and antimony, neighboring slabs interact through van der Waals interactions like in Sb_2Te_3 (cf. Figure 1). The structure of the binary phase 9P- Sb_2Te (= Sb_6Te_3) ($n = 0, k = 2$; $P\bar{3}m1$, $a = 4.272 \text{ \AA}$, $c = 17.633 \text{ \AA}$)^[35] corresponds to an alternating stacking sequence of two A7-type antimony layers and one Sb_2Te_3 block. GeSb_4Te_4 represents the hitherto unknown compound with $n = k = 1$ and combines alternating building blocks form stable GeSb_2Te_4 with A7-type antimony layers as described above. All three phases are 9P-type structures, however, their compositions are different. The two-dimensional metrics of the hexagonal atom layers, represented by the a lattice parameter, varies only slightly. In contrast, the c lattice parameters depend on the number of van der Waals gaps present per unit cell. These correspond to enlarged layers spacing relative to those in rocksalt-type blocks. Thus, the average thickness of one hexagonal layer, c/N ($N =$ number of layers per unit cell; $c =$ lattice parameter), depends on the composition as described elsewhere.^[12, 30] This relationship may facilitate structure analyses and allows the identification of the Ramsdell type from powder patterns even when superstructure reflections are not clearly visible as c/N can be calculated from the strong basic-structure reflections.^[30] The three 9P-type phases follow this rule. The c lattice parameter of GeSb_4Te_4 (17.483 \AA) which has two van der Waals gaps per unit cell lies between those of $\text{Ge}_2\text{Sb}_2\text{Te}_5$ (one van der Waals gap per unit cell, $c = 17.239 \text{ \AA}$) and Sb_2Te (three van der Waals gaps per unit cell, $c = 17.633 \text{ \AA}$).

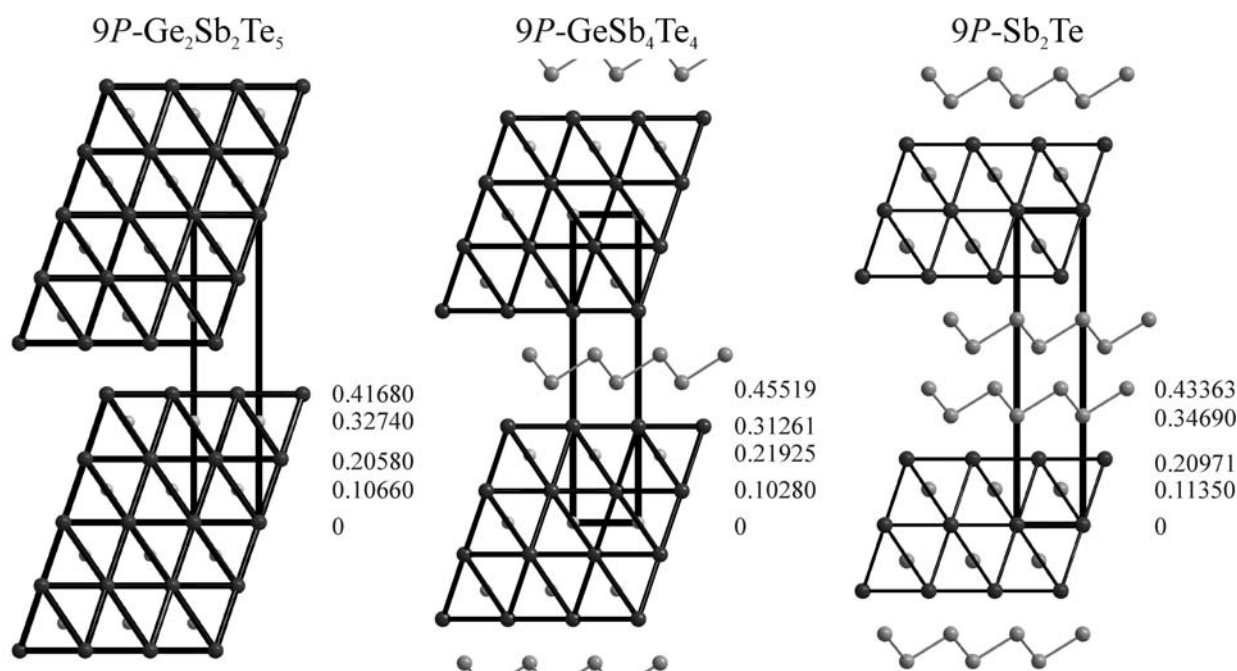


Figure 4. Comparison of the 9P-type structures of $\text{Ge}_2\text{Sb}_2\text{Te}_5$, GeSb_4Te_4 and Sb_2Te ; the z coordinates of corresponding atom layers are given (x and y coordinates see Table 3).

Although the three variants of the 9P-type can be distinguished by their lattice parameters, this does not allow a straightforward structure solution. As described above, the $\text{Ge}_2\text{Sb}_2\text{Te}_5$ structure type represents a false minimum in the structure refinement of GeSb_4Te_4 . The correct structure solution has the best R value but wrong non-congruent structure models may come close to it. This is illustrated in Figure 5. It shows a comparison of powder patterns simulated according to the three structure models. For all atom positions, the same isotropic displacement parameter was used. For easier comparison of intensities, identical lattice parameters were assumed, so that the reflection positions are the same for all models. Although there are characteristic intensity differences, especially concerning weak reflections, the powder patterns are very similar. In single-crystal structure refinements, this means that similar R values will result for the three models.

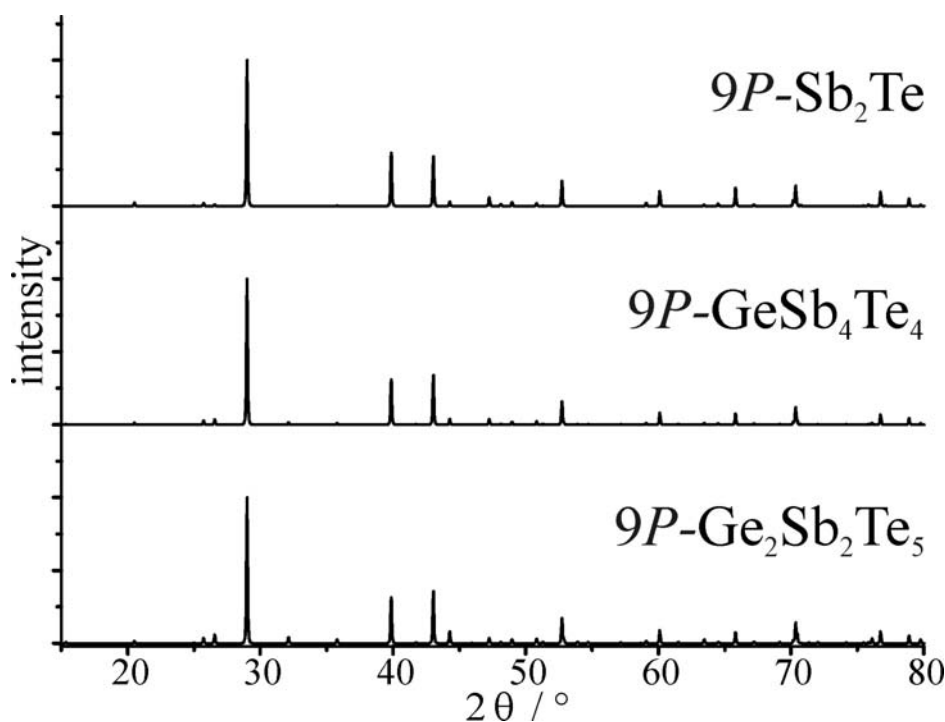


Figure 5. Calculated powder patterns for the $9P$ -type structures of $\text{Ge}_2\text{Sb}_2\text{Te}_5$, GeSb_4Te_4 and Sb_2Te (details see text).

Figure 4 also gives the atom coordinates z for the three $9P$ -type structures. Although they are incongruent, the structures exhibit many similar interatomic vectors and thus similar Patterson functions, i.e. similar diffraction patterns. The diffraction patterns of $9P\text{-Ge}_2\text{Sb}_2\text{Te}_5$ and $9P\text{-GeSb}_4\text{Te}_4$ are most similar in the low-angle region whereas $9P\text{-Ge}_2\text{Sb}_2\text{Te}_5$ and $9P\text{-Sb}_2\text{Te}$ are most similar in the high-angle region. This highlights the necessity of high-quality datasets with high resolution in order to avoid false minima in refinements and to obtain significantly worse R values for wrong models. Unfortunately, layered compounds often do not form crystals that are suitable for the collection of such data. This emphasizes the importance of chemical analyses which allow distinguishing the phases more easily than any other method because of their different compositions.

3.2.2.4 Stability of GeSb_4Te_4

According to the ternary phase diagram,^[11, 18, 19, 20] GeSb_4Te_4 is not stable in the solid state. Germanium has been reported to precipitate from such samples after long-time annealing at 525-615 °C. However, the kinetic stability of the phase is remarkable. Upon annealing at 500 °C for several days, no germanium could be detected. According to both DSC and DTA measurements, no significant exothermal structural changes towards the thermodynamically stable state have been detected before the sample starts to melt incongruently at ca. 540 °C (onset). The endothermic heat flow peaks at ca. 550 and 580 °C before the phase is completely

liquid around 590 °C. This indicates the stepwise formation of related phases during the incongruent melting process. This finding is consistent with temperature dependent X-ray powder diffraction data (cf. Figure 6). At ca. 550 °C the reflections become weaker and the intensity of the background increases because of the presence of a liquid phase. The strong reflections corresponding to the simple rhombohedral basic structure of all layered phases in the system Ge/Sb/Te remain until the sample melts completely. This indicates that the decomposition products of a peritectic reaction exhibit structures that are closely related to that of GeSb_4Te_4 . Probably they correspond to thermodynamically stable phases. At high temperatures, no germanium precipitation is expected.

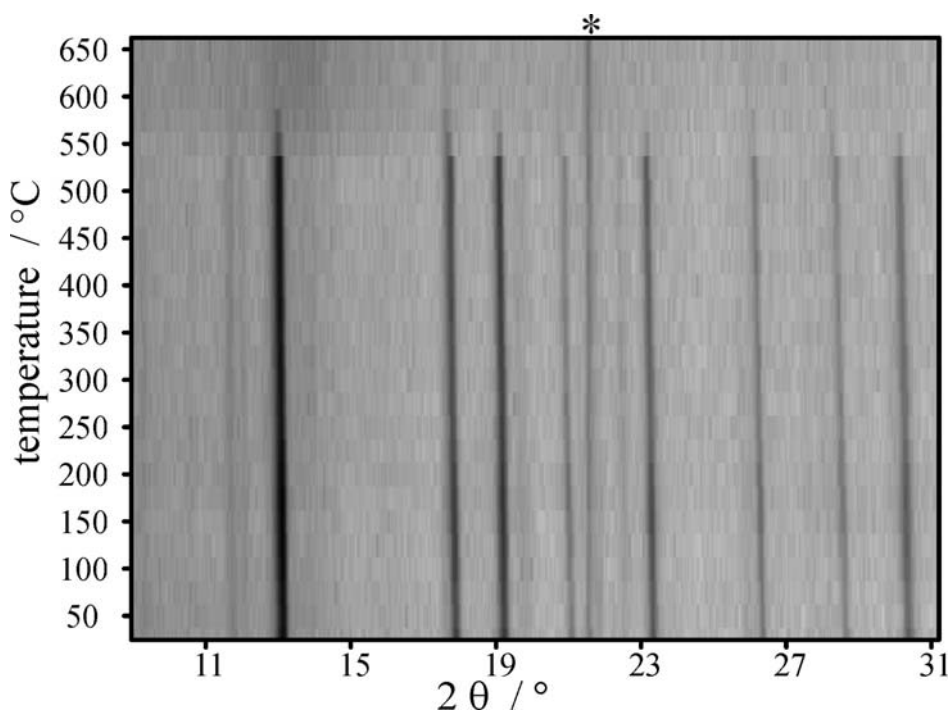


Figure 6. Temperature dependent X-ray powder diffraction pattern of GeSb_4Te_4 (the asterisk indicates a reflection that originates from the experimental setup).

3.2.2.5 Electrical conductivity

Electrical conductivity measurements in the temperature range from 10 K to 300 K show metallic characteristics, indicated by the increase of the resistance with increasing temperature (cf. Figure 7). The residual resistivity ratio $\rho(300\text{K})/\rho(10\text{K})$ is 1.6. Anisotropic conductivity (parallel and perpendicular to the stacking direction) was reported for the layered phases $(\text{Sb}_2\text{Te}_3)_m(\text{Sb}_2)_k$ ^[24] and can be expected for GeSb_4Te_4 as well. Because of preferred orientation in the sample, the rather low absolute value of the conductivity ($33 \text{ S}\cdot\text{cm}^{-1}$ at room temperature) may not be very meaningful. However, in combination with the metallic characteristics it probably indicates a degenerate semiconductor. The small differences in electronegativity imply a narrow band gap and positional disorder may further narrow it by tailing of band states.

Metalloid conduction was also reported for stable phases $(\text{GeTe})_n(\text{Sb}_2\text{Te}_3)_m$ ^[11] although their optical properties reveal a narrow band gap.^[36] The absolute values of their conductivities are in the range of 1300 to 2400 $\text{S}\cdot\text{cm}^{-1}$ whereas those for the compounds $(\text{Sb}_2\text{Te}_3)_m(\text{Sb}_2)_k$ are even higher (1500–6000 $\text{S}\cdot\text{cm}^{-1}$).^[24] However, related tellurides like AgSbTe_2 (30 $\text{S}\cdot\text{cm}^{-1}$)^[37] exhibit conductivities close to that of GeSb_4Te_4 .

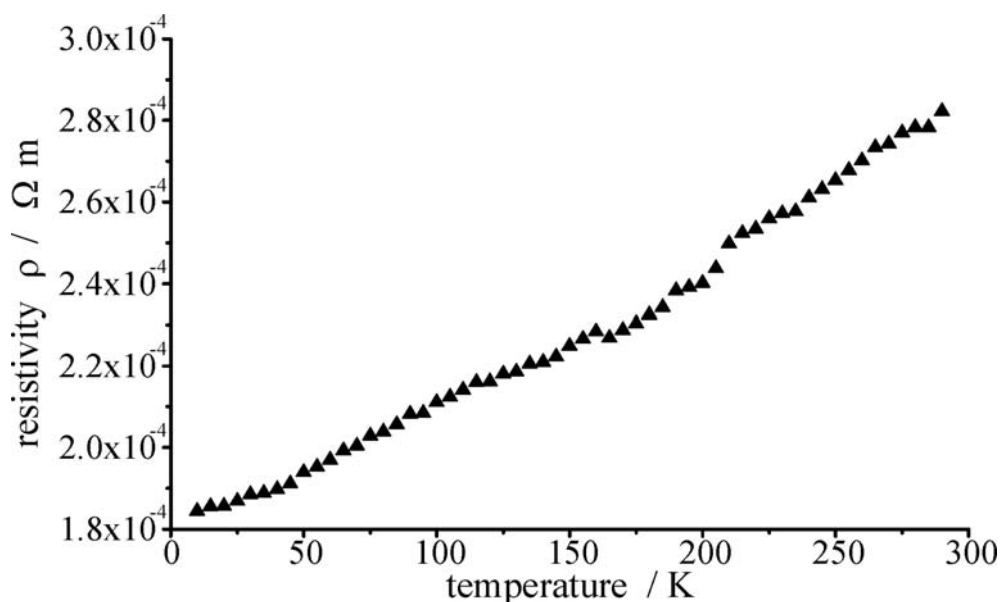


Figure 7. Temperature dependence of the specific resistivity of GeSb_4Te_4 in the temperature range from 10 K to 300 K, indicating metallic behavior.

3.2.3 Conclusions

The synthesis and characterization of GeSb_4Te_4 and $\text{Ge}_{2-x}\text{Sb}_{2+x}\text{Te}_5\cdot\text{Sb}_8$ ($x = 0.43$)^[9] show that new phases in the system Ge/Sb/Te can be found if quenched samples are annealed at low temperatures. They exhibit a combination of building blocks found in the homologous series of stable phases $(\text{GeTe})_n(\text{Sb}_2\text{Te}_3)_m$ and additional A7-type antimony layers. Although they are probably metastable, homogeneous samples can be obtained and do not decompose up to 540 °C. This is probably due to the fact that the precipitation of germanium is hindered because the nucleation of diamond-type germanium domains requires long-distance diffusion and coherent exsolution is impossible because of the very different crystal structures. This route should allow the synthesis of a series of compounds $(\text{GeTe})_n(\text{Sb}_2\text{Te}_3)_m(\text{Sb}_2)_k$ with $n, m, k \neq 0$. Stacking disorder is not pronounced in GeSb_4Te_4 but can be expected in related phases which might be interesting thermoelectrics when domain structures are formed. In fact, some phases that are usually synthesized by sputtering subsequent layers on a substrate might be obtained in a simple way by the technique presented here.

The crystal structure determination showed that weak reflections are important to distinguish non-congruent structure types with the same number of atom layers per unit cell. We have shown that it is almost impossible to derive correct structure models from X-ray data without relying on further information. Only to some extent, this is due to the similar form factors of antimony and tellurium. Moreover, the diffraction patterns are so similar that false minima can easily occur in structure analyses. This is most relevant when crystals from inhomogeneous samples are used for structure analysis. Chemical analysis is mandatory in such cases. As *Arndt Simon* often stated, the preparation of homogeneous samples from stoichiometrically weighted starting materials is probably the best analysis in solid-state chemistry.

3.2.4 Experimental section

3.2.4.1 Synthesis

Samples were prepared by heating the corresponding mixtures of the pure elements germanium (99.999 %, Sigma Aldrich), antimony (99.999 %, Smart Elements) and tellurium (99.999 %, Alfa Aesar) in sealed silica glass ampoules under argon to 950 °C. The resulting melts were quenched to room temperature in water.

Homogenous bulk samples (cf. Figure 2) of GeSb_4Te_4 were obtained by subsequent annealing at 500 °C for 150 h. Single crystals for structure determination of $9P\text{-GeSb}_4\text{Te}_4$ were obtained from a rather rapidly cooled sample with the nominal composition GeSb_6Te_4 (crystal growth from a stoichiometric melt is impossible, cf. section on sample characterization). As the crystals were of good quality, further annealing proved unnecessary in this case. In the powder pattern of this sample the superstructure reflections appeared broadened and indicated that the sample is inhomogeneous, the majority phase was highly disordered.

3.2.4.2 EDX analyses

EDX spectra were obtained with a JSM-6500F (Jeol, USA) scanning electron microscope with EDX detector (model 7418, Oxford Instruments, Great Britain). For each crystal or fragment of the ingot, respectively, the results of five point analyses were averaged and the error limits were estimated from their variance.

3.2.4.3 X-ray diffraction

X-ray powder patterns were recorded with a Huber G670 Guinier camera equipped with a fixed imaging plate and integrated read-out system using Cu- $K_{\alpha 1}$ radiation (Ge monochromator, $\lambda = 1.54051 \text{ \AA}$). Specimens were prepared by crushing representative parts of the samples and fixing the powder on Mylar foils using silicone grease. The phase homogeneity was assessed and lattice parameters were determined by pattern fitting (Rietveld method) using the program TOPAS.^[38] Temperature-dependent powder diffraction experiments were performed with a STOE Stadi P powder diffractometer equipped with an imaging plate system using Mo- $K_{\alpha 1}$ radiation (Ge monochromator, $\lambda = 0.71093 \text{ \AA}$) in Debye–Scherrer geometry. Powdered specimens were filled into silica glass capillaries with 0.3 mm diameter and sealed with silicone grease under argon. During measurement, the samples were heated up to 650 °C in a graphite furnace and then cooled to room temperature.

For single crystal structure determination, lamina shaped crystals were isolated from the crushed ingots, mounted on glass fibers and checked for quality by Laue photographs with a Buerger precession camera. For the best crystals, intensity data were collected with a STOE IPDS-I diffractometer with imaging plate detector using Mo- K_{α} radiation (graphite monochromator, $\lambda = 0.71093 \text{ \AA}$). A numerical absorption correction based on measured crystal faces was applied after optimizing the crystal shape based on equivalent reflections.^[39, 40] Final full-matrix least-squares refinements of models developed from the initial solutions (see above) were executed with SHELXL.^[41] The refinements yield similar results for the two crystals investigated, details about data collection and refinement are given in Table 1 for the better crystal. Lattice parameters determined from powder data have been used for the refinement and the calculation of interatomic distances. Further information on the crystal structure investigation may be obtained from the Fachinformationszentrum Karlsruhe, 76344 Eggenstein-Leopoldshafen, Germany, by quoting the deposition number CSD-420989, the names of the authors, and the citation of the paper.

3.2.4.4 Thermal analysis

The thermal behavior of the samples was studied up to 650 °C by differential thermal analysis and thermogravimetry (DTA-TG) with a Setaram TG-92 instrument. The measurement was conducted under helium at a scanning rate of $10 \text{ K} \cdot \text{min}^{-1}$ using alumina crucibles. In this temperature range, the weight loss was not significant. Differential scanning calorimetry (DSC) was carried out in an aluminum crucible on a Setaram DSC 141.

3.2.4.5 Electrical conductivity measurement

Measurements of the electrical conductivity were carried out using the conventional DC four-point current-reversal method between 10 and 300 K. A fragment of an ingot of a homogeneous polycrystalline GeSb₄Te₄ sample was polished to a platelet of about 4 x 4 x 0.1 mm. Contact to the experimental setting was established with silver wires using an silver containing conductive paste. Cooling and heating curves were identical within the error limits. The resistivity was calculated by scaling according to the absolute value obtained at 300 K by a complete analysis according to *van der Pauw* from multiple measurements taking into account the sample thickness.^[42]

3.2.5 References

- [1] D. Lencer, M. Salinga, B. Grabowski, T. Hickel, J. Neugebauer, M. Wuttig, *Nat. Mater.* **2008**, *7*, 972.
- [2] M. Wuttig, C. Steimer, *Appl. Phys. A* **2007**, *87*, 411.
- [3] T. Matsunaga, R. Kojima, N. Yamada, K. Kifune, Y. Kubota, Y. Tabata, M. Takata, *Inorg. Chem.* **2006**, *45*, 2235.
- [4] M. Wuttig, N. Yamada, *Nat. Mater.* **2007**, *6*, 824.
- [5] A. V. Kolobov, *Nat. Mater.* **2008**, *7*, 351.
- [6] J. Tominaga, P. Fons, A. Kolobov, T. Shima, T. C. Chong, R. Zhao, H. K. Lee, L. Shi, *Jpn. J. Appl. Phys.* **2008**, *47*, 5763.
- [7] C. T. Chong, L. P. Shi, X. S. Miao, P. K. Tan, R. Zhao, Z. P. Cai, *Jpn. J. Appl. Phys.* **2000**, *39*, 737.
- [8] H. Yang, C. T. Chong, R. Zhao, H. K. Lee, J. Li, K. G. Lim, L. Shi, *Appl. Phys. Lett.* **2009**, *94*, 203110.
- [9] M. N. Schneider, M. Seibald, O. Oeckler, *Dalton Trans.* **2009**, 2004.
- [10] K. Kifune, Y. Kubota, T. Matsunaga, N. Yamada, *Acta Crystallogr. Sect. B* **2005**, *61*, 492.
- [11] L. E. Shelimova, O. G. Karpinsky, P. P. Konstantinov, M. A. Kretova, E. S. Avilov, V. S. Zemskov, *Inorg. Mater.* **2001**, *37*, 342.
- [12] L. E. Shelimova, O. G. Karpinsky, M. A. Kretova, V. I. Kosyakov, V. A. Shestakov, V. S. Zemskov, F. A. Kuznetsov, *Inorg. Mater.* **2000**, *36*, 768.
- [13] P. P. Konstantinov, L. E. Shelimova, E. S. Avilov, M. A. Kretova, V. S. Zemskov, *Inorg. Mater.* **2001**, *37*, 662.

- [14] D. L. Medlin, G. J. Snyder, *Curr. Opin. Colloid Interface Sci.* **2009**, *14*, 226.
- [15] E. S. Landry, M. I. Hussein, A. J. H. McGaughey, *Phys. Rev. B* **2008**, *77*, 184302.
- [16] H. Böttner, G. Chen, R. Venkatasubramanian, *MRS Bull.* **2006**, *31*, 211.
- [17] T. C. Harman, P. J. Taylor, M. P. Walsh, B. E. LaForge, *Science* **2002**, *297*, 2229.
- [18] V. I. Kosyakov, V. A. Shestakov, L. E. Shelimova, F. A. Kuznetsov, V. S. Zemskov, *Inorg. Mater.* **2000**, *36*, 1004.
- [19] B. Legendre, C. Hancheng, S. Bordas, M. T. Clavaguera-Mora, *Thermochim. Acta* **1984**, *78*, 141.
- [20] S. Bordas, M. T. Clavaguera-Mora, B. Legendre, C. Hancheng, *Thermochim. Acta* **1986**, *107*, 239.
- [21] T. Chattopadhyay, J. X. Boucherle, H. G. von Schnering, *J. Phys. C: Solid State Phys.* **1987**, *20*, 1431.
- [22] C. S. Barrett, P. Cucka, K. Haefner, *Acta Crystallogr.* **1963**, *16*, 451.
- [23] T. L. Anderson, H. B. Krause, *Acta Crystallogr. Sect. B* **1974**, *30*, 1307.
- [24] P. F. P. Poudeu, M. G. Kanatzidis, *Chem. Commun.* **2005**, *21*, 2672.
- [25] D. Harker, *Z. Kristallogr.* **1934**, *89*, 175.
- [26] P. Bayliss, *Am. Mineral.* **1991**, *76*, 257.
- [27] O. G. Karpinsky, L. E. Shelimova, M. A. Kretova, J.-P. Fleurial, *J. Alloys Compd.* **1998**, *268*, 112.
- [28] S. Kuypers, G. Van Tendeloo, J. Van Landuyt, S. Amelinckx, *J. Solid State Chem.* **1988**, *76*, 102.
- [29] F. Hulliger in: *Physics and Chemistry of Materials with Layered Structures* (Ed.: F. Levy), Vol. 5, Reidel, Dordrecht, **1976**, p. 195.
- [30] M. N. Schneider, O. Oeckler, *Z. Anorg. Allg. Chem.* **2008**, *634*, 2557.
- [31] T. Matsunaga, N. Yamada, *Phys. Rev. B* **2004**, *69*, 104111.
- [32] T. Matsunaga, R. Kojima, N. Yamada, K. Kifune, Y. Kubota, M. Takata, *Appl. Phys. Lett.* **2007**, *90*, 161919.
- [33] A. Bondi, *J. Phys. Chem.* **1964**, *68*, 441.
- [34] T. Matsunaga, N. Yamada, Y. Kubota, *Acta Crystallogr. Sect. B* **2004**, *60*, 685.
- [35] V. Agafonov, N. Rodier, R. Céolin, R. Bellissent, C. Bergman, J. P. Gaspard, *Acta Crystallogr., Sect. C* **1991**, *47*, 1141.
- [36] B.-S. Lee, J. R. Abelson, S. G. Bishop, D.-H. Kang, B.-K. Cheong, K.-B. Kim, *J. Appl. Phys.* **2005**, *97*, 093509.

- [37] K. Hoang, S. D. Mahanti, J. R. Salvador, M. G. Kanatzidis, *Phys. Rev. Lett.* **2007**, *99*, 156403.
- [38] A. Coelho, *TOPAS-Academic*, V. 4.1; Coelho Software, Brisbane, **2007**.
- [39] *X-RED*, Revision 1.10, Stoe & Cie. GmbH, Darmstadt **1998**.
- [40] *X-SHAPE*, Revision 1.03, Stoe & Cie. GmbH, Darmstadt, **1998**.
- [41] G. M. Sheldrick, *Acta Crystallogr. Sect. A* **2008**, *64*, 112.
- [42] L. J. van der Pauw, *Philips Res. Rep.* **1958**, *13*, 1.

3.3 A new series of long-range ordered metastable phases in the system M-Sb-Te (M = Ge, Ag)

Matthias N. Schneider, Markus Seibald, Oliver Oeckler

Dalton Transactions **2009**, 2004-2011.

Dedicated to Professor I.-P. Lorenz on the occasion of his 65th birthday

Abstract

New phases with the general formula $(\text{MTe})_n(\text{Sb}_2\text{Te}_3)(\text{Sb}_2)_4$ ($n = 0, 1, 2, \dots$; $\text{M} = \text{Ge}, \text{Ag}$) have been synthesized by quenching stoichiometric melts of the pure elements and subsequent annealing. These phases represent a combination of the well-known homologous series $(\text{Sb}_2\text{Te}_3)_m(\text{Sb}_2)_k$ and $(\text{GeTe})_n(\text{Sb}_2\text{Te}_3)_m$, including substitution with Ag. Their layered crystal structures contain rocksalt-type building blocks $(\text{MTe})_n(\text{Sb}_2\text{Te}_3)$ alternating with antimony slabs which represent sections of the A7 structure type of elementary antimony. These blocks, which are stacked along the threefold axis of the trigonal crystals, vary in size according to the composition. Powder diffraction patterns allow predictions concerning the symmetry and periodicity of the stacking sequence. Single-crystal structure refinements of the members $\text{Ge}_{2-x}\text{Sb}_{2+x}\text{Te}_5\text{Sb}_8$ ($x = 0.43$; $R\bar{3}m$, $a = 4.258(1) \text{ \AA}$, $c = 97.23(2)$, $R = 4.38\%$) and $\text{Ag}_x\text{Sb}_{3-x}\text{Te}_4\text{Sb}_8$ ($x = 0.24$; $P\bar{3}m1$, $a = 4.282(1) \text{ \AA}$, $c = 28.638(5)$, $R = 5.38\%$) reveal completely ordered superstructures with extremely long periodicities containing slabs similar to those in $\text{Ge}_2\text{Sb}_2\text{Te}_5$ and GeSb_2Te_4 , respectively, alternating with four antimony layers. According to the ternary phase diagram the phases are metastable but thermal analyses do not evidence phase separation or structural phase transformations before incongruent melting, which indicates that the structures are kinetically very stable. Although the phases are valence compounds, temperature dependence of resistance shows metallic like behaviour in the range of 300 – 10 K, which probably indicates degenerate semiconductivity.

Copyright: © 2009 Royal Society of Chemistry

3.3.1 Introduction

Owing to a range of tuneable properties, chalcogenides are the materials of choice for a variety of applications, including photovoltaic devices, phase-change materials for data storage, thermoelectrics and others. In recent years, thermoelectric materials have become an interesting perspective for the reversible exchange of heat and electricity. With rising efficiency, represented by the so-called figure of merit ZT , new possibilities for thermopower devices arise. The thermoelectric properties correlate with the structures of the compounds on different length scales. "Exotic" structures such as quantum dots or multi-layer thin films promise high figure of merits (up to 3 and more) at moderate temperatures. Such superstructures have, for example, been generated in $\text{Sb}_2\text{Te}_3/\text{Bi}_2\text{Te}_3$ thin films by chemical vapour deposition (CVD) or molecular beam epitaxy (MBE).^[1,2] However, for large-scale industrial application, it would be desirable to gain high ZT values in bulk materials using easy and inexpensive preparation methods. Tellurides, such as $\text{AgPb}_m\text{SbTe}_{m+2}$, PbTe or Bi_2Te_3 , and many others are the class of thermoelectrics that shows the highest values of ZT (up to 1.5 in a reasonable temperature range) accessible for bulk material so far.^[3,4] Sb_2Te_3 (as well as Bi_2Te_3) is a stable compound that crystallizes in a variant of the tetradymite ($\text{Bi}_2\text{Te}_2\text{S}$) structure type (see Fig. 1) with three slabs per unit cell stacked along $[001]$ (hexagonal setting of the rhombohedral space group $R\bar{3}m$, $a = 4.264(1) \text{ \AA}$, $c = 30.46(1) \text{ \AA}$). Each slab contains an alternating sequence of three hexagonal Te layers and two hexagonal Sb layers, which yields three "van der Waals gaps" per unit cell located between the Te layers terminating the individual slabs^[5,6] (however, the bonding is not only van der Waals type, as bond lengths indicate rather strong Te–Te interactions, see also below). Slabs with Sb_2Te_3 (Bi_2Te_3) type structures are also common building blocks in the crystal structures of ternary tellurides of the group 14 and 15 elements.^[7,8] The tetrel or pentel positions can also host elements such as Sn, Pb, Ag, In^[9–14] or Bi and As,^[15–17] respectively. Furthermore, Te may be replaced by other chalcogens such as Se.^[18]

In the ternary system Ge–Sb–Te, whose phase diagram has been investigated in detail,^[7,19–21] there are two homologous series of layered compounds with the general formulae $(\text{Sb}_2\text{Te}_3)_m(\text{Sb}_2)_k$ and $(\text{GeTe})_n(\text{Sb}_2\text{Te}_3)_m$.^[6,8,22,23] Their trigonal structures consist of Sb_2Te_3 slabs stacked along the threefold axis, which either alternate with additional A7-type layers Sb_2 (similar to the layers in grey As with A7 structure) or are expanded to thicker rocksalt-type blocks by formal insertion of GeTe units (see Fig. 1). The combination of all three building elements, including substituted variants, has not been reported so far and, from a

thermodynamical point of view, should be impossible regarding the phase diagrams.^[7,19-21] New, probably metastable phases $(MTe)_n(Sb_2Te_3)_m(Sb_2)_k$ ($M = Ge$ or other elements, see above) would, however, extend the structural chemistry and might allow for additional tuning of thermoelectric properties which have been reported for phases such as $AgPb_mSbTe_{m+2}$ ($m = 0$ to 18) and $Ag_{3-x}Sb_{1+x}Te_4$ ($x = 0$ to 2)^[12,24] or $GeSb_2Te_4$ and $Ge_2Sb_2Te_5$.^[23,25] Here we report on the new phases $Ge_{2-x}Sb_{2+x}Te_5 \cdot Sb_8$ ($x = 0.43$) and $Ag_xSb_{3-x}Te_4 \cdot Sb_8$ ($x = 0.24$) which, according to our knowledge, are the first members of a class of compounds composed of three types of building units.

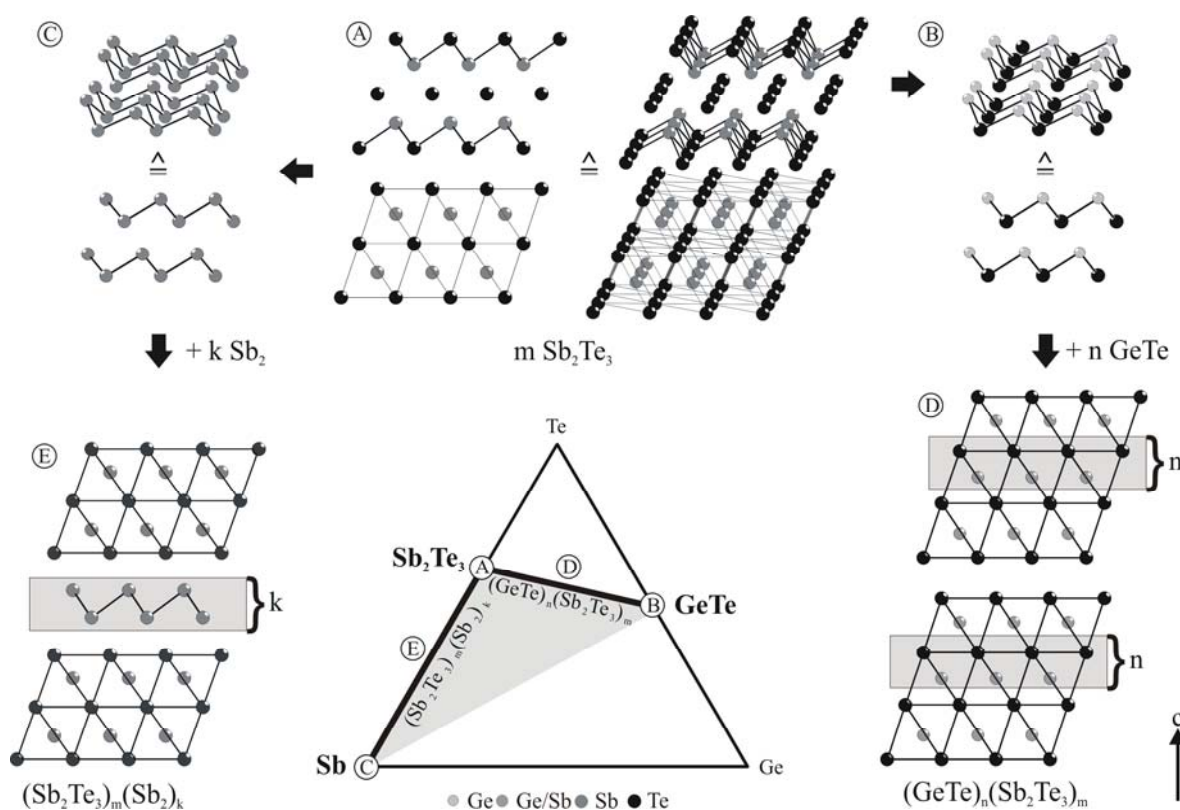


Figure 1. Ternary phase diagram (schematic representation) Ge-Sb-Te and structural relationships in homologous series of the binary system Sb-Te and the pseudobinary section GeTe-Sb₂Te₃: formal insertion of GeTe units into Sb₂Te₃ slabs leads to compounds (GeTe)_n(Sb₂Te₃)_m (D) with rocksalt-type slabs, whereas formal insertion of Sb₂ units between Sb₂Te₃ slabs leads to phases (Sb₂Te₃)_m(Sb₂)_k (E) containing two types of slabs; perspective views and projections of the basic phases Sb, GeTe and Sb₂Te₃ along $\langle 100 \rangle$ are depicted to show the similarity of the layered structures to A7-type layers (for Sb (C) and GeTe (B) the shortest bonds are drawn; for Sb₂Te₃ (A) the upper part of the corresponding drawing highlights the shortest bonds, whereas the lower part highlights the coordination polyhedra).

3.3.2 Experimental

3.3.2.1 Synthesis and chemical analysis

Mixtures of the pure powdered elements Ag (99.99%, Smart Elements) or Ge (99.999%, Sigma Aldrich), Sb (99.999%, Smart Elements) and Te (99.999%, Alfa Aesar) were heated in sealed silica glass ampoules under argon atmosphere with a rate of $15\text{ }^{\circ}\text{C min}^{-1}$ to $850\text{ }^{\circ}\text{C}$. This temperature was maintained for 4 h, then the melts were cooled to $350\text{ }^{\circ}\text{C}$ with a rate of $0.1\text{ }^{\circ}\text{C min}^{-1}$. After annealing at $350\text{ }^{\circ}\text{C}$ for 15 h, the samples were cooled to room temperature by switching off the furnace. Initially, crystals of $\text{Ge}_{2-x}\text{Sb}_{2+x}\text{Te}_5\cdot\text{Sb}_8$ ($x = 0.43$) = $\text{Ge}_{1.57}\text{Sb}_{10.43}\text{Te}_5 \approx \text{Ge}_9\text{Sb}_{61}\text{Te}_{29}$ and $\text{Ag}_x\text{Sb}_{3-x}\text{Te}_4\cdot\text{Sb}_8$ ($x = 0.24$) = $\text{Ag}_{0.24}\text{Sb}_{10.76}\text{Te}_4 \approx \text{Ag}_2\text{Sb}_{72}\text{Te}_{27}$ were isolated from ingots with the nominal compositions $\text{M}_{12}\text{Sb}_{59}\text{Te}_{29}$ ($\text{M} = \text{Ag}$ or Ge). The compositions of these crystals were derived from the structure determinations described below and confirmed by elemental analyses done by EDX spectroscopy using a JSM-6500F (Jeol, USA) scanning electron microscope with EDX detector (model 7418, Oxford Instruments, Great Britain). The average composition obtained from various point analyses on several crystallites isolated from the bulk samples yielded the compositions $\text{Ge}_{11}\text{Sb}_{59}\text{Te}_{29}$ and $\text{Ag}_4\text{Sb}_{70}\text{Te}_{26}$, respectively. No standards were used, but the setup had been checked with homogeneous samples of $\text{Ge}_2\text{Sb}_2\text{Te}_5$ and GeSb_2Te_4 which showed that the reliability of the analyses is about 2 atom%.

The original $\text{Ag}_{12}\text{Sb}_{59}\text{Te}_{29}$ sample contained impurities of AgTe_2 (see below), however, homogenous bulk samples of both compounds can be prepared by melting stoichiometric amounts of the pure elements with the compositions derived from the single-crystal structure determination using analogous temperature treatment or by quenching stoichiometric melts in water. The homogeneity was proved by X-ray powder patterns (see below). Crystals from these ingots exhibit the same structure and composition as the original ones.

3.3.2.2 Thermal analysis

The thermal behaviour of finely ground samples was studied by differential thermoanalysis and thermogravimetry (DTA-TG) using a Setaram TG-92 equipped with a protected DTA-TG rod. The measurement was conducted under He atmosphere at a scanning rate of $10\text{ }^{\circ}\text{C min}^{-1}$ using alumina crucibles. All temperatures of thermal effects are given as onset temperatures of the signals. In addition, differential scanning calorimetry (DSC) measurements were carried out in aluminium crucibles using a Setaram DSC 141. Both methods do not show any significant signals before incongruent melting of the specimens.

3.3.2.3 Conductivity measurements

Electrical conductivity measurements were carried out employing the conventional DC four-point current-reversal method between 10 and 300 K. A part of the crushed polycrystalline ingot of each specimen was polished to a platelet of about $5 \times 5 \times 0.1 \text{ mm}^3$. Contact to the experimental setting was established with Ag wires and Ag-containing conductive paste. Cooling and heating curves were identical within the error limits. The specific conductivity was calculated by scaling according to the absolute value obtained at 300 K by a complete analysis according to van der Pauw^[26] from multiple measurements taking into account the sample thickness.

3.3.2.4 X-ray characterization

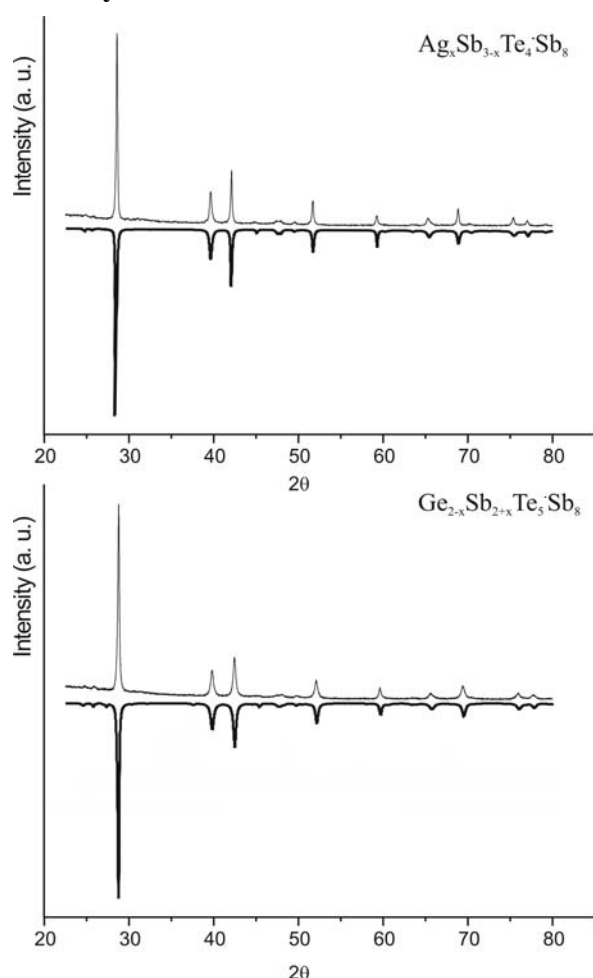


Figure 2. Powder diffraction patterns ($\text{Cu-K}\alpha_1$ radiation) of $\text{Ag}_x\text{Sb}_{3-x}\text{Te}_4\text{Sb}_8$ ($x = 0.24$) and $\text{Ge}_{2-x}\text{Sb}_{2+x}\text{Te}_5\text{Sb}_8$ ($x = 0.43$). The experimental powder patterns (upwards) match well with simulated powder patterns (downwards) which were calculated from the single-crystal refinement results taking into account slight preferred orientation along (001).

X-Ray powder patterns were recorded on a Huber G670 powder diffractometer equipped with an imaging plate system using $\text{Cu-K}\alpha_1$ radiation (Ge monochromator, $\lambda = 1.54051 \text{ \AA}$) in Guinier geometry or on a STOE Stadi P powder diffractometer with linear PSD using $\text{Mo-K}\alpha_1$ radiation (Ge monochromator, $\lambda = 0.71093 \text{ \AA}$) in Debye–Scherrer geometry. Specimens were prepared by crushing representative parts of the samples and fixing the powder on Mylar foils with silicone grease. The powder data were evaluated using the program WIN^{XPOW} .^[27] The X-ray powder patterns of $\text{Ge}_{2-x}\text{Sb}_{2+x}\text{Te}_5\text{Sb}_8$ ($x=0.43$) specimens indicate homogeneity for all samples investigated, including the original one with a slightly deviating composition $\text{Ge}_{12}\text{Sb}_{59}\text{Te}_{29}$ which might indicate a certain range of homogeneity.

For the Ag substituted compound $\text{Ag}_x\text{Sb}_{3-x}\text{Te}_4\cdot\text{Sb}_8$ ($x = 0.24$), small amounts of an impurity phase AgTe_2 were identified in the powder pattern of the original sample $\text{Ag}_{12}\text{Sb}_{59}\text{Te}_{29}$, which contained an excess of Ag and Te compared to the composition of the crystals (see also above). The stoichiometric mixture of the elements, however, leads to homogenous samples for both compounds according to powder diffraction experiments. The large c lattice parameters, a great number of extremely weak reflections and severe peak overlap impeded the proof of the homogeneity by a Rietveld refinement. Thus, the powder patterns corresponding to the models obtained from single-crystal structure refinements were simulated with the program package EXPGUI (GSAS).^[28,29] The reflection positions and intensities match well with the experimental diagrams if a small amount of preferred orientation along (001) is taken into account. The plate-like shape of the crystallites resulting from the layered structure obviously leads to this preferred orientation on the Mylar foil. Experimental and calculated powder patterns are shown in Fig. 2 and substantiate the homogeneity of the samples.

For single crystal analysis, irregularly shaped single crystals were isolated from the crushed ingots, mounted on glass fibres and checked for quality by Laue photographs on a Buerger precession camera. Intensity data of the best crystals were collected on a STOE IPDS-I diffractometer with imaging plate detector using Mo- $K\alpha$ radiation (graphite monochromator, $\lambda = 0.71093 \text{ \AA}$). Semiempirical absorption corrections based on equivalent reflections were applied^[30] before the structures were solved by direct methods.^[31] Full-matrix least-squares refinements of models developed from the initial solutions (see below) were executed with SHELXL.^[32] Details about data collection and final refinement are given in Table 1. Further information may be obtained from the Fachinformationszentrum Karlsruhe, D-76344 Eggenstein-Leopoldshafen (Germany), by quoting the deposition numbers CSD-419748 ($\text{Ge}_{4.71}\text{Sb}_{31.29}\text{Te}_{15}$) and CSD-419749 ($\text{Ag}_{0.24}\text{Sb}_{10.76}\text{Te}_4$), the names of the authors, and the citation of the paper.

Table 1. Crystallographic data on the structure refinements of 51R-Ge_{2-x}Sb_{2+x}Te₅Sb₈ (x = 0.43) and 15P-Ag_xSb_{3-x}Te₄Sb₈ (x = 0.24) at 293 K.

Formula	Ge _{1.57} Sb _{10.43} Te ₅	Ag _{0.24} Sb _{10.76} Te ₄
Formula mass (in g mol ⁻¹)	2021.98	1846.32
Crystal system / Space group	trigonal / $R\bar{3}m$	trigonal / $P\bar{3}m1$
Cell parameters (in Å)	$a = 4.258(1)$, $c = 97.23(2)$	$a = 4.282(1)$, $c = 28.636(5)$
Cell volume (in Å ³)	1526.7(6)	454.7(2)
X-ray density (in g cm ⁻³)	6.598	6.742
Absorption coefficient (in mm ⁻¹)	22.880	22.215
Formula units (per unit cell)	3	1
$F(000)$	2526.5	768
Diffractometer	IPDS I	IPDS I
Radiation (in Å)	MoK α ($\lambda = 0.71073$)	MoK α ($\lambda = 0.71073$)
2θ range (in °)	$5.0 < 2\theta < 53.5$	$5.7 < 2\theta < 59.8$
$R_{\text{int}} / R_{\sigma}$	0.0690, 0.0288	0.1040, 0.0462
Absorption correction	semiempirical	semiempirical
Measured reflections	3700	4373
Independent data / parameters	513 / 29	601 / 26
Refinement	full-matrix least-squares on F^2	full-matrix least-squares on F^2
R indices [$I > 2\sigma(I)$] ^(a,b)	$R1 = 0.0438$, $wR1 = 0.1037$	$R1 = 0.0538$, $wR1 = 0.1023$
R indices [all data] ^(a,b)	$R1 = 0.0570$, $wR1 = 0.1100$	$R1 = 0.0839$, $wR1 = 0.1207$
Goof [all data]	1.286	1.064
Residual electron density (max. / min) (in eÅ ⁻³)	+2.764/-2.681	+ 1.094/ - 1.465

$$^a) R1 = \sum |F_o - F_c| / \sum |F_o|$$

$$^b) wR2 = [\sum [w(F_o^2 - F_c^2)^2] / \sum [w(F_o^2)^2]]^{1/2}; w = 1 / [\sigma^2(F_o^2) + (aP)^2 + bP] \text{ with } P = [\text{Max}(0, F_o^2) + 2F_c^2] / 3$$

3.3.3 Results and discussion

3.3.3.1 Powder patterns and structural homologies

GeTe, Sb₂Te₃ and Sb₂ units are combined in the homologous series (Sb₂Te₃)_m(Sb₂)_k and (GeTe)_n(Sb₂Te₃)_m (*cf.* Fig. 1) to yield trigonal structures with various stacking sequences of atom layers and whole building blocks, respectively, along the threefold axis. This arrangement is possible because in the various block elements there are almost identical hexagonal 2D atom layers extending parallel (001). We concluded that the combination of all three building units should be feasible and lead to a new series (MTe)_n(Sb₂Te₃)_m(Sb₂)_k. According to the homologies found for (Sb₂Te₃)_m(Sb₂)_k and (GeTe)_n(Sb₂Te₃)_m, which are described in detail elsewhere,^[6,8,22,23] powder patterns indicate the number of layers N per translational period; and an average layer thickness c/N (in general about 1.9 Å but depending on the composition) can be obtained by indexing the strongest reflections based on an “average” A7 type unit cell.^[33] Since the exact value of c/N strongly depends on the type and number of characteristic building block types present, the sequence of typical slabs, the lattice parameters and the space groups of the

structures can be predicted. We expanded this idea to the new class of compounds $(\text{MTe})_n(\text{Sb}_2\text{Te}_3)_m(\text{Sb}_2)_k$. The number N of atom layers per translational period must be a multiple of the number of atom layers within the individual building blocks. The formula units MTe or Sb_2 contribute two layers each, whereas five layers must be taken into account per Sb_2Te_3 unit. As the ubiquitous ABC stacking sequence of the single atom layers superimposes a periodicity that is a multiple of three, one translational period comprises three times the calculated number of layers if $2n + 5m + 2k$ is not a multiple of three. The resulting space group is $R\bar{3}m$ (with $Z = 3$), whereas it is $P\bar{3}m1$ (with $Z = 1$) in case $2n + 5m + 2k$ is a multiple of three.^[17,33,34] The powder patterns of the specimens investigated correspond to patterns estimated from these rules by relating the composition with a theoretically expected number of layers per unit cell ($51R\text{-Ge}_{2-x}\text{Sb}_{2+x}\text{Te}_5\cdot\text{Sb}_8$ and $15P\text{-Ag}_x\text{Sb}_{3-x}\text{Te}_4\cdot\text{Sb}_8$). However, for the bulk samples slight deviations due to stacking disorder of the building blocks and a certain range of homogeneity without changing the stacking sequence can be expected.^[15,35] It seems obvious that the more or less ordered arrangement of possible block elements can easily vary and might strongly depend on the details of the reaction conditions. Bi_4Te_3 , for example, shows a periodical sequence of alternating Bi_2 and Bi_2Te_3 slabs ("one to one") whereas in Sb_4Te_3 pairs of Sb_2 slabs alternate with pairs of Sb_2Te_3 -slabs ("two to two").^[6] A non-periodical arrangement of structural units or a variation of block sizes would primarily affect weak "superstructure" reflections that are not easy to detect precisely in powder patterns. Therefore, single-crystal structure analysis is the most appropriate tool to determine or confirm the exact arrangement of the predicted block elements in phases of the type $(\text{MTe})_n(\text{Sb}_2\text{Te}_3)_m(\text{Sb}_2)_k$. Our single crystal diffraction experiments on the samples discussed here do not show any pronounced diffuse scattering, which excludes a high degree of disorder. However, we also observed disordered phases $(\text{MTe})_n(\text{Sb}_2\text{Te}_3)_m(\text{Sb}_2)_k$ (especially for $m = 1$ and large values, *i.e.* up to 12, for either m or k) which exhibit remarkable diffuse scattering between the strong reflections instead of superstructure reflections. This is most pronounced for quenched samples and indicates disorder of the building elements. Powder patterns simulated from the results of the single crystal structure refinements match well with the powder patterns experimentally observed (*cf.* Fig. 2 and experimental section). The decisive features are the weak reflections which seemingly disappear, *i.e.* turn into almost continuous diffuse intensity, in disordered samples.

3.3.3.2 Single-crystal structure refinement

The initial structure solutions corresponded to the number of layers per unit cell expected from the analysis of the powder patterns for both $51R\text{-Ge}_{2-x}\text{Sb}_{2+x}\text{Te}_5\cdot\text{Sb}_8$ and $15P\text{-Ag}_x\text{Sb}_{3-x}\text{Te}_4\cdot\text{Sb}_8$. However, the similar atomic formfactors of Sb and Te do not allow a straightforward differentiation of these elements. Fortunately, an unequivocal identification of the structural building blocks present along [001] in the layered structure is possible by comparing the interatomic distances obtained from the initial solutions with well-known binary compounds such as Sb_2Te_3 , SbTe , Sb_2Te and Sb_8Te_3 ^[5,6,22] on the one hand and ternary compounds with rocksalt-type slabs such as GeSb_2Te_4 or $\text{Ge}_2\text{Sb}_2\text{Te}_5$ ^[23,25] on the other hand. According to this comparison, which is partially shown in Fig. 3, the atom types were assigned to the possible positions obtained from structure solution. An adequate structure model with $\text{Ge}_2\text{Sb}_2\text{Te}_5$ -type blocks separated by four A7-type Sb_2 layers was found for the phase $\text{Ge}_{2-x}\text{Sb}_{2+x}\text{Te}_5\cdot\text{Sb}_8$. In the same way, a reasonable structural model assembled of GeSb_2Te_4 -type slabs, containing three cation layers and four Te layers, with four A7-type Sb_2 layers was derived for $\text{Ag}_x\text{Sb}_{3-x}\text{Te}_4\cdot\text{Sb}_8$. The distribution of Ge/Sb and Ag/Sb on the cation sites is quite clear from the refinement of site occupancy factors, which were constrained to full occupancy for all cation positions. In principle, void cation sites are as well possible, however, assuming no voids leads to refined compositions that are in good agreement with the overall composition given by the chemical analysis and the preparation of homogeneous samples with the corresponding composition. The final structure refinements converged at $R = 4.38\%$ for $51R\text{-Ge}_{2-x}\text{Sb}_{2+x}\text{Te}_5\cdot\text{Sb}_8$ and $R = 5.38\%$ for $15P\text{-Ag}_x\text{Sb}_{3-x}\text{Te}_4\cdot\text{Sb}_8$, respectively. Wyckoff positions, atomic coordinates, site occupancies, and displacement parameters for $\text{Ge}_{2-x}\text{Sb}_{2+x}\text{Te}_5\cdot\text{Sb}_8$ and $\text{Ag}_x\text{Sb}_{3-x}\text{Te}_4\cdot\text{Sb}_8$ are given in Tables 2 and 3, respectively.

Table 2. Wyckoff positions, atomic coordinates, site occupancy, equivalent isotropic displacement factors and anisotropic displacement parameters (in \AA^2) for $51R\text{-Ge}_{2-x}\text{Sb}_{2+x}\text{Te}_5\cdot\text{Sb}_8$ ($x = 0.43$).

atom	Wyck.	x	y	Z	s.o.f.	U_{eq}	U_{11}	U_{22}	U_{33}	U_{12}	U_{13}	U_{23}
Ge1/Sb1	6c	0	0	0.35180(2)	0.56(2)/0.44(2)	0.0263(7)	0.0254(8)	0.0254(8)	0.0282(10)	0.0127(4)	0	0
Ge2/Sb2	6c	0	0	0.05859(2)	0.23(2)/0.77(2)	0.0264(6)	0.0184(7)	0.0184(7)	0.0423(11)	0.0092(4)	0	0
Te1	3a	0	0	0	1	0.0144(4)	0.0153(6)	0.0153(6)	0.0126(7)	0.0076(3)	0	0
Te2	6c	0	0	0.70272(1)	1	0.0179(4)	0.0165(5)	0.0165(5)	0.0206(6)	0.0083(2)	0	0
Te3	6c	0	0	0.40790(2)	1	0.0227(4)	0.0153(5)	0.0153(5)	0.0375(8)	0.0077(2)	0	0
Sb3	6c	0	0	0.76599(1)	1	0.0184(4)	0.0143(5)	0.0143(5)	0.0265(7)	0.0072(2)	0	0
Sb4	6c	0	0	0.11505(1)	1	0.0184(4)	0.0152(5)	0.0152(5)	0.0249(7)	0.0076(2)	0	0
Sb5	6c	0	0	0.47221(1)	1	0.0147(4)	0.0138(5)	0.0138(5)	0.0166(7)	0.0069(2)	0	0
Sb6	6c	0	0	0.82136(1)	1	0.0121(4)	0.0110(5)	0.0110(5)	0.0144(6)	0.0055(2)	0	0

Table 3. Wyckoff positions, atomic coordinates, site occupancy, equivalent isotropic displacement factors and anisotropic displacement parameters (in Å²) for 15*P*-Ag_xSb_{3-x}Te₄Sb₈ (*x* = 0.24).

atom	Wyck.	x	y	Z	s.o.f.	U_{eq}	U_{11}	U_{22}	U_{33}	U_{12}	U_{13}	U_{23}
Sb1	1 <i>a</i>	0	0	0	1	0.0262(5)	0.0259(7)	0.0259(7)	0.0267(9)	0.0130(3)	0	0
Ag2/Sb2	2 <i>d</i>	2/3	1/3	0.13472(6)	0.12(9)/ 0.88(9)	0.0310(7)	0.0213(7)	0.0213(7)	0.0502(12)	0.0107(4)	0	0
Te1	2 <i>d</i>	1/3	2/3	0.06246(5)	1	0.0175(3)	0.0155(4)	0.0155(4)	0.0215(5)	0.0077(2)	0	0
Te2	2 <i>c</i>	0	0	0.19164(5)	1	0.0180(4)	0.0156(5)	0.0156(5)	0.0227(6)	0.0078(2)	0	0
Sb3	2 <i>d</i>	1/3	2/3	0.27267(5)	1	0.0174(4)	0.0137(4)	0.0137(4)	0.0247(6)	0.0068(2)	0	0
Sb4	2 <i>d</i>	2/3	1/3	0.32588(5)	1	0.0186(4)	0.0141(5)	0.0141(5)	0.0278(7)	0.0070(2)	0	0
Sb5	2 <i>c</i>	0	0	0.40724(4)	1	0.0170(4)	0.0155(4)	0.0155(4)	0.0200(6)	0.0077(2)	0	0
Sb6	2 <i>d</i>	1/3	2/3	0.46023(4)	1	0.0129(3)	0.0113(4)	0.0113(4)	0.0160(6)	0.0056(2)	0	0

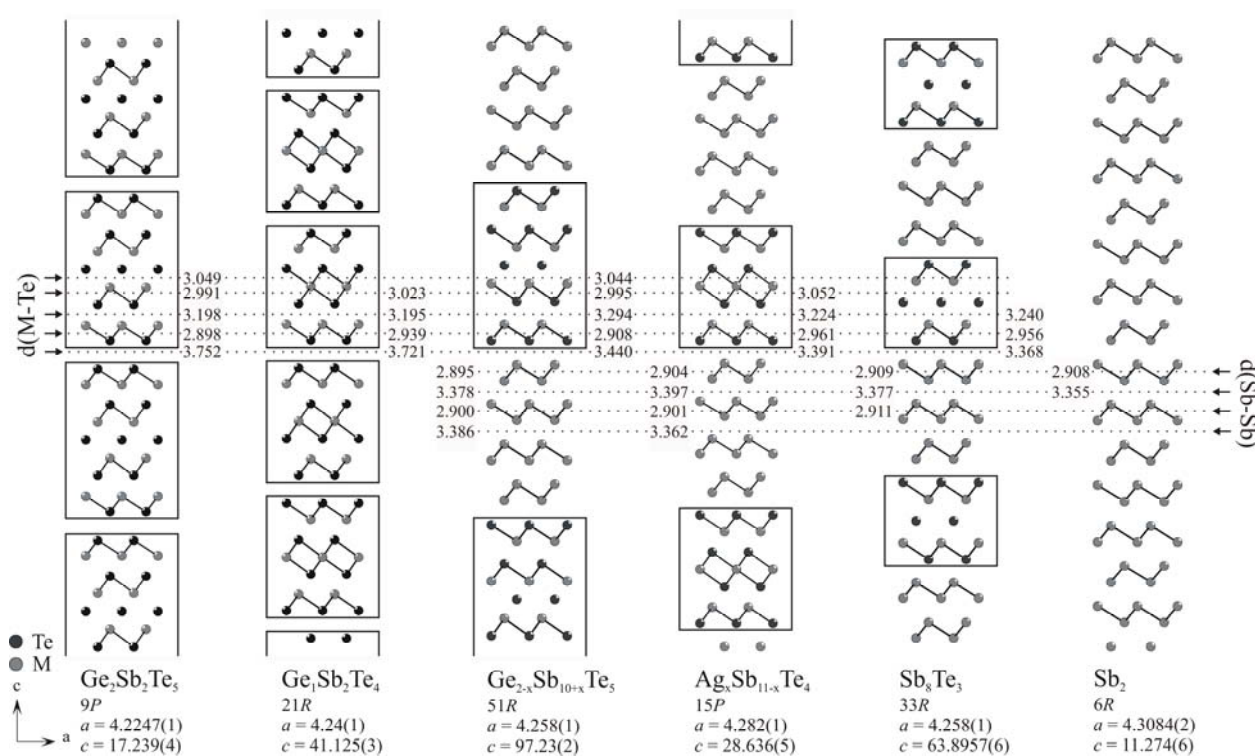


Figure 3. Comparable interatomic distance sets (in Å) for exemplary compounds of the series (GeTe)_n(Sb₂Te₃)_m, (Sb₂Te₃)_m(Sb₂)_k and (MTe)_n(Sb₂Te₃)_m(Sb₂)_k; distances M-Te are given on the right hand side and distances Sb-Sb on the left hand side of representative sections of the structures. All standard deviations are < 0.002 Å. For the new phases, the distances given have been taken from the final refinement results, however the distances obtained from initial solution did not significantly differ from these values. The boxes indicate the rocksalt-type slabs. Short bonds are drawn to indicate the layer structure and its inversion (cf. Fig. 1 for a clear correlation of the projections by comparison with perspective views of structure parts). The phases, their structure types as well as their lattice parameters are given at the bottom.

3.3.3.3 Structure description

The new compounds of the type $(MTe)_n(Sb_2Te_3)_m(Sb_2)_k$, ($n = 1, 2, m = 1, k = 4$) crystallize with long-range ordered stacking sequences of semimetallic and rather ionic hexagonal atom layers parallel to (001). Their structures can be viewed as ordered arrangement of blocks of four A7-type Sb_2 layers alternating with one $(MTe)_n(Sb_2Te_3)_m$ ($n = 1$ or $2, m = 1$) block, yielding $51R$ and $15P$ structures with a "four to one" building block composition. The structures are shown in Fig. 4.

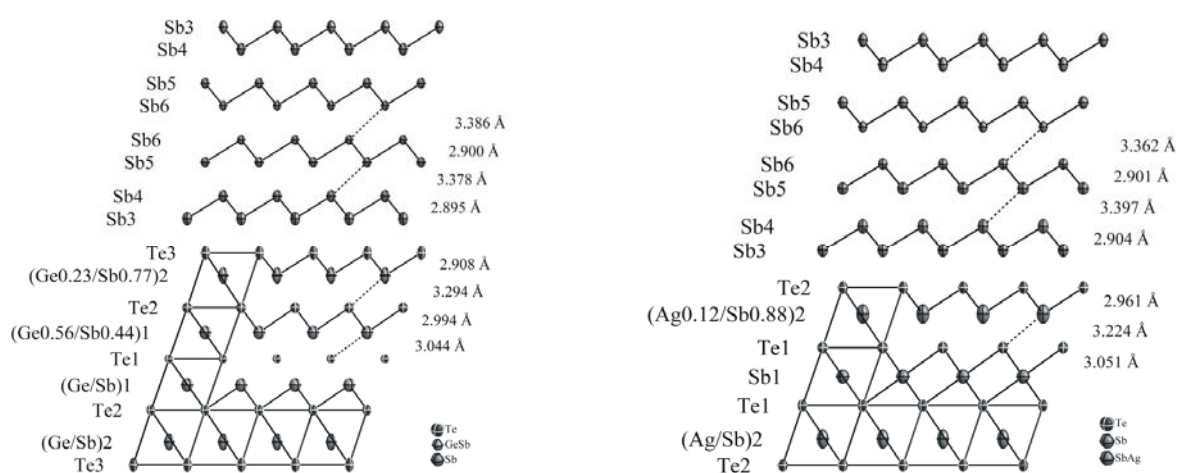


Figure 4. Projections of the $51R$ and $15P$ crystal structures of $Ge_{2-x}Sb_{2+x}Te_5Sb_8$ (left) and $Ag_xSb_{3-x}Te_4Sb_8$ (right) along $[010]$ (cf. Fig. 1 for a clarification of the style): displacement ellipsoids are drawn at 90% probability level; interatomic distances show no esd. > 0.002 Å and site occupation are indicated if deviating from full occupation.

Rocksalt-type slabs of the type $(MTe)_n(Sb_2Te_3)_m$ (with $m=1$ and $n = 1$ or 2) include an alternating sequence of $n + 2m$ cation layers and $n + 3m$ anion layers. The cations exhibit distorted octahedral coordination resulting in a network of $[MTe_6]$ corresponding to a distorted rocksalt structure comparable to that of $GeTe$ which is an ordered variant of the A7 type.^[37] A distortion towards the typical $3 + 3$ coordination of A7 phases can be observed with increasing distance from the block centre. Short bond lengths $M-Te$ occur towards the adjacent "pure" A7-type Sb_2 slabs and longer $M-Te$ distances are observed towards the block centre (cf. Fig. 3). Due to the mirror plane in the centre of the $Ag_xSb_{3-x}Te_4$ block, an almost undistorted octahedron can be found around $Sb1$ in $Ag_xSb_{3-x}Te_4Sb_8$. Similar distance variations have been observed for compounds $(GeTe)_n(Sb_2Te_3)_m$ and correspond to the increasing formation of A7-type $M-Te$ double layers with increasing distance from the centres of the rocksalt-type blocks, induced by the rising influence of neighbouring structural units with a lower degree of ionic bonding.^[6,23,33] These double layers are quite similar to A7-layers in elemental Sb (cf. Fig. 1 and 3), especially with intra-layer distances being very similar (however, the difference is large enough to

distinguish atoms in rocksalt-type blocks and A7-type Sb_2 layers in structure determinations). This structural similarity allows for a strain-free intergrowth of $(\text{MTe})_n(\text{Sb}_2\text{Te}_3)_m$ elements with blocks of A7-type Sb_2 layers. The van der Waals like gap between consecutive building units is essentially the same for $\text{Ge}_{2-x}\text{Sb}_{2+x}\text{Te}_5\cdot\text{Sb}_8$ and $\text{Ag}_x\text{Sb}_{3-x}\text{Te}_4\cdot\text{Sb}_8$ with distances $\text{Sb}-\text{Te}$ of 3.440 and 3.391 Å respectively. The sum of van der Waals radii for Sb (2.00 Å) and Te (2.06 Å)^[38] is 4.06 Å, which is greater than the distances observed. Therefore, they indicate that there is not only van der Waals bonding but a high degree of polar covalence. Typical lengths of strong M-Te bonds within the Te containing units lie in the range of about 2.8–2.9 Å for phases $(\text{GeTe})_n(\text{Sb}_2\text{Te}_3)_m$ and $(\text{Sb}_2\text{Te}_3)_m(\text{Sb}_2)_k$.^[6,8,22,23] Within the $(\text{Sb}_2)_4$ blocks in both new compounds, the distance sets corresponding to four A7-type layers of antimony show a variation of the short and long distances with proximity to the Te-network (*cf.* Fig. 3 and 4) similar to those found in the homologous series $(\text{Sb}_2\text{Te}_3)_m(\text{Sb}_2)_k$.^[6,22] These distances are almost identical to those in elementary antimony. The results obtained indicate the possibility to perfectly combine the blocks $(\text{MTe})_n(\text{Sb}_2\text{Te}_3)_m$ and $(\text{Sb}_2)_k$ in a new homologous series $(\text{MTe})_n(\text{Sb}_2\text{Te}_3)_m(\text{Sb}_2)_k$ for which, depending on the exact composition, differently sized building blocks can be expected.

The two phases studied in this work exhibit differences in cation site occupancy within the $(\text{MTe})_n(\text{Sb}_2\text{Te}_3)_m$ building blocks. In $\text{Ge}_{2-x}\text{Sb}_{2+x}\text{Te}_5\cdot\text{Sb}_8$, all cation positions show a mixed occupancy with Ge and Sb. The slight preference of Sb to occupy positions closer to the van der Waals like gap is consistent with results for compounds $(\text{GeTe})_n(\text{Sb}_2\text{Te}_3)_m$.^[23,25] The higher formal charge of Sb^{III} compared to Ge^{II} makes it more suitable to occupy cation positions neighbouring terminal Te layers since Sb^{III} can better satisfy the coordination of Te atoms in layers that are only uniaxially surrounded by cations. Therefore, the ratio Ge/Sb on these positions is lowered. Recently, we showed^[33] that a given structure type in the series $(\text{GeTe})_n(\text{Sb}_2\text{Te}_3)_m$ can be realized with remarkable deviations from the ideal composition. Therefore, the excess of Sb in the $\text{Ge}_{2-x}\text{Sb}_{2+x}\text{Te}_5$ slab (compared to ideal $\text{Ge}_2\text{Sb}_2\text{Te}_5$) is consistent with the synthesis conditions. In contrast to $\text{Ge}_{2-x}\text{Sb}_{2+x}\text{Te}_5\cdot\text{Sb}_8$, mixed occupancy of cation positions was not observed on all cation positions of $\text{Ag}_x\text{Sb}_{3-x}\text{Te}_4\cdot\text{Sb}_8$. Although Ag^{I} has a lower formal charge than Ge^{II} , it obviously prefers the position close to the terminal Te layers. Sb and Ag obviously do not occupy exactly the same position as indicated by the prolate displacement ellipsoid. However, the ratio Ag/Sb is much lower than in case of Ge/Sb mixing. Probably this explains why the rocksalt-type blocks in $\text{Ag}_x\text{Sb}_{3-x}\text{Te}_4\cdot\text{Sb}_8$ show a stronger deviation from the idealized composition AgSb_2Te_4 than those in $\text{Ge}_{2-x}\text{Sb}_{2+x}\text{Te}_5\cdot\text{Sb}_8$ with respect to the ideal formula $\text{Ge}_2\text{Sb}_2\text{Te}_5$. The cation position in the $\text{Ag}_x\text{Sb}_{3-x}\text{Te}_4$ block centre is, according to our results, solely occupied by Sb. Similar ordering of Ag- and Sb-cations was supposed for a

theoretical rhombohedral structure of $\text{Ag}_{0.5}\text{Sb}_{0.5}\text{Te}$.^[12,39] The cation ordering might be due to a size effect since it is extremely unlikely that Ag and Sb have the same effective size in such compounds. Ag^{I} is larger than Sb^{III} and the distortion of Te_6 octahedra is energetically favourable near the van der Waals like gap. This is consistent with the elongated distances M–Te of 3.224 and 2.961 Å compared to corresponding distances M–Te of 3.195 and 2.939 Å found in GeSb_2Te_4 (see also Fig. 3). Probably this also explains why only a small amount of Sb can be substituted by Ag.

3.3.3.5 Metastability of phases $(\text{MTe})_n(\text{Sb}_2\text{Te}_3)_m(\text{Sb}_2)_k$

According to the phase ternary phase diagram^[7,19–21] (*cf.* Fig. 1) there are no thermodynamically stable phases whose compositions deviate significantly from those of the homologous series on the pseudo-binary lines $(\text{GeTe})_n(\text{Sb}_2\text{Te}_3)_m$ and $(\text{Sb}_2\text{Te}_3)_m(\text{Sb}_2)_2$. The long-range ordered arrangement of A7-type Sb slabs and rocksalt-type building blocks therefore corresponds to kinetically stabilized phases. The compounds $(\text{MTe})_n(\text{Sb}_2\text{Te}_3)_m(\text{Sb}_2)_k$ are probably quenched intermediate states of phase separation processes which finally lead to the stable phases $(\text{MTe})_n(\text{Sb}_2\text{Te}_3)_m$ and Sb. Complete phase separation is very slow as, of course, complete building blocks cannot be rearranged and “isolate” parts of the structure from each other. Comparable to spinodal decomposition, partial phase separation without well-defined phase boundaries slowly continues on the atomic scale if enough energy for atom diffusion is supplied during annealing. This is in accordance with reports on the ternary phase diagram, since most samples studied to construct the diagram were annealed for up to 8 months at temperatures up to 500 °C,^[7,19–21] giving enough time for phase separation. An intermediate state of spinodal decomposition may be long-ordered by short-range diffusion during annealing at lower temperatures or for a short time only. Our thermoanalytical measurements (DTA) revealed that $\text{Ag}_x\text{Sb}_{3-x}\text{Te}_4\cdot\text{Sb}_8$ ($x = 0.24$) = $\text{Ag}_{0.24}\text{Sb}_{10.76}\text{Te}_4$ melts incongruently at 525 °C and $\text{Ge}_{2-x}\text{Sb}_{2+x}\text{Te}_5\cdot\text{Sb}_8$ ($x = 0.43$) = $\text{Ge}_{1.57}\text{Sb}_{10.43}\text{Te}_5$ melts incongruently at 529 °C. The melting points are lower than the melting points described for the pseudobinary lines $(\text{GeTe})_n(\text{Sb}_2\text{Te}_3)_m$ and $(\text{Sb}_2\text{Te}_3)_m(\text{Sb}_2)_2$, which can be expected for a mixture of different building blocks. Annealing at temperatures approximately 200 °C below the melting points for several hours does not affect the structure and homogeneity of the specimens according to powder patterns. This indicates that the layered structure is kinetically stable and does not easily separate into the thermodynamically stable phases. The melts partially evaporate above 700 °C, indicated by a mass loss according to TG.

3.3.3.6 Electrical properties

Electrical conductivity measurements show metallic characteristics for both phases, indicated by the increase of the resistance with increasing temperature (*cf.* Fig. 5). The residual resistivity ratio $\rho_s(300\text{ K})/\rho_s(10\text{ K})$ is 1.54 for $15P\text{-Ag}_x\text{Sb}_{3-x}\text{Te}_4\cdot\text{Sb}_8$ and 2.06 for $51R\text{-Ge}_{2-x}\text{Sb}_{2+x}\text{Te}_5\cdot\text{Sb}_8$. Positional disorder in the rocksalt-type slabs can raise the resistivity at low temperatures and thus explain these small values.

The metallic conductivity seems, at first sight, somewhat unusual since assuming Ge^{II} , Ag^{I} and Sb^{III} , both compounds are valence compounds that obey the 8-*N* rule and one would expect semiconducting behaviour. However, the absolute values of the conductivity (588 S cm^{-1} for $15P\text{-Ag}_x\text{Sb}_{3-x}\text{Te}_4\cdot\text{Sb}_8$ and 2500 S cm^{-1} for $51R\text{-Ge}_{2-x}\text{Sb}_{2+x}\text{Te}_5\cdot\text{Sb}_8$ at 300 K) are rather low compared to typical metals and may well indicate that in fact the compounds are degenerate semiconductors. The small difference in electronegativity implies a narrow band gap and positional disorder may further narrow it by tailing of band states. Metallic like conduction was also reported for stable phases $(\text{GeTe})_n(\text{Sb}_2\text{Te}_3)_m$ although their optical properties reveal a narrow band gap.^[40] This seemingly contradictory result is typical for degenerate semiconductors. The absolute values are in the same range as those found for the homologous series $(\text{GeTe})_n(\text{Sb}_2\text{Te}_3)_m$ and $(\text{Sb}_2\text{Te}_3)_m(\text{Sb}_2)_k$. Conductivities are given in Table 4 for comparison. Phases with remarkable thermoelectric properties in the systems Sb–Te and M–Sb–Te (M=Ge, Ge/Ag, Ag/Pb, Bi...) are closely related to our compounds and exhibit conductivities in the same range.

Table 4. Specific electrical conductivity σ of phases from the homologous series $(\text{GeTe})_n(\text{Sb}_2\text{Te}_3)_m$, $(\text{Sb}_2\text{Te}_3)_m(\text{Sb}_2)_k$ and their basic building units in comparison with the values found for $15P\text{-Ag}_x\text{Sb}_{3-x}\text{Te}_4\cdot\text{Sb}_8$ and $51R\text{-Ge}_{2-x}\text{Sb}_{2+x}\text{Te}_5\cdot\text{Sb}_8$ (in Scm^{-1}).

Phase	n:m:k	σ	Phase ^[7]	n:m:k	σ	Phase ^[6]	n:m:k	σ	Phase	n:m:k	σ
$\text{Ge}_{2-x}\text{Sb}_{10+x}\text{Te}_5$	2:1:4	2500	$\text{Ge}_2\text{Sb}_2\text{Te}_5$	2:1:0	2400	SbTe	0:2:1	3500	Sb_2Te_3 ^[7]	0:1:0	5000
$\text{Ag}_x\text{Sb}_{11-x}\text{Te}_4$	1:1:4	588	GeSb_2Te_4	1:1:0	2250	Sb_4Te_3	0:1:1	3000	GeTe ^[7]	1:0:0	6750
			GeSb_4Te_7	1:2:0	2020	Sb_2Te	0:1:2	1500	$\text{Ag}_{0.5}\text{Sb}_{0.5}\text{Te}$ ^[41]	1:0:0	30
			$\text{GeSb}_6\text{Te}_{10}$	1:3:0	1300	Sb_8Te_9	0:1:3	6000	Sb ^[42]	0:0:1	28000

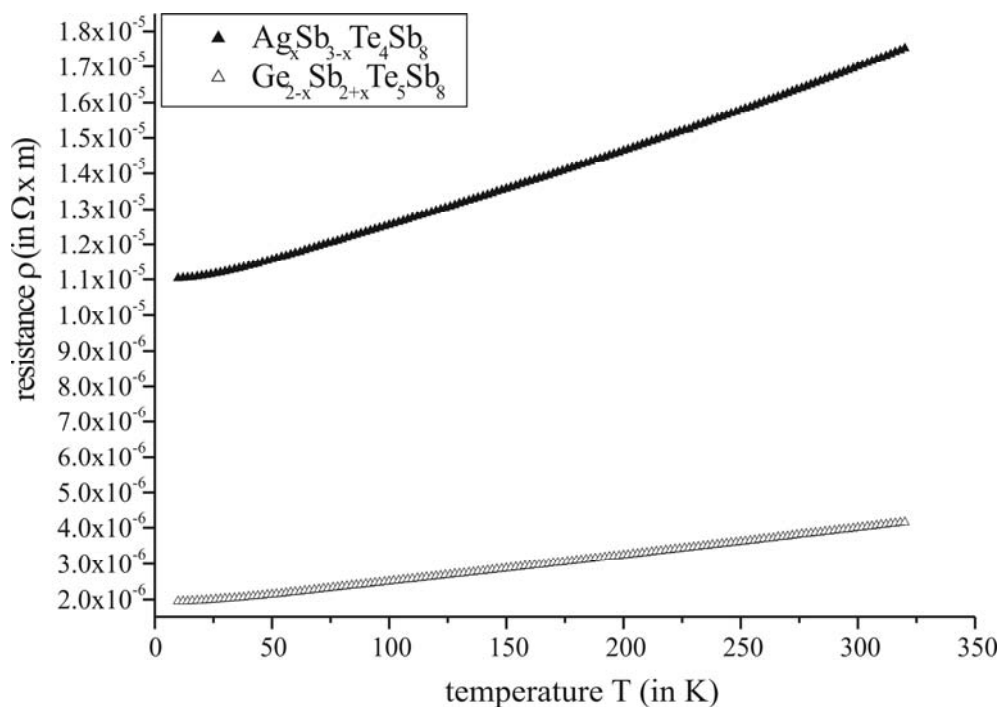


Figure 5. Temperature dependence of the specific resistance of $\text{Ge}_{2-x}\text{Sb}_{2+x}\text{Te}_5\text{Sb}_8$ and $\text{Ag}_x\text{Sb}_{3-x}\text{Te}_4\text{Sb}_8$ in the temperature range 10K to 300K.

Obviously several factors do influence the conductivity. The frequency of different building block types (see the influence of GeTe , Sb_2Te_3 or Sb_2 concentration, Table 4) is related to the electrical properties of the materials. Substitution of the elements and ordering on their atomic positions play an additional role. The higher degree of cation ordering (see above) is probably the main reason why $\text{Ag}_x\text{Sb}_{3-x}\text{Te}_4\text{Sb}_8$ shows a lower conductivity than $\text{Ge}_{2-x}\text{Sb}_{2+x}\text{Te}_5\text{Sb}_8$.

Strongly anisotropic conductivity (parallel and perpendicular to the stacking direction) was reported for the layered phases $(\text{Sb}_2\text{Te}_3)_m(\text{Sb}_2)_k$ ^[6] and an influence of the stacking sequence can be expected, but to our knowledge has yet not been studied for these materials.

3.3.4 Conclusion

$\text{Ge}_{2-x}\text{Sb}_{2+x}\text{Te}_5\text{Sb}_8$ ($x = 0.43$) and $\text{Ag}_x\text{Sb}_{3-x}\text{Te}_4\text{Sb}_8$ ($x = 0.24$) unite the building elements MTe ($= \text{GeTe}$ or $\text{Ag}_{0.5}\text{Sb}_{0.5}\text{Te}$), Sb_2Te_3 and Sb_2 known from stable phases on the (pseudo)binary lines GeTe to Sb_2Te_3 and Sb_2Te_3 to Sb in a 1 : 4 stacking sequence of distorted rocksalt-type M-Sb-Te slabs and A7-type Sb layers. For phases $(\text{MTe})_n(\text{Sb}_2\text{Te}_3)_m(\text{Sb}_2)_k$ the composition as well as the thermal treatment probably determine the occurrence of the distinct building units. The substitution of Ge by $\text{Ag}_{0.5}\text{Sb}_{0.5}$ has a strong influence on occupancy of cation positions. Ag containing phases show a stronger tendency towards cation ordering including a higher degree of ionicity and thus a higher resistivity.

Although, according to the phase diagram, these long-periodically ordered phases are metastable, they are kinetically stable at room temperature. Thermoanalytical studies show that their long-range order is stable up to the incongruent melting point at approximately 525 °C (at least for some hours). In our opinion the phases are long-periodically ordered superstructures formed by short-range diffusion after quenching an intermediate state of spinodal decomposition. This leads to “*in situ* multilayer formation”, comparable to that which is usually generated by CVD or MBE methods in thin films (although those layers are thicker). Fine-tuning the combination of block frequencies, substitution and thermal treatment might well open new ways to “multilayer bulk materials”. Structure–property relationships have yet to be fully understood, but our electrical conductivity measurements, in comparison with previously reported ones (*cf.* Table 4) indicate that an adjustment of physical properties of these materials is possible by varying the composition and cation ordering in distorted rocksalt-type telluride blocks with different thickness in combination with an introduction of semimetallic character by insertion of A7-type antimony blocks. This is especially interesting since strongly related telluride phases are promising candidates for bulk thermoelectric materials with high performance. Phases $(\text{MTe})_n(\text{Sb}_2\text{Te}_3)_m(\text{Sb}_2)_k$ therefore unite interesting structural chemistry with relevant physical properties and might pave the way to new fields of applications.

3.3.5 References

- [1] H. Böttner, G. Chen and R. Venkatasubramanian, *MRS Bull.* **2006**, *31*, 211.
- [2] R. Venkatasubramanian, E. Siivola, T. Colpitts and B. O’Quinn, *Nature* **2001**, *413*, 597.
- [3] G. S. Nolas, J. Poon and M. G. Kanatzidis, *MRS Bull.* **2005**, *31*, 199.
- [4] T. M. Tritt and M. A. Subramanian, *MRS Bull.* **2006**, *31*, 188.
- [5] T. L. Anderson and H. B. Krause, *Acta Crystallogr. Sect. B* **1974**, *30*, 1307.
- [6] P. F. P. Poudeu and M. G. Kanatzidis, *Chem. Commun.* **2005**, 2672
- [7] L. E. Shelimova, O. G. Karpinsky, P. P. Konstantinov, M. A. Kretova, E. S. Avilov and V. S. Zemskov, *Inorg. Mater.* **2001**, *37*, 342.
- [8] L. E. Shelimova, O.G.Karpinsky, M. A. Kretova, V. I.Kosyakov, V. A. Shestakov, V. S. Zemskov and F. A. Kuznetsov, *Inorg. Mater.* **2000**, *36*, 768.
- [9] T. B. Zhukova and A. I. Zaslavskii, *Sov. Phys. Crystallogr.* **1972**, *15*, 796.
- [10] J. Navrátil, I. Klichová, S. Karamazov, J. Šrámková and J. Horák, *J. Solid State Chem.*, **1998**, *140*, 29.
- [11] T. Matsunaga and N. Yamada, *Jpn. J. Appl. Phys.* **2002**, *41*, 1674.

- [12] E. Quarez, K.-F. Hsu, R. Pcionek, N. Frangis, E. K. Polychroniadis and M. G. Kanatzidis, *J. Am. Chem. Soc.* **2005**, *127*, 9177.
- [13] H. Tashiro, M. Harigaya, Y. Kageyama, K. Ito, M. Shinotsuka, K. Tani, A. Watada, N. Yiwata, Y. Nakata and S. Emura, *Jpn. J. Appl. Phys.* **2002**, *41*, 3758.
- [14] S. Geller, A. Jayaraman and G. W. Hull, *J. Phys. Chem. Solids* **1965**, *26*, 353.
- [15] S. Kuypers, G. Van Tendeloo, J. Van, Landuyt and S. Amelinckx, *J. Solid State Chem.* **1988**, *76*, 102.
- [16] S. Kuypers, G. Van Tendeloo, J. Van, Landuyt and S. Amelinckx, *J. Solid State Chem.* **1988**, *73*, 192.
- [17] O. G. Karpinskii, L. E. Shelimova, M. A. Kretova and J.-P. Fleurial, *J. Alloys Compd.* **1998**, *265*, 170.
- [18] T. E. Svechnikova, L. E. Shelimova, P. P. Konstantinov, M. A. Kretova, E. S. Avilov, V. S. Zemskov, C. Stiewe and E. Müller, *Inorg. Mater.* **2006**, *42*, 1311.
- [19] S. Bordas, M. T. Clavaguera-Mora, B. Legendre and C. Hancheng, *Thermochim. Acta* **1986**, *107*, 239.
- [20] V. I. Kosyakov, V. A. Shestakov, L. E. Shelimova, F. A. Kuznetsov and V. S. Zemskov, *Inorg. Mater.* **2000**, *36*, 1004.
- [21] B. Legendre, C. Hancheng, S. Bordas and M. T. Clavaguera-Mora, *Thermochim. Acta* **1984**, *78*, 141.
- [22] K. Kifune, Y. Kubota, T. Matsunaga and N. Yamada, *Acta Crystallogr. Sect. B* **2005**, *61*, 492.
- [23] O. G. Karpinskii, L. E. Shelimova, M. A. Kretova and J.-P. Fleurial, *J. Alloys Compd.* **1998**, *268*, 112.
- [24] H. Matsushita, E. Hagiwara and A. Katsui, *J. Mater. Sci.* **2004**, *39*, 6299.
- [25] T. Matsunaga, N. Yamada and Y. Kubota, *Acta Crystallogr. Sect. B* **2004**, *60*, 685.
- [26] L. J. van der Pauw, *Philips Res. Rep.* **1958**, *13*, 1.
- [27] *WINXPOW*, Stoe & Cie GmbH, Darmstadt, **2005**.
- [28] A. C. Larson and R. B. Von Dreele, *Los Alamos National Laboratory Report LAUR.*, **2000**, 86–748.
- [29] B. H. Toby, *J. Appl. Crystallogr.* **2001**, *34*, 210.
- [30] *XPREP, Version 6.12*, Siemens Analytical X-ray Instruments Inc., Madison, WI, USA, **1996**.
- [31] M. C. Burla, M. Camalli, B. Carrozzini, G. L. Casciarano, C. Giacovazzo, G. Polidori and R. Spagna, *J. Appl. Crystallogr.* **2003**, *36*, 1103.

-
- [32] G. M. Sheldrick, *Acta Crystallogr. Sect. A* **2008**, *64*, 112.
- [33] M. N. Schneider and O. Oeckler, *Z. Anorg. Allg. Chem.* **2008**, *634*, 2557.
- [34] L. E. Shelimova, O. G. Karpinsky, M. A. Kretova and E. S. Avilov, *J. Alloys Compd.* **1996**, *243*, 194.
- [35] B. J. Kooi and J. T.M. De Hosson, *J. Appl. Phys.* **2002**, *92*, 3584.
- [36] C. S. Barrett, P. Cucka and K. Haefner, *Acta Crystallogr.* **1963**, *16*, 451.
- [37] T. Chattopadhyay, J. X. Boucherle and H. G. von Schnering, *J. Phys. C: Solid State Phys.* **1987**, *20*, 1431.
- [38] A. Bondi, *J. Phys. Chem.* **1964**, *68*, 441.
- [39] S. Geller and J. H. Wernick, *Acta Crystallogr.* **1959**, *12*, 46.
- [40] B.-S. Lee, J. R. Abelson, S. G. Bishop, D.-H. Kang, B.-K. Cheong and K.-B. Kim, *J. Appl. Phys.* **2005**, *97*, 093509.
- [41] K. Hoang, S. D. Mahanti, J. R. Salvador and M. G. Kanatzidis, *Phys. Rev. Lett.* **2007**, *99*, 156403.
- [42] L. D. Ivanova and Y. V. Granatkina, *Inorg. Mater.* **2007**, *43*, 247.

3.4 The layered tellurides $39R\text{-M}_{0.067}\text{Sb}_{0.667}\text{Te}_{0.266}$ ($M = \text{Ge}, \text{Sn}$): element distribution and thermoelectric properties

Matthias N. Schneider, Felix Fahrnbauer, Tobias Rosenthal, Markus Döblinger, Christian Stiewe, and Oliver Oeckler

Chemistry - A European Journal **2012**, *18*, 1209-1218.

Abstract

The isostructural phases $39R\text{-Ge}_{0.067}\text{Sb}_{0.667}\text{Te}_{0.266}$ ($R\bar{3}m$, $a = 4.2649(1)$, $c = 75.061(2)$ Å) and $39R\text{-Sn}_{0.067}\text{Sb}_{0.667}\text{Te}_{0.266}$ ($R\bar{3}m$, $a = 4.2959(1)$, $c = 75.392(2)$ Å) have been prepared by quenching stoichiometric melts of the pure elements and subsequent annealing at moderate temperatures. Their structures are comparable to “superlattices” synthesized by layer-per-layer deposition on a substrate. They show no stacking disorder according to electron microscopy. The structure of the metastable layered phases are similar to that of $39R\text{-Sb}_{10}\text{Te}_3$ (= $\text{Sb}_{0.769}\text{Te}_{0.231}$), which contains four A7 (gray arsenic) type layers of antimony alternating with Sb_2Te_3 slabs. Joint refinements on single-crystal diffraction data using synchrotron radiation at several K edges have been performed in order to enhance the scattering contrast. They show that the element distribution on some atom positions is disordered whereas otherwise the structures are long-range ordered. The variation of the element concentration correlates with the variation of interatomic distances. Z-contrast scanning transmission electron microscopy (HAADF-STEM) on $39R\text{-Ge}_{0.067}\text{Sb}_{0.667}\text{Te}_{0.266}$ confirms the presence of concentration gradients. The carrier type of the isostructural metal (A7-type lamellae) – semiconductor (Ge/Sn doped Sb_2Te_3 slabs) heterostructures varies from n-type ($\text{Ge}_{0.067}\text{Sb}_{0.667}\text{Te}_{0.266}$) to p-type ($\text{Sn}_{0.067}\text{Sb}_{0.667}\text{Te}_{0.266}$). Although the absolute values of the Seebeck coefficient reach $\sim 50\text{-}70$ $\mu\text{V/K}$ and electrical conductivity is relatively high, the two isotopic phases exhibit a maximal thermoelectric figure of merit (ZT) of 0.06 at 400 °C as their thermal conductivity ($\kappa \sim 8 - 9.5$ W/mK at 400 °C) interestingly lies in between that of antimony and pure Sb_2Te_3 .

Keywords: layered compounds; synchrotron radiation; electron microscopy; X-ray diffraction; thermoelectric materials

Copyright: © 2012 WILEY-VCH Verlag GmbH & Co. KGaA

3.4.1 Introduction

During the past decades, tellurides have received much attention in various fields of materials science. Their applications range from solar-cell technology, e.g. based on cadmium telluride^[1,2] to the fields of phase-change materials for data storage, dominated by metastable germanium antimony tellurides.^[3,4,5] Lead and bismuth tellurides are the standard thermoelectric materials which are currently applied; however, there is a huge demand for improved materials. In ideal thermoelectrics, a high electrical conductivity (σ) needs to be combined with a high Seebeck coefficient (S) and a low total thermal conductivity (κ).^[6,7,8] However, as all these properties depend on the charge carrier concentration, they cannot be varied independently. The efficiency of thermoelectric generators depends on the dimensionless figure of merit $ZT = S^2\sigma T\kappa^{-1}$ which is ~ 1 for the materials used industrially today. New developments often concern κ because the power factor $S^2\sigma$ is hard to optimize as its improvement simultaneously leads to a high electronic part of the thermal conductivity. The total thermal conductivity can, up to a certain extent, be independently optimized by reducing its phononic part, i. e. the so-called lattice thermal conductivity. One approach is the fabrication of extended nano- and microstructures, e. g. in layered "superlattice" structures with various translation periodicities.^[9,10,11] Thin lamellar building blocks, which can be described as rocksalt-type slabs of ~ 10 Å thickness are present in bulk materials like Bi_2Te_3 or solid solutions $\text{Bi}_{2-x}\text{Sb}_x\text{Te}_3$. Such "lamellae" can be described as a sequence of five hexagonal anion (Te) and cation (Bi and Sb, respectively) layers; they are interconnected through van der Waals gaps between the anion layers terminating successive slabs. Whereas the lattice thermal conductivity of $\text{Bi}_{2-x}\text{Sb}_x\text{Te}_3$ single crystals is $0.83 \text{ Wm}^{-1}\text{K}^{-1}$ for $x = 1.5$,^[12] multilayer systems $\text{Sb}_2\text{Te}_3\text{-Bi}_2\text{Te}_3$ prepared by vapour deposition have been reported to reach ZT values up to ~ 2.4 which is mainly due to their extremely low lattice thermal conductivity of $\sim 0.24 \text{ Wm}^{-1}\text{K}^{-1}$.^[8,11,13] The periodicity of the layer stacking is ~ 60 Å corresponding to 5 lamellae of Sb_2Te_3 (~ 50 Å) and one lamella of Bi_2Te_3 (~ 10 Å); however, the preparation of such samples is difficult to reproduce.^[8,11] Recently, attempts have been made to mimic the structural features and associated properties of such thin-film "superlattices" in bulk materials, e.g. in the system Pb-Sb-Te, where phase separation phenomena are supposed to yield self-assembled lamellar structures.^[8,11,14,15] In this context, long-periodically ordered layered structures of stable binary or ternary antimony tellurides are interesting as their crystal structures contain lamellar slabs as distinct building units. Antimony-rich antimony tellurides with the general formula $(\text{Sb}_2\text{Te}_3)_m(\text{Sb}_2)_k$ consist of Sb_2Te_3 -type slabs arranged in between gray-arsenic-type antimony layers similar to those in elemental antimony as shown in Figure 1.^[16,17,18] For

example, $42R\text{-Sb}_4\text{Te}_3$ ($m = 1, n = 1$) or $9P\text{-Sb}_2\text{Te}$ ($m = 1, n = 2$) exhibit lamellae which are stacked with (primitive) translation periods of $\sim 28 \text{ \AA}$ and $\sim 17 \text{ \AA}$, respectively. Pseudo-binary phases $(\text{GeTe})_n(\text{Sb}_2\text{Te}_3)_m$ contain slabs built up from an alternating sequence of cation (Ge, Sb) and anion (Te) layers (the number of layers per slab depends on the composition), separated by van der Waals gaps similar to those in Sb_2Te_3 .^[19-21] Typical examples like $21R\text{-GeSb}_2\text{Te}_4$ or $33R\text{-Ge}_3\text{Sb}_2\text{Te}_6$ contain lamellae with a thickness of $\sim 13 \text{ \AA}$ and $\sim 21 \text{ \AA}$, respectively.^[22,23] The structural features of both series of compounds can be combined in phases of the type $(\text{GeTe})_n(\text{Sb}_2\text{Te}_3)_m(\text{Sb}_2)_k$ as recently shown for $9P\text{-GeSbTe}_4$ ($m = 1, n = 1, k = 1$) or $51R\text{-Ge}_{1.57}\text{Sb}_{2.43}\text{Te}_5\text{Sb}_8$ ($m = 1, n \sim 3, k = 4$) (lamellar periodicities $\sim 17 \text{ \AA}$ and $\sim 32 \text{ \AA}$, respectively).^[24,25] In general, the periodicity of the lamella sequence depends on the composition and can be derived from the crystallographic lattice parameters. Although the basic structural features of these structures as depicted in Figure 1 are well understood, the elucidation of the element distribution remains a challenging question since mixed site occupancies on cation sites are common and elements with similar electron count, e.g. Sb, Sn and Te cannot be distinguished by conventional X-ray diffraction. As recently demonstrated for $21R\text{-SnSb}_2\text{Te}_4$, resonant X-ray scattering is an elegant way to reveal the element distribution in multinary antimony tellurides because the scattering contrast can be significantly increased using wavelengths at the K absorption edges of the relevant elements.^[26]

Concerning bulk materials, we have already shown that germanium antimony tellurides with $ZT \sim 1.3$ can be obtained by inducing nanostructures via phase transitions that involve vacancy diffusion and nanoscale twinning.^[27] We now aim at synthesizing and characterizing multinary antimony tellurides as model systems for nano- and microscopic "superlattice" structures which might provide a facile route towards bulk materials with improved thermoelectric characteristics.

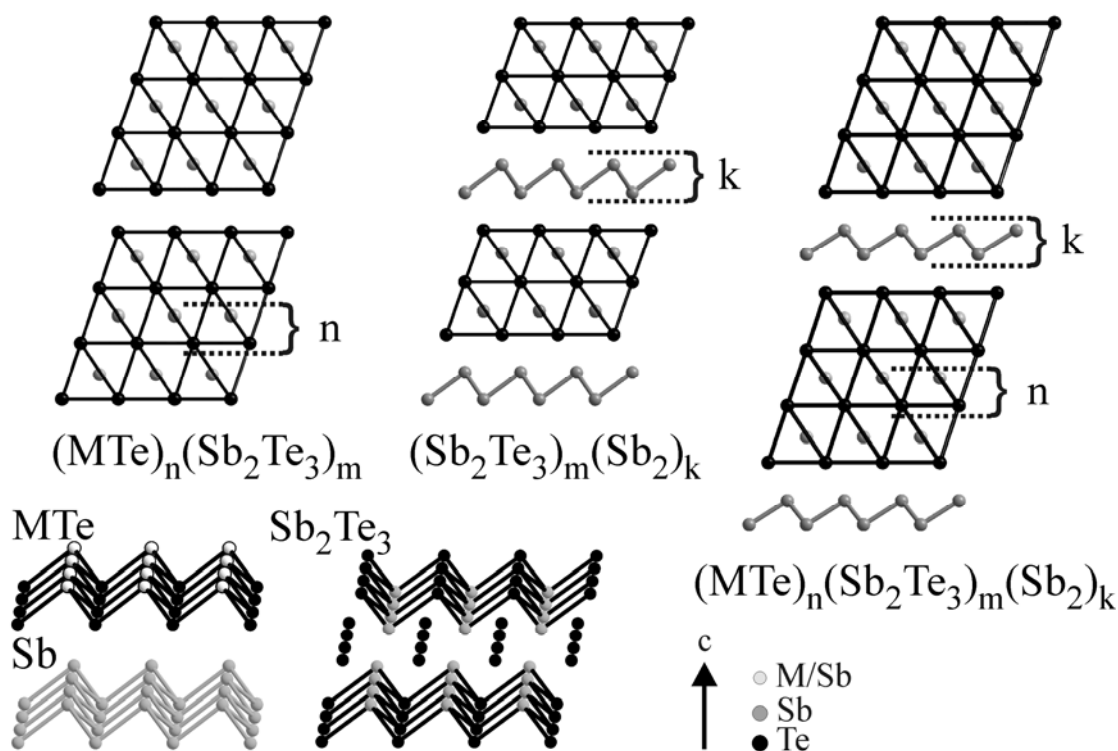


Figure 1. Structural relationship between compounds $(MTe)_n(Sb_2Te_3)_m$, $(Sb_2Te_3)_m(Sb_2)_k$, and $(MTe)_n(Sb_2Te_3)_m(Sb_2)_k$ ($M = Ge, Sn, Ag/Sb, \dots$); the layered phases which contain structural motifs of the rocksalt-type structures as well as corrugated honeycomb nets similar to elemental Sb are shown as projections along [010] (top). As depicted in perspective view (bottom), local atom environments in the layers are similar to the $GeTe$ type and Sb type, respectively. The building unit of Sb_2Te_3 is shown for comparison.

3.4.2 Results and discussion

3.4.2.1 Synthesis, homogeneity and stability

The phases $M_{0.067}Sb_{0.667}Te_{0.266}$ ($M = Ge, Sn$) can be prepared by quenching stoichiometric melts and subsequently annealing the samples for about one week. X-ray powder patterns of such samples are dominated by very intense reflections corresponding to the (rather meaningless) α -Hg-type basic structure of all compounds $(GeTe)_n(Sb_2Te_3)_m$ and $(Sb_2Te_3)_m(Sb_2)_k$ (this has been discussed in more detail for Bi compounds, see ref. [28]). These patterns are also typical for disordered compounds,^[29] however, the powder patterns of the title compounds clearly show the rather weak reflections indicative of the ordered $39R$ -type stacking sequence. Based on the refined structure models from single-crystal data (see below), Rietveld refinements of the powder patterns (Figure 2) confirm the homogeneity of the samples. The atom coordinates were not refined for these fits, however, a certain degree of preferred orientation along [001], probably introduced by grinding and sample preparation, needs to be taken into account. Further annealing up to a few weeks does not yield additional changes according to powder diffraction patterns.

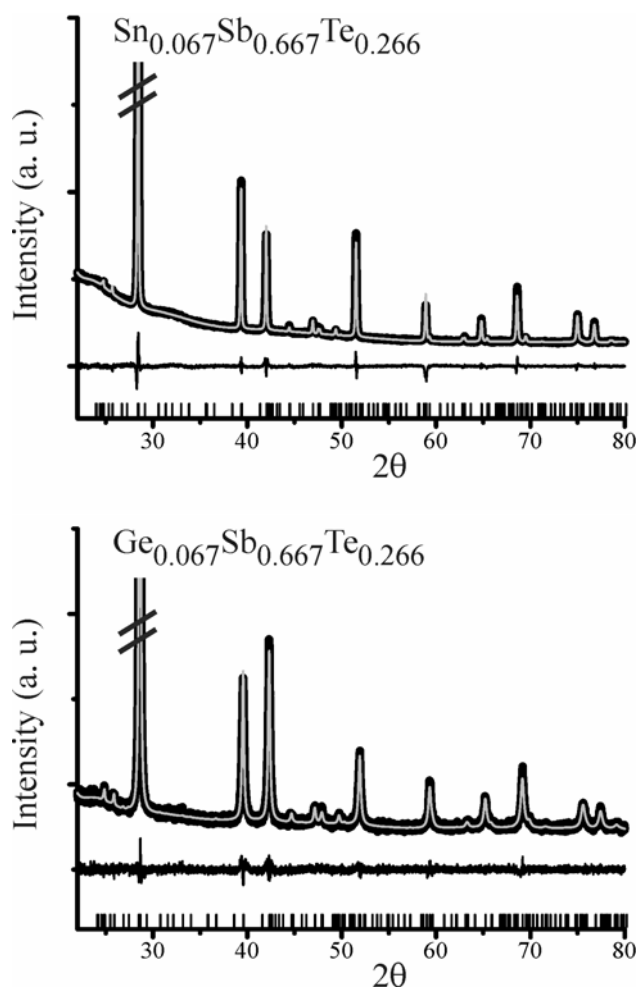


Figure 2. Results of the Rietveld refinements (gray) on the experimental powder patterns (Cu- $K_{\alpha 1}$ radiation, black, the most intense reflection is truncated in order to better visualize the weak ones) of $39R\text{-Ge}_{0.067}\text{Sb}_{0.667}\text{Te}_{0.266}$ ($R\bar{3}m$, $a = 4.2649(1)$ Å, $c = 75.061(2)$ Å, $R_p = 0.0116$, $wR_p = 0.0149$) and $39R\text{-Sn}_{0.067}\text{Sb}_{0.667}\text{Te}_{0.266}$ ($R\bar{3}m$, $a = 4.2959(1)$ Å, $c = 75.392(1)$ Å, $R_p = 0.0199$, $wR_p = 0.0321$) with the structure models obtained by the single crystal structure refinements. The positions of the Bragg reflections are indicated by vertical bars (bottom).

Thermoanalytical measurements (DTA) do not show any significant heat flow before incongruent melting that starts at 529 °C for $M = \text{Ge}$ and at 538 °C for $M = \text{Sn}$. The maximum of the exothermal heat flow occurs at 535 °C ($M = \text{Ge}$) and 546 °C ($M = \text{Sn}$), respectively, before the samples become completely liquid. At low temperatures, the phase diagrams^[30,31,32,33] suggest the formation of the so called δ -phase which has a certain range of homogeneity with respect to the Sb and Te content but may also contain several distinct layered structures.^[16,17] Small amounts of Ge or Sn might be incorporated; their solubility in antimony tellurides is much more pronounced at elevated temperatures. However, at low temperatures, phase separation is extremely slow as long-range diffusion processes and the precipitation of a pure element with a very different crystal structure would be required. For phase-diagram determination, samples were annealed up to 8 months at 500 °C.^[30,32] Annealing finely ground samples for three weeks near the melting point (at 520 °C) does not lead to the precipitation of Ge or

Sn; however, the powder patterns suggest the presence of an inhomogeneous mixture of various layered phases. Thus, thermal analysis as well as annealing experiments indicate that $39R\text{-M}_{0.067}\text{Sb}_{0.667}\text{Te}_{0.266}$ ($M = \text{Ge}, \text{Sn}$) are long-range ordered and kinetically very inert phases. In contrast to many other multinary antimony tellurides, they do not show significant stacking disorder, but the mixed site occupancies still indicate a pronounced degree of random chemical disorder.

3.4.2.2 Electron microscopy and diffraction

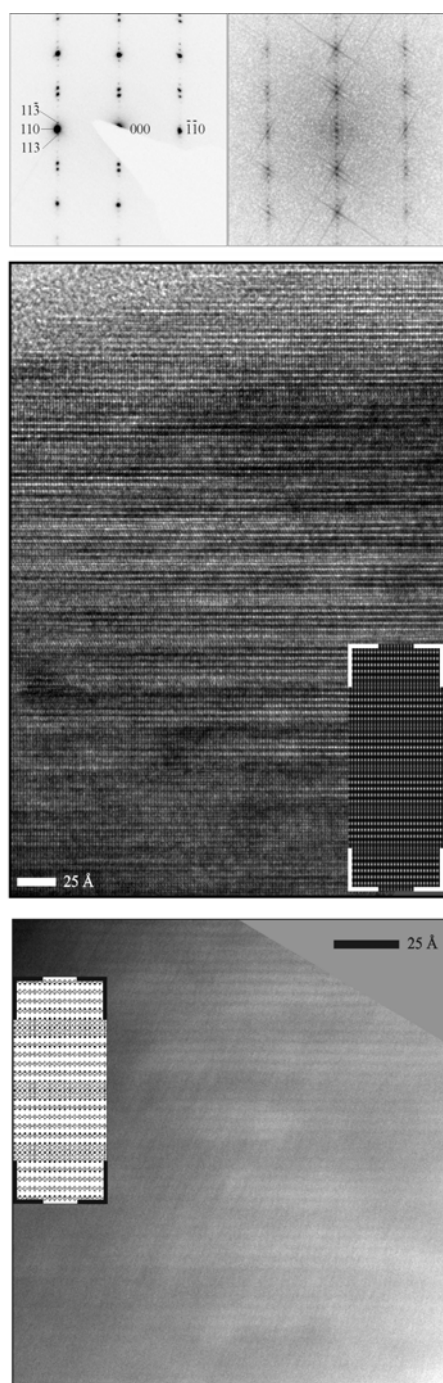


Figure 3. Electron microscopy of $39R\text{-Ge}_{0.067}\text{Sb}_{0.667}\text{Te}_{0.266}$: SAED pattern (top left, zone axis $[210]$), section of a HRTEM image (middle, inset: shows a simulation based on the refined structure model at a defocus value of -40 nm, thickness 34 nm) with corresponding Fourier transform (top right) and a STEM-HAADF image (bottom right, inset shows the structure along $[210]$ for comparison; Ge/Sb depicted as gray spheres, Te depicted as black spheres)

As diffuse scattering due to stacking disorder may seem insignificant in powder patterns, the conclusions drawn may be misleading, which has also been discussed for layered antimony tellurides.^[29] Therefore, we have investigated the samples by means of electron microscopy and diffraction, which is most suitable to both detect weak diffuse scattering and directly image stacking faults (see Figure 3). Selected-area electron diffraction (SAED) patterns of $39R\text{-Ge}_{0.067}\text{Sb}_{0.667}\text{Te}_{0.266}$ do not show diffuse streaking and in addition confirm the $39R$ -type structure with high intensities for every 13th basic-structure (α -Hg type) reflection along $[001]^*$. Even in polycrystalline aggregates, rows of reflections along $[001]^*$ are free of streaks. High-resolution transmission electron microscopy (HRTEM) reveals an ordered sequence of structural building units. This is confirmed by image simulations based on the results of the structure refinement described in the following section. The correspondence between the Fourier transform of the HRTEM images and many SAED patterns proves that all crystallites investigated exhibit the same ordered stacking sequence.

For $39R\text{-Ge}_{0.067}\text{Sb}_{0.667}\text{Te}_{0.266}$, a first insight into the element distribution can be obtained from Z contrast (STEM-HAADF) images where the grayscale corresponds to the atomic number (electron density). The brighter areas in Figure 3 (bottom)

correspond to higher electron density. The variation of the contrast correlates with structural building units of $\text{Sb}_{10}\text{Te}_3$ (cf. Figure 4). The major part of the lightest element Ge is located in the rocksalt-like Sb_2Te_3 blocks, whereas gray-arsenic-type Sb layers exhibit a slightly larger layer spacing and are hence separated by darker lines. However, the boundaries between rocksalt-type and arsenic-type blocks appear blurred. This suggests a wave-like distribution of the light Ge atoms which excellently matches the result of the resonant X-ray study (see below).

3.4.2.3 X-ray diffraction data analysis

According to the initial structure solution on laboratory data, both $\text{Ge}_{0.067}\text{Sb}_{0.667}\text{Te}_{0.266}$ and $\text{Sn}_{0.067}\text{Sb}_{0.667}\text{Te}_{0.266}$ exhibit a $39R$ -type structure similar to that of $\text{Sb}_{10}\text{Te}_3$ ($=\text{Sb}_{0.769}\text{Te}_{0.231}$, $R\bar{3}m$, $a = 4.289 \text{ \AA}$, $c = 75.51 \text{ \AA}$).^[29] Concerning the assignment of atom types in long-range ordered Sb-rich antimony tellurides, characteristic interatomic distances can usually be used to distinguish Sb and Te and thus to differentiate rocksalt-type sections, e.g. as in Sb_2Te_3 , and additional corrugated honeycomb Sb nets. In the case of $39R\text{-M}_{0.067}\text{Sb}_{0.667}\text{Te}_{0.266}$ ($M = \text{Ge}, \text{Sn}$), a comparison with known binary and ternary compounds reveals that, at first sight, the building blocks stacked along $[001]$ are similar to those found in $39R\text{-Sb}_{10}\text{Te}_3$ (cf. Figure 4). However, as three elements are present and the distance set is not unambiguous in this case, the similar form factors of Sn, Sb and Te impede the reliable element assignment based on conventional X-ray data. Hence, the scattering contrast was enhanced by collecting additional single-crystal data sets with synchrotron radiation very close to the K absorption edges of the elements present in order to obtain very pronounced resonant scattering effects. For $M = \text{Sn}$, resonant scattering data were collected at all relevant absorption edges (Sn, Sb, Te) to unambiguously refine mixed site occupancies for all atom positions. For $M = \text{Ge}$, only Sb and Te are difficult to distinguish, therefore one resonant dataset, preferably at the Sb edge (for a discussion concerning the optimal edge see refs. [26,34]), and non-resonant (in this case, laboratory) data are sufficient. Although the dispersion correction factors $\Delta f'$ and $\Delta f''$ of the resonant scatterers depend slightly on their chemical environment, especially close to the absorption edges, it is optimal to measure very close to the edge and refine the affected $\Delta f'$ values in joint refinements based on all data. As shown for SnSb_2Te_4 ,^[26] this method is very robust with respect to the refined element distribution. Also in the present case, manual variation of $\Delta f'$ by ± 0.5 did not change the structure model more than a few standard deviations. $\Delta f'$ and $\Delta f''$ values were taken from various databases and averaged.^[35,36] $\Delta f'$ of the elements at their K edges were refined with respect to the corresponding dataset in the joint refinements using JANA2006,^[37] they did not change significantly (refined values are between -7.4 and -8.2 e with standard deviations around

0.1 e). During the refinement, no sum formula constraint was applied but site occupancies were fixed to full occupancy. After initial refinements including all atom types on all positions, all site occupancies were positive or zero within a 2σ range; in the final refinements, site occupancies smaller than 1σ were set to zero in order to eliminate unnecessary parameters and correlations. The final refinements including anisotropic displacement parameters for all atoms converged at $R = 0.0495$ for $39R\text{-Ge}_{0.067}\text{Sb}_{0.667}\text{Te}_{0.266}$ and $R = 0.0396$ for $39R\text{-Sn}_{0.067}\text{Sb}_{0.667}\text{Te}_{0.266}$, referring to all observed data in all datasets. The chemical compositions calculated from site occupancies are $\text{Ge}_{0.073}\text{Sb}_{0.625}\text{Te}_{0.303}$ and $\text{Sn}_{0.071}\text{Sb}_{0.660}\text{Te}_{0.269}$, respectively. As several sites contribute, the relative standard deviations are about 8% in total, however, within that error limit, the refined formulae match with the nominal composition and the results from EDX spectroscopy on the crystals used for the diffraction experiments (cf. *Experimental Section*). Crystal data and refinement details are given in Table 1, atom positions and displacement parameters are summarized in Tables 2 and 3, respectively. Refined site occupancies are also illustrated in Figure 4.

Table 1. Crystallographic data on the structure refinement of $39R\text{-Sn}_{0.067}\text{Sb}_{0.667}\text{Te}_{0.266}$ and $39R\text{-Ge}_{0.067}\text{Sb}_{0.667}\text{Te}_{0.266}$ at 293 K.

Compound	$39R\text{-Sn}_{0.067}\text{Sb}_{0.667}\text{Te}_{0.266}$				$39R\text{-Ge}_{0.067}\text{Sb}_{0.667}\text{Te}_{0.266}$	
Refined composition	$\text{Sn}_{0.071(6)}\text{Sb}_{0.66(5)}\text{Te}_{0.27(2)}$				$\text{Ge}_{0.073(6)}\text{Sb}_{0.63(5)}\text{Te}_{0.30(2)}$	
Formula mass (in g mol^{-1})	123.1				120.0	
Crystal system	Trigonal				trigonal	
Space group	$R\bar{3}m$				$R\bar{3}m$	
Cell parameters (in Å)	$a = 4.2959(1), c = 75.392(2)$				$a = 4.2649(1), c = 75.061(2)$	
Cell volume (in Å ³)	1204.94(5)				1182.40(5)	
Formula units (per unit cell)	39				39	
$F(000)$	1996.7				1947.6	
X-ray density (in g cm^{-3})	6.61				6.57	
Parameters / constraints	31 / 23				27 / 12	
Resolution	0.75 Å, $\sin\theta/\lambda = 0.665$				0.70 Å, $\sin\theta/\lambda = 0.711$	
R [all data with $I > 3\sigma(I)$ in all datasets] ^(a)	0.049				0.040	
R [all data in all datasets] ^(a)	0.094				0.078	
wR [all data in all datasets] ^(b)	0.110				0.057	
GooF [all data in all datasets]	1.91				1.66	
$\Delta\rho_{\min}/\Delta\rho_{\max}$ (in $\text{e}\text{Å}^{-3}$)	-1.49/+2.22				-2.16/+1.76	
Wavelength (in Å)	0.38970	0.40662	0.42460	0.71073	0.406629	0.71073
Absorption coefficient (in mm^{-1})	23.8	20.4	6.9	21.8	20.7	22.6
Measured / independent reflections	4397 / 465	2486 / 468	2814 / 467	2678 / 451	3508 / 539	3663 / 542
R_{int}	0.040	0.066	0.058	0.065	0.100	0.065
R_{σ}	0.031	0.049	0.038	0.036	0.044	0.036
R [$I > 2\sigma(I)$] ^(a)	0.043	0.057	0.051	0.049	0.035	0.046
R [all data] ^(a)	0.053	0.151	0.110	0.077	0.072	0.088
wR [$I > 2\sigma(I)$] ^(b)	0.095	0.120	0.117	0.087	0.046	0.060
wR [all data] ^(b)	0.099	0.132	0.123	0.091	0.050	0.065

^{a)} $R = \sum |F_o - F_c| / \sum |F_o|$ ^{b)} $wR = [\sum [w(F_o - F_c)^2] / \sum [w(F_o)^2]]^{1/2}$

Table 2. Wyckoff positions, atomic coordinates, equivalent isotropic and anisotropic displacement parameters (in \AA^2 , $U_{13}=U_{23}=0$) for $39R\text{-Sn}_{0.067}\text{Sb}_{0.667}\text{Te}_{0.266}$; atom labels correspond to Figure 4, where in addition the site occupancies are given.

atom	Wyck.	x	y	z	U_{eq}	$U_{11} = U_{22} = 2 U_{12}$	U_{33}
M1	$3a$	0	0	0	0.0196(4)	0.0182(6)	0.0223(7)
M2	$6c$	2/3	1/3	0.02530(2)	0.0316(4)	0.0260(5)	0.0428(7)
M3	$6c$	1/3	2/3	0.048031(14)	0.0222(4)	0.0199(5)	0.0268(5)
M4	$6c$	0	0	0.078908(17)	0.0275(4)	0.0191(5)	0.0442(8)
M5	$6c$	2/3	1/3	0.099284(16)	0.0262(4)	0.0187(5)	0.0411(7)
M6	$6c$	1/3	2/3	0.130811(12)	0.0202(4)	0.0183(5)	0.0240(5)
M7	$6c$	0	0	0.151199(13)	0.0185(4)	0.0169(5)	0.0216(5)

Table 3. Wyckoff positions, atomic coordinates, equivalent isotropic and anisotropic displacement parameters (in \AA^2 , $U_{13}=U_{23}=0$) for $39R\text{-Ge}_{0.067}\text{Sb}_{0.667}\text{Te}_{0.266}$; atom labels correspond to Figure 4, where in addition the site occupancies are given.

atom	Wyck.	x	y	z	U_{eq}	$U_{11} = U_{22} = 2 U_{12}$	U_{33}
M1	$3a$	0	0	0	0.0196(3)	0.0198(4)	0.0191(5)
M2	$6c$	2/3	1/3	0.026044(8)	0.0288(3)	0.0244(4)	0.0377(5)
M3	$6c$	1/3	2/3	0.049139(10)	0.0202(3)	0.0192(4)	0.0222(5)
M4	$6c$	0	0	0.079808(13)	0.0278(3)	0.0217(4)	0.0400(5)
M5	$6c$	2/3	1/3	0.100477(10)	0.0215(3)	0.0181(4)	0.0285(5)
M6	$6c$	1/3	2/3	0.131367(11)	0.0190(3)	0.0173(4)	0.0226(5)
M7	$6c$	0	0	0.151500(10)	0.0189(3)	0.0172(4)	0.0223(5)

3.4.2.4 Structure description and element distribution

The characteristic crystal chemical feature of the two isostructural compounds $\text{M}_{0.067}\text{Sb}_{0.667}\text{Te}_{0.266}$ ($\text{M} = \text{Ge}, \text{Sn}$) is the long-range ordered $39R$ stacking sequence of hexagonal atom layers that extend parallel (001). A simplified description classifies the layer sequence as a stacking of alternating Sb_2Te_3 -type slabs which consist of two cation and three anion layers and four corrugated honeycomb layers with gray arsenic type (one such layer comprises two shifted planar hexagonal atom layers) as shown in Figure 4. These layers are quite similar to those in elemental antimony, (intra-layer distance 2.908 \AA , inter-layer distance 3.355 \AA).^[18] The layers that are further away from the Sb_2Te_3 -type slab are more similar to those in the element, those that interact with the slab are more strongly distorted.

Within the Sb_2Te_3 -type slab, the cations exhibit a 3+3 coordination with short Sb-Te distances towards the Te layer terminating the slab. This can be explained with the one-sided coordination of the Te atoms involved. The Sb-Te distances towards the central Te atom layer are longer, and the latter exhibits an almost ideal octahedral coordination. This situation is rather similar to that in $\text{Sb}_{10}\text{Te}_3$, neither the introduction of Sn nor that of Ge significantly affects the distance set.^[29]

With respect to the general formula $(\text{MTe})_n(\text{Sb}_2\text{Te}_3)_m(\text{Sb}_2)_k$, $\text{M}_{0.067}\text{Sb}_{0.667}\text{Te}_{0.266} = \text{MSb}_{10}\text{Te}_4$ corresponds to $n = m = 1$ and $k = 4$, suggesting four corrugated honeycomb antimony layers between 7-layer rocksalt-like blocks as in GeSb_2Te_4 or SnSb_2Te_4 .^[22,26] However, the actual

structure does not match this prediction. Although, for instance, *9P*-GeSb₄Te₄ and *51R*-Ge_{2-x}Sb_{2+x}Te₅Sb₈ prove that such structural combinations are possible,^[24,25] the title compounds are closer to Sb₁₀Te₃, which once more shows that simple rules for structure prediction often fail for metastable compounds. This may be complicated by a certain range of homogeneity and minute deviations from the ideal composition as shown for Ge₄Sb₂Te₇ whose layer sequence corresponds to that expected for Ge₃Sb₂Te₆.^[20] Although the compounds (MTe)_n(Sb₂Te₃)_m (M = Ge, Sn) exhibit mixed cation sites even in thermodynamically stable phases, the cation distribution is not completely random: Sb prefers the sites in the vicinity of the van der Waals gaps.

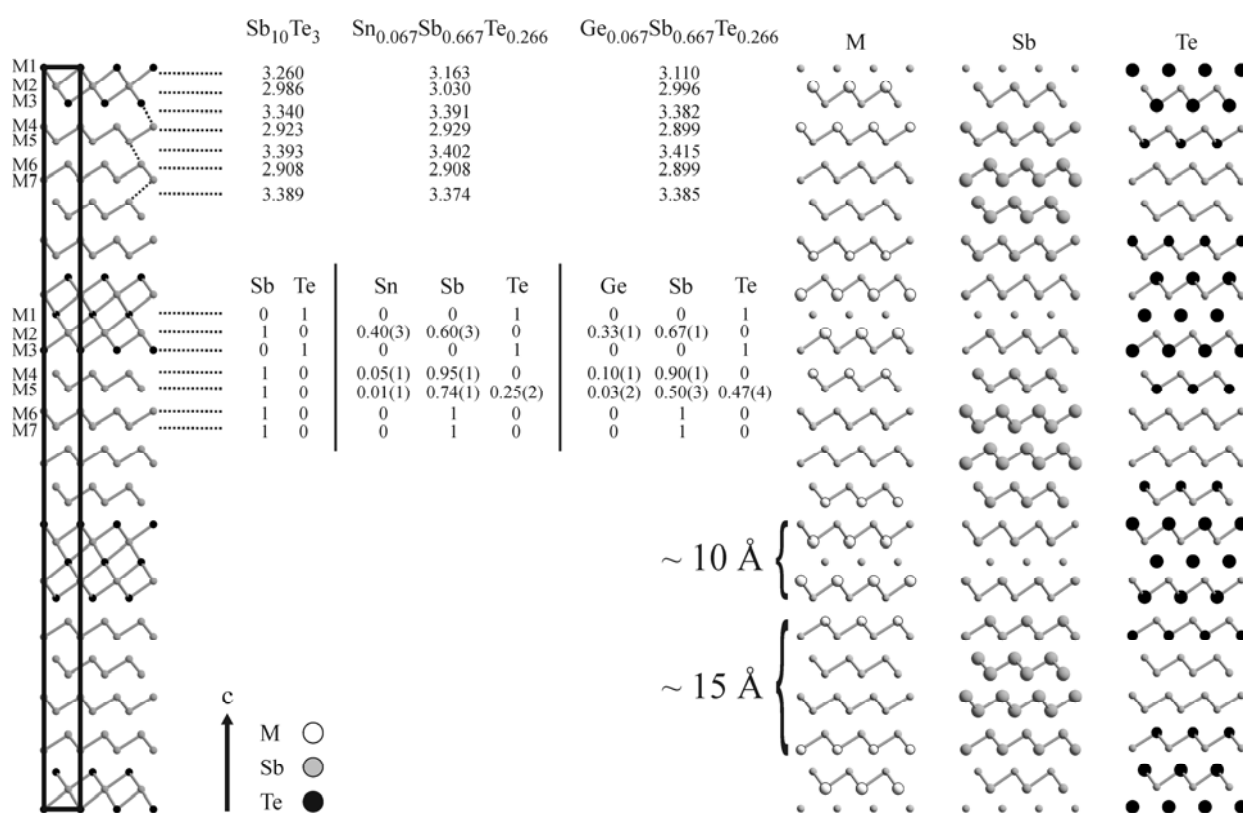


Figure 4. Atom distribution and selected interatomic distances (top, middle) in the refined structure models of *39R*-M_{0.067}Sb_{0.667}Te_{0.266} (M = Ge, Sn) projected along [010] in comparison with Sb₁₀Te₃ (left, all distances are given in Å, all e.s.d.s < 0.003 Å). The site occupation factors for *39R*-M_{0.067}Sb_{0.667}Te_{0.266} derived from the joint refinements on synchrotron data are given in the center of the figure (the amount of Ge and Sn on position M5 is insignificant and not considered further). For comparison the occupancies in Sb₁₀Te₃ are also shown. The schematic representation on the left depicts the element distribution, the slight difference between the Ge and Sn compounds is neglected; small gray spheres indicate that the corresponding element is absent on this position; enlarged spheres for M = Ge or Sn (white), Sb (gray), Te (black) represent the site occupancies, the size of the spheres is proportional to the occupancy. The brackets indicate the rocksalt-type slab and the gray arsenic type layers, which are formally present.

The single-crystal data (see above) clearly reveal the element distribution in $M_{0.067}Sb_{0.667}Te_{0.266}$ ($M = Ge, Sn$). The occupancy factors correspond to concentration gradients as visualized in Figure 4. Interestingly, the arsenic-type layers do not exclusively contain Sb atoms. In part, the site occupancies may suggest that a certain proportion of corrugated honeycomb Sb layers is substituted by GeTe layers, which are simply a binary variant of the gray arsenic type layers and exhibit a very similar periodicity perpendicular to the stacking direction [001]: $a = 4.308 \text{ \AA}$ for antimony and 4.164 \AA for GeTe (compare Figure 1).[18,38] As both Sb and GeTe layers are charge neutral, one might expect that the formal replacement of Sb in the arsenic-type layers by Ge and/or Te is coupled. However, the oxidation state of Sb is variable; it may also be cationic near Te. Thus, charge neutrality does not necessarily require to fully replace Sb by Ge or Sn on positions that neighbor those where Sb is replaced by Te. In fact, the element concentrations vary rather smoothly in both the Sb_2Te_3 -type and the arsenic-type slabs, resembling a wave-like concentration modulation. It is, therefore, just a simplification to distinguish the different types of slabs, the real structure is not well described as a stacking sequence of individual slabs. However, the variation which comprises both interatomic distances and occupancy factors is not smooth enough to be easily described as a commensurately modulated structure with a 3+1D superspace approach. This would be an unnecessary complication and cannot be used to simplify the refinement as very high satellite orders would be required unless observed reflections are omitted and the data/parameter ratio would not be reduced due to the complexity of the "modulation". Cation-anion separation becomes less pronounced with increasing distance from the center of the formal Sb_2Te_3 -type slabs. In fact, locally these might be extended by GeTe-type layers on both sides to form slabs similar to those in $Ge_2Sb_2Te_5$.^[39] In the same way as the distortion of the arsenic-type layers depends on the location within the stacking sequence, the site occupancies depend on the surrounding of the corresponding positions in the layer sequence. In the Sb_2Te_3 -type slab, cation positions show a preferred occupancy for Ge and Sn which decreases towards the center of the arsenic-type block. There, Sb is much more prevalent. No significant amount of Ge, Sn or Te in the arsenic-type layers that are not next to the Sb_2Te_3 -type slabs was found. The concentration gradient is slightly less pronounced for $M = Sn$ as compared to $M = Ge$. In layered "superlattice" structures prepared by sputtering or similar techniques, interdiffusion between adjacent building blocks does not seem significant.^[40,41] In contrast, both title compounds exhibit a rather continuous transition from predominantly ionic rocksalt-like Sb_2Te_3 -type slabs to predominantly metallic antimony slabs. This bears similarity to an initial stage of spinodal decomposition.

3.4.2.5 Thermoelectric properties

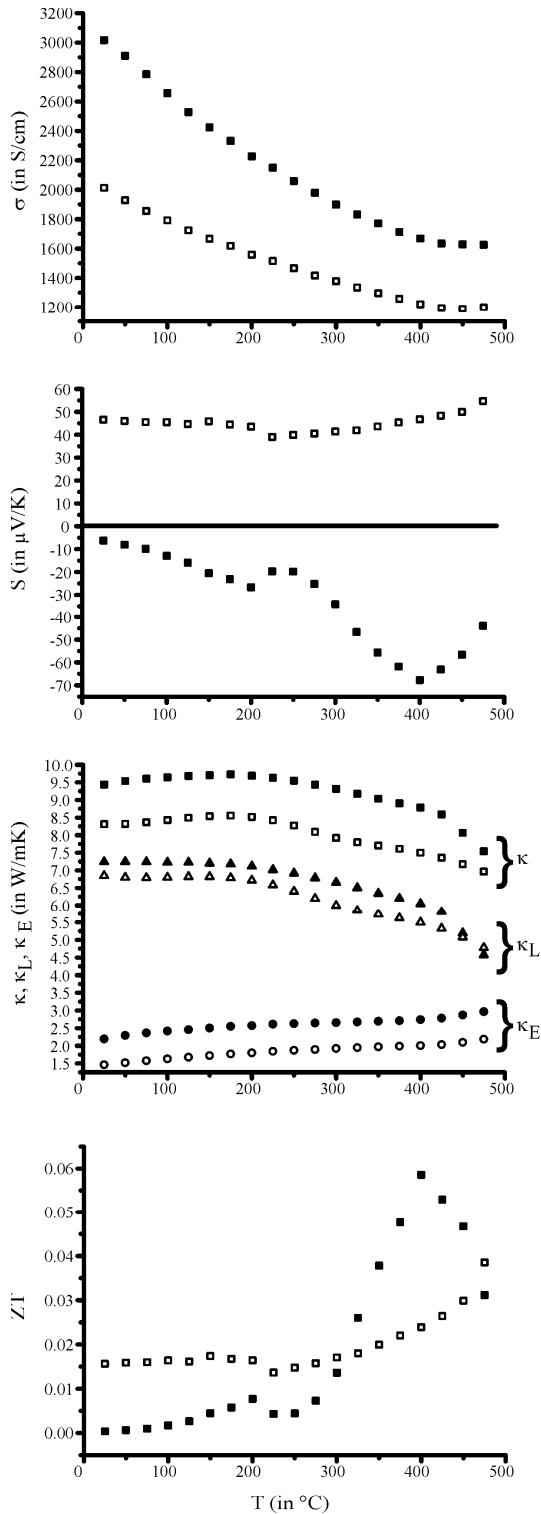


Figure 5. Thermoelectric characteristics of $39R\text{-M}_{0.067}\text{Sb}_{0.667}\text{Te}_{0.266}$ (filled symbols for $M = \text{Ge}$, empty symbols for $M = \text{Sn}$), from top to bottom: electrical conductivity, Seebeck coefficient, thermal conductivity (squares: total, triangles: phononic contribution, circles: electronic contribution) and overall thermoelectric figure of merit.

The measurement of the electrical conductivity σ suggests that the atom distribution changes slightly upon heating, because for both $\text{Sn}_{0.067}\text{Sb}_{0.667}\text{Te}_{0.266}$ and $\text{Ge}_{0.067}\text{Sb}_{0.667}\text{Te}_{0.266}$, σ exhibits a certain hysteresis, it appears slightly higher during cooling as compared to heating. This is probably due to cation diffusion processes which have also been observed for other metastable tellurides.^[42] However, as the difference is smaller than 10% on average, it is numerically insignificant and thus heating and cooling curves were averaged. The electrical conductivities at room temperature amount to $\sim 3000 \text{ Scm}^{-1}$ for $M = \text{Ge}$ and $\sim 2000 \text{ Scm}^{-1}$ for $M = \text{Sn}$, the temperature characteristics are metallic, corresponding to small-bandgap semiconductors (Figure 5, top). The absolute values are rather high, but are comparable to those of other stable layered structures of the series $(\text{MTe})_n(\text{Sb}_2\text{Te}_3)_m$ ($M = \text{Ge}, \text{Sn}$) and $(\text{Sb}_2\text{Te}_3)_m(\text{Sb}_2)_k$ (e.g. SnSb_2Te_4 1904 Scm^{-1} , GeSb_2Te_4 2810 Scm^{-1} , Sb_4Te_3 3000 Scm^{-1})^[16,43,44] or metastable ones like $\text{Ge}_{1.57}\text{Sb}_{2.43}\text{Te}_5\text{-Sb}_8$ (2500 Scm^{-1}).^[24] The electrical conductivity of the Ge compound is significantly higher; this trend is the same for the pair of stable compounds $\text{GeSb}_2\text{Te}_4 / \text{SnSb}_2\text{Te}_4$. The Seebeck coefficients of both $39R\text{-M}_{0.067}\text{Sb}_{0.667}\text{Te}_{0.266}$ phases at room temperature, $-6.3 \mu\text{VK}^{-1}$ for $M = \text{Ge}$ and $46.6 \mu\text{VK}^{-1}$ for $M = \text{Sn}$, are close to the values reported for layered binary and ternary phases

M-Sb-Te (M = Ge, Sn) which range from approximately 10 to 40 μVK^{-1} .^[43,44] Whereas the Seebeck coefficient is positive and almost independent of the temperature for M = Sn, it is negative over the whole temperature range for M = Ge, indicating that deficiency electrons (holes) are the major charge carriers in the Sn compound (Figure 5, second graph). The highest absolute value is observed for M = Ge at 400 °C. The differences between the Ge and the Sn compound might be due to slight variations of the stoichiometry or crystallite shape and size effects. The hole concentration in Sb_2Te_3 was reported to increase upon Sn doping, while Ge doping decreases it.^[45,46] This is in accordance with the behavior observed for $39R\text{-M}_{0.067}\text{Sb}_{0.667}\text{Te}_{0.266}$ phases. Both compounds exhibit thermal conductivities κ between 8 and 10 $\text{WK}^{-1}\text{m}^{-1}$ at ambient temperature which slightly decrease upon heating. As for most semiconductors, κ is dominated by the phononic contribution κ_L , which decreases more strongly upon heating than the overall κ , whereas the electronic contribution κ_E increases slightly (Figure 5, third graph). The layered compounds $(\text{GeTe})_n(\text{Sb}_2\text{Te}_3)_m$ ($k = 2 - 4 \text{WK}^{-1}\text{m}^{-1}$) and $21R\text{-SnSb}_2\text{Te}_4$ ($k = 2 \text{WK}^{-1}\text{m}^{-1}$) exhibit slightly lower k values,^[43,44] whereas elemental antimony shows a thermal conductivity between $\sim 23 \text{WK}^{-1}\text{m}^{-1}$ (bulk material) and $14 \text{WK}^{-1}\text{m}^{-1}$ (thin film).^[47] The measured values of the $39R\text{-M}_{0.067}\text{Sb}_{0.667}\text{Te}_{0.266}$ phases are in this range and similar to the value measured for Sb_2Te ($8 \text{WK}^{-1}\text{m}^{-1}$, thin film).^[47] Both compounds exhibit rather low thermoelectric figures of merit ZT with a maximum of 0.06 at 400 °C for the Ge compound (Figure 5, bottom). Comparable stable long range-ordered Ge-Sb-Te ($ZT = \sim 0.2$) and Sn-Sb-Te ($ZT = \sim 0.01$) phases exhibit similar ZT values.^[43,44]

3.4.3 Conclusion

Whereas partial phase separation in bulk samples, especially by spinodal decomposition, often leads to layered nano- or microstructures that are highly disordered with respect to the sequence of structural building blocks, the isostructural metastable phases $39R\text{-Ge}_{0.067}\text{Sb}_{0.667}\text{Te}_{0.266}$ and $39R\text{-Sn}_{0.067}\text{Sb}_{0.667}\text{Te}_{0.266}$, which can be obtained by simply quenching stoichiometric melts and subsequently annealing the bulk samples, crystallize as long-periodically ordered layered structures. Lamellae of gray arsenic type (predominantly composed of antimony, thickness $\sim 15 \text{Å}$) and Sb_2Te_3 -type slabs (thickness $\sim 10 \text{Å}$) alternate without significant stacking disorder. The phases obtained by our facile route are structurally comparable to “superlattice” structures of thin film samples prepared by layer-by-layer deposition on a substrate. In contrast to the formally isostructural $39R\text{-Sb}_{10}\text{Te}_3$ the corrugated honeycomb Sb nets in the vicinity of Sb_2Te_3 building block are partially substituted by GeTe or SnTe, locally extending them to slabs $\text{M}_2\text{Sb}_2\text{Te}_5$

(M = Ge, Sn). This blurs the distinct interface between the subunits composed of Sb and Sb₂Te₃ doped with Ge and Sn. The resulting wave-like concentration variation is probably due to diffusion processes related to the preference of Te and Ge/Sn to form an alternating cation-anion sequence. Similar interdiffusion effects between distinct lamellae can be expected in "superlattice" structures, for example activated by thermal cycling of multi-layer thermoelectrics.

An intriguing feature of the title compounds with respect to their properties is their nature as (semi-)metal (gray arsenic type layers) - semiconductor (Ge, Sn doped Sb₂Te₃ slabs) heterostructures. For analogous structures (M₂Te₃)_m(M₂)_k (M = Sb, Bi) it was already shown that the "metallicity" of these materials can be increased with rising k, i.e. a larger fraction of the metallic constituent.^[16,48] The present investigation shows that the carrier type of such structures can also be altered from n-type (electrons) to p-type (holes) by doping the corresponding semiconductor, in this case with Ge or Sn, respectively. The electronic properties of such "bulk superlattice" materials may thus be adjusted by varying the composition which should allow the further optimization of the power factor $S^2\sigma$. Recently, a theoretical study on the thermal conductivity of semimetal (Sb) - semiconductor (Bi₂Te₃) "superlattice nanowires" showed that reducing the lengths of Sb and Bi₂Te₃ segments should lower the thermal conductivity.^[49] Although we have investigated bulk samples, this prediction is experimentally confirmed by the measurements of thermal conductivity of the title compounds which lies in between the thermal conductivity of pure Sb and that of the compounds (MTe)_n(Sb₂Te₃)_m (M = Ge, Sn) with variable lengths of individual lamellae (smallest one ~ 10 Å for n = 0). In comparison to optimized thermoelectrics, the rather high thermal conductivity impedes high *ZT* values for the title compounds despite their good electrical conductivity and reasonable Seebeck coefficients. To overcome this problem, additional micro- and nanostructuring (e.g. texture, twin boundaries, partial defect ordering) could be a possible solution as shown for metastable Ge-Sb-Te phases with compositions close to those used in data storage devices, which can be nanostructured by appropriate thermal treatment.^[27] The extension of such structure-property relationships to layered phases, although it would require additional tedious investigations, might be an intriguing aspect for future investigations. It is interesting to note that atomically controlled "superlattice" structures have also been discussed for data storage media.^[50,51-53] The key feature of these layered structures is that different lamellae vary in their crystallization properties, which could allow the optimization of the materials. Hence, the title compounds are not only interesting model systems for chalcogenide thermoelectrics but can also contribute to the understanding of other possible applications for "superlattice" structures.

3.4.4 Experimental section

3.4.4.1 Synthesis and elemental analysis

Homogenous bulk samples of $M_{0.067}Sb_{0.667}Te_{0.266}$ ($M = Ge, Sn$) can be prepared by melting stoichiometric mixtures of the elements Ge (99.999%, Sigma Aldrich), Sn (99.99%, Smart Elements), Sb (99.999%, Smart Elements) and Te (99.999%, Alfa Aesar) in sealed silica glass ampoules under argon atmosphere at 950 °C, quenching in air and annealing at a temperature of 500 °C for one week. Energy-dispersive X-ray spectroscopy (EDX) was performed using a JSM-6500F (Jeol, USA) scanning electron microscope with EDX detector (model 7418, Oxford Instruments, Great Britain). The averaged values of 3-5 point analyses on the single crystals used for X-ray data collection correspond to the formulae $Ge_{0.072(3)}Sb_{0.675(5)}Te_{0.253(3)}$ and $Sn_{0.071(5)}Sb_{0.676(4)}Te_{0.253(3)}$, respectively, which agree well with the compositions $Ge_{0.067}Sb_{0.667}Te_{0.266}$ and $Sn_{0.067}Sb_{0.667}Te_{0.266}$ given by initial weight. For the measurement of thermoelectric properties, ingots were prepared from stoichiometric melts of the elements which were solidified in silica ampoules with flat bottom to obtain disc-shaped ingots with diameters of approximately 15 mm and thicknesses of 3-6 mm. The ingots were annealed at 500 °C for approximately 7 days before they were polished to flat plates for the measurements. The powder diffraction patterns of these materials do not differ significantly from those of the corresponding samples used for the other investigations.

3.4.4.2 Thermal analysis

A Setaram TG-92 instrument was used to study the thermal behavior of the samples up to 800 °C by differential thermal analysis and thermogravimetry (DTA-TG). The measurements were conducted under helium at a heating rate of 10 K·min⁻¹ on powdered material in alumina crucibles. In the investigated temperature range, the weight loss was not significant.

3.4.4.3 X-ray powder diffraction

X-ray powder patterns were recorded on a Huber G670 Guinier camera equipped with a fixed imaging plate and integrated read-out system using Cu-K_{α1} radiation (Ge monochromator, $\lambda=1.54056$ Å). Specimens were prepared by crushing representative parts of the samples and fixing powdered specimens on Mylar foils using silicone grease. Evaluation of the powder data was done using the program WINX^{POW}.^[54] Lattice parameters were determined by pattern fitting

(Rietveld method) using the program TOPAS with structure models obtained from the single crystal structure analyses.^[55] Results can be seen in Figure 2.

3.4.4.4 Single-crystal X-ray crystallography

For single crystal analysis, irregularly shaped plate-like single crystals were mechanically isolated from the ingots and checked for quality by Laue photographs on a Buerger precession camera after mounting them on glass fibers. Laboratory single crystal intensity data were collected on a STOE IPDS-I diffractometer with imaging plate detector using Mo-K α radiation (graphite monochromator, $\lambda = 0.71093$ Å). Synchrotron data of the same crystals were collected at beamline ID11 (ESRF, Grenoble, undulator beam) on a Huber diffractometer setup with vertical rotation axis and Frelon2K CCD detector. Resonant scattering data sets were collected at the K edges of Sn (0.424607 Å, 29.200 keV), Sb (0.406629 Å, 30.491 keV) and Te (0.389700 Å, 31.814 keV) for Sn_{0.067}Sb_{0.667}Te_{0.266} and at the Sb K edge for Ge_{0.067}Sb_{0.667}Te_{0.266}. A detector offset was used to obtain high-angle data. After conversion of the frames, the data were indexed using SMART and integrated using SAINT.^[56] Semiempirical absorption corrections based on equivalent reflections were applied to the laboratory data before the structures were solved with direct methods.^[57] As remaining beamtime between other projects was used, the measurement parameters (exposure time, number of frames) for the data collections and thus the quality of the individual datasets vary slightly. The structure was initially solved (without assigning element types) from laboratory data.^[58] After scaling, combining and correcting the synchrotron data of each wavelength using SADABS,^[59] joint multiple-wavelength refinements were performed using JANA2006.^[37] Details on the refinement are discussed in the section *Results and Discussion*, and further information may be obtained from the Fachinformationszentrum Karlsruhe, D-76344 Eggenstein-Leopoldshafen (Germany), by quoting the deposition numbers CSD-423076 and CSD-423077 for Sn_{0.067}Sb_{0.667}Te_{0.266} and Ge_{0.067}Sb_{0.667}Te_{0.266}, respectively, the names of the authors, and the citation of the paper. As there is no cif standard for multiple-wavelength joint refinements, the data that vary for different wavelengths (e.g. the absorption coefficient), have been given for laboratory data in the deposited files, whereas the atomic parameters result from the joint refinement.

3.4.4.5 Electron microscopy

Specimens were prepared by dispersing an ethanol suspension of finely powdered specimen on copper grids coated with holey carbon film which were mounted on a double tilt holder with maximum tilt angle of $\pm 30^\circ$. Selected-area electron diffraction (SAED) and high-resolution

transmission electron microscopy (HRTEM) were carried out on a FEI Titan 80–300 equipped with a field emission gun operating at 300 kV. In addition, scanning transmission electron microscopy (STEM) using a high-angle annular dark field detector (HAADF) was performed to obtain Z contrast images. TEM images were recorded using a Gatan UltraScan 1000 (2k×2k) camera, for HAADF-STEM, a Fischione detector with an inner semi-angle of 32 mrad was used. For the simulation of high resolution images, the multi-slice method as implemented in the EMS program package was used.^[60]

3.4.4.6 Thermoelectric properties

Both commercial and in-house-built facilities were used to determine the temperature dependence of the electrical and thermal conductivities as well as the Seebeck coefficient, which were investigated in the range from room temperature up to approx. 500 °C under vacuum. To avoid Peltier influences on the measurement, the electrical conductivity was measured by a four-point-probe setup using an AC method. The Seebeck coefficient was measured using a small temperature gradient across the sample while slowly changing the environment temperature in order to obtain Seebeck coefficients for each mean sample temperature. Type-R thermocouples attached directly to the sample's surface were used for both temperature measurements and the Seebeck voltage was picked up via the Pt lines. The thermal conductivity was calculated from measurements of the thermal diffusivity by a laser-flash apparatus (Netzsch LFA 427), the heat capacity determined by differential scanning calorimetry (Netzsch DSC 404) and the samples' density measured using a Mohr's balance. Experimental errors are estimated at 2% for the electrical conductivity, 5% for the Seebeck coefficient and 7% for the thermal conductivity. The electronic contribution of the thermal conductivity was calculated according to the Wiedemann-Franz law for non-degenerate semiconductors.

3.4.5 References

- [1] D. Bonnet, P. Meyers, *J. Mater. Res.* **1998**, *13*, 2740.
- [2] M. A. Green, *J. Mater. Sci. - Mater. Electron.* **2007**, *18*, S15.
- [3] D. Lencer, M. Salinga, M. Wuttig, *Adv. Mater.* **2011**, *23*, 2030.
- [4] S. Raoux, W. Wojciech, D. Ielmini, *Chem. Rev.* **2009**, *110*, 240.
- [5] W. Bensch, M. Wuttig, *Chem. Unserer Zeit* **2010**, *44*, 92.
- [6] A. V. Shevelkov, *Russ. Chem. Rev* **2008**, *77*, 1.
- [7] J. R. Sootsman, D. Y. Chung, M. G. Kanatzidis, *Angew. Chem. Int. Ed.* **2009**, *48*, 8616.

- [8] G. J. Snyder, E. S. Toberer, *Nat. Mater.* **2008**, 7, 105.
- [9] D. L. Medlin, G. J. Snyder, *Curr. Opin. Colloid Interface Sci.* **2009**, 14, 226.
- [10] M. S. Dresselhaus, G. Chen, M. Y. Tang, R. Yang, H. Lee, D. Wang, Z. Ren, J.-P. Fleurial, P. Gogna, *Adv. Mater.* **2007**, 19, 1.
- [11] M. G. Kanatzidis, *Chem. Mater.* **2010**, 22, 648.
- [12] Č. Drašar, A. Hovorková, P. Lošťák, H. Kong, C.-P. Li, C. Uher, *J. Appl. Phys.* **2008**, 104, 023701.
- [13] R. Venkatasubramanian, E. Siivola, T. Colpitts, B. O'Quinn, *Nature* **2001**, 413, 597.
- [14] J. R. Szczech, J. M. Higgins, S. Jin, *J. Mater. Chem.* **2011**, 21, 4037.
- [15] S. K. Bux, J.-P. Fleurial, R. B. Kaner, *Chem. Commun.* **2010**, 46, 8311.
- [16] P. F. P. Poudeu, M. G. Kanatzidis, *Chem. Commun.* **2005**, 21, 2672.
- [17] K. Kifune, Y. Kubota, T. Matsunaga, N. Yamada, *Acta Crystallogr. Sect. B* **2005**, 61, 492.
- [18] C. S. Barrett, P. Cucka, K. Haefner, *Acta Crystallogr.* **1963**, 16, 451-453.
- [19] T. L. Anderson, H. B. Krause, *Acta Crystallogr. Sect. B* **1974**, 30, 1307-1310.
- [20] M. N. Schneider, O. Oeckler, *Z. Anorg. Allg. Chem.* **2008**, 634, 2557-2561.
- [21] L. E. Shelimova, O. G. Karpinsky, M. A. Kretova, V. I. Kosyakov, V. A. Shestakov, V. S. Zemskov, F. A. Kuznetsov, *Inorg. Mater.* **2000**, 36, 768.
- [22] O. G. Karpinsky, L. E. Shelimova, M. A. Kretova, J.-P. Fleurial, *J. Alloys Compd.* **1998**, 268, 112.
- [23] T. Matsunaga, R. Kojima, N. Yamada, K. Kifune, Y. Kubota, M. Takata, *Appl. Phys. Lett.* **2007**, 90, 161919.
- [24] M. N. Schneider, M. Seibald, O. Oeckler, *Dalton Trans.* **2009**, 2004.
- [25] M. N. Schneider, O. Oeckler, *Z. Anorg. Allg. Chem.* **2010**, 636, 137.
- [26] O. Oeckler, M. N. Schneider, F. Fahrnbauer, G. Vaughan, *Solid State Sci.* **2011**, 13, 1157.
- [27] M.N. Schneider, T. Rosenthal, C. Stiewe, O. Oeckler, *Z. Kristallogr.* **2010**, 225, 463.
- [28] H. Lind, S. Lidin, *Solid State Sci.* **2003**, 5, 47.
- [29] M. N. Schneider, M. Seibald, P. Lagally, O. Oeckler, *J. Appl. Crystallogr.* **2010**, 43, 1012.
- [30] B. Legendre, C. Hancheng, S. Bordas and M. T. Clavaguera-Mora, *Thermochim. Acta* **1984**, 78, 141.
- [31] V. I. Kosyakov, V. A. Shestakov, L. E. Shelimova, F. A. Kuznetsov and V. S. Zemskov, *Inorg. Mater.* **2000**, 36, 1004.

- [32] S. Bordas, M. T. Clavaguera-Mora, B. Legendre and C. Hancheng, *Thermochim. Acta* **1986**, *107*, 239.
- [33] A. Stegherr, *Philips Res. Repts. Suppl.* **1969**, *6*, 1.
- [34] R. Wulf, *Acta Crystallogr. Sect. A* **1990**, *46*, 681.
- [35] B. L. Henke, E. M. Gullikson, J.C. Davis, *Atomic Data and Nuclear Data Tables* **1993**, *54*, 181.
- [36] C. T. Chantler, K. Olsen, R. A. Dragoset, J. Chang, A. R. Kishore, S. A. Kotochigova, D. S. Zucker, X-Ray Form Factor, Attenuation and Scattering Tables, Version 2.1, National Institute of Standards and Technology, Gaithersburg MD, **2005**.
- [37] V. Petricek, M. Dusek, L. Palatinus, *JANA2006 - The crystallographic computing system*, Institute of Physics, Praha, Czech Republic, **2006**.
- [38] T. Chattopadhyay, J. X. Boucherle, H. G. von Schnering, *J. Phys. C: Solid State Phys.* **1987**, *20*, 1431.
- [39] T. Matsunaga, N. Yamada, Y. Kubota, *Acta Crystallogr. Sect. B* **2004**, *60*, 685.
- [40] H. Böttner, G. Chen, R. Venkatasubramanian, *MRS Bull.* **2006**, *31*, 211.
- [41] F. R. Harris, S. Standridge, C. Feik, D. C. Johnson, *Angew. Chem. Int. Ed.* **2003**, *42*, 5296.
- [42] O. Oeckler, M. N. Schneider, T. Rosenthal, C. Stiewe, *Z. Anorg. Allg. Chem.* **2010**, *636*, 2095.
- [43] J. Oestreich, *Ph.D. Thesis*, University of Konstanz, Germany, **2001**.
- [44] P. P. Konstantinov, L. E. Shelimova, E. S. Avilov, M. A. Kretova, V. S. Zemskov, *Inorg. Mater.* **2001**, *37*, 662.
- [45] V. A. Kulbachinskiĭ, A. Y. Kaminskiĭ, P. M. Tarasov, P. Lostak, *Phys. Solid State* **2006**, *48*, 833.
- [46] J. L. Cui, H. Fu, X. L. Liu, D. Y. Chen, W. Yang, *Curr. Appl. Phys.* **2009**, *9*, 1170.
- [47] M. Kuwahara, O. Suzuku, N. Takethosi, T. Yagi, P. Fons, J. Tominaga, T. Baba, *Jpn. J. Appl. Phys.* **2007**, *46*, 6863.
- [48] J. W. G. Bos, H. W. Zandbergen, M.-H. Lee, N. P. Ong, R. J. Cava, *Phys. Rev. B* **2007**, *75*, 195203.
- [49] D. Pinisetty, R. V. Devireddy, *Acta Mater.* **2010**, *58*, 570.
- [50] T. C. Chong, L. P. Shi, X. S. Miao, P. K. Tan, R. Zhao, Z. P. Cai, *Jpn. J. Appl. Phys.* **2000**, *39*, 737.
- [51] T. C. Chong, L. P. Shi, R. Zhao, P. K. Tan, J. M. Li, H. K. Lee, X. S. Miao, A. Y. Du, C. H. Tung, *Appl. Phys. Lett.* **2006**, *88*, 122114.

-
- [52] H. Yang, T. C. Chong, R. Zhao, H. K. Lee, J. Li, K. G. Lim, L. Shi, *Appl. Phys. Lett.* **2009**, *94*, 203110.
- [53] M. Hase, Y. Miyamoto, J. Tominaga, *Phys. Rev. B* **2009**, *79*, 174112.
- [54] *WINXPOW, Version 2.12*, Stoe & Cie. GmbH, Darmstadt, **2005**.
- [55] A. Coelho, *TOPAS -Academic, V. 4.1*; Coelho Software, Brisbane, **2007**.
- [56] *SAINT, v6.01*, Bruker AXS, Madison USA **1999**.
- [57] *XPREP, Version 6.12*, Siemens Analytical X-ray Instruments Inc., Madison, Wisconsin, USA, **1996**.
- [58] G. M. Sheldrick, *Acta Crystallogr. Sect. A* **2008**, *64*, 112.
- [59] *SADABS, v2.03*, Bruker AXS, Madison USA **1999**.
- [60] P. Stadelmann, *Ultramicroscopy* **1987**, *21*, 131.

4 From phase-change materials to thermoelectrics

4.1 Overview

The rational synthesis of new solid-state compounds with special properties is an idea that often resounds throughout the community of solid-state scientists. However, the discovery of novel materials remains challenging as the potential of theoretical approaches for the *a priori* prediction of new compounds and their properties is still rather limited. The search for new materials with specific properties is often tedious and involves a lot of experimental trial and error. Nevertheless, various concepts often serve as guides during such a search. The synthesis of novel materials might be inspired by nature.^[1-3] New preparative routes might be bio-inspired and for example copy biomineralization processes under laboratory conditions. They can also be geo-inspired by concepts and findings of modern mineralogy, e.g. the natural formation of textures on variable length scales, e.g. by precipitation, spinodal decomposition or phase transitions, may be mimicked to obtain nano- or microstructured materials. The formation of nano- and microstructures by partial decomposition or exsolution is also an intriguing approach to lower the thermal conductivity of thermoelectrics as demonstrated by examples such as $\text{AgPb}_m\text{SbTe}_{2+m}$ (LAST-m), $\text{NaPb}_m\text{SbTe}_{2+m}$ (SALT-m) or AgSbTe_2 and $\text{Pb}_2\text{Sb}_6\text{Te}_{11}$.^[4-8] In addition to nature, technology may also provide inspiration concerning the search for new materials. For example, the properties of well-characterized and understood compounds that are applied for a specific purpose can be optimized for new applications. Such approaches include various doping experiments with additional elements, intercalation or change of the nano-/microstructure.

In this context, compounds whose composition are comparable to those of phase-change materials, especially GeTe-rich phases $(\text{GeTe})_n(\text{Sb}_2\text{Te}_3)$ ($n = 12$), have been shown to exhibit interesting thermoelectric properties as discussed in Chapter 4.2. They are small-bandgap semiconductors that exhibit moderate thermal conductivities and therefore meet two basic requirements for thermoelectrics (cf. Chapter 1). For phase-change materials a moderate electrical conductivity allows for switching between amorphous and crystalline modifications by electrical heating and ensures that stored information can be read applying read-out currents. For thermoelectrics the electrical part of the thermal conductivity remains for low small-bandgap

semiconductors while simultaneously enough electrical conductivity to use the thermoelectric effect is present. Whereas in phase-change materials a small thermal conductivity enables the writing of sharp recording marks when the material is locally heated, in thermoelectrics the small thermal conductivity ensures that the temperature gradient necessary to use the thermoelectric effect is sustained during application. The highly disordered crystalline phases of phase-change materials exhibit simple average structures which are metastable with respect to the formation of long-periodic layered structures. Partial stabilization yields pronounced nano- or microstructures which further reduce the thermal conductivity (see also Chapter 5). Thin-film samples of metastable crystalline modifications are suitable to study their phase-change characteristics but less suitable for thermoelectric investigations or detailed real-structure analysis. Therefore, bulk material is required to confirm the hypothesis that the chemical systems used as phase-change materials are promising thermoelectrics, both concerning the structural characterization as well as for physical measurements. In this work, various synthetic approaches have been compared.

GeTe-rich compounds on the pseudobinary section GeTe - Sb₂Te₃ exhibit a stable rocksalt-type structure at elevated temperatures,^[9,10] which can be investigated *in situ*. Such high-temperature modifications of (GeTe)_n(Sb₂Te₃) compounds exist for $n \geq 3$, e. g. Ge₃Sb₂Te₆ ($n = 3$). 21R-GeSb₂Te₄ ($n = 1$) and 9P-Ge₂Sb₂Te₅ ($n = 2$) do not show phase transitions to a cubic high-temperature phase before melting. The transition temperatures between cubic rocksalt-type and trigonal layered phases decrease with increasing n , as will be discussed in more detail in Chapter 5. Rietveld refinements on diffraction patterns of Ge₃Sb₂Te₆ ($n = 3$, transition temperature ~575 °C) and Ge₁₂Sb₂Te₁₅ ($n = 12$, transition temperature ~475 °C) collected at 600 °C confirm that the high-temperature modifications exhibit rocksalt-type average structures. Single crystals were obtained by chemical transport reactions using iodine or SbI₃ as transport agent or by crystal formation during the annealing process in the stability range of the high-temperature modifications (cf. Chapter 4.2, Chapter 5.4 and Chapter 5.5). Above the transition temperatures to the cubic high-temperature phases, single crystals ($n = 12$ cf. Chapter 4.2 and $n = 6, = 12, = 15$ cf. Chapter 5.5) do not exhibit pronounced diffuse scattering, i. e. little short-range order: Te atoms occupy the anion positions whereas Ge atoms, Sb atoms as well as cation vacancies are randomly distributed on cation sites. Thus, the high-temperature phases are characterized by a large concentration of cation vacancies. Upon slow cooling, the stable trigonal layered structures are obtained. Formally, this involves the ordering of cation defects in 2D extended defect layers which are parallel. The stacking sequence of the Te layers changes and there are significant structural distortions around the resulting van der Waals gaps. These separate the rocksalt-type

slabs in the ordered structures described in Chapters 1 and 2, respectively. Rapid quenching partially prevents the formation of stable trigonal layered structures for compounds that exhibit cubic high-temperature modifications. Quenching melts (in air or liquid nitrogen) with $n < 3$, i. e. compounds with no cubic high-temperature phase, yields the corresponding trigonal layered structures ($n = 1$: $21R$ -type, $n = 2$: $9P$ -type) with a pronounced degree of stacking faults. As shown for GeBi_2Te_4 ($n = 1$, cf. Chapter 4.3), whose stable trigonal layered phase corresponds to a $21R$ -type.^[11] even melt-spinning experiments with very high cooling rates do not yield metastable samples with simple average structures. Although powder diffraction shows the normal $21R$ -type structure electron microscopy reveals that very small domains are present. Quenching of $\text{Ge}_3\text{Sb}_2\text{Te}_6$ in air or liquid nitrogen yields a mixture of a phase with cubic metrics and a highly disordered layered trigonal phase with broad reflections. The cubic phase vanishes at ~ 270 °C and long-range ordered $33R$ - $\text{Ge}_3\text{Sb}_2\text{Te}_6$ forms at ~ 420 °C. Recent results^[12] indicate that melt-spinning impedes the formation of the layered phase and yields primarily the (pseudo-)cubic modification. In contrast, rapid quenching of the high-temperature modification of $\text{Ge}_{12}\text{Sb}_2\text{Te}_{15}$ in air or water yields a homogenous highly disordered phase that is kinetically inert up to ~ 325 °C when a trigonal layered structure (with pronounced stacking disorder) is formed (also refer to Chapter 5.2). Whereas the quenched phases are pseudo-cubic according to powder diffraction, single-crystal diffraction as well as electron microscopy reveal nanoscale twin domains with trigonal structure that are associated with a cubic to rhombohedral phase transition. This multiple twinning is accompanied by short-range order of cation defects in finite intersecting layers that leads to characteristic diffuse scattering which will be discussed in Chapter 5.

Quenched samples of $(\text{GeTe})_n(\text{Sb}_2\text{Te}_3)$ ($n = 3, 4.5, 7, 12, 19$, cf. Chapter 4.2 and Chapter 5.3) exhibit rather high thermoelectric figures of merit ZT . For $n = 12$ and 19 , a maximum value of 1.3 is reached at 450 °C. This is comparable to modern thermoelectrics.^[13-17] This implies that metastable GeTe-rich Ge-Sb-Te materials may be promising for thermoelectric applications. However, at elevated temperatures the nanostructure of the materials is not long-time stable as diffusion processes are activated above ~ 300 °C in such materials (cf. Chapter 5). Below 300 °C, the thermoelectric figure of merit of compounds $(\text{GeTe})_n(\text{Sb}_2\text{Te}_3)$ ($n = 3, 4.5, 7, 12, 19$) is about one magnitude smaller than the maximum values at 450 °C. A detailed discussion of the corresponding structure-property relationships will be given in Chapter 5.

The cubic to rhombohedral phase transition is naturally accompanied by a volume and density change, respectively. Other phase transitions of, for instance, metastable cubic $\text{Ge}_2\text{Sb}_2\text{Te}_5$ (prepared as thin-film sample) include the pressure-induced amorphization at (~ 15 GPa, at room

temperature) followed by the formation of a body-centred phase at ~ 30 GPa. In contrast, stable $9P$ - $\text{Ge}_2\text{Sb}_2\text{Te}_5$ remains crystalline upon compression and transforms to an orthorhombic structure at ~ 17 GPa before a body-centred phase is obtained at ~ 33 GPa.^[18-21] These findings imply that pressure is an interesting parameter for synthetic approaches especially when it is combined with high temperatures and quenching steps. This assumption is corroborated by high-pressure experiments on GeBi_2Te_4 . According to Rietveld refinement, a sample of GeBi_2Te_4 obtained by quenching a stoichiometric melt under a constant pressure of 12 GPa (i. e. by switching of the furnace) exhibits a CuPt-type structure (cf. Chapter 1.2). Electron microscopy reveals a pronounced nanostructure which explains why the "average structure" can only be described with very prolate atomic displacement ellipsoids. At ambient pressure, the sample transforms into $21R$ - GeBi_2Te_4 above 200 °C. This indicates that a highly disordered high-pressure high-temperature phase is partially retained. Variation of the thermal treatment applied under constant pressure of 12 GPa allows one to alter the domain sizes and orientations as well as the defect layer arrangements. Although the small volume of high-pressure samples impedes the complete thermoelectric characterization of the thermoelectric properties, the dependency of their electrical conductivity on the micro-/nanostructure is very pronounced. The characteristics of the electrical conductivity changes from metallic to semiconducting behavior with decreasing domain size and a more random orientation distribution of domains. Scattering of the electrons at the domain or grain boundaries becomes predominant and the electrical conductivity decreases as the mean free path of electrons decreases. These results show that metastable germanium bismuth tellurides and germanium antimony tellurides are intriguing precursors for thermoelectrics with extended nanostructures, and also exhibit interesting properties themselves without further processing.

References for chapter 4.1

- [1] E. Dujardin, S. Mann, *Adv. Mater.* **2002**, *14*, 775.
- [2] L. A. Estroff, A. D. Hamilton, *Chem. Mater.* **2001**, *13*, 3227.
- [3] W. Depmeier, *Cryst. Res. Technol.* **2009**, *44*, 1122.
- [4] A. C. Bruce, J. K. Matthew, L. H. Joel, H. Mi-Kyung, C. Duck-Young, G. K. Mercuri, *Adv. Funct. Mater.* **2009**, *19*, 1254.
- [5] C. J. Vineis, A. Shakouri, A. Majumdar, M. G. Kanatzidis, *Adv. Mater.* **2010**, *22*, 3970.
- [6] P. F. P. Poudeu, J. D'Angelo, A. D. Downey, J. L. Short, T. P. Hogan, M. G. Kanatzidis, *Angew. Chem. Int. Ed.* **2006**, *45*, 3835.

-
- [7] T. Ikeda, V. A. Ravi, L. A. Collins, S. M. Haile, G. J. Snyder, *J. Electron. Mater.* **2007**, *36*, 716.
- [8] S. N. Zhang, T.J. Zhu, S. H. Yang, C. Yu, X. B. Zhao, *J. Alloys Compds.* **2010**, *499*, 215.
- [9] T. Matsunaga, N. Yamada, Y. Kubota, *Acta Crystallogr. Sect. B* **2004**, *60*, 685.
- [10] T. Matsunaga, H. Morita, R. Kojima, N. Yamada, K. Kifune, Y. Kubota, Y. Tabata, J.-J. Kim, M. Kobata, E. Ikenaga, K. Kobayashi, *J. Appl. Phys.* **2008**, *103*, 093511.
- [11] L. E. Shelimova, O. G. Karpinskii, P. P. Konstantinov, E. S. Avilov, M. A. Kretova, V. S. Zemskov, *Inorg. Mater.* **2004**, *40*, 451.
- [12] T. Schröder, publication in preparation.
- [13] A. V. Shevelkov, *Russ. Chem. Rev.* **2008**, *77*, 1.
- [14] K. Nielsch, J. Bachmann, J. Kimling, H. Böttner, *Adv. Energy Mater.* **2011**, *1*, 713.
- [15] M. G. Kanatzidis, *Chem. Mater.* **2010**, *22*, 648.
- [16] G. J. Snyder, E. S. Toberer, *Nat. Mater.* **2008**, *7*, 105.
- [17] J. R. Sootsman, D. Y. Chung, M. G. Kanatzidis, *Angew. Chem. Int. Ed.* **2009**, *48*, 8616.
- [18] A. V. Kolobov, J. Haines, A. Pradel, M. Ribes, P. Fons, J. Tominaga, Y. Katayama, T. Hammouda, T. Uruga, *Phys. Rev. Lett.* **2006**, *97*, 035701.
- [19] Y. Q. Cheng, M. Xu, H. W. Sheng, Y. Meng, X. D. Han, E. Ma, *Appl. Phys. Lett.* **2009**, *95*, 131904.
- [20] M. Krbal, A. V. Kolobov, J. Haines, P. Fons, C. Levelut, R. Le Parc, M. Hanfland, J. Tominaga, A. Pradel, M. Ribes, *Phys. Rev. Lett.* **2009**, *103*, 115502.
- [21] M. Krbal, A. V. Kolobov, P. Fons, J. Haines, A. Pradel, M. Ribes, A. A. Piarristeguy, C. Levelut, R. Le Parc, V. Agafonov, M. Hanfland, J. Tominaga, *Phys. Rev. B* **2011**, *83*, 024105.

4.2 From phase-change materials to thermoelectrics?

Matthias N. Schneider, Tobias Rosenthal, Christian Stiewe, and Oliver Oeckler

Zeitschrift für Kristallographie **2010**, 225, 463-470.

Abstract

Metastable tellurides play an important role as phase-change materials in data storage media and non-volatile RAM devices. The corresponding crystalline phases with very simple basic structures are not stable as bulk materials at ambient conditions, however, for a broad range of compositions they represent stable high-temperature phases. In the system Ge/Sb/Te, rocksalt-type high-temperature phases are characterized by a large number of vacancies randomly distributed over the cation position, which order as 2D vacancy layers upon cooling. Short-range order in quenched samples produces pronounced nanostructures by the formation of twin domains and finite intersecting vacancy layers. As phase-change materials are usually semimetals or small-bandgap semiconductors and efficient data storage requires low thermal conductivity, bulk materials with similar compositions and properties can be expected to exhibit promising thermoelectric characteristics. Nanostructuring by phase transitions that involve partial vacancy ordering may enhance the efficiency of such thermoelectrics. We have shown that germanium antimony tellurides with compositions close to those used as phase-change materials in rewritable Blu-Ray Discs, e. g. $(\text{GeTe})_{12}\text{Sb}_2\text{Te}_3$, exhibit thermoelectric figures of merit of up to $ZT = 1.3$ at 450 °C if a nanodomain structure is induced by rapidly quenching the cubic high-temperature phase. Structural changes have been elucidated by X-ray diffraction and high-resolution electron microscopy.

Copyright: © 2010 Oldenbourg Wissenschaftsverlag

4.2.1 Introduction

4.2.1.1 Thermoelectrics

In the past decade, an increasing number of research projects have focused on both the synthesis and the optimization of thermoelectric materials. These may be used to reversibly interconvert thermal and electrical energy, the ultimate goals being electric power generation from waste heat and the construction of efficient cooling devices. In this context, structure-property relationships concerning thermoelectricity have received increasing attention of materials scientists as understanding the phenomenon on the atomic as well as the nanoscale is the basis for any targeted optimization. Efficient thermoelectrics should combine high electrical conductivity (σ) and high Seebeck coefficients (S). Furthermore, the thermal conductivity (κ) should be as low as possible. The interplay of these specifications is represented by the dimensionless figure of merit $ZT = S^2 T \sigma \kappa^{-1}$ which is directly related to the efficiency of thermoelectric generators.

All relevant properties depend on the charge carrier concentration and cannot be altered independently. Concerning σ and κ , the best compromise are small-bandgap semiconductors or semimetals. As the electronic part of κ is proportional to σ , only its phononic part can be somehow independently varied.

Table 1. Comparison of tellurides used as thermoelectrics or as phase-change materials. Compounds without references are discussed in reviews.^[1-5, 31-40]

thermoelectric materials	phase-change materials
<p>M-Te (M = Ge, In, Ga, Pb, Bi, Sb) GeTe₄, [19] InTe₄, [20] GaTe₄, [20] PbTe, Bi₂Te₃, Sb₂Te₃, (Bi₂)_m(Bi₂Te₃)_n, [21], (Sb₂)_m(Sb₂Te₃)_n [22]</p>	<p>M-Te (M = Au, Ge, Sb) Au₅Te₉₅, [23] GeTe, GeTe₄, [23] Sb₂Te, Sb₇Te₃</p>
<p>M-Sb-Te (M = Ag, Ge, Ag/Ge, Ga, Pb) AgSbTe₂, (GeTe)_n(Sb₂Te₃)_m (GST), [24,25] (AgSbTe₂)_{1-x}(GeTe)_x (TAGS), Ga_mSb_nTe_{1.5(m+n)}, [26] Pb₂Sb₆Te₁₁, GeSb₁₀₀Te₁₅₀ [27]</p>	<p>M-Sb-Te (M = Ag, Ge, Sn, In) AgSbTe₂, [28] (GeTe)_n(Sb₂Te₃)_m (GST), SnSb₂Te₄, Ge_{7.1}Sb_{76.0}Te_{16.9} In₃SbTe₂ [29]</p>
<p>M-Bi-Te (M = Ge, Sn, Pb, Cs) (GeTe)_n(Bi₂Te₃)_m (GBT), [30], (SnTe)_n(Bi₂Te₃)_m, [30] (PbTe)_n(Bi₂Te₃)_m, [30] CsBi₄Te₆</p>	<p>M-Bi-Te (M = Ge) (GeTe)_n(Bi₂Te₃)_m (GBT)</p>
<p>M-Tl-Te (M = Ag, Sn, Bi) Ag₉TlTe₆, Tl₂SnTe₅, Tl₉BiTe₆</p>	<p>M-In-Sb-Te (M = Ag) Ag₅In₅Sb₆₀Te₃₀, Ag_{3.4}In_{3.7}Sb_{76.4}Te_{16.5} (AIST)</p>
<p>M-Pb-(M')-Sb-Te (M = Ag, Na, K; M' = Sn) AgPb_mSbTe_{2+m} (LAST), AgPb_mSn_nSbTe_{2+m+n} (LASTT), NaPb_mSbTe_{2+m} (SALT), NaPb_mSn_nSbTe_{2+m+n} (SALTT), KPb_mSbTe_{2+m} (PLAT)</p>	<p>M-M'-Sn-Te (M = Au M'=Ge) Au₂₅Ge₄Sn₁₁Te₆₀</p>

One way to increase ZT is the incorporation of atoms that are located in voids that are larger than necessary to accommodate them. These so-called ‘rattling’ atoms may effectively scatter phonons and thus reduce κ . Several classes of compounds such as skutterudites (e.g., CoSb_3), clathrates (e.g., $\text{Na}_8\text{Si}_{46}$) or half Heusler alloys (e.g., TiNiSn) provide promising candidates as summed up in various recent reviews.^[1–5] However, practical applications are still dominated by tellurides such as PbTe or Bi_2Te_3 which show a sufficient concentration of carriers and exhibit a rather low thermal conductivity owing to the presence of heavy atoms. Based on these conventional thermoelectrics with ZT in the range of ~ 1 , a broad range of new tellurides with promising properties has been prepared (see Table 1). Most of these materials exhibit a high degree of disorder on various length scales. Nanostructuring by partial decomposition or exsolution on the nanoscale led to ZT values up to ~ 2 , the most prominent examples being $\text{AgPb}_m\text{SbTe}_{2+m}$ (LAST- m) or $\text{NaPb}_m\text{SbTe}_{2+m}$ (SALT- m).^[6,7] Other examples such as $\text{Pb}_2\text{Sb}_6\text{Te}_{11}$ exhibit layered structures.^[8] Precipitates and domain or grain boundaries, respectively, are essential as corroborated by thermoelectrics which combine high power factors $S^2\sigma$ with drastically reduced lattice thermal conductivity due to increased phonon scattering at interfaces. This approach has successfully been demonstrated for layer-like systems such as $\text{Sb}_2\text{Te}_3/\text{Bi}_2\text{Te}_3$ superlattices, PbTe/PbSe quantum dot superlattices or nanocomposites of crystalline GeTe in an amorphous matrix with overall composition GeTe_4 .^[9–11] Such approaches (recent reviews [12–18]): strongly depend on the interplay of thermodynamics and kinetics and always mean approaching (but not reaching) the equilibrium state from a metastable one. Unstable but kinetically inert tellurides obviously offer a good starting point to follow this concept.

4.2.1.1 Phase-change materials

Metastable tellurides play another important role as phase-change materials (PCMs) in the recording layers of many rewritable data storage media (e.g., DVD-RW, DVD-RAM, BD-RE) and novel non-volatile random-access memory (RAM) devices.^[31–40] PCMs allow switching between amorphous and crystalline modifications which differ in optical and electrical properties, respectively. According to theoretical calculations and X-ray absorption fine structure (EXAFS) investigations,^[41–48] $\text{Ge}/\text{Sb}-\text{Te}-\text{Ge}/\text{Sb}-\text{Te}$ squares and even-membered larger rings are present in the amorphous modification. Although distorted octahedral coordination is predominant for most atoms, tetrahedral coordination of Ge has been evidenced and led to the hypothesis of an ‘umbrella-flip’ mechanism for the phase change between the amorphous and crystalline phases.^[49–53] The metastable crystalline modifications of various PCMs exhibit simple average structures, such as the A7 (gray As) type (e.g., $\text{Ag}_{3.4}\text{In}_{3.7}\text{Sb}_{76.4}\text{Te}_{16.5}$ or $\text{Ge}_{7.1}\text{Sb}_{76.0}\text{Te}_{16.9}$)

^[39] or the rocksalt type (e.g., GeSb_2Te_4 or $\text{Ge}_2\text{Sb}_2\text{Te}_5$) ^[54–56] which may be rhombohedrally distorted towards a GeTe-type structure (e.g., $\text{Ge}_8\text{Sb}_2\text{Te}_{11}$).^[57] These simple average structures are accessible from amorphous ones via short diffusion pathways, which is a requirement for the fast phase transition. As chemically very different atom types share the same Wyckoff position, the question of short-range ordering arises, both concerning of the elements and the vacancies, including the accompanying local distortion and relaxation, respectively. Vacancies are crucial for the stabilization of these materials and a statistical distribution as well as an arrangement in planar defect planes have been discussed.^[58–64] The stable phases formed upon annealing of the metastable crystalline materials often exhibit ordered layered structures such as *21R*- GeSb_2Te_4 , *21R*- GeBi_2Te_4 or *9P*- $\text{Ge}_2\text{Sb}_2\text{Te}_5$.^[65–69] These structures can be described as a stacking sequence of distorted rocksalt-type slabs with van der Waals gaps in between Te layers terminating the slabs. These gaps can be viewed as 2D infinite layers of cation vacancies associated with relaxation. However, in other cases equilibrium conditions correspond to a mixture of two or more different phases. For example, GeTe-rich GST materials do not form single-phase materials when reaching the thermodynamically stable state but separate into the long-periodically ordered compound $\text{Ge}_9\text{Sb}_2\text{Te}_{12}$ and an additional phase with a GeTe-type structure.^[57] Although the stable modifications do not occur during the write-erase cycle, they need to be taken into consideration as they are the ‘thermodynamic trap’ to be avoided. The kinetic inertness of metastable tellurides is essential for PCMs.

The properties of the materials depend, of course, on the electronic structure of the materials. The reversible phase transition amorphous to metastable crystalline is either induced by laser irradiation or by an electric current. In general, small-bandgap semiconductors or semimetals are required. Especially in RAM devices, intermediate electrical conductivity ensures sufficient currents but still allows ‘resistance heating’. The writing process involves the amorphization of small recording marks in a crystalline matrix, whereas erasing means recrystallization. For the sake of high spatial resolution and short write and erase times, low thermal conductivity of the PCMs is important in order to obtain high temperatures in very small areas. The metastability of both modifications is essential and ensures the reversibility of the process which would be interrupted once the stable phases are formed.

Several reviews show impressively that tellurides dominate the field of PCMs.^[31–40] For example, $\text{Ag}_5\text{In}_5\text{Sb}_{60}\text{Te}_{30}$ and $\text{Ag}_{3.4}\text{In}_{3.7}\text{Sb}_{76.4}\text{Te}_{16.5}$ are used for DVD-RW media, whereas germanium antimony tellurides (GST materials) are employed in CD-RWs (e.g. $\text{Ge}_{7.1}\text{Sb}_{76}\text{Te}_{16.9}$), DVD-RAMs (GeSb_2Te_4 or $\text{Ge}_2\text{Sb}_2\text{Te}_5$) and Blu-Ray Discs (GeTe-rich materials like $\text{Ge}_8\text{Sb}_2\text{Te}_{11}$). The relevant materials are summarized in Table 1, which also contains further

examples that exhibit rapid phase-change behavior but are currently not used due to slightly inferior properties. Interestingly, the combinations of elements used for efficient PCMs are rather similar to those employed in thermoelectrics with high figures of merit. This fact is reflected in several basic properties. For both applications, semimetals or small-bandgap semiconductors with low thermal conductivity are required. For a few examples, such as AgSbTe_2 , $\text{Ge}_2\text{Sb}_2\text{Te}_5$ or GeTe_4 , more or less stable modifications have been shown to possess interesting thermoelectric properties,^[3,25] whereas their metastable modifications are well known PCMs. The striking similarities between both classes of materials rise the question if metastable modifications of PCMs are intriguing precursors for efficient thermoelectrics. Whereas the formation of thermodynamically stable modifications is a drawback concerning PCM applications, the partial equilibration by exsolution or short-range vacancy ordering might be associated with the formation of nanostructures in bulk material. Such processes may yield interesting thermoelectrics, however, not much is known about the thermoelectric properties of PCMs and materials obtained from such ‘precursors’ by approaching stable states.

4.2.2 Structure of metastable GST bulk materials with different GeTe content and their thermoelectric properties

4.2.2.1 Structural aspects

Concerning the investigation of thermoelectric properties, it is a drawback that most metastable phases of PCMs are only accessible as thin films prepared by sputtering techniques. Therefore, it is desirable to find compounds whose metastable modifications are accessible as bulk material. Most GST materials with metastable, slightly distorted rocksalt-type average structures correspond to compositions that lie on the pseudobinary line $(\text{GeTe})_n(\text{Sb}_2\text{Te}_3)_m$, i.e. all elements exhibit normal valence states. Rewriting the formula so that it reflects the cation and anion positions of the rocksalt-type shows that the concentration of vacancies decreases with decreasing Sb content: $(\text{Ge}_{n/(3m+n)}\text{Sb}_{2m/(3m+n)}\square_{m/(3m+n)})\text{Te}$, whereas the cation to anion ratio converges to 1 when approaching pure GeTe as shown in Fig. 1 for $m = 1$.

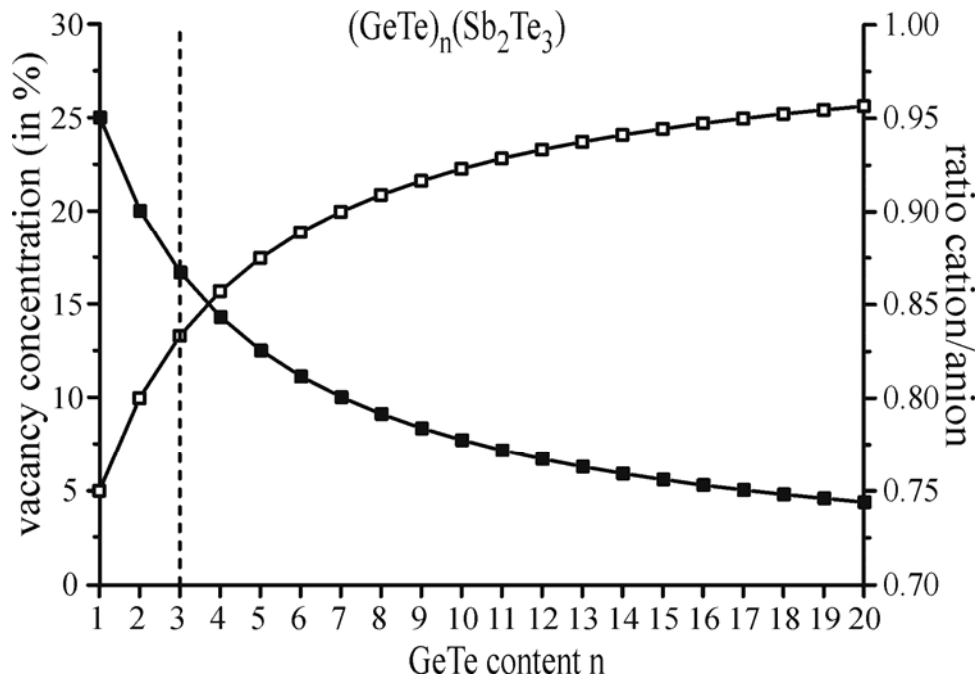


Figure 1. Concentration of vacancies in metastable rocksalt-type structures with compositions $(\text{GeTe})_n\text{Sb}_2\text{Te}_3$ (solid squares) and anion/cation ratio (empty squares) depending on the GeTe content n in the range $n = 1 - 20$. For $n \geq 3$ (broken line), there are stable cubic high-temperature modifications.

The vacancy concentration has an impact on the existence and stability of different atomic as well as nanostructures. The spacing between van der Waals gaps that can be viewed as 2D extended cation defect planes in the stable modifications increases with increasing GeTe content; the overall stacking sequence (Ramsdell symbol) depends on n and m .^[69,70] On the other hand, the average structure of metastable crystalline GeTe-rich PCM phases produced by magnetron sputtering corresponds to the rocksalt type for $n \leq 6$, whereas phases with $n \geq 8$ exhibit a rhombohedrally distorted rocksalt-type resembling the structure of GeTe.^[57] Similar to GeTe, these phases have a cubic rocksalt-type modification at high temperatures. If this high-temperature phase is rapidly quenched to room temperature, the transition to the stable layered phase is hindered due to the multiple twinning associated with a cubic to rhombohedral phase transition. Stresses between the nanoscale rhombohedral twin domains impede lattice relaxation and long-range two-dimensional defect ordering.^[71] The metrics remain almost cubic but short-range layer formation takes place. Concerning the use of this partial phase transition to optimize the thermoelectric properties of $(\text{GeTe})_n\text{Sb}_2\text{Te}_3$ compounds, it is interesting to determine the range of n in which a stable cubic high-temperature modification does exist and in which cases it can be quenched to pseudocubic metastable bulk material.

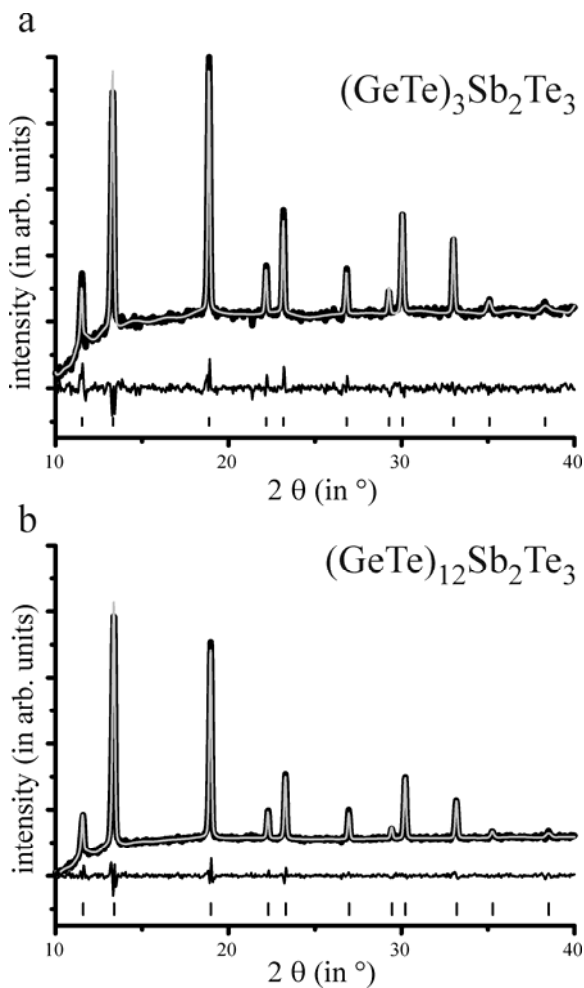


Figure 2. Result of Rietveld fits (gray) of experimental powder diffraction patterns (black) measured at 600 °C (background from the furnace subtracted) of (a) $(\text{GeTe})_3\text{Sb}_2\text{Te}_3$ and (b) $(\text{GeTe})_{12}\text{Sb}_2\text{Te}_3$ with difference curve and reflection markers (bottom).

$\text{Ge}_3\text{Sb}_2\text{Te}_6$, rapid quenching in air or liquid nitrogen does neither yield the stable modification nor a homogenous distorted rocksalt-type structure. Powder diffraction patterns of quenched samples indicate a mixture of a cubic and a layered rhombohedral phase. However, the rhombohedral phase is strongly disordered as indicated by the diffuse broadening of its reflections. Upon heating this material, the cubic phase vanishes at ~ 270 °C, whereas $33R\text{-Ge}_3\text{Sb}_2\text{Te}_6$ forms from the disordered rhombohedral phase at ~ 420 °C as shown in Fig. 3a. The cubic phase forms at ~ 575 °C and transforms back to $33R\text{-Ge}_3\text{Sb}_2\text{Te}_6$ without significant hysteresis.

For the most prominent PCMs GeSb_2Te_4 and $\text{Ge}_2\text{Sb}_2\text{Te}_5$ (i.e., $n < 3$), no phase transition from their stable $21R$ type and $9P$ type structures to cubic high temperature modifications has been reported in the literature. This is in accordance with temperature-dependent X-ray powder diffraction and DTA experiments which we performed in the course of this study. No phase transitions were observed up to the melting points. However, for the stable ambient temperature phase of $33R\text{-Ge}_3\text{Sb}_2\text{Te}_6$ ($n = 3$), which was obtained by annealing a sample at 500 °C, both methods indicate a phase transition to a cubic phase at ~ 575 °C, which melts at ~ 615 °C. The rocksalt-type of the high-temperature phase was confirmed by a Rietveld refinement on a powder diffraction pattern recorded at 600 °C (cf. Fig. 2a), assuming that Te occupies the anion position and Ge, Sb and vacancies share the cation position. Details of the structure refinement are given in Table 2. Whereas slow cooling from the melt yields long-range ordered $33R\text{-Ge}_3\text{Sb}_2\text{Te}_6$,

Table 2. Experimental details and results of the Rietveld refinements for the high-temperature phases of $(\text{GeTe})_n\text{Sb}_2\text{Te}_3$ with $n = 3$ and 12 , respectively.

	$(\text{GeTe})_3\text{Sb}_2\text{Te}_3$	$(\text{GeTe})_{12}\text{Sb}_2\text{Te}_3$
sum formula	$\text{Ge}_3\text{Sb}_2\text{Te}_6$	$\text{Ge}_{12}\text{Sb}_2\text{Te}_{15}$
structure type		NaCl (B1)
crystal system		Cubic
space group		$Fm\bar{3}m$
temperature		600 °C
lattice parameters	$a = 6.1140(6) \text{ \AA}$	$a = 6.0826(5) \text{ \AA}$
cell volume	$228.54(7) \text{ \AA}^3$	$225.04(6) \text{ \AA}^3$
formula weight	1226.87 g/mol	3028.58 g/mol
Z	2/3	4/15
observed reflections		22
refined parameters		62
diffractometer	Stoe STADI P, Ge(111) monochromator	
radiation	Mo $K_{\alpha 1}$ ($\lambda = 0.7093 \text{ \AA}$)	
2 θ range	10 – 50°	
background function	Shifted Chebyshev (48 parameters)	
R_p	0.029	0.026
wR_p	0.044	0.041

$(\text{GeTe})_{12}\text{Sb}_2\text{Te}_3$ exhibits an analogous rocksalt-type high-temperature phase (cf. Table 2) which has also been confirmed by a Rietveld refinement (Fig. 2b) using data measured at 600 °C. In contrast to $(\text{GeTe})_3\text{Sb}_2\text{Te}_3$, rapid quenching of this phase (or directly quenching the melt) yields a homogeneous (stress-stabilized) pseudo-cubic phase whose average structure corresponds to a rhombohedrally distorted rocksalt-type. Slow cooling as well as annealing at 400 °C, however, leads to a relaxed rhombohedral layered structure. Temperature dependent powder diffraction (cf. Fig. 3b) starting from quenched samples indicate a transformation to the relaxed structure at ~ 325 °C and the phase transition to the cubic high-temperature phase at ~ 475 -500 °C, which is significantly lower than for $(\text{GeTe})_3\text{Sb}_2\text{Te}_3$.

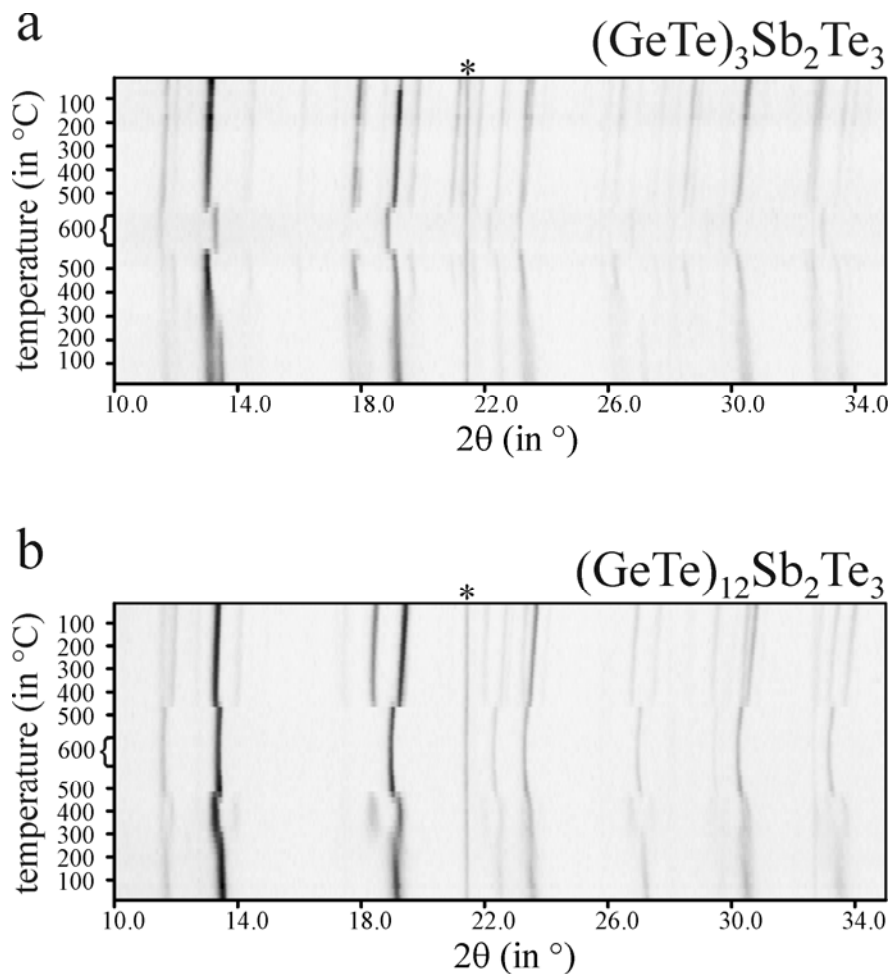


Figure 3. Comparison of in situ temperature dependent powder diffraction patterns (heating and subsequent cooling shown from bottom to top): (a) a sample of $(\text{GeTe})_3\text{Sb}_2\text{Te}_3$ quenched from the melt after heating to $950\text{ }^\circ\text{C}$; (b) a sample of $(\text{GeTe})_{12}\text{Sb}_2\text{Te}_3$ quenched after annealing at $500\text{ }^\circ\text{C}$ for 20 h (samples of $(\text{GeTe})_{12}\text{Sb}_2\text{Te}_3$ quenched from the melt are not significantly different). The asterisk marks a reflection from the furnace. The reflections of the (pseudo-)cubic quenched phases (bottom) can be identified by comparison with those of the cubic high-temperature phase (middle): they are the only ones observed for quenched $(\text{GeTe})_{12}\text{Sb}_2\text{Te}_3$ whereas they correspond to a minor phase for $(\text{GeTe})_3\text{Sb}_2\text{Te}_3$. Note that the reflection broadening for the main phase in quenched $(\text{GeTe})_3\text{Sb}_2\text{Te}_3$ vanishes around $420\text{ }^\circ\text{C}$.

Single crystals of $(\text{GeTe})_{12}\text{Sb}_2\text{Te}_3$ (composition verified by EDX) were grown from starting material with the same composition by chemical transport in the stability region of the high temperature and subsequently quenched to room temperature. Their structure is similar to that of GeTe-rich single crystals isolated from pseudo-cubic bulk material.^[71] The average structure is rhombohedral (GeTe type, $R\bar{3}m$, $a = 4.237(3)\text{ \AA}$, $c = 10.29(1)\text{ \AA}$) with pseudo-cubic metrics due to stresses resulting fourfold twinning. Their diffraction patterns exhibit pronounced diffuse streaks along the pseudocubic $\langle 111 \rangle$ directions as shown in Fig. 4a. Very similar diffraction patterns have been obtained by selected-area electron diffraction (SAED). Figure 5 shows that these correspond to nanostructured crystals as described in detail recently.^[71] The corresponding high-resolution images show that vacancies tend towards short-range order in finite layers that

extend perpendicular to the (pseudo-)cubic $\langle 111 \rangle$ directions. This involves a (local) symmetry reduction, however, the corresponding twin domains are very small.

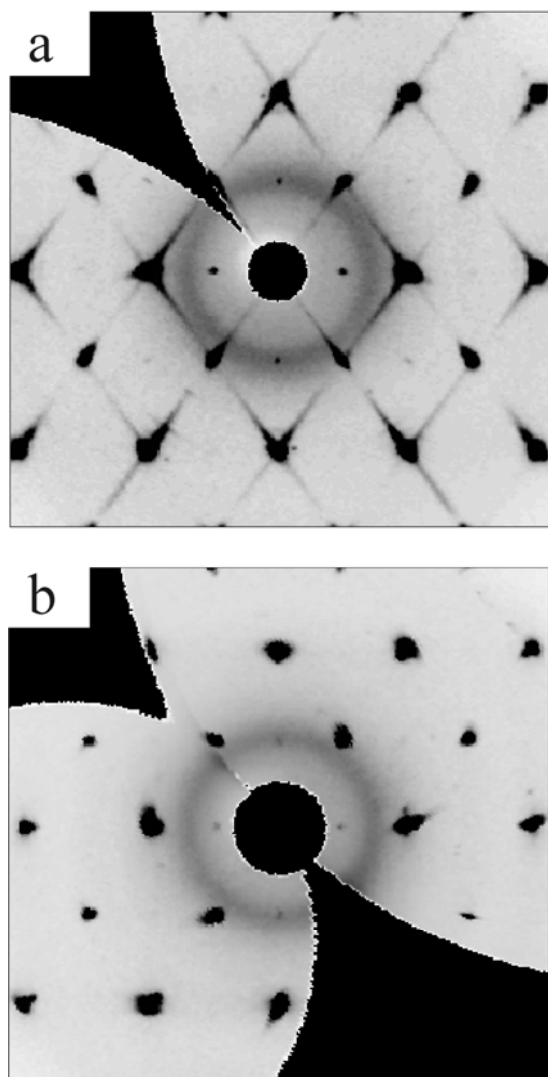


Figure 4. Reciprocal lattice sections hhl (with respect to pseudocubic indexing) reconstructed from area-detector data of a $(\text{GeTe})_{12}\text{Sb}_2\text{Te}_3$ single crystal grown by chemical transport: (a) quenched crystal at room temperature with diffuse streaks along $\langle 111 \rangle$; (b) measurement at 550 °C (cubic high-temperature phase, no diffuse streaks).

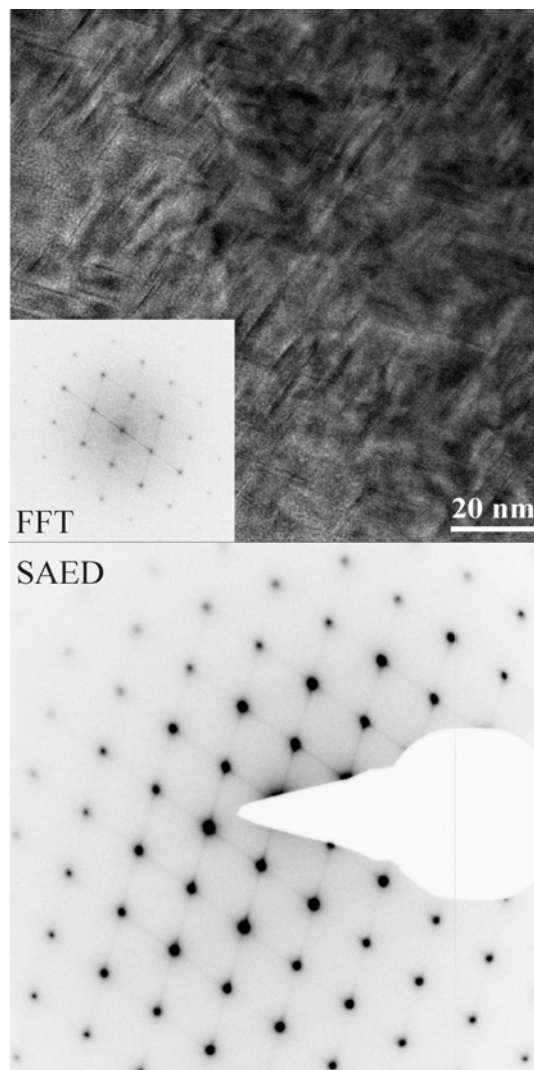


Figure 5. SAED pattern (bottom) and HRTEM image (top, with corresponding Fourier transform) of quenched $(\text{GeTe})_{12}\text{Sb}_2\text{Te}_3$. The zone axis $[110]$ (pseudocubic indexing) corresponds to the reciprocal lattice sections hhl .

However, X-ray diffraction patterns recorded in the stability range of the high temperature phase (550 °C , cf. Fig. 4b) do not show diffuse streaks. This indicates that at this temperature there are no planar defects, i.e., no significant short-range ordering of vacancies. Ge, Sb and vacancies are probably randomly distributed over all cation sites.

4.2.2.2 Thermoelectric properties

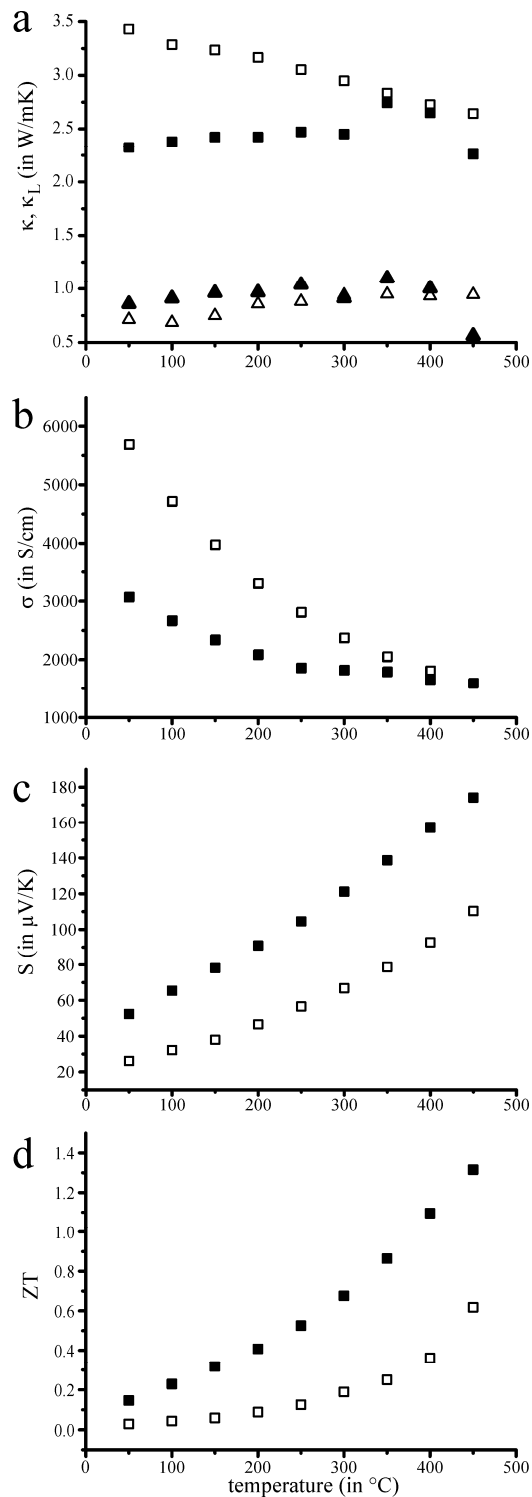


Figure 6. Thermoelectric characteristics for (GeTe)₁₂Sb₂Te₃ (solid squares) and (GeTe)₃Sb₂Te₃ (empty squares): (a) thermal conductivity (additional triangles represent the lattice part κ_L); (b) electrical conductivity; (c) Seebeck coefficient; (d) overall thermoelectric figure of merit.

The nanostructuring by planar defect planes in quenched material as indicated by HRTEM and diffuse scattering can be expected to reduce the thermal conductivity of the materials and increase the thermoelectric efficiency. Very high electrical conductivities were measured for both of the samples (Fig. 6b), with lower values for (GeTe)₁₂Sb₂Te₃, probably due to a more pronounced scattering of charge carriers because of the nanodomain structure. The temperature dependences of the electrical conductivities show metallic behavior, corresponding to highly doped semiconductors.

The Seebeck coefficient for both samples is positive over the complete temperature range under investigation, proving the deficiency electrons (holes) as the major charge carriers (Fig. 6c). At each temperature, the Seebeck coefficient values of (GeTe)₁₂Sb₂Te₃ are almost double compared to (GeTe)₃Sb₂Te₃. This surprising result has been checked in a repeated measurement run to improve the reliability. The reason for this behavior of the Seebeck coefficient is not yet completely understood and will be investigated in more detail in further studies. The overall thermal conductivity matches the picture of the electrical

conductivity with smaller values for $(\text{GeTe})_{12}\text{Sb}_2\text{Te}_3$. Calculating the electrical contribution of the thermal conductivity using the Wiedemann-Franz law for non-degenerate semiconductors allows the identification of the lattice thermal conductivity as displayed in Fig. 6a. No significant difference in κ_L could be found between both samples. Although the domain structure is more pronounced for $(\text{GeTe})_{12}\text{Sb}_2\text{Te}_3$, the higher concentration of vacancies in $(\text{GeTe})_3\text{Sb}_2\text{Te}_3$ probably compensates for the higher degree of long-range order. Therefore, the difference in the overall thermal conductivity is due to the difference in the electrical one, leading to an almost uninfluenced ratio of σ/κ .

Both compounds exhibit rather high overall figures of merit ZT as compared to long-range ordered stable GST phases, where maximum ZT values of about ~ 0.2 have been measured.^[24,25] The high value of $ZT = 1.3$ at 450 °C for $(\text{GeTe})_{12}\text{Sb}_2\text{Te}_3$ is due to the increased Seebeck coefficient, as can be seen from Fig. 6c and d, making this class of materials very promising for thermoelectric applications.

4.2.3 Conclusion

Several conclusions can be drawn from the comparison of GeTe-poor and GeTe-rich $(\text{GeTe})_n\text{Sb}_2\text{Te}_3$ materials. Only materials with $n \geq 3$ exhibit a stable cubic high-temperature modification with randomly distributed cation defects. 2D vacancy ordering is energetically favored, therefore, the transition temperature to the high-temperature phase is higher for compounds with high vacancy concentrations (~ 575 °C for $n = 3$ vs. ~ 500 °C for $n = 12$). If the vacancy concentration is rather high (e.g., $(\text{GeTe})_3\text{Sb}_2\text{Te}_3$), the high-temperature modification cannot be completely quenched to a pseudocubic phase, in contrast to phases with fewer vacancies like $(\text{GeTe})_{12}\text{Sb}_2\text{Te}_3$ which require longer diffusion pathways to reach the stable layered compounds. The pseudocubic phases are kinetically inert as stresses impede metric relaxation and vacancy diffusion.^[71] The partial transition from the randomly disordered high-temperature phase to the layered stable phase can be used to induce nanostructuring which influences both the thermal as well as the electric conductivity. The composition of $(\text{GeTe})_{12}\text{Sb}_2\text{Te}_3$ is close to that of PCMs employed in rewritable BluRay-Discs. As pointed out in the introduction, the requirements for PCMs and thermoelectrics are comparable. If the cubic phases of PCMs are used as precursors for nanostructured thermoelectrics, one can expect efficient materials. We have shown this for quenched $(\text{GeTe})_{12}\text{Sb}_2\text{Te}_3$, which exhibits promising ZT values at high temperatures, and, to a lesser extent, for $(\text{GeTe})_3\text{Sb}_2\text{Te}_3$. We believe that this is

a promising concept for the search of new nanostructures chalcogenide or pnictide thermoelectrics.

4.2.4 Experimental

4.2.4.1 Synthesis

Bulk samples of $(\text{GeTe})_3\text{Sb}_2\text{Te}_3$ (= $\text{Ge}_3\text{Sb}_2\text{Te}_6$) and $(\text{GeTe})_{12}\text{Sb}_2\text{Te}_3$ (= $\text{Ge}_{12}\text{Sb}_2\text{Te}_{15}$) were prepared by melting stoichiometric amounts of the elements Ge (99.999%, Sigma Aldrich), Sb (99.999%, Smart Elements) and Te (99.999%, Alfa Aesar) in sealed silica glass ampoules under Ar atmosphere. After melting the mixtures at 950 °C (ca. 2 h), the ampoules were quenched in water. The nanostructured samples were obtained by reheating to 500 °C for 20 h and quenching in water again. Other samples were annealed at the temperatures given in the text.

Single crystals of $(\text{GeTe})_{12}\text{Sb}_2\text{Te}_3$ were grown by chemical transport using iodine as transport agent. Stoichiometric $(\text{GeTe})_{12}\text{Sb}_2\text{Te}_3$ (ca. 110 mg, see above) was sealed in evacuated silica ampoules of approximate 20 cm in length and 15 mm diameter as starting material. Small amounts (ca. 10 mg) of SbI_3 were added to generate I_2 by decomposition at elevated temperatures (a similar procedure has been used for GeSb_4Te_7 [72]). The octahedral single crystals grew in a temperature gradient from 600 to 550 °C (i.e., in the stability range of the high-temperature phase) within 15–20 h and were subsequently quenched to room temperature by removing the ampoule from the furnace.

Ingots for the measurement of thermoelectric properties were prepared by melting stoichiometric mixtures of the elements under inert atmosphere in ampoules with flat base which allow to solidify the melts into disc-shaped ingots with diameter of approximately 15 mm and thickness of 3–6 mm. After melting at 950 °C and quenching, these ingots were annealed at 500 °C for 20 h and quenched to room temperature in air. For thermoelectric measurements, they were polished to flat plates. Powder diffraction patterns of these materials do not differ significantly from those of the corresponding samples used for the other investigations.

4.2.4.2 Scanning electron microscopy and chemical analysis

Energy dispersive X-ray spectroscopy was done with a JSM-6500F (Jeol, USA) scanning electron microscope (SEM) equipped with an energy-dispersive X-ray (EDX) detector (model 7418, Oxford Instruments, Great Britain). The compositions of the bulk samples were confirmed by averaging three point analyses on crystallites isolated from bulk material. The resulting atom

ratios Ge : Sb : Te are 29 : 18 : 53 for $(\text{GeTe})_3\text{Sb}_2\text{Te}_3$ (calculated: 27.3 : 18.2 : 54.6) and 48 : 5 : 47 for $(\text{GeTe})_{12}\text{Sb}_2\text{Te}_3$ (calculated: 41.4 : 6.8 : 51.7), the deviations are within the usual error limits for samples with rough surfaces. The composition of single crystals $(\text{GeTe})_{12}\text{Sb}_2\text{Te}_3$ grown by transport reactions was determined as Ge : Sb : Te = 43 : 7 : 50 by analyzing flat crystal faces. No iodine impurities were detected.

4.2.4.3 X-ray diffraction

X-ray powder patterns were recorded on a Huber G670 Guinier camera equipped with a fixed imaging plate and integrated read-out system using $\text{Cu-K}_{\alpha 1}$ radiation (Ge monochromator, $\lambda = 1.54051 \text{ \AA}$). Specimens were prepared by fixing powdered parts of the samples on Mylar foils using silicone grease. Temperature-dependent powder patterns were recorded using a STOE Stadi P powder diffractometer with a linear position-sensitive detector (PSD) using $\text{Mo-K}_{\alpha 1}$ radiation (Ge monochromator, $\lambda = 0.71093 \text{ \AA}$) equipped with a graphite furnace. The powdered samples were filled into silica glass capillaries with 0.3 mm diameter which were sealed with silicone grease under argon atmosphere. During the measurements, the samples were heated up to 600 °C (5 °C/min), where several measurements were carried out (at least 90 min altogether) and then cooled to room temperature with a rate of 5 °C/min. Powder patterns were evaluated using WIN^{XPOW}.^[73] Rietveld pattern fitting was carried out using the program TOPAS.^[74]

Single crystals obtained from chemical transport reactions were sealed in silica glass capillaries under argon atmosphere and checked for quality by Laue photographs on a Buerger precession camera. Intensity data were collected on a Stoe IPDS I diffractometer using Mo-K_{α} radiation (graphite monochromator, $\lambda = 0.71073 \text{ \AA}$). High temperature measurements were performed using a heated gas flow around the crystals (Stoe Heatstream). Reciprocal space sections were reconstructed using the diffractometer software.

4.2.4.4 Transmission electron microscopy

Finely ground samples were dispersed in ethyl alcohol suspension and subsequently dispersed on copper grids coated with holey carbon film. The grids were mounted on a double tilt holder with a maximum tilt angle of 30°. Selected-area electron diffraction (SAED) and high-resolution electron microscopy (HRTEM) were carried out on a FEI Titan 80–300 equipped with a field emission gun operating at 300 kV. The images were recorded using a Gatan UltraScan 1000 (2k x 2k) camera.

4.2.4.5 Thermal analysis

The thermal behavior of the samples was studied up to 700 °C by differential thermal analysis and thermo-gravimetry (DTA-TG) with a Setaram TG-92 instrument. The measurement was conducted under helium at a scanning rate of 10 K · min⁻¹ using alumina crucibles. In this temperature range, the weight loss was not significant.

4.2.4.6 Thermoelectric properties

The temperature dependence of the electrical and thermal conductivity as well as the Seebeck coefficient and the figure of merit were investigated in the range from room temperature up to approx. 500 °C under vacuum using various facilities, both commercial and in-house-built ones. The electrical conductivity was measured by a four-point-probe setup above room temperature using an AC method in order to avoid Peltier influences on the measurement. Seebeck coefficient investigation was performed using a small temperature gradient across the sample while slowly changing the environment temperature. This way Seebeck coefficient values for each mean sample temperature are obtained. The thermal conductivity was calculated from measurements of the thermal diffusivity by a Laser Flash Apparatus (Netzsch LFA 427) and heat capacity determined by Differential Scanning Calorimetry (Netzsch DSC 404).

4.2.5 References

- [1] G. S. Nolas, J. Poon, M. G. Kanatzidis, *MRS Bull.* **2006**, *31*, 199.
- [2] T. M. Tritt, M. A. Subramanian, *MRS Bull.* **2006**, *31*, 188.
- [3] J. R. Sootsman, D. Y. Chung, M. G. Kanatzidis, *Angew. Chem. Int. Ed.* **2009**, *48*, 8616.
- [4] V. A. Shevelkov, *Russ. Chem. Rev.* **2008**, *77*, 1.
- [5] G. J. Snyder, E. S. Toberer, *Nat. Mater.* **2008**, *7*, 105.
- [6] A. C. Bruce, J. K. Matthew, L. H. Joel, H. Mi-Kyung, C. Duck-Young, G. K. Mercuri, *Adv. Funct. Mater.* **2009**, *19*, 1254.
- [7] P. F. P. Poudeu, J. D'Angelo, A. D. Downey, J. L. Short, T. P. Hogan, M. G. Kanatzidis, *Angew. Chem. Int. Ed.* **2006**, *45*, 3835.
- [8] T. Ikeda, V. A. Ravi, L. A. Collins, S. M. Haile, G. J. Snyder, *J. Electron. Mater.* **2007**, *36*, 716.
- [9] R. Venkatasubramanian, E. Siivola, T. Colpitts, B. O'Quinn, *Nature* **2001**, *413*, 597.
- [10] H. Böttner, G. Chen, R. Venkatasubramanian, *MRS Bull.* **2006**, *31*, 211.

-
- [11] T. J. Zhu, F. Yan, X. B. Zhao, S. N. Zhang, Y. Chen, S. H. Yang, *J. Phys.* **2007**, *D40*, 6094.
- [12] J. Sommerlatte, K. Nielsch, H. Böttner, *Phys. J.* **2007**, *6*, 35.
- [13] A. Bulusu, D. G. Walker, *Superlattice Microst.* **2008**, *44*, 36.
- [14] A. Majumdar, *Science* **2004**, *303*, 777.
- [15] M. S. Dresselhaus, G. Chen, M. Y. Tang, R. Yang, H. Lee, D. Wang, Z. Ren, J.-P. Fleurial, P. Gogna, *Adv. Mater.* **2007**, *19*, 1.
- [16] D. L. Medlin, G. J. Snyder, *Curr. Opin. Colloid Interface Sci.* **2009**, *14*, 226.
- [17] M. G. Kanatzidis, *Chem. Mater.* **2010**, *22*, 648.
- [18] Y. C. Lan, A. J. Minnich, G. Chen, Z. F. Ren, *Adv. Funct. Mater.* **2010**, *20*, 357.
- [19] T. J. Zhu, F. Yan, X. B. Zhao, S. N. Zhang, Y. Chen, S. H. Yang, *J. Phys.* **2007**, *D40*, 6094.
- [20] S. K. Hsiung, R. Wang, *J. Appl. Phys.* **1978**, *49*, 280.
- [21] J. W. G. Bos, H. W. Zandbergen, M.-H. Lee, N. P. Ong, R. J. Cava, *Phys. Rev.* **2007**, *B75*, 195203.
- [22] P. F. P. Poudeu, M. G. Kanatzidis, *Chem. Commun.* **2005**, *21*, 2672.
- [23] T. Shima, T. Kikukawa, T. Nakano, J. Tominaga, *Jpn. J. Appl. Phys.* **2006**, *45*, 136.
- [24] P. P. Konstantinov, L. E. Shelimova, E. S. Avilov, M. A. Kretova, V. S. Zemskov, *Inorg. Mater.* **2001**, *37*, 662.
- [25] F. Yan, T. J. Zhu, X. B. Zhao, S. R. Dong, *Appl. Phys. A* **2007**, *88*, 425.
- [26] J. L. Cui, X. L. Liu, W. Yang, D. Y. Chen, H. Fu, P. Z. Ying, *J. Appl. Phys.* **2009**, *105*, 063703
- [27] J. L. Cui, H. Fu, X. L. Liu, D. Y. Chen, W. Yang, *Curr. Appl. Phys.* **2009**, *9*, 1170.
- [28] R. Detemple, D. Wamwangi, M. Wuttig, G. Bihlmayer, *Appl. Phys. Lett.* **2003**, *83*, 2572.
- [29] Y. Maeda, H. Andoh, I. Ikuta, H. Minemura, *J. Appl. Phys.* **1988**, *64*, 1715.
- [30] L. E. Shelimova, O. G. Karpinskii, P. P. Konstantinov, E. S. Avilov, M. A. Kretova, V. S. Zemskov, *Inorg. Mater.* **2004**, *40*, 451.
- [31] M. Wuttig, *Nat. Mater.* **2005**, *4*, 265.
- [32] D. Lencer, M. Salinga, B. Grabowski, T. Hickel, J. Neugebauer, M. Wuttig, *Nat. Mater.* **2008**, *7*, 972.
- [33] M. Wuttig, C. Steimer, *Appl. Phys. A* **2007**, *87*, 411.
- [34] M. Wuttig, N. Yamada, *Nat. Mater.* **2007**, *6*, 824.
- [35] S. Raoux, R. M. Shelby, J. Jordan-Sweet, B. Munoz, M. Salinga, Y.-C. Chen, Y.-H. Shih, E.-K. Lai, M.-H. Lee, *Microelectron. Eng.* **2008**, *85*, 2330.

- [36] S. Raoux, *Annu. Rev. Mater. Res.* **2009**, *39*, 9.1.
- [37] S. Raoux, W. Wojciech, D. Ielmini, *Chem. Rev.* **2009**, *110*, 240.
- [38] M. Frumar, B. Frumarova, T. Wagner, M. Hrdlicka, *J. Mater. Sci: Mater. Electron* **2007**, *18*, 169.
- [39] T. Matsunaga, N. Yamada, *Jpn. J. Appl. Phys.* **2004**, *43*, 4704.
- [40] T. Matsunaga, N. Yamada, *Jpn. J. Appl. Phys.* **2002**, *41*, 1674.
- [41] P. J v ri, I Kaban, J. Steiner, B. Beuneu, A. Sch ps, A. Webb, *J. Phys.: Condens. Matter* **2007**, *19*, 335212.
- [42] S. Caravati, M. Bernasconi, T. D. Kuhne, M. Krack, M. Parrinello, *Appl. Phys. Lett.* **2007**, *91*, 171906.
- [43] K. Kohary, V. M. Burlakov, D. G. Pettifor, *Phys. Rev. B* **2005**, *71*, 235309.
- [44] F. Sava, A. L rinczi, J. Ovonic, *Res.* **2006**, *2*, 4.
- [45] S. Hosokawa, T. Ozaki, K. Hayashi, N. Happo, M. Fujiwara, K. Horii, P. Fons, A. V. Kolobov, J. Tominaga, *Appl. Phys. Lett.* **2007**, *90*, 131913.
- [46] J. Akola, R. O. Jones, S. Kohara, S. Kimura, K. Kobayashi, M. Takata, T. Matsunaga, R. Kojima, N. Yamada, *Phys. Rev. B* **2009**, *80*, 020201.
- [47] J. Akola, R. O. Jones, *Phys. Rev. B* **2007**, *76*, 235201.
- [48] J. Akola, R. O. Jones, *Phys. Rev. B* **2009**, *79*, 134118.
- [49] A. V. Kolobov, P. Fons, A. I. Frenkel, A. L. Ankudinov, J. Tominaga, T. Uruga, *Nat. Mater.* **2004**, *3*, 703.
- [50] A. V. Kolobov, P. Fons, J. Tominaga, A. I. Frenkel, A. L. Ankudinov, T. Uruga, J. Ovonic, *Res.* **2005**, *1*, 21.
- [51] V. A. Kolobov, P. Fons, J. Tominaga, T. Uruga, *J. Non-Cryst. Solids* **2006**, *352*, 1612.
- [52] E. T. Kim, J. Y. Lee, Y. T. Kim, *Appl. Phys. Lett.* **2007**, *91*, 101909.
- [53] W. Wenig, M. Wuttig, *Materials Today* **2008**, *11*, 20.
- [54] T. Matsunaga, N. Yamada, *Phys. Rev. B* **2004**, *69*, 104111.
- [55] T. Matsunaga, N. Yamada, Y. Kubota, *Acta Crystallogr. Sect. B* **2004**, *60*, 685.
- [56] T. Matsunaga, R. Kojima, N. Yamada, K. Kifune, Y. Kubota, Y. Tabata, M. Takata, *Inorg. Chem.* **2006**, *45*, 2235.
- [57] T. Matsunaga, H. Morita, R. Kojima, N. Yamada, K. Kifune, Y. Kubota, Y. Tabata, J.-J. Kim, M. Kobata, E. Ikenaga, K. Kobayashi, *J. Appl. Phys.* **2008**, *103*, 093511.
- [58] W. Wenig, A. Pamungkas, R. Detemple, C. Steimer, S. Blugel, M. Wuttig, *Nat. Mater.* **2006**, *5*, 56.

- [59] M. Wuttig, D. Lüsebrink, D. Wamwangi, W. Wenig, M. Gilleßen, R. Dronskowski, *Nat. Mater.* **2007**, *6*, 122.
- [60] Z. Sun, J. Zhou, R. Ahuja, *Phys. Rev. Lett.* **2006**, *96*, 055507.
- [61] Z. Sun, S. Kyrsta, D. Music, R. Ahuja, J. M. Schneider, *Solid State Commun.* **2007**, *143*, 240.
- [62] S. Shamoto, N. Yamada, T. Matsunaga, T. Proffen, J. W. Richardson, J.-H. Chung, T. Egami, *Appl. Phys. Lett.* **2005**, *86*, 081904.
- [63] S. I. Shamoto, K. Kodama, S. Iikubo, T. U. Taguchi, N. Yamada, T. Proffen, *Jpn. J. Appl. Phys.* **2006**, *45*, 8789.
- [64] J.-H. Eom, Y.-G. Yoon, C. Park, H. Lee, J. Im, D.-S. Suh, J.-S. Noh, Y. Khang, J. Ihm, *Phys. Rev. B* **2006**, *73*, 214202.
- [65] O. G. Karpinskii, L. E. Shelimova, M. A. Kretova, V. S. Zemskov, *Inorg. Mater.* **2000**, *36*, 1108.
- [66] O. G. Karpinsky, L. E. Shelimova, M. A. Kretova, J.-P. Fleurial, *J. Alloys Compd.* **1998**, *268*, 112.
- [67] O. G. Karpinsky, L. E. Shelimova, M. A. Kretova, J.-P. Fleurial, *J. Alloys Compd.* **1998**, *265*, 170.
- [68] L. E. Shelimova, O. G. Karpinsky, P. P. Konstantinov, M. A. Kretova, E. S. Avilov, V. S. Zemskov, *Inorg. Mater.* **2001**, *37*, 342.
- [69] L. E. Shelimova, O. G. Karpinsky, M. A. Kretova, V. I. Kosyakov, V. A. Shestakov, V. S. Zemskov, F. A. Kuznetsov, *Inorg. Mater.* **2000**, *36*, 768.
- [70] M. N. Schneider, O. Oeckler, *Z. Anorg. Allg. Chem.* **2008**, *634*, 2557.
- [71] M. N. Schneider, P. Urban, A. Leineweber, M. Doeblinger, O. Oeckler, *Phys. Rev. B* **2010**, *81*, 184102.
- [72] M. Frumar, L. Tichy, M. Matyas, J. Zelizko, *Phys. Stat. Sol.* **1974**, *22*, 535.
- [73] *WINXPOW, Version 2.12*, Stoe & Cie. GmbH, Darmstadt, **2005**.
- [74] A. Coelho, *TOPAS-Academic, V. 4.1*; Coelho Software, Brisbane, **2007**.

4.3 Nanostructures in metastable GeBi_2Te_4 obtained by high-pressure synthesis and rapid quenching and their influence on physical properties

Thorsten Schröder, Matthias N. Schneider, Tobias Rosenthal, Andreas Eisele, Christian Gold, Ernst-Wilhelm Scheidt, Wolfgang Scherer, Rico Berthold, Oliver Oeckler

Physical Review B **2011**, *84*, 184104.

Abstract

We report on a new metastable modification of GeBi_2Te_4 obtained by high-pressure high-temperature synthesis. It crystallizes in the CuPt type; different nanostructures are induced by various temperature programs under a constant pressure of 12 GPa. The particle size changes from <10 nm in quenched samples to >100 nm for melts slowly crystallized under high pressure. The smaller the domains the more random is their orientation distribution. The nanostructure has a high impact on the temperature characteristics of the electrical resistivity. The domain size determines whether the compounds are metallic or semiconducting. In the latter case the semiconducting behavior is due to the scattering of electrons at domain and/or grain boundaries. Intermediate behavior that starts off metal-like and changes to semiconducting at higher temperature has been observed for samples thermally quenched from the solid state at high pressure. Resistivity measurements of the high-pressure samples involving multiple heating and cooling sequences lead to a significant reduction of internal stress and finally approach a state which is characterized by $\rho(T)$ hysteresis. Our results show the large influence of the domain size and the grain boundary concentration on the properties of the materials and reveal how properties like the thermoelectric figure of merit (ZT) depend on the preparation technique. By the microstructuring of stable GeBi_2Te_4 , the ZT value drops by one order of magnitude.

Copyright: © 2011 American Physical Society

4.3.1 Introduction

Tellurides play important roles in various fields of application such as phase-change materials (PCMs) for data storage as well as a broad range of high-performance thermoelectrics. Interestingly, most of the relevant tellurides are not thermodynamically stable. Metastability is, for example, a crucial property of PCMs used in optical as well as electrical rewritable storage devices (DVD-RW, BD-RE, PCRAM, etc.).^[1,2] The recording and erasing process involves the fast and reversible switching between amorphous and metastable disordered crystalline phases with simple average structures which exhibit the A7 (gray arsenic) or the rocksalt structure type. Metastability and disorder are essential to reach extremely short switching times for writing or erasing large amounts of data, as no long-distance diffusion is required and both structural states are inert enough to guarantee reliable long-time data storage. The required material properties of PCMs are, at least in part, similar to those that are crucial in the field of thermoelectrics.^[3] However, it remains unclear if the thermoelectric effect itself is important in electrically switchable PCMs.

The long-time goal of most research activities on thermoelectrics, which interconvert thermal and electrical energy, is the generation of electrical energy from waste heat. The efficiency of thermoelectrics depends on the dimensionless figure of merit $ZT = S^2T/\rho\kappa$ (with the Seebeck coefficient S , the electrical resistivity ρ , and the thermal conductivity κ). As all these quantities depend on the charge-carrier concentration, they cannot be optimized independently. The electrical resistivity and the electronic part of the thermal conductivity are inversely proportional to each other according to the Wiedemann-Franz law. Therefore, the only way to decrease the overall thermal conductivity without significantly increasing the electrical resistivity is to influence the phononic part of the thermal conductivity. This can be achieved, for instance, by introducing nanostructures. Phase transitions associated with the formation of long-periodically ordered structures, twinning, or (partial) decomposition may yield nanostructures that scatter phonons rather effectively and therefore enhance the thermoelectric properties. Nanostructures are, of course, metastable states, especially if they are obtained by partial stabilization of highly disordered metastable phases. This can be accomplished by various quenching techniques. However, care must be taken not to completely reach the fully ordered equilibrium state.^[4–11]

In addition to the common characteristic feature that the compounds are metastable, many efficient thermoelectrics [e.g., $\text{AgPb}_m\text{SbTe}_{2+m}$ (LAST),^[12] $\text{NaPb}_m\text{SbTe}_{2+m}$ (SALT),^[13] $(\text{AgSbTe}_2)_{1-m}(\text{GeTe})_m$ (TAGS),^[14] or Bi_2Te_3] contain more or less the same chemical elements in similar ratios as well-known PCMs [e.g., $(\text{GeTe})_n(\text{Sb}_2\text{Te}_3)$ (GST),^[15–17] $\text{Ag}_{3.4}\text{In}_{3.7}\text{Sb}_{76.4}\text{Te}_{16.5}$

(AIST)].^[18] Inspired by GST-based PCMs in PC-RAM and BD-RE devices, the investigation of the thermoelectric properties of $(\text{GeTe})_{12}\text{Sb}_2\text{Te}_3$ yielded ZT values of ~ 1.3 at 450°C .^[3] These compounds exhibit cubic high-temperature phases with Ge, Sb, and vacancies disordered on the cation sites of the rocksalt-type structure, which can be quenched as pseudocubic bulk material. The high ZT value can be related to short-range vacancy ordering effects. Similar metastable rocksalt-type phases of GBT (Ge/Bi/Te) materials have been reported for thin-film samples obtained by sputtering and exhibit rapid phase-change behavior that can be induced by laser irradiation.¹⁹ However, in this case the rocksalt-type phase does not exist as a stable high-temperature phase (it is in fact unstable at any temperature). Therefore, quenching experiments using bulk samples do not yield cubic or pseudocubic phases, but rather the stable rhombohedral layered modifications, which are similar to stable GST phases. Therefore, it is essential to apply methods beyond conventional solid-state synthesis to obtain metastable GBT compounds as bulk materials. Fast quenching methods such as melt-spinning as well as high-pressure experiments seem promising in order to obtain different nanostructures that can be correlated with the corresponding thermoelectric properties.

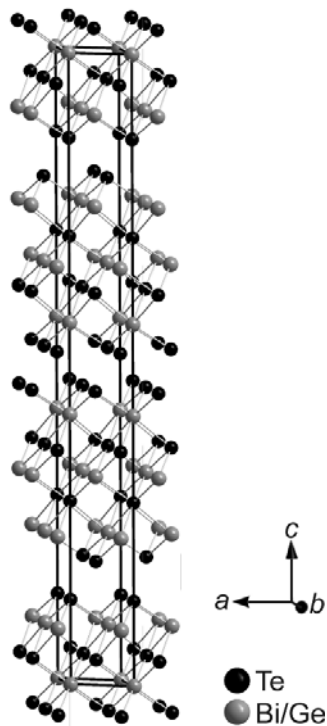


Figure 1. Crystal structure of stable 21R-type GeBi_2Te_4 (the small percentage of anti-site disorder is neglected).

In this report we focus on GeBi_2Te_4 , which is one of the peritectic compounds that can be found on the pseudobinary line $\text{GeTe}-\text{Bi}_2\text{Te}_3$ in the Ge/Bi/Te phase diagram. The stable modification of GeBi_2Te_4 crystallizes in a rhombohedral long-range ordered 21R-type structure (space group $R\bar{3}m$, no. 166) with 21 hexagonal atom layers in each unit cell (Fig. 1).^[20] These 21 layers form three blocks of seven layers each, which can be described as a distorted cutout of the rocksalt-structure type due to the octahedral coordination of the cations. Adjacent blocks are linked via van der Waals gaps by tellurium · · · tellurium interactions. In contrast to this stable phase, the metastable cubic modification found for thin-film sample experiments corresponds to a rocksalt-type structure $(\text{Ge}_{0.25}\text{Bi}_{0.5}\square_{0.25})\text{Te}$ displaying cation defects.^[19,21] A phase transition toward the stable state therefore involves a vacancy rearrangement. Layer-like defect ordering and subsequent relaxation leads to the formation of the

van der Waals gaps. Intermediate structures between the cubic and the 21R-type phases could be

observed for $\text{Ge}_2\text{Bi}_2\text{Te}_5$ in annealing experiments on thin films.^[22] They involve a shear deformation which may also be important for the phase-change mechanism.

4.3.2 Experimental details

4.3.2.1 Synthesis

Bulk samples with the nominal composition GeBi_2Te_4 were prepared by heating a stoichiometric mixture (e.g., 0.3 g) of the pure elements (germanium 99.999%, Sigma Aldrich; bismuth 99.999%, Smart Elements; tellurium 99.999%, Alfa Aesar) in sealed silica glass ampoules to 950 °C under argon atmosphere. The resulting melts were quenched to room temperature in water and used as starting material for the following syntheses. After quenching, some ingots were annealed at 500 °C to obtain the stable 21R-type modification.

High-pressure experiments were performed using the multianvil technique with a hydraulic press (Voggenreiter, Mainleus, Germany).^[23–26] Quenched GeBi_2Te_4 was powdered, loaded into a cylindrical capsule of hexagonal boron nitride (Henze, Kempten, Germany) and sealed with a BN cap. The capsule was centered within two nested graphite tubes, which acted as an electrical resistance furnace. The remaining volume at both ends of the sample capsule was filled with two cylindrical pieces of magnesium oxide. The arrangement was placed into a zirconia tube and then transferred into a pierced Cr_2O_3 -doped MgO octahedron (edge length 14 mm, Ceramic Substrates & Components, Isle of Wight, Great Britain). Eight truncated tungsten carbide cubes (truncation edge length 8 mm) separated by pyrophyllite gaskets served as anvils for the compression of the octahedron. Two plates of molybdenum provided electrical contact for the graphite tubes. The assembly was compressed up to a constant pressure of 12 GPa in 350 minutes. At this pressure, three temperature programs were applied (see Table 1). Samples were prepared by heating to 850 °C and subsequently (1) quenching the melt by turning off the furnace (melt-quenched samples), or (2) cooling the sample to 200 °C within 5 hours and then turning off the furnace (solid-quenched samples). A third type of high-pressure samples was prepared by (3) cooling the samples to room temperature within 4 hours (slowly cooled samples). After the temperature program the pressure was reduced to ambient pressure within 1050 minutes.

Table 1. High-pressure sample overview.

denotation	pressure	temperature program
melt-quenched	12 GPa	quenched from melt (850 °C)
solid-quenched	12 GPa	quenched from 200 °C
slowly cooled	12 GPa	slowly cooled from 850 °C to RT

A melt-spinning apparatus (model SC, Bühler, Germany) was used in order to obtain high quenching rates (up to approximately 10^9 K/s) at ambient pressure. Powdered GeBi_2Te_4 was loaded into a tantalum blast pipe, which was placed over a rotating copper wheel (60 Hz). Both the tantalum blast pipe and the copper wheel were placed in a recipient, which was evacuated and/or filled with argon. The powder was melted using a water-cooled high-frequency coil (high frequency generator Himmel HIT 12, Himmelwerk Hoch- & Mittelfrequenzanlagen GmbH, Germany) and then sprayed onto the rotating copper wheel under an argon pressure of 500 mbar by applying an excess argon pressure connected to the tantalum blast pipe. The melt hits the copper wheel and solidifies immediately. Flat particles with the size of about $5 \times 2 \times 0.2 \text{ mm}^3$ were hurled away from the wheel onto a collecting tray.

4.3.2.2 Energy dispersive x-ray analysis

Energy dispersive X-ray (EDX) spectra were recorded using a JSM-6500F (Jeol, USA) scanning electronmicroscope with EDX detector (model 7418, Oxford Instruments, Great Britain). For each particle or fragment of the ingot, respectively, the results of five point analyses were averaged and the error limits were estimated from their variance.

4.3.2.3 X-ray diffraction

X-ray powder patterns were recorded with a Huber G670 Guinier camera equipped with a fixed imaging plate and integrated read-out system using $\text{Cu-}K_{\alpha 1}$ radiation (Ge monochromator, $\lambda = 1.54059 \text{ \AA}$). Specimens were prepared by crushing representative parts of the samples and fixing the powder on Mylar foils using silicone grease. Low-temperature measurements between 10 and 300 K were obtained using a cryo cooling system (Cooling head, CTI-Cyrogenics, model 22 CP). The phase homogeneity was assessed and lattice parameters were determined by pattern fitting (Rietveld method) using the program TOPAS.^[27] Temperature-dependent powder-diffraction experiments at temperatures above 300 K were performed with a STOE Stadi P powder diffractometer equipped with an imaging plate detector system using $\text{Mo-}K_{\alpha 1}$ radiation (Ge monochromator, $\lambda = 0.71093 \text{ \AA}$) in Debye–Scherrer geometry. Powdered specimens were filled into silica glass capillaries with 0.3mm diameter and sealed with silicone grease under argon atmosphere. During the measurement, the samples were heated up to 600 °C in a graphite furnace and then cooled to room temperature with a heating/cooling rate of 5 K/min.

4.3.2.4 Transmission electron microscopy

For transmission electron microscopy studies, finely ground samples were dispersed in ethanol and distributed on copper grids coated with a holey carbon film (S166-2, Plano GmbH, Germany). The grids were fixed on a double tilt holder. Selected area electron diffraction (SAED) and high resolution transmission electron microscopy (HRTEM) were done on a JEM2011 (Jeol Ltd., Japan) with a tungsten thermal emitter and an acceleration voltage of 200 kV equipped with a TVIPS CCD (model 114, resolution: $1\text{k} \times 1\text{k}$). Further HRTEM, SAED, and EDX measurements were done on a Titan 80-300 (FEI, USA) with a field-emission gun operated at 300 kV equipped with a TEM TOPS 30 EDX spectrometer (EDAX, Germany). Images were recorded using an UltraScan 1000 camera (Gatan, USA, resolution $2\text{k} \times 2\text{k}$). HRTEM and SAED data was evaluated using the Digital Micrograph and EMS software,^[28,29] for STEM and EDX data the program ES Vision was used.^[30]

4.3.2.5 Electrical and thermal transport measurements

The temperature dependent resistivity $\rho(T)$ of various stable and metastable GeBi_2Te_4 modifications were measured by a standard four-probe dc method employing a constant current of 5 mA and using a physical property measurement system (PPMS, Quantum Design). The data were collected in the temperature range of 2–300 K by cooling and heating sequences in which the temperature changed at a rate of 0.5K/min. The uncertainty of the absolute electrical resistivity values (approximately 20–30%) has been estimated by taking into account the errors in specifying the sample dimensions.

The thermoelectric power $S(T)$ and the thermal conductivity $\kappa(T)$ of samples crystallizing in the stable GeBi_2Te_4 modification were measured simultaneously using the commercial thermal transport option of the PPMS. This is based on a relaxation method employing one heater and two thermometers to determine the induced thermal voltage and the temperature gradient along the sample in a temperature range between 4 and 300 K. These measurements were carried out using bar-shaped samples with typical dimensions of about $1 \times 2 \times 5 \text{ mm}^3$ during a heating process at a rate of 0.5 K/min. The total accuracy of $S(T)$ and $\kappa(T)$ is about 5%.

4.3.3 Results and discussion

4.3.3.1 Structure of quenched HP-GeBi₂Te₄

The powder diffraction pattern of a sample obtained by quenching the melt of GeBi₂Te₄ under a constant pressure of 12 GPa (i.e., switching off the furnace) could be indexed assuming a rhombohedral unit cell with $a = 4.3508(3)$ Å and $c = 11.234(2)$ Å. Starting from an α -GeTe-type structure model (space group $R3m$), which allows many degrees of freedom, Ge, Bi, and vacancies were placed on the cation position (occupancy factors 0.25 for Ge and 0.5 for Bi) and Te (fully occupied) on the anion position. The occupancy factors were derived from the nominal composition, which is confirmed by the EDX results (for all GeBi₂Te₄ samples between Ge_{0.9(1)}Bi_{2.2(1)}Te₄ and Ge_{1.1(1)}Bi_{2.0(1)}Te₄). The Rietveld refinement (shown in Fig. 2) turned out that there is no evidence for noncentrosymmetry of the average structure, as in contrast to α -GeTe, all cation-anion distances are equal within two standard deviations. Therefore, the average structure seems not to be layered, and the space group can be identified as $R3m$ (no. 166). Details of the Rietveld analysis and the refined atomic parameters are given in Tables 2 and 3, respectively.

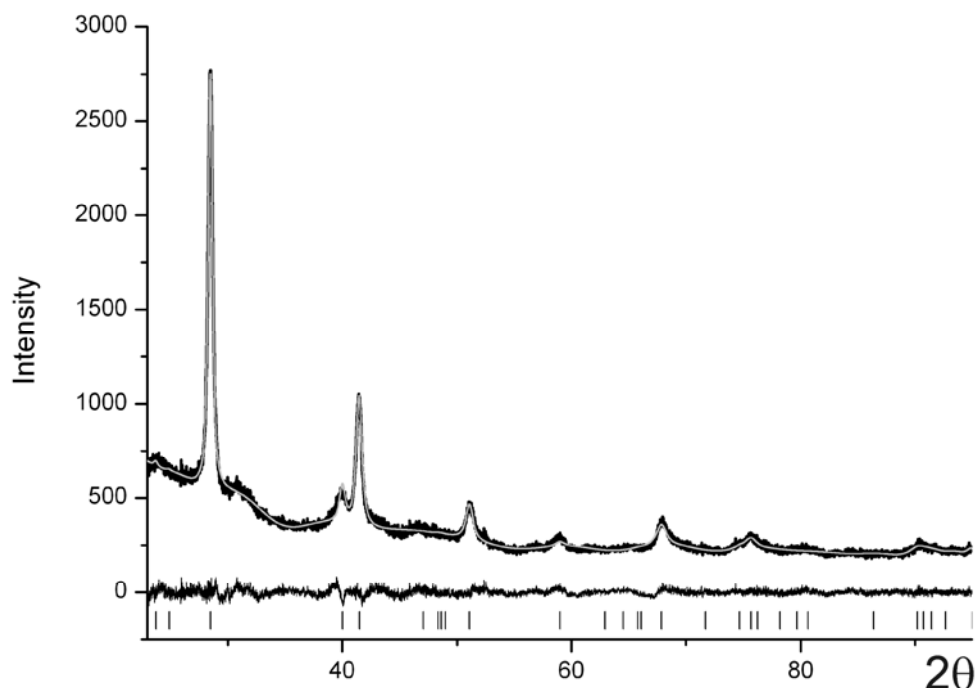


Figure 2. Rietveld refinement of melt-quenched HP-GeBi₂Te₄: experimental powder pattern (black), calculated pattern (gray), and difference plot (black) and tick marks (black, straight lines).

Table 2. Crystal data and Rietveld refinement of melt-quenched GeBi₂Te₄.

sum formula	GeBi ₂ Te ₄
molar mass (in g/mol)	1000.97
lattice parameters (in Å)	$a = 4.3508(3)$ Å; $c = 11.234(2)$
cell volume (in Å ³)	184.16(5)
radiation	Cu-K _{α1} ($\lambda = 1.540596$ Å)
density (in g/cm ³)	6.769(2)
space group	$R\bar{3}m$ (no. 166)
2 theta range	22° < 2 θ < 95°
number of reflections	32
refined parameters	12 structural / 36 background
constraints	2
profile function	fundamental parameter approach
step width (2 θ)	0.005°
R_{wp}, R_p	0.0135; 0.0104

Table 3. Atom positions and displacement parameters of HP-GeBi₂Te₄.

atom	Wyck.	x y z	s.o.f.	U_{eq}	$U_{11} = U_{22} = 2U_{12}$	U_{33}	$U_{13}=U_{23}$
Te	3a	0 0 0	1	0.15(2)	0.017(11)	0.48(7)	0
Bi/Ge	3b	0 0 1/2	Bi 0.5 Ge 0.25	0.18(2)	0.008(11)	0.43(6)	0

The average structure model derived from Bragg reflections corresponds to the CuPt-type structure, a rhombohedrally distorted variant of the rocksalt type, derived from the latter by stretching the unit cell along $\langle 111 \rangle$. In fact the powder pattern contains no significant evidence for different scattering densities on anion and cation positions, as disordered germanium, bismuth, and vacancies lead to an average electron count of 49.5 at the cation position, and tellurium involves 52 electrons on the anion position. Thus, the structure might formally be described assuming the α -Hg type with just one Wyckoff position for all atoms, however, electron-diffraction patterns clearly show the CuPt type's reflections hkl with $h, k, l = 2n + 1$ whose intensity (similar to the rocksalt case) can only be observed in case of different scattering densities for cation and anion sites (see the next section). Of course, a certain degree of antisite disorder cannot be excluded; however, such phenomena have been thoroughly investigated for Ge/Sb/Te phases, where the amount of antisite disorder is either very small or not significant.^[17,31] Although the refinement fits the experimental data, the structure model does not correspond to an ordered compound, and the disorder goes far beyond the cation disorder itself. The “average” structure from Bragg data can only be described with very prolate atomic displacement ellipsoids, as can be seen in Fig. 3; so in fact there is no average structure with, at least in part, “normal” atom positions. These results suggest that a cubic rocksalt-type phase is formed under high pressure but partially relaxes to a layered trigonal structure as soon as the pressure is released. The short-range order in this phase may locally correspond to the structure

of the stable room temperature phase. Obviously, the high vacancy concentration of 25% on the cation sites does not allow a completely random vacancy distribution at ambient conditions.

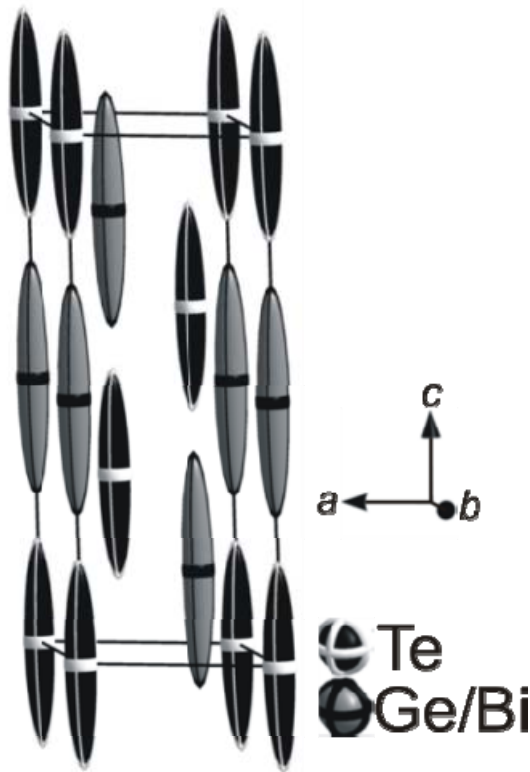


Figure 3. “Average” structure model of metastable HP-GeBi₂Te₄ as determined from Bragg data (displacement ellipsoids for 99% probability).

The powder-diffraction patterns of the slowly cooled and solid-quenched samples, respectively, do not differ significantly from those of samples that were quenched from the melt, although the micro/nanostructures are significantly different (see subsequent discussion). However, Table 4 shows that the lattice parameters of the average structures vary slightly. All trigonal c/a ratios are almost equally far from that of the trigonal setting of a unit cell with cubic metrics (2.45). Figure 4 shows that temperature-dependent powder diffraction experiments and *ex-situ* annealing of high-pressure samples (for 36 hours at 300 °C) prove that the high-pressure phase is metastable at ambient pressure. The reflections of the layered 21R-type structure reappear when the metastable compound is heated over 200 °C.

Table 4. Comparison of the lattice parameters of various high-pressure samples (cf. text).

denotation	a (Å)	c (Å)	c/a	Volume (Å ³)
melt-quenched	4.3502(4)	11.234(2)	2.582	184.05(5)
solid-quenched	4.347(2)	11.184(5)	2.573	183.1(2)
slowly cooled	4.3495(5)	11.043(3)	2.539	180.93(7)

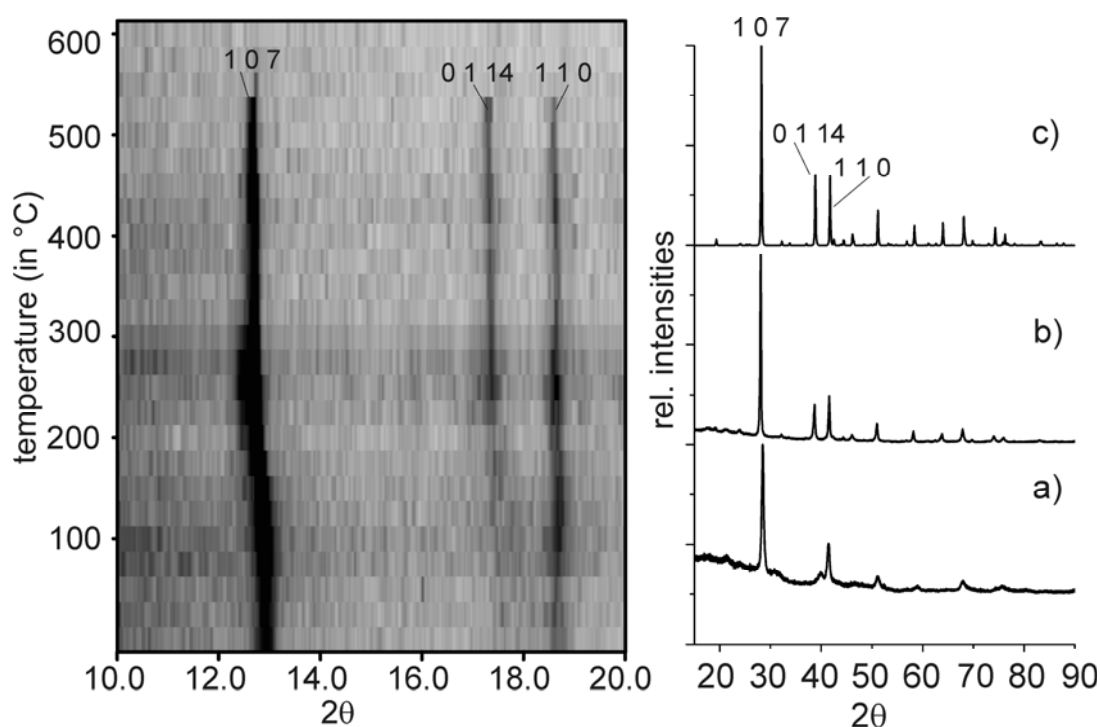


Figure 4. Temperature-dependent PXRD (left, room temperature to 600 °C, Mo- $K_{\alpha 1}$ radiation - intensity from 0 (white) to maximum (black)) of the melt-quenched HP phase; PXRD (Cu- $K_{\alpha 1}$ radiation) of the melt-quenched sample (right): a) as removed from the press, b) after annealing for 36 h at 300 °C, c) calculated powder pattern of 21R-type GeBi_2Te_4 .

4.3.3.2 Nucleation mechanism and nanostructuring

The nanostructure of the melt-quenched sample, which is shown in Fig. 5(a), is characterized by a broad range of different domain orientations with domain sizes < 10 nm. The domains are intergrown, but there are no coherent domain walls. Therefore, the SAED pattern corresponds to the combination of multiple patterns and not to a single crystallite. A few grains with larger domains can be found, but they are rare exceptions. Thus, quenching the melt under a high constant pressure leads to nucleation dominated growth.

The solid-quenched sample exhibits larger and more anisotropic domains with average dimensions ≥ 10 nm. Therefore, it is possible to obtain single crystalline SAED patterns, as shown in Fig. 5(b), if larger domains are selected. These patterns contain reflections hkl with $h, k, l = 2n + 1$, which implies that there are different scattering densities for anion and cation sites, respectively. There are no pronounced diffuse streaks in the SAED patterns. Thus, there is no pronounced intermediate-range order corresponding to extended vacancy layers or van der Waals gaps within the domains as they are known from the stable trigonal phases. Probably the lack of vacancy ordering limits the maximal domain size as vacancies might aggregate at domain boundaries. The crystallites are larger than the ones in the melt-quenched HP sample; yet, the

domains are still randomly oriented. The domain shape is more anisotropic than in the melt-quenched sample.

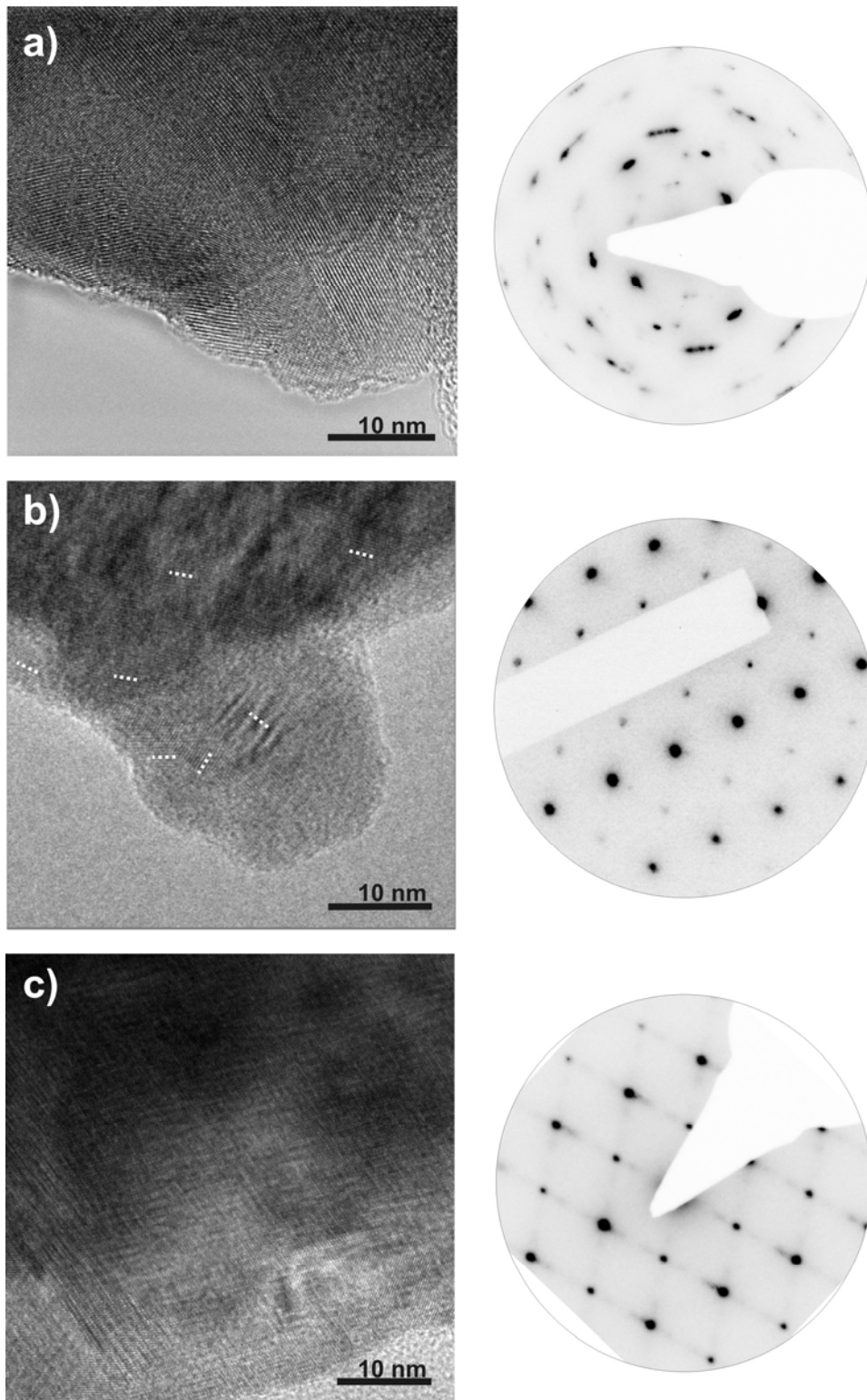


Figure 5. HRTEM images (left) and the corresponding SAED (right) a) of the melt-quenched sample (Titan 80-300); b) of the solid-quenched sample, some domain orientations are highlighted with white dashed lines (JEM 2011); c) of the slow cooled sample; here different domain orientations overlap (Titan 80-300).

Figure 5(c) shows that the slowly cooled sample has large crystallites ≥ 100 nm. Twinned areas next to single-domain areas can be observed. All slowly cooled samples exhibit extended vacancy layers that lead to van der Waals gaps if the adjacent Te atom layers relax. Therefore, diffuse streaks can be observed in the corresponding SAED patterns. These large domains indicate fast growth crystallization rather than nucleation dominated growth. The relative orientation of the twin domains corresponds to the $\langle 111 \rangle$ directions of a pseudocubic structure. This corroborates the assumption that there is a cubic high-pressure phase of GeBi_2Te_4 which, upon a phase transition toward a trigonal phase, involves fourfold twinning according to the *translationengleiche* cubic \rightarrow rhombohedral group-subgroup relationship.

The powder X-ray diffraction (PXRD) pattern of melt-spun GeBi_2Te_4 corresponds to that of the ordered $21R$ -type structure and not to the PXRD patterns of the high-pressure samples. Yet, melt-spun GeBi_2Te_4 exhibits small intergrown domains, the smallest ones with a diameter of ~ 10 nm, as shown in Fig. 6. Larger domains are also present. The domain orientation changes within one grain, however, not as randomly as in the quenched high-pressure samples.

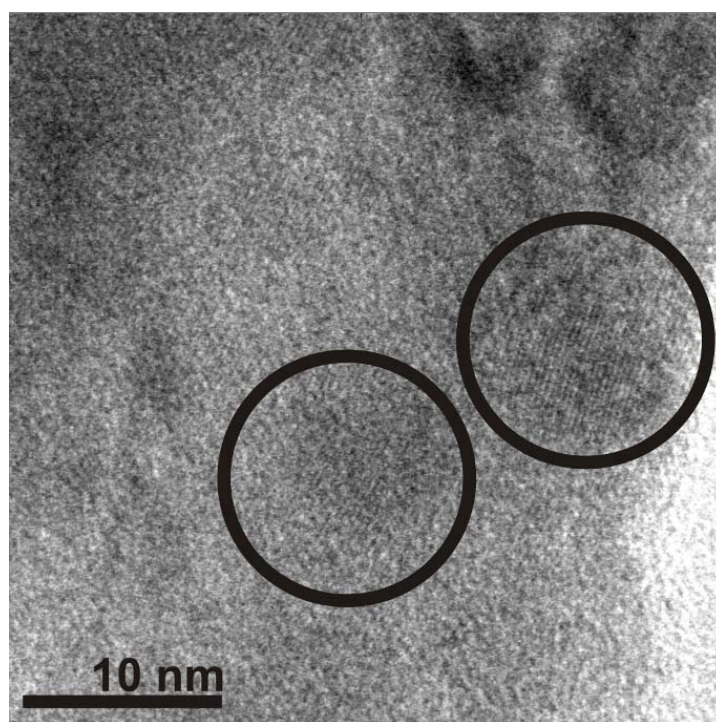


Figure 6. HRTEM image of a melt-spun sample of GeBi_2Te_4 ; two well-ordered domains of the stable layered phase are highlighted by black circles.

4.3.3.3 Influence of the nanostructure on the electrical resistivity

The following section conduces to the understanding of the influence of the nanostructure of the metastable modifications of HP-GeBi₂Te₄ on the temperature-dependent resistivity $\rho(T)$. Therefore the resistivity of three different metastable quenched samples—slowly cooled, solid-quenched, and meltquenched— were synthesized and compared with an annealed ingot as well as a melt-spun particle, both crystallizing in the stable modification.

1. Stable and melt-spun modification of GeBi₂Te₄

The resistivity of an annealed ingot of the stable ambient-pressure modification of GeBi₂Te₄ is plotted vs temperature in the range between 2 and 300 K in Fig. 7(a). The decrease of $\rho(T)$ with decreasing temperature suggests metal-like behavior. However, the high residual resistivity ρ_0 of about 0.3 m Ω cm together with the small residual resistivity ratio of $RRR=\rho(300\text{ K})/\rho(2\text{ K}) = 2.52$ suggest the presence of severe disorder. The metallic conductivity behavior depends on two different scattering processes. The temperature-independent residual resistivity ρ_0 originates from the scattering of conduction electrons by defects (impurity atoms, grain boundaries, etc.). In the present case this is probably due to the Ge/Bi disorder at the cation sites. The second—temperature-dependent—process is due to the scattering of conduction electrons by phonon excitations. These two processes yield the description of simple metals via the Bloch-Grüneisen (BG) relation

$$\rho_{\text{BG}}(T) = \rho_0 + \frac{4B}{\Theta_D} \left(\frac{T}{\Theta_D} \right)^5 \int_0^{\Theta_D/T} \frac{z^5 dz}{(e^z - 1)(1 - e^{-z})}$$

where B is the temperature-independent electron-phonon interaction strength, Θ_D the Debye-temperature, and $z = \hbar\omega/k_B T$.

The insert of Fig. 7(a) depicts the resistivity behavior $\rho(T)$ of the stable GeBi₂Te₄ modification in comparison with a corresponding data fit employing the BG relationship. The BG relation fits the experiment sufficiently well only at temperatures below ~ 40 K. For higher temperatures, $\rho(T)$ displays larger values than those expected by the BG relation for metallic behavior. This suggests an onset of semiconducting behavior at elevated temperatures in accordance with the high residual resistivity and the small RRR value. Furthermore, $\rho(T)$ of the annealed ingot reflects fully reversible behavior between cooling and heating sequences only below 40 K in the region where experimental data can be fitted by the BG relation. This reversibility can also be retrieved in the metastable modifications of GeBi₂Te₄ (see subsequent discussion).

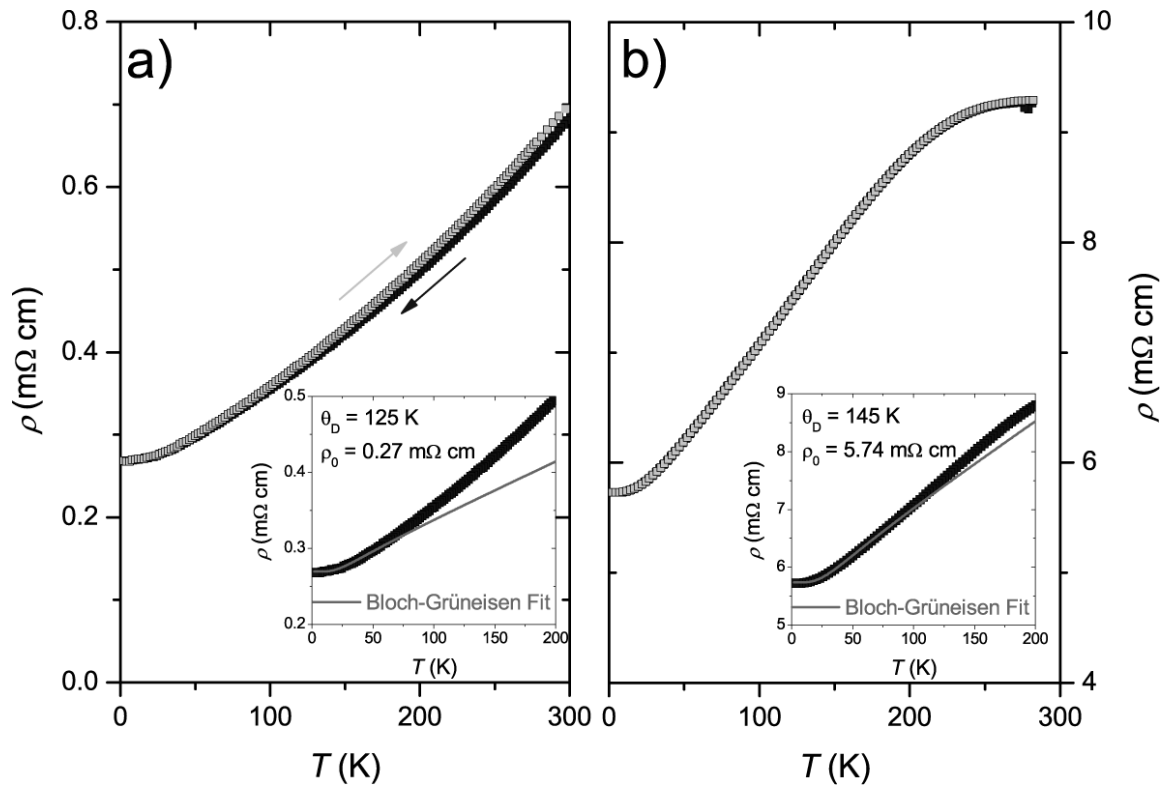


Figure 7. Comparison of the temperature-dependent resistivity of a) an annealed ingot of 21R-type GeBi_2Te_4 and of b) a melt-spun particle of GeBi_2Te_4 . The inserts show the low-temperature behavior together with a fit according to the Bloch-Grüneisen relationship (solid line). The arrows denote cooling and heating sequences, respectively.

The deviation from metallic behavior above a certain temperature becomes more evident in the resistivity of the melt-spun particle [see Fig. 7(b)], although in this case the BG relation fits the experimental data well up to ~ 60 K. However, the residual resistivity ρ_0 increases by a factor of 20 in comparison to the annealed ingot. Furthermore, $\rho(T)$ of the melt-spun particle starts to saturate already at $\sim 9.3 \text{ m}\Omega \text{ cm}$ in the high-temperature regime. The higher resistivity can be attributed to the reduction of the grain size (up to 10 nm) and can therefore be related to the increasing number of domain and grain boundaries acting as scattering centers. The saturation below room temperature is in line with a transition from metal-like to a degenerate semiconducting behavior, as supported by the description via the BG formalism [see insert Fig. 7(b)] at low temperatures, which also takes the temperature dependency of the charge carrier density into account.^[32] Such a two-regime behavior was recently reported for Ge-based clathrate I compounds as well as Sb-based skutterudites.^[33–35]

These results point out that the nanostructure, e.g., the domain size and the relative orientation, influence the temperature characteristics of the resistivity behavior even if the crystal structure is maintained (21R type).

2. Metastable quenched HP-GeBi₂Te₄

All three high-pressure samples are characterized by pronounced irreversible temperature dependencies of $\rho(T)$ for repeated cooling and heating cycles in the temperature range between 44 and 260 K. This is shown for the slowly cooled sample of HP-GeBi₂Te₄ in Fig. 8. There is a drastic change of the hysteretic behavior when the $\rho(T)$ sequences of cycle one and two are compared. However, already after the third cooling/heating sequence the hysteresis curves remain rather invariant. There is, however, a subtle decrease of the resistivity [and of the $\rho(T)$ minima at ca. 35–38 K] with increasing number of cooling/heating cycles.

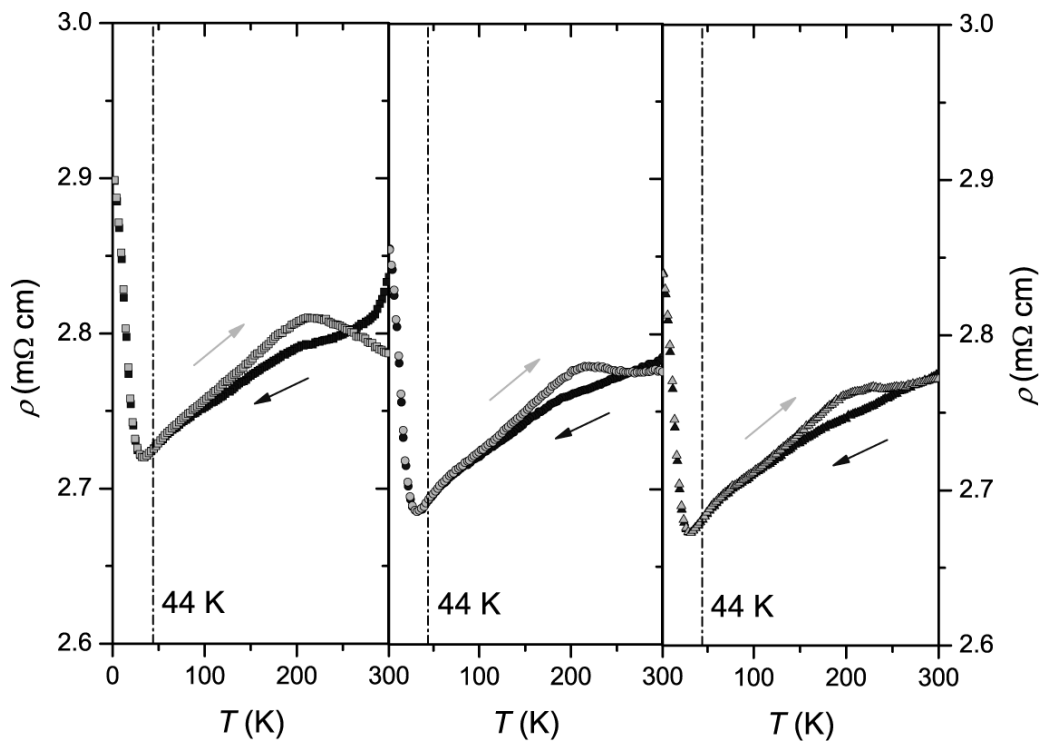


Figure 8. Temperature dependent resistivity of a slowly cooled HP-GeBi₂Te₄ sample; from left to right three successive cooling (black) and heating (gray) sequences, approaching a final state.

In the final state after more than three successive cooling and heating sequences, the resistivity $\rho(T)$ shows a metal-like behavior above 35 K and an insulating one for lower temperatures, similar to the behavior observed, e.g., for didymium skutterudites (Pr,Nd)(Fe,Co)₄Sb₁₂ and (Pr,Nd)(Fe,Ni)₄Sb₁₂.^[36] Below 44 K heating and cooling curves show reversibility, while above 44 K a hysteresis with a maximal splitting of 0.014 mΩ cm at ~208 K occurs. One may speculate that the $\rho(T)$ behavior in the reversible regions is mainly controlled by the intrinsic resistivity of the grains, whereas above 44 K the resistivity of the grain boundaries starts to dominate, as observed in the case of the stable GeBi₂Te₄ modification [see previous discussion, Fig. 7(a)].

In Fig. 9 the temperature-dependent resistivity behavior of three metastable high-pressure samples of GeBi_2Te_4 obtained by different cooling/quenching procedures is compared. All three samples are characterized by a hysteretic $\rho(T)$ behavior, which also depends on the number of cooling/heating sequences applied (*vide supra*; Fig. 8). However, in order to study exclusively the competition between the intrinsic resistivity of the domains with that of the grain boundaries, only those $\rho(T)$ cooling/heating curves were depicted in Fig. 9, which remained invariant after several measuring cycles. All of the three samples possess reversible temperature dependence below ~ 40 K. Above that temperature, the temperature characteristics of the resistivity changes from metallic-like (slowly cooled) to semiconducting (melt-quenched sample). Hence, the temperature-dependent resistivity behavior critically depends on the sample history, especially on the cooling/quenching approach applied. In contrast the hysteretic behavior above 40 K remains a characteristic feature of all the three different samples.

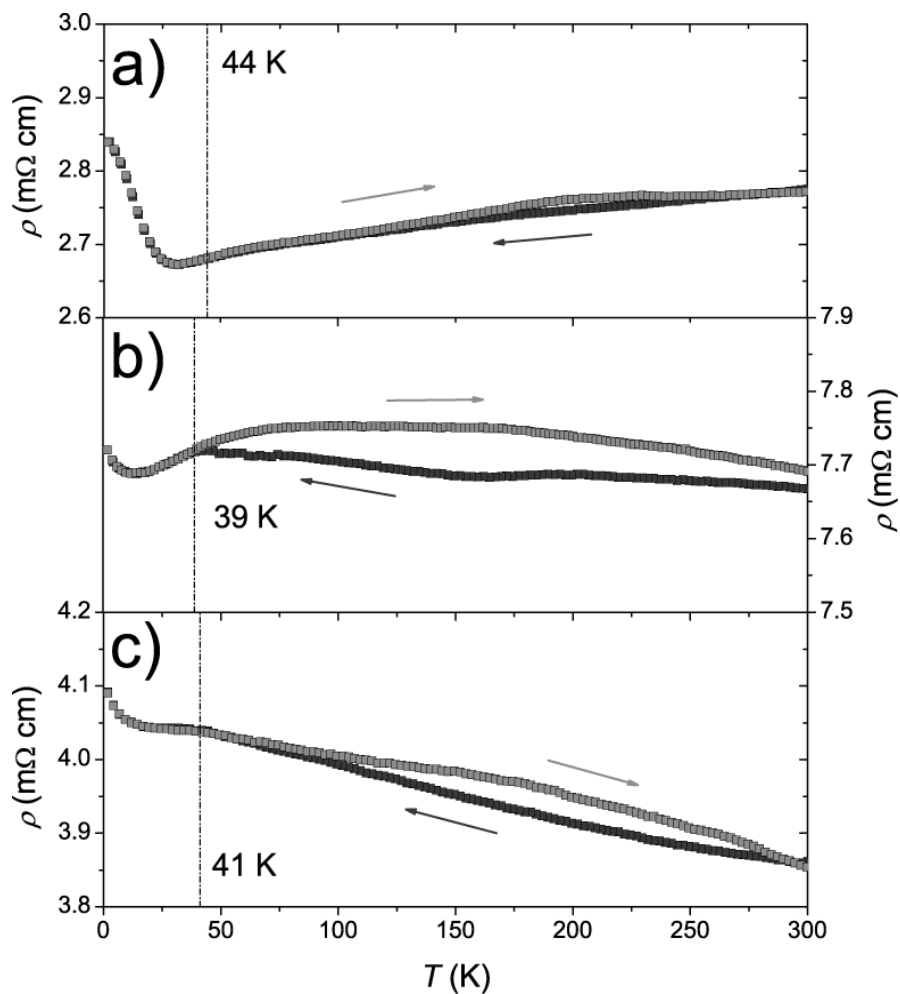


Figure 9. Final state of the cooling (black) and heating (gray) sequences of the temperature dependent resistivity of a) slowly cooled b) solid-quenched and c) melt-quenched high-pressure samples of GeBi_2Te_4 .

The occurrence of such hysteresis effects could be due to either a first-order phase transition or the presence of internal stress. A first-order phase transition can be excluded based on temperature-dependent x-ray experiments, which do not reveal any significant change in the powder-diffraction pattern down to 15 K (except for a trivial change of lattice parameters), as well as by specific heat studies (not shown here), which do not indicate any phase transformation. Therefore, the hysteretic $\rho(T)$ behavior is probably due to the internal stress of the grains. The extent of the hysteresis changes drastically with an increasing domain size and the number of their relative orientation in the different samples. Accordingly, the slowly cooled sample is characterized by the smallest hysteresis splitting of all three samples [see Fig. 9(a)]. This is consistent with the expected small change of internal stress as a consequence of the large domain size (≥ 100 nm) and the presence of only few domain orientations, as evidenced by the HRTEM studies. A similar, but more pronounced splitting is therefore found in case of the melt-quenched sample [see Fig. 9(c)], which is characterized by very small particles (<10 nm) showing many different orientations. However, the solid-quenched sample reveals the strongest splitting of all metastable GeBi_2Te_4 compounds [see Fig. 9(b)]. This is probably a result of the strongly anisotropic size of the grains.

Due to this type of nanostructuring, the total resistivity of these samples is not only affected by the intrinsic structure and disorder of the domains but also by a contribution of the microscopic nature of the domain and/or grain boundaries. The change of the residual resistivity in Fig. 9 suggests that also the dominant scattering mechanisms might differ in the three samples. The slowly cooled high-pressure sample exhibits the lowest residual resistivity and the most pronounced similarity to the stable modification [e.g., metallic conductivity at ambient temperature; see Fig. 7(a)]. This is basically due to the fact that this sample exhibits the largest domains of the three high-pressure systems and displays a disordered pseudocubic-layered structure. The melt-quenched sample, however, shows semiconducting behavior between 41 K and room temperature in spite of the isotropy and rather random orientation of its domains. The temperature dependence of the resistivity is therefore dominated by the grain boundaries' contributions. The solid-quenched sample indicates the highest residual resistivity of all the high-pressure species under investigation. This remarkably high value in combination with the pronounced grain anisotropy implies a coexistence of both scattering mechanisms discussed (see previous discussion). The $\rho(T)$ behavior of the solid-quenched modification, however, marks an intermediate behavior and thus adopts to the low-temperature behavior of the slowly cooled and mimics the high-temperature behavior of the melt-quenched one.

4.3.3.4 Influence of grain boundaries on ZT

In order to investigate the influence of the sample preparation techniques on the thermoelectric figure of merit ZT , the thermal and electrical transport properties of three characteristic samples were measured between 4 K and room temperature. In this respect the annealed ingot of stable 21R-type GeBi_2Te_4 represents a benchmark sample, which is compared with two pellet samples (samples two and three). Sample two is a pellet pressed of 21R- GeBi_2Te_4 powder, while the third sample is a pellet composed of cold-pressed powder of the melt-spun 21R- GeBi_2Te_4 . It was not possible to perform such measurements with the high-pressure samples due to their small sample volumes.

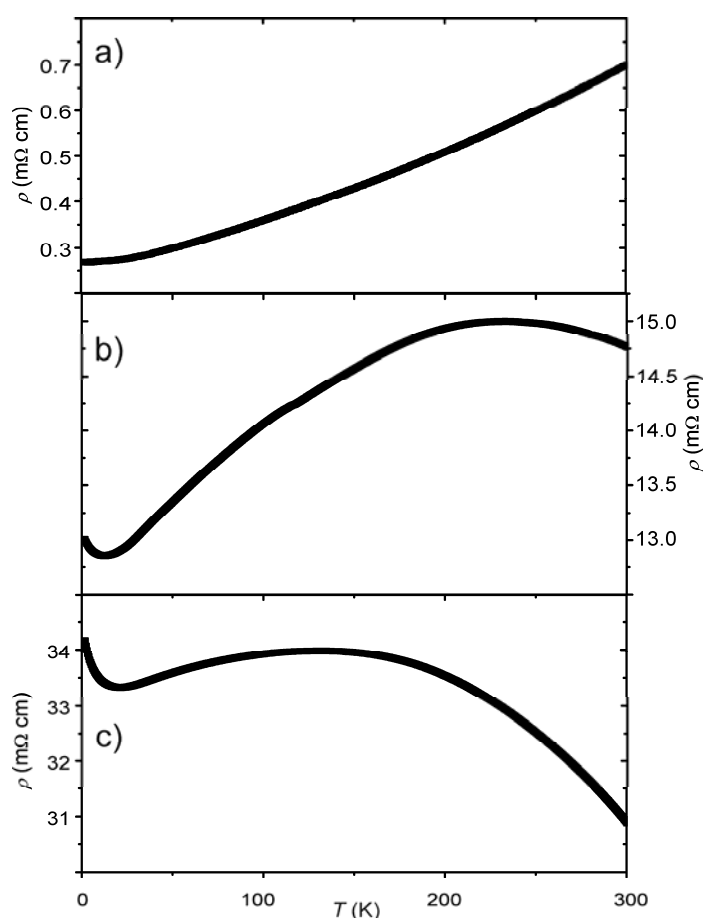


Figure 10. Comparison of the temperature dependent resistivity $\rho(T)$ (heating from 2 to 300 K) of a) an annealed ingot of GeBi_2Te_4 , b) a pressed powder pellet of 21R- GeBi_2Te_4 and c) a pressed powder pellet of melt-spun GeBi_2Te_4 .

A comparison of the $\rho(T)$ behavior of these three samples is plotted in Figs. 10(a)–10(c). The $\rho(T)$ behavior of the annealed ingot and that of the melt-spun sample were already characterized as metal-like in Fig. 7. In contrast, $\rho(T)$ of the two pellets do not show metal-like conductivity behavior. In addition, ρ_0 increases by a factor of about 30 and 60 in the case of both pellet samples, irrespective of the sample's origin (stable modification or melt-spun 21R- GeBi_2Te_4 sample, respectively). Two closely related control parameters might be responsible for observation of semiconducting behavior, namely the nano- or microstructure formation by different synthesis routes and the process of pellet pressing itself. Both lead to an increasing number of grain boundaries and therefore trigger the increase of ρ_0 and the change of the $\rho(T)$ behavior.

These observations are consistent with the thermal conductivity $\kappa(T)$ behavior shown in Figs. 11(a) and 11(b). The total thermal conductivity κ_{total} of solids can be expressed as the sum of an electrical κ_{el} as well as a phononic κ_{ph} contribution. The electrical contribution was estimated from the electrical resistivity (cf. Fig. 10) via the Wiedemann-Franz law. Subtracting this part from the experimentally determined total thermal conductivity yields the phononic contribution.

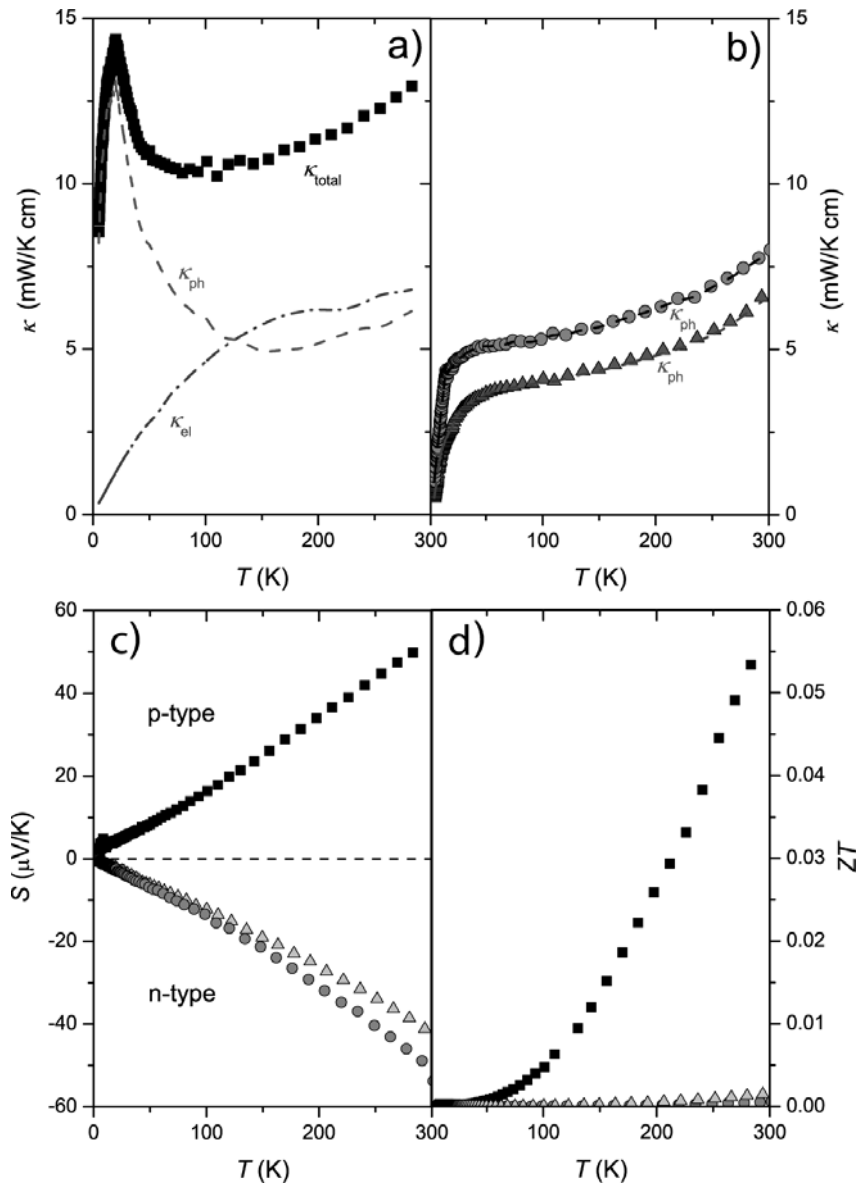


Figure 11. Temperature characteristics a) of the total thermal conductivity, κ_{total} , (black squares), the phonon contribution, κ_{ph} , (dashed line) and electronic contribution, κ_{el} , (dashed and dotted line) for the annealed ingot of GeBi_2Te_4 ; b) of κ_{total} for the pressed powder pellet of 21R-type GeBi_2Te_4 (gray circles) and the powder pressed pellet of melt-spun GeBi_2Te_4 (gray triangles) and the phonon contributions (dashed lines, dark gray); c) of the Seebeck coefficient and d) of the ZT value for the annealed ingot (black squares), the pressed powder pellet of 21R-type GeBi_2Te_4 (gray circles) and the pressed powder pellet of melt-spun GeBi_2Te_4 (light gray triangles).

In Fig. 11(a) κ_{total} of the annealed ingot of the stable modification is composed of significant contributions from κ_{ph} and κ_{el} . While at room temperature both parts coexist and contribute approximately by the amount to κ_{total} , a phonon-dominated state is observed below 50 K. The maximum of κ_{ph} at about 13 K displays the onset of phonon umklapp scattering which effectuates a decrease of κ_{ph} above a certain temperature. Such kind of maximum depends only weakly on the Debye temperature and occurs well below $\Theta_D/10$. The low-temperature slope of κ_{ph} thus indicates defect scattering and becomes large when the number of defects is small.

A comparison with the $\kappa(T)$ results of the two pellets indicate an overall and significant reduction of $\kappa_{\text{total}}(T)$ [Fig. 11(b)]. Generally, κ_{ph} of the thermal conductivity of both samples follows the pattern of κ_{total} while the κ_{el} contribution vanishes, as expected in light of the high resistivity values observed. Furthermore, the change of the low-temperature slope of κ_{ph} hints to an increase of phonon scattering at boundaries and/or point defects. Hence, the reduced thermal conductivity of the pellet-pressed samples originates mainly from the enhancement of these scattering processes.

The thermopower $S(T)$ of the three samples is depicted in Fig. 11(c). For the annealed ingot of the stable modification, an increase of the thermopower up to about $+50 \mu\text{V/K}$ at room temperature can be observed. The positive sign of $S(T)$ between 4 and 300 K reveals the characteristic behavior of a p -type material. The featureless, almost linear temperature dependence of $S(T)$ indicates the absence of any significant correlations within the charge carriers and is expected for the diffusion thermopower above the Debye temperature (125 K). In this temperature region electron-phonon scattering is the dominant-scattering mechanism and given by

$$S_d(T > \Theta_D) = \frac{\pi^2 k_B^2 2m_e}{|e| \hbar^2 (3n\pi^2)^{2/3}} \cdot T$$

with $k_B = 1.38065 \cdot 10^{-23} \text{ J/K}$, $m_e = 9.10938 \cdot 10^{-31} \text{ kg}$, $e = 1.60218 \cdot 10^{-19} \text{ C}$, and $\hbar = 6.62607 \cdot 10^{-34} \text{ Js}$. According to this equation, the slope below 300 K yields a density of charge carriers of $3.4 \cdot 10^{21} \text{ cm}^{-3}$.

In contrast to its influence on $\rho(T)$ and $\kappa(T)$, the method of synthesis has no drastic influence on $S(T)$ except for the remarkable change of sign in the thermopower of the pellets from positive (p -type) to negative (n -type). The absolute values of $S(T)$, as well as the carrier concentration ($\sim 10^{21} \text{ cm}^{-3}$) of the pellet samples, remain more or less the same.

The ZT values for the three samples calculated from the present results are shown in Fig. 11(d). For the annealed ingot of the stable modification a ZT value of 0.055 was reached at room

temperature. The ZT values of both pellet samples were found to be one order of magnitude lower, which disqualifies these samples from thermoelectric applications. Significant scattering of the charge carriers on grain boundaries results in high resistivity values for the micro- or nanostructured samples and, as a consequence, in a small electronic contribution to the thermal conductivity.

4.3.4 Conclusion

Quenching melts of GeBi_2Te_4 at high pressure yields metastable samples whose average structure is related to the rocksalt-type, similar to samples obtained by laser irradiation of thin films for PCM applications. Partial relaxation toward the stable trigonal-layered modification leads to a rhombohedrally distorted crystal structure. The metastable state can be completely relaxed by annealing. Concerning PCMs, the nucleation mechanisms are important. “Nucleation dominated growth” begins spontaneously at different spots in the amorphous phase and therefore leads to a multitude of grains, which have no crystallographic relation to each other. We have shown that the crystallization of melts during rapid quenching is very similar; an intermediate solid amorphous phase might be discussed for bulk samples as well but cannot be confirmed by our experiments. The domain size and therefore probably the nucleation mechanism depends on the temperature regime, including quenching rates, which were applied under a constant pressure of 12 GPa. The nanostructures obtained and especially the corresponding domain and grain boundaries have a large influence on the temperature characteristics of the electrical resistivity. In the high-pressure compounds the characteristics of the electrical resistivity changes from metal-like to semiconducting behavior with decreasing domain size and more randomly oriented domains, because the resistivity becomes more dominated by scattering of the electrons at the domain or grain boundaries. The temperature regime during the synthesis therefore determines at which temperature this type of scattering becomes dominant. However, multiple heating and cooling sequences in the course of the resistivity measurements show that the system seems to approach a final state. Apparently, internal stress needs to be reduced before the measurements yield invariant $\rho(T)$ sequences but even after the stabilization a hysteretic behavior remains.

As a consequence, the preparation technique has a large influence on the ZT value, as shown by measurements on samples that exhibit the stable-layered structure. The thermal conductivity is influenced by the electronic contribution, which decreases significantly in pressed pellets with many grain boundaries; however, it is accompanied by the corresponding increase of the electrical resistivity. Therefore, the ZT value drops by more than an order of magnitude because

the phononic contribution becomes dominant. These findings illustrate the importance of the thermal conditioning of thermoelectrics, especially in order to ensure sufficient electrical conductivity. It is often difficult to reproduce thermoelectric materials with distinct properties because different methods of synthesis (like hot press, high-pressure experiments, or conventional solid-state preparation techniques), annealing times, and temperatures lead to various amounts of grain boundaries and therefore strong deviations in ZT .

4.3.5 References

- [1] W. Bensch, M. Wuttig, *Chem. Unserer Zeit* **2010**, *44*, 92.
- [2] S. Raoux, *Annu. Rev. Mater. Res.* **2009**, *39*, 9.
- [3] M. N. Schneider, T. Rosenthal, C. Stiewe, O. Oeckler, *Z. Kristallogr.* **2010**, *225*, 463.
- [4] J. Sommerlatte, K. Nielsch, H. Böttner, *Phys. J.* **2007**, *6*, 35.
- [5] A. Bulusu, D. G. Walker, *Superlattices Microstruct.* **2008**, *44*, 36.
- [6] A. Majumdar, *Science* **2004**, *303*, 777.
- [7] M. S. Dresselhaus, G. Chen, M. Y. Tang, R. Yang, H. Lee, D. Wang, Z. Ren, J.-P. Fleurial, P. Gogna, *Adv. Mater.* **2007**, *19*, 1.
- [8] D. L. Medlin, G. J. Snyder, *Curr. Opin. Colloid Interface Sci.* **2009**, *14*, 226.
- [9] M. G. Kanatzidis, *Chem. Mater.* **2010**, *22*, 648.
- [10] Y. C. Lan, A. J. Minnich, G. Chen, Z. F. Ren, *Adv. Funct. Mater.* **2010**, *20*, 357.
- [11] J. R. Sootsman, D. Y. Chung, M. G. Kanatzidis, *Angew. Chem. Int. Ed.* **2009**, *48*, 8616.
- [12] A. C. Bruce, J. K. Matthew, L. H. Joel, H. Mi-Kyung, C. Duck-Young, G. K. Mercuri, *Adv. Funct. Mater.* **2009**, *19*, 1254.
- [13] P. F. P. Poudeu, J. D'Angelo, A. D. Downey, J. L. Short, T. P. Hogan, M. G. Kanatzidis, *Angew. Chem. Int. Ed.* **2006**, *45*, 3835.
- [14] F. D. Rosi, J. P. Dismukes, E. F. Hockings, *Electron Eng.* **1960**, *79*, 450.
- [15] T. Matsunaga, N. Yamada, *Phys. Rev. B* **2004**, *69*, 104111.
- [16] T. Matsunaga, N. Yamada, Y. Kubota, *Acta Crystallogr. Sect. B* **2004**, *60*, 685.
- [17] T. Matsunaga, R. Kojima, N. Yamada, K. Kifune, Y. Kubota, Y. Tabata, M. Takata, *Inorg. Chem.* **2006**, *45*, 2235.
- [18] T. Matsunaga, Y. Umetani, N. Yamada, *Phys. Rev. B* **2001**, *64*, 184116.
- [19] T. Matsunaga, N. Yamada, *Jpn. J. Appl. Phys.* **2004**, *43*, 4704.
- [20] L. E. Shelimova, O. G. Karpinskii, P. P. Konstantinov, E. S. Avilov, M. A. Kretova, V. S. Zemskov, *Inorg. Mater.* **2004**, *5*, 451.

-
- [21] S.-I. Shamoto, N. Yamada, T. Matsunaga, T. Proffen, *Phys. B* **2006**, 385-385, 574.
- [22] C. W. Sun, J. Y. Lee, Y. T. Kim, *Phys. Stat. Sol. RRL* **2009**, 3, 254.
- [23] D. Walker, M. A. Carpenter, C. M. Hitch, *Am. Mineral.* **1990**, 75, 1020.
- [24] D. Walker, *Am. Mineral.* **1991**, 76, 1092.
- [25] D. C. Rubie, *Phase Trans.* **1999**, 68, 431.
- [26] H. Huppertz, *Z. Naturforsch. B* **2001**, 56, 697.
- [27] *TOPAS-Academic, V. 4.1*, Coelho Software, Brisbane, Australia **2007**.
- [28] *Digital Micrograph 3.6.1*, Gatan Software, Pleasanton, California, USA, **1999**.
- [29] P. A. Stadelmann, *Ultramicroscopy* **1987**, 21, 131.
- [30] *ESVision, 4.0.164*, Emispec Systems Inc., Tempe, Arizona, USA, **1994–2002**.
- [31] P. P. Konstantinov, L. E. Shelimova, E. S. Avilov, M. A. Kretova, V. S. Zemskov, *Inorg. Mater.* **2001**, 37, 662.
- [32] N. Melnychenko-Koblyuk, A. Grytsiv, St. Berger, H. Kaldarar, H. Michor, F. Röhrbacher, E. Royanian, E. Bauer, P. Rogl, H. Schmid, G. Giester, *J. Phys. Condens. Matter* **2007**, 19, 046203.
- [33] C. Candolfi, U. Aydemir, M. Baitinger, N. Oeschler, F. Steglich, Yu. Grin, *J. Electron. Mater.* **2010**, 39, 2039.
- [34] A. Grytsiv, P. Rogl, St. Berger, Ch. Paul, H. Michor, E. Bauer, G. Hilscher, C. Godart, P. Knoll, M. Musso, W. Lottermoser, A. Saccone, R. Ferro, T. Roisnel, H. Noel, *J. Phys. Condens. Matter* **2002**, 14, 7071.
- [35] G. Rogl, A. Grytsiv, E. Bauer, P. Rogl, M. Zehetbauer, *Intermetallics* **2010**, 18, 394.
- [36] G. Rogl, A. Grytsiv, E. Bauer, P. Rogl, M. Zehetbauer, *Intermetallics* **2010**, 18, 57.

5 Characterization of the real structure of metastable germanium antimony tellurides and its influence on their properties

5.1 Overview

Although materials science focuses on the discovery and optimization of new materials, the fundamental understanding of structure-property relationships has always been an important objective. This, of course, requires detailed structure elucidation ranging from the macroscopic to the atomic scale and may involve the question how properties change with temperature or compositional variations. In this context, disorder on various length scales plays a key role for thermoelectrics as short-range order significantly influences the properties of the materials, especially their thermal conductivity.

As demonstrated in Chapter 2, long-periodic layered structures represent the stable modifications of phases $(\text{GeTe})_n\text{Sb}_2\text{Te}_3$ (at least for $0 < n < 4$) at ambient conditions.^[1-4] With respect to the oxidation states Ge^{II} , Sb^{III} and Te^{II} , these phases are normal-valence compounds. Ge and Sb atoms are distributed over fully occupied cation positions in distorted rocksalt-type slabs that are separated by van der Waals gaps between Te atom layers. The compounds $(\text{GeTe})_n\text{Sb}_2\text{Te}_3$ with $n \geq 3$ exhibit stable high-temperature polymorphs with a rocksalt-type average structure as discussed in Chapter 4.^[5] In contrast to the long-periodic layered structures which contain no significant amount of cation defects, the given cation/anion ratio requires the presence of $1/n+3$ cation defects per n cation positions in the NaCl-type phases if anion positions are fully occupied by Te atoms.^[6,7] Ge and Sb atoms share the cation positions with vacancies in a randomly disordered fashion. Whereas slow cooling of the high-temperature modifications yields the trigonal long-periodic layered structures, quenching yields metastable modifications as discussed in Chapter 4. These metastable polymorphs crystallize with pseudo-cubic metrics; their diffraction pattern exhibits alternating weak and strong reflections characteristic for the rocksalt type. The assumption of a rocksalt-type structure, however, is just an approximation. The symmetry reduction $Fm\bar{3}m$ (NaCl type) $\xrightarrow{t^4}$ $R\bar{3}m$ (CuPt type) $\xrightarrow{t^2}$ $R3m$ (GeTe type) leads to fourfold or eightfold twinning, respectively. Short-range order of cation defects yields pronounced nanostructures as revealed by high-resolution electron microscopy (HRTEM) in combination with STEM-HAADF (scanning transmission electron microscopy with high-angle

annular dark-field detector) imaging, (cf. Chapter 5.1 and Chapter 5.2) and the analysis of diffuse X-ray scattering (cf. Chapter 5.3 and Chapter 5.4). The pseudo-cubic diffraction pattern thus results from the superposition of the intensities of individual twin domains with trigonal average structure. The axis ratio a_t/c_t does not significantly deviate from that of a cubic structure in trigonal setting ($a_t = a_c \cdot 2^{-1/2}$, $c_t = a_c \cdot 3^{1/2}$, the index c indicates a cubic setting whereas the index t indicates a trigonal setting).

The nanostructure of quenched $(\text{GeTe})_n\text{Sb}_2\text{Te}_3$ ($n = 4.5, 7, 12, 19$, cf. Chapters 5.1 and 5.2) are characterized by finite cation defect layers with various orientation distributions. The chemical composition is one important factor that influences the structures. For low GeTe contents ($n = 4.5, 7$), the high concentration of defects leads to high correlations between them. Furthermore, short diffusion pathways yield pronounced short-range order that leads to a parallel arrangement of extended almost equidistant cation defect layers. For higher GeTe contents ($n = 12, 19$), they are parallel to all $\langle 111 \rangle_c$ directions of the pseudo-cubic average structure which leads to intersecting defect layers. As demonstrated for $(\text{GeTe})_{12}\text{Sb}_2\text{Te}_3$ (cf. Chapter 5.1), this nanoscale twinning leads to stresses that stabilize the pseudo-cubic metrics of individual domains. Powder diffraction patterns therefore show anisotropic microstrain broadening. The relaxation of the resulting microstrain towards the rhombohedral equilibrium lattice parameters in addition requires vacancy diffusion and a rearrangement of the Te-atom layer stacking sequence. The lateral extension of the cation defect layers decreases with increasing GeTe-content n and the variance of the inter-layer spacings increases with the increasing diffusion pathways required to form the hypothetical long-range ordered layered compounds (exemplified by $(\text{GeTe})_n\text{Sb}_2\text{Te}_3$ with $n = 12, 19$).

In accordance with cation defect layers evidenced by TEM, X-ray diffraction patterns of quenched crystals $(\text{GeTe})_n\text{Sb}_2\text{Te}_3$ with $n = 5, 6, 12, 15$ (Chapter 5.3 and Chapter 5.4) exhibit structured diffuse streaks that interconnect Bragg reflections along all $\langle 111 \rangle_c$ directions. These correspond to the superposition of streaks along the $[001]_t$ directions of individual trigonal domains. The intensity distribution on each diffuse streak resembles to a "comet" with a maximum located at the low-angle side of Bragg positions accompanied by a slightly structured "tail". Whereas a statistical analysis of the defect layer distribution and the structure relaxation in their vicinity, i. e. interatomic distances, is difficult by means of TEM, the analysis of diffuse scattering characterizes real-structure effects from the complete crystal volume. In this work, a disorder model for the simulation of the diffuse scattering was developed using structure information from the corresponding stable modifications, i. e. long-periodic layered structures

(cf. Chapter 2) and rocksalt-type high-temperature modifications (cf. Chapter 4) as well as the knowledge that cation defect layers are present.

The parameters of the model describe the overall metrics, the concentration and distribution of defect layers, atom displacements in their vicinity and the stacking sequence of Te atom layers around the planar defects. These parameters were varied in order to derive simple rules for the interpretation of the diffuse scattering. The details given in Chapter 5.3 can be summed up as follows:

- 1) The distance between the diffuse maximum and the Bragg positions decreases with increasing distance between cation defect layers (i. e. increasing n). Increasing variance of the inter-layer spacing reduces the intensity modulation in the "tail of the diffuse comet".
- 2) The displacement of neighboring atom layers towards the planar defects yield "comets" on the low-angle side and vice versa. The streaks are, of course, more intense for larger deviations from the average structure.
- 3) A rocksalt-type basic structure with its characteristic diffraction pattern can only be obtained if the planar defects correspond to "missing" cation layers in the cubic ABC stacking sequence of the Te atom layers. The formation of a van der Waals gap comparable to that in the stable low-temperature modifications requires a hexagonal ABAB stacking around the gap. An increasing amount of hexagonal transitions leads to the increasing broadening and splitting of the Bragg reflections which then merge with the diffuse scattering.

Based on these rules, the real structure of crystals $(\text{GeTe})_n\text{Sb}_2\text{Te}_3$ with different GeTe content n was determined by simulating diffraction patterns and comparing them with experimental reciprocal sections or the measured intensity along the streaks. Crystals of $(\text{GeTe})_2\text{Sb}_2\text{Te}_3$ obtained from stoichiometric melts quenched in liquid nitrogen exhibit almost equidistant van der Waals gaps whose average distance that corresponds to that in the long-range ordered phase, and hexagonal transitions between Te atoms layers around the gaps predominate. In contrast, the cubic Te atom layer sequence is retained across the cation defect layers in crystals of $(\text{GeTe})_{12}\text{Sb}_2\text{Te}_3$ grown in the stability range of the cubic high-temperature phase and subsequently quenched. The large variance of the inter-layer spacings matches well with the observations by electron microscopy (cf. Chapter 5.1 and Chapter 5.2).

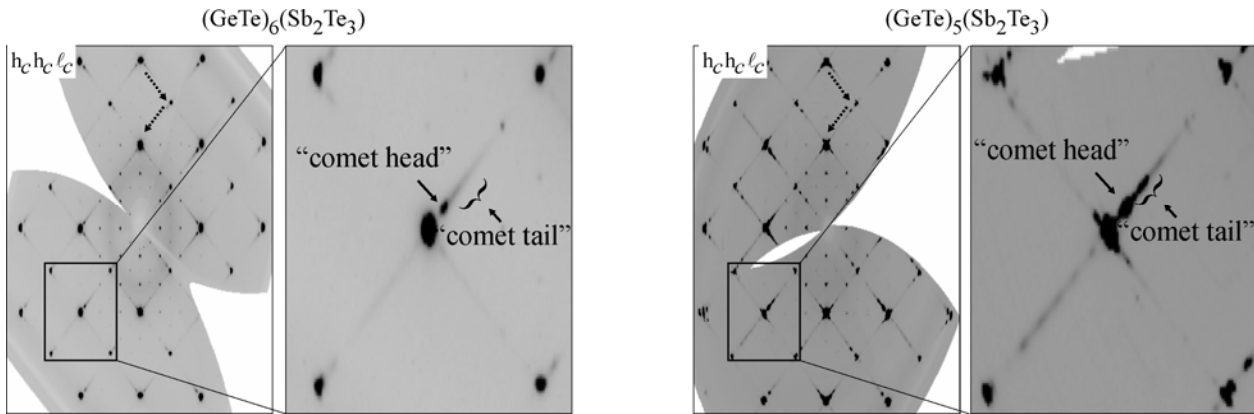


Figure 1. Comparison of synchrotron experimental reciprocal sections " $h_c h_c \ell_c$ ": The intensity distribution corresponds to the superposition of intensities from individual domains with 1D disordered trigonal structure ($[001]_t$ directions are indicated by broken arrows). The enlargement shows the diffuse intensity distribution around a strong "pseudo-cubic" Bragg reflection. Towards the low angle-side a diffuse maximum ("comet head" accompanied by a "comet tail" is observed). The "comet tail" shows a clear modulation in its intensity for the crystal with lower GeTe-content.

Synchrotron diffraction data of quenched crystals $(\text{GeTe})_n\text{Sb}_2\text{Te}_3$ with $n = 5$ and 6 have been used to quantitatively extract the intensity of the streaks. Selected streaks of trigonal domains $h_t k_t \ell_t$ ($h_t = 0, 1, 2$; $h_t = k_t$ or $h_t = -k_t$) were compared with simulated intensities. For $n = 5$ the crystal exhibits a narrow distribution of cation defect layers, the average distance corresponding to an ordered compound with $n = 4$. Atom displacements in the vicinity of the cation defect layers yield interatomic Te-Te distances that are significantly smaller than the sum of van der Waals radii. This situation is comparable to that around the van der Waals gap of long-periodic layered structures. In the $[(\text{Ge,Sb})\text{Te}_6]$ octahedra next to the defect layer, the 3+3 coordination also corresponds to that observed in the stable layered phases. Whereas $(\text{GeTe})_5\text{Sb}_2\text{Te}_3$ contains approximately equal amounts of cubic and hexagonal transitions between Te atom layers around the cation defect layers, $(\text{GeTe})_6\text{Sb}_2\text{Te}_3$ exhibits almost exclusively cubic transitions. For the latter, the position of the "comet" head corresponds to the structure of an ordered phase with $n = 5$; and the smooth "comet tail" indicates a large variance of inter-defect-layer spacings. The atom displacements around the defect plane are a bit smaller than those in $(\text{GeTe})_5\text{Sb}_2\text{Te}_3$, which means that the Te-Te distances in cubic transitions are closer to the sum of van der Waals radii. Summing up, both TEM and diffuse scattering data from quenched phases $(\text{GeTe})_n\text{Sb}_2\text{Te}_3$ ($n \geq 3$) show the real structure deviates significantly from the average rocksalt-type structure. In cases where both cubic and hexagonal transitions between Te atom layers across the cation defect layers occur, there is no well-defined average structure. The real structures of these metastable phases correspond to an "intermediate state" of the phase transition from the rocksalt-type high-

temperature modification with random cation defect distribution to the long-periodic layered structures characterized by van der Waals gaps between distorted rocksalt-type slabs. Thus, it is not surprising that pseudocubic quenched phases can only be obtained for compounds with rocksalt-type high-temperature polymorphs.

Upon slowly heating quenched samples $(\text{GeTe})_n\text{Sb}_2\text{Te}_3$ (e. g. in temperature-programmed powder diffraction experiments), they relax to the thermodynamically stable trigonal phases. As discussed in Chapter 5.2, the corresponding transition temperatures depend only slightly on the composition and lie around 300 °C for $n = 6 - 17$. For $3 < n < 6$ the transition temperature is lightly higher (cf. Chapter 4.2). The transition temperature to the cubic high-temperature phase, in contrast, decreases with increasing n : it drops from 500 °C for $n = 7$ to 410 °C for $n = 17$. The high-temperature phases can be undercooled; upon slow cooling, the trigonal layered phases form at temperatures between 460 °C for $n = 7$ and 250-275 °C for $n = 17$.

In contrast to temperature programmed powder diffraction, microfocus Laue diffraction can *in situ* detect the structural changes during the phase transitions as discussed in Chapter 5.4. In a quenched crystal of $(\text{GeTe})_6\text{Sb}_2\text{Te}_3$, diffuse streaks occur only along one of the pseudocubic $\langle 111 \rangle_c$ directions and thus indicate that domains with parallel not equidistantly spaced planar defect are larger than the beam size of 1 μm . Between 250 °C and 300 °C, these streaks gradually transform into a series of sharp reflections characteristic for a long-periodically ordered layered structure. From 500 °C on these reflections become weak and at 550 °C a rocksalt-type high-temperature phase with random distribution of vacancies is found. In contrast, a quenched crystal of $(\text{GeTe})_{12}\text{Sb}_2\text{Te}_3$ exhibits broadened Bragg reflections and weak diffuse streaks along all $\langle 111 \rangle_c$ directions. The streaks gain intensity at 350 °C, and Bragg reflections that correspond to a hR lattice become sharp at 400 °C. This is consistent with increasing long-range order towards the stable layered phase. Upon further increasing temperature, the diffuse streaks do not change up to 450 °C when their intensity decreases and the high-temperature phase is approached and finally reached at 500 °C. Upon cooling, diffuse streaks reappear at 430-370 °C. Due to the higher vacancy concentration in (pseudo-)cubic $(\text{GeTe})_6\text{Sb}_2\text{Te}_3$, the diffusion pathways required to form the parallel and equidistantly spaced van der Waals gaps of the stable phase are shorter than for $(\text{GeTe})_{12}\text{Sb}_2\text{Te}_3$. Thus, the ordering process requires longer times in the latter compound, and the time during the heating experiments is not sufficient to transform the diffuse streaks into characteristic reflections of a long-periodic layered structure.

In contrast to these observations, diffraction patterns of a $(\text{GeTe})_{15}\text{Sb}_2\text{Te}_3$ crystal are not pseudocubic but, due to multiple twinning, show groups of reflections resulting from domains with rhombohedral metrics. There is little diffuse scattering, and thus short-range order is not very

pronounced. Above 330 °C, additional Bragg reflections of the rocksalt-type high-temperature phase appear between the reflections of each group and gain intensity as the splitting of the original reflections and thus the rhombohedral distortion decreases with increasing temperature. The rocksalt-type high-temperature modification is reached at 400 °C. Upon cooling this crystal behaves rather similar to $(\text{GeTe})_{12}\text{Sb}_2\text{Te}_3$, reflection broadening and slight streaking occur below 330 °C. This indicates that the original crystal was a growth twin formed below the stability range of the cubic phase. Whereas the formation of long-periodic layered phases from the (pseudo-)cubic ones (from the metastable quenched polymorphs upon heating and for the stable high-temperature polymorph upon cooling) obviously depend on diffusion processes and hence are kinetically controlled, the transition to the high-temperature phase is thermodynamically controlled. The random arrangement of cation defects in the high-temperature phase (cf. Chapter 4) leads to “incomplete” anion-centered polyhedra in which Te-atoms exhibit an “unsaturated” coordination. To reach such an unfavourable situation, with increasing amount of cation defects an increasing amount of energy must be provided for the order-disorder transition which explains why the transition temperature to the high-temperature phases decrease with increasing GeTe-content.

As demonstrated in Chapter 5.3, quenched samples ($n = 3, 4.5, 7, 12, 19$) exhibit similar Seebeck coefficients that indicate p-type semiconductivity. Whereas at 150 °C below the temperature of ~ 300 °C at which diffusion processes set in (hence at 150 °C) the Seebeck coefficients range from 20 to 90 μVK^{-1} , rather high values of 100-200 μVK^{-1} are reached 150 °C above the temperature where diffusion processes occur (hence at 450 °C). The electrical conductivities (σ) correspond to metallic behavior. The overall thermal conductivities κ range from 1 to 3.2 W/mK at 150 °C, whereas at 450 °C they range from 1.4 to 2.6 W/mK. The lowest phononic thermal conductivity κ_L at 150 °C was found for $(\text{GeTe})_{4.5}\text{Sb}_2\text{Te}_3$ and may be attributed to the high defect concentration and pronounced short-range order. At this temperature, $n = 4.5$ yields the highest figure of merit of $ZT = 0.3$. At higher temperature, the stable layered phase forms and leads to a significant increase of κ_L so that ZT is only 0.5 at 450 °C. $(\text{GeTe})_{19}\text{Sb}_2\text{Te}_3$, on the contrary, has a rather high κ_L and thus a small ZT of 0.02 at 150 °C due to the low defect concentration. With increasing temperature, however, the low defect concentration does not lead to the formation of trigonal layered structures and κ_L decreases. In combination with the high Seebeck coefficient, this phase reaches $ZT = 1.3$ at 450 °C. However, at such high temperatures, the nanostructure is not long-time stable so that for practical applications one would be restricted to temperatures below ~ 300 °C where the figure of merit of quenched samples does not exceed ~ 0.5 . The comparison of quenched samples with annealed (at 400 °C) ones with the same composition

shows that quenching is crucial for the nanostructure formation. For $(\text{GeTe})_{12}\text{Sb}_2\text{Te}_3$, κ_L of quenched samples with pronounced nanostructure is lower than that of annealed samples (with parallel van der Waals gaps) below 300 °C, where diffusion effects are negligible. Once diffusion processes are activated at approximately 300 °C (see above), the thermal conductivities of quenched samples with $n = 7, 12$ and 19 develop discontinuously and show pronounced hysteresis as discussed in Chapter 5.4. This may be attributed to the high atomic mobility that influences the thermal conductivities. The diffusion processes also change the charge carrier concentration so that the Seebeck coefficients and the electrical conductivities also exhibit discontinuous and hysteretic behavior.

The thermoelectric characteristics of quenched samples $(\text{GeTe})_n\text{Sb}_2\text{Te}_3$ are comparable to those of pseudobinary compounds GeTe-AgSbTe_2 which are often referred to as TAGS (Te-Sb-Ge-Ag). Below ~ 300 °C the thermoelectric figures of merit of these optimized solid solutions range below ~ 1 and reach high values of ~ 1.5 at 450 °C.^[8,9] Similar ZT-values are also found for inhomogenous nanostructured SALT-materials (Na-Sb-Pb-Te) or LAST-materials (Pb-Sb-Ag-Te).^[10,11] All these materials are comparable to phases $(\text{GeTe})_n\text{Sb}_2\text{Te}_3$ and are discussed as high-performance thermoelectrics.^[12,13]

References for Chapter 5.1

- [1] O. G. Karpinsky, L. E. Shelimova, M. A. Kretova, J.-P. Fleurial, *J. Alloys Compd.* **1998**, 268, 112.
- [2] T. Matsunaga, N. Yamada, Y. Kubota, *Acta Crystallogr. Sect. B* **2004**, 60, 685.
- [3] T. Matsunaga, R. Kojima, N. Yamada, K. Kifune, Y. Kubota, M. Takata, *Appl. Phys. Lett.* **2007**, 90, 161919.
- [4] L. E. Shelimova, O. G. Karpinsky, M. A. Kretova, V. I. Kosyakov, V. A. Shestakov, V. S. Zemskov, F. A. Kuznetsov, *Inorg. Mater.* **2000**, 36, 768.
- [5] T. Matsunaga, H. Morita, R. Kojima, N. Yamada, K. Kifune, Y. Kubota, Y. Tabata, J.-J. Kim, M. Kobata, E. Ikenaga, K. Kobayashi, *J. Appl. Phys.* **2008**, 103, 093511.
- [6] T. Matsunaga, R. Kojima, N. Yamada, K. Kifune, Y. Kubota, Y. Tabata, M. Takata, *Inorg. Chem.* **2006**, 45, 2235.
- [7] T. Matsunaga, N. Yamada, *Jpn. J. Appl. Phys.* **2002**, 41, 1674.
- [8] Y. Chen, T. J. Zhu, S. H. Yang, S. N. Zhang, W. Miao, X. B. Zhao, *J. Electron. Mater.* **2010**, 39, 1719.
- [9] S. H. Yang, T. J. Zhu, C. Yu, J. J. Shen, Z. Z. Yin, X. B. Zhao, *J. Electron. Mater.* **2011**, 40, 1244.

- [10] A. C. Bruce, J. K. Matthew, L. H. Joel, H. Mi-Kyung, C. Duck-Young, G. K. Mercuri, *Adv. Funct. Mater.* **2009**, *19*, 1254.
- [11] P. F. P. Poudeu, J. D'Angelo, A. D. Downey, J. L. Short, T. P. Hogan, M. G. Kanatzidis, *Angew. Chem. Int. Ed.* **2006**, *45*, 3835.
- [12] M. G. Kanatzidis, *Chem. Mater.* **2010**, *22*, 648.
- [13] J. R. Sootsman, D. Y. Chung, M. G. Kanatzidis, *Angew. Chem. Int. Ed.* **2009**, *48*, 8616.

5.2 Influence of stress and strain on the kinetic stability and phase transitions of cubic and pseudocubic Ge-Sb-Te materials

Matthias N. Schneider, Philipp Urban, Andreas Leineweber, Markus Döblinger, and Oliver Oeckler

Physical Review B **2010**, *81*, 184102.

Abstract

Rewritable data-storage media and promising nonvolatile random-access memory are mainly based on phase-change materials (PCMs) which allow reversible switching between two metastable (amorphous and crystalline) modifications accompanied by a change in physical properties. Although the phase-change process has been extensively studied, it has not been elucidated how and why the metastable crystalline state is kinetically stabilized against the formation of thermodynamically stable phases. In contrast to thin-film investigations, the present study on bulk material allows to demonstrate how the cubic high-temperature phase of GeTe-rich germanium antimony tellurides (GST materials) is partially retained in metastable states obtained by quenching of bulk samples. We focus on compositions such as $\text{Ge}_{0.7}\text{Sb}_{0.2}\text{Te}$ and $\text{Ge}_{0.8}\text{Sb}_{0.13}\text{Te}$, which are important materials for Blu-ray disks. Bulk samples allow a detailed structural characterization. The structure of a multiply twinned crystal isolated from such material has been determined from x-ray diffraction data ($\text{Ge}_{0.7}\text{Sb}_{0.2}\text{Te}$, $R3m$, $a=4.237 \text{ \AA}$, $c=10.29 \text{ \AA}$). Although the metrics is close to cubic, the crystal structure is rhombohedral and approximates a layered GeTe-type atom arrangement. High-resolution transmission electron microscopy (HRTEM) on quenched samples of $\text{Ge}_{0.8}\text{Sb}_{0.13}\text{Te}$ reveal nanoscale twin domains. Cation defects form planar domain boundaries. The metastability of the samples was proved by *in situ* temperature-dependent powder diffraction experiments, which upon heating show a slow phase transition to a trigonal layered structure at ca. 325 °C. HRTEM of samples annealed at 400 °C shows extended defect layers that lead to larger domains of one orientation which can be described as a one-dimensionally disordered long-periodical-layered structure. The stable cubic high-temperature modification is formed at about 475 °C. Powder diffraction on samples of $\text{Ge}_{0.8}\text{Sb}_{0.13}\text{Te}$ with defined particle sizes reveal that the formation of the stable superstructure phase is influenced by stress and strain induced by the twinning and volume change due to the cubic \rightarrow rhombohedral

phase transition upon quenching. The associated peak broadening is larger for small crystallites that allow relaxation more readily. Consequently, the degree of rhombohedral distortion as well as the appearance of superstructure reflections upon annealing is more pronounced for small crystallites. The same is true for samples which were slowly cooled from 500 °C. Hence, the lattice distortion accompanying the phase transition toward a stable trigonal superstructure is, to a certain degree, inhibited in larger crystallites. This kinetic stabilization of metastable states by stress effects is probably relevant for GST phase-change materials.

Copyright: © 2010 by the American Physical Society

5.2.1 Introduction

Rapid data storage using phase-change recording media and nonvolatile random-access memory is a key technology. The phase-change materials (PCMs) involved have to meet the basic requirement that a reversible phase transition between two structurally different phases is related to a change in physical properties.^[1–4] For all materials under development, this phase change is based on the transition between amorphous phases and metastable crystalline phases with simple average structures.^[5,6] The metastability of the phases that contribute to the write-erase cycle is essential in order to reversibly induce the phase change that allows to code information in solid state. According to the phase diagrams, all materials that are currently used exhibit corresponding thermodynamically stable states, either as additional modifications or involving phase separation.^[7–10] The stable compounds do not contribute to the data-storage process but present an energetical minimum which is disadvantageous for the phase-change behavior. Since they must be avoided, it is essential that the kinetic stabilization of metastable phases periods. On the other hand, they must allow for fast phase change. Numerous investigations have attempted to elucidate the mechanism of the transition used for data storage,^[11–14] however, it remains unclear why the systems under investigation do not reach the thermodynamic equilibrium during their application.

Most studies have focused on alloys in the system Ge-Sb-Te (GST materials).^[15] Concerning many analytical methods, it is a drawback that the metastable phases are not easily accessible by solid-state synthesis, but mostly have to be prepared as thin films, e.g., by magnetron sputtering. The crystalline phases in the system Ge-Sb-Te can be classified according to their structures. A rocksalt-type (B1) lattice with Te atoms occupying the anion site and Ge/Sb sharing the cation site has been reported for metastable crystalline phases occurring in the phase-change cycle.^[3,16,17] Their composition generally lies on or very close to the pseudobinary section GeTe-Sb₂Te₃ in the ternary phase diagram, where normal valence compounds are located. Thus, a varying content of cation vacancies is intrinsic as there are more Te atoms than Ge and Sb atoms in this AB structure. The vacancy distribution has been discussed in detail.^[3,11,16,18,19] A statistical distribution as well as partial defect ordering two-dimensional arrays have been reported based on DFT calculations.^[17,20,21] For both models, local distortions accompany the vacancies.

For GeTe-rich samples obtained by scraping off thin films produced by sputtering, it has recently been shown that the metastable “cubic” B1-type phases, in fact, exhibit a slight rhombohedral distortion.^[22] Comparable to pure GeTe,^[23] a stable undistorted cubic high-temperature

modification does exist; the transition temperature between the rhombohedral and the cubic phases increases with rising GeTe content. Furthermore, a B1-type crystalline phase Ge_4SbTe_5 ($=\text{Ge}_{0.8}\text{Sb}_{0.2}\text{Te}$), has been described,^[15,24–26] this composition point slightly deviates from the compositions corresponding to the pseudobinary GeTe-Sb₂Te₃ line.

However, at low temperatures these modifications are metastable: reaching the thermodynamic equilibrium involves phase separation. For example, annealing the metastable phase $\text{Ge}_8\text{Sb}_2\text{Te}_{11}$ (GeTe:Sb₂Te₃=8:1) leads to separation into GeTe and a phase with composition $\text{Ge}_6\text{Sb}_2\text{Te}_9$ (GeTe:Sb₂Te₃=6:1), which, under these conditions, is probably the ternary phase with the lowest Sb content.^[22] It exhibits a long periodically ordered structure which is representative for a range of phases $(\text{GeTe})_n(\text{Sb}_2\text{Te}_3)_m(\text{Sb}_2)_k$. These ordered compounds can exhibit surprisingly large translation periods. They include homologous series of antimony-rich antimony tellurides ($n=0$) (Refs. 27–29) and stable compounds with $k=0$ that contain rigid rocksalt-like building blocks of alternating Te and Ge/Sb layers.^[28,30,31] For $n, m, k \neq 0$, the latter are separated by additional antimony layers.^[32] These phases are accessible as bulk material, however, the long-range ordering of the building blocks can be limited and both stacking disorder as well as varying site occupancies have been described.^[31,33,34] These effects probably depend on the exact composition and thermal treatment.

Although frequently disordered, the thermodynamically stable phases contain distorted rocksalt-type slabs rather similar to metastable crystalline phase-change materials and exhibit a similar chemical composition. However, PCMs fortunately do not adopt the thermodynamically stable structures during write-erase cycles. The present study on GeTe-rich bulk samples emphasizes the role of microstrain regarding the inhibition of the cubic-to-rhombohedral phase transition. Mechanical stress as a consequence of the phase transitions influences the kinetics, impedes long-range ordering, and may be important in phase change devices as well.

5.2.2 Experimental details

5.2.2.1 Synthesis

Bulk samples of $\text{Ge}_{0.8}\text{Sb}_{0.2}\text{Te}$ ($=\text{Ge}_4\text{SbTe}_5$, $\text{GeTe}:\text{Sb}_2\text{Te}_3:\text{Sb}_2 = 24:2:1$), $\text{Ge}_{0.7}\text{Sb}_{0.2}\text{Te}$ ($\text{GeTe}:\text{Sb}_2\text{Te}_3 = 7:1$), and $\text{Ge}_{0.8}\text{Sb}_{0.13}\text{Te}$ ($\text{GeTe}:\text{Sb}_2\text{Te}_3 = 12:1$) were prepared by melting stoichiometric amounts of the pure elements Ge (99.999%, Sigma Aldrich), Sb (99.999%, Smart Elements), and Te (99.999%, Alfa Aesar) in sealed silica glass ampoules under argon atmosphere at 950 °C (~2 h). After quenching to room temperature in water, the samples were annealed at 500 °C ($\text{Ge}_{0.8}\text{Sb}_{0.13}\text{Te}$) or 550 °C ($\text{Ge}_{0.8}\text{Sb}_{0.2}\text{Te}$, $\text{Ge}_{0.7}\text{Sb}_{0.2}\text{Te}$) for 20 h in a tube furnace and quenched in water again. Some samples of $\text{Ge}_{0.8}\text{Sb}_{0.13}\text{Te}$ were ground and separated into fractions with different grain sizes by sieving and subsequently annealed under Ar as described below. These samples were not ground again after annealing and no sintering was observed.

5.2.2.2 Scanning electron microscopy and chemical analysis

Images of the samples were recorded using JSM-6500F (Jeol, USA) scanning electron microscope (SEM) equipped with an energy-dispersive x-ray (EDX) detector (model 7418, Oxford Instruments, Great Britain). The composition of the bulk samples was confirmed by EDX spectroscopy. All analyses of $\text{Ge}_{0.7}\text{Sb}_{0.2}\text{Te}$ and $\text{Ge}_{0.8}\text{Sb}_{0.13}\text{Te}$ corresponded to the stoichiometry of the weighted sample within an error limit of 2–4 at. %. For the analysis of the single crystal from a heterogeneous sample with the nominal composition $\text{Ge}_{0.8}\text{Sb}_{0.2}\text{Te}$ (see below), three-point measurements were averaged.

5.2.2.3 X-ray diffraction

X-ray powder patterns were recorded on a Huber G670 Guinier camera equipped with a fixed imaging plate and integrated read-out system using $\text{Cu } K\alpha_1$ radiation (Ge monochromator, $\lambda=1.54051 \text{ \AA}$) in Guinier geometry. Specimens were prepared by fixing powdered specimens on Mylar foils using silicone grease. Lattice parameters were determined by pattern fitting (Rietveld method) using the program TOPAS.^[35] Temperature-dependent powder diffraction experiments were done on a STOE Stadi P powder diffractometer equipped with an imaging plate system using $\text{Mo } K\alpha_1$ radiation (Ge monochromator, $\lambda=0.71093 \text{ \AA}$) in Debye-Scherrer geometry. Powdered specimens were filled into silica glass capillaries with 0.3 mm diameter and sealed

with silicone grease under argon atmosphere. During measurement the samples were heated up to 600 °C in a graphite furnace and then cooled to room temperature.

Irregularly shaped crystals obtained by crushing a quenched sample of Ge₄SbTe₅ were checked for quality by Laue photographs on a Buerger precession camera after mounting them on glass fibers. Intensity data were collected on a Nonius-Kappa CCD diffractometer using Mo *K* α radiation (graded multilayer x-ray optics, $\lambda=0.71093$ Å). Semiempirical absorption corrections based on equivalent reflections^[36] were applied before structure refinements with SHELX.^[37] Details concerning the data collection and refinement are summarized in Tables 1 and 2.^[38]

Table 1. Crystal data and refinement details for Ge_{0.7}Sb_{0.2}Te.

formula	Ge _{0.7} Sb _{0.2} Te
molar mass in g mol ⁻¹	204.7 g/mol
crystal system	Trigonal
space group	<i>R3m</i>
cell parameters in Å	$a = 4.237(3), c = 10.29(1)$
cell volume in Å ³	160.0(2)
formula units / cell	3
X-ray density in g cm ⁻³	6.314
abs. coefficient in mm ⁻¹	25.60
<i>F</i> (000)	253.8
crystal size in mm ³	0.03 x 0.03 x 0.02
diffractometer	Nonius Kappa-CCD
radiation, monochromation	Mo-K α ($\lambda = 0.71073$ Å), graded multilayer X-ray optics
temperature in K	293(2)
2 θ range in deg	11.8 – 66.3
total no. of reflections	2240
independent / observed reflections	99 / 97
refined parameters	12
GOF	1.090
<i>R</i> values [$I > 2\sigma(I)$]	$R1 = 0.0319, wR2 = 0.0750$
all data	$R1 = 0.0329, wR2 = 0.0764$
max./min. residual electron density in e Å ⁻³	1.085 / -1.567

Table 2. Atom coordinates, occupation factors, and displacement factors (in Å²) Ge_{0.7}Sb_{0.2}Te.

Atom	Wyckof f site	<i>x = y</i>	<i>z</i>	<i>f.o.f.</i>	<i>U</i> _{eq}	<i>U</i> ₁₁ = <i>U</i> ₂₂	<i>U</i> ₃₃	<i>U</i> ₂₃ = <i>U</i> ₁₃	<i>U</i> ₁₂ = ½ <i>U</i> ₁₁
Ge/Sb	3 <i>a</i>	0	0.4808(3)	Ge 0.70 Sb 0.20	0.0221(7)	0.0214(11)	0.024(2)	0	0.0107(5)
Te	3 <i>a</i>	0	0	1	0.0290(4)	0.0284(8)	0.0302(18)	0	0.0142(4)

5.2.2.4 Transmission electron microscopy

The samples were finely dispersed in ethyl alcohol suspension and subsequently dispersed on copper grids coated with holey carbon film. The grids were mounted on a double tilt holder with a maximum tilt angle of 30°. Selected-area electron diffraction (SAED) and high-resolution transmission electron microscopy (HRTEM) were carried out on a FEI Titan 80-300 equipped with a field emission gun operating at 300 kV. The images were recorded using a Gatan UltraScan 1000 (2k x 2k) camera.

5.2.3 Results and discussion

5.2.3.1 Electroneutrality and phase separation

According to literature,^[24–26] a cubic B1-type phase $\text{Ge}_{0.8}\text{Sb}_{0.2}\text{Te}$ ($=\text{Ge}_4\text{SbTe}_5$, $\text{GeTe}:\text{Sb}_2\text{Te}_3:\text{Sb}_2 = 24:2:1$) can be obtained as bulk material. However, we were not able to obtain single-phase samples with this composition. Instead, x-ray powder diffraction patterns of various both quenched and annealed samples always indicated formation of elemental Ge in the samples. Optical microscopy on polished samples shows dark spots due to Ge precipitation. In contrast to thin-film samples, where a B1-type material without cation vacancies has been reported with anion to cation ratio^[1,24–26] our results are in accordance with the ternary phase diagram. Metastable phases are, of course, not well described by phase diagrams, however, the latter indicate the precipitation of Ge, which can be explained regarding the charge Sb^{III} , and $\text{Te}^{-\text{II}}$. For $\text{Ge}_{0.8}\text{Sb}_{0.2}\text{Te}$, the charge balance between anions (–2) and cations (average charge +2.2) does not correspond to a valence compound whereas all stable phases on the pseudobinary section $(\text{GeTe})_n(\text{Sb}_2\text{Te}_3)_m$ are valence compounds per definition. Hence, the electron count suggests that $\text{Ge}_{0.8}\text{Sb}_{0.2}\text{Te}$ is expected to be metastable against phase separation. Electroneutrality can, in principle, be achieved by precipitation of either Ge or Sb. The Ge precipitation observed is easy to detect as Ge crystallizes in a cubic diamond type ($F\bar{d}\bar{3}m$) which does not allow coherent intergrowth. In contrast, spinodal Sb exsolution might be kinetically favored (but has not been observed for this composition) because its layerlike gray arsenic-type structure ($A7$, $R\bar{3}m$) is closely related to the structure of stable trigonal germanium antimony tellurides. The similar metrics perpendicular to the rhombohedral axis (differences < 2%) allows coherent intergrowth that may even lead to new long-range ordered intergrowth phases, especially for higher Sb contents as in $\text{Ge}_{1.57}\text{Sb}_{2.43}\text{Te}_5\text{Sb}_8$.^[32]

From these considerations, single-phase samples require at least a composition on the pseudobinary section $\text{GeTe}-\text{Sb}_2\text{Te}_3$, e.g., $\text{Ge}_{0.7}\text{Sb}_{0.2}\text{Te}$ ($\text{GeTe}:\text{Sb}_2\text{Te}_3 = 7:1$) and $\text{Ge}_{0.8}\text{Sb}_{0.13}\text{Te}$

(GeTe:Sb₂Te₃ = 12:1). In any case, thermal treatment of these samples does not lead to the formation of Sb or Ge but rather to separation into interrelated ordered compounds on the mentioned line. However, in a (pseudo)cubic B1 structure, the Sb content of these phases leads to cation vacancies (Ge_{1-x}Sb_{2x/3}V_{x/3}Te).

5.2.3.2 Average crystal structure of the quenched samples

Quenched bulk samples with the composition Ge_{0.8}Sb_{0.2}Te (=Ge₄SbTe₅, GeTe:Sb₂Te₃:Sb₂ = 24:2:1) contain precipitated Ge (as mentioned above), however, small single crystals of a ternary phase can be isolated from the ingots. To confirm the average structure of the (pseudo)cubic phase we performed single-crystal diffraction experiments on such metastable single crystals. EDX spectroscopy yields a composition Ge_{0.71(1)}Sb_{0.195(10)}Te which corresponds very well to an electroneutral formula Ge_{0.7}Sb_{0.2}Te and indicates phase separation according to Ge_{0.8}Sb_{0.2}Te → Ge_{0.7}Sb_{0.2}Te + 0.1 Ge. At first sight, the average structure of Ge_{0.7}Sb_{0.2}Te is a B1 rocksalt type with a lattice constant of $a_c = 5.991(1)$ Å (the subscript c denotes the cubic setting). Since such compounds can be regarded as a Sb-doped variant of GeTe, a rhombohedral structure model has been suggested for the related phase Ge₈Sb₂Te₁₁=Ge_{0.72}Sb_{0.18}Te (Ref. 22) in analogy to the displacive phase transition between β and α GeTe (Ref. 23), which involves a symmetry reduction from $Fm\bar{3}m$ to $R3m$. A simple distortion of the cF lattice along $\langle 111 \rangle_c$ yields a centrosymmetric hR lattice. In single crystals, such a *translationengleiche* group-subgroup relationship of index 4 ($t4$) usually involves fourfold twinning. The formation of a polar layered GeTe-type structure requires further symmetry reduction from $R\bar{3}m$ to $R3m$ ($t2$), leading to additional inversion twinning. Both $R\bar{3}m$ and $R3m$ contain two independent atom positions corresponding to the anion (Te) and cation (Ge+Sb+vacancies) sublattices, respectively. Whereas the deviation from the cubic metrics is relatively small, the trigonal symmetry of twin domains and their relative orientation are quite obvious in SEM images of fragments from the ingot as shown in Fig. 1.

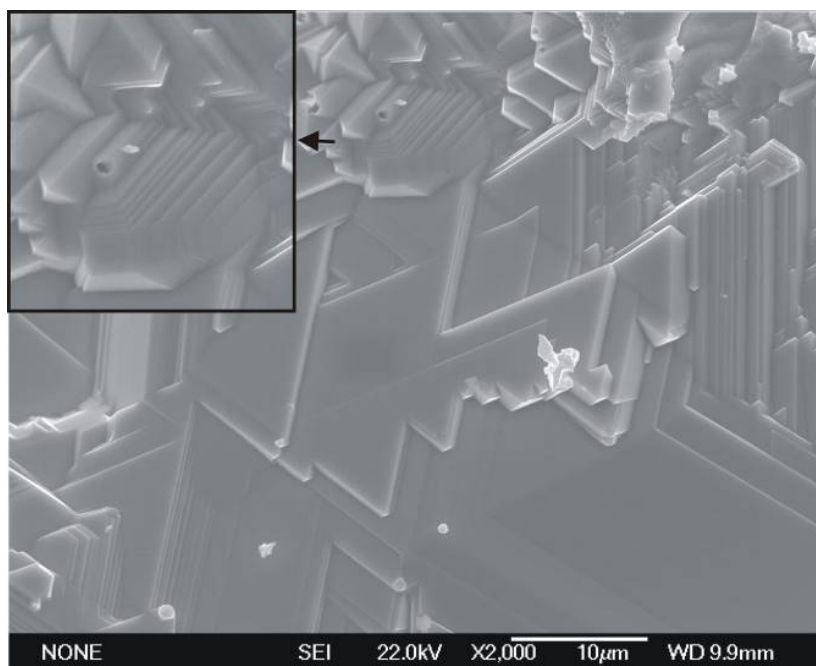


Figure 1. SEM image of a fragment of an ingot with the composition $\text{Ge}_{0.7}\text{Sb}_{0.2}\text{Te}$; the trigonal morphology of plate-shaped domains and their multiple twinning to form pseudocubic arrangements (see magnified inset) is easily seen.

Structure refinements have been performed using different models in space groups $Fm\bar{3}m$, $R\bar{3}m$, and $R3m$, respectively. In order to comply with the cubic Laue symmetry of the diffraction data as well as with group-subgroup relationships, fourfold pseudomerohedral twinning for the rhombohedral models must be considered. The relative volume fractions of the four domains refined to 0.241(4):0.251(4):0.265(4):0.243(4). Additional inversion twinning in the case of $R3m$ could not be taken into account as refinements became unstable, however, Flack parameters indicate that inversion twinning is present. In preliminary refinements, full Ge/Sb occupancy has been assumed for cation as well as anion positions for better comparison of different models. Although at first glance the refinement assuming a B1-type rocksalt structure seems satisfactory [$Fm\bar{3}m$, 38 independent data, 3 parameters; $R1(\text{all})=0.062$], symmetry reduction and accounting for twinning improve the residuals significantly [$R\bar{3}m$: 99 independent data, 8 parameters, $R1(\text{all})=0.045$; $R3m$: 99 independent data (Friedel pairs averaged), 11 parameters, $R1(\text{all})=0.033$]. Although the final model in $R3m$ has more parameters, the improvement of the data fit is statistically significant. This result confirms the reasonable assumption of a GeTe-type structure. If the Ge and Sb fractions on the cation site are refined with the constraint of total charge neutrality [$2 \text{ sof}(\text{Ge}) + 3 \text{ sof}(\text{Sb}) = 2 \text{ sof}(\text{Te})$], the resulting composition is $\text{Ge}_{0.689(1)}\text{Sb}_{0.207(1)}\text{Te}$. This is consistent with the EDX result, however, in combination with the twin fractions the refinement requires strong damping. Therefore, the slightly idealized composition $\text{Ge}_{0.7}\text{Sb}_{0.2}\text{Te}$ was fixed in the final refinement. As the metrical rhombohedral

distortion cannot be quantified from a twinned crystal (which apparently exhibits the cubic metrics), the lattice parameters used for the calculation of interatomic distances and angles were determined from powder data (see below). Crystallographic details are given in Table 1, atom positions, site occupancies, and displacement parameters are given in Table 2.

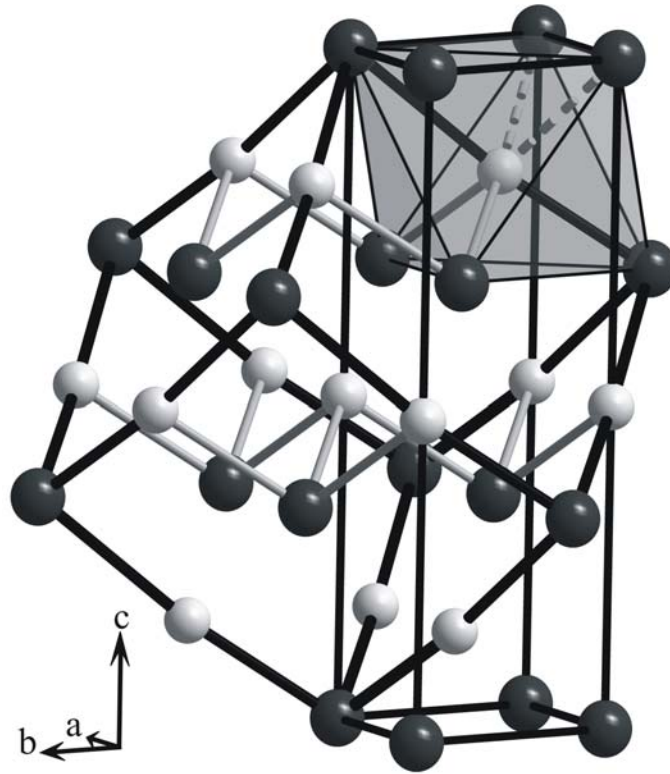


Figure 2. Representation of the crystal structure of quenched $\text{Ge}_{0.7}\text{Sb}_{0.2}\text{Te}$ (white spheres: cation position with Ge, Sb and vacancy occupation, dark spheres: Te): both the rhombohedral (hexagonal setting, upright) and the pseudocubic rocksalt-type unit cells are outlined, GeTe-type layers are indicated by interconnection of the atoms with the shortest interatomic distances, some of the longer interatomic distances are also indicated (gray fragmented “bonds” that highlight the pseudo-octahedral coordination of the cations).

In the final GeTe-type structure model (cf. Fig. 2), the coordination octahedron around Ge/Sb is distorted, resulting in three short distances Ge/Sb-Te [$2.879(2)$ Å] and three long distances Ge/Sb-Te [$3.105(2)$ Å] with angles Te-Ge/ Sb-Te of $94.76(7)^\circ$ and $86.05(7)^\circ$ at the cation. Thus, the structural deviation from the B1-type is much larger than the deviation from the cubic metrics. The distances and angles correspond well to the values for $\text{Ge}_8\text{Sb}_2\text{Te}_{11}$ ($R3m$, $a_h=4.203$ Å, $c_h=10.458$ Å at 92 K; the subscript h denotes hexagonal setting) that were obtained by Rietveld refinement on powder data (distances Ge/Sb-Te: 2.883 and 3.101 Å, angles Te-Ge/Sb-Te: 93.6° and 85.3°).^[22]

5.2.3.3 *In situ* temperature-dependent powder diffraction study

The powder patterns of quenched GeTe-rich phases with electroneutral compositions such as $\text{Ge}_{0.7}\text{Sb}_{0.2}\text{Te}$ and $\text{Ge}_{0.8}\text{Sb}_{0.13}\text{Te}$ indicate single-phase products with pseudocubic metrics consistent with the single-crystal experiment, the ac lattice parameter being approximately 5.99 Å, corresponding to $a_h \approx 4.235$ Å and $c_h \approx 10.37$ Å (again, the indices c and h indicate cubic and hexagonal setting, respectively). The slight rhombohedral distortion along $[111]_c$ is manifested in the anisotropic peak broadening of the pseudocubic reflections (see below). It corresponds to approximate rhombohedral lattice parameters $a_h = 4.237$ Å and $c_h = 10.29$ Å for $\text{Ge}_{0.7}\text{Sb}_{0.2}\text{Te}$ and $a_h = 4.237$ Å and $c_h = 10.36$ Å for $\text{Ge}_{0.8}\text{Sb}_{0.13}\text{Te}$ (for comparison: GeTe :^[23] $a_h = 4.164$ Å and $c_h = 10.692$ Å). *In situ* temperature-dependent powder diffraction experiments prove that this structural state is metastable. The kinetic stabilization of the pseudocubic phase is more pronounced for $\text{Ge}_{0.8}\text{Sb}_{0.13}\text{Te}$ (cf. Fig. 3), therefore we chose this sample for a detailed investigation. Upon heating, structural changes are observed as reported earlier.^[22] The anisotropically broadened reflections of $\text{Ge}_{0.8}\text{Sb}_{0.13}\text{Te}$ split into the typical strong reflections corresponding to a clearly rhombohedral GeTe-type pattern at approximately 325 °C. As detailed below, this is the average structure of a disordered superstructure phase that includes blocks of various GeTe-rich compounds $(\text{GeTe})_n(\text{Sb}_2\text{Te}_3)$. Clearly visible superstructure reflections are not expected as no long-time annealing has been applied. A second phase transition to a phase with regular cubic metrics occurs at about 475 °C. Peak integrals of this cubic high-temperature phase and the quenched (pseudo)cubic phase correspond well, but the absence of anisotropic broadening indicates a genuine stable rocksalt-type phase at high temperatures. Upon slow cooling of the sample to room temperature, the more or less disordered block structure with pronounced rhombohedral distortion is obtained instead of a (pseudo)cubic state. Weak additional reflections of a phase very similar to GeTe were sometimes observed.

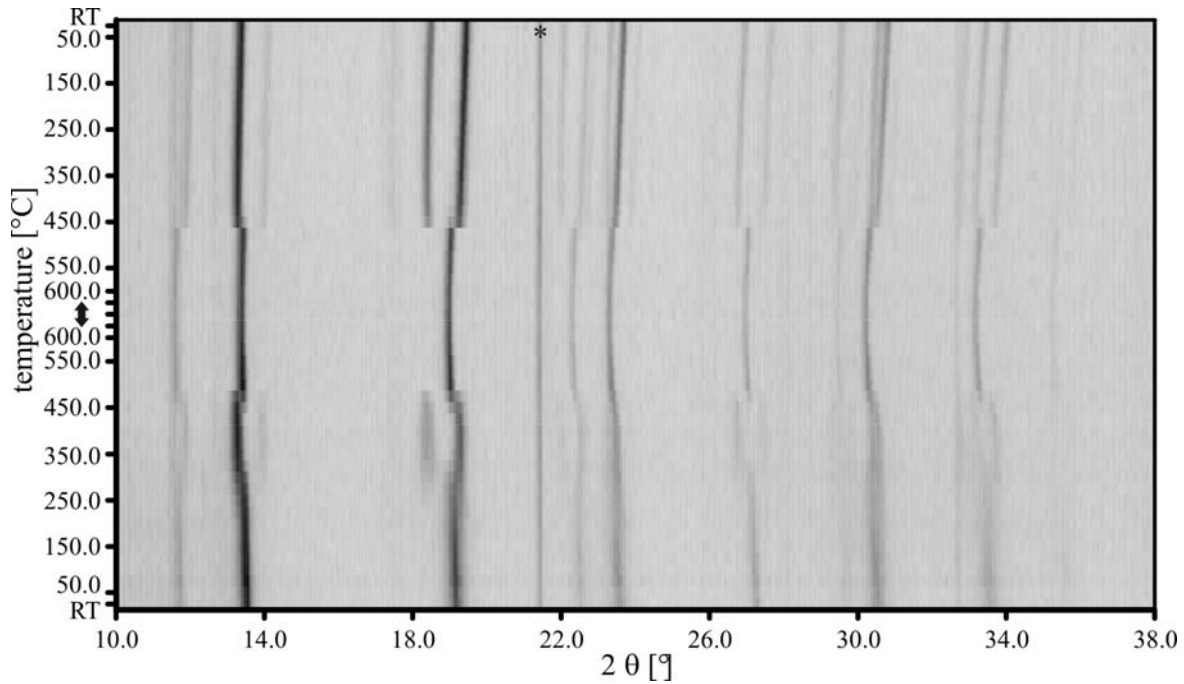


Figure 3. Temperature programmed powder diffraction experiment (Mo- $K_{\alpha 1}$ radiation) of a quenched sample $\text{Ge}_{0.8}\text{Sb}_{0.13}\text{Te}$ (from bottom to top, heating and cooling ramp $5\text{ }^{\circ}\text{C}/\text{min}$). At $600\text{ }^{\circ}\text{C}$, several patterns were recorded and later added to obtain more precise lattice parameters of the high-temperature phase (see Supplementary Material). One reflection from the furnace material is indicated by an asterisk.

5.2.3.4 Transmission electron microscopy

HRTEM images of a $\text{Ge}_{0.8}\text{Sb}_{0.13}\text{Te}$ specimen quenched from $500\text{ }^{\circ}\text{C}$ show a disordered domain structure with parquet-like appearance (cf. Fig. 4, top). It can be interpreted in terms of planar defects, and similar effects have been reported for copper gallium chalcogenides.^[39] From the structures of the corresponding stable phases as well as from theoretical calculations^[7,17,28,33,34,40-42] it seems obvious that cation vacancies tend to arrange as planar defect layers accompanied by local distortions in the crystal structure. In fact, the van der Waals gaps between the rocksalt-type blocks in $(\text{GeTe})_n(\text{Sb}_2\text{Te}_3)$ phases can be viewed as defect layers, if the shift between adjacent Te atom layers is considered as a relaxation. The partial cation defect ordering in $\text{Ge}_{0.8}\text{Sb}_{0.13}\text{Te}$ extends in planes $\{\{111\}_c$, i.e., parallel to the single hexagonal atom layers of the cubic ABC stacking sequence. Interpenetrating nanodomains with different orientations inhibit long-periodic ordering of the layer faults and on average, the resulting disordered structure maintains cubic metrics (see below). The domains are much smaller than in $\text{Ge}_{0.7}\text{Sb}_{0.2}\text{Te}$ (cf. Fig. 2), and crystals of $\text{Ge}_{0.8}\text{Sb}_{0.13}\text{Te}$ would not be suitable for twin refinements as the x-rays' length of coherence exceeds the domain size. Therefore, the elementary mesh of the $h\bar{h}l_c$ electron diffraction pattern (cf. Fig. 5, bottom) exhibits no significant deviation from the expected $1/\sqrt{2}$ lattice parameter ratio. The elongation of the Bragg maxima along $\langle 111 \rangle$ can be

attributed to local rhombohedral distortion. The statistical distribution of the planar defects leads to diffuse lines interconnecting the Bragg intensities along $\langle 111 \rangle$, consistent with the Fourier transform of the HRTEM image.

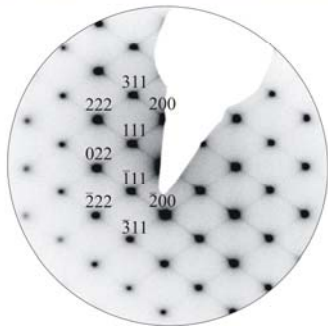
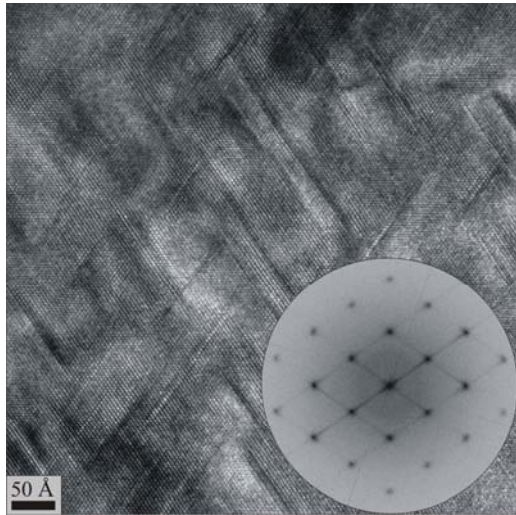


Figure 4. HRTEM image of a $\text{Ge}_{0.8}\text{Sb}_{0.13}\text{Te}$ specimen as quenched from 500°C (top, inset: Fourier transform) and the corresponding SAED pattern (bottom, indices of some Bragg positions are given).

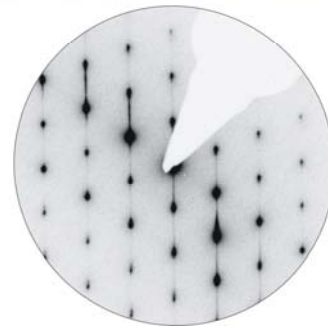
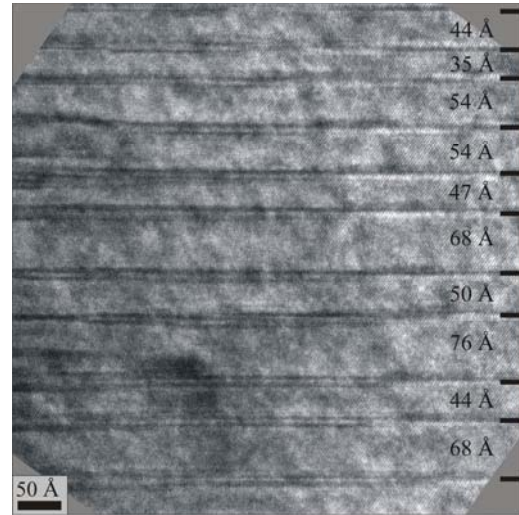


Figure 5. HRTEM image of a $\text{Ge}_{0.8}\text{Sb}_{0.13}\text{Te}$ specimen annealed at 400°C for 20h and subsequently quenched (top, the spacings of cation defect layers are indicated, they yield an average of 54 \AA) and the corresponding SAED pattern (bottom).

After further annealing of the samples previously quenched from 500°C (stability region of the cubic high-temperature phase) at 400°C (below the transition temperature to the cubic high-temperature modification) for 20 h, the planar defects adopt a strongly preferred orientation perpendicular to the $[001]_h$ direction of a rhombohedral GeTe-type unit cell (cf. Fig. 5, $[001]_h$ corresponds to one of the $\langle 111 \rangle_c$ directions, h and c indicate hexagonal and cubic setting, respectively). The defect layers appear as rather broad lines as the relaxation around them continues into several atom layers of the rocksalt-type slabs. As measured in HRTEM images, the average distance between the defect layers is about 54 \AA , but in contrast to a well-defined superstructure they are not arranged periodically and their distance varies up to 30 \AA around the

average value. Similar one-dimensional disorder has been reported, for example, for the phases GeSb_2Te_4 , $\text{Ge}_2\text{Sb}_2\text{Te}_5$, or $\text{Ge}_3\text{Sb}_2\text{Te}_{6.33}$,^[34] Consequently, the SAED patterns show diffuse streaks along c_h^* . An idealized hypothetical superstructure corresponding to the given composition can be derived by homology principles as described in detail in the literature.^[28,31] The number of cation defects and thus the frequency of van der Waals gaps depends on the Sb content and, in this case, leads to rather thick rocksalt-type slabs. For the composition $\text{Ge}_{0.8}\text{Sb}_{0.13}\text{Te}=(\text{GeTe})_{12}(\text{Sb}_2\text{Te}_3)$, an $87R$ type with a c_h lattice constant of approximately 165.3 Å is expected as the average thickness for two-dimensional hexagonal atom layers in these long periodically ordered structures is about 1.9 Å. In such an $87R$ -type structure, one c_h translation period contains three rocksalt-type slabs comprising 29 atom layers each. Consequently, the distance between the van der Waals gaps, i.e., the cation defect layers, is expected to be 55.1 Å. This agrees well with the experimentally determined average value, although this is just an approximation as a certain degree of GeTe exsolution cannot be excluded.

5.2.3.5 Influence of the powder-particle size on the establishment of the rhombohedral distortion

The transformation between the quenched pseudocubic state and the rhombohedral superstructure phase depends on time and temperature. The pseudocubic state itself differs from the cubic high-temperature phase by the formation of a GeTe-type structural distortion and by formation of the planar defect layers $\{111\}_c$, which both can be expected to drive a rhombohedral distortion of the lattice metrics. However, the formation of the rhombohedrally distorted GeTe-type state is realized in twin domains differing by the orientation of the $[001]_h$ direction corresponding to different $\langle 111 \rangle_c$ directions. In this state, the planar defect layers are aligned perpendicular $[001]_h$ of the corresponding rhombohedral domain. Within the small-domain-sized microstructure, each domain is hindered to establish its stress-free rhombohedrally distorted metrics (equilibrium lattice parameters), and the metrical misfit between the different domains leads to locally varying deviations from the equilibrium lattice parameters to pseudocubic ones (microstrain accompanied by microstress). Depending on the domain size and actual domain microstructure, this either leads to an incomplete rhombohedral splitting or merely to the anisotropic microstrain broadening of the reflections in a powder diffraction pattern that would be expected for a cubic phase.

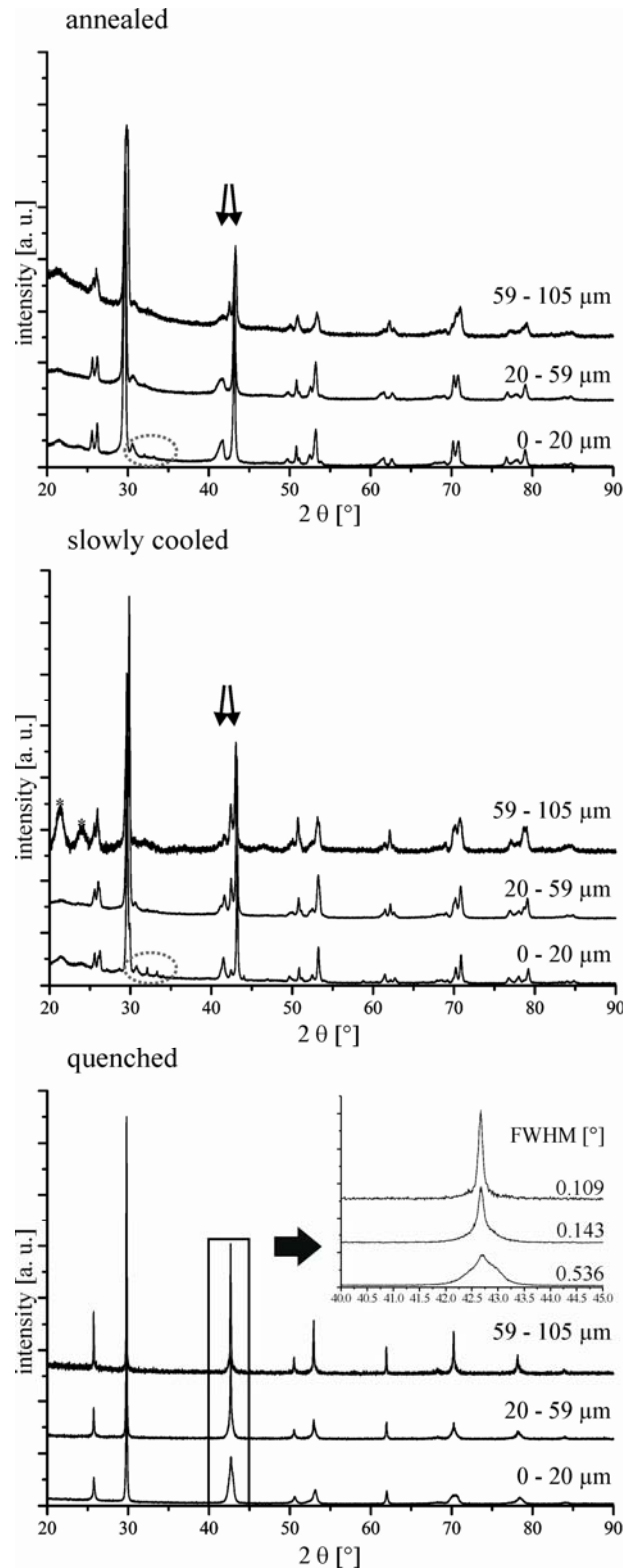


Figure 6. Powder diffraction patterns of fractions of $\text{Ge}_{0.8}\text{Sb}_{0.13}\text{Te}$ samples with grain sizes 0-20 μm , 20-59 μm and 59-105 μm : quenched from 500°C (bottom, with anisotropic peak broadening depending on the grain size, inset: 220_c reflection and its FWHM), slowly cooled from 500°C to 250°C (middle) and quenched after annealing at 400°C for 20h (top); The slowly cooled and annealed samples show rhombohedral reflection splitting (indicated by arrows for the 104_h and 110 reflections) and superstructure reflections (marked for the batches with the smallest grain sizes by dotted ellipses at an exemplary position).

Indeed the powder diffraction patterns (Fig. 6, bottom) of the quenched samples exhibit anisotropic broadening with the hhh_c (111 and 222) reflections being very broad and the $h00_c$ (200 and 400) reflections being narrowest. This anisotropy of the broadening reflects the fact that the $h00_c$ reflections do not split upon a rhombohedral distortion, whereas for hhh_c this splitting will be largest (e.g., 003_h and 101_h originating from 111_c). In the experimental pattern (Fig. 6, bottom), the broadening is highlighted for the strong 220_c reflection which formally splits into the 104_h and 110_h reflections. The order dependence of the line broadening of the hhh_c reflections in Williamson-Hall plots^[43] (not shown) clearly confirms the microstrain character of the line broadening as expected for varying d spacings in the specimen. However, a quantitative evaluation of the line broadening is complicated by coherent-diffraction effects between the small domains and by the stacking faults.^[44–46] Moreover, the planar defect layers may also lead to layer-fault-induced line broadening, however, this is apparently not large in the present case.

The free surface, which depends on the size of the powder particles, is a decisive factor concerning possible relaxation of the stresses in domains which, in turn, allows for better establishment of the rhombohedral distortion. Therefore, powder samples of $\text{Ge}_{0.8}\text{Sb}_{0.13}\text{Te}$ were separated into fractions with defined grain sizes of 0–20 μm , 20–59 μm , and 59–105 μm before they were annealed in the stability region of the cubic modification (at 500 °C) and subsequently quenched in water. No further grinding was applied; therefore, the peak shapes are not biased by grinding effects which may otherwise have a strong influence. In fact, the powder batches with the smallest particle size (which is definitely larger than the domain size, cf. Fig. 4) exhibit the largest line broadening with respect to an unbroadened cubic pattern, and are thus closest to the rhombohedral pattern (Fig. 6, bottom). Particle-size broadening can be neglected as the reflections that do not split in the rhombohedral system remain sharp.

The pseudocubic rhombohedral state with more or less pronounced microstrain broadening is kinetically stable at ambient temperature. However, upon annealing (400 °C for 20 h) the domains of the pseudocubic state coarsen and optimize their mutual arrangement. This way the stress-free rhombohedral lattice parameters are approached (similar to the observations in the course of the high-temperature powder diffraction experiments, see above). At the same time the defect-layers reorient perpendicular to the $[001]_h$ direction of the larger domains and order in a long-range fashion so that superstructure reflections appear. This occurs most readily for the smallest powder-particle-size batch, where the superstructure reflections are best visible (Fig. 6, top). Apparently, the free surfaces enhance the coarsening and the defect-layer ordering, similar to abnormal grain growth.^[47] In additional experiments, similar powder batches of $\text{Ge}_{0.8}\text{Sb}_{0.13}\text{Te}$ were slowly cooled from 500 to 250 °C and then quenched by removing them from the furnace.

The changes observed in the powder patterns of these samples are even more pronounced than for annealed samples.

In the course of the present investigations, two different ternary phases have been observed: the cubic high-temperature phase and the metastable disordered pseudocubic or clearly distorted phase with a GeTe-type basic structure. A long-range ordered phase containing periodically arranged planar defect layers would constitute a third phase that has not been observed in its ideal state. We note that the pseudocubic GeTe-type state and the rhombohedrally distorted GeTe-type state without clear indication of long-range order should be regarded as the same phase, however, with different microstructures. Indeed, the lattice parameters observable by diffraction methods are sometimes determined by the microstructure, e.g., in Pd₆B.^[48] However, it is impossible to clearly distinguish a long-range ordered phase with a certain amount of disorder from a GeTe-type phase with defect layers that does not exhibit long-range periodicity.

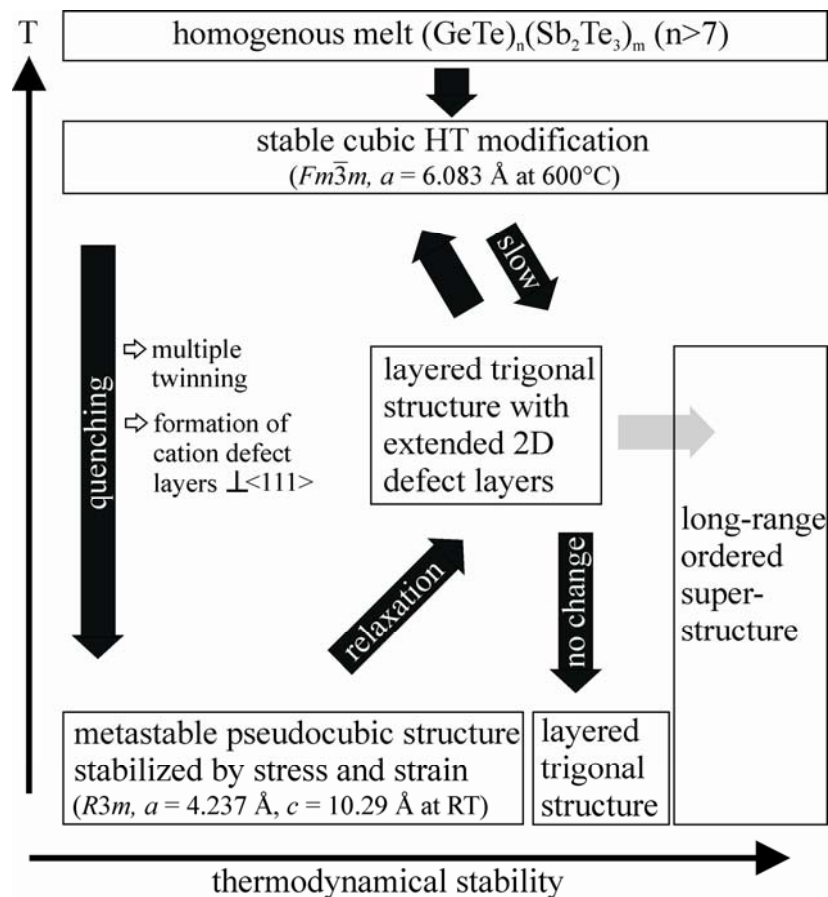


Figure 7. Phase relations and transformations between the cubic high-temperature phase, the metastable pseudocubic or rhombohedral phase, and the stable trigonal layered superstructure of GeTe-rich GST materials as observed for bulk samples.

5.2.4 Conclusions

The present study shows that bulk samples of quenched GeTe-rich GST materials exhibit phase relationships and transformations (cf. Fig. 7) between metastable states and stable trigonal phases that are very similar to those observed in thin films of phase-change materials on rewritable datastorage media.^[22] If the cubic high-temperature phase is quenched, the phase transition to a rhombohedral phase leads to twin domains, which has been shown by HRTEM as well as by the first single-crystal structure refinement of a metastable GST phase in its pseudocubic state. Temperature-dependent powder diffraction experiments have clearly revealed that in this case the formation of the stable ordered phases is inhibited by stress that arises from the formation of twin domains due to the anisotropic distortion associated with the formation of the rhombohedral phase. Thus, the realignment into areas with long-periodic parallel defect layers is hindered in large powder particles or compact bulk material, whereas the necessary relaxation occurs more readily in small powder particles. Surface effects may also play a role. Summing up, the transition kinetics is strongly affected by stress effects.

In PCM data-storage devices, only small regions of thin films are actually melted and quickly recrystallized (i.e., quenched) to code information, hence, the surrounding matrix can lead to anisotropic stress.^[49–51] Pressures during the write-erase cycle have been estimated to reach up to several gigapascal.^[52–54] A strong mechanical force, which results mainly from interactions between substrate and capping cannot be neglected within the phase-change material itself. In this context, our results show that stress and strain effects in GST phases are not only important for the write-erase cycle but also with respect to the kinetic inhibition of the formation of the stable trigonal phases. Thus, they play a decisive role in PCMs and are not only interesting with respect to adhesion between the storage layer and its surrounding. Comparable strain effects have been investigated, for example, in ferroelectric or ferroelastic materials,^[55,56] metals,^[57,58] and alloys,^[59] and shown to influence the electrical behavior of perovskites.^[60] Concerning phase-change materials, most research has concentrated on the amorphous-crystalline transitions so far. However, to understand their crystal chemistry and physics, it is also essential to take into account the transitions between metastable and stable crystalline modifications, especially since the latter involve the impetus of thermodynamics. This insight into the interplay of kinetics and thermodynamics of GST materials might also be interesting with respect to their potential thermoelectric properties.^[30] Therefore, it seems promising to further investigate this relationship.

5.2.5 References

- [1] M. Wuttig, C. Steimer, *Appl. Phys. A: Mater. Sci. Process.* **2007**, *87*, 411.
- [2] M. Wuttig, *Nature Mater.* **2005**, *4*, 265.
- [3] M. Wuttig, N. Yamada, *Nature Mater.* **2007**, *6*, 824.
- [4] A. L. Greer, N. Mathur, *Nature (London)* **2005**, *437*, 1246.
- [5] T. Matsunaga, N. Yamada, *Jpn. J. Appl. Phys., Part 1* **2002**, *41*, 1674.
- [6] T. Matsunaga, N. Yamada, *Jpn. J. Appl. Phys., Part 1* **2004**, *43*, 4704.
- [7] L. E. Shelimova, O. G. Karpinsky, P. P. Konstantinov, M. A. Kretova, E. S. Avilov, V. S. Zemskov, *Inorg. Mater.* **2001**, *37*, 342.
- [8] V. I. Kosyakov, V. A. Shestakov, L. E. Shelimova, F. A. Kuznetsov, V. S. Zemskov, *Inorg. Mater.* **2000**, *36*, 1004.
- [9] B. Legendre, C. Hancheng, S. Bordas, M. T. Clavaguera-Mora, *Thermochim. Acta* **1984**, *78*, 141.
- [10] S. Bordas, M. T. Clavaguera-Mora, B. Legendre, C. Hancheng, *Thermochim. Acta* **1986**, *107*, 239.
- [11] A. V. Kolobov, P. Fons, A. I. Frenkel, A. L. Ankudinov, J. Tominaga, T. Uruga, *Nature Mater.* **2004**, *3*, 703.
- [12] A. V. Kolobov, P. Fons, J. Tominaga, and T. Uruga, *J. Non-Cryst. Solids* **2006**, *352*, 1612.
- [13] J. Hegedüs, S. R. Elliott, *Nature Mater.* **2008**, *7*, 399.
- [14] W. Welnic, M. Wuttig, *Mater. Today* **2008**, *11*, 20.
- [15] D. Lencer, M. Salinga, B. Grabowski, T. Hickel, J. Neugebauer, M. Wuttig, *Nature Mater.* **2008**, *7*, 972.
- [16] T. Matsunaga, R. Kojima, N. Yamada, K. Kifune, Y. Kubota, Y. Tabata, M. Takata, *Inorg. Chem.* **2006**, *45*, 2235.
- [17] Z. Sun, J. Zhou, R. Ahuja, *Phys. Rev. Lett.* **2006**, *96*, 055507.
- [18] T. Matsunaga, N. Yamada, *Phys. Rev. B* **2004**, *69*, 104111.
- [19] T. Matsunaga, N. Yamada, and Y. Kubota, *Acta Crystallogr., Sect. B: Struct. Sci.* **2004**, *60*, 685.
- [20] M. Wuttig, D. Lüsebrink, D. Wamwangi, W. Welnic, M. Gilleßen, R. Dronskowski, *Nature Mater.* **2007**, *6*, 122.
- [21] Z. Sun, S. Kyrsta, D. Music, R. Ahuja, J. M. Schneider, *Solid State Commun.* **2007**, *143*, 240.

- [22] T. Matsunaga, H. Morita, R. Kojima, N. Yamada, K. Kifune, Y. Kubota, Y. Tabata, J.-J. Kim, M. Kobata, E. Ikenaga, K. Kobayashi, *J. Appl. Phys.* **2008**, *103*, 093511.
- [23] T. Chattopadhyay, J. X. Boucherle, H. G. von Schnering, *J. Phys. C* **1987**, *20*, 1431.
- [24] J. González-Hernández, E. López-Cruz, M. Yáñez-Limón, D. Strand, B. B. Chao, S. R. Ovshinsky, *Solid State Commun.* **1995**, *95*, 593.
- [25] E. Morales-Sánchez, E. F. Prokhorov, J. González-Hernández, A. Mendoza-Galván, *Thin Solid Films* **2005**, *471*, 243.
- [26] D. Wamwangi, W. K. Njoroge, M. Wuttig, *Thin Solid Films* **2002**, *408*, 310.
- [27] P. F. P. Poudeu, M. G. Kanatzidis, *Chem. Commun. (Cambridge)* **2005**, 2672.
- [28] L. E. Shelimova, O. G. Karpinsky, M. A. Kretova, V. I. Kosyakov, V. A. Shestakov, V. S. Zemskov, F. A. Kuznetsov, *Inorg. Mater.* **2000**, *36*, 768.
- [29] K. Kifune, Y. Kubota, T. Matsunaga, N. Yamada, *Acta Crystallogr., Sect. B: Struct. Sci.* **2005**, *61*, 492.
- [30] P. P. Konstantinov, L. E. Shelimova, E. S. Avilov, M. A. Kretova, V. S. Zemskov, *Inorg. Mater.* **2001**, *37*, 662.
- [31] M. N. Schneider, O. Oeckler, *Z. Anorg. Allg. Chem.* **2008**, *634*, 2557.
- [32] M. N. Schneider, M. Seibald, O. Oeckler, *Dalton Trans.* **2009**, 2004.
- [33] S. Kuypers, G. van Tendeloo, J. van Landuyt, S. Amelinckx, *J. Solid State Chem.* **1988**, *76*, 102.
- [34] B. J. Kooi, J. T. M. De Hosson, *J. Appl. Phys.* **2002**, *92*, 3584.
- [35] A. Coelho, *TOPAS-ACADEMIC*, V. 4.1, Coelho Software, Brisbane, **2007**.
- [36] G. M. Sheldrick, *SADABS*, Version 2.10, Bruker AXS Inc., Madison, Wisconsin, **2001**.
- [37] G. M. Sheldrick, *Acta Crystallogr., Sect. A: Found. Crystallogr.* **2008**, *64*, 112.
- [38] Further details may be obtained from Fachinformationszentrum Karlsruhe, 76344 Eggenstein-Leopoldshafen, Germany [fax: +49 7247-808-666; e-mail: crysdata@fiz-karlsruhe.de, http://www.fiz-karlsruhe.de/request_for_deposited_data.html] on quoting the reference number CSD-420919.
- [39] L. Kienle, V. Duppel, A. Simon, H. J. Deiseroth, *Z. Anorg. Allg. Chem.* **2003**, *629*, 1412.
- [40] B. J. Kooi, W. M. G. Groot, J. T. M. De Hosson, *J. Appl. Phys.* **2004**, *95*, 924.
- [41] Y. J. Park, J. Y. Lee, Y. T. Kim, *Appl. Surf. Sci.* **2006**, *252*, 8102.
- [42] Y. J. Park, J. Y. Lee, Y. T. Kim, *Appl. Surf. Sci.* **2006**, *253*, 714.
- [43] G. K. Williamson, W. H. Hall, *Acta Metall.* **1953**, *1*, 22.
- [44] H. Boysen, *J. Phys.: Condens. Matter* **2007**, *19*, 275206.

-
- [45] D. Rafaja, V. Klemm, G. Schreiber, M. Knapp, R. Kuzel, *J. Appl. Crystallogr.* **2004**, *37*, 613.
- [46] A. Leineweber, E. J. Mittemeijer, M. Knapp, C. Baetz, *Philos. Mag.* **2007**, *87*, 1821.
- [47] C. V. Thompson, H. J. Frost, and F. Spaepen, *Acta Metall.* **1987**, *35*, 887.
- [48] T. G. Berger, A. Leineweber, E. J. Mittemeijer, C. Sarbu, V. Duppel, P. Fischer, *Z. Kristallogr.* **2006**, *221*, 450.
- [49] A. V. Kolobov, *Nature Mater.* **2008**, *7*, 351.
- [50] I. M. Park, J. K. Jung, S. O. Ryu, K. J. Choi, B. G. Yu, Y. B. Park, S. M. Han, Y. C. Joo, *Thin Solid Films* **2008**, *517*, 848.
- [51] W. K. Njoroge, H.-W. Wöltgens, M. Wuttig, *J. Vac. Sci. Technol. A* **2002**, *20*, 230.
- [52] Q. Guo, M. H. Li, Y. Li, L. P. Shi, T. C. Chong, J. A. Kalb, C. V. Thompson, *Appl. Phys. Lett.* **2008**, *93*, 221907.
- [53] T. P. L. Pedersen, J. Kalb, W. K. Njoroge, D. Wamwangi, M. Wuttig, F. Spaepen, *Appl. Phys. Lett.* **2001**, *79*, 3597.
- [54] J. Kalb, F. Spaepen, T. P. L. Pedersen, and M. Wuttig, *J. Appl. Phys.* **2003**, *94*, 4908.
- [55] T. Lookman, S. R. Shenoy, K. Ø. Rasmussen, A. Saxena, A. R. Bishop, *Phys. Rev. B* **2003**, *67*, 024114.
- [56] L. W. Chang, M. McMillen, J. M. Gregg, *Appl. Phys. Lett.* **2009**, *94*, 212905.
- [57] B. Clausen, C. N. Tomé, D. W. Brown, S. R. Agnew, *Acta Mater.* **2008**, *56*, 2456.
- [58] Z. Budrovic, H. van Swygenhoven, P. M. Derlet, S. van Petegem, B. Schmitt, *Science* **2004**, *304*, 273.
- [59] S. A. Kibey, L. L. Wang, J. B. Liu, H. T. Johnson, H. Sehitoglu, D. D. Johnson, *Phys. Rev. B* **2009**, *79*, 214202.
- [60] K. H. Ahn, T. Lookman, A. R. Bishop, *Nature* **2004**, *428*, 401.

5.3 Real structure and thermoelectric properties of GeTe-rich germanium antimony tellurides

Tobias Rosenthal, Matthias N. Schneider, Christian Stiewe, Markus Döblinger, and Oliver Oeckler

Chemistry of Materials **2011**, *23*, 4349-4356.

Abstract

Quenched Ge-Sb-Te (GST) compounds exhibit strongly disordered metastable structures whose average structure corresponds to a distorted rocksalt type with trigonal symmetry. Depending on the composition and thermal treatment, the metrics remain more or less pseudocubic. The corresponding stable phases show regular sequences of distorted rocksalt-type blocks that formally result from layer-like cation defect ordering. These thermodynamically stable layered phases can gradually be approached by annealing the metastable (pseudo)cubic compounds that are accessible by quenching high-temperature phases. The relaxation of Te atoms in the vicinity of the defect layers leads to van der Waals gaps rather than defect layers in an undistorted matrix. The partially ordered phases obtained show defect layers with an average distance and arrangement depending on the composition and the thermal treatment of the samples. This variation of the nanostructure influences the lattice thermal conductivity (κ_L) and thus the thermoelectric figure of merit (ZT). This results in ZT values up to 1.3 at 450 °C for bulk samples of $\text{Sb}_2\text{Te}_3(\text{GeTe})_n$ ($n = 12$ and 19). The stability ranges of the various phases have been examined by temperature programmed X-ray powder diffraction and can be understood in conjunction with the changes of the nanostructure involved. The real structure of phases $\text{Sb}_2\text{Te}_3(\text{GeTe})_n$ ($n = 3-19$) has been investigated by high-resolution electron microscopy (HRTEM) and scanning transmission electron microscopy (STEM)-high-angle annular dark-field (HAADF) with respect to the stoichiometry and synthesis conditions. The correlation of the nanostructure with the thermoelectric properties opens an interesting perspective for tuning thermoelectric properties.

Keywords: GST materials; thermoelectric properties; TEM, real structure elucidation; structure-property relationships

Copyright: © 2011 American Chemical Society

5.3.1 Introduction

5.3.1.1 Tellurides as thermoelectrics

Tellurides have been the predominant materials for thermoelectric applications in the past decade. PbTe, Bi₂Te₃, and Sb₂Te₃ are well-established examples that still dominate the market.^[1] In order to secure the future energy supply, the sustainable usage of energy is becoming increasingly important.^[2] Thermoelectric materials make electric power generation from waste heat possible, e.g., in cars and airplanes, leading to lower fuel consumption. In addition, they may become increasingly popular in energy-efficient cooling and heating devices. The bottleneck for all applications is the efficiency of the transformation between heat and electric energy, which depends on the thermoelectric figure of merit (*ZT*) of the material used. At a given temperature *T*, it is defined as:

$$ZT = \frac{S^2 \sigma}{\kappa} T$$

The major problem is the interdependence of the material properties determining *ZT*. The electrical conductivity (σ) and the electronic part of the thermal conductivity (κ_e), which corresponds to heat transport by electrons, are linked by the Wiedemann-Franz law. Both properties correlate with the Seebeck coefficient (*S*), as all these properties depend on the charge carrier concentration. The phononic part of the thermal conductivity (κ_L) reflects the heat that is transported by phonons. Since it depends on various structural features, it seems to be the most promising approach to reduce κ_L by increased phonon scattering. Therefore, many new approaches rely on nanostructuring and doping. Novel element combinations, e.g., Ag/Sb/Pb/Te (LAST, *ZT* up to 2)^[3] or Ag/Ge/Sb/Te (TAGS, *ZT* up to 1.54), and structuring processes (e.g., spin-milled, ball-milled and hot pressed crystalline ingots of Bi-Sb-Te alloys with *ZT* up to 1.45) have led to drastic improvements in recent years. However, there is still an urgent need for bulk materials with high *ZT* values at various temperatures.

5.3.1.2 Sb₂Te₃(GeTe)_n as phase-change materials

For rewritable optical data storage media, GST (Ge-Sb-Te) materials have been used for more than a decade^[6,7] because the fast reversible phase change between metastable crystalline and amorphous phases can be induced in a favorable energy range. Compared to rewritable DVDs, the GeTe content has been increased for rewritable Blu-Ray discs in order to (1) optimize the bit density by enhancing the difference in reflectivity between both phases and (2) obtain higher

stability of the amorphous phase (recording marks), corresponding to a longer life cycle.^[8] The fast reversible phase change can also be induced by electric pulses, and the structural states can be identified by their different resistivity.^[9,10] As the information is preserved by structural changes, GST materials are very promising candidates for nonvolatile PC-RAM devices.^[11-14] Besides this well-known phase change between amorphous and metastable crystalline phases, GeTe-rich GST materials exhibit another phase transformation between a rocksalt-type high-temperature and a layered low-temperature modification.

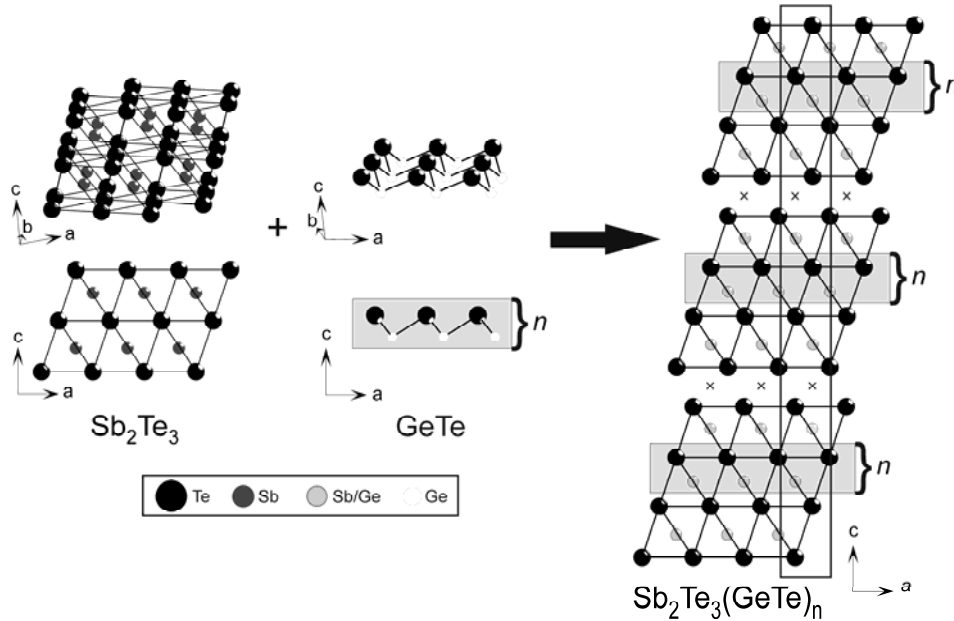


Figure 1. Tetradymite-like Sb_2Te_3 slabs (left) are formally enlarged by inserting GeTe-type layers in the blocks. The resulting structure (right) consists of distorted rocksalt-type building blocks with a thickness depending on the GeTe content n (the crosses indicate the position of the formal “vacancies” in the van der Waals gaps). For Sb_2Te_3 itself, n equals 0.

5.3.1.3 Structure and properties of $\text{Sb}_2\text{Te}_3(\text{GeTe})_n$

The structures of materials with the composition $\text{Sb}_2\text{Te}_3(\text{GeTe})_n$ can be described as a combination of tetradymite-type Sb_2Te_3 ^[15] and GeTe, a binary variant of the A7 (gray arsenic) structure type. The tetradymite-like Sb_2Te_3 blocks can formally be enlarged by inserting GeTe, resulting in the pseudobinary homologous series $\text{Sb}_2\text{Te}_3(\text{GeTe})_n$ with distorted rocksalt-type building blocks of a thickness depending on n (Figure 1). These blocks are separated by van der Waals gaps between the Te layers terminating the individual building blocks. The distance between these Te layers and the following cation layers are rather short, leading to a 3 + 3 coordination of these cations and an arrangement resembling that in GeTe itself. The Te-Te distances between adjacent building blocks are significantly shorter than the sum of the van der Waals radii and indicate partially covalent bonding. Although these trigonal, thermodynamically stable phases contain no structural vacancies, the strongly distorted octahedral voids between

these Te layers can formally be viewed as layer-like ordered cation-position “vacancies”.^[16,17] The cubic rocksalt-type high-temperature phases are highly disordered with Ge, Sb, and vacancies occupying the cation positions and Te occupying the anion positions. The vacancy concentration depends on the ratio GeTe/Sb₂Te₃ (n).^[18,19] In GeTe rich ($n > 3$) GST phase-change materials, the structure of the crucial metastable crystalline phase is similar to the high-temperature rocksalt-type phase. It is kinetically inert at ambient conditions, providing long-time data storage on rewriteable optical media.

In recent years, the thermoelectric behavior of some GST materials has been investigated.^[20] HRTEM investigations of spark plasma sintered Sb₂Ge_{0.02}Te₃ revealed a large number of randomly distributed nanodomains, coupled with a 0.3 W/mK decrease in thermal conductivity compared to pure Sb₂Te₃. Consequently, the ZT value of Sb₂Te₃ increases from 0.74 to 0.84 at 492 K when doped with small amounts of Ge.^[21] Recent investigations indicate ZT values up to 1.3 at 720 K for Ge-rich compositions ($n \sim 12$).^[22]

5.3.2 Experimental section

Bulk samples of Sb₂Te₃(GeTe) _{n} ($3 \leq n \leq 19$) were prepared by melting (950 °C, 2 h) stoichiometric amounts of the elements Ge (99.999%, Sigma Aldrich), Sb (99.999%, Smart Elements), and Te (99.999%, Alfa Aesar) in silica glass ampules sealed under Ar atmosphere. Nanostructured samples were obtained by annealing the initially quenched samples at 500-550 °C (i.e., in the stability range of the cubic high-temperature phase) for 2 days and quenching in water. The relaxed (trigonal) samples with less pronounced nanostructuring were annealed for 2 days at 400 °C and slowly cooled in the furnace (2 h). A fraction of each sample was used for electron microscopy. Ingots for thermoelectric measurements were prepared under analogous conditions in silica glass ampules with flat bottom. The ingots obtained were disk-shaped with a diameter around 15 mm and a thickness of 2-6 mm. They were polished to obtain flat discs with a constant thickness. X-ray powder diffraction patterns matched those from corresponding samples used for other investigations.

The composition of the samples was verified by energy-dispersive X-ray spectroscopy (EDX). Typical analyses deviate less than 5 atom % from values corresponding to the starting mixture. Data acquisition was done using a JSM-6500F (Jeol, Japan) scanning electron microscope equipped with an EDX detector (model 7418, Oxford Instruments, UK).

For transmission electron microscopy, samples were finely ground, dispersed in ethanol, and subsequently transferred on a copper grid coated with holey carbon film. Selected area electron diffraction (SAED) and high-resolution electron microscopy (HRTEM) were done on a

JEM2011 (Jeol Ltd., Japan) with an tungsten thermal emitter and an acceleration voltage of 200 kV equipped with a TVIPS CCD camera (model 114, resolution: 1k x 1k). Further HRTEM, SAED, EDX, and scanning transmission electron microscopy (STEM) using a high-angle annular dark-field (HAADF) detector was done on a Titan 80-300 (FEI, USA) with a field emission gun operated at 300 kV equipped with a TEMTOPS 30 EDX spectrometer (EDAX, Germany). Images were recorded on an UltraScan 1000 camera (Gatan, USA, resolution: 2k x 2k). HRTEM and SAED data were evaluated using the Digital Micrograph^[23] and EMS^[24] software; for STEM and EDX data, the program ES Vision^[25] was used.

X-ray powder diffraction (XRPD) patterns were recorded from ground samples fixed on Mylar foils using silicone grease. Data were collected on a G670 Guinier camera (Huber, Germany) equipped with a fixed imaging plate detector with an integrated read-out system using Cu K_{α1} radiation (Ge monochromator, $\lambda = 1.54051 \text{ \AA}$).

Temperature programmed XRPD patterns were collected using powdered samples filled into silica glass capillaries with a diameter of 0.3 mm and sealed with silicone grease under Ar. Data were collected using a Stadi P powder diffractometer (Stoe & Cie. GmbH, Germany) with a linear position-sensitive detector (PSD) and a graphite furnace using Mo K_{α1} radiation (Ge monochromator, $\lambda = 0.71093 \text{ \AA}$). The samples were heated from room temperature to 600 °C (10°/min) and subsequently cooled to room temperature in the same way. Data were collected every 25 °C with 10 min acquisition time. Powder patterns were analyzed with WIN^{XPOW}^[26].

Thermoelectric properties were measured up to 450 °C under vacuum using commercial and in-house-built facilities of the DLR (Cologne, Germany). The Seebeck coefficient was measured by establishing a small temperature gradient across the sample while the temperature was changed slowly and continuously. Type-R thermocouples attached directly to the sample's surface were used for both temperature measurement (T1 and T2) and Seebeck voltage (U_S) pickup via the Pt lines. The sample's Seebeck coefficient was then calculated as

$$S_{sample} = \frac{U_S}{\Delta T} - S_{Pt} \quad \Delta T = |T_2 - T_1|$$

Electrical conductivity σ was calculated from the sample's resistance R, measured using an AC method in order to reduce Peltier influences and a four-point-probe setup to avoid cable and contact resistances affecting the measurement. When the cross-section A of the sample and the distance l of the probe tips are taken into account, the electrical conductivity follows as $\sigma = l/A R$. Thermal conductivity κ was calculated from measurements of the thermal diffusivity D_{th} using a laser-flash apparatus (LFA 427, Netzsch GmbH & Co., Germany), the heat capacity c_p in a differential scanning calorimeter (DSC 404, Netzsch GmbH & Co., Germany), and the density ρ using a Mohr's balance: $\kappa = D_{th} \cdot \rho \cdot c_p$.

5.3.3 Results and discussion

5.3.3.1 Stability of the phases $\text{Sb}_2\text{Te}_3(\text{GeTe})_n$ ($3 \leq n \leq 17$)

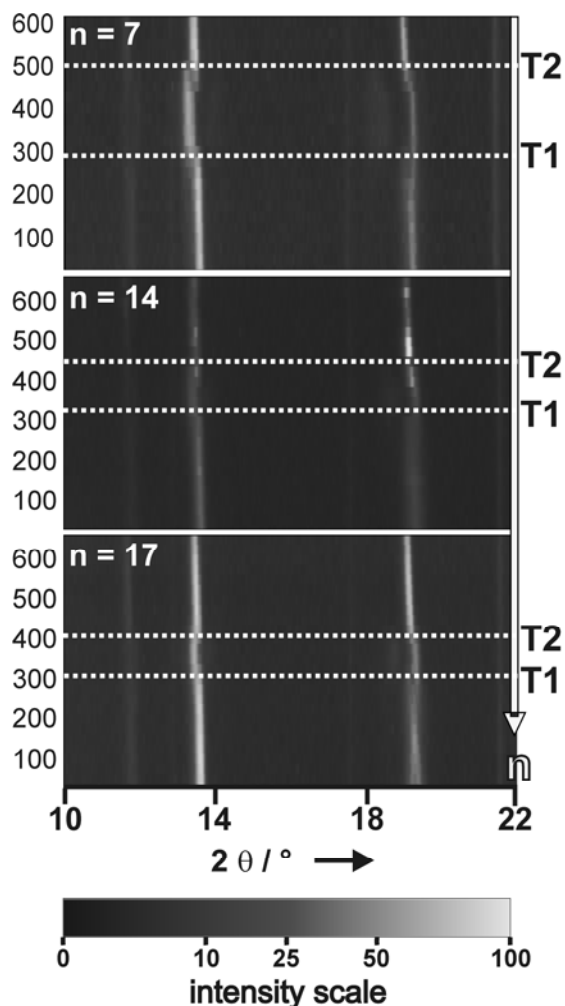


Figure 2. Heating section of the temperature-dependent PXRD of different $\text{Sb}_2\text{Te}_3(\text{GeTe})_n$ samples with the transition temperatures T1 and T2 (left: temperatures in $^{\circ}\text{C}$).

Temperature-dependent XRPD investigations of quenched samples of $\text{Sb}_2\text{Te}_3(\text{GeTe})_n$ ($3 \leq n \leq 17$) were performed in order to determine the existence range of the different phases (Table 1). Two changes occur when the quenched samples are heated (T1, T2) (Figure 2) and one during cooling (T3) (Table 1). All transformation temperatures depend on the composition, indicating the influence of the thickness of the distorted rocksalt-type building blocks and the vacancy concentration on the stability of each phase, respectively. Starting from quenched pseudocubic samples, diffusion processes occur at T1 when the quenched sample with short-range ordered vacancies relaxes to the thermodynamically stable trigonal phase (see below), which transforms to the cubic high-temperature phase when the sample reaches the latter's stability region (T2). When it is slowly cooled below that stability range, the transformation from the cubic to the trigonal phase occurs (T3). This phase transition is delayed because the high-temperature phase can be undercooled ($T3 < T2$).

Table 1. Phase transformation temperatures of $\text{Sb}_2\text{Te}_3(\text{GeTe})_n$ ($3 \leq n \leq 17$) from temperature programmed XRPD

Composition	T1 (in $^{\circ}\text{C}$)	T2 (in $^{\circ}\text{C}$)	T3 (in $^{\circ}\text{C}$)
$\text{Sb}_2\text{Te}_3(\text{GeTe})_3$	375	560	550
$\text{Sb}_2\text{Te}_3(\text{GeTe})_7$	250-320	500	460
$\text{Sb}_2\text{Te}_3(\text{GeTe})_{12}$	325	475-500	460
$\text{Sb}_2\text{Te}_3(\text{GeTe})_{14}$	325	450	320
$\text{Sb}_2\text{Te}_3(\text{GeTe})_{17}$	300	410	250-275

With increasing GeTe content n , the cubic phase obviously becomes more stable and more inert at lower temperatures: it is reached at lower temperatures (T_2) upon heating and can be increasingly undercooled (T_3 decreases). GeTe itself cannot be undercooled as it exhibits no vacancies.^[27] Its transition temperature (ca. 390 °C for slightly Te-rich samples) between the rhombohedral and the cubic phase continues the trend given by samples with increasing n .

The diffusion pathways required to reach the trigonal phase with more or less equidistant van der Waals gaps depend on the block size. Due to the long diffusion pathways involved, the cubic phase can be increasingly undercooled and partially retained at room temperature by quenching the samples if the GeTe content is higher (i.e., thicker blocks). The transition from the trigonal to the cubic phase requires a rearrangement of the Te substructure and the introduction of randomly distributed structural vacancies on cation positions. This process is governed by thermodynamics rather than by kinetics. Trigonal phases of all samples investigated can be long-time annealed at 400 °C without phase transition to the cubic high-temperature phase.

5.3.3.2 Influence of thermal treatment on the nanostructure

The microstructure of $\text{Sb}_2\text{Te}_3(\text{GeTe})_{12}$ samples with different thermal treatment have been investigated by TEM. Samples quenched from temperatures in the existence range of the cubic high-temperature phase show intersecting defect layers perpendicular to all pseudocubic [111] directions in the HRTEM images. A parquet-like structure is formed, and corresponding diffuse intensities are observed in the SAED patterns (Figure 3). The defect layers are directly imaged by Z contrast in STEM-HAADF images (electron-rich areas appear brighter). A similar HRTEM investigation of samples that were annealed in the existence range of the trigonal phase (400 °C) show parallel van der Waals gaps with irregular distances, which can only formally be viewed as “defect layers”. Accordingly, the corresponding SAED patterns show diffuse intensities only in the direction orthogonal to the layers (Figure 3). Slowly cooled samples resemble those obtained by annealing quenched ones.

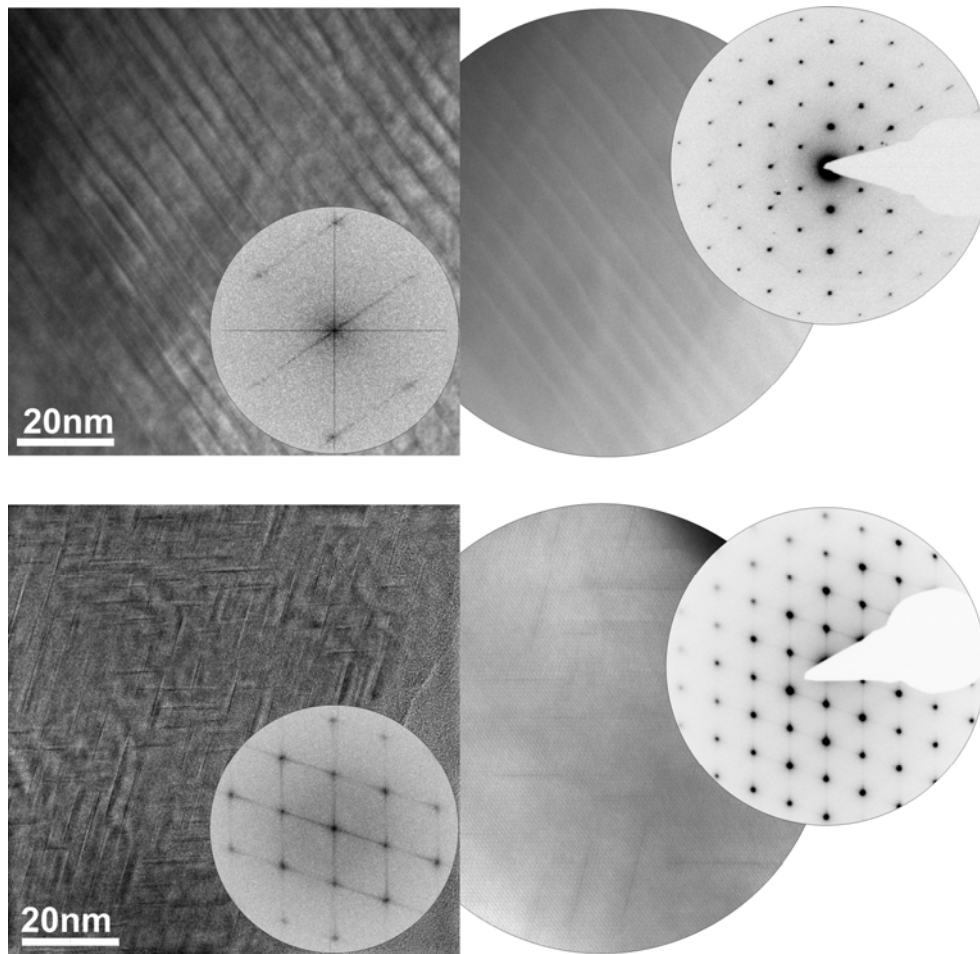


Figure 3. Comparison of two samples of $\text{Sb}_2\text{Te}_3(\text{GeTe})_{12}$ with different thermal treatment (top: annealed at 400°C for 20h; bottom: quenched from 500°C); each with HRTEM image (left, insert: corresponding Fourier transform), STEM-HAADF image (middle) and SAED (right).

The different arrangements of the defect layers or van der Waals gaps, respectively, are a consequence of the diffusion processes that occur during the phase changes associated with the thermal treatment. The disorder-order phase transition from the cubic high-temperature phase with random distribution of the vacancies to the long-range ordered trigonal structures, which are thermodynamically stable at room-temperature, requires a reconstructive phase transition including a rearrangement of the anion substructure. During this phase transformation, the short-range order gradually increases when the vacancies are arranged in two-dimensional layers by diffusion in the solid state. In quenched phases, the defect layers are finite and arranged perpendicular to all $[111]$ directions of the original cubic phase, forming the parquet-like structure consisting of multiple intersecting defect layers. Annealing quenched phases leads to further diffusion and thus to an extension of the defect layers toward the thermodynamically stable trigonal phase with an ideally symmetric, equidistant arrangement of van der Waals gaps. Summing up, the structure of the quenched phases combines features of both stable (low and

high temperature) phases even though it cannot be observed as an intermediate state during the phase transition at equilibrium conditions.

Investigations of the phase diagram Ge-Sb-Te showed that such samples need up to 8 months of annealing to reach the trigonal thermodynamically stable phase.^[28] Therefore, it is possible to obtain various stages between the structure of quenched samples and the stable phase by controlling the annealing conditions. This transformation is hindered because the cubic structure is locally preserved, owing to stresses caused by multiple twinning that is unavoidable in quick transitions from the cubic high-temperature to the rhombohedral phase (translationengleiche group-subgroup relationship).^[30] When the quenched pseudocubic samples are heated, the mobility of vacancies increases and stresses are relieved during the transformation to the stable trigonal structure (T1 in Table 1).

In situ TEM experiments show that the defect layers present in samples quenched from the cubic high-temperature phase disappear when the sample is exposed to the highly energetic electron beam for about 1 min (Figure 4). This is similar to the behavior described for $\text{Ge}_2\text{Sb}_2\text{Te}_5$.^[29]

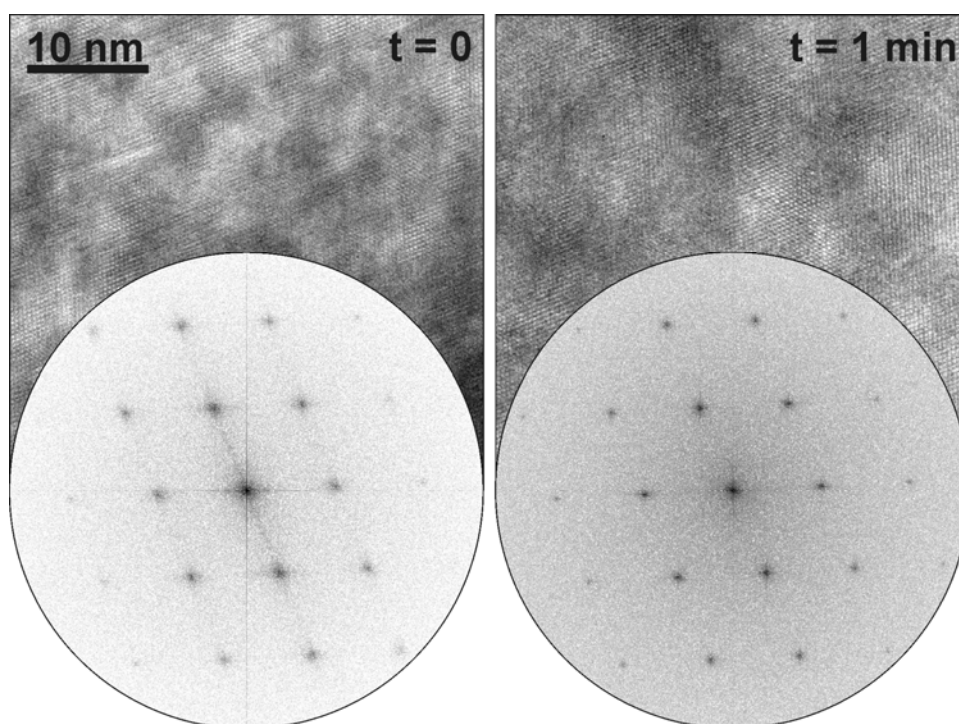


Figure 4. Quenched sample with diffuse intensities in the corresponding Fourier transform and defect layers in HRTEM (left); after prolonged exposition (1 min) to the electron beam, there are no diffuse intensities in the Fourier transform and no defect layers in HRTEM (right).

5.3.3.3 Influence of the composition on the nanostructure of quenched $\text{Sb}_2\text{Te}_3(\text{GeTe})_n$ samples

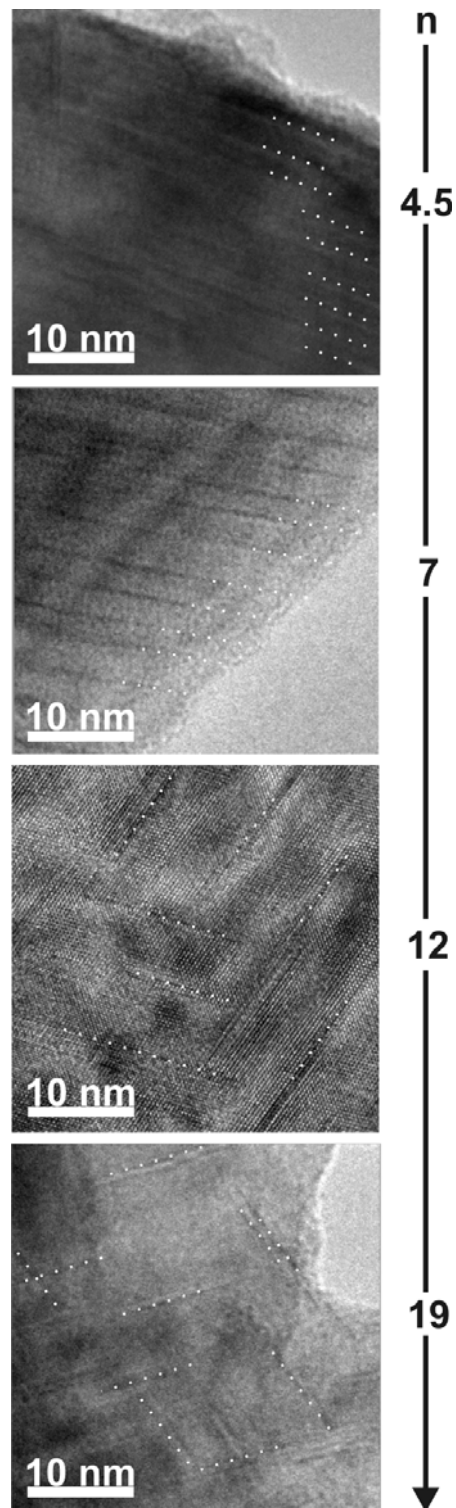


Figure 5. HRTEM images of different $\text{Sb}_2\text{Te}_3(\text{GeTe})_n$ samples with similar thermal treatment (top to bottom $n = 4.5; 7; 12; 19$; the defect layers are highlighted with white dotted lines) – they become fewer and less regularly spaced with increasing n .

The nanostructure of $\text{Sb}_2\text{Te}_3(\text{GeTe})_n$ ($n = 4.5-19$) samples quenched from the cubic phase not only depends on the thermal treatment but also on the composition (n) of the samples. Higher GeTe contents result in fewer defects in the high-temperature phase and larger blocks in the trigonal phase with strongly varying thicknesses. Higher defect concentrations at lower GeTe contents correspond to an increased number of van der Waals gaps with more regular spacing (Figure 5). This change in the variance of the spacing results from the increasing diffusion pathways which are necessary to reach the ideal, thermodynamically stable trigonal phase. Samples with a higher GeTe content must be annealed much longer in order to reach this state, and therefore, the block thickness distribution is more irregular as compared to samples with the same thermal treatment and a lower GeTe content.

Increased diffusion pathways have a second effect on the microstructure. The probability of intersecting defect layers with different orientations increases when the diffusion pathways necessary to form the stable phase increase. Therefore, the fraction of domains with intersecting defect layers forming parquet-like structures increases with the GeTe content.

Thus, in addition to the thermal treatment, the composition is an important factor that determines the nanostructure of $\text{Sb}_2\text{Te}_3(\text{GeTe})_n$.

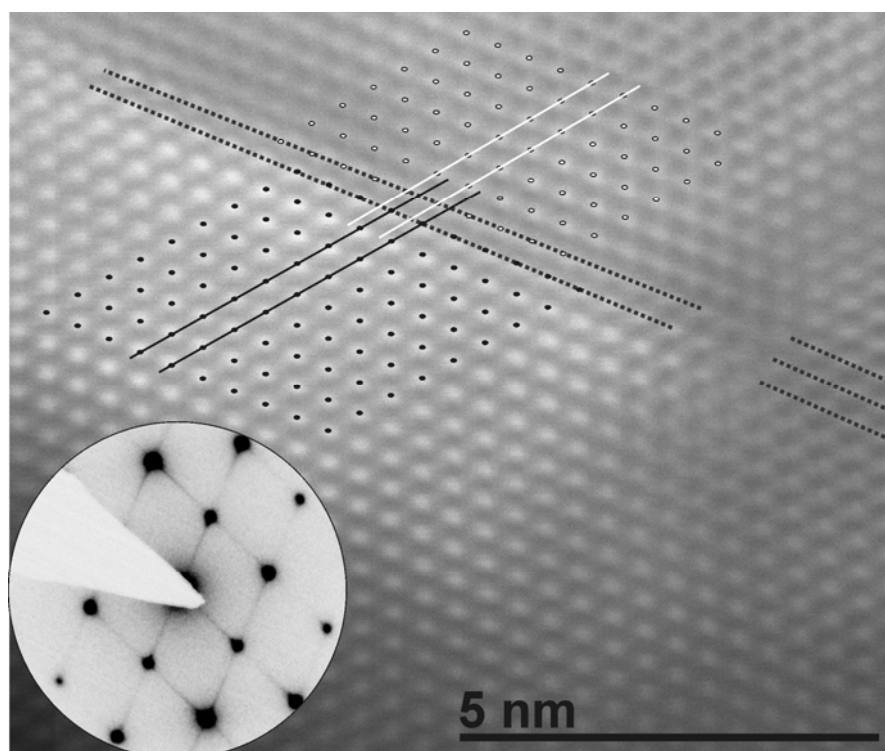


Figure 6. HAADF-STEM image (pseudo-cubic zone axis $\langle 110 \rangle$, with corresponding SAED of the whole crystallite) of $\text{Sb}_2\text{Te}_3(\text{GeTe})_{12}$; the atom rows on either side of the defect layer are marked (gray and white dotted lines); at the defect layer the structure is shifted by $1/3$ of the distance between the atom rows parallel to the defect layer; the image also shows the relaxation of the defect layer (black lines).

5.3.3.4 Structural relaxation around the defect layers in $\text{Sb}_2\text{Te}_3(\text{GeTe})_{12}$.

We reported in earlier works that the relaxation and/or shift of Te atom layers upon “vacancy ordering” leads to van der Waals gaps rather than defect layers in an undistorted matrix.^[22,30] High-resolution imaging both by HRTEM and STEM-HAADF shows that the magnitude of relaxation between the distorted rocksalt-like building blocks depends on the lateral extension of the “vacancy” layers. Where they terminate, the relaxation is hindered by the surrounding bulk and the Te atom positions of the rocksalt-type phase are approximately retained. For the same reason, no relaxation occurs if the defect layers extend over just a few unit cells. Whenever defect layers extend over larger areas, Te-Te contacts are formed and the structure is partially relaxed (Figure 6). The relaxation includes a shift of $1/3$ of the distance between the rows of atom columns parallel to the defect layers. This shift corresponds to the structure around the van der Waals gaps in stable trigonal phase (compare Figure 1), whose structures were derived from

single-crystal data.^[31,32] This proves the van der Waals character of extended defect layers whereas less extended ones are rather similar to “point defects” (point defect = a type of defect as opposed to a planar defect or a line defect) with little influence on the surrounding lattice.

5.3.3.5 Influence of the microstructure on the thermoelectric characteristics of $\text{Sb}_2\text{Te}_3(\text{GeTe})_n$ ($n = 3-19$)

The thermoelectric properties of $\text{Sb}_2\text{Te}_3(\text{GeTe})_n$ ($n = 3, 4.5, 7, 12, 19$) samples, each quenched from its cubic high-temperature phase, show that the nanostructures resulting from different compositions (Figure 7) have diverse and, in part, complex consequences.

For all samples of $\text{Sb}_2\text{Te}_3(\text{GeTe})_n$ with $n = 3-19$, the Seebeck coefficients (S) are quite similar and increase continuously with the temperature reaching $100-200 \mu\text{VK}^{-1}$ at $450 \text{ }^\circ\text{C}$. They correspond to p-type semiconductors. For $n = 19$, the increase with the temperature is most pronounced. Such values are common for materials with high ZT values, e.g., TAGS (Te-Ag-Ge-Sb) compounds with $S = 160-220 \mu\text{V/K}$ at $450 \text{ }^\circ\text{C}$, the exact values depending on the composition and sample treatment.^[33,34] Water quenched and rapidly solidified (melt-spun) samples of layered $\text{Sb}_2\text{Te}_3(\text{GeTe})_n$ with $n = 1$ or 2 reach $S = 60-110 \mu\text{V/K}$ at $450 \text{ }^\circ\text{C}$.^[35]

The temperature dependence of the electrical conductivity (σ) corresponds to metallic behavior. Upon heating, σ decreases down to $800-2000 \text{ S/cm}$ at $450 \text{ }^\circ\text{C}$, which is also similar to TAGS compounds ($800-1200 \text{ S/cm}$ at $450 \text{ }^\circ\text{C}$)^[33,34] and optimized $\text{Sb}_2\text{Te}_3(\text{GeTe})_n$ ($n = 1, 2$) ($1500-2000 \text{ S/cm}$ at $450 \text{ }^\circ\text{C}$).^[35] The electrical conductivity decreases with the GeTe content for $n = 3, 4.5, 7$, probably as a consequence of the increasingly inhomogeneous spacings between defect layers (see above). Further increasing the GeTe content ($n = 12, 19$) increases σ , probably because the defect layer concentration gets rather small and its influence on the metallic character becomes less dominant. The fact that $\text{Sb}_2\text{Te}_3(\text{GeTe})_{12}$ exhibits the maximal electrical conductivity is probably the result of a complex interplay of different factors.

As the positive effect of a high electrical conductivity σ is compensated by a higher electronic part of the thermal conductivity κ_e , the phononic part (lattice thermal conductivity κ_L) is crucial for ZT . The overall thermal conductivities of the compounds $\text{Sb}_2\text{Te}_3(\text{GeTe})_n$ ($n = 3-19$) range from 1 to 3.5 W/mK , the lattice part amounts to $0.2-1.3 \text{ W/mK}$ at $450 \text{ }^\circ\text{C}$. For TAGS, the overall thermal conductivity ranges from 1.5 to 2.8 with a lattice part around 0.4 at $450 \text{ }^\circ\text{C}$.^[33,34]

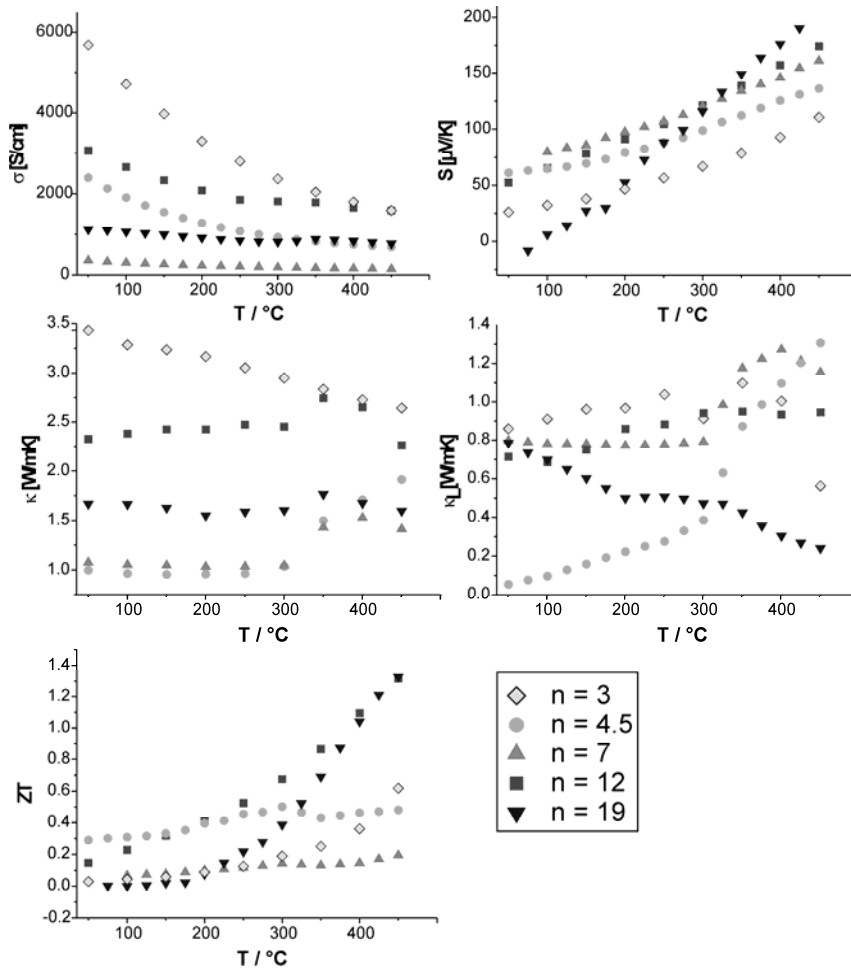


Figure 7. Thermoelectric characteristics of quenched $\text{Sb}_2\text{Te}_3(\text{GeTe})_n$ ($n = 3 - 19$) samples; electric conductivity (σ) (top left); Seebeck coefficient (S) (top right); thermal conductivity (κ) (middle left); lattice thermal conductivity (κ_L) (middle right) and the resulting thermoelectric figure of merit (ZT , bottom).

In general, more pronounced nanostructuring is expected to cause more phonon scattering and thus reduce κ_L , thereby increasing ZT . Higher defect concentrations should have a similar effect. $\text{Sb}_2\text{Te}_3(\text{GeTe})_3$ has the highest overall thermal conductivity of the samples investigated. Its cubic high-temperature phase exhibits a maximum cation defect concentration; however, it cannot be quenched to a pseudocubic one with highly disordered defect planes. Therefore, quenched samples of $\text{Sb}_2\text{Te}_3(\text{GeTe})_3$ are not significantly different from annealed ones and exhibit an almost completely ordered trigonal structure with equidistant van der Waals gaps. Since such an ordered arrangement has less potential to suppress the phonon proliferation, $\text{Sb}_2\text{Te}_3(\text{GeTe})_3$ has the highest lattice (κ_L) and overall (κ) thermal conductivity. This results in a relatively low ZT value. Therefore, the rather low ZT of more or less long-range ordered phases $\text{Sb}_2\text{Te}_3(\text{GeTe})_n$ with $n = 1$ or 2 (~ 0.2 at 450°C)^[35] is not surprising.

Since ZT of all compounds investigated increases with temperature, the temperature dependence of κ_L is crucial. $\text{Sb}_2\text{Te}_3(\text{GeTe})_{4.5}$ has a very low κ_L and thus the highest ZT at room temperature, probably due to the high defect concentration combined with disorder. However, in this case, the diffusion pathways are rather short so that the transition to the stable trigonal phase causes κ_L to increase significantly with the temperature. That outweighs the increasing Seebeck coefficient and results in a comparably low ZT at higher temperatures. The same effect is observed for $\text{Sb}_2\text{Te}_3(\text{GeTe})_7$ which has a higher κ_L at room temperature due to the reduced defect concentration and therefore a lower ZT value. The overall low thermal conductivity is not helpful as it comes with a low electrical conductivity. The lower defect concentration also means less pronounced effects of structural changes at higher temperatures since the diffusion pathways are significantly increased compared to $\text{Sb}_2\text{Te}_3(\text{GeTe})_{4.5}$. The compounds with higher GeTe contents ($n = 12, 19$) increasingly show the parquet-like structure, owing to intersecting finite defect layers as a result of the even longer diffusion pathways hypothetically required to form the thermodynamically stable trigonal phase. The diffusion processes are, of course, more pronounced at higher temperatures, which results in an increased κ_L , except for $\text{Sb}_2\text{Te}_3(\text{GeTe})_{19}$, where there is little diffusion due to the low defect concentration. The strongly increasing Seebeck coefficient of the compounds with $n = 12$ and 19 leads to the steep increase of ZT at higher temperatures. As a result, the ZT values reach 1.3 at 450°C for both $\text{Sb}_2\text{Te}_3(\text{GeTe})_{19}$ and $\text{Sb}_2\text{Te}_3(\text{GeTe})_{12}$.

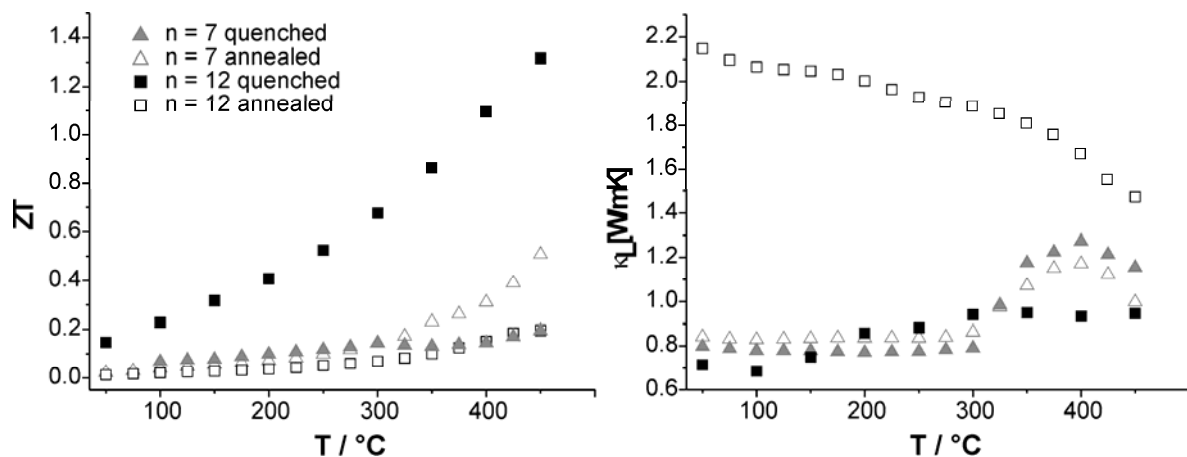


Figure 8. Comparison of the thermoelectric characteristics of quenched samples of $\text{Sb}_2\text{Te}_3(\text{GeTe})_n$ ($n = 7, 12$) with those of annealed and slowly cooled ones; left side: thermoelectric figure of merit (ZT); right side: lattice thermal conductivity (κ_L).

In order to analyze the influence of the nanostructure on the thermoelectric properties independent of the chemical composition and the associated carrier concentration, samples with identical composition but different thermal treatment were investigated. Quenched samples of $\text{Sb}_2\text{Te}_3(\text{GeTe})_{12}$ and $\text{Sb}_2\text{Te}_3(\text{GeTe})_7$ have a higher ZT value at room temperature than those annealed at 400 °C (in the stability range of the trigonal phase) and slowly cooled afterward (Figure 8). The Seebeck coefficients are influenced very little by the thermal treatment and almost identical for the samples investigated. Up to 300 °C, i.e., in the temperature range where diffusion effects are negligible, the lattice thermal conductivity of the quenched samples is significantly lower, reflecting the high degree of phonon scattering by the finite defect layers with irregular spacings. This effect is much more pronounced in $\text{Sb}_2\text{Te}_3(\text{GeTe})_{12}$ than it is in $\text{Sb}_2\text{Te}_3(\text{GeTe})_7$. This is obviously due to the parquet-like structure of quenched $\text{Sb}_2\text{Te}_3(\text{GeTe})_{12}$ which is neither present in annealed samples nor in quenched $\text{Sb}_2\text{Te}_3(\text{GeTe})_7$.

The electrical conductivity σ of annealed and slowly cooled $\text{Sb}_2\text{Te}_3(\text{GeTe})_{12}$ is lower than that of quenched samples. For $\text{Sb}_2\text{Te}_3(\text{GeTe})_7$, however, σ nearly doubles between 300 and 400°C, resulting in a higher ZT value at high temperatures than that of quenched samples. The slowly cooled samples exhibit a structure that is closer to the thermodynamically stable layered structure than that of the quenched sample. Most defect layers in slowly cooled $\text{Sb}_2\text{Te}_3(\text{GeTe})_{12}$ are already ordered and form van der Waals gaps, which results in long diffusion pathways for the remaining disordered defects. This results in a decreasing lattice thermal conductivity with increasing temperatures, comparable to the situation in quenched $\text{Sb}_2\text{Te}_3(\text{GeTe})_{19}$. Thus, the high ZT value of quenched $\text{Sb}_2\text{Te}_3(\text{GeTe})_{12}$ is a consequence of the reduced thermal conductivity in combination with a high electrical conductivity.

5.3.4 Conclusion

The nanostructure of $\text{Sb}_2\text{Te}_3(\text{GeTe})_n$ ($n = 3-19$) can be tuned both by varying the composition and by changing the thermal treatment of the samples. Cation defects tend to form layers, which become van der Waals gaps if they are extended enough to allow the relaxation of the surrounding structure. Quenching from highly disordered cubic high-temperature phases leads to finite intersecting defect layers forming a parquet-like structure, which (especially for $n = 12$) leads to a significant reduction of the lattice thermal conductivity. The concentration and arrangement of the defect layers have substantial influence on the thermoelectric properties. The temperature dependence of the individual contributions varies in a rather complicated way. Although this makes predictions rather difficult, the complex interplay of different structural

features correlates with the properties and is very valuable for an a posteriori understanding many observed effects.

The Seebeck coefficient of all compounds investigated rises with increasing temperature, especially for high GeTe contents, and indicates p-type semiconductors. Materials with intermediate n such as $\text{Sb}_2\text{Te}_3(\text{GeTe})_7$ have the lowest electric conductivity. As their lattice thermal conductivity increases with temperature, they interestingly exhibit the lowest ZT values at high temperatures, in addition to those (e.g., $n = 3$) that exhibit fully ordered structures independent of the thermal treatment. A high defect concentration leads to a relatively homogeneous arrangement of parallel “defect layers” which correspond to van der Waals gaps and result in an increased electric conductivity. The high defect concentration induces a low lattice thermal conductivity in case enough disorder remains in quenched pseudocubic samples. This holds for GeTe contents as low as $n = 4.5$; further decreasing n is not helpful as short diffusion pathways usually yield highly ordered structures (as shown for $n = 3$). The increased mobility of the atoms at higher temperatures emphasizes the importance of order_disorder effects and causes a more or less pronounced transition to the thermodynamically stable phase with equidistant van der Waals gaps around ~ 300 °C. In compounds with higher GeTe contents, the reduced defect concentration increases the electrical conductivity while the long diffusion pathways required to form extended defect layers result in intersecting finite defect layers and a more pronounced nanostructure, decreasing the lattice thermal conductivity (especially for $n = 19$). Therefore, the compounds $\text{Sb}_2\text{Te}_3(\text{GeTe})_{12}$ and $\text{Sb}_2\text{Te}_3(\text{GeTe})_{19}$ have rather low ZT values at room temperature but reach the highest ZT values up to 1.3 in the high-temperature range. Although due to limited long- time stability above ~ 300 °C, this value has little meaning for the application in actual time ZT values of about 0.7 in the temperature interval where the nanostructures are long-time stable still seems promising. Probably, the properties can be further enhanced by doping with additional elements, even if such efforts might further complicate the situation. In contrast to other multinary telluride systems, germanium antimony tellurides do not tend to exhibit phase separation (e.g., precipitates) and, despite the nanostructuring, remain chemically homogeneous.

5.3.5 References

- [1] G. J. Snyder, E. S. Toberer, *Nat. Mater.* **2008**, 7, 105.
- [2] F. Schüth, *Positionspapier Koordinierungskreis Chemische Energieforschung*, **2009**.
- [3] K. F. Hsu, S. Loo, F. Guo, W. Chen, J. S. Dyck, C. Uher, T. Hogan, E. K. Polychroniadis, M. G. Kanatzidis, *Science* **2004**, 303, 818.
- [4] J. P. Heremans, V. Jovovic, E. S. Toberer, A. Sarmat, K. Kurosaki, A. Charoenphakdee, S. Yamanaka, G. J. Snyder, *Science* **2008**, 321, 554.
- [5] B. Poudel, Q. Hao, Y. Ma, Y. Lan, A. Minnich, B. Yu, X. Yan, D. Wang, A. Muto, D. Vashaee, X. Chen, J. Liu, M. S. Dresselhaus, G. Chen, Z. Ren, *Science* **2008**, 320, 634.
- [6] M. Wuttig, N. Yamada, *Nat. Mater.* **2007**, 6, 824.
- [7] S. Raoux, *Annu. Rev. Mater. Res.* **2009**, 39, 9.1.
- [8] L. van Pieteron, M. H. R. Lankhorst, M. van Schijndel, A. E. T. Kuiper, J. H. J. Roosen, *J. Appl. Phys.* **2005**, 97, 083520.
- [9] S. R. Ovshinsky, *Phys. Rev. Lett.* **1968**, 21, 1450.
- [10] W. Welnic, M. Wuttig, *Mater. Today* **2008**, 11, 20.
- [11] S. Raoux, R. M. Shelby, J. Jordan-Sweet, B. Munoz, M. Salinga, Y.-C. Chen, Y.-H. Shih, E.-K. Lai, M.-H. Lee, *Microelectron. Eng.* **2008**, 85, 2330.
- [12] M. Wuttig, C. Steimer, *Appl. Phys. A: Mater. Sci. Process.* **2007**, 87, 411.
- [13] A. L. Lacaíta, D. Wouters, *J. Phys. Status Solidi A* **2008**, 205, 2281.
- [14] M. Terao, T. Morikawa, T. Ohta, *Jpn. J. Appl. Phys.* **2009**, 48, 080001.
- [15] T. L. Anderson, H. B. Krause, *Acta Crystallogr.* **1974**, C47, 1141.
- [16] O. G. Karpinsky, L. E. Shelimova, M. A. Kretova, J.-P. Fleurial, *J. Alloys Compd.* **1998**, 268, 112.
- [17] L. E. Shelimova, O. G. Karpinsky, M. A. Kretova, V. I. Kosyakov, V. A. Shestakov, V. S. Zemskov, F. A. Kuznetsov, *Inorg. Mater.* **2000**, 36, 768.
- [18] T. Matsunaga, H. Morita, R. Kojima, N. Yamada, K. Kifune, Y. Kubota, Y. Tabata, J.-J. Kim, M. Kobata, E. Ikenaga, K. Kobayashi, *J. Appl. Phys.* **2008**, 103, 093511.
- [19] S. Raoux, W. Wojciech, D. Ielmini, *Chem. Rev.* **2010**, 110, 240.
- [20] F. Yan, T. J. Zhu, X. B. Zhao, S. R. Dong, *Appl. Phys. A: Mater. Sci. Process.* **2007**, 88, 425.
- [21] J. L. Cui, H. Fu, X. L. Liu, D. Y. Chen, W. Yang, *Curr. Appl. Phys.* **2009**, 9, 1170.
- [22] M. N. Schneider, T. Rosenthal, C. Stiewe, O. Oeckler, *Z. Kristallogr.* **2010**, 225, 463.
- [23] *DigitalMicrograph 3.6.1*; Gatan Software: Brisbane, Australia, **2007**.

-
- [24] P. A. Stadelmann, *Ultramicroscopy* **1987**, *21*, 131.
- [25] *ESVision*, 4.0.164; Emispec Systems Inc.: Tempe, AZ, **1994-2002**.
- [26] *WINXPOW*, Version 2.12; Stoe & Cie. GmbH: Darmstadt, Germany, **2005**.
- [27] T. Chattopadhyay, J. X. Boucherle, H. G. von Schnering, *J. Phys. C: Solid State Phys.* **1987**, *20*, 1431.
- [28] S. Bordas, M. T. Clavaguera-Mora, B. Legendre, C. Hancheng, *Thermochim. Acta* **1986**, *107*, 239.
- [29] B. J. Kooi, W. M. G. Groot, J. T. M. De Hosson, *J. Appl. Phys.* **2004**, *95*, 924.
- [30] M. N. Schneider, P. Urban, A. Leineweber, M. Döblinger, O. Oeckler, *Phys. Rev. B* **2010**, *81*, 184102.
- [31] K. A. Agaev, A. G. Talybov, *Sov. Phys. Cryst.* **1966**, *11*, 400.
- [32] M. N. Schneider, O. Oeckler, *Z. Anorg. Allg. Chem.* **2008**, *634*, 2557.
- [33] Y. Chen, T. J. Zhu, S. H. Yang, S. N. Zhang, W. Miao, X. B. Zhao, *J. Electron. Mater.* **2010**, *39*, 1719.
- [34] S. H. Yang, T. J. Zhu, C. Yu, J. J. Shen, Z. Z. Yin, X. B. Zhao, *J. Electron. Mater.* **2011**, *40*, 1244.
- [35] F. Yan, T. J. Zhu, X. B. Zhao, S. R. Dong, *Appl. Phys. A: Mater. Sci. Process.* **2007**, *88*, 425.

5.4 Diffuse X-ray scattering and the real structure of GeTe-rich metastable germanium antimony tellurides $(\text{GeTe})_n\text{Sb}_2\text{Te}_3$ ($2 > n > 12$)

M. N. Schneider, P. Urban, Marten Seemann, J. Wright, O. Oeckler

Journal of Applied Crystallography (to be submitted).

Abstract

Metastable phases $(\text{GeTe})_n\text{Sb}_2\text{Te}_3$ ($n \geq 3$) with $1/n+3$ cation vacancies per anion can be obtained by quenching rocksalt-type high-temperature polymorphs. They exhibit interesting thermoelectric properties and are related to phase-change materials for data storage. The average structure of quenched crystals can be approximated by the rocksalt type. Diffraction patterns are an incoherent superposition of intensities from individual domains with trigonal average structure but pseudo-cubic metrics. The fourfold twinning is mirrored in structured diffuse streaks that interconnect Bragg reflections along the [001] directions of individual disordered trigonal domains. The diffuse streaks exhibit a "comet-like" shape with a maximum of the diffuse intensity located at the low-angle side of Bragg positions ("comet head") accompanied by a diffuse "comet tail". 2D extended cation defect ordering leads to parallel but not equidistantly spaced planar faults. Based on a stacking fault approach, a model to simulate the diffuse scattering was developed. The parameters of the model describe the overall metrics, the concentration and distribution of cation defect layers, atom displacements in their vicinity and the stacking sequence of Te atom layers around the planar defects. These parameters were varied in order to derive simple rules for the interpretation of the diffuse scattering. The distance between Bragg position and "comet head" increases with increasing frequency of planar faults. A sharp distance distribution of the planar faults leads to an intensity modulation along the "comet tail" which, for low values of n approximate superstructure reflections. The displacement of atom layers towards the planar defects yields "comets" on the low-angle side and vice versa. A rocksalt-type average structure can only be obtained if the planar defects correspond to "missing" cation layers in the cubic ABC stacking sequence of the Te atom layers. An increasing amount of hexagonal ABAB stacking around the cation defect layers leads to an increasing broadening and splitting of some Bragg reflections which then overlap with the diffuse scattering.

Based on these rules, the diffuse scattering of $(\text{GeTe})_n\text{Sb}_2\text{Te}_3$ ($n = 2, 5, 6, 12$) crystals was analyzed by comparison of simulated and experimental reciprocal sections as well as streaks $h_t k_t \ell_t$ ($h_t = 0, 1, 2$; $h_t = \pm k_t$) extracted from synchrotron data. With decreasing GeTe content n , the distance between faults and its variance decreases which indicates the increasing correlation between defects with increasing defect concentration. With increasing amounts of cation defects, the ABC stacking sequence of the Te atom layers across the defect layers becomes dominant. Whereas the rocksalt-type polymorphs contain a random cation defect arrangement, the long-periodic layered structures exhibit rocksalt-type slabs separated by van der Waals gaps. These can be formally regarded as an equidistant arrangement of cation defect layers with hexagonal ABAB stacking sequence of the Te atom layers across the gap accompanied by displacements of atom layers towards the gap. The metastable phases, hence, correspond to "intermediate" states between the high-temperature and room-temperature modifications.

5.4.1 Introduction

Disordered metastable germanium antimony tellurides (GST materials) with rocksalt-type average structures or slightly distorted variants thereof play an essential role as phase-change materials for rewriteable data storage. Data is stored by producing amorphous recording marks in crystalline layers by laser irradiation or electrical currents and erased by recrystallization.^[1-5] Furthermore, some quenched GST materials exhibit interesting thermoelectric properties which allow one to convert thermal energy into electrical energy.^[6, 7] The composition of these materials lies on or very close to the pseudobinary line GeTe - Sb₂Te₃ where normal valence compounds are located in the ternary phase diagram Ge/Sb/Te.^[8, 9] The properties of these materials strongly depend on the composition which in turn determines the real structure and thus the electrical and thermal properties. For example, disorder may lead to the localization of charge carriers or enhance phonon scattering.^[6, 7, 10-12]

For compounds (GeTe)_nSb₂Te₃ with $n < 3$, metastable rocksalt-type phases can only be obtained as thin films, whereas they represent thermodynamically stable high-temperature phases for $n \geq 3$.^[9] The transition temperatures to the high-temperature modifications depend on the composition and decrease with increasing n , from 560 °C for Ge₃Sb₂Te₆ to 450 °C for Ge₁₄Sb₂Te₁₇.^[6] Whereas quenching the rocksalt-type high-temperature modification of GeTe-rich ($n \geq 20$) pseudobinary compounds or GeTe itself yields the rhombohedral ambient-temperature modifications, quenching the high-temperature modifications of (GeTe)_nSb₂Te₃ in the range $3 \leq n < 19$ leads to metastable samples. Such phases, e. g. (GeTe)₇Sb₂Te₃ = Ge_{0.7}Sb_{0.2}Te, are pseudocubic according to their powder diffraction patterns. Single-crystal data have revealed that their (average) structure is trigonal and corresponds to the GeTe structure type (space group $R\bar{3}m$).^[13] The phase transitions from the cubic high-temperature phases to the rhombohedral structures lead to multiple twinning according to the group-subgroup relationship $Fm\bar{3}m$ (NaCl type) $\xrightarrow{t^4}$ $R\bar{3}m$ (CuPt type) $\xrightarrow{t^2}$ $R\bar{3}m$ (GeTe type). The first step of the symmetry reduction allows a rhombohedral distortion along $\langle 111 \rangle_c$ (the index c indicates the cubic setting whereas the index t indicates the trigonal setting). This leads to distorted coordination octahedra, which still exhibit equal cation-anion distances in the CuPt structure type^[14]; however, the metric deviation from the cubic rocksalt type is not very pronounced. Further symmetry reduction leads to the non-centrosymmetric GeTe type where layers perpendicular $[001]_t$ are formed. If cations and anions are not differentiated, these layers are similar to those in gray arsenic with the typical 3+3 coordination. Neglecting the deviations from the average structure, the compounds can approximately be described as highly disordered rocksalt-type

structures where tellurium atoms occupy the anion positions and germanium atoms, antimony atoms and voids share the cation position. Cation vacancies are present as suggested by the cation/anion ratio $n+2/n+3$ and lead to some “incomplete” anion-centered polyhedra. Consequently, local distortions are much more pronounced than that those of the average structure. The distribution of the cation defects has been controversially discussed.^[10, 12, 15-19] In metastable phases $(\text{GeTe})_n\text{Sb}_2\text{Te}_3$ ($n \geq 3$) obtained by quenching bulk samples from the stability range of the rocksalt-type high temperature modification, high-resolution electron microscopy (HRTEM) revealed short-range cation defect ordering that produces extended nanostructures and also involves twinning. In each domain, parallel but not equidistant cation defect layers are formed perpendicular to the pseudo-cubic $\langle 111 \rangle_c$ directions, accompanied by atom displacements in their vicinity. In single-crystal diffraction patterns, these planar faults lead to pronounced diffuse streaks between Bragg reflections. The intensity distribution along the streaks contains information about local distortions and the space-averaged statistical distribution of 2D extended defects which complement the local information accessible by HRTEM.

5.4.2 Experimental

5.4.2.1 Sample preparation and characterization

All samples were prepared by initially melting the elements Ge (99.999%, Sigma Aldrich), Sb (99.999%, Smart Elements) and Te (99.999%, Alfa Aesar) in sealed silica glass ampoules under Ar atmosphere. Highly disordered crystals of $(\text{GeTe})_2\text{Sb}_2\text{Te}_3$ were obtained by pouring a stoichiometric melt (950 °C) in liquid nitrogen to rapidly cool the sample. Multiply twinned crystal fragments of disordered $(\text{GeTe})_2\text{Sb}_2\text{Te}_3 = \text{Ge}_{0.2}\text{Sb}_{0.2}\text{Te}$ were mechanically isolated from such quenched samples.

Crystals with variable n in the range between 3 - 12 were be obtained by physical vapor deposition. A melt with elemental ratio $\text{Ge}:\text{Sb}:\text{Te} = 1.44:2:5$ was quenched by cooling the ampoule in water and about 100 mg of the powdered product was sealed in an silica glass ampoule (length 10 cm, diameter 10 mm, Ar atmosphere), kept at 628 °C for 4 h and then slowly cooled to 618 °C (within 6 h). After holding this temperature for 75 h, the ampoule containing octahedral crystals was quenched in air. Among others, crystals of $(\text{GeTe})_5\text{Sb}_2\text{Te}_3 = \text{Ge}_{0.63}\text{Sb}_{0.25}\text{Te}$ were obtained. Crystals of $(\text{GeTe})_6\text{Sb}_2\text{Te}_3 = \text{Ge}_{0.67}\text{Sb}_{0.22}\text{Te}$ and $(\text{GeTe})_{12}\text{Sb}_2\text{Te}_3 = \text{Ge}_{0.8}\text{Sb}_{0.13}\text{Te}$ were grown in the stability ranges of their high-temperature phases by chemical transport reactions and subsequently quenched. The starting material was $(\text{GeTe})_{12}\text{Sb}_2\text{Te}_3$ prepared by heating a stoichiometric mixture to 950 °C, quenching the ampoule in air and

powdering the ingot obtained. Together with a small amount (~ 10 mg) of SbI_3 as transport agent, the material (typically 100 mg) was sealed in silica glass ampoules (length 15-20 cm, diameter 10-15 mm). Crystals of $(\text{GeTe})_6\text{Sb}_2\text{Te}_3 = \text{Ge}_{0.67}\text{Sb}_{0.22}\text{Te}$ were obtained using a two-zone furnace with a temperature gradient from 600 °C to 520 °C within 29 hours and subsequently removing the ampoule from the furnace. Crystals of $(\text{GeTe})_{12}\text{Sb}_2\text{Te}_3 = \text{Ge}_{0.8}\text{Sb}_{0.13}\text{Te}$ were grown using the natural temperature gradient of a tube furnace from 600 °C to ~ 450 °C within 17 hours and subsequently quenching the ampoule in air.

All methods yielded crystals with sizes of up to $0.5 \times 0.5 \times 0.5$ mm³. The elemental ratios of the crystals selected for the diffraction experiments was confirmed by energy dispersive X-ray spectroscopy (EDX) on crystal faces oriented approximately perpendicular to the electron beam using a JSM-6500F scanning electron microscope (Jeol, USA) with EDX detector (model 7418, Oxford Instruments, Great Britain). The results were averaged from at least 3 point analyses. The single-crystal diffraction patterns (see below) of compounds $(\text{GeTe})_n\text{Sb}_2\text{Te}_3$ ($n \geq 3$) with similar composition are similar and do not depend on the method of crystal growth if it takes place in the stability region of the high-temperature modifications before quenching.

5.4.2.2 Single-crystal data collection and processing

Laboratory single-crystal datasets of many crystals with various compositions were collected using a STOE IPDS-I diffractometer with imaging plate detector using Mo-K_α or Ag-K_α radiation (graphite monochromator, $\lambda = 0.71073$ Å or $\lambda = 0.56087$ Å, respectively) to confirm the quality of the crystals selected for synchrotron experiments and to classify different diffraction patterns according to the composition and method of crystal growth.

Synchrotron data of selected single crystals were collected at beamline ID11 of the ESRF (Grenoble) on a heavy-duty Huber diffractometer with vertical rotation axis equipped with a Frelon2K CCD detector.^[20] The X-ray optics at the undulator beamline give a good stability of the beam and a small band pass required for high-resolution single-crystal scattering experiments. Data to determine the average structure as well as to extract diffuse intensities were collected with wavelengths 0.40681 Å, i. e. close to the Sb K edge, and 0.56356 Å (energies 30.477 keV and 22.000 keV, respectively). A detector offset was used to obtain additional high-angle data. After conversion of the frames, the data were indexed using SMART and integrated using SAINT.^[21] They were scaled, combined and corrected for absorption using SADABS.^[22] SHELX97^[23] was used for full-matrix least-squares refinements (cf. following sections). Dispersion correction factors were interpolated from various databases.^[24, 25] Crystal data and refinement details are summarized in Tables 1 and 2.

Table 1. Crystallographic data on the structure refinement of quenched crystals (GeTe)₅Sb₂Te₃ and (GeTe)₆Sb₂Te₃ at 293 K.

Formula	(GeTe) ₅ Sb ₂ Te ₃ = Ge _{0.63} Sb _{0.25} Te	(GeTe) ₆ Sb ₂ Te ₃ = Ge _{0.67} Sb _{0.22} Te
Formula mass (in g mol ⁻¹)	203.41	203.51
Crystal system / Space group	cubic, $Fm\bar{3}m$	
Cell parameters (in Å)	6.003(5)	6.007(4)
Cell volume (in Å ³)	216.4(3)	216.8(2)
Formula units (per unit cell)	4	
$F(000)$	339	339
X-ray density (in g cm ⁻³)	6.24	6.24
Parameters / restraints	4 / 0	
Resolution	0.50 Å, $\sin\theta/\lambda =$ 1.010	0.51 Å, $\sin\theta/\lambda =$ 1.036
Wavelength (in Å)	0.40681	
Absorption coefficient (in mm ⁻¹)	13.08	13.22
Extinction coefficient (EXTI)	0.12(3)	0.057(10)
Measured / independent reflections	1195 / 69	1303 / 73
$R_{\text{int}} / R_{\sigma}$	0.0316 / 0.0127	0.0323 / 0.0128
$RI [I > 2\sigma(I)]^{(a)}$	0.0370	0.0204
$RI [\text{all data}]^{(a)}$	0.0370	0.0204
$wR2 [I > 2\sigma(I)]^{(b)}$	0.0876	0.0478
$wR2 [\text{all data}]^{(b)}$	0.0876	0.0478
GooF [all data]	1.290	1.184
Residual electron density (min. / max.) (in eÅ ⁻³)	-1.196 / 1.792	-1.361 / 0.156

$$^a) RI = \sum |F_o - F_c| / \sum |F_o|$$

$$^b) wR2 = [\sum [w(F_o^2 - F_c^2)^2] / \sum [w(F_o^2)^2]]^{1/2}; w = 1 / [\sigma^2(F_o^2) + (aP)^2 + bP] \text{ with } P = [\text{Max}(0, F_o^2) + 2F_c^2] / 3$$

Table 2. Atom coordinates, occupation factors, and displacement parameters (in Å²) for quenched crystals (GeTe)₅Sb₂Te₃ and (GeTe)₆Sb₂Te₃.

Atom	Wyck. site	x	y	z	f.o.f	U_{eq}		
					Ge _{0.63} Sb _{0.25} Te	Ge _{0.67} Sb _{0.22} Te	Ge _{0.63} Sb _{0.25} Te	Ge _{0.67} Sb _{0.22} Te
Ge/Sb	4a	0	0	0	0.62 / 0.25	0.67 / 0.22	0.0357(6)	0.0449(4)
Te	4b	1/2	1/2	1/2	1		0.0174(4)	0.0211(2)

For the reconstruction of reciprocal lattice sections and the extraction of streaks along $\langle 111 \rangle_c = [001]_t$ (corresponding to individual domain orientations), e.g. $h_t k_t \ell_t$ ($h_t = 0, 1, 2$; $h_t = k_t$; $h_t = -k_t$) the synchrotron data were subjected to a data reduction procedure using the ImageD11 program suite^[26] and new home-written scripts from *M. Seemann*. Peaks harvested from the diffraction images were transformed to scattering vectors subsequently used to index the reflections and determine the orientation matrix. The latter was used to generate a reconstructed reciprocal volume file from the experimental data. The reciprocal volume file contains the observed intensities at the corresponding coordinates in reciprocal space which can be extracted and depicted in two-dimensional sections. To obtain streaks along different lattice directions, intensities within a cylinder along the streak were extracted from the volume file. Intensities within the radius of this cylinder were summed up for each point along the streak. Data points intersected by the radius were proportionally taken into account. Both reciprocal sections as well as extracted streak intensities therefore directly correspond to measured intensities and were not subjected to any corrections.

5.4.2.3 Treatment of diffuse scattering data and calculation of diffraction patterns from disordered structures

DIFFAX was used to model disordered structures by a stacking fault approach that uses a general recursion algorithm (a modified version of the Hendricks-Teller formalism^[27]) to calculate the corresponding diffraction patterns.^[28] The program treats a crystalline 1D disordered solid as a stacking sequence of ordered layers interconnected by appropriate stacking vectors in a crystallographic reference coordinate system. Disorder is introduced by assigning transition probabilities between individual layers. The formalism then exploits the recurring pattern in an ordered or disordered arrangement of defined layers to compute the average interference wavefunction scattered by each layer with a given layer structure factor taking into account the stacking probabilities. Powder diffraction patterns, reciprocal lattice sections or streaks along the stacking direction can be simulated. Experimental streaks $h_t k_t \ell_t$ ($h_t = 0, 1, 2$ $h_t = k_t$ $h_t = -k_t$) parallel to $[001]_t$ of different trigonal domains can be directly compared to the corresponding simulated streaks. For reciprocal lattice sections the incoherent superposition of diffraction patterns from individual domains was introduced in the simulations by superimposing simulated reciprocal sections according to the twin law. The influence of various parameters on the diffuse scattering is discussed below.

5.4.3 Determination of the average structure of metastable

(GeTe)_nSb₂Te₃ (n = 5 and 6)

Metastable phases (GeTe)_nSb₂Te₃ (n ≥ 3) obtained by quenching their stable high-temperature modifications exhibit average structures that can be approximated by a distorted rocksalt-type. Upon quenching, pseudomerohedral twinning according to the group-subgroup relationship $Fm\bar{3}m$ (NaCl type) $\xrightarrow{t^4}$ $R\bar{3}m$ (CuPt type) $\xrightarrow{t^2}$ $R3m$ (GeTe type) leads to strain effects which stabilize the cubic metrics against relaxation towards rhombohedral metrics.^[13] The individual domains exhibit rhombohedral metrics with an a_t/c_t ratio only slightly deviating from that of the trigonal setting of a cubic cell ($a_t/c_t = 0.408$) as evidenced by the characteristic broadening of Bragg reflections. As shown by HRTEM and space-resolved Laue diffraction, the twin domains are rather small and exhibit pronounced short-range order of cation defects as will be discussed in later sections.^[6, 29, 30] The superposition of the reflections from individual domains yields groups of reflections that are not clearly separated but rather accumulate in intensities resembling to broadened Bragg reflections (see also section 4 and 5). The intensity distribution corresponds to a cF lattice and indicates a significant scattering contrast between anion and cation positions. If full occupancy of anion positions with Te atoms is assumed, the scattering contrast between cation and anion positions depends on the ratio Ge / Sb which also determines the concentration of cation vacancies if charge neutrality is retained according to the formula (GeTe)_nSb₂Te₃. Different compositions on the pseudobinary section GeTe - Sb₂Te₃, however, exhibit just very small differences in the scattering densities on the Wyckoff positions of a simple AB type. The scattering contrast ranges from 34 and 52 electrons on cation and anion positions, respectively, in a hypothetical rocksalt-type structure of Sb₂Te₃ (formally 33 % vacancies) to 32 and 52 electrons on cation and anion positions, respectively, in the rocksalt-type modification of GeTe (0 % vacancies). This implies that the Bragg data do not contain significant information about the composition whereas the diffuse intensity distribution yields some information on the amount of defects present as detailed in the following sections. For the determination of the average structure, synchrotron single-crystal data of each crystal were collected at a wavelength of 0.40681 Å. This allows one to obtain high-resolution data and is close to the Sb K absorption edge, where anomalous dispersion enhances the scattering contrast between Sb and Te. In order to comply with the cubic Laue symmetry, possible pseudomerohedral twinning according to the group-subgroup relationship described above was considered for structure refinements on crystals (GeTe)_nSb₂Te₃ with n = 5 and n = 6 in the space groups $Fm\bar{3}m$ (NaCl type), $R\bar{3}m$ (CuPt type), and $R3m$ (GeTe type). During refinements, full

occupancy of anion positions with Te atoms was assumed, whereas the Ge/Sb ratio was fixed to match the idealized compositions $(\text{GeTe})_5\text{Sb}_2\text{Te}_3 = \text{Ge}_{0.63}\text{Sb}_{0.25}\text{Te}$ and $(\text{GeTe})_6\text{Sb}_2\text{Te}_3 = \text{Ge}_{0.67}\text{Sb}_{0.22}\text{Te}$ which match well with the elemental ratios of the crystals determined by EDX-spectroscopy ($\text{Ge}_{0.68(1)}\text{Sb}_{0.27(1)}\text{Te}$ and $\text{Ge}_{0.67(2)}\text{Sb}_{0.23(2)}\text{Te}$, respectively). The site occupancies were fixed to match the compositions as the residuals do not significantly improve if the occupancy of Ge or Sb is tentatively refined. With the given reflection / parameter ratios, the trigonal models do not significantly improve the residuals so that the average structure can well be approximated assuming the rocksalt type. Crystallographic details are given in Table 1 and Table 2. As can be seen from Table 2, the atomic displacement factors are rather large, which indicates local distortions of the structure. This implies that a chemically more reasonable structural description needs to take into account short-range order phenomena, as discussed in the following sections.

5.4.4 Diffuse Scattering

5.4.4.1 Diffraction patterns of disordered phases $(\text{GeTe})_n\text{Sb}_2\text{Te}_3$

To analyze the diffuse scattering of crystals $(\text{GeTe})_n\text{Sb}_2\text{Te}_3$, laboratory as well synchrotron data were compared with simulated data as described below. Reciprocal lattice sections $h_c h_c \ell_c$ (c: cubic setting, t: trigonal setting) for crystals with $n = 2, 12$ (laboratory data) and $n = 5, 6$ (synchrotron data) are discussed in detail in section 5 and shown in Figures 6 and 7, respectively. The diffuse scattering corresponds to the pseudocubic Laue symmetry. Diffuse streaks are oriented along all $\langle 111 \rangle_c$ directions due to the superposition of intensities from the individual trigonal twin domains. The lateral broadening of the diffuse streaks is not significantly different from that of the Bragg reflections, which indicates that the intensity distribution observed can be described as 1D disorder. The intensity distribution on the diffuse streaks exhibits the following features:

- 1) The diffuse maxima near the Bragg position can be approximately described as very broadened satellite reflections. For all crystals, a maximum corresponding to a “first order satellite” is observed at $h_t k_t (\ell_t - \delta)$ ($h_t = k_t$ or $h_t = -k_t$); the distance $-\delta$ from the Bragg position depends on the composition and is larger for lower GeTe contents n . For $n = 6$ and 12 , no maxima corresponding to distinct “higher order satellites” are observed, instead, there is a rapidly declining smooth tail so that the streaks resemble “comets” with head and tail. For $n = 2$

and 5 Bragg reflections correspond to not clearly separated groups, e.g. are asymmetrically broadened. Diffuse "comets" exhibit several side maxima (cf. Fig 6 and 7).

2) The intensity distribution of these features is highly asymmetric with respect to the Bragg position. Whereas at the low angle side the diffuse "comets" are clearly visible, at the high angle side no clearly visible "comets" are found. Intense diffuse "comets" accompany strong Bragg reflections and weak diffuse "comets" are observed next to weak Bragg reflections. With increasing diffraction angle the intensity of the diffuse scattering declines less than the Bragg intensities.

3) Additional sections of diffuse streaks are located approximately in the middle between Bragg peaks. These are relatively weak compared to the "comets". For $n = 6$ and 12 they are almost not visible and exhibit no modulation in the intensity, whereas they are clearly visible for $n = 2$ and 5 and show a distinct structuring, i.e. several maxima.

5.4.4.2 Modelling of diffuse scattering in metastable $(\text{GeTe})_n\text{Sb}_2\text{Te}_3$ phases

As there are rather few characteristic features in the diffuse intensity distribution, it can be expected that a reasonable description of the real structure requires just a small parameter set. Knowledge on the structural chemistry of stable layered $(\text{GeTe})_n\text{Sb}_2\text{Te}_3$ compounds helps to develop an adequate model as the short-range order in metastable modifications can be assumed to be related to the structure of the stable ones. Whereas high-temperature modifications with $n > 3$ exhibit disordered rocksalt-type structures ($Fm\bar{3}m$, $a \approx 6 \text{ \AA}$) with a random distribution of germanium, antimony and vacancies on cation sites,^[7, 9] the stable ambient-temperature structures do not contain cation defects. The long-periodically ordered trigonal layered structures of e.g. GeSb_2Te_4 , $\text{Ge}_2\text{Sb}_2\text{Te}_5$, or $\text{Ge}_4\text{Sb}_2\text{Te}_7$.^[8, 31-34] exhibit equidistantly spaced van der Waals gaps between Te atom layers that separate distorted rocksalt-type slabs with Sb and Ge (but no vacancies) disordered on cation positions. The thickness of the slabs depends on the composition.^[31, 33] Within an alternating sequence of $n+2$ cation and $n+3$ anion layers per slab, a cubic ABC stacking sequence of Te atom layers is realized. However, at the van der Waals gaps the Te-atom layers exhibit a hexagonal ABA stacking. The cation atom positions in the vicinity of the van der Waals gap are shifted towards it. The cation positions are occupied by germanium and antimony atoms; however, antimony prefers positions next to the van der Waals gap. The phase transition between the high-temperature and the layered ambient-temperature modifications is reconstructive and formally involves the ordering of cation vacancies in infinitely extended planes, coupled to significant distortions around these "planar faults". This

can be described in terms of atom displacements along the stacking direction, i.e. the trigonal axis, and additional shearing parallel to the defect plane.^[6, 35] Taking into account this prior knowledge, models used to simulate diffraction patterns of metastable quenched crystals require a parameter set that determines the following structural features:

- 1) the metrics of the average structure
- 2) the degree of disorder, i.e. the distribution of distances between planar faults
- 3) the frequency of planar faults given by the composition $(\text{GeTe})_n\text{Sb}_2\text{Te}_3$
- 4) the shift of atom positions along the stacking direction surrounding the planar faults and thus defining the local structure (= cation defect layers and displaced atoms in their vicinity)
- 5) the impact of the planar faults on the element distribution
- 6) the arrangement of atom layers over the formal defect plane ABC-V-ABC vs. ABC-V-BCA

At first glance, it may seem reasonable to stack distorted rocksalt-type slabs with variable thicknesses whose structures can be extracted from various known layered structures in order to construct a disordered structure. However, in such a model each layer needs to be individually modified if the parameter set is to be altered. Furthermore, it is rather complex to define all "inter-layer" stacking vectors between individual slabs in a way that ensures overall pseudo-cubic metrics. In order to avoid such a complex parameter set, the real structure was described by treating the short-range order of cation defects (which yields cation defect layers) and accompanying local distortions as a formation of planar faults in a "matrix" with pseudo-cubic metrics. Although relaxation occurs in the environment of the cation defect layers, the surrounding matrix remains approximately undistorted. The effect of the cation defect layers on the adjacent structure was assumed to be independent of the distance between the planar faults. Such a model has a straightforward parameter set that can be varied in simulations; basically only two layer types are necessary to implement it. Using appropriate stacking vectors and transition probabilities, an alternating sequence of layers describing the environment of planar faults ("planar fault layer") and "matrix" slabs can be generated. The "planar fault layers" used here include the symmetrically relaxed structure around the cation defect layers. Two fault types are required to describe stacking sequence around the cation defect layer V, i. e. ABC-V-ABC vs. ABC-V-BCA (A, B, C corresponds to Te atom positions). The "matrix" layers describe rocksalt-type slabs of different thickness that act as spacers between the "planar fault layers". Thus, atom displacements in the vicinity of the cation defect layer are introduced by the modifications within the "planar fault layer", whereas the distance distribution between planar faults can be varied by different more or less frequent "matrix" layers. Figure 1 depicts the essential concept of the model.

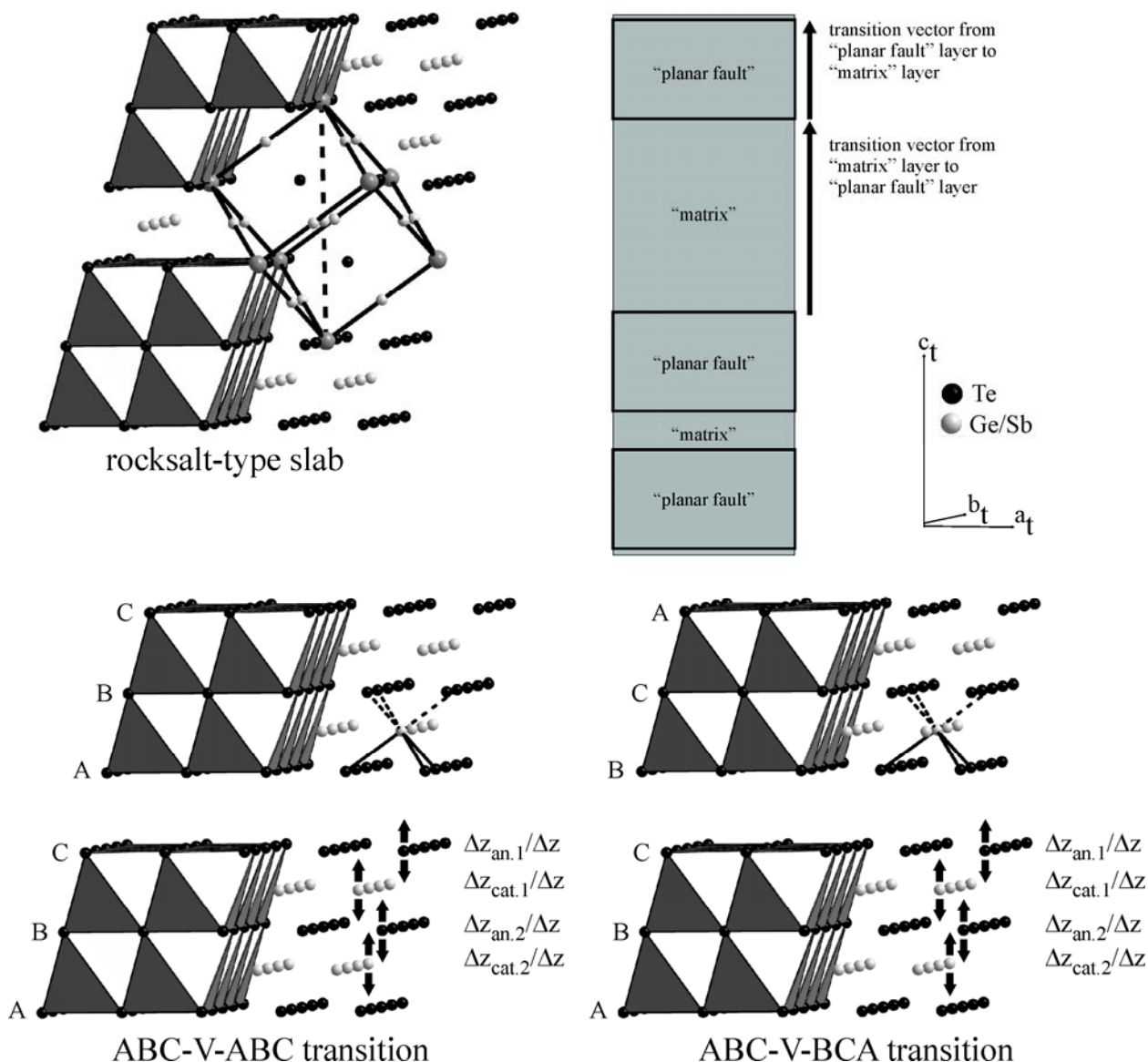


Figure 1. Schematic representation of the stacking fault model; top left: a section of the rocksalt-type with its cubic unit cell (black lines, Te atoms at the corners are depicted dark gray), one of the $\langle 111 \rangle_c$ directions is indicated by a broken line and corresponds to a possible orientation of the $[001]_t$ direction of a twin domain with trigonal average structure but pseudo-cubic axis ratio $a_t/c_t = 0.408$ (for a cubic metric in trigonal setting) – such rocksalt-type slabs with variable number of alternating cation and anion layers are used as “matrix” layers in the stacking model, whereas planar faults correspond to cation defect layers which are accompanied by centrosymmetrical displacements of atom positions in their vicinity. The displacements of cations and anions can be expressed as the ratio of the absolute shifts $\Delta z_{cat.}$ or $\Delta z_{an.}$, respectively, and Δz (with respect to the z coordinates in the average structure) between two consecutive atoms in the average structure ($\Delta z_{cat.}/\Delta z$ or $\Delta z_{an.}/\Delta z$, positive values indicate a shift towards the cation defect layer): cubic sequence (ABC-V-ABC, bottom left) or hexagonal sequences of Te-atom layers (ABC-V-ABC, bottom right) at the cation defect layers (=V) are possible. In the structure model, “matrix” layers and “planar fault layers” are interconnected by appropriate stacking vectors as schematically shown (top right). The frequency of the different layers is defined by corresponding probabilities.

5.4.4.3 Influence of different structural features on the diffuse scattering

In order to study the influence of different structural features on the intensity distribution of the diffuse scattering, the corresponding parameters were independently varied. As a first step, all parameters except one were left unchanged in series of simulations. The model crystal was assumed to exhibit an average structure with $a_t = 4.2251 \text{ \AA}$ and $c_t = 10.3493 \text{ \AA}$ corresponding to a rocksalt-type cell with $a_c = 5.9752 \text{ \AA}$, a typical value for metastable GeTe-rich phases $(\text{GeTe})_n\text{Sb}_2\text{Te}_3$. Such a model is, in principle, suitable to simulate data of ordered long-periodic layered structures and different polytypes or disordered stacking variants thereof. However, the simulations discussed here focus on the real structure of pseudocubic domains whose metrics can be adjusted by varying the reference coordinate system. The amount and statistical distribution of planar faults, the relaxation accompanying them, and the Te-atom stacking sequence around them can be independently varied. Trigonal metrics with different a_t/c_t ratios might be extracted from the Bragg data and also taken into account.

1. The distribution of planar faults

An equidistant and parallel arrangement of cation defect layers (with or without relaxation around them) yields an ordered long-periodic layered structure. Figure 2 (bottom) depicts the positions of reflections along the $0_t0_t\ell_t$ streak of such an ordered crystal of $(\text{GeTe})_9\text{Sb}_2\text{Te}_3$. Cation defect layers are separated by 23 atom layers in a continuous ABC stacking sequence; and accompanied by a relaxation of neighboring atom positions towards the defect layers. Thus, there are three distorted 23-layer rocksalt-type slabs per unit cell of the corresponding 69R polytype. There are show strong reflections of the basic rocksalt-type structure as well as characteristic "superstructure" reflections. A normalized Gaussian distribution (Equation 1) of the planar faults was assumed, including a variance σ around a mean value μ corresponding to the distance between the cation defect layers in long-periodically ordered structures ($\mu = 2n+5$; only values within a 3σ interval were taken into account). In this symmetrical distribution, the average distance μ between the cation defect layers along $[001]_t$ represents the most frequently occurring block size.

$$f(d) = \frac{1}{\sqrt{2\pi\sigma^2}} \cdot e^{-\frac{1}{2}\left(\frac{d-\mu}{\sigma}\right)^2}$$

Equation 1. Gaussian probability density function: d = number of atom layers between cation defect layers; d is proportional to the GeTe content n : $d = 2n+5$, μ = mean number of atomic layers per rocksalt-type slab in a hypothetical ordered arrangement, σ = variance.

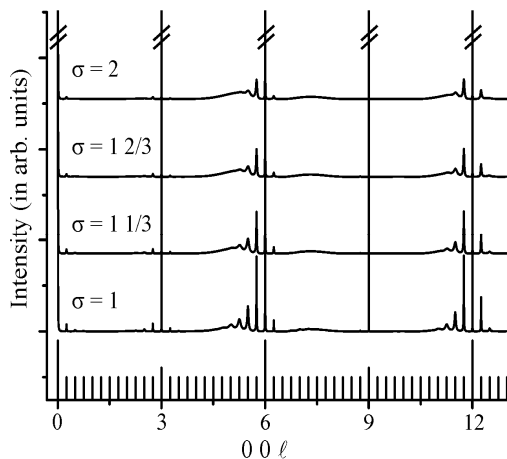


Figure 2. Change of diffuse scattering in the $0_t 0_t l_t$ streak with increasing variance of the Gaussian distance distribution in a model crystal $(\text{GeTe})_9\text{Sb}_2\text{Te}_3$ ($+\Delta z_{\text{cat},1}/\Delta z = 18\%$, $+\Delta z_{\text{an},1}/\Delta z = 15.6\%$, and 100% ABC-V-ABC stacking); the $0_t 0_t l_t$ streak is shown as its intensity distribution is independent from the ratio of Te-Te transitions across the cation defect layer (cf. section 5.4.4.3, 5).

With increasing σ , the "superstructure" reflections broaden and form a tail which accompanies a maximum in the diffuse intensity distribution located at $h_t k_t (l_t - \delta)$ ($h_t = k_t$ or $h_t = -k_t$) where δ gives the distance between Bragg position and "comet". At $h_t k_t (l_t + \delta)$ ($h_t = k_t$ or $h_t = -k_t$) only weak intensities resemble to a "comet" on the high-angle side. Only at very high diffraction angles they become clearly visible. As shown in Figure 2, the diffuse intensity distribution is strongly structured for small values of σ and shows several maxima whereas for larger values of σ only one maximum remains as the head of a "comet" with a continuous tail. The position of the maximum does not depend on σ but only on μ (see below).

2. The defect concentration

Whereas a symmetrical distribution of planar faults around a mean distance μ does not influence the position of the diffuse maximum. Figures 6 and 7 show how the position of the "comet head" $h_t k_t (l_t - \delta)$ ($h_t = k_t$ or $h_t = -k_t$) with respect to the Bragg position depends on the composition. Assuming that all cation defects $(\text{GeTe})_n\text{Sb}_2\text{Te}_3$ are ordered in 2D extended layers, the $1/(n+3)$ defects per anion yield an average thickness of the rocksalt-type slabs of $\mu = 2n+5$ atom layers. Figure 3 depicts the $0_t 0_t l_t$ streak of disordered model crystals with $n = 6, 9$ and 12 in comparison to the Bragg positions of hypothetical polymorphs with slabs of equal thickness. With increasing n and thus increasing μ , the distance $-\delta$ between the diffuse maximum and the Bragg position $h_t k_t l_t$ decreases. The maxima of the diffuse intensity coincide with the Bragg positions of the corresponding hypothetical ordered structures with $\mu = 2n+5$. The ordered arrangement of voids in a superstructure of the rocksalt type (with no hexagonal Te-atom layer sequences) yields a distance $\delta_s = 6/(\mu+1) c^*$ between neighboring reflections. Thus, μ can easily be extracted from experimental data.

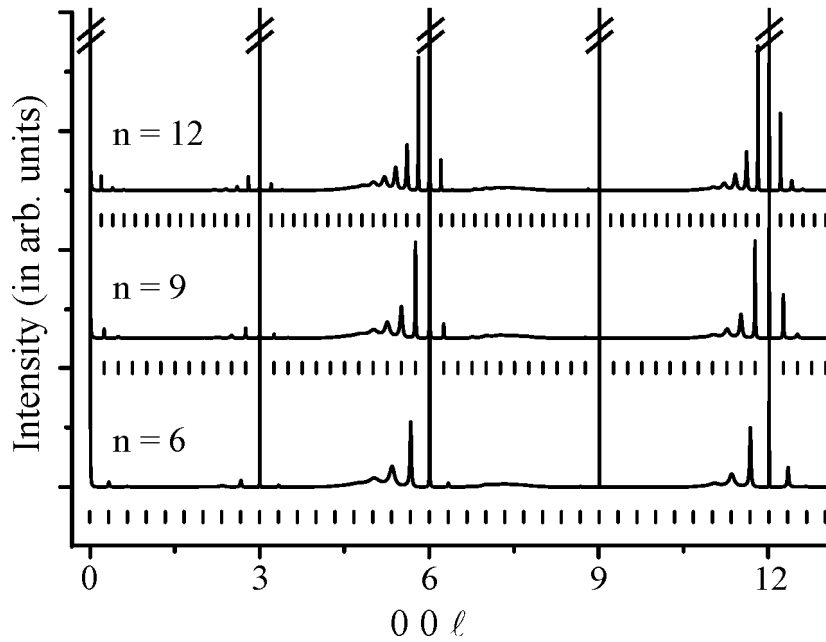


Figure 3. Change of the diffuse intensity along the $0_t 0_t \ell_t$ streak with increasing GeTe content n of $(\text{GeTe})_n\text{Sb}_2\text{Te}_3$ (with $\sigma = 1$, $+\Delta z_{\text{cat.1}}/\Delta z = 18\%$, $+\Delta z_{\text{an.1}}/\Delta z = 15.6\%$, and 100% ABC-V-ABC stacking); the $0_t 0_t \ell_t$ streak is shown as its intensity distribution is independent from the ratio of Te-Te transitions across the cation defect layer (cf. section 5.4.4.3, 5).

3. The structure relaxation around the planar faults

The 2D ordering of cation vacancies is accompanied by symmetrical atom displacements near the planar faults, mirrored in a shift of the z coordinates. A shift Δz_i of the atom position i from its value $z_{i_average}$ in the undistorted average structure to $z_{i_shifted}$ yields the relative displacement $\Delta z_i/\Delta z$, Δz being the difference between the z coordinates of two consecutive atom layers in the average structure. Positive values of $\Delta z_i/\Delta z$ are defined as a shift towards the cation defect layer. Of course, the shift of the anion positions neighboring the defect layer determines the Te-Te distance across the van der Waals gap. Additional shifts of adjacent atom layers yield distorted $[(\text{Ge,Sb})\text{Te}_6]$ octahedra. Simulations have shown that only the anion ($\Delta z_{\text{an.1}}$) cation ($\Delta z_{\text{cat.1}}$) positions next to the defect plane exhibit large shifts that change the diffuse intensity distribution significantly; smaller shifts of next neighbor anion ($\Delta z_{\text{an.2}}$) and cation ($\Delta z_{\text{cat.2}}$) positions therefore can at first be neglected. To assess the influence of the atom displacements, the atom coordinates were stepwise altered starting from the coordinates in the average structure. Only displacements that lead to reasonable interatomic distances were considered. The $0_t 0_t \ell_t$ streak of a model crystal no relaxation (all $\Delta z_i/\Delta z = 0$) around the defect layers shows weak diffuse intensity symmetrically distributed around Bragg positions, as depicted in Figure 4. If the Te-Te atom-layer distance is not changed with respect to the average structure ($\Delta z_{\text{an.1}}/\Delta z = 0$), longer distances (Ge,Sb)-Te towards the cation defect layer ($\Delta z_{\text{cat.1}}/\Delta z < 0$) yield “comets” on the

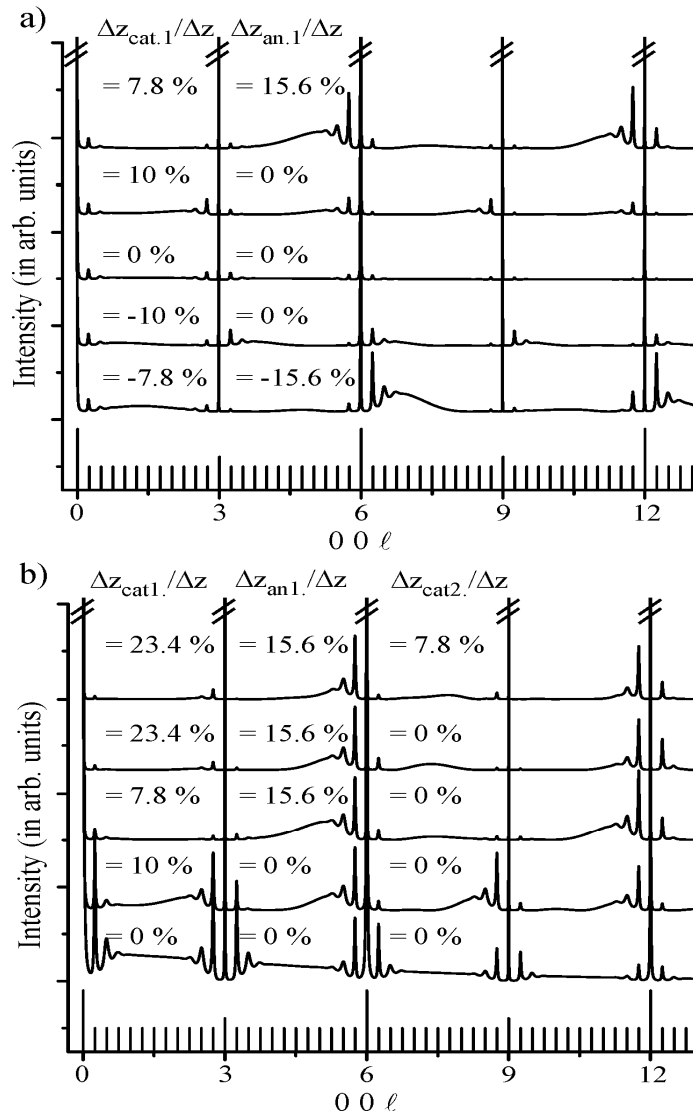


Figure 4. Change of the diffuse streak $0_t\ 0_t\ \ell_t$ with varying displacement of neighboring anions and cations for $(\text{GeTe})_9\text{Sb}_2\text{Te}_3$ ($\sigma = 3$, 100 % ABC-V-ABC stacking); the $0_t\ 0_t\ \ell_t$ streak is shown as its intensity distribution is independent from the ratio of Te-Te transitions across the cation defect layer (cf. section 5.4.4.3, 5): a) change of the diffuse scattering with the direction of the displacements ($\pm \Delta z_{\text{cat.1}}/\Delta z$ and $\pm \Delta z_{\text{an.1}}/\Delta z$, positive shifts resemble displacement towards the defect cation layer); the intensities simulated are not normalized to illustrate the stronger effect of the anion displacement. b) change of the diffuse scattering when several atom layers are shifted towards the cation defect layers ($+\Delta z_{\text{cat.1}}/\Delta z$, $+\Delta z_{\text{an.1}}/\Delta z$ and $+\Delta z_{\text{an.2}}/\Delta z$); to clarify the influence diffuse intensities were normalized on the "comet" head accompanying the Bragg position with $\ell = 6$.

high-angle side of Bragg reflections, whereas for shorter distances Ge/Sb-Te towards the defect layer ($\Delta z_{\text{cat.1}}/\Delta z > 0$) the diffuse maximum is located at the low-angle side (cf. Figure 4). Similarly, the expansion of the Te-Te distance between the slabs yields "comets" on the high-angle side, whereas a contraction, i.e. the formation of van der Waals or partially covalent bonds, yields diffuse maxima on the low-angle side, even if a symmetrical sixfold coordination of cation positions is retained, i.e. $\Delta z_{\text{an.1}}/\Delta z = 2 \Delta z_{\text{cat.1}}/\Delta z$. Due to the more pronounced overall displacement such a model yields, of course, stronger integral diffuse intensities which are further intensified if chemically reasonable anion and cation shifts are applied which combine Te-Te bonding and a 3+3 cation coordination, as shown in Figure 4.

The diffuse features around $h_t\ k_t$ ($\ell_t + 1/2$) are much weaker than the "comets" and almost invisible for small displacements, but become clearly visible when $\Delta z_i/\Delta z$ and thus the overall intensity of the diffuse scattering increases; however, the intensity ratio between strong and weak diffuse features around one Bragg reflection is not significantly

affected by the magnitude of $\Delta z_i/\Delta z$. Whereas the Bragg intensities decrease with ℓ , the diffuse intensity rather increases. This effect is more pronounced for larger atomic displacements. Although the diffuse intensity primarily depends in the displacement of the atom positions neighboring the defect layer ($\Delta z_{an,1}$ and $\Delta z_{cat,1}$, respectively), the relative intensity of the "comet tail" decreases with respect to its "head" if further atom layers (e.g. $\Delta z_{an,2}$ and $\Delta z_{cat,2}$) are shifted to yield reasonable interatomic distances (cf. Figure 4). The function describing the atom shifts around the planar fault then becomes more like a cosine. The "comets" can then be viewed as diffuse satellites of a modulated structure, the first one being dominant for a cosine-like modulation function.

4. The impact of planar faults on the element distribution

In addition to the distortions around the planar faults, vacancy ordering might influence the Ge/Sb ratios on the cation sites. However, simulations have shown that such effects only slightly affect the diffuse intensity in contrast to the much more pronounced influence of atomic displacements. It was therefore neglected and even excellent data are not likely to contain significant information about the cation distribution from diffuse scattering.

5. The Te-atom layer stacking sequence around defect planes

Whereas 2D cation defect ordering in a rocksalt-type structure does not change the Te-atom layer stacking sequence and formally yields a cubic arrangement ABC-V-ABC around the defect plane, the hexagonal arrangement ABC-V-BCA known from the van der Waals gaps in ordered layered structures might also occur. Both types of planar faults exhibit the same 2D periodicity and thus a diffraction pattern where diffuse as well as Bragg intensity is located only at integer h_t and k_t values. Whereas for the $0_t 0_t \ell_t$ streak the structure factor of both sequences is identical, streaks with $h_t, k_t \neq 0$ exhibit significantly different intensities depending on the ratio of cubic and hexagonal transitions. Simulated streaks $1_t -1_t \ell_t$ and $2_t -2_t \ell_t$ for random distribution of different ratios of the two transitions (in steps of 10 %) are depicted in Figure 5. Typical diffuse "comets" are observed in all streaks $h_t k_t \ell_t$ with $h_t, k_t \neq 0$ or $k_t = 0$ and $h_t = k_t$ or $h_t = -k_t$ if there are only ABC-V-ABC transitions.

If exclusively hexagonal ABC-V-BCA transitions are assumed, the diffraction patterns are significantly different. Around positions $-h_t + k_t + \ell_t = 3n$, two strong peaks are observed. The introduction of hexagonal transitions between the slabs alters the metrics of the average structure and thus different Bragg positions. The trigonal axis ratio a_t/c_t corresponding to a cubic cell with

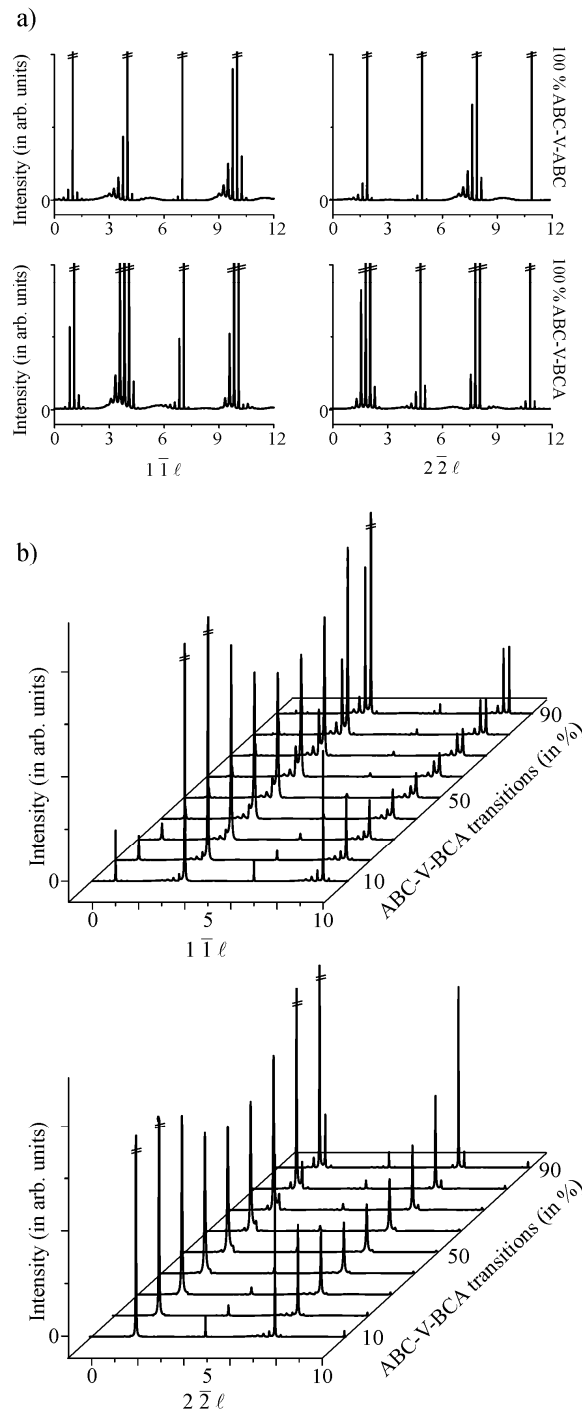


Figure 5. Change of the diffuse scattering in the $1\bar{1}\ell$ and $2\bar{2}\ell$ streaks with increasing percentage of hexagonal ABC-V-BCA transitions between the rocksalt-type slabs in disordered model crystals of $(\text{GeTe})_n\text{Sb}_2\text{Te}_3$ (with $n = 9$, $\sigma = 1$, $+\Delta z_{\text{cat.1}}/\Delta z = 18\%$, $+\Delta z_{\text{an.1}}/\Delta z = 15.6\%$): a) comparison of diffuse intensity in the $1\bar{1}\ell$ and $2\bar{2}\ell$ streaks for ABC-V-ABC or ABC-V-BCA transitions only (the intense Bragg peaks are not completely shown), b) change of the $1\bar{1}\ell$ and $2\bar{2}\ell$ streaks with increasing amount of ABC-V-BCA transitions (strong Bragg peaks cut off).

$a_c = 5.9752 \text{ \AA}$ cannot be recovered by changing the reference basis vectors. The distance between the two strong peaks around $-h_t + k_t + \ell_t = 3n$ is proportional to $1/\mu+1$ ($\mu =$ mean distance between planar faults, see section 5.4.4.3, 1): they are located at $\ell_{t_{\text{low}}} = \ell_t - 2/3(6/(\mu+1))$ and $\ell_{t_{\text{high}}} = \ell_t + 1/3(6/(\mu+1))$ in the streaks with $h_t = \pm k_t = 1$ whereas they are situated at $\ell_{t_{\text{low}}} = \ell_t - 1/3(6/(\mu+1))$ and $\ell_{t_{\text{high}}} = \ell_t + 2/3(6/(\mu+1))$ in the rods with $h_t = \pm k_t = 2$ with respect to integer ℓ_t for a model crystal with ABC-V-ABC transitions only. In streaks with $h_t = \pm k_t = 1$, the reflection at the low-angle side are less intense, whereas the intensity distribution is reversed for streaks $h_t = \pm k_t = 2$.

Of both cubic and hexagonal transitions are present, the ratio between ABC-V-ABC and ABC-V-BCA transitions influences the distance between the "double" peaks characteristic for hexagonal transitions and their relative intensities. Increasing the amount of hexagonal transitions in a disordered model crystal increases the splitting. For small amounts of hexagonal transitions, the Bragg reflections corresponding to 100% cubic transitions are only significantly broadened, amounts $\geq \sim 30\%$ lead to two distinct peaks.

Independent of the degree of splitting, the "double peak" is accompanied by "comets" at $\ell_{t_high} + \delta$ and $\ell_{t_low} - \delta$ with $\delta = 6/(\mu+1) c^*$, respectively.

5.4.5 Examples for matching simulated and experimental data

5.4.5.1 Cubic vs. hexagonal stacking around planar faults in $(\text{GeTe})_2\text{Sb}_2\text{Te}_3$ and $(\text{GeTe})_{12}\text{Sb}_2\text{Te}_3$

The comparison of samples $(\text{GeTe})_n\text{Sb}_2\text{Te}_3$ with significantly different vacancy concentrations provides an instructive example how the defect concentration as well as the ratio between ABC-V-ABC and ABC-V-BCA transitions at defect planes influence the diffraction patterns. Pseudocubic crystals of GeTe-rich samples ($n \geq 3$) can be obtained by quenching the high-temperature modification, which does not exist for $n = 2$ [7]); however, quenching a melt with $n = 2$ in liquid nitrogen yields highly disordered layered phases – probably multiple growth twins – that are ideally suited for comparison. Here, a crystalline fragment with the approximate composition $\text{Ge}_{0.4}\text{Sb}_{0.4}\text{Te} = \text{Ge}_2\text{Sb}_2\text{Te}_5$ (EDX: $\text{Ge}_{0.33(1)}\text{Sb}_{0.49(1)}\text{Te}$) with seemingly pseudo-cubic metrics (cF , $a \approx 5.9870(7) \text{ \AA}$) was investigated. Reciprocal lattice sections perpendicular $\langle 110 \rangle_c$ (cf. Figure 6) resemble those of rocksalt-type structures with alternating strong ($h_c k_c \ell_c$ all even) and weak ($h_c k_c \ell_c$ all odd) intensities; however, groups of several reflections are observed at the corresponding positions. These are interconnected by streaks along $\langle 111 \rangle_c$ that exhibit rather irregular series of maxima. As described in section 5.4.3.1, this diffraction pattern corresponds to superimposed patterns of twin domains with 1D disordered trigonal structures. In Figure 6, an experimental diffraction pattern is compared with two simulated ones, each obtained by superimposing the intensities of twin domains. Both simulations assume the same distribution of planar faults ($n = 2$, $\sigma = 2/3$) with equal structural distortions ($+ \Delta z_{an1}/\Delta z = 15.6 \%$, $+ \Delta z_{cat1}/\Delta z = 18 \%$, $+ \Delta z_{an2}/\Delta z = 0 \%$, $+ \Delta z_{cat2}/\Delta z = 6 \%$). For the model crystal with exclusively cubic ABC-V-ABC transitions, the Bragg reflections of individual domains coincide upon superposition, which yields a rocksalt-type Bragg diffraction pattern and "comet"-like diffuse features at the low angle side of the Bragg positions. This intensity distribution, however, does not correspond to the experimentally observed diffraction pattern. A much more realistic simulation is obtained assuming only hexagonal ABC-V-BCA transitions. The associated deviation from the pseudo-cubic metric of the average structure leads to the characteristic peak splitting in streaks $h_t k_t \ell_t$ with $h_t, k_t \neq 0$ and $h_t = \pm k_t$) as described in section 5.4.4.3, 5. The superposition of simulated intensities of individual domains hence yields groups of strong reflections that are accompanied by additional diffuse maxima, more pronounced at the low

angle side. Whereas the rather large distance between strong reflections and diffuse maxima corroborates the high frequency of planar faults expected for $n = 2$, the pronounced maxima on the diffuse streaks along $[001]_t$ indicate a rather sharp distance distribution of planar faults. Thus, rapidly quenched $\text{Ge}_2\text{Sb}_2\text{Te}_5$ contains fourfold twins of a disordered variant of the stable long-range ordered layered modification with van der Waals gaps with hexagonal Te-atom layer stacking around them.

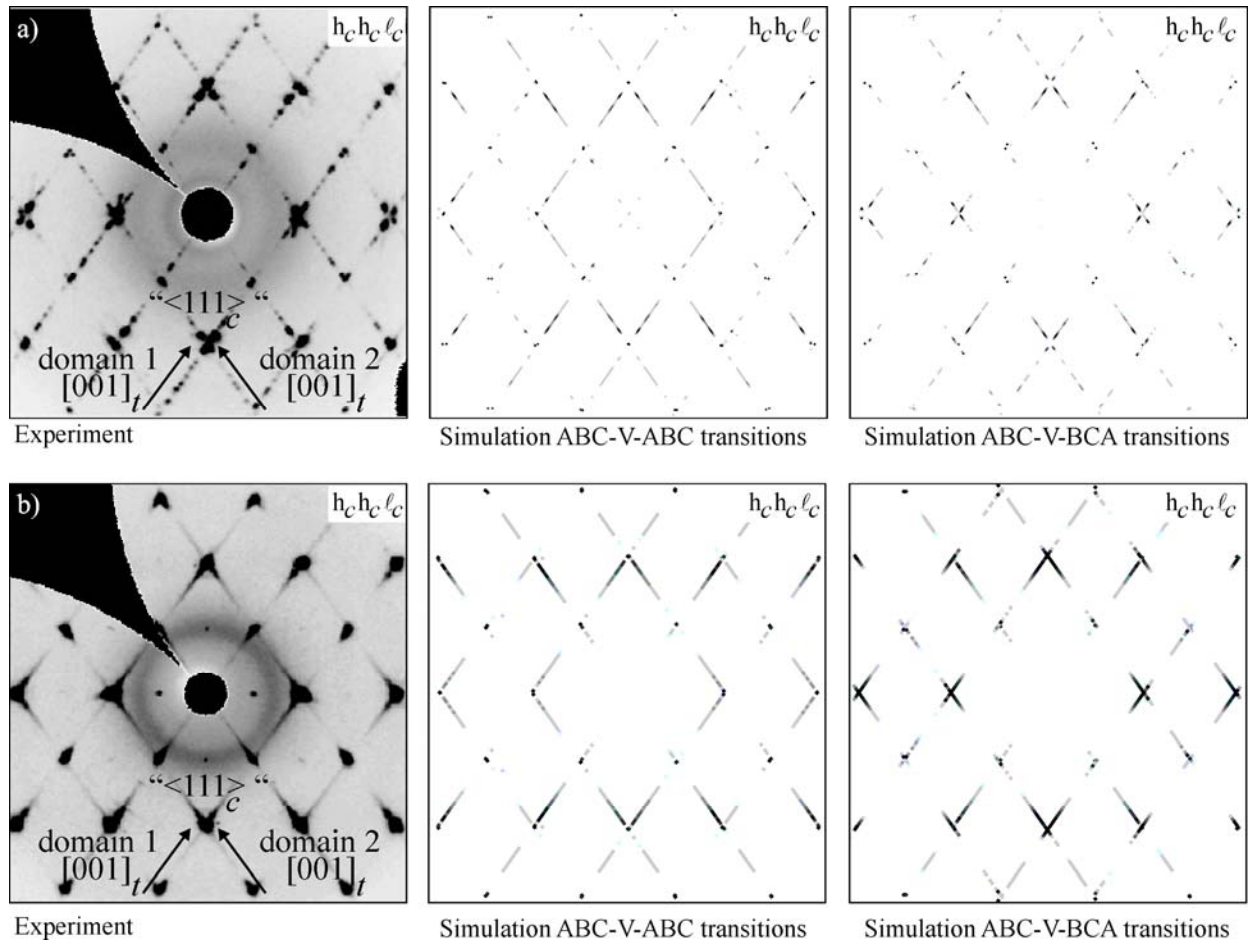


Figure 6. Reciprocal lattice sections $h_c h_c l_c$ extracted from laboratory data of $(\text{GeTe})_2\text{Sb}_2\text{Te}_3$ (a, left) and $(\text{GeTe})_{12}\text{Sb}_2\text{Te}_3$ (b, left) in comparison with simulated data for model crystals with the same defect concentrations that exhibit either exclusively cubic ABC-V-ABC (centre) or exclusively hexagonal ABC-V-BCA (right) transitions of Te atom layers at the cation defect layer. (see text); $[001]_t$ directions parallel $\langle 111 \rangle_c$ are indicated in the experimental sections.

The diffraction pattern of an octahedral crystal of $\text{Ge}_{12}\text{Sb}_2\text{Te}_{15} = \text{Ge}_{0.8}\text{Sb}_{0.13}\text{Te}$ (EDX: $\text{Ge}_{0.87(1)}\text{Sb}_{0.13(1)}\text{Te}$) was grown in the stability range of the rocksalt-type high-temperature modification and subsequently quenched looks very different (cf. Figure 6). The reflections corresponding to the rocksalt-type average structure are broadened but not split (cF with $a = 5.962(1) \text{ \AA}$). There are typical diffuse "comets"; however, they are not clearly separated from

the Bragg reflections. Whereas the broadening of the Bragg reflections might be attributed to twinning on the nanoscale, the small distance between Bragg intensities and the maximum of the diffuse intensity is due to the large spacing between planar faults as discussed in section 5.4.4.3, 1. The diffuse streaks along $[001]_t$ are not structured which indicates a broad distribution of planar faults (cf. section 5.4.4.3, 2). Figure 6 shows a comparison of experimental and, for two model crystals, simulated data generated by superimposing intensities from individual domains. Both model crystals contain the same distribution of defect layers ($n = 12$, $\sigma = 1/3$) and show equal structural distortions (cf. section 5.4.4.3, 3) around them ($+ \Delta z_{an.1}/\Delta z = 15.6\%$, $+ \Delta z_{cat.1}/\Delta z = 18\%$, $+ \Delta z_{an.2}/\Delta z = 0\%$, $+ \Delta z_{cat.2}/\Delta z = 6\%$). The models exhibit exclusively cubic ABC-V-ABC or hexagonal ABC-V-BCA transitions in the Te-atom sequence at the defect plane, respectively. The simulated data for the cubic stacking sequence correspond well to the intensity features experimentally observed. Bragg intensities of individual domains are at the same position and "comets" on the low angle side are close to the strong reflections. Similar to the previous example a change of the metrics of the average structure results if the model crystal contains hexagonal transitions and impedes the complete overlap of Bragg reflections of individual domains. Instead, groups of strong reflections accompanied by diffuse streaking yield asymmetrical "crosses" which do not match with the experimental pattern. This indicates that the crystal with $n = 12$ predominantly contains cubic ABC-V-ABC transitions and the structure is more closely related to the cubic high-temperature modification than to the stable long-periodic layered structures with hexagonal ABC-V-BCA transitions of Te-atom layers at the van der Waals gaps.

5.4.5.2 Fitting simulated to experimental synchrotron data of $(\text{GeTe})_5\text{Sb}_2\text{Te}_3$ and $(\text{GeTe})_6\text{Sb}_2\text{Te}_3$

Whereas the comparison of simulated diffraction data with reciprocal sections reconstructed from laboratory data suffices to approximately assess the frequency and distribution of planar faults and the Te-atom stacking sequence around them, a more detailed evaluation of the diffuse scattering requires synchrotron data with high intensity and good spatial resolution. Such data were acquired for $(\text{GeTe})_5\text{Sb}_2\text{Te}_3 = \text{Ge}_{0.63}\text{Sb}_{0.25}\text{Te}$ and $(\text{GeTe})_6\text{Sb}_2\text{Te}_3 = \text{Ge}_{0.67}\text{Sb}_{0.22}\text{Te}$. Both crystals approximately exhibit a rocksalt type (cf. section 5.4.3) with pronounced short-range defect ordering.

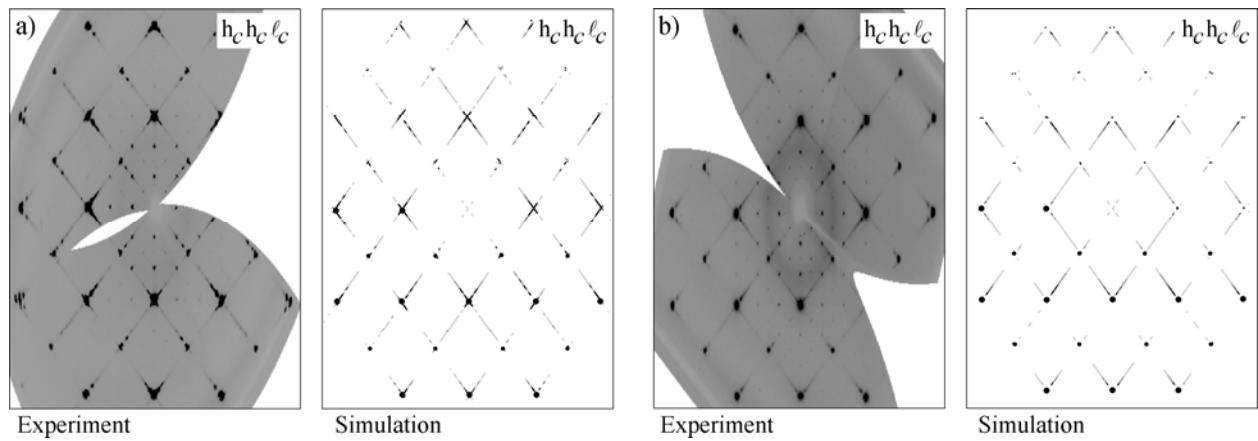


Figure 7. Reciprocal lattice sections $h_c h_c l_c$ extracted from synchrotron data of $(\text{GeTe})_5\text{Sb}_2\text{Te}_3$ (a, left part) and $(\text{GeTe})_6\text{Sb}_2\text{Te}_3$ (b, left part) in comparison with simulated data of optimized model crystals (a and b, respectively, right); in the lower left part of the simulations the broadening strong and weak reflections are marked with black circles to match the experimental broadening whereas the upper right part shows only the superimposed, simulated intensities.

The intensity distribution in the $h_c h_c l_c$ reciprocal section of $(\text{GeTe})_5\text{Sb}_2\text{Te}_3 = \text{Ge}_{0.63}\text{Sb}_{0.25}\text{Te}$ (cf. Figure 7, left), like that of $(\text{GeTe})_{12}\text{Sb}_2\text{Te}_3$, resembles that of the rocksalt type. The structured diffuse streaks along all $\langle 111 \rangle_c$ directions indicate a fourfold twin of trigonal domains with stacking disorder perpendicular $[001]_t$. The asymmetrical shape of the rocksalt-type reflections indicates a deviation from the ideal a_t/c_t ratio of a cubic structure in trigonal setting. As discussed above, such deviations may result from the presence of hexagonal ABC-V-BCA transitions in the cubic arrangement of Te-atom layers (cf. section 5.1). The distance between Bragg intensities and the "comet heads" at their low-angle side is in accordance with a low GeTe content. The presence of several maxima on the diffuse streaks corroborates a sharp distance distribution of the planar faults. As the experimental intensities along a streak can be more conveniently analyzed than that of reciprocal lattice sections, the intensity was integrated along the streaks reconstructed from synchrotron data (cf. Figure 8). The streak $00l_t$, which is not affected by the type of transitions between Te-atom layers terminating the distorted rocksalt-type slabs, yields a mean distance $\mu = 13$ atom layers between cation defect layers according to $\delta = 6/(\mu+1) c^*$. This corresponds to a long-periodic layered structure with $n = 4$, whereas from the composition $(\text{GeTe})_5\text{Sb}_2\text{Te}_3$ with $n = 5$, for a long periodic-layered structure a mean distance of $\mu = 2n + 5 = 15$ atom layers would be expected. Such predictions from the composition; however, are not always accurate, as has been demonstrated for $(\text{GeTe})_4\text{Sb}_2\text{Te}_3$.^[31] A long-periodic layered structure with $\mu = 13$ atom layers in between van der Waals gaps would be expected for this composition; however, a certain range of homogeneity due to mixed site occupancies allows for a deviation from this structure prediction. Single-crystal diffraction did

reveal an long-periodically ordered structure with $\mu = 11$ atom layers, structurally related to the stable phase of $(\text{GeTe})_3\text{Sb}_2\text{Te}_3$.^[36] In metastable phases such effects can be assumed to be even more pronounced which explains why the diffuse scattering corroborates a distance of 13 atom layers between cation defect layers. A narrow distance distribution between planar faults described by a Gaussian function with $\sigma = 2/3 n$ yields a simulated streak similar to the experimentally observed one. This means that the planar faults are almost equidistantly spaced. A good agreement between experimentally and simulated intensities is obtained by shifting the atoms positions in the vicinity of the cation defect layers were shifted by $+\Delta z_{\text{an.1}}/\Delta z = 15.6\%$, $+\Delta z_{\text{cat.1}}/\Delta z = 18\%$, $+\Delta z_{\text{an.2}}/\Delta z = 0\%$, $+\Delta z_{\text{cat.2}}/\Delta z = 6\%$. This corresponds to a Te-Te distance of 3.798 \AA across the cation defect layer, which is significantly smaller than the sum of van der Waals radii (about 4 \AA)^[37] and agrees well with Te-Te distances observed in stable modifications which range in between 3.721 and 3.773 \AA .^[9, 31, 32, 34, 36, 38] Typical short and longer distances in the distorted $(\text{Ge,Sb})\text{Te}_6$ octahedra directly neighbouring the van der Waals gaps in these structures are 2.833 - 2.939 \AA and 3.173 - 3.209 \AA , respectively, which is in good agreement with the corresponding distances (2.964 and 3.177 \AA) in the model crystal. In the neighbouring $(\text{Ge,Sb})\text{Te}_6$ octahedra only cations were displaced in the model crystal ($\Delta z_{\text{cat.2}}$) yielding short and long interatomic distances of 2.929 \AA and 3.049 \AA , respectively. In long-periodic layered phases for which a similar 3+3 coordination is observed, the short distances range between 2.887 - 2.991 \AA and the long distances between 3.049 - 3.095 \AA .

In contrast to the $00\ell_t$ streaks, the $1\bar{1}\ell_t / \bar{1}1\ell_t$ and $2\bar{2}\ell_t / \bar{2}2\ell_t$ streaks contain information about the ratio of cubic ABC-V-ABC and hexagonal ABC-V-BCA transitions. Peak splitting at rocksalt-type positions $h_t k_t \ell_t$ with $-h_t + k_t + \ell_t = 3n$ ($h_t, k_t \neq 0, h_t = \pm k_t$) (cf. Figure 8) indicates that the crystal contains both types of transitions (cf. section 5.4.4.3, 5). However, at these positions intensities from different twin domains overlap which impedes the extraction of the absolute intensities of one domain. Yet, simulated data with equal probability for ABC-V-ABC and ABC-V-BCA Te-atom transitions match the experiment and prove that both types of transitions are present at the cation defect layer. The match between experimental and simulated reciprocal lattice sections with additional intensity features (cf. Figure 7) is also convincing. Thus, the diffuse scattering from quenched $(\text{GeTe})_5\text{Sb}_2\text{Te}_3 = \text{Ge}_{0.63}\text{Sb}_{0.25}\text{Te}$ clearly indicates that the real structure corresponds to an intermediate between the cubic high-temperature phase and the stable long-periodic layered polymorph.

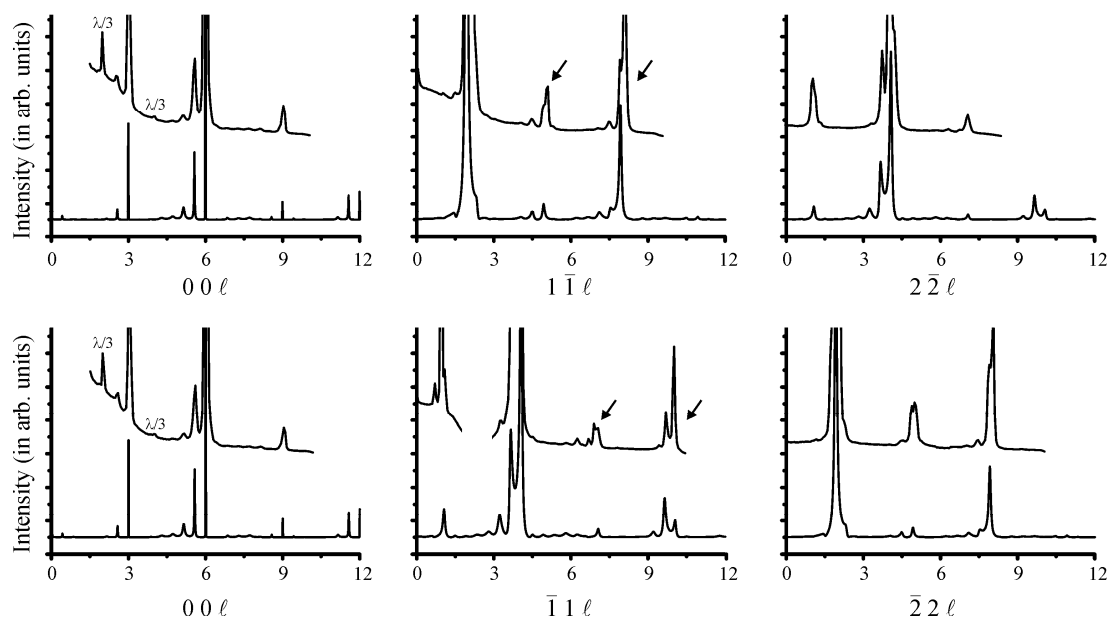


Figure 8. Experimental intensity along diffuse streaks $00l_t$ (the equal directions $-l_t = l_t$ are both depicted to corroborate the symmetry expected for this streak) and $1\bar{1}l_t / \bar{1}1l_t$ as well as $2\bar{2}l_t / \bar{2}2l_t$ ($l_t > 0$) of the crystal $(\text{GeTe})_5\text{Sb}_2\text{Te}_3$ (top histogram in each graph) in comparison to corresponding simulated intensities (bottom in each graph). $\lambda/3$ reflections (observed due to the high beam intensity) are indicated. Black arrows indicate intensity from twin domains with different orientation that cannot be separated. The model used for the simulation is discussed in the text.

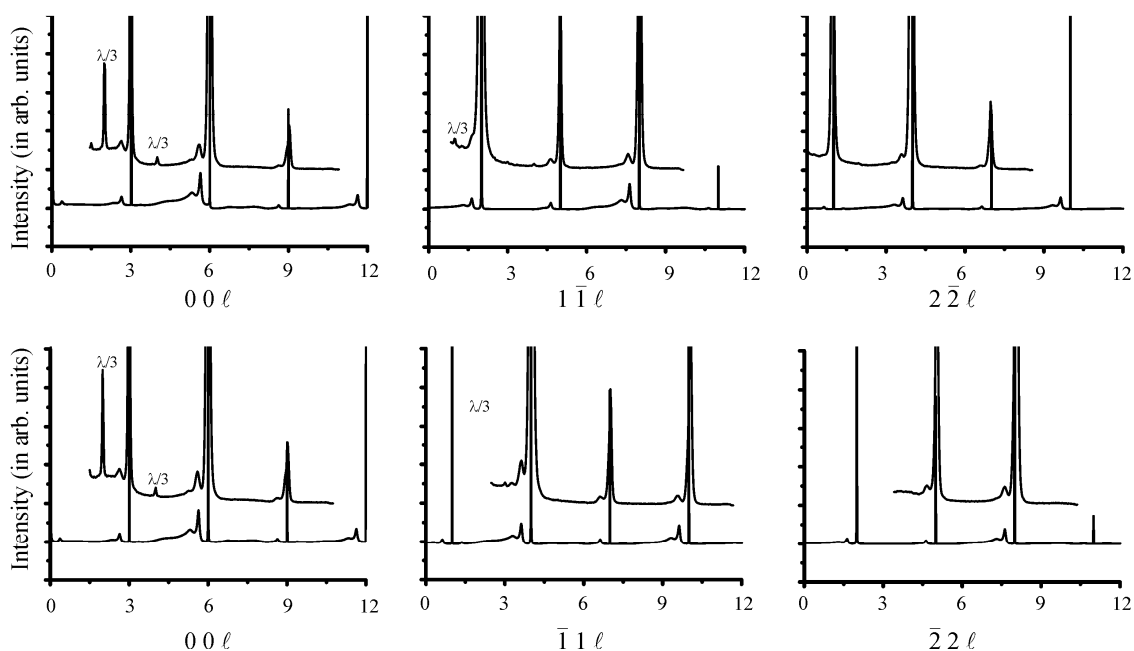


Figure 9. Experimental diffuse streaks along $00l_t$ (the equal directions $-l_t = l_t$ are both depicted to corroborate the symmetry expected for this streak), and $1\bar{1}l_t / \bar{1}1l_t$ as well as $2\bar{2}l_t / \bar{2}2l_t$ ($l_t > 0$) of the crystal $(\text{GeTe})_6\text{Sb}_2\text{Te}_3$ (top histogram in each graph) in comparison to corresponding simulated intensities (bottom histogram in each graph). $\lambda/3$ reflections (observed due to the high beam intensity) are indicated. The model used for the simulation is discussed in the text.

In contrast to $(\text{GeTe})_5\text{Sb}_2\text{Te}_3$, a reciprocal section $h_c h_c \ell_c$ of $(\text{GeTe})_6\text{Sb}_2\text{Te}_3 = \text{Ge}_{0.67}\text{Sb}_{0.22}\text{Te}$ reveals rather sharp Bragg reflections of the pseudo-cubic average structure (cf. Figure 7) and thus does not indicate a deviation from the cubic metrics. Diffuse "comets" are located at the low-angle side of the Bragg reflections. The distance between "comets" and Bragg reflections in the streak $00\ell_t$ (cf. Figure 9) indicates a mean distance $\mu = 15$ atom layers between cation defect layers which corresponds to $n = 5$. Similar to the previous sample, diffuse scattering indicates a certain homogeneity range. The "comet heads" are distinct maxima accompanied by a tail with a smooth intensity distribution. A broad Gaussian function with $\sigma = 5/3 n$ describing the distance distribution of planar faults yields an adequate match between experimental and simulated intensities if atom positions in the vicinity of the cation defect layers are displaced by $+\Delta z_{\text{an}1}/\Delta z = 10.8\%$, $+\Delta z_{\text{cat}1}/\Delta z = 13.2\%$, $+\Delta z_{\text{an}2}/\Delta z = 0\%$, $+\Delta z_{\text{cat}2}/\Delta z = 6\%$. The Te-Te distance is 3.927 \AA , whereas shorter and longer interatomic distances (Ge,Sb)-Te in the first and second $[(\text{Ge,Sb})\text{Te}_6]$ octahedra neighboring the defect layer are $2.964 \text{ \AA} / 3.125 \text{ \AA}$ and $2.929 \text{ \AA} / 3.049 \text{ \AA}$, respectively. The resulting distortion around the cation defect layer is less pronounced than for the previous example with $n = 5$, indicating that atom positions are closer to those of the average structure.

Whereas the streaks $1\bar{1}\ell_t / \bar{1}1\ell_t$ and $2\bar{2}\ell_t / \bar{2}2\ell_t$ $(\text{GeTe})_5\text{Sb}_2\text{Te}_3$ revealed the presence of $\sim 50\%$ hexagonal ABC-V-BCA transitions, such transitions are negligible in $(\text{GeTe})_6\text{Sb}_2\text{Te}_3$. In combination with the broader distance distribution of planar faults and smaller displacements of atoms, this indicates that the structure of $(\text{GeTe})_6\text{Sb}_2\text{Te}_3$ is closer related to the rocksalt-type high-temperature phase with random cation and vacancy distribution than to the stable long-periodically ordered layered structures with their equidistant spacing of van der Waals gaps.

5.4.6 Conclusion

Layer-like cation defect ordering in metastable germanium antimony tellurides $(\text{GeTe})_n\text{Sb}_2\text{Te}_3$ yields structural features comparable to those that are characteristic for trigonal layered modifications stable at ambient temperature. On the other hand, other features resemble the rocksalt-type high-temperature phases. Their structures, especially for $n \gg 3$, therefore represent a snapshot of the atom rearrangements occurring during the equilibrium phase transition between the thermodynamically stable polymorphs of compositions.

In the rocksalt-type high-temperature modification, the Te atom coordination is incomplete due to the random arrangement of cation defects. Such an arrangement is unfavorable at low temperatures but can occur at high-temperature phases, probably due to its higher entropy. For

very small GeTe contents $n < 3$ too many incomplete anion centred polyhedra would be present in a high-temperature phase; such compositions melt before a rocksalt-type structure could be stable. This consideration also explains why the transition temperatures to the high-temperature phases decrease with increasing cation/anion ratio $n+2/n+3$ when incomplete coordination spheres become less frequent.

In long-periodic layered structures, however, no cation defects are present. Distorted rocksalt-type slabs terminated by Te atom layers are only formally separated by missing cation layers in the alternating cation and anion sequence. Although the Te atoms at such a “defect layer” are coordinated by cations from one side only, a change of the Te-atom stacking sequence yields a hexagonal ABC-V-BCA transition and homonuclear Te-Te interactions become favorable. This partially covalent interaction leads to Te-Te distances significantly shorter than the sum of the van der Waals radii and renders this structural arrangement thermodynamically stable.

The equilibrium phase transition from the high-temperature phase therefore yields long-periodic layered phases, but requires long-range diffusion for the structural rearrangements associated. These diffusion processes are hindered if the high-temperature phase is quenched. For high defect concentrations, however, diffusion pathways to form extended vacancy layers are shorter, and the real structure of quenched samples resembles the long-periodic layered phases. For low defect concentrations, diffusion pathways are longer and the real structure of quenched samples is closer to that of the high-temperature phase.

The results obtained from the analysis of diffuse scattering allows one to obtain insight in the complex interplay of thermodynamics and kinetics of phase transitions and emphasized that the characterization of the average structure is not enough to understand the properties of these materials. The simple rules for the interpretation of diffuse streaks of pseudocubic germanium antimony tellurides described in this report can contribute to a better understanding of such interesting thermoelectrics and also contribute to the understanding of metastable crystalline phases of phase-change materials that play an essential role in write and erase cycles in data storage media.

5.4.7 References

- [1] W. Bensch, M. Wuttig, *Chem. Unserer Zeit* **2010**, *44*, 92.
- [2] M. Wuttig, N. Yamada, *Nat. Mater.* **2007**, *6*, 824.
- [3] D. Lencer, M. Salinga, M. Wuttig, *Adv. Mater.* **2011**, *23*, 2030.
- [4] S. Raoux, *Annu. Rev. Mater. Res.* **2009**, *39*, 9.1.

- [5] S. Raoux, W. Wojciech, D. Ielmini, *Chem. Rev.* **2009**, *110*, 240.
- [6] T. Rosenthal, M. N. Schneider, C. Stiewe, M. Döblinger, O. Oeckler, *Chem. Mater.* **2011**, *23*, 4349.
- [7] M. N. Schneider, T. Rosenthal, C. Stiewe, O. Oeckler, *Z. Kristallogr.* **2010**, *225*, 463.
- [8] L. E. Shelimova, O. G. Karpinsky, P. P. Konstantinov, M. A. Kretova, E. S. Avilov, V. S. Zemskov, *Inorg. Mater.* **2001**, *37*, 342.
- [9] T. Matsunaga, H. Morita, R. Kojima, N. Yamada, K. Kifune, Y. Kubota, Y. Tabata, J.-J. Kim, M. Kobata, E. Ikenaga, K. Kobayashi, *J. Appl. Phys.* **2008**, *103*, 093511.
- [10] M. Wuttig, D. Lüsebrink, D. Wamwangi, W. Welnic, M. Gilleßen, R. Dronskowski, *Nat. Mater.* **2007**, *6*, 122.
- [11] T. Siegrist, P. Jost, H. Volker, M. Woda, P. Merkelbach, C. Schlockermann, M. Wuttig, *Nat. Mater.* **2011**, *10*, 202.
- [12] S. Shamoto, N. Yamada, T. Matsunaga, T. Proffen, J. W. Richardson, J.-H. Chung, T. Egami, *Appl. Phys. Lett.* **2005**, *86*, 081904.
- [13] M. N. Schneider, P. Urban, A. Leineweber, M. Döblinger, O. Oeckler, *Phys. Rev. B* **2010**, *81*, 184102.
- [14] C. H. Johansson, J. O. Linde, *Ann. Phys.* **1927**, *387*, 449.
- [15] T. Matsunaga, R. Kojima, N. Yamada, K. Kifune, Y. Kubota, Y. Tabata, M. Takata, *Inorg. Chem.* **2006**, *45*, 2235.
- [16] W. Welnic, A. Pamungkas, R. Detemple, C. Steimer, S. Blugel, M. Wuttig, *Nat. Mater.* **2006**, *5*, 56.
- [17] Z. Sun, S. Kyrsta, D. Music, R. Ahuja, J. M. Schneider, *Solid State Commun.* **2007**, *143*, 240.
- [18] S. I. Shamoto, K. Kodama, S. Iikubo, T. U. Taguchi, N. Yamada, T. Proffen, *Jpn. J. Appl. Phys.* **2006**, *45*, 8789.
- [19] J.-H. Eom, Y.-G. Yoon, C. Park, H. Lee, J. Im, D.-S. Suh, J.-S. Noh, Y. Khang, J. Ihm, *Phys. Rev. B* **2006**, *73*, 214202.
- [20] J. C. Labiche, O. Mathon, S. Pascarelli, M. A. Newton, G. G. Ferre, C. Curfs, G. B. M. Vaughan, A. Homs, D. F. Carreiras, *Rev. Sci. Instrum.* **2007**, *78*, 11.
- [21] a) J.L. Chambers, K.L. Smith, M.R. Pressprich, Z. Jin, *SMART*, V.5.625. Bruker AXS, Madison, USA, **1997-2001**. b) *SAINTE*, V6.01, Bruker AXS, Madison, USA, **1999**.
- [22] *SADABS*, V2.03, Bruker AXS, Madison, USA, **1999**
- [23] G. M. Sheldrick, *Acta Crystallogr. Sect. A* **2008**, *64*, 112.

-
- [24] C. T. Chantler, K. Olsen, R. A. Dragoset, J. Chang, A. R. Kishore, S. A. Kotochigova, D. S. Zucker, **2005**.
- [25] B. L. Henke, E. M. Gullikson, J. C. Davis, *At. Data Nucl. Data Tables* **1993**, *54*, 181.
- [26] J. P. Wright, unpublished work.
- [27] S. Hendricks, E. Teller, *J. Chem. Phys.* **1942**, *10*, 147.
- [28] M. M. J. Treacy, J. M. Newsam, M. W. Deem, *Proc. R. Soc. Lond. A* **1991**, *433*, 499.
- [29] M. N. Schneider, X. Biquard, C. Stiewe, T. Schröder, P. Urban, O. Oeckler, *Chem. Commun.* **accepted**.
- [30] M. N. Schneider, X. Biquard, C. Stiewe, T. Schröder, P. Urban, O. Oeckler, *Chem. Commun.* **2012**.
- [31] M. N. Schneider, O. Oeckler, *Z. Anorg. Allg. Chem.* **2008**, *634*, 2557.
- [32] T. Matsunaga, N. Yamada, Y. Kubota, *Acta Crystallogr. Sect. B* **2004**, *60*, 685.
- [33] L. E. Shelimova, O. G. Karpinsky, M. A. Kretova, V. I. Kosyakov, V. A. Shestakov, V. S. Zemskov, F. A. Kuznetsov, *Inorg. Mater.* **2000**, *36*, 768.
- [34] O. G. Karpinsky, L. E. Shelimova, M. A. Kretova, J.-P. Fleurial, *J. Alloys Compd.* **1998**, *268*, 112.
- [35] C. W. Sun, J. Y. Lee, Y. T. Kim, *Phys. Stat. Sol. RRL* **2009**, *3*, 254.
- [36] T. Matsunaga, R. Kojima, N. Yamada, K. Kifune, Y. Kubota, M. Takata, *Appl. Phys. Lett.* **2007**, *90*, 161919.
- [37] A. Bondi, *J. Phys. Chem.* **1964**, *68*, 441.
- [38] T. Matsunaga, N. Yamada, *Phys. Rev. B* **2004**, *69*, 104111.

5.5 From metastable to stable modifications – *in situ* Laue diffraction investigation of diffusion processes related to the phase transitions of GeTe-rich $(\text{GeTe})_n(\text{Sb}_2\text{Te}_3)$ ($n = 6 < n < 15$) crystals

Matthias N. Schneider, Xavier Biquard, Christian Stiewe, Thorsten Schröder, Philipp Urban, and Oliver Oeckler

Chemical Communications **2012**, 48, 2192-2194.

Abstract

Temperature dependent phase transitions of germanium antimony tellurides $(\text{GeTe})_n\text{Sb}_2\text{Te}_3$ ($n = 6, 12, 15$) have been investigated by *in situ* microfocus Laue diffraction. Diffusion processes involving cation defect ordering at ~ 300 °C lead to different nanostructures which can be correlated to changes of the thermoelectric characteristics.

Copyright: © 2011 Royal Society of Chemistry

5.5.1 Introduction

Thermodynamically stable phases of GeTe-rich compounds in the pseudobinary system $(\text{GeTe})_n\text{Sb}_2\text{Te}_3$ ($n > 3$) exhibit rocksalt-type average structures at elevated temperatures but crystallize in trigonal long-periodically ordered layered structures at room temperature (cf. Fig. 1).^[1,2] The latter exhibit no cation vacancies but are rather composed of distorted rocksalt-type slabs with $2n + 5$ alternating cation and anion layers which are interconnected by van der Waals gaps between Te atom layers terminating the slabs. In contrast, the high-temperature phases contain $1/(n + 3)$ cation defects randomly distributed over one crystallographic site.³ Both modifications are related by a phase transition which involves diffusion—formally of cation defects which form 2D extended layers at low temperature—and by the alteration of the cubic stacking sequence of Te atom layers to yield van der Waals gaps. Metastable modifications obtained by quenching the high-temperature phases represent an “intermediate state” of this phase transition. They exhibit domains with a trigonally distorted rocksalt-type average structure which are eightfold twinned according to the group–subgroup relationship $Fm\bar{3}m \rightarrow R\bar{3}m \rightarrow R3m$.^[4] The deviation from the cubic metrics becomes more pronounced with increasing n .^[1] Diffraction patterns of such quenched samples exhibit pseudo-cubic symmetry resulting from the incoherent superposition of intensities from individual domains. Short-range ordering of cation defects produces nanostructures characterized by more or less extended intersecting vacancy layers perpendicular to the pseudo-cubic $\langle 111 \rangle$ directions (cf. Fig. 1), as indicated by diffuse scattering and corroborated by electron microscopy.^[3,4]

Metastable modifications play an important role in write–erase cycles of modern data storage media such as Blu-Ray Discs or non-volatile PC-RAM. Furthermore, they are an intriguing class of thermoelectrics with figures of merit ZT of up to 1.3.^[4,5] Both these applications strongly depend on physical properties related to the real structure of the materials.^[6,7] As it is mainly associated with the defect distribution, it is of great interest to study temperature-dependent diffusion processes associated with the phase transitions of $(\text{GeTe})_n\text{Sb}_2\text{Te}_3$ compounds.

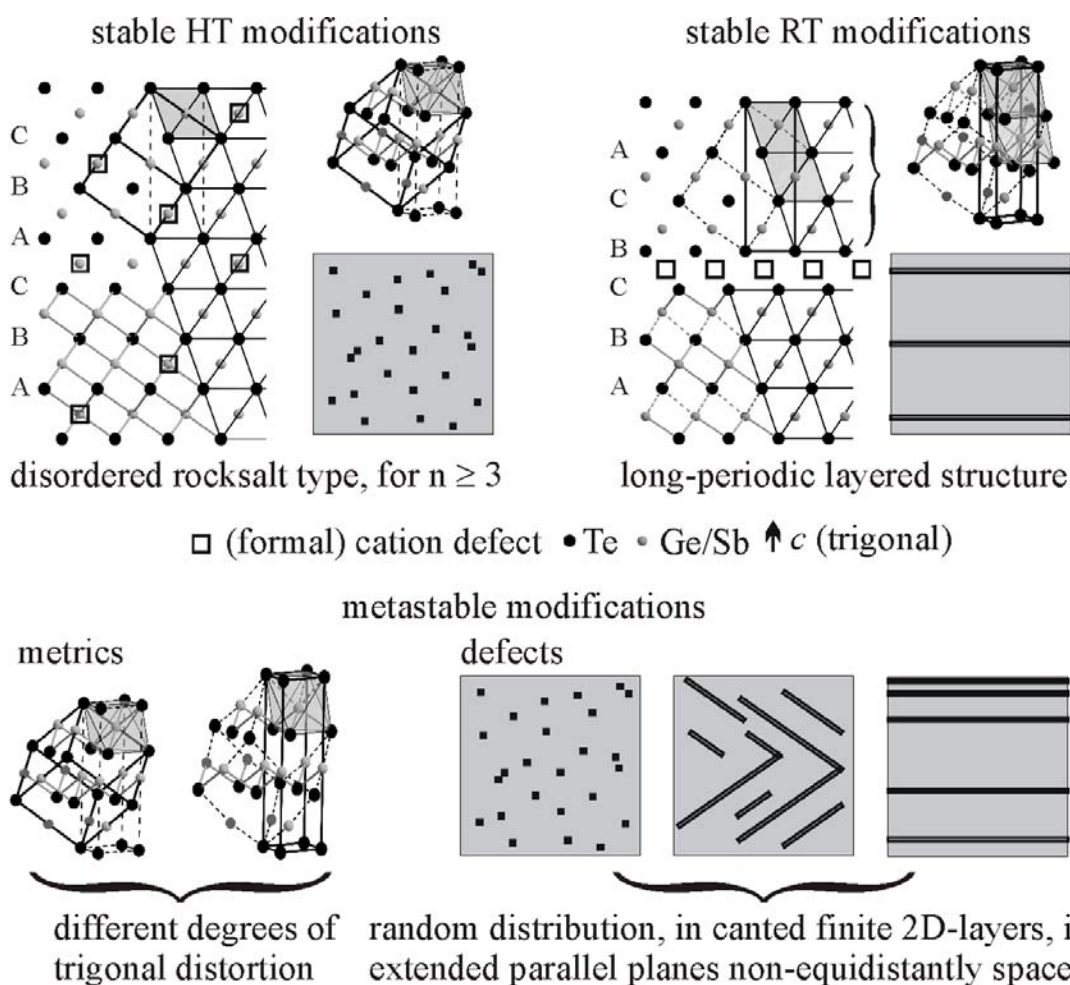


Figure 1. Structures of different modifications of $(\text{GeTe})_n\text{Sb}_2\text{Te}_3$ phases: sections of stable phases (top, along $[010]$, trigonal setting), the perspective views indicate the rocksalt-type building units. Cubic and trigonal cells are outlined for comparison. A schematic representation shows the formal cation defect distribution; average structure of metastable phases with more or less pronounced distortion (bottom left, perspective view) and schematic representations of different cation defect distributions in metastable modifications (bottom right).

Micro-focus white-beam (Laue) diffraction using synchrotron radiation is an intriguing method for such investigations. Micro-focusing partially excludes space-averaging effects typical for conventional X-ray diffraction experiments, whereas due to the polychromatic beam large areas of reciprocal space are recorded in a single diffraction pattern. Therefore, micro-focus Laue diffraction is ideally suited for the in situ temperature-dependent investigation of diffusion phenomena. Laue diffraction patterns of various GeTe-rich $(\text{GeTe})_n\text{Sb}_2\text{Te}_3$ crystals grown by chemical transport reactions were collected at BM32 (ESRF, Grenoble) using a micro-beam (focus $< 1 \times 1 \text{ mm}^2$) in a temperature range from room temperature to approximately $600 \text{ }^\circ\text{C}$ and a temperature accuracy of $\pm 15 \text{ }^\circ\text{C}$. Details of the sample preparation and the experimental setup can be found in the ESI.

5.5.2 Results and discussion

Laue diffraction patterns collected from a crystal of $\text{Ge}_{0.65(3)}\text{Sb}_{0.22(1)}\text{Te} = (\text{GeTe})_6\text{Sb}_2\text{Te}_3$, which was originally grown in the stability range of the cubic high-temperature phase and subsequently quenched (cf. Fig. 2), show asymmetrically broadened reflections which are interconnected by diffuse streaks. The variation of both the asymmetric broadening as well as the diffuse scattering in diffraction patterns collected at different positions on the sample corresponds to the presence of individual twin domains which are at least as large as the area irradiated by the micro-beam.

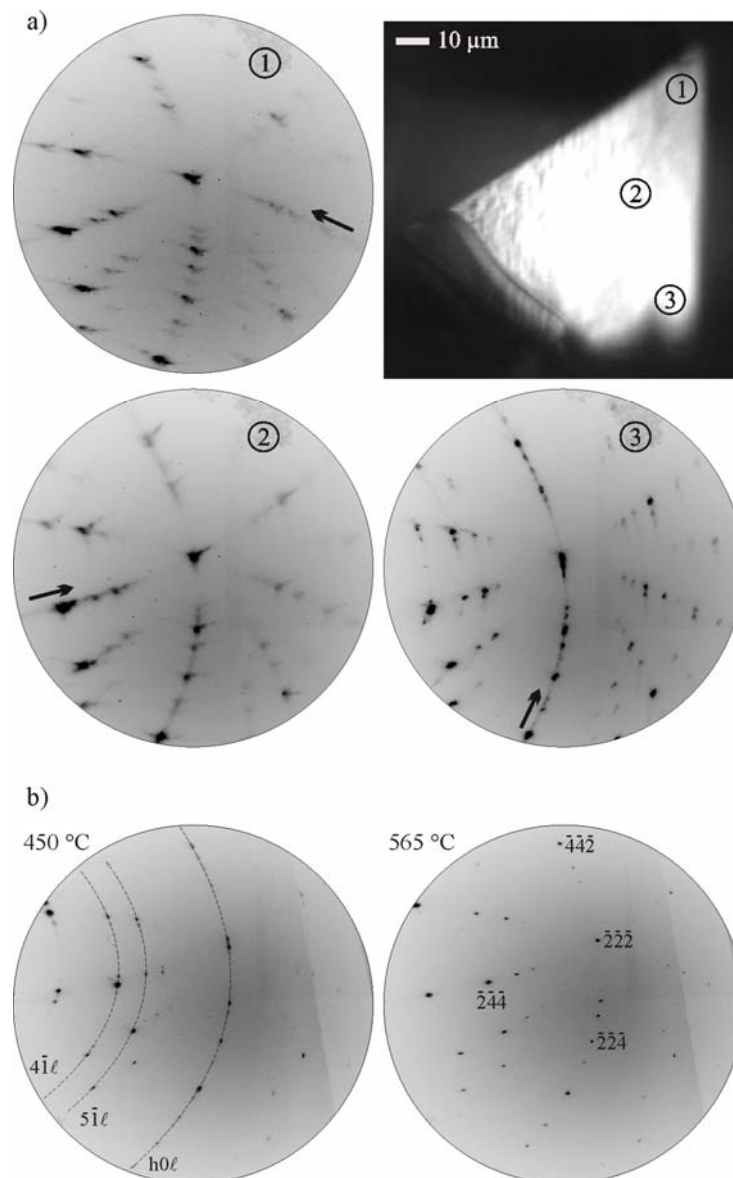


Figure 2. a) Optical microscopy image of the $(\text{GeTe})_5(\text{Sb}_2\text{Te}_3)$ crystal used for the investigation (top right) and three room-temperature Laue diffraction patterns collected from the positions indicated by the numbers (black arrows indicate the main orientation of diffuse streaks); b) diffraction patterns collected from position 3 (slightly different section of the complete pattern) at 450 °C (selected rays of the $h\bar{1}l$ plane and the $h0l$ zone are indicated) and at 565 °C with selected indices

The broadening of the Bragg reflections is related to the varying metric distortion of individual domains along one of the pseudocubic $\langle 111 \rangle$ directions. It is further enhanced due to short-range order. The orientation of the structured diffuse streaks between the Bragg positions continues to the asymmetric broadening and indicates the presence of extended planar defects which are parallel but not equidistant. Upon heating, at a rate of $10 \text{ }^\circ\text{C min}^{-1}$ (cf. Fig. S1a), between 250 and 300 $^\circ\text{C}$ the diffuse streaks gradually transform into a series of rather sharp reflections characteristic of a long-periodically ordered layered structure (cf. Fig. 2, bottom left). Although the Laue experiment does not allow one to determine the absolute lattice parameters, the reflections observed in zones with variable l roughly match with a $51R$ -type structure.^[1] This is in accordance with the cation/anion ratio of $(\text{GeTe})_6\text{Sb}_2\text{Te}_3$ which determines the thickness of the rocksalt-type slabs.^[2] However, such a structure prediction on the basis of simple rules is limited by non-stoichiometry^[8] so that details of the long-periodic structure cannot unequivocally be determined. At $\sim 500 \text{ }^\circ\text{C}$, the characteristic reflections of the layered structure become weak and at 550 $^\circ\text{C}$ the cubic high-temperature modification is formed. The diffraction pattern above this temperature (Fig. 2, bottom right) can be indexed assuming a cF lattice with $a = 6.00 \text{ \AA}$ (cf. Fig. S2a) in accordance with lattice parameters reported for such high-temperature modifications.^[1,3] The absence of structured diffuse scattering confirms the random arrangement of the cation defects.

A similar experiment with a metastable $\text{Ge}_{0.83(4)}\text{Sb}_{0.14(1)}\text{Te} = (\text{GeTe})_{12}\text{Sb}_2\text{Te}_3$ crystal (cf. Fig. S1b and S3w) shows very broad reflections at room temperature whose broadening does not exhibit a preferred direction and there are no distinct diffuse streaks with specific orientations. These data indicate the absence of domains with parallel planar defects larger than the beam size. They rather correspond to twinning on the nanoscale. Upon heating, the diffuse intensities become more structured at 350 $^\circ\text{C}$ and gradually develop into streaks between Bragg reflections. At 400 $^\circ\text{C}$, the Bragg reflections are sharp and correspond to an hR lattice with $a/c = 0.404$ ($a = 4.25 \text{ \AA}$, $c = 10.52 \text{ \AA}$). They are interconnected by diffuse streaks along c^* corresponding to 2D cation defect ordering that results in parallel but not equidistant defect planes. When the temperature is further increased by approx. $10 \text{ }^\circ\text{C min}^{-1}$, the diffuse streaks

do not transform into rows of sharp reflections. Instead, from 450 $^\circ\text{C}$ on their intensity gradually decreases. The absence of structured diffuse scattering at 500 $^\circ\text{C}$ indicates a random defect distribution in a high-temperature modification; the Bragg reflections can be indexed based on a rocksalt-type cell with $a = 6.00 \text{ \AA}$ (cf. Fig. S2b). Thermal cycling experiments reveal that the high-temperature modification of the sample can be undercooled to about 30 $^\circ\text{C}$ before a 1D disordered layered structure is reformed. Diffuse streaks become clearly visible between 430–

370 °C. Upon reheating, the intensity of these diffuse streaks decreases from 500 °C on; however, the rocksalt-type phase without diffuse scattering forms at slightly higher temperature compared to the initial heating. The high-temperature modification of $\text{Ge}_{0.65(3)}\text{Sb}_{0.22(1)}\text{Te} = (\text{GeTe})_6\text{Sb}_2\text{Te}_3$ can also be undercooled to about 30 °C, however, no thermal cycling experiments were performed.

Although both $(\text{GeTe})_6\text{Sb}_2\text{Te}_3$ and $(\text{GeTe})_{12}\text{Sb}_2\text{Te}_3$ exhibit a similar high-temperature modification, the real structure of quenched crystals is significantly different. As a consequence of the higher vacancy concentration, short-range defect ordering is more pronounced in $(\text{GeTe})_6\text{Sb}_2\text{Te}_3$ and yields extended, parallel defect planes, whereas in $(\text{GeTe})_{12}\text{Sb}_2\text{Te}_3$, the diffraction data indicate a nanostructure with finite intersecting defect layers.^[4,7] The diffusion pathways required to form a long-periodically ordered structure are shorter for $(\text{GeTe})_6\text{Sb}_2\text{Te}_3$. Therefore, the ordered structure appears within a few seconds when diffusion sets in at 300 °C. Although diffusion is activated in a similar temperature range in $(\text{GeTe})_{12}\text{Sb}_2\text{Te}_3$, extended defect layers are not formed until the cubic high-temperature phase appears when heating quenched crystals by 10 °C min⁻¹. In this case, the formation of a long periodically ordered structure requires prolonged annealing times.^[1,3,4]

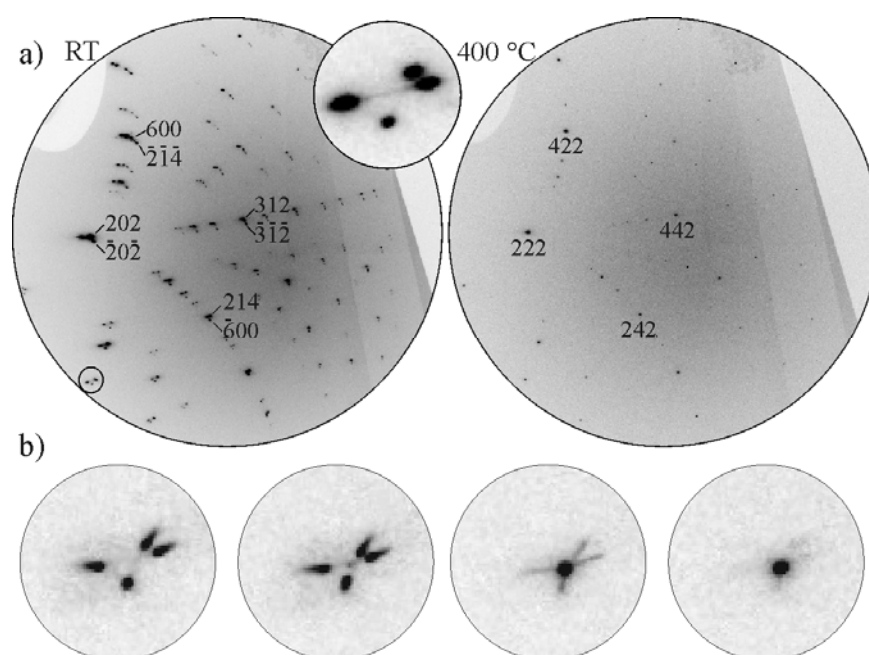


Figure 3. a) Laue diffraction patterns of $(\text{GeTe})_{15}(\text{Sb}_2\text{Te}_3)$ collected at room temperature and at 415 °C, the inset shows an enlarged group of reflections from different domains (exemplarily indices of some reflections are given); b) changing intensity distribution of the reflection group indicated in a) between 330 and 340 °C (left to right) during heating.

Laue diffraction patterns of quenched $\text{Ge}_{0.84(1)}\text{Sb}_{0.12(1)}\text{Te} = (\text{GeTe})_{15}\text{Sb}_2\text{Te}_3$ crystals (Fig. 3) do not show strongly broadened Bragg reflections at room temperature, in contrast to samples with

lower GeTe content. The diffraction patterns exhibit groups of reflections which result from the superposition of the intensities from individual domains with unit cells clearly deviating from pseudo-cubic metrics. Reflections belonging to individual domains can be indexed based on an hR cell with $a = 4.22 \text{ \AA}$ and $c = 10.57 \text{ \AA}$ (cf. Fig. S4). The ratio $a/c = 0.399$ lies between that of α -GeTe ($a/c = 0.389$)^[9] and that of a cubic cell in hR setting ($a/c = 0.408$). Whereas no diffuse scattering is observed between groups of reflections, there are weak diffuse streaks that interconnect the reflections of one group. These are due to domain-wall scattering (cf. Fig. 3 and Fig. S4). Upon heating the sample above 330 °C, additional Bragg reflections of the rocksalt-type high temperature phase appear in between the reflections of each group and gain intensity as the rhombohedral distortion of the individual domains decreases. At 400 °C only reflections which can be indexed with a cF cell with $a = 6.00 \text{ \AA}$ are observed (cf. Fig. 3 and S2c).

In contrast to samples with lower GeTe contents, $(\text{GeTe})_{15}\text{Sb}_2\text{Te}_3$ does not show nanostructures with pronounced short-range correlated cation defects. At all temperatures, there was no diffuse scattering indicative of extended planar faults. Intrinsic cation defects can be assumed to concentrate at domain boundaries. However, slightly below the transition temperature to the cubic high-temperature modification, trigonal and cubic domains coexist. Although the $(\text{GeTe})_{15}\text{Sb}_2\text{Te}_3$ crystal can be viewed as a multiply twinned Sb_2Te_3 -doped variant of GeTe, the phase transition is different from the continuous, displacive rhombohedral to cubic transition of GeTe at $\sim 432 \text{ °C}$ ^[9,10] as it requires diffusion of defects from domains boundaries to form the disordered rocksalt type. Upon cooling the crystal below 330 °C, the sharp reflections of the high-temperature modification significantly broaden and the diffraction patterns resemble those observed for $(\text{GeTe})_{12}\text{Sb}_2\text{Te}_3$ at room temperature (cf. Fig. S5). This indicates that a nano-domain transformation twin is formed, whereas before heating a growth twin was present.

Metastable Ge–Sb–Te phases are p-type semiconductors with rather low thermal conductivities, κ , rendering them promising candidates for thermoelectric materials. Fig. 4 shows the temperature dependence of κ of samples $(\text{GeTe})_n\text{Sb}_2\text{Te}_3$ ($n = 7, 12, 19$) quenched from their high-temperature phases as well as the Seebeck coefficient and the electrical conductivity of $(\text{GeTe})_{12}\text{Sb}_2\text{Te}_3$ during heating (for experimental details refer to ESI). The dependency of the thermoelectric properties on the composition is discussed elsewhere.^[7] The thermal conductivity curves are discontinuous: above 300 °C, κ increases by $\sim 0.2 \text{ W mK}^{-1}$ and decreases again at higher temperature. At similar temperatures, both the Seebeck coefficient as well as the electrical conductivity of $(\text{GeTe})_{12}\text{Sb}_2\text{Te}_3$ change discontinuously and show a hysteretic behavior in this temperature range.

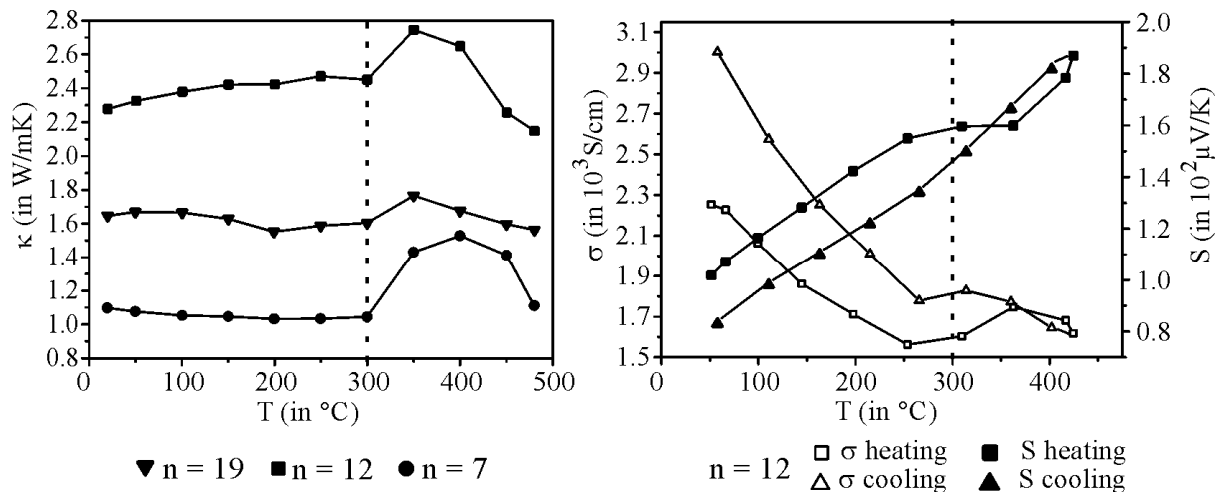


Figure 4. Thermal conductivities of quenched samples $(\text{GeTe})_n(\text{Sb}_2\text{Te}_3)$ ($n = 7, 12, 19$) up to a temperature of 480 °C (top) and temperature dependency of the Seebeck coefficient as well as the electrical conductivity of metastable $(\text{GeTe})_{12}(\text{Sb}_2\text{Te}_3)$: during heating up to 450 °C (bottom)

5.5.3 Conclusion

Several conclusions can be drawn from our experiments: the high-temperature phase transitions of $(\text{GeTe})_n\text{Sb}_2\text{Te}_3$ ($n > 3$) involve the rearrangement of cation defects and therefore are predominantly order–disorder transitions rather than displacive phase transitions such as that of GeTe. For all compositions, independent of the real structure, diffusion processes are activated at ~ 300 °C. This is mirrored in the thermoelectric characteristics. The diffusion processes influence the thermal conductivities and also alter the electronic structure. The hysteresis of the properties concurs with the limited mobility of defects. Our investigation clearly demonstrates that investigations of the average structure, e.g. by powder diffraction, are not sufficient to fully understand the temperature dependencies of the structure–property relationships of these materials because the diffusion processes and thus the changes of the real-structure are predominantly reflected as diffuse scattering.

5.5.4 References

- [1] D. T. Matsunaga, H. Morita, R. Kojima, N. Yamada, K. Kifune, Y. Kubota, Y. Tabata, J.-J. Kim, M. Kobata, E. Ikenaga, K. Kobayashi, *J. Appl. Phys.* **2008**, *103*, 093511.
- [2] O. G. Karpinsky, L. E. Shelimova, M. A. Kretova, J.-P. Fleurial, *J. Alloys Compd.* **1998**, *268*, 112.
- [3] M. N. Schneider, T. Rosenthal, C. Stiewe, O. Oeckler, *Z. Kristallogr.* **2010**, *225*, 463.

- [4] M. N. Schneider, P. Urban, A. Leineweber, M. Döblinger, O. Oeckler, *Phys. Rev. B* **2010**, *81*, 184102.
- [5] D. Lencer, M. Salinga, M. Wuttig, *Adv. Mater.* **2011**, *23*, 2030.
- [6] T. Siegrist, P. Jost, H. Volker, M. Woda, P. Merkelbach, C. Schlockermann, M. Wuttig, *Nat. Mater.* **2011**, *10*, 202.
- [7] T. Rosenthal, M. N. Schneider, C. Stiewe, M. Döblinger, O. Oeckler, *Chem. Mater.* **2011**, *23*, 4349.
- [8] M. N. Schneider, O. Oeckler, *Z. Anorg. Allg. Chem.* **2008**, *634*, 2557.
- [9] T. Chattopadhyay, J. X. Boucherle, H. G. von Schnering, *J. Phys. C: Solid State Phys.* **1987**, *20*, 1431.
- [10] A. V. Kolobov, M. Krbal, P. Fons, J. Tominaga, T. Uruga, *Nat. Chem.* **2011**, *3*, 311.

5.5.5 Supporting information

5.5.5.1 Experimental

Synthesis of crystalline samples

GeTe-rich metastable $(\text{GeTe})_n\text{Sb}_2\text{Te}_3$ bulk samples with $n \geq 3$ were prepared by melting stoichiometric amounts of the elements Ge (99.999%, Sigma Aldrich), Sb (99.999%, Smart Elements) and Te (99.999%, Alfa Aesar) in sealed silica glass ampoules under Ar atmosphere. After melting the mixtures at 950 °C, the ampoules were quenched in air. From samples obtained this way, octahedral crystals $(\text{GeTe})_n\text{Sb}_2\text{Te}_3$ $n \geq 3$ with size of about $0.5 \times 0.5 \times 0.5 \text{ mm}^3$ can be grown by chemical transport reactions. The crystal $\text{Ge}_{0.65(3)}\text{Sb}_{0.22(1)}\text{Te} = (\text{GeTe})_6\text{Sb}_2\text{Te}_3$ was grown from approximately 100 mg of powdered material with initial elemental ratio of Ge:Sb:Te = 1.44:2:5 in an silica glass ampoule (length 10 cm, diameter 10 mm) under Ar atmosphere. The material was kept at 628 °C for 4 h then slowly cooled to 618 °C (within 6 h). After holding this temperature for 75 h, the sample was quenched in air. This way GeTe-poor crystals are obtained, n varies between 3 and 12. For GeTe-rich crystals such as $\text{Ge}_{0.83(4)}\text{Sb}_{0.14(1)}\text{Te} = (\text{GeTe})_{12}\text{Sb}_2\text{Te}_3$ and $\text{Ge}_{0.84(1)}\text{Sb}_{0.12(1)}\text{Te} = (\text{GeTe})_{15}\text{Sb}_2\text{Te}_3$ different procedures were used. Powdered starting material (ca. 100 mg, the initial elemental ratio for both crystals Ge:Sb:Te = 12:2:15) was sealed in evacuated silica glass ampoules (length 15-20 cm, diameter 10-15 mm). SbI_3 (< 10 weight%) was added to generate the transport agent I_2 by decomposition at elevated temperatures. Octahedral single crystals $\text{Ge}_{0.83(4)}\text{Sb}_{0.14(1)}\text{Te} = (\text{GeTe})_{12}\text{Sb}_2\text{Te}_3$ grew in a two-zone furnace (temperature gradient from 600 to 500 °C, 24 h) and were subsequently quenched to room temperature by removing the ampoule from the furnace. Growth twinned crystals

$\text{Ge}_{0.84(1)}\text{Sb}_{0.12(1)}\text{Te} = (\text{GeTe})_{15}\text{Sb}_2\text{Te}_3$ were obtained in a standard tube furnace by heating the side of the silica glass ampoule containing the starting material to 615 °C (10 days) whereas the side was situated outside the furnace. Both these techniques allow to reproducibly synthesize single crystals used for the investigations.

For the measurement of thermoelectric properties, stoichiometric melts of the elements were solidified in silica ampoules with flat bottom to obtain disc-shaped ingots with diameters of approximately 15 mm and thicknesses of 3-6 mm. The ingots were heated to the stability range of the high temperature modification and subsequently quenched to room temperature in water to obtain metastable samples. For thermoelectric measurements, they were polished to flat plates.

X-ray diffraction and EDX spectroscopy

Laboratory single-crystal intensity data were collected on a STOE IPDS-I diffractometer with imaging plate detector using Mo- K_α or Ag- K_α radiation (graphite monochromator, $\lambda = 0.71093 \text{ \AA}$ and $\lambda = 0.56087 \text{ \AA}$) to check the crystal quality before selecting appropriate samples for the synchrotron investigations. This way single crystals of the given compositions and with the characteristic diffraction patterns described in the text can be reproduced. The compositions of the crystals used for the experiments were checked by energy dispersive X-ray spectroscopy (EDX). EDX analyses were performed using a JSM-6500F (Jeol, USA) scanning electron microscope with EDX detector (model 7418, Oxford Instruments, Great Britain). The averaged values of 3-7 point analyses on the single crystals used for X-ray data collection at BM32 (ESRF, Grenoble) correspond to the formulae $\text{Ge}_{0.65(3)}\text{Sb}_{0.22(1)}\text{Te} = (\text{GeTe})_6\text{Sb}_2\text{Te}_3$, $\text{Ge}_{0.83(4)}\text{Sb}_{0.14(1)}\text{Te} = (\text{GeTe})_{12}\text{Sb}_2\text{Te}_3$ and $\text{Ge}_{0.84(1)}\text{Sb}_{0.12(1)}\text{Te} = (\text{GeTe})_{15}\text{Sb}_2\text{Te}_3$, respectively.

Laue diffraction at BM32

The Laue diffraction patterns were collected at ESRF on BM32 with a white beam (energies from 5 keV to 25 keV) focused via KB mirrors to a size of about $1 \times 1 \mu\text{m}^2$ on the sample (<http://www.esrf.eu/UsersAndScience/Experiments/CRG/BM32/>). The sample was inclined 40° with respect to the beam and the CCD camera (165 x 165 mm) was placed approximately 70 mm above the samples, which were fixed in silica capillaries filled with argon attached to silica glass or silicon holders with high-temperature cement. A domed hot stage (Anton Paar) was used for heating the samples. Its temperature was calibrated using a thermocouple fixed to the furnace in the same fashion as the samples (with an estimated error for the temperature of about ± 10 °C). At exposure times of about 1 second per image and read-out times of about 5 seconds, about ten diffraction images per minute can be collected yielding an approximate temperature

resolution of 1°C using a heating rate of approximately 10 °C/min. As a microfocused beam was used for the experiments, so that only small volumes diffracted in a single exposure. Therefore even small samples shifts resulting from the dilation of the heating stage affect the diffraction pattern and the sample position had to be optimized repeatedly during the heating process. Data evaluation and treatment was performed using the software packages X-ray Microdiffraction Analysis Software (X-MAS; N. Tamura, R. S. Celestre, A. A. MacDowell, H. A. Padmore, R. Spolenak, B. C. Valek, N. Meier Chang, *J. Synchrotron Rad.* **2003**, *10*, 137) and the Laue Daresbury Software Suite (modified for the CCD-detector data, J. R. Helliwell, J. Habash, D. W. J. Cruickshank, M. M. Harding, T. J. Greenhough, J. W. Campbell, I. J. Clifton, M. Elder, P. A. Machin, M. Z. Papiz, and S. Zurek, *J. Appl. Crystallogr.* **1989**, *22*, 483). For indexing exemplary diffraction patterns, the (approximate) sample-detector distance for room temperature as well as high temperature diffraction patterns was determined from a silicon or germanium reference fixed on the sample holders using X-MAS. For further indexing, the Laue Daresbury Software Suite was used. Initially, a cubic cell with $a_{\text{cubic}} = 6.00 \text{ \AA}$ in trigonal setting ($a_{\text{trigonal}} = (1/\sqrt{2})a_{\text{cubic}}$; $c_{\text{trigonal}} = (\sqrt{3})a_{\text{cubic}}$) was used for indexing the diffraction patterns of the high-temperature modifications. Although a white beam diffraction experiment does not allow one to obtain the absolute lattice parameters, the unit cell parameters (i.e. c , with a fixed) were refined to determine the deviation from the axis ratio $a_{\text{trigonal}}/c_{\text{trigonal}} = (1/\sqrt{2})/(\sqrt{3})$. For the high-temperature modifications, there was no significant deviation, hence the patterns were indexed based on a cF -lattice $a_{\text{cubic}} = 6.00 \text{ \AA}$. Simulated spot positions match well with the observed ones (cf. Fig. 2S). To index the diffraction patterns of other not long-periodically ordered structures, the axis ratio of the trigonal average structure $a_{\text{trigonal}}/c_{\text{trigonal}}$ was manually varied in between 0.408 (cubic, β -GeTe) and 0.389 (rhombohedral, α -GeTe) to find the best match between observed and predicted spot positions (cF. Fig. 3S and 4S). For the diffraction patterns indicative of a long-periodically ordered structure, an initial cell can be derived from a structural prediction based on the composition described in detail elsewhere (L. E. Shelimova, O. G. Karpinsky, M. A. Kretova, V. I. Kosyakov, V. A. Shestakov, V. S. Zemskov, F. A. Kuznetsov, *Inorg. Mater.* **2000**, *36*, 768; M. N. Schneider, O. Oeckler, *Z. Anorg. Allg. Chem.* **2008**, *634*, 2557). For the composition $(\text{GeTe})_6\text{Sb}_2\text{Te}_3$ a 51R-type ($a \approx 4.2 \text{ \AA}$, $c \approx 93.8 \text{ \AA}$) layered structure is expected. This cell allows one approximately index the Bragg reflections characteristic for the long-periodically ordered structure. However, they are rather broad so that the indexing is not unequivocal with respect to closely related stacking sequences. All lattice parameters given in the text contain two digits as given by the Laue Daresbury Software Suite and with an estimated

error < 0.03. For the trigonal phases, the axis ratios $a_{\text{trigonal}}/c_{\text{trigonal}}$ which are not affected by detector distance errors are given in addition.

Thermoelectric characterization

To determine the temperature dependency of the thermoelectric properties, both commercial and in-house built facilities were used to characterize the electrical and the thermal conductivities as well as the Seebeck coefficient in the range from room temperature to approx. 500 °C under vacuum. In order to avoid Peltier influences on the measurement a four point-probe setup above room temperature using an AC method was used to measure the electrical conductivity. The Seebeck coefficient was determined using a small temperature gradient across the sample while slowly changing the environmental temperature, in order to the values for each mean temperature. The thermal conductivity was calculated from measurements of the thermal diffusivity by a Laser Flash Apparatus (Netzsch LFA 427) and heat capacity determined by Differential Scanning Calorimetry (Netzsch DSC 404). The samples' density was measured using a Mohr's balance.

5.5.5.2 Additional Figures

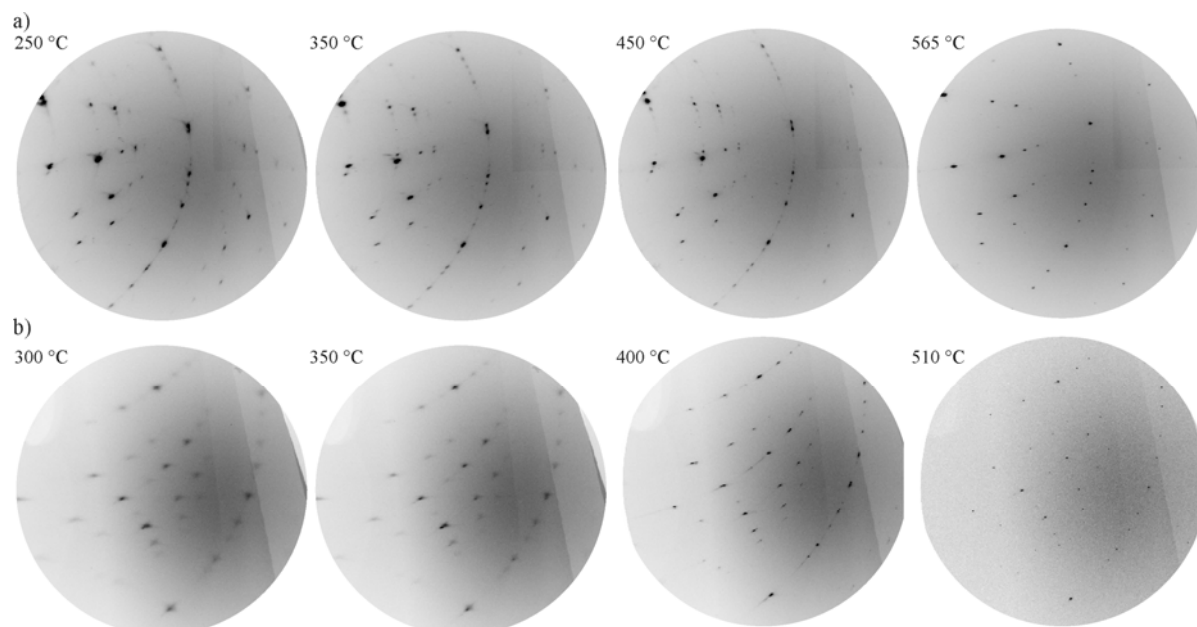


Figure S1. Enlarged sections of the experimental Laue diffraction patterns collected during heating a) $\text{Ge}_{0.65(3)}\text{Sb}_{0.22(1)}\text{Te} = (\text{GeTe})_6\text{Sb}_2\text{Te}_3$, and b) $\text{Ge}_{0.83(4)}\text{Sb}_{0.14(1)}\text{Te} = (\text{GeTe})_{12}\text{Sb}_2\text{Te}_3$; the temperatures at which the selected diffraction patterns were collected are depicted next to the diffraction patterns

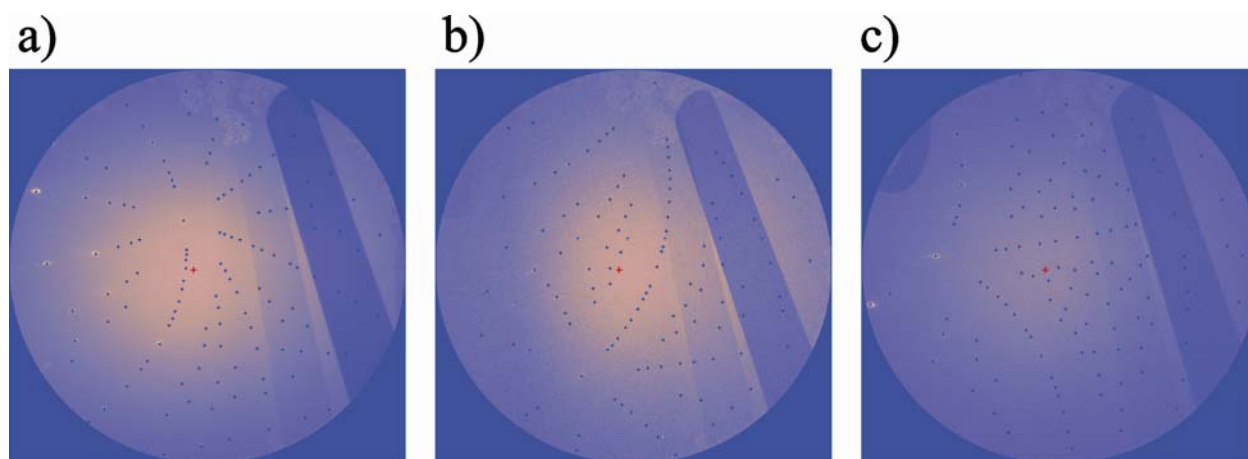


Figure S2. Experimental Laue diffraction patterns of the high-temperature modifications of a) $\text{Ge}_{0.65(3)}\text{Sb}_{0.22(1)}\text{Te} = (\text{GeTe})_6\text{Sb}_2\text{Te}_3$ (565 °C), b) $\text{Ge}_{0.83(4)}\text{Sb}_{0.14(1)}\text{Te} = (\text{GeTe})_{12}\text{Sb}_2\text{Te}_3$ (515 °C), and c) $\text{Ge}_{0.84(1)}\text{Sb}_{0.12(1)}\text{Te} = (\text{GeTe})_{15}\text{Sb}_2\text{Te}_3$ (415 °C) with simulated reflection positions corresponding to a cubic cell ($a = 6.00 \text{ \AA}$) derived from a combined approach using the software packages X-MAS and the Laue Daresbury Software suite which allow one to index the reflections of the crystal in the corresponding orientation.

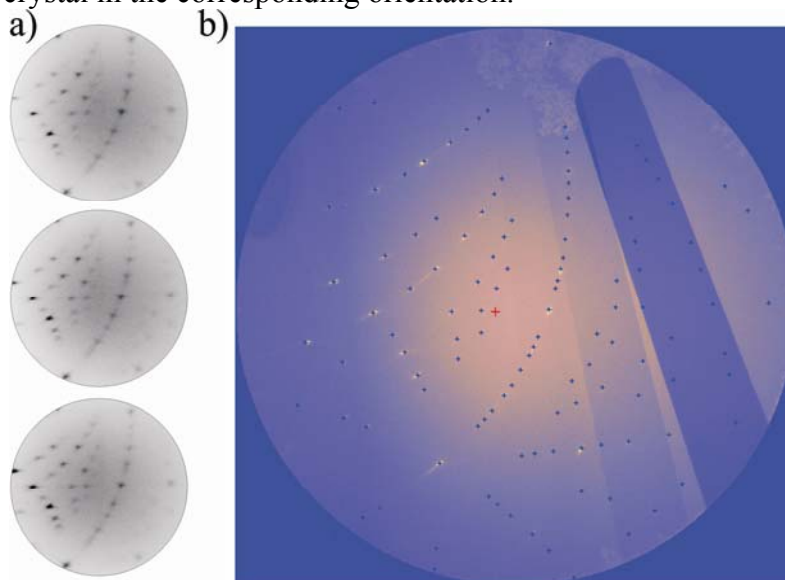


Figure S3. a) Laue diffraction patterns of $\text{Ge}_{0.83(4)}\text{Sb}_{0.14(1)}\text{Te} = (\text{GeTe})_{12}\text{Sb}_2\text{Te}_3$ collected from different positions on the sample at room temperature; b) Experimental diffraction pattern from the same crystal collected at 400 °C overlaid with reflection positions simulated by the Laue Daresbury Software suite which was used to index the reflections (hR $a = 4.25 \text{ \AA}$, $c = 10.52 \text{ \AA}$ $a/c = 0.404$)

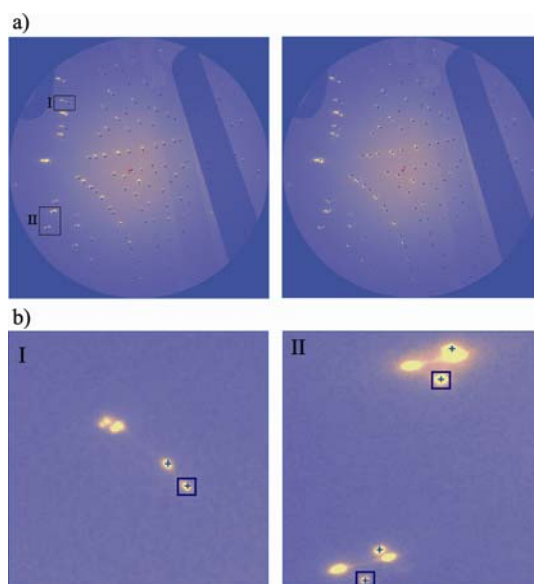


Figure S4. a) Laue diffraction pattern of $\text{Ge}_{0.84(1)}\text{Sb}_{0.12(1)}\text{Te} = (\text{GeTe})_{15}\text{Sb}_2\text{Te}_3$ collected at room temperature; the pattern is depicted twice as the individual patterns are overlaid with the reflection positions of one domain each which can be individually indexed (hR $a = 4.22 \text{ \AA}$, $c = 10.57 \text{ \AA}$ $a/c = 0.399$) b) enlarged sections indicated in a); (I) a group of reflections which shows that all domain orientations expected for a fourfold twin according to the group-subgroup scheme $Fm\bar{3}m - R\bar{3}m - R3m$ contribute to the diffraction patterns (two orientations are indexed as indicated by crosses only and a cross-square combination); (II) Groups of several reflections belonging to different domain orientations which are interconnected by diffuse six diffuse streaks as expected for six different domain wall orientation possible in a fourfold twin.

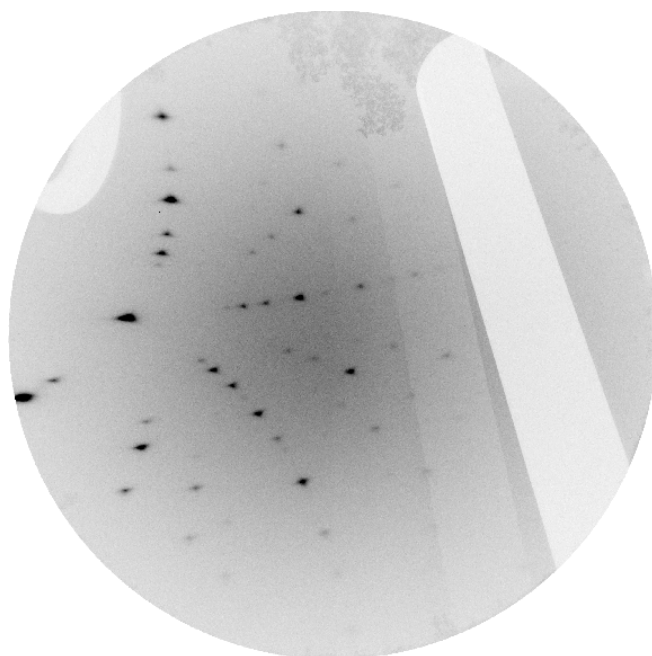


Figure S5. Diffraction pattern of a $\text{Ge}_{0.84(1)}\text{Sb}_{0.12(1)}\text{Te} = (\text{GeTe})_{15}\text{Sb}_2\text{Te}_3$ crystal after cooling from the cubic high-temperature phase (see text and compare with Fig. 3a) at $260 \text{ }^\circ\text{C}$

6 Conclusion and prospects

In the course of this work, a broad spectrum of analytical methods yielded various insights into the structural chemistry of pnictogen tellurides. The structure elucidation of stable layered compounds (Chapter 2) provided the basis for a comprehensive investigation of metastable polymorphs. Novel, metastable compounds with long-periodically ordered layered structures with the general formula $(\text{MTe})_n(\text{Sb}_2\text{Te}_3)_m(\text{Sb}_2)_k$ ($\text{M} = \text{Ge}, \text{Sn}, \text{Ag/Sb}$) contain structural building units similar to those that are present in the pseudobinary series of stable compounds $(\text{MTe})_n(\text{Sb}_2\text{Te}_3)$ and $(\text{Sb}_2\text{Te}_3)_m(\text{Sb}_2)_k$ (Chapter 3). The knowledge of structural details of such building units facilitated the structure elucidation of materials that can be viewed as model systems for "superlattices" with extremely long stacking periodicities which are otherwise prepared by layer-per-layer deposition. It turned out that for some of these layered pnictogen tellurides, the determination of interatomic distances is not unambiguous. In the case of (pseudo-) homometry, two non-congruent structure models yield (almost) the same diffraction pattern. For such different models, however, reasonable atom assignments yield different compositions so that chemical analysis can identify the correct model. In this process, mixed site occupancies on cation positions play an important role and were shown to be a characteristic feature of most ternary pnictogen tellurides. The cation distribution on the crystallographic sites is neither ordered nor random, but significantly influenced by van der Waals gaps. These are accompanied by characteristic interatomic distance sets in their vicinity, and their spacing defines the periodicities of such structures. If the compounds contain elements with similar atomic numbers, the element distribution cannot be reliably elucidated by standard X-ray diffraction. Therefore, resonant diffraction using synchrotron radiation was used, e. g., to elucidate the distribution of Sn, Sb and Te in $21R\text{-SnSb}_2\text{Te}_4$. The experience from this rather simple compound helped during the characterization of two isostructural complex phases. Although the structure of the compounds $39R\text{-MSb}_{10}\text{Te}_4$ ($\text{M} = \text{Ge}, \text{Sn}$) is related to that of $39R\text{-Sb}_{10}\text{Te}_3$, the latter contains antimony and tetradymite-type slabs that are clearly separated whereas in the new phases, antimony layers are partially substituted by GeTe or SnTe, respectively. The resulting concentration gradient resembles an interdiffusion of distorted rocksalt-type slabs typical for $(\text{MTe})_n(\text{Sb}_2\text{Te}_3)$ and antimony slabs characteristic for $(\text{Sb}_2\text{Te}_3)_m(\text{Sb}_2)_k$, and hence represents a snapshot of diffusion processes which might also occur in "multilayer" compounds that are discussed as thin-film "superlattice" thermoelectrics or phase-change materials with new device hierarchy, to name the most prominent ones with respect to this work. It would be interesting to further study such diffusion processes that influence the element distribution in stable and

metastable long-periodic layered structures in future works, for example by temperature dependent synchrotron diffraction experiments.

As diffusion processes often accompany phase transitions towards stable modifications, it is essential to prevent them in order to obtain kinetically inert metastable phases (Chapter 4). Phases $(\text{GeTe})_n(\text{Sb}_2\text{Te}_3)$ ($n \geq 3$) exhibit rocksalt-type high-temperature modifications that contain $1/n+3$ cation defects per anion which are randomly distributed, whereas their trigonal long-periodically ordered polymorphs, which are stable at ambient conditions, do not contain significant amounts of cation vacancies. The phase transition between both modifications formally involves the layer-like ordering of cation defects, associated with the rearrangement of the anion-layer stacking sequence from a cubic towards a hexagonal stacking across the defect layers. This yields van der Waals gaps between rocksalt-type slabs with a partially covalent interaction between Te atoms. At ambient conditions, this arrangement is more stable than a random distribution of cation defects which is always associated with "incomplete" anion centred polyhedra. Due to the higher entropy, the latter arrangement can be stable at high temperatures, and the transition temperatures consequently increase with increasing defect concentration. Quenching high-temperature modifications with n ($n \geq 3$) partially hinders the formation of long-periodic layered structures and yields metastable samples with seemingly simple average structure corresponding to a rhombohedrally distorted rocksalt-type. Although the metrics does not significantly deviate from the cubic one, multiple twinning yields domains with disordered trigonal structure. Quenching GeBi_2Te_4 ($n = 2$) under high pressure also yields a metastable modification that exhibits a distorted rocksalt type; however, the distortion is more pronounced and the average structure corresponds to the CuPt type. This finding indicates that further disordered high-temperature phases exist under non-ambient pressure conditions.

The metastable modifications of both germanium bismuth tellurides and germanium antimony tellurides exhibit comparable real-structure effects. Short-range order of cation defects leads to nanostructures characterized by cation defect layers (Chapter 5) that can be viewed as snapshots of the diffusion processes involved in phase transitions. The comparison of simulated and experimental diffuse scattering intensities from quenched phases $(\text{GeTe})_n(\text{Sb}_2\text{Te}_3)$ ($n = 2, 5, 6, 12$) corroborates this assumption. With decreasing n , a higher correlation between cation defects leads to a more pronounced similarity between the real structure and the long-periodically ordered layered phases. In such cases, almost equidistantly spaced van der Waals gaps are present, whereas for larger values of n , "missing" cation layers in a cubic anion-layer stacking sequence are present and the almost randomly distributed. It might be an intriguing future project to refine the corresponding disorder models on the experimental diffuse scattering data, possibly based on

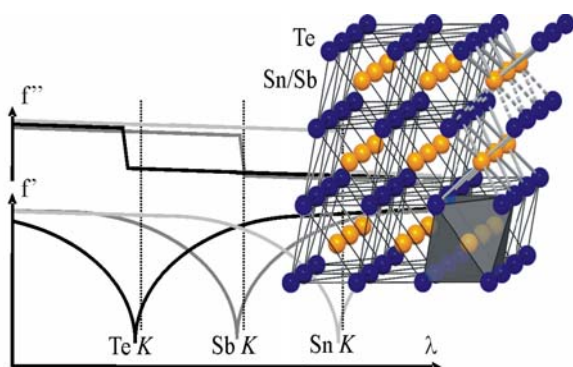
the models used for simulations in this work. In this context, it would be a challenging plan to extract additional information from anomalous dispersion effects on the diffuse scattering. As shown by in-situ temperature dependent micro-focused Laue diffraction, the real structure of quenched crystals $(\text{GeTe})_n(\text{Sb}_2\text{Te}_3)$ ($6 < n < 15$) significantly changes upon heating when diffusion processes set in at approximately 300 °C. The diffusion processes have been monitored by the change of the diffuse scattering; and this method seems promising to further study other time-dependent structural rearrangements correlated with phase transitions.

The real structures of the metastable materials investigated in this work significantly influence their properties and render them an intriguing class of new thermoelectrics. Their nanostructures lead to rather low thermal conductivities while their electronic structures yield high Seebeck coefficients. When diffusion is activated at elevated temperatures and the nanostructures become unstable, the thermal conductivity changes significantly, i.e. increases and the electrical conductivity as well as the Seebeck coefficient exhibit a hysteretic behavior. GeTe-rich phases with compositions comparable to those of phase-change materials used in non-volatile RAM devices or Blu-Ray discs exhibit figures of merit ZT of ~ 1.3 at 450 °C, mostly due to very high Seebeck coefficients of $\sim 180 \mu\text{V/K}$. It would be very interesting to obtain insight into the electronic structure that leads to these Seebeck coefficients; however, theoretical calculations for such disordered materials are almost impossible. Angular resolved photoelectron spectroscopy (ARPES) might be an intriguing approach. From the preparative chemist's point of view, it could be promising to alter the thermal conductivity not only by nanostructuring the material but also by doping with lighter or heavier elements in order to introduce new phonon scattering centres. Such an approach need not be restricted to temperatures where the atom arrangement, i. e. the real structure, is kinetically inert. High figures of merit can also be expected at temperatures where dynamic disorder is activated. This work has demonstrated that the investigation of structure-property relationships for multinary pnictogen tellurides needs to go hand in hand with the structural characterization of both stable and metastable compounds. Understanding the complex interplay of interesting structures and intriguing properties will for sure remain a rewarding approach.

7 Summary

7.1 Resonant X-ray diffraction to distinguish Sn, Sb and Te in 21R-SnSb₂Te₄

Chapter 2.2 (Page 14)



Anomalous dispersion terms at the K-edges of Sn, Sb and Te and a rocksalt-type slab of 21R-SnSb₂Te₄.

Crystals of 21R-SnSb₂Te₄ ($R\bar{3}m$, $a = 4.298(1)$, $c = 41.57(1)$ Å, $R1 = 0.028$) were grown by chemical transport using SbI₃ as transport agent. The periodicity of the layered structure is defined by van der Waals gaps between rocksalt-type slabs that comprise four anion and three cation layers. The atom distribution was determined by means of resonant single-crystal diffraction at the K-absorption edges of the elements present. Five datasets were used in a joint refinement. Sb atoms are distributed

over all cation sites but prefer those in the vicinity of the van der Waals gap. The determination of the element distribution in 21R-SnSb₂Te₄ by means of resonant X-ray diffraction can be regarded as case study for the application of this elegant technique with respect to the structural elucidation of multinary antimony tellurides.

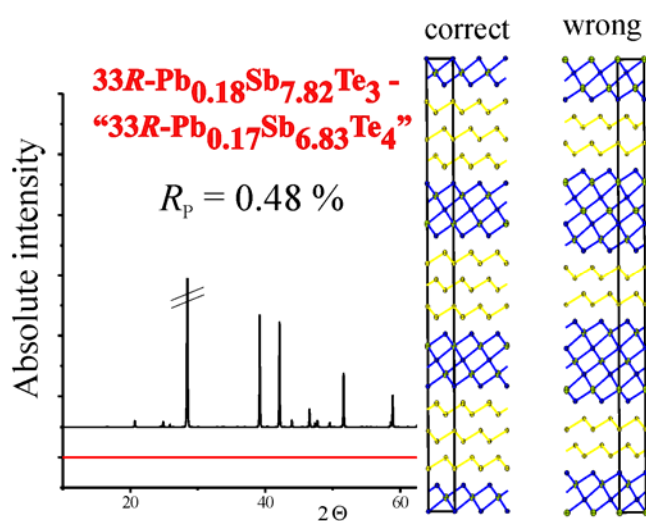
7.2 Limitations of structure predictions based on the composition of germanium antimony tellurides

Chapter 2.3 (Page 26)

For pseudobinary compounds (GeTe)_n(Sb₂Te₃)_m rules for predicting the structure of the stable layered structures have been devised based on their stoichiometry and crystal chemistry. However, although, a 39R layer stacking is expected for Ge₄Sb₂Te₇, powder diffraction data of bulk material Ge₄Sb₂Te₇ obtained by quenching a stoichiometric melt and subsequent annealing indicate a 33R-type structure. Single crystal diffraction confirms that the layered structure is closely related to that of 33R-Ge₃Sb₂Te₆ ($R\bar{3}m$, $a = 4.1891(5)$ Å, $c = 62.169(15)$, $R1 = 0.047$). Mixed occupancy of cation positions with Ge and Sb and possibly defects cause this unusual range of homogeneity in the kinetically stable compound.

7.3 Homometry and stacking disorder in antimony tellurides

Chapter 2.4 (Page 39)



Almost homometric structure models of $\text{Pb}_{0.18}\text{Sb}_{7.82}\text{Te}_3$; difference of PXRD intensities simulated with the correct and wrong model

Ambiguities in the interpretation of diffraction data from long-range ordered layered chalcogenides can arise from almost homometric structure models, which can be refined equally well on experimental data sets, as demonstrated for $39R\text{-Sb}_{10}\text{Te}_3$ ($R\bar{3}m$, $a = 4.2874(6)$ Å, $c = 64.300(16)$ Å, $R1 = 0.0298$). Mixed site occupancies may further reduce the differences between the calculated diffraction patterns of non-congruent

structure models as shown for $33R\text{-(Sb}_{0.978(3)}\text{Pb}_{0.022(3)})_8\text{Te}_3$ ($R\bar{3}m$, $a = 4.2890(10)$, $c = 75.51(2)$ Å, $R1 = 0.0615$). In both cases, chemical analysis proves the correct structure as reasonable atom assignments lead to different compositions for the almost homometric models. Further pitfalls for the structure elucidation can result from stacking disorder of tetradymite and A7 (gray arsenic) type building units and leads to powder diffraction patterns which can be misinterpreted in terms of 3D randomly disordered almost isotropic structures with a simple $\alpha\text{-Hg}$ type basic structure.

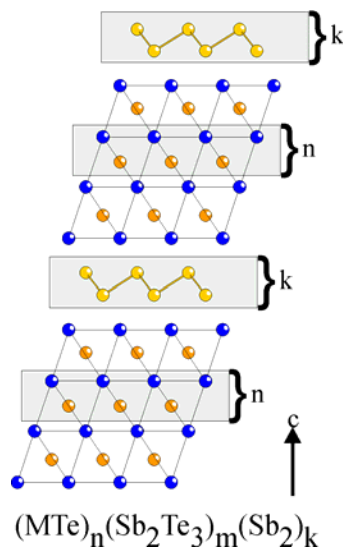
7.4 A new metastable long-periodic layered germanium antimony telluride $9P\text{-GeSb}_4\text{Te}_4$

Chapter 3.2 (Page 63)

Homogeneous samples of the new phase $9P\text{-GeSb}_4\text{Te}_4$ can be obtained by quenching a stoichiometric melt and subsequent annealing at 500 °C. They exhibit metallic conductivity (33 Scm^{-1} at room temperature). Single-crystal X-ray structure analysis ($P\bar{3}m1$, $a = 4.2466(2)$ Å, $c = 17.483$ Å, $R1 = 0.0355$) reveals that the compound consists of antimony layers similar to those in elemental Sb that alternate with rocksalt-type slabs related to those in $21R\text{-GeSb}_2\text{Te}_4$. Although this new member in the series of long-periodic layered germanium antimony tellurides is not thermodynamically stable according to the phase diagram, it is remarkably inert up to 540 °C, where it starts to melt incongruently.

7.5 Long-range ordered metastable phases as models for "superlattices"

Chapter 3.3 (Page 81)

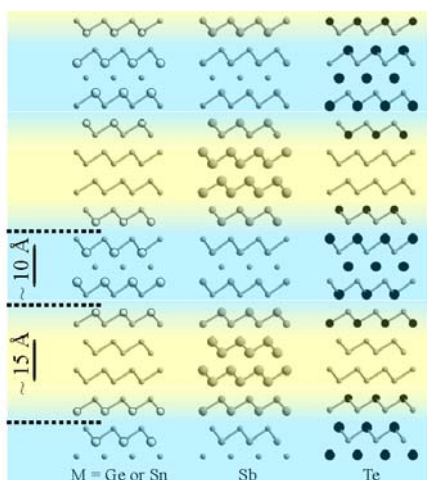


Schematic representation of new metastable compounds $(MTe)_n(Sb_2Te_3)_m(Sb_2)_k$;

make them comparable to "superlattice" metal (A7-type lamellae) – semiconductor (rocksalt-type slabs) heterostructures prepared by layer-per-layer deposition.

7.6 Concentration gradients of the elements in new metastable layered tellurides $39R-M_{0.067}Sb_{0.667}Te_{0.266}$ (M = Ge, Sn)

Chapter 3.4 (Page 99)



Representation of the concentration gradients in $39R-M_{0.067}Sb_{0.667}Te_{0.266}$ (M=Ge, Sn)

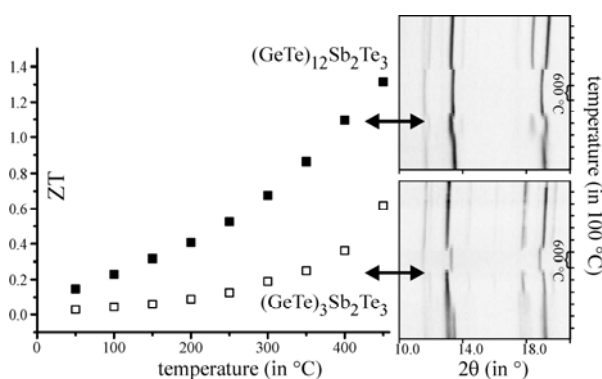
Single-crystal structure refinements on $51R-Ge_{2-x}Sb_{2+x}Te_5Sb_8$ ($x = 0.43$; $R\bar{3}m$, $a = 4.258(1)$ Å, $c = 97.23(2)$ Å, $R = 4.38\%$; $n=2$, $k=4$) and $15P-Ag_xSb_{3-x}Te_4Sb_8$ ($x = 0.24$; $P\bar{3}m1$, $a = 4.282(1)$ Å, $c = 28.638(5)$ Å, $R = 5.38\%$; $n=1$, $k=4$) reveal that these metastable compounds contain structure elements known from the pseudobinary series $(GeTe)_n(Sb_2Te_3)_m$ (including substitution of Ge with Ag/Sb) and $(Sb_2Te_3)_m(Sb_2)_k$. Although the phases are valence compounds, the temperature dependence of resistance shows metallic behavior ($51R$ -type structure: 2500 Scm^{-1} , $15P$ -type structure: 588 Scm^{-1} at room temperature). Partial spinodal decomposition might be the reason for their extremely long stacking periodicities that

Structure refinements on resonant single-crystal diffraction data reveal that the isostructural phases $39R-Ge_{0.067}Sb_{0.667}Te_{0.266}$ ($R\bar{3}m$, $a = 4.2649(1)$, $c = 75.061(2)$ Å) and $39R-Sn_{0.067}Sb_{0.667}Te_{0.266}$ ($R\bar{3}m$, $a = 4.2959(1)$, $c = 75.392(2)$ Å) exhibit structures that are similar to that of $39R-Sb_{10}Te_3$ ($= Sb_{0.769}Te_{0.231}$). Four gray arsenic type layers of antimony alternate with Sb_2Te_3 slabs, but are partially substituted by GeTe and SnTe. A wave-like element distribution results which, for $39R-Ge_{0.067}Sb_{0.667}Te_{0.266}$, was corroborated by Z-contrast (HAADF-STEM) imaging. The concentration gradient of the elements can be regarded as a model for interdiffusion in

“superlattice” heterostructures. The phases exhibit a thermoelectric figure of merit (ZT) of 0.06 at 400 °C; their thermal conductivity ($\kappa \sim 8 - 9.5$ W/mK at 400 °C) lies in between that of elemental antimony and pure Sb_2Te_3 .

7.7 Similarities between phase-change materials and thermoelectrics

Chapter 4.1 (Page 124)



In situ temperature programmed powder diffraction and ZT values of $(\text{GeTe})_n(\text{Sb}_2\text{Te}_3)$ ($n = 3, 12$).

Metastable crystalline phase-change materials are usually small-bandgap semiconductors that exhibit low thermal conductivities. These properties are also required for good thermoelectrics. For phases $(\text{GeTe})_n(\text{Sb}_2\text{Te}_3)$ ($n \geq 3$) with compositions comparable to phase-change materials used in Blu-Ray discs and PC-RAM devices, rocksalt-type high-temperature polymorphs with a high concentration of randomly distributed cation

vacancies can be quenched to yield bulk samples that are better suited for a thermoelectric characterization than thin-film samples. *In situ* temperature dependent powder diffraction proves the metastability of such samples. They exhibit pronounced nanostructures that result from the formation of twin domains and finite intersecting vacancy layers. In contrast, in slowly cooled or annealed samples (below the transition temperature to the high-temperature polymorph), vacancies order in parallel layers. A comparative investigation of the thermoelectric properties of metastable $(\text{GeTe})_n(\text{Sb}_2\text{Te}_3)$ ($n = 3, 12$) demonstrates that initially quenched materials can exhibit figures of merit of up to $ZT = 1.3$ at 450 °C, as found for $(\text{GeTe})_n\text{Sb}_2\text{Te}_3$ with $n = 12$ or 19. Metastable germanium antimony tellurides are therefore intriguing disordered precursors for nanostructured thermoelectrics.

7.8 High-pressure synthesis of metastable germanium bismuth tellurides

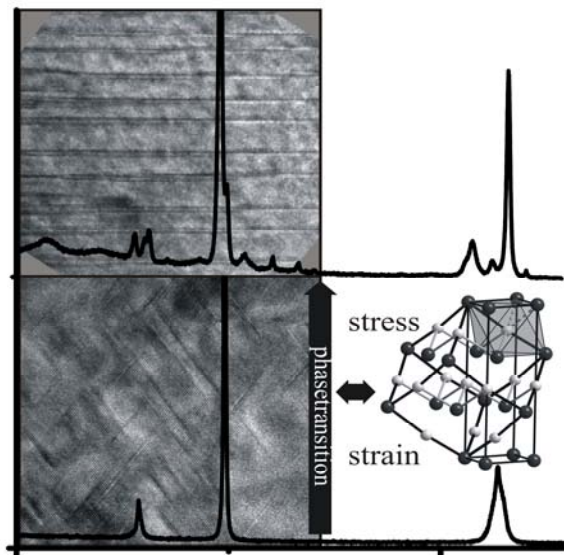
Chapter 4.2 (Page 142)

Metastable samples of GeBi_2Te_4 with simple average structures cannot be obtained by thermal quenching under ambient pressure; however, a new metastable modification with CuPt-type average structure was obtained by high-pressure high-temperature synthesis using a Walker-type multi-anvil press. They exhibit pronounced nanostructures that depend on the thermal treatment applied under a constant pressure of 12 GPa, e.g. the particle size changes from < 10 nm in

quenched samples to > 100 nm for melts slowly crystallized. The temperature characteristics of the electrical conductivity changes from metallic to semiconducting behavior with decreasing domain size which is accompanied by a more random orientation distribution of domains. A comparative investigation of annealed ingots and pressed powder pellets of stable $21R$ - GeBi_2Te_4 reveals that with an increasing amount of grain boundaries, the ZT value drops by more than one order of magnitude.

7.9 Influence of stress and strain on the stability of metastable germanium antimony tellurides

Chapter 5.2 (Page173)



HRTEM images and powder diffraction patterns of quenched as well as annealed samples of $(\text{GeTe})_{12}(\text{Sb}_2\text{Te}_3)$ and average structure of metastable $(\text{GeTe})_7(\text{Sb}_2\text{Te}_3)$.

Metastable crystalline modifications of $(\text{GeTe})_n(\text{Sb}_2\text{Te}_3)$ ($n = 7, 12$) have been obtained by quenching the corresponding high-temperature polymorphs. Despite the pseudocubic metrics, the average structure of individual domains in a multiply twinned metastable crystal $(\text{GeTe})_7(\text{Sb}_2\text{Te}_3)$ is rhombohedral and approximates a layered GeTe-type atom arrangement $(\text{Ge}_{0.7}\text{Sb}_{0.2}\text{Te}_3, R3m, a = 4.237 \text{ \AA}, c = 10.29 \text{ \AA}, R1 = 0.0319)$. Powder diffraction patterns of samples of $(\text{GeTe})_{12}(\text{Sb}_2\text{Te}_3)$ with defined particle sizes reveal that the rearrangement of cation defects, which is required to form a parallel

arrangement of vacancy layers is influenced by microstrain that hinders necessary relaxation. After annealing at $400 \text{ }^\circ\text{C}$, cation defect layers adopt a non-equidistant parallel arrangement as shown by HR-TEM. These findings show that metastable phases interesting as phase-change materials and nanostructured thermoelectrics are kinetically stabilized by microstrain.

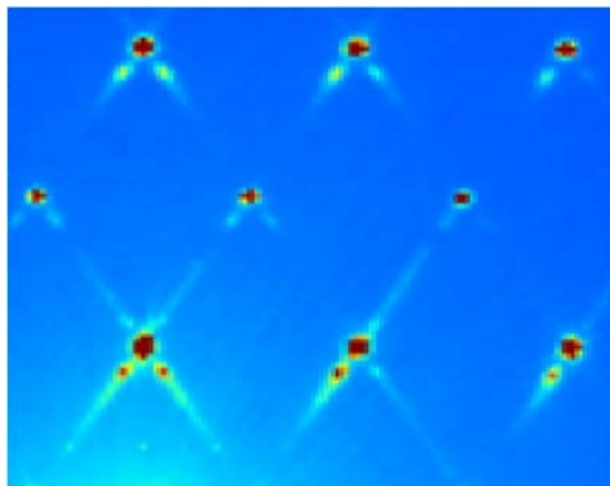
7.10 Real structure and properties of quenched germanium antimony tellurides

Chapter 5.3 (Page 194)

Both the composition and the thermal treatment of quenched samples $(\text{GeTe})_n\text{Sb}_2\text{Te}_3$ ($n = 3-19$) significantly influences their nanostructures. For example, a more random distribution of defect layers results for larger GeTe contents. A parallel arrangement of defect layers characteristic for stable layered phases can gradually be approached by annealing metastable bulk material at temperatures below the stability range of the high-temperature modifications which lies at lower temperatures for larger values of n . Variations of the nanostructures influence the lattice thermal conductivity (κ_L) and thus the thermoelectric figure of merit (ZT). At temperatures below 300 °C the nanostructures are stable and ZT -values up to ~ 0.6 are found due to moderate thermal conductivities. Nevertheless even above the temperature at which diffusion is activated increasing Seebeck coefficients yield ZT values up to 1.3 at 450 °C for GeTe-rich samples.

7.11 Analysis of diffuse scattering from metastable germanium antimony tellurides

Chapter 5.4 (Page 212)



Characteristic $h_c h_c l_c$ reciprocal section with "comet-like" diffuse streaks at the low angle side of Bragg reflections.

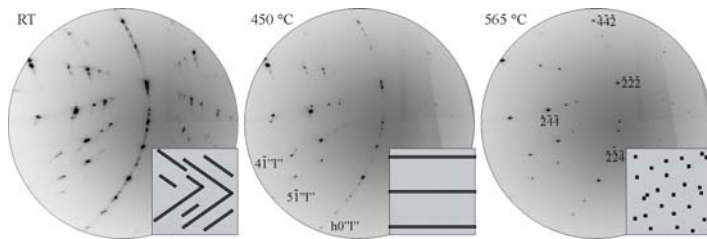
Pseudocubic diffraction patterns of quenched crystals of $(\text{GeTe})_n\text{Sb}_2\text{Te}_3$ ($n = 2; 5, 6, 12$) are an incoherent superposition of intensities from twin domains with trigonal average structure but (pseudo-)cubic metrics. Short-range order of vacancies yields a 1D disordered arrangement of defect layers that leads to "comet-like" diffuse intensity features, e.g. a maximum ("comet head") that is accompanied by strongly broadened side maxima ("comet tail") at the low-angle side of

Bragg reflections. The analysis of diffuse scattering reveals that a decreasing GeTe content leads to real structures that are comparable to the stable long-periodic layered structures, i. e. almost equidistantly spaced van der Waals gaps with hexagonal stacking of Te-atom layers around them are predominant. For GeTe-rich samples, planar defects correspond to "missing" cation layers in the cubic ABC stacking sequence of the Te-atom layers. These real structures correspond to

different “frozen” states of the phase transition from stable high-temperature to the stable room-temperature modifications.

7.12 In situ Laue diffraction investigation of diffusion processes involved in the phase transitions of germanium antimony tellurides

Chapter 5.5 (Page 240)



Laue diffraction pattern during heating of a metastable crystal and schematic representation of the defect distribution.

The change of the real structures of metastable $(\text{GeTe})_n\text{Sb}_2\text{Te}_3$ ($n = 6, 12, 15$) crystals upon heating was investigated by microfocused Laue diffraction. Diffusion processes involving cation defect ordering are activated at ~ 300 °C which is also

mirrored in the thermoelectric characteristics of the materials. For low GeTe contents, a parallel equidistant arrangement of defect layers readily forms upon heating whereas for larger GeTe contents this process requires longer annealing times due to increased diffusion pathways. The formation of a stable layered structure therefore is kinetically controlled. Upon further increasing the temperature, the equilibrium phase transition to the high-temperature phase is observed. Although it involves the diffusion of defects, it is thermodynamically controlled as a random arrangement of cation defects leads to energetically unfavorable "incomplete" anion centred polyhedra. A higher defect concentration therefore leads to higher transition temperatures. The results show that phase transitions of Ge-Sb-Te materials are order-disorder transitions that involve a complex interplay of kinetics and thermodynamics.

8 Appendix

8.1 Publications within this thesis

- 12) **Diffuse X-ray scattering and its interpretation with respect to the real structure of GeTe-rich metastable germanium antimony tellurides**
M. N. Schneider, P. Urban, M. Seemann, J. Wright, O. Oeckler
J. Appl. Crystallogr. **2012** (to be submitted).
- 11) **From metastable to stable modifications – *in situ* Laue diffraction investigation of diffusion processes related to the phase transitions of GeTe-rich (GeTe)_n(Sb₂Te₃) (n = 6 < n < 15) crystals**
M. N. Schneider, X. Biquard, C. Stiewe, T. Schröder, P. Urban, O. Oeckler
Chem. Commun. **2012**, 48, 2192-2194.
- 10) **The layered tellurides 39R-M_{0.067}Sb_{0.667}Te_{0.266} (M = Ge, Sn): element distribution and thermoelectric properties**
M. N. Schneider, F. Fahrnbauer, T. Rosenthal, M. Döblinger, C. Stiewe, O. Oeckler
Chem. Eur. J. **2012**, 18, 1209-1218.
- 9) **Nanostructures in metastable GeBi₂Te₄ obtained by high-pressure synthesis and rapid quenching and their influence on physical properties**
T. Schröder, M. N. Schneider, T. Rosenthal, A. Eisele, C. Gold, E.-W. Scheidt, W. Scherer, R. Berthold, O. Oeckler
Phys. Rev. B **2011**, 84, 184104.
- 8) **Real structure and thermoelectric properties of GeTe-rich Germanium Antimony Tellurides**
T. Rosenthal, M. N. Schneider, C. Stiewe, M. Döblinger, O. Oeckler
Chem. Mater. **2011**, 23, 4349-4356.
- 7) **Atom distribution in SnSb₂Te₄ by resonant X-ray diffraction**
O. Oeckler, M. N. Schneider, F. Fahrnbauer, G. Vaughan
Solid State Sci. **2011**, 13, 1157-1161.
- 6) **From phase-change materials to thermoelectrics?**
M. N. Schneider, T. Rosenthal, C. Stiewe, O. Oeckler
Z. Kristallogr. **2010**, 225, 463-470.
- 5) **Ambiguities in the structure determination of antimony tellurides arising from almost homometric structure models and stacking disorder**
M. N. Schneider, M. Seibald, P. Lagally, O. Oeckler
J. Appl. Crystallogr. **2010**, 43, 1012-1020.

- 4) **The influence of stress and strain on the kinetic stability and phase transitions of cubic and pseudocubic Ge-Sb-Te materials**
M. N. Schneider, P. Urban, A. Leineweber, M. Döblinger, O. Oeckler
Phys. Rev. B **2010**, *81*, 184102.
- 3) **GeSb₄Te₄ – a new 9P-type phase in the system Ge-Sb-Te**
M. N. Schneider, O. Oeckler
Z. Anorg. Allg. Chem. **2010**, *636*, 137 – 143.
- 2) **A new series of long-range ordered metastable phases in the system M-Sb-Te (M = Ge, Ag)**
M. N. Schneider, M. Seibald, O. Oeckler
Dalton Trans. **2009**, 2004 – 2011.
- 1) **Unusual solid solutions in the system Ge-Sb-Te : The crystal structure of 33R-Ge_{4-x}Sb_{2-y}Te₇ (x, y ≈ 0.1) is isostructural to that of Ge₃Sb₂Te₆**
M. N. Schneider, O. Oeckler
Z. Anorg. Allg. Chem. **2008**, *634*, 2557 – 2561.

8.2 Contributions to conferences

- 26) **Order-disorder transitions in GeTe-rich germanium antimony tellurides elucidated by *in situ* Laue microdiffraction**
P. Urban, M. N. Schneider, T. Schröder, X. Biquard, O. Oeckler
Joint Meeting of the German Crystallographic Society (DGK), the German Mineralogical Society (DMG) and the Austrian Mineralogical Society (ÖMG), Salzburg (Österreich) **2011**.
- 25) **The influence of the microstructure on the thermoelectric properties of (GeTe)_nSb₂Te₃ (4 < n < 20) compounds – a TEM investigation**
T. Rosenthal, M. N. Schneider, O. Oeckler
GDCh-Wissenschaftsforum Chemie Bremen **2011**.
- 24) **Thermoelectric properties of metastable Ge/Sb/Te and Ge/Bi/Te compounds**
T. Schröder, M. N. Schneider, T. Rosenthal, P. Urban, F. Fahrnbauer, C. Stiewe, C. Gold, E.-W. Scheidt, W. Scherer, O. Oeckler
9th European Conference on Thermoelectrics, Thessaloniki (Griechenland) **2011**.
- 23) **Influence of real-structure effects on the properties of metastable tellurides**
O. Oeckler, T. Schröder, T. Rosenthal, M. N. Schneider
Trilateral Seminar “Advances in Inorganic Crystal Chemistry”, St. Petersburg (Russland) **2011**.
- 22) **Wie Kristalle aufräumen - zeit- und orts aufgelöste Laue-Beugungsexperimente an fehlgeordneten Ge/Sb/Te-Phasen**
M. N. Schneider, X. Biquard, T. Schröder, P. Urban, O. Oeckler:
Festkörperchemie-Treffen “Hemdsärmelkolloquium”, Dresden **2011**.

- 21) **Real-structure effects, diffusion processes and thermoelectric properties of tetradymite-type tellurides and related compounds**
O. Oeckler, M. N. Schneider, T. Rosenthal, T. Schröder, P. Urban, F. Fahrnbauer, C. Stiewe, M. Döblinger
Minerals as Advanced Materials II, Kirovsk (Russland) **2010**.
- 20) **From Phase-Change Materials to Thermoelectrics?**
O. Oeckler, M. N. Schneider, T. Schröder, T. Rosenthal, F. Fahrnbauer, C. Stiewe
3rd International Symposium on Structure-Property Relationships in Solid State Materials, Stuttgart **2010**.
- 19) **Transmission electron microscopy on stable and metastable Ge/Sb/Te phases**
T. Rosenthal, M. N. Schneider, O. Oeckler
26th European Crystallographic Meeting, Darmstadt **2010**.
- 18) **Resonant diffraction study of concentration gradients in multinary antimony tellurides**
M. N. Schneider, F. Fahrnbauer, O. Oeckler
26th European Crystallographic Meeting, Darmstadt **2010**.
- 17) **Real structure of metastable Ge-Sb-Te and Ge-Bi-Te materials**
M. N. Schneider, T. Rosenthal, T. Schröder, O. Oeckler
European Phase Change and Ovonic Symposium, Mailand (Italien) **2010**.
- 16) **Improving Materials: Effect of Lithium Intercalation on Layered Tellurides**
L. K. Sposato M. N. Schneider, O. Oeckler
240th ACS National Meeting & Exposition, Boston (USA) **2010**.
- 15) **Einfluss der Mikro- und Nanostruktur auf thermoelektrische Eigenschaften von Germaniumantimontelluriden**
O. Oeckler, M. N. Schneider, T. Rosenthal, C. Stiewe
15. Vortragstagung der Fachgruppe Festkörperchemie und Materialforschung der Gesellschaft Deutscher Chemiker, Berlin **2010**.
- 14) **Metastabile Phasen von GeBi₂Te₄ durch Kristallisation unter Hochdruck**
T. Schröder, M. N. Schneider, A. Eisele, O. Oeckler
15. Vortragstagung der Fachgruppe Festkörperchemie und Materialforschung der Gesellschaft Deutscher Chemiker, Berlin **2010**.
- 13) **Fehlordnungsvarianten und Nanostrukturen von GeBi₂Te₄ und deren Einfluss auf den elektrischen Widerstand**
T. Schröder, M. N. Schneider, T. Rosenthal, A. Eisele, C. Gold, E.-W. Scheidt, W. Scherer, O. Oeckler
15. Vortragstagung der Wöhler-Vereinigung, Freiburg **2010**.
- 12) **TEM-Untersuchungen zur Nanostruktur GeTe-reicher Germaniumantimontelluride und deren partieller Defektausordnung**
T. Rosenthal, M. N. Schneider, O. Oeckler
Hirschegg-Seminar für Festkörperchemie, Hirschegg **2010**.

- 11) **Resonante Röntgenbeugung an Zinnantimonelluriden**
M. N. Schneider, F. Fahrnbauer, O. Oeckler
Hirschegg-Seminar für Festkörperchemie, Hirschegg 2010. - eigener Vortrag -
- 10) **Multinary Layered Tellurides with Almost Homometric Structures**
M. N. Schneider, O. Oeckler
25th European Crystallographic Meeting, Istanbul (Türkei) 2009.
- 9) **Concentration Modulations and Short-Range vs. Long-Range Order in Layered Tellurides**
O. Oeckler, M. N. Schneider
25th European Crystallographic Meeting, Istanbul (Türkei) 2009.
- 8) **Langreichweitige Konzentrationsmodulationen in metastabilen Schichttelluriden**
O. Oeckler, M. N. Schneider, P. Lagally
Wissenschaftsforum Chemie 2009, Frankfurt 2009.
- 7) **Bulk synthesis and kinetic stabilization of metastable GST and GBT phases by stress and strain**
M. N. Schneider, O. Oeckler
European Phase Change and Ovonic Symposium, Aachen 2009.
- 6) **Kinetic stabilization of metastable GST phases by stress and strain**
O. Oeckler, M. N. Schneider, P. Urban
12th European Conference on Solid State Chemistry, Münster 2009.
- 5) **Metastabile (pseudo-)kubische Antimonelluride und verwandte Phasen**
O. Oeckler, P. Urban, T. Schröder, M. N. Schneider
Hirschegg-Seminar für Festkörperchemie, Hirschegg 2009.
- 4) **Langreichweitige Überstrukturen mit Fehlordnung – Konzentrationsmodulationen in partiell entmischten [Ge-Sb-]Telluriden**
M. N. Schneider, O. Oeckler
Hirschegg-Seminar für Festkörperchemie, Hirschegg 2009.
- 3) **Realstruktur fehlgeordneter Telluride im B1- oder A7-Typ**
M. N. Schneider, O. Oeckler
14. Vortragstagung der Fachgruppe Festkörperchemie und Materialforschung der Gesellschaft Deutscher Chemiker, Bayreuth 2008.
- 2) **Metastabile Überstrukturphasen im System Ge-Sb-Te**
M. N. Schneider, M. Seibald, O. Oeckler
14. Vortragstagung der Wöhler-Vereinigung, Garching/München 2008.
- 1) **Fehlgeordnete Telluride im Kochsalz-Typ?**
M. N. Schneider, O. Oeckler
Hirschegg-Seminar für Festkörperchemie, Hirschegg 2008.

Matthias Nikolaus Schneider

Personal Data

Date and Place of Birth October 22, 1981; Munich, Germany
Parents Dieter and Heidemarie Schneider
Citizenship German

Education/Course of studies

Primary School 1988-1992 Ernst-Reuter-Grundschule, Munich
Higher Education 1992-2001 Luitpold-Gymnasium, Munich
Abitur in 2001
University Education 2002-2006 Basic studies in chemistry and biochemistry,
LMU Munich
Bachelor of Science in 2006
Bachelor thesis
"Unerwartete Umlagerungsreaktionen und CH-Aktivierung bei der
Synthese neuer Ferrocenylliganden"
2006-2008 Graduate studies in chemistry,
LMU, Munich
Master of Science in 2008
Master thesis
"An den Grenzen der kristallinen Stabilität - Überstrukturbildung und
Fehlordnung im System Ge-Sb-Te"
since 2008 PhD student
LMU, Munich

Additional information

Scientific awards 2011 *Römer-Preis*, Dr. Klaus Römer-Stiftung
(doctoral thesis)
2008 *Römer-Preis*, Dr. Klaus Römer-Stiftung
(master thesis)
12/2010-5/2011 Scholarship *Abschluss-Stipendium*, LMU
Civilian Service 2001-2002 Sanitätshelfer (equiv. EMT-Basic), Malteser-
Hilfsdienst, Munich